STEADY FLOW IN SHALLOW CHANNEL BENDS

Part I : Text

Proefschrift

ter verkrijging van de graad van doctor in
de technische wetenschappen aan de
Technische Hogeschool Delft,
op gezag van de rector magnificus
prof. ir. B.P.Th. Veltman,
voor een commissie aangewezen door het
college van dekanen te verdedigen op
woensdag 17 juni 1981 te 14.00 uur

door

Hubrecht Johannis de Vriend
civiel ingenieur,

geboren te Oudelande

Dit proefschrift is goedgekeurd door de promotor
prof. dr. ir. J.P.Th. Kalkwijk

Met dank aan Hil en Jet

STELLINGEN

1.

Voor de bepaling van het zandtransport in open waterlopen met behulp van merkstoffen, kan thans nog niet algemeen worden aangegeven of radioactieve merkers of luminoforen moeten worden gebruikt.

2.

Bij zandtransport-metingen met merkstoffen voor rivieren zoals de Nederlandse bovenrivieren moeten luminoforen worden gebruikt.

3.

Bij de ontwikkeling van bodemtransportmeters moet uitdrukkelijk rekening worden gehouden met het stochastische karakter van het transportverschijnsel.

4.

De door COLBY en HEMBREE gebruikte benaming „modified Einstein-procedure" werkt verwarrend.

COLBY, B. R. and C. H. HEMBREE, „Computations of total sediment discharge in the Niobrara River". U.S. Dept. of the Interior. Water-Supply-paper No. 1357 U.S. Geol. Survey 1955.

5.

Bij praktische berekeningen met betrekking tot niet-permanent bodemtransport in open waterlopen, is het gebruik van een pseudo-viscositeitsmethode sterk aan te bevelen.

6.

De invloed van regime-wijzigingen op de bodemligging van een rivierensysteem met vrijwel gefixeerde oevers, kan worden bestudeerd met een combinatie van een wiskundig- en een fysisch model. Een opzet waarbij het hoofdaccent op het wiskundig model valt, is aan te bevelen.

7

De afleidingen met betrekking tot de bedvormende afvoer van een rivier, zoals deze voorkomen in het Nedeco-rapport over de Niger en de Benue, kunnen beduidend worden vereenvoudigd door niet a priori uit te gaan van de vergelijking van MEYER-PETER en MUELLER.

Nedeco, „River Studies and recommendations on the improvement of Niger and Benue". North Holland Publishing Company, Amsterdam, 1959.

8.

De door VOLLMERS onderzochte oplossingen voor de aansluiting van een kanaal of een haven aan een bovenrivier, hebben voor Nederlandse omstandigheden vrijwel geen praktische betekenis .

VOLLMERS, H. J. „Systematik der Masznahmen zur Verringerung der Schwebstoffablagerungen in Binnenhafenmündungen". Proefschrift, Karlsruhe, 1963.

9.

Voor het ontwerpen van een optimaliseringstechniek voor waterbeheersingsplannen ten behoeve van waterschappen, kan de door het Waterloopkundig Laboratorium ontwikkelde methode voor de berekening van de waterbeweging in een systeem van open leidingen, als uitgangspunt dienen.

MEYER, TH. J. G. P., C. B. VREUGDENHIL and M. DE VRIES, „A method of computation for non-stationary flow in open-channel networks". I.A.H.R. Leningrad 1965, paper 3.28.

10.

Het is sterk aan te bevelen de student in de weg- en waterbouwkunde tijdens de propaedeuse te onderwijzen in de beginselen van het moderne rekenen.

ABSTRACT

Making use of a mathematical model solving the complete Navier-Stokes equations for steady flow in coiled rectangular pipes, fully-developed laminar flow in shallow curved channels is analysed physically and mathematically. Transverse convection of momentum by the secondary flow is shown to cause important deformations of the main velocity distribution. The model is also used to investigate simplified computation methods for shallow channels. The usual 'shallow water approximation' is shown to fail here, but a method starting from similarity hypotheses for the main and the secondary flow works well. On the basis of this method, a simplified mathematical model of steady turbulent flow in river bends is developed and verified using the results of laboratory experiments and fully three-dimensional flow computations. This model works well for shallow and mildly curved channels, but it shows important shortcomings if the channel is less shallow or sharplier curved.

CONTENTS (PART I)

CONTENTS (PART II)

Summary

As a contribution to the development of a mathematical model of the flow and the bed topography in river bends, steady flow in curved channels is analysed physically and mathematically and a computation method for this flow is developed.
After formulating and normalizing the system of differential equations that describes the flow in general (chapter 2), fully-developed laminar flow in curved rectangular ducts is analysed on the basis of solutions of the full Navier-Stokes equations for this flow case (chapter 3). This analysis leads to the conclusion, that the transverse convection of momentum by the secondary flow can give rise to considerable deformations of the main velocity distribution: the main velocity maximum tends to shift from the inner to the outer bend and from the water surface downwards. These deformations are shown to increase with the Dean number, defined as the Reynolds number multiplied by the square root of the curvature ratio. Other curvature effects, such as the 'bend resistance', are explained from this redistribution of the main velocity.
In chapter 3 it is also shown, that the sidewall regions, and especially the one near the inner wall, play an important part in the main flow redistribution process in curved rectangular channels. As a consequence, the usual 'shallow water approximation', in which the sidewall regions are ignored, are not applicable to flow in not too mildly curved rectangular channels, not even if they are shallow. This is illustrated and elaborated in chapter 4, where some other simplified computation methods for fully-developed laminar flow in shallow rectangular curved ducts are investigated, as well. A method based on similarity hypotheses for the main and the secondary flow appears to yield satisfactory results.
In chapter 5, the main and the secondary velocity components in developing curved channel flow are defined and the similarity hypotheses from chapter 4 are applied to the main and the secondary velocity distributions. This forms the basis of a computational model of developing laminar flow in curved rectangular channels, on the analogy of the aforementioned computation method for fully-developed curved flow.

Some of the most important simplifying assumptions underlying this model are verified using a sensitivity analysis. This leads to the conclusion that the depth-averaged main flow computation can better be uncoupled from the computation of the magnitude and the direction of the bottom shear stress, the latter making higher demands upon the description of the main velocity profile and the secondary flow. Finally, a global and qualitative comparison of the model predictions with measured depth-averaged main velocity distributions in turbulent curved channel flow yields encouraging results.

In order to make the next step to a mathematical model of the flow in a river bend, an adequate turbulence model has to be formulated. Postulating that this model must be as simple as possible, it is based on a mixing length hypothesis (chapter 6). When compared with measurements in straight channels with a shallow rectangular cross-section, it appears to work well. In addition, the influence of the most important assumptions in this turbulence model is investigated using a sensivity analysis. This makes clear, that the secondary flow intensity highly depends on the overall mean value and the vertical distribution of the turbulence viscosity.

Making use of this turbulence model and on the analogy of the mathematical model of developing laminar flow, a simplified model of turbulent flow in curved channels of shallow rectangular cross-section is developed in chapter 7. Once again, the most important simplifying assumptions are verified through a sensivity analysis. A preliminary comparison with measured data gives rise to a moderate optimism about the model performance.

As a last step (for the time being) towards a mathematical model of the flow in a river bend, the model described in chapter 7 is generalized to channels of more or less arbitrary, but shallow cross-sectional shape. This is achieved by transforming the cross-section to a rectangle. Though this gives rise to additional terms in the differential equations, the character of the mathematical system remains unalterad and the solution procedure can be essentially the same as in chapter 7. On comparison with measured data from straight trapezoidal channels, however, the turbulence model appears to need modification. This is done by introducing

lateral diffusion into the turbulence viscosity.
In chapter 9, the model is verified using the results of various laboratory experiments and of fully three-dimensional mathematical simulations of two of these experiments. The model appears to work well for shallow and mildly curved channels, but it shows important shortcomings in case of less shallow and sharplier curved flow. An analysis of these shortcomings makes clear, that the similarity hypotheses underlying the model do not apply to developing curved flow with a strong interaction between the main and the secondary flow, in spite of their approval for fully-developed curved flow, even at higher Dean numbers. Removing this defect, if possible at all, makes the model so expensive, that such cases can just as well be simulated mathematically with a fully three-dimensional model.
On the other hand, the model can be simplified drastically in case of shallow, gently curved rivers with mildly sloping banks. Since many rivers meet these requirements, or can be schematized as such, a strongly simplified and economic model like this is very attractive as part of a mathematical model of the flow and the bed topography in curved alluvial rivers.
Finally, chapter 10 resumes the most important conclusions and some of their practical implications. Furthermore, recommendations are made for the practical application of the simplified mathematical models and suggestions for further research are given.

NOTATION

A	total dynamic viscosity
A_t	dynamic turbulence viscosity
A_0	dynamic turbulence viscosity in uniform rectilinear shear flow
$\overline{A}_0$	mean turbulence viscosity in uniform rectilinear shear flow
B	channel width
c	constant in the stream function equation of the secondary flow
C	Chezy's coefficient
C'	disturbance of C due to depth variations
C_0	value of C for the reference depth of flow
d	reference depth of flow
De	Dean number ($= Re\sqrt{\varepsilon}$)
De_0	effective Dean number ($\simeq Re_0\sqrt{\varepsilon}$)
E	constant in wall function approximation for turbulent flow
f_1, f_2	perturbations of the vertical distribution of the main velocity
g	acceleration due to gravity
h	local depth of flow
k_m, k_s	bottom shear stress factors for the main and the secondary flow
k_{sn}	secondary flow convection factor (strongly simplified model)
L, L_t	length scale of transverse bottom level variations
L_m	mixing length
$l_{0.1}$	length needed for 90% reduction of the secondary flow intensity
p	pressure
P	pressure scale
Q	discharge
r	normalized radial coordinate
R	radial coordinate
R_c	radius of curvature of the channel axis
R_0	characteristic radius of curvature
R_e	Reynolds number ($= Vd/\nu$)
Re_0	effective Reynolds number ($= \rho Vd/\overline{A}_0$)
s	longitudinal coordinate
S	length scale of longitudinal flow variations
t	time
$T_{s'}, T_{s's'}$, etc.	factors due to transformation of the cross-section

u	normalized longitudinal velocity component
$\tilde{u}$	known estimate of u
$\bar{u}$	depth-averaged value of u
$u' = u/l$	
u_m, u_s	main and secondary flow constituents of u
$u_0, u_1, \ldots, u_k$	perturbations of u
u_τ	normalized longitudinal bottom friction velocity
U_τ	resultant normalized bottom friction velocity
$u_{\tau l}$, $u_{\tau r}$	normalized longitudinal sidewall friction velocity (left, right)
$u_{\tau w}$	normalized longitudinal wall friction velocity
v	normalized transverse velocity component
V	velocity scale
v_m, v_s	main and secondary flow constituents of v
V_{res}	resultant horizontal velocity
v_R, v_ϕ, v_z	velocity components in cylindrical coordinate system
v'_R, v'_ϕ, v'_z	turbulent fluctuations of velocity components
$v_0, v_1, \ldots, v_k$	perturbations of v
$\tilde{v}_0$	transverse velocity factor at the bend exit
v_τ	normalized transverse bottom friction velocity
V_τ, v_{τ}	resultant bottom friction velocity
$v_{\tau m}$, $v_{\tau s}$	main and secondary flow constituents of v_τ
w	normalized vertical velocity
w_m, w_s	main and secondary flow constituents of w
$w_{\tau l}$, $w_{\tau r}$	normalized vertical sidewall friction velocity (left, right)
y, y'	transverse coordinate
y^+	dimensionless wall distance
$\tilde{y}$	wall distance
z	vertical coordinate
z_b	bottom level
z_s	water surface elevation
a	normalized turbulence viscosity
a'	vertical distribution function of the turbulence viscosity
D	lateral diffusivity in the turbulence viscosity equation
e	normalized total flow energy
f	vertical distribution function of the main velocity

$\tilde{f}$ known estimate of f

$F = \int_{-1}^{\zeta} f \, d\zeta$

g vertical distribution function of the secondary flow

h normalized local depth of flow

i_s secondary flow intensity ($= \frac{1}{2}|\overline{v_s}|$)

k Nikuradse sand roughness

l_m normalized mixing length

n normal coordinate in streamline coordinate system

n' normal coordinate after transformation of the cross-section

p normalized total pressure

$\overline{p}$ depth-averaged value of p

$\overline{\overline{p}}$ cross-sectional mean value of p

r_s, r_n radius of curvature of the streamlines and the normal lines of the depth-averaged main velocity field

s streamwise coordinate in the streamline coordinate system

s' streamwise coordinate after transformation of the cross-section

u_m normalized streamwise velocity component

v normalized normal velocity component (in App. B and I: $v/\tilde{v}_0$)

v_m, v_s main and secondary flow constituents of v

z normalized vertical coordinate after transformation of the cross-section

α underrelaxation factor

α_i inclination of the main flow isovels

α_s inclination of the streamlines of the secondary flow

α_τ direction of the bottom shear stress

α_v direction of the velocity at the bottom

γ overall mean turbulence viscosity factor

$\delta, \delta_l, \delta_r$ wall layer thickness (bottom, left wall, right wall)

$\Delta\phi$ total bend angle

ϵ curvature ratio d/R_c

ζ normalized vertical coordinate

ζ_b normalized bottom level

ζ_s normalized water surface elevation

ζ^* level of zero horizontal velocity

η dynamic viscosity of the fluid

ι longitudinal slope factor

ι_0 value of ι in fully-developed straight channel flow

κ Von Karman's constant

λ normalized length scale of secondary flow decay

ν kinematic viscosity of the fluid

ξ normalized transverse coordinate

ξ' normalized transverse coordinate after transformation of the cross-section

ρ mass density of the fluid

$\sigma = s/\varepsilon Re$ normalized longitudinal coordinate

$\sigma_{\phi\phi}, \sigma_{RR}, \sigma_{zz}$ normal components of the stress tensor

$\tau_{R\phi}, \tau_{\phi z}, \tau_{Rz}$ shear components of the stress tensor

$\tau_b, \tau_{b_{res}}$ bottom shear stress

$\tau_{b\xi}, \tau_{b\phi}$ normalized components of the bottom shear stress

$\tau_{b\xi_m}, \tau_{b\phi_m}$ normalized bottom shear stress components due to the main flow

$\tau_{l\phi}, \tau_{r\phi}$ normalized longitudinal components of the sidewall shear stress

$\tau_{l\zeta}, \tau_{r\zeta}$ normalized vertical components of the sidewall shear stress

ϕ tangential coordinate

ϕ' tangential coordinate after transformation of the cross-section

Φ stream function of the depth-averaged main flow

ϕ_{tot} total bend angle

ψ normalized stream function of the secondary flow

$\psi' = Re\ \psi$

Ψ degree of development of the secondary flow intensity

$\psi_0, \psi_1, \ldots, \psi_k$ perturbations of ψ

$\bar{\omega}, \bar{\omega}_m$ depth-averaged main flow vorticity

ω_s secondary flow vorticity

$\omega_s' = Re\ \omega_s$

∇^2 Laplace operator

1. Introduction

1.1. Relevance of the investigations

The increasing use of rivers (navigation, water supply, waste discharge, cooling water, etc.; see Jansen, 1979) has made their control and improvement increasingly important. The measures needed to achieve this, however, become more and more complicated and require ever more accurate predictions of their effects on the flow and the channel topography.

A complicated and most interesting phenomenon to be dealt with in such predictions is the essentially three-dimensional flow pattern in a curved stream (bends, bifurcations) and its interaction with an alluvial channel bed. The characteristic helical flow pattern drastically influences the dispersion of suspended or dissolved matter and the bed topography in a bend often differs strongly from the one in a straight reach, such that it can even become limitative to the navigability of the river. Hence an efficient and accurate prediction method for the flow and the bed topography in curved alluvial streams is almost indispensable when considering river improvement measures.

Hitherto, the decision on such measures used to be based on predictions obtained from hydraulic scale models, even though the complicated flow pattern in a bend can give rise to scale effects that make the model results hard to interpret. The increasing facilities of electronic computers, however, provide the possibility to develop mathematical models, in which there is no question of scale effects. Though such models are not likely to replace hydraulic scale models completely, at least in the near future, they will facilitate the understanding of the physical phenomena and, when applied in combination with hydraulic scale models, they will induce a greater flexibility of the model investigations.

For most alluvial rivers, the mathematical description of the interaction between the flow and the bed topography can be based on the alternate application of a quasi-steady flow computation, a sediment transport model and a computation of the bed level variation (Jansen, 1979). In each of these elements, the channel curvature gives rise

to important complications, most of which are insufficiently understood. Therefore, the three elements can better be developed separately, before being composed to a bed formation model for curved alluvial rivers. The flow computation element is subject of the present thesis.

The development of a mathematical model of the bed formation in curved alluvial channels is one of the projects of the River Research Group of the joint hydraulic research programme T.O.W. (Toegepast Onderzoek Waterstaat), in which Rijkswaterstaat, the Delft Hydraulics Laboratory and the Delft University of Technology participate. Within this framework, the flow modelling is mainly concentrated in the Laboratory of Fluid Mechanics of the Delft University of Technology, Department of Civil Engineering.

1.2. Previous work

Flow in bends of pipes and open channels, with its striking helical character, has fascinated scientific investigators for a long time past. In the second half of the nineteenth century, Boussinesq (1868) published a correct mathematical analysis of mildly curved laminar flow in wide ducts and channels, and Thomson (1876, 1877, 1879) was the first to draw the right conclusion about the cause of river meandering from observations of spiral flow in river bends and curved experimental channels.
This has been the start of a more or less continuous flow of publications initially in two almost independent series, one concerning the flow in curved ducts, with the emphasis on hydrodynamics, and one dealing with river flow, from a more hydraulic and geophysical point of view. Though not directly relevant to river engineering, the former group of publications should not be ignored. It contains a great deal of experimental information (Eustice, 1911; White, 1929; Taylor, 1929; Adler, 1934 and many others; see also chapter 3) that can contribute to the understanding of curved flow phenomena, also in river bends. Moreover, this group has a considerably longer tradition of mathematical modelling (Dean, 1927 and many others after him; see also Smith, 1976) and it is usually first in applying new computation techniques

(Patankar et al., 1974), which can also be of use in river bend models.

The second group is closely connected to river engineering. Here the developments have proceeded somewhat slowlier, at least from the point of view of mathematical modelling. For a long time, publications in this group have reported only empirical observations and laboratory experiments, with at most a rather primitive mathematical analysis (Fargue, 1908; Beyerhaus, 1922; Hinderks, 1927; Blue et al., 1934; Mockmore, 1944; Shukry, 1949 and many others). Apart from the application of potential flow theory to the main flow and the water surface configuration in river bends (Böss, 1934 & 1938), it was only in 1943 and 1947 that Van Bendegom*) published a proper mathematical description of the secondary flow and a prediction method for the flow and the bed topography in alluvial channel bends.

Some 10 years later, a most important development in the mathematical modelling of curved channel flow took place in the USSR, with Ananyan (1957; Engl. transl. 1965) and Rozovskii (1957; Engl. transl. 1961) as the most prominent exponents. They introduced the use of perturbation methods (with the curvature ratio d/R_c as a perturbation parameter) in mathematical models of flow in river bends (cf. Dean, 1927; see also chapter 4). Especially Rozovskii's outstanding monograph contains many brilliant ideas and is still one of the most-cited works on this subject.

Many computational methods published since (and, in a way, also Van Bendegom's method) can be classified as perturbation methods for small curvature ratios (Yen, 1965; De Vriend, 1973; Engelund, 1974; Ikeda, 1975; De Vriend, 1976 & 1977; Falcón, 1979; see also chapter 4). The essential feature all these methods have in common is the assumption that, in a first approximation, the main flow is not influenced by the secondary circulation. As will be shown in

*) Unfortunately, these publications are written in Dutch. Only after the latter had been translated into English (1963), it became more widely known, but it still has not received the international estimation it deserves (see also; Allen. 1978).

the present thesis (chapter 4), this is a misconception in case of not very mildly curved channels.
Although the role of secondary flow convection in the redistribution of the main velocity in a bend was recognized rather early (Einstein et al., 1954; Rozovskii, 1961; Fox et al., 1968; Callander, 1978), it was incorporated only recently in a simplified mathematical model (Kalkwijk et al., 1980), and that only for the specific case of gently curved non-rectangular channels with mildly sloping banks. More generally applicable simplified models accounting for this effect, however, are still missing.
Along with the increase of computer facilities, fully three-dimensional computation methods have become increasingly important, also for curved channel flow (Patankar et al., 1974 & 1975; Pratap et al., 1975; Leschziner et al., 1979; see also De Vriend et al., 1981). Hitherto, however, such computations have been incidental *), as they are too expensive for routine computations, at least for the time being. Besides, computations for channels with a more or less arbitrary cross-sectional shape, as would be needed in a river bend model, have not been reported yet.

1.3. The present investigations

The present investigations comprise the analysis and the computation of steady flow in curved ducts and channels, with the object to improve the insight into the physical phenomena and to develop a simplified computation mehtod that can be incorporated in a mathematical model of the flow and the bed topography in alluvial river bends.
After formulating and normalizing the basic system of differential equations and boundary conditions, a mathematical and physical analysis of fully-developed laminar flow in curved rectangular ducts

*) Unfortunately, these computations are seldomly followed by a physical analysis of the results, which could have contributed considerably to a proper understanding of curved channel flow.

is made on the basis of solutions of the full Navier-Stokes equations. As the laminar and the time-mean turbulent flow patterns show globally the same features in a bend and the most important phenomena to be considered are mainly a matter of convection, the conclusions drawn from this analysis are likely to apply to turbulent flow, as well, at least qualitatively. These full Navier-Stokes solutions will also be used to verify various approximative computation methods and simplifying assumptions. This is to yield a simplified computation method that can be applied in the mathematical model. In the first instance, this model is developed for laminar flow in curved rectangular channels, in order to have continuity with the foregoing investigations and to avoid too many complications at a time. As far as possible, the sensitivity of the model to the underlying assumptions will be tested and a qualitative comparison will be made with measured data from turbulent flow experiments. Subsequently, the modelling of turbulence is considered and the suggested turbulence model is tested for straight rectangular channels. The resulting model is to be incorporated in a mathematical model of turbulent flow in curved rectangular channels, on the analogy of the laminar flow model. Once again, the sensitivity of this model to the underlying assumptions will be tested and a global comparison with laminar flow computations and measured data will be made. Next, the model will be extended to non-rectangular channels with a more or less arbitrarily shaped shallow cross-section. The resulting mathematical model will be verified by comparing its results with measured data from various laboratory experiments in rectangular and non-rectangular curved flumes and with the results of a fully three-dimensional mathematical simulation of two of the rectangular channel experiments. The shortcomings of the model will be analysed and remedial suggestions will be made.
Finally, the investigations will be evaluated and the most important conclusions and their practical implications will be resumed. In addition, recommendations for the practical application of simplified mathematical models and suggestions for further research will be given.

2. General mathematical formulation

2.1. Channel geometry and coordinate system

The present investigations mainly concern the essential features of flow in river bends and its mathematical modelling. From this point of view a more or less arbitrary channel pattern is likely to be only a complicating factor of no essential importance. Therefore considerations are limited to channels of constant width, with a longitudinal axis consisting of a series of circular arcs*). For the same reason the free surface is approximated by a frictionless horizontal plate ("rigid-lid-approximation"), which implies that the Froude number is assumed small.

Accordingly, the coordinate system to be used in the mathematical model consists of a series of cylindrical systems, each with a vertical axis through the centre of curvature of the relevant part of the channel axis (see figure 1). For the sake of simplicity, the model will be described here for a single channel section with a cicular axis of radius R_c, using a cylindrical coordinate system (R,ϕ,z) with the z-axis pointing vertically upwards and $z = 0$ at the surface (figure 2).

2.2. Conservation of mass and momentum

Three-dimensional incompressible fluid flow can be described mathematically by a system of four differential equations representing the conservation of mass and of the three components of momentum. If t denotes time, v_R, v_ϕ and v_z the velocity components, σ_{RR}, $\sigma_{\phi\phi}$, σ_{zz}, $\tau_{R\phi}$, τ_{Rz} and $\tau_{\phi z}$ the components of the stress tensor, ρ the mass density of the fluid and g the acceleration due to gravity, these equations can be written as (Bird et al., 1960)

---

*) The radius of curvature of such an arc can be chosen infinitely large to yield a straight channel section.

$$\frac{\partial v_\phi}{\partial t} + \frac{v_\phi}{R}\frac{\partial v_\phi}{\partial \phi} + v_R\frac{\partial v_\phi}{\partial R} + v_z\frac{\partial v_\phi}{\partial z} + \frac{v_R v_\phi}{R} =$$

$$\frac{1}{\rho}\left[\frac{1}{R}\frac{\partial \sigma_{\phi\phi}}{\partial \phi} + \frac{\partial \tau_{R\phi}}{\partial R} + \frac{\partial \tau_{\phi z}}{\partial z} + 2\frac{\tau_{R\phi}}{R}\right] \qquad (2.1)$$

$$\frac{\partial v_R}{\partial t} + \frac{v_\phi}{R}\frac{\partial v_R}{\partial \phi} + v_R\frac{\partial v_R}{\partial R} + v_z\frac{\partial v_R}{\partial z} - \frac{v_\phi^2}{R} =$$

$$\frac{1}{\rho}\left[\frac{1}{R}\frac{\partial \tau_{R\phi}}{\partial \phi} + \frac{\partial \sigma_{RR}}{\partial R} + \frac{\partial \tau_{Rz}}{\partial z} + \frac{\sigma_{RR}}{R} - \frac{\sigma_{\phi\phi}}{R}\right] \qquad (2.2)$$

$$\frac{\partial v_z}{\partial t} + \frac{v_\phi}{R}\frac{\partial v_z}{\partial \phi} + v_R\frac{\partial v_z}{\partial R} + v_z\frac{\partial v_z}{\partial z} =$$

$$\frac{1}{\rho}\left[\frac{1}{R}\frac{\partial \tau_{\phi z}}{\partial \phi} + \frac{\partial \tau_{Rz}}{\partial R} + \frac{\partial \sigma_{zz}}{\partial z} + \frac{\tau_{Rz}}{R}\right] - g \qquad (2.3)$$

$$\frac{1}{R}\frac{\partial v_\phi}{\partial \phi} + \frac{\partial v_R}{\partial R} + \frac{v_R}{R} + \frac{\partial v_z}{\partial z} = 0 \qquad (2.4)$$

For steady laminar flow the time-derivatives in equations (2.1) through (2.3) can simply be omitted. Steady turbulent flow, however, is essentially time-dependent, though the turbulence-averaged quantities do not vary with time. In that case the above time-dependent momentum equations must be integrated over a time-interval that is much larger than the turbulence time scale to yield momentum equations for the turbulence-averaged quantities.

In addition to terms with the turbulence-averaged velocity and stress components similar to the ones in (2.1) through (2.3), however, these equations contain terms with the time-mean products of the velocity fluctuations (see, for instance; Hinze, 1975). As these terms are similar to the stress-terms in the time-dependent equations, the tensor with elements $-\rho\,\overline{v_\phi'^2}$, $-\rho\,\overline{v_R'^2}$, $-\rho\,\overline{v_z'^2}$, $-\rho\,\overline{v_R'v_\phi'}$, $-\rho\,\overline{v_R'v_z'}$, $-\rho\,\overline{v_\phi'v_z'}$ is called the Reynolds stress tensor.

Anticipating on what is stated in chapter 6 on the modelling of the Reynolds stresses, the so-called Boussinesq hypothesis is adopted: on the analogy of the relation between the viscous stress tensor and the rate-of-strain tensor through the molecular viscosity η(see, for instance; Landau et al., 1975), the Reynolds stress tensor is related to the rate-of-strain tensor of the turbulence-averaged flow through a scalar turbulence viscosity A_t (Hinze, 1975).
Hence, if p denotes the isotropic pressure,

$$\sigma_{\phi\phi} - \rho \overline{v_\phi'^2} = - p + 2(\eta + A_t)(\frac{1}{R} \frac{\partial v_\phi}{\partial \phi} + \frac{v_R}{R}) \tag{2.5}$$

$$\sigma_{RR} - \rho \overline{v_R'^2} = - p + 2(\eta + A_t) \frac{\partial v_R}{\partial R} \tag{2.6}$$

$$\sigma_{zz} - \rho \overline{v_z'^2} = - p + 2(\eta + A_t) \frac{\partial v_z}{\partial z} \tag{2.7}$$

$$\tau_{R\phi} - \rho \overline{v_R' v_\phi'} = (\eta + A_t)(\frac{1}{R} \frac{\partial v_R}{\partial \phi} + \frac{\partial v_\phi}{\partial R} - \frac{v_\phi}{R}) \tag{2.8}$$

$$\tau_{Rz} - \rho \overline{v_R' v_z'} = (\eta + A_t)(\frac{\partial v_R}{\partial z} + \frac{\partial v_z}{\partial R}) \tag{2.9}$$

$$\tau_{\phi z} - \rho \overline{v_\phi' v_z'} = (\eta + A_t)(\frac{1}{R} \frac{\partial v_z}{\partial \phi} + \frac{\partial v_\phi}{\partial z}) \tag{2.10}$$

, where v_R, v_ϕ, v_z and p are turbulence-averaged quantities now. Substitution of these expressions into the turbulence-averaged momentum equations yields, after some elaboration and for $A = \eta + A_t$,

$$\frac{v_\phi}{R} \frac{\partial v_\phi}{\partial \phi} + v_R \frac{\partial v_\phi}{\partial R} + v_z \frac{\partial v_\phi}{\partial z} + \frac{v_R v_\phi}{R} = - \frac{1}{\rho} \frac{1}{R} \frac{\partial p}{\partial \phi} + \frac{A}{\rho} (\nabla^2 v_\phi - \frac{v_\phi}{R^2} + \frac{2}{R^2} \frac{\partial v_R}{\partial \phi}) +$$

$$+ \frac{1}{\rho}\{\frac{2}{R}\frac{\partial A}{\partial \phi}(\frac{1}{R}\frac{\partial v_\phi}{\partial \phi} + \frac{v_R}{R}) + \frac{\partial A}{\partial R}(\frac{1}{R}\frac{\partial v_R}{\partial \phi} + \frac{\partial v_\phi}{\partial R} - \frac{v_\phi}{R}) +$$

$$+ \frac{\partial A}{\partial z}(\frac{\partial v_\phi}{\partial z} + \frac{1}{R}\frac{\partial v_z}{\partial \phi})\} \qquad (2.11)$$

$$\frac{v_\phi}{R}\frac{\partial v_R}{\partial \phi} + v_R\frac{\partial v_R}{\partial R} + v_z\frac{\partial v_R}{\partial z} - \frac{v_\phi^2}{R} = -\frac{1}{\rho}\frac{\partial \rho}{\partial R} + \frac{A}{\rho}(\nabla^2 v_R - \frac{v_R}{R^2} - \frac{2}{R^2}\frac{\partial v_\phi}{\partial \phi}) +$$

$$+ \frac{1}{\rho}\{\frac{1}{R}\frac{\partial A}{\partial \phi}(\frac{1}{R}\frac{\partial v_R}{\partial \phi} + \frac{\partial v_\phi}{\partial R} - \frac{v_\phi}{R}) + 2\frac{\partial A}{\partial R}\frac{\partial v_R}{\partial R} +$$

$$+ \frac{\partial A}{\partial z}(\frac{\partial v_R}{\partial z} + \frac{\partial v_z}{\partial R})\} \qquad (2.12)$$

$$\frac{v_\phi}{R}\frac{\partial v_z}{\partial \phi} + v_R\frac{\partial v_z}{\partial R} + v_z\frac{\partial v_z}{\partial z} = -\frac{1}{\rho}\frac{\partial \rho}{\partial z} - g + \frac{A}{\rho}\nabla^2 v_z +$$

$$+ \frac{1}{\rho}\{\frac{1}{R}\frac{\partial A}{\partial \phi}(\frac{\partial v_\phi}{\partial z} + \frac{1}{R}\frac{\partial v_z}{\partial \phi}) + \frac{\partial A}{\partial R}(\frac{\partial v_z}{\partial R} + \frac{\partial v_R}{\partial z}) + 2\frac{\partial A}{\partial z}\frac{\partial v_z}{\partial z}\} \qquad (2.13)$$

, in which $\nabla^2 = \frac{1}{R^2}\frac{\partial^2}{\partial \phi^2} + \frac{\partial^2}{\partial R^2} + \frac{1}{R}\frac{\partial}{\partial R} + \frac{\partial^2}{\partial z^2}$

2.3. Boundary conditions

The boundary conditions arising from the impermeability of the "water surface" and the vanishing of the shear stress tangent to this surface can be formulated as

$$v_z\Big|_{z=0} = 0 \qquad (2.14)$$

and

$$(A\frac{\partial v_\phi}{\partial z})\Big|_{z=0} = 0; \qquad (A\frac{\partial v_R}{\partial z})\Big|_{z=0} = 0 \qquad (2.15)$$

, respectively. As the surface is kept fixed, it must be considered as a frictionless rigid plate exerting normal stresses on the fluid. Consequently, the dynamic free surface condition $p\big|_{z=0} = 0$ is not applicable here*).
The boundary conditions at the fixed boundaries stem from the impermeability of these boundaries and the no-slip conditions. If the maximum channel width occurs at the surface, this yields

$$v_R = 0; \quad v_\phi = 0; \quad v_z = 0 \quad \text{for} \quad z = -h \text{ and}$$

$$\text{for } R = R_c \pm \frac{B}{2} \text{ **)} \qquad (2.16)$$

, in which h is the local depth of flow and B is the channel width.

In addition to these "cross-sectional" boundary conditions, inflow and outflow conditions must be formulated. Most of these conditions will be given in a later stage. Only the discharge Q is mentioned here, since it plays a part in the integral condition of continuity (cf. equation (2.4))

$$\int_{R_c - B/2}^{R_c + B/2} dR \int_{-h}^{0} v_\phi dz = Q \qquad (2.17)$$

and it will be used in the normalization of the system of differential equations and boundary conditions.

---

*) After the velocities and the pressures have been computed, this dynamic condtion can be used to estimate the elevation of the actual free surface (cf. De Vriend, 1976).

**) The latter conditon applies only if there are vertical sidewalls.

2.4. Normalization

In order to find out which parameters characterize the flow and to get an insight into the relative magnitude of the various terms, the mathematical system described in the foregoing paragraphs is normalized, i.e. each term of the equations is written as the product of a constant scale-factor and a variable dimensionless quantity of the order of magnitude $0(1)$*).

It seems appropriate to carry out this normalization by adopting an adequate scale-factor for each variable, either dependent or independent, and applying it to any term in which the relevant variable occurs. So if f is a function of x, these two variables are normalized by

$$f(x) = F * f(x) \qquad \text{and} \qquad x = X * x \tag{2.18}$$

, F and X being constant scale-factors. Now it is assumed that the n-th derivative of f with respect to x can be normalized using the same scale-factors F and X, so

$$\frac{d^n f}{dx^n} = \frac{F}{X^n} * \frac{d^n f}{dx^n} \qquad \text{with} \qquad \frac{d^n f}{dx^n} = 0(1) \tag{2.19}$$

for any n occurring in the system.

For most of the variables in the present system this approach works well, but it gives rise to problems for the radial coordinate R, which occurs here in three essentially different types of terms, viz.

- terms introduced by the use of curvilinear coordinates (in general: terms containing a factor $\frac{1}{R}$ that is not coupled to $\frac{\partial}{\partial \phi}$),
- terms containing a tangential derivative $\frac{1}{R^n} \frac{\partial^n}{\partial \phi^n}$,
- terms with a radial derivative $\frac{\partial^n}{\partial R^n}$.

---

*) A quantity f is of the order $0(\varepsilon^n)$ if $\lim_{\varepsilon \downarrow 0} \frac{f}{\varepsilon^n}$ exists.

The normalization of R in either type of terms should be considered separately. If R tends to infinity, the terms of the first type vanish. Hence the factor $\frac{1}{R}$ in these terms can be normalized by

$$\frac{1}{R} = \frac{1}{R_0}\frac{1}{r} \qquad \text{with} \qquad \frac{1}{r} = 0(1) \tag{2.20}$$

, in which R_0 is a characteristic radius of curvature for the flow to be considered (in case of a single circular bend, for instance, the radius of curvature of the channel axis is an appropriate scale-factor).
For the terms with radial derivatives, especially the diffusion terms near the sidewalls, which do not vanish if R_0 tends to infinity, another normalization is needed. To that end an additional transverse coordinate y is introduced

$$R = R_c + y \tag{2.21}$$

, so that $\frac{\partial}{\partial R} = \frac{\partial}{\partial y}$. As the diffusion of momentum will be mainly due to friction at the fixed boundaries, the depth-of-flow scale d will be an adequate scale-factor for y as long as the channel aspect ratio d/B is of the order 0(1), i.e. the channel is not deep and narrow. Hence

$$y = d.\xi \qquad \text{and} \qquad \frac{\partial^n}{\partial R^n} = \frac{1}{d^n}\frac{\partial^n}{\partial \xi^n} \qquad \text{with} \qquad \frac{\partial^n}{\partial \xi^n} = 0(1) \tag{2.22}$$

, where d can be taken as the overall mean depth of flow, for instance. For the same reason d is chosen as a scale-factor for z:

$$z = d.\zeta \qquad \text{and} \qquad \frac{\partial^n}{\partial z^n} = \frac{1}{d^n}\frac{\partial^n}{\partial \zeta^n} \qquad \text{with} \qquad \frac{\partial^n}{\partial \zeta^n} = 0(1) \tag{2.23}$$

The overall mean velocity V is taken as a scale-factor for the tangential velocity component

$$v_\phi = Vu \qquad \text{with} \qquad V = \frac{Q}{Bd} \tag{2.24}$$

In addition to this tangential velocity component, radial and vertical components will occur in curved channel flow. On the assumption that all deviations from fully-developed straight channel flow*) are due to curvature, these transverse velocity components are normalized by

$$v_R = V \frac{d}{R_0} v \qquad \text{and} \qquad v_z = V \frac{d}{R_0} w \tag{2.25}$$

The total viscosity A is normalized using its overall mean value $\bar{A}_0$ in the equivalent uniform rectilinear shear flow:

$$A = \bar{A}_0 \alpha \tag{2.26}$$

The pressure p, or rather the total pressure $p + \rho gz$, and the longitudinal coordinate $s = R(\phi-\phi_0)$, in which ϕ_0 is the value of ϕ at the beginning of the channel section considered, should be normalized in such a way, that the longitudinal pressure gradient in the ϕ-wise momentum equation (2.11) is appropriately represented. In the limit case of fully-developed flow in an infinitely wide straight channel, this equation reduces to

$$0 = -\frac{1}{\rho}\frac{\partial p}{\partial s} + \frac{A}{\rho}\frac{\partial^2 v_\phi}{\partial z^2} + \frac{1}{\rho}\frac{\partial A}{\partial z}\frac{\partial v_\phi}{\partial z} \tag{2.27}$$

---

*) Flow through a prismatic straight channel of the same cross-sectional shape, with the same bottom roughness and the same discharge as in the curved channel to be considered; the secondary flow due to turbulence in channels of non-circular cross-sectional shape (see chapter 6) is left out of consideration here.

If the scale-factors for p + ρgz and s are formally indicated by P and S, respectively, this equation can be written as

$$0 = - \frac{P}{\rho S} \frac{\partial p}{\partial s} + \frac{\bar{A}_0 V}{\rho d^2} \left(a \frac{\partial^2 u}{\partial \zeta^2} + \frac{\partial a}{\partial \zeta} \frac{\partial u}{\partial \zeta} \right) \tag{2.28}$$

As the mathematical model should include this limit case, the scale-factors of the pressure gradient term and the vertical diffusion terms in (2.28) are chosen equal. On the other hand, all velocity variations with s are deviations from the equivalent fully-developed straight channel flow, i.e. they are due to the channel curvature. Therefore R_0 is an appropriate scale-factor for s, so that

$$S = R_0 \quad \text{and} \quad P = \bar{A}_0 V \frac{R_0}{d^2} = \rho V^2 \frac{1}{Re_0} \frac{R_0}{d} \tag{2.29}$$

, in which Re_0 denotes the "effective" Reynolds number $\rho V d / \bar{A}_0$.

Defining the curvature ratio ε as d/R_0, the normalized system of differential equations and boundary conditions becomes

$$\frac{1}{r} \frac{\partial u}{\partial \phi} + \frac{\partial v}{\partial \xi} + \frac{\varepsilon}{r} v + \frac{\partial w}{\partial \zeta} = 0 \tag{2.30}$$

$$\varepsilon Re_0 \left(\frac{u}{r} \frac{\partial u}{\partial \phi} + v \frac{\partial u}{\partial \xi} + w \frac{\partial u}{\partial \zeta} + \frac{\varepsilon}{r} uv \right) = - \frac{1}{r} \frac{\partial p}{\partial \phi} +$$

$$+ a \left\{ \frac{\partial^2 u}{\partial \zeta^2} + \frac{\partial^2 u}{\partial \xi^2} + \frac{\varepsilon^2}{r^2} \frac{\partial^2 u}{\partial \phi^2} + \frac{\varepsilon}{r} \frac{\partial u}{\partial \xi} - \frac{\varepsilon^2}{r^2} u + \frac{\varepsilon^3}{r^2} 2 \frac{\partial v}{\partial \phi} \right\} +$$

$$+ 2 \frac{\varepsilon^2}{r} \frac{\partial a}{\partial \phi} \left(\frac{1}{r} \frac{\partial u}{\partial \phi} + \frac{\varepsilon}{r} v \right) + \frac{\partial a}{\partial \xi} \left(\frac{\partial u}{\partial \xi} - \frac{\varepsilon}{r} u + \frac{\varepsilon^2}{r} \frac{\partial v}{\partial \phi} \right) +$$

$$+ \frac{\partial a}{\partial \zeta} \left(\frac{\partial u}{\partial \zeta} + \frac{\varepsilon^2}{r} \frac{\partial w}{\partial \phi} \right) \tag{2.31}$$

$$\varepsilon^3 Re_0 \left(\frac{u}{r}\frac{\partial v}{\partial \phi} + v\frac{\partial v}{\partial \xi} + w\frac{\partial v}{\partial \zeta}\right) - \varepsilon^2 Re_0 \frac{u^2}{r} =$$

$$-\frac{\partial p}{\partial \xi} + \varepsilon^2 \alpha \left\{\frac{\partial^2 v}{\partial \zeta^2} + \frac{\partial^2 v}{\partial \xi^2} + \frac{\varepsilon^2}{r^2}\frac{\partial^2 v}{\partial \phi^2} + \frac{\varepsilon}{r}\frac{\partial v}{\partial \xi} - \frac{\varepsilon^2}{r^2} v - \frac{\varepsilon}{r^2} 2\frac{\partial u}{\partial \phi}\right\} +$$

$$+ \frac{\varepsilon^2}{r}\frac{\partial \alpha}{\partial \phi}\left(\frac{\partial u}{\partial \xi} - \frac{\varepsilon}{r} u + \frac{\varepsilon^2}{r}\frac{\partial v}{\partial \phi}\right) + 2\varepsilon^2 \frac{\partial \alpha}{\partial \xi}\frac{\partial v}{\partial \xi} + \varepsilon^2 \frac{\partial \alpha}{\partial \zeta}\left(\frac{\partial v}{\partial \zeta} + \frac{\partial w}{\partial \xi}\right) \qquad (2.32)$$

$$\varepsilon^3 Re_0 \left(\frac{u}{r}\frac{\partial w}{\partial \phi} + v\frac{\partial w}{\partial \xi} + w\frac{\partial w}{\partial \zeta}\right) =$$

$$-\frac{\partial p}{\partial \zeta} + \varepsilon^2 \alpha \left\{\frac{\partial^2 w}{\partial \zeta^2} + \frac{\partial^2 w}{\partial \xi^2} + \frac{\varepsilon^2}{r^2}\frac{\partial^2 w}{\partial \phi^2} + \frac{\varepsilon}{r}\frac{\partial w}{\partial \xi}\right\} + \frac{\varepsilon^2}{r}\frac{\partial \alpha}{\partial \phi}\left(\frac{\partial u}{\partial \zeta} + \frac{\varepsilon^2}{r}\frac{\partial w}{\partial \phi}\right) +$$

$$+ \varepsilon^2 \frac{\partial \alpha}{\partial \xi}\left(\frac{\partial v}{\partial \zeta} + \frac{\partial w}{\partial \xi}\right) + 2\varepsilon^2 \frac{\partial \alpha}{\partial \zeta}\frac{\partial w}{\partial \zeta} \qquad (2.33)$$

$$\int_{-B/2d}^{B/2d} d\xi \int_{-h}^{0} u\, d\zeta = \frac{B}{d} \quad \text{with} \quad h = h/d \qquad (2.34)$$

$$u = 0; \quad v = 0; \quad w = 0 \quad \text{at} \quad \zeta = -h \quad \text{and at} \quad \xi = \pm \frac{B}{2d} \qquad (2.35)$$

$$w = 0; \quad \alpha \frac{\partial u}{\partial \zeta} = 0; \quad \alpha \frac{\partial v}{\partial \zeta} = 0 \quad \text{at} \quad \zeta = 0 \qquad (2.36)$$

3. The mechnism of the velocity redistribution in a bend

3.1. Relevance of the investigation

A large number of curved flow experiments, both in laminar and in turbulent flow, in open channels as well as in closed conduits, has shown that, in addition to the secondary circulation, the flow curvature gives rise to a systematic deformation of the main velocity distribution, even if the shape of the cross-section is constant along the bend. As it is hardly possible to refer to all experimental evidence at this point, some key references will be given. For laminar flow: Mori et al. (1965) for bends in circular pipes, Mori et al. (1971) and Humphrey et al. (1977) for square pipes, Asfari (1968) for a rectangular open channel. For turbulent flow: Mori et al. (1967) for circular pipes, Howard et al. (1975) for rectangular pipes, Shukry (1949) and Fox et al. (1968) for rather narrow rectangular open channels, Francis et al. (1973) and De Vriend (1979b) for shallow rectangular open channels.
Even though there are some unresolved problems left (Götz, 1975; De Vriend, 1979b; see also chapters 6 and 9), a qualitatively and quantitatively acceptable explanation can be given for the secondary flow (Boussinesq (1868) and many others later). For the main velocity redistribution, however, no satisfactory explanation has been given so far. Fully three-dimensional numerical simulations of curved flow experiments (Patankar et al., 1974 & 1975; Pratap 1975; Pratap et al., 1975; Leschziner et al., 1979) lead to rather good predictions of the measured velocity distributions, but the results of these computations were not analysed far enough to give a physical explanation of the velocity redistribution. On the other hand, Rozovskii (1961) and recently Falcón (1979) and Kalkwijk et al. (1980) showed that this explanation can be found in the transverse transport of main flow momentum by the secondary flow. Their approaches, however, hold good for channels with gently sloping banks or in the central region of very shallow rectangular channels, but without further adjustments they are not applicable to the present rectangular channels.

Therefore, considering that a proper understanding of the important phenomena is indispensable for the development of a simplified mathematical model, the main velocity redistribution and its influence on the magnitude and the distribution of the bed shear stress have to be analysed first.

3.2. Method of analysis

In order to avoid unnecessary complications, the analysis of the main velocity redistribution will be carried out for the simplest possible case: fully-developed laminar flow in rectangular channels with a rigid-lid approximation for the water surface. The fully-developed flow stage (i.e. the velocity and the transverse pressure distribution show no more streamwise variations) is hardly reached in natural rivers, as is shown by most of the experiments cited in paragraph 3.1. Although streamwise variations play a specific role in the velocity redistribution (see chapter 5), they are eliminated in the first instant, in order to isolate what is expected to be the most important cause of the redistribution: the secondary flow.
The mathematical model eventually aimed at will have to describe turbulent flow. The mathematical description of turbulence, however, is a complicating factor introducing a great deal of uncertainty into the model (see chapter 6). On the other hand, the secondary flow and the velocity redistribution in laminar curved flow are qualitatively similar to the ones in turbulent flow (cf. the literature cited in par. 3.1). Therefore the present analysis is carried out for laminar flow, which is described quite well by the Navier-Stokes equations (Landau et al., 1975; Rouse, 1965).
The **most** important tool for the analysis is a newly developed computational model solving the complete Navier-Stokes equations for steady fully-developed laminar flow in coiled rectangular pipes, which was tested using the results of experiments and of computations with other mathematical models. It will be described briefly in paragraph 3.3; for a more extensive description reference is made to the relevant background report (De Vriend, 1978a). This mathematical

approach provides the possibility of extensive parameter variations and of omitting terms from the equations in order to assess the influence of the various aspects of the elementary phenomena (convection, diffusion). Besides, the mathematical model can be used in a later stage, when investigating simplified computation methods (see chapter 4).

3.3. Mathematical model of fully-developed laminar flow

The mathematical description of steady fully-developed laminar flow in a coiled rectangular pipe can simply be derived from the general system of equations given in chapter 2. For laminar flow the total viscosity A is equal to the molecular viscosity η and the effective Reynolds number Re_0 is equal to the "molecular" Reynolds number Re. So if all tangential derivatives except the longitudinal pressure gradient are omitted, the normalized system (2.30) through (2.36) reduces to

$$\frac{\partial v}{\partial \xi} + \frac{\varepsilon}{r} v + \frac{\partial w}{\partial \zeta} = 0 \tag{3.1}$$

$$\varepsilon Re \left(v \frac{\partial u}{\partial \xi} + w \frac{\partial u}{\partial \zeta} + \frac{\varepsilon}{r} uv\right) = - \frac{1}{r} \frac{\partial p}{\partial \phi} + \frac{\partial^2 u}{\partial \zeta^2} + \frac{\partial^2 u}{\partial \xi^2} + \frac{\varepsilon}{r} \frac{\partial u}{\partial \xi} - \frac{\varepsilon^2}{r^2} u \tag{3.2}$$

$$\varepsilon^3 Re \left(v \frac{\partial v}{\partial \xi} + w \frac{\partial v}{\partial \zeta}\right) - \varepsilon^2 Re \frac{u^2}{r} =$$

$$- \frac{\partial p}{\partial \xi} + \varepsilon^2 \left(\frac{\partial^2 v}{\partial \zeta^2} + \frac{\partial^2 v}{\partial \xi^2} + \frac{\varepsilon}{r} \frac{\partial v}{\partial \xi} - \frac{\varepsilon^2}{r^2} v\right) \tag{3.3}$$

$$\varepsilon^3 Re \left(v \frac{\partial w}{\partial \xi} + w \frac{\partial w}{\partial \zeta}\right) = - \frac{\partial p}{\partial \zeta} + \varepsilon^2 \left(\frac{\partial^2 w}{\partial \zeta^2} + \frac{\partial^2 w}{\partial \xi^2} + \frac{\varepsilon}{r} \frac{\partial w}{\partial \xi}\right) \tag{3.4}$$

$$\int_{-B/2d}^{B/2d} d\xi \int_{-1}^{0} u d\zeta = \frac{B}{d} \tag{3.5}$$

$$u = 0; \quad v = 0; \quad w = 0 \quad \text{at} \quad \zeta = -1 \quad \text{and at} \quad \xi = \pm \frac{B}{2d} \tag{3.6}$$

$$w = 0; \quad \frac{\partial u}{\partial \zeta} = 0; \quad \frac{\partial v}{\partial \zeta} = 0 \quad \text{at} \quad \zeta = 0 \tag{3.7}^{*})$$

The equation of continuity (3.1) concerns only the two secondary velocity components, so a scalar stream function can be used to describe the secondary flow. Although there are other possibilities (see, for instance: De Vriend, 1973a & 1973b), the stream function ψ' is defined in such a way that the streamlines of the secondary circulation are lines of constant ψ':

$$v = -\frac{1}{r}\frac{\partial \psi'}{\partial \zeta} \quad \text{and} \quad w = \frac{1}{r}\frac{\partial \psi'}{\partial \xi} \tag{3.8}$$

, so that

$$\left.\frac{d\zeta}{d\xi}\right|_{d\psi'=0} = -\frac{\frac{\partial \psi'}{\partial \xi}}{\frac{\partial \psi'}{\partial \zeta}} = \frac{w}{v} \tag{3.9}$$

Elimination of the pressure from equations (3.3) and (3.4) yields a transport equation for the secondary flow vorticity ω_s', reading

$$\varepsilon Re \left(v \frac{\partial \omega_s'}{\partial \xi} + w \frac{\partial \omega_s'}{\partial \zeta} - \frac{\varepsilon}{r} v\omega_s'\right) + Re \frac{\partial}{\partial \zeta}\left(\frac{u^2}{r}\right) =$$

$$\frac{\partial^2 \omega_s'}{\partial \zeta^2} + \frac{\partial^2 \omega_s'}{\partial \xi^2} + \frac{\varepsilon}{r}\frac{\partial \omega_s'}{\partial \xi} - \frac{\varepsilon^2}{r^2}\omega_s' \tag{3.10}$$

---

*) As the flow in a rectangular pipe of height 2d ($-d \leq z \leq d$) is symmetric about the axis $z = 0$, these "rigid lid" surface conditions for "open" channel flow can also be considered as symmetry conditions for flow in a rectangular pipe of double height.

with $\omega_s' = \frac{\partial w}{\partial \xi} - \frac{\partial v}{\partial \zeta}$, or, regarding (3.8),

$$\omega_s' = \frac{1}{r}\left(\frac{\partial^2 \psi'}{\partial \zeta^2} + \frac{\partial^2 \psi'}{\partial \xi^2} - \frac{\varepsilon}{r}\frac{\partial \psi'}{\partial \xi}\right) \tag{3.11}$$

According to equation (3.10), the vertical derivative of the centripetal acceleration term in equation (3.3) is the only source of secondary flow vorticity. For low Reynolds numbers the source term in (3.10) is proportional to Re, so that it is obvious to define

$$\psi = \frac{\psi'}{Re} \quad \text{and} \quad \omega_s = \frac{\omega_s'}{Re} \tag{3.12}$$

, where ψ and ω_s can be expected to be independent of Re if Re is small.
Making use of these definitions, the system (3.1) through (3.7) can be replaced by

$$\varepsilon Re^2 \left\{-\frac{1}{r}\frac{\partial \psi}{\partial \zeta}\left(\frac{\partial u}{\partial \xi} + \frac{\varepsilon}{r}u\right) + \frac{1}{r}\frac{\partial \psi}{\partial \xi}\frac{\partial u}{\partial \zeta}\right\} = -\frac{1}{r}\frac{\partial p}{\partial \phi} + \nabla^2 u - \frac{\varepsilon^2}{r^2}u \tag{3.13}^*)$$

$$\varepsilon Re^2 \left\{-\frac{1}{r}\frac{\partial \psi}{\partial \zeta}\left(\frac{\partial \omega_s}{\partial \xi} - \frac{\varepsilon}{r}\omega_s\right) + \frac{1}{r}\frac{\partial \psi}{\partial \xi}\frac{\partial \omega_s}{\partial \zeta}\right\} + \frac{\partial}{\partial \zeta}\left(\frac{u^2}{r}\right)) =$$

$$\nabla^2 \omega_s - \frac{\varepsilon^2}{r^2}\omega_s \tag{3.14}$$

$$\nabla^2 \psi - 2\frac{\varepsilon}{r}\frac{\partial \psi}{\partial \xi} = r\omega_s \tag{3.15}$$

---

*) As all velocity variations with ϕ are dropped, the operator ∇^2 reduces to $\frac{\partial^2}{\partial \zeta^2} + \frac{\partial^2}{\partial \xi^2} + \frac{\varepsilon}{r}\frac{\partial}{\partial \xi}$.

$$\int_{-B/2d}^{B/2d} d\xi \int_{-1}^{0} u\,d\zeta = \frac{B}{d} \tag{3.16}$$

$$\frac{\partial u}{\partial \zeta} = 0 \quad \text{at} \quad \zeta = 0; \quad u = 0 \text{ at } \zeta = -1 \text{ and at } \xi = \pm \frac{B}{2d} \tag{3.17}$$

$$\psi = 0 \quad \text{and} \quad \frac{\partial \psi}{\partial \zeta} = 0 \quad \text{at} \quad \zeta = -1 \tag{3.18}$$

$$\psi = 0 \quad \text{and} \quad \frac{\partial \psi}{\partial \xi} = 0 \quad \text{at} \quad \xi = \pm \frac{B}{2d} \tag{3.19}$$

$$\psi = 0 \quad \text{and} \quad \frac{\partial^2 \psi}{\partial \zeta^2} = 0 \quad \text{at} \quad \zeta = 0 \tag{3.20}$$

$$v = -\frac{Re}{r}\frac{\partial \psi}{\partial \zeta}; \qquad w = \frac{Re}{r}\frac{\partial \psi}{\partial \xi} \tag{3.21}$$

$$\nabla^2\left(p + \varepsilon^3 Re\,\frac{v^2+w^2}{2}\right) =$$

$$\varepsilon^3 Re\,\left(w\frac{\partial \omega_s}{\partial \xi} + \frac{\varepsilon}{r} w\omega_s - v\frac{\partial \omega_s}{\partial \zeta} + \omega_s^2\right) + \frac{\varepsilon^2 Re}{r}\frac{\partial u^2}{\partial \xi} \tag{3.22}$$

$$\frac{\partial p}{\partial \xi} = \varepsilon^2 \frac{\partial^2 v}{\partial \zeta^2} \quad \text{at} \quad \zeta = -1; \quad \frac{\partial p}{\partial \zeta} = 0 \quad \text{at } \zeta = 0;$$

$$\frac{\partial p}{\partial \zeta} = \varepsilon^2 \left(\frac{\partial^2 w}{\partial \xi^2} + \frac{\varepsilon}{r}\frac{\partial w}{\partial \xi}\right) \quad \text{at} \quad \xi = \pm \frac{B}{2d} \tag{3.23}$$

The velocity components u, v and w and the pressure p are solved from this system, which seems mathematically more attractive than (3.1) through (3.7): if equations (3.14) and (3.15) are combined to one fourth-order equation for ψ, only this equation and the longitudinal momentum equation (3.13) have to be solved simultaneously, whereas the system (3.1)

through (3.7) requires the simultaneous solution of four differential equations (see, for instance, Joseph et al., 1975). Equation (3.13) and the equation for ψ

$$\frac{\partial^4\psi}{\partial\xi^4} + 2\frac{\partial^4\psi}{\partial\xi^2\partial\zeta^2} + \frac{\partial^4\psi}{\partial\zeta^4} + 2\frac{\varepsilon}{r}\left(\frac{\partial^3\psi}{\partial\xi^3} + \frac{\partial^3\psi}{\partial\xi\partial\zeta^2}\right) + 3\frac{\varepsilon^2}{r^2}\frac{\partial^2\psi}{\partial\xi^2} - 3\frac{\varepsilon^3}{r^3}\frac{\partial\psi}{\partial\xi} =$$

$$\varepsilon Re^2\left\{-\frac{1}{r}\frac{\partial\psi}{\partial\zeta}\left(\frac{\partial^3\psi}{\partial\xi\partial\zeta^2} + \frac{\partial^3\psi}{\partial\xi^3} - 2\frac{\varepsilon}{r}\frac{\partial^2\psi}{\partial\zeta^2} - 3\frac{\varepsilon}{r}\frac{\partial^2\psi}{\partial\xi^2} + 3\frac{\varepsilon^2}{r^2}\frac{\partial\psi}{\partial\xi}\right) + \right.$$

$$\left. + \frac{1}{r}\frac{\partial\psi}{\partial\xi}\left(\frac{\partial^3\psi}{\partial\zeta^3} + \frac{\partial^3\psi}{\partial\xi^2\partial\zeta} - \frac{\varepsilon}{r}\frac{\partial^2\psi}{\partial\xi\partial\zeta}\right)\right\} + \frac{\partial u^2}{\partial\zeta} \qquad (3.24)$$

, which are two coupled non-linear partial differential equations, must be solved iteratively. Therefore the following iterative procedure has been used to solve the system (3.13) through (3.24):

a. estimate ψ; taking $\psi \equiv 0$, for instance, is rather interesting, since in that case step b yields the main velocity distribution without influence of convection.

b. solve u and $\frac{\partial p}{\partial\phi}$ (which can easily be shown to be a constant) from the longitudinal momentum equation (3.13) and the integral condition of continuity (3.16), imposing conditions (3.17) at the boundaries;

c. solve ψ from equation (3.24) with conditions (3.18) through (3.20);

d. repeat steps b and c until the termination criterion

$$\max\left\{\left|u^{(n)} - u^{(n-1)}\right|\right\} < \delta \qquad (\delta << 1) \qquad (3.25)$$

is satisfied*);

*) In the actual computations the convergence of the iteration procedure was improved by "underrelaxation", i.e. by taking into account only a fraction of the changes in u from one iteration step to another. So if $\tilde{u}^{(n)}$ is the solution of (3.13) in the n-th iteration step,

$$u^{(n)} = \alpha\tilde{u}^{(n)} + (1 - \alpha)\, u^{(n-1)} \qquad (0 < \alpha \leq 1)$$

e. determine the secondary velocity components from (3.21).
f. solve the transverse pressure distribution from equation (3.22) with boundary conditions (3.23).

Further details of this procedure are given in the relevant background report (De Vriend, 1978a).

3.4. Verification of the model and applicability

As was stated before, the present model is nothing new in the field of fully-developed laminar flow computations. Therefore it will suffice here to state that the mathematical model was verified in three different ways:

- by comparing its results for small values of the Dean number $De = Re\sqrt{\varepsilon}$ with analytical solutions given by Itō (1951), Cuming (1952) and De Vriend (1973a & 1973b),
- by comparing its results with those from other numerical models described by Cheng et al. (1970), Joseph et al. (1975) and Cheng et al. (1976),
- by comparing its results with measured data given by Mori et al. (1971).

For a more extensive description of this verification reference is made to De Vriend (1978a).

From the aforementioned comparisons it became evident that for low and intermediate Dean numbers ($De < 60$) the model gives a good description of fully-developed laminar flow in coiled pipes with a rectangular cross-section of not very high aspect ratio d/B. In contrast with similar models solving equations (3.14) and (3.15) instead of the stream function equation (3.24) (Cheng et al., 1976; see also Roache, 1972), the convergence of the present iteration procedure becomes very poor if the Dean number exceeds the value 60. Regarding the requirements to the mathematical model of turbulent flow in natural river bends, however, this limitation is acceptable, as can be shown by the following reasoning.

In laminar curved flow the Dean number indicates the importance of the convective transport of momentum by the secondary flow with respect to the molecular diffusion (see equations (3.13) and (3.24)). Likewise, in turbulent flow the Dean number should

indicate the importance of convection with respect to turbulent diffusion, i.e. it should be based on the effective Reynolds number Re_0 (see chapters 2 and 6). According to Engelund (1964 & 1974), this effective Reynolds number can be estimad by

$$Re_0 = 13 \frac{C}{\sqrt{g}} \tag{3.26}$$

, in which C denotes Chezy's factor. In practice $C/\sqrt{g}$ will range from 10 to 20 and in natural rivers the ratio of the channel width to the radius of curvature will not exceed 0.5 (Leopold et al., 1964; see also Jansen, 1979). So in the most extreme case the depth-to-width ratio may not exceed 0.1 in order to have an effective Dean number smaller than 60. This is thought to be an acceptable limitation.
It should be noted that in various flume experiments the effective Dean number is considerably larger than 60 (Shukry (1949): 150; Fox et al. (1968): 130; Rozovskii (1961): 70), so that the mathematical model is not likely to apply to these flow cases.

3.5. Influence of the Dean number

In the longitudinal momentum equation (3.13) as well as in the vorticity transport equation (3.14) and the stream function equation (3.24) for the secondary flow, the parameter εRe^2 indicates the importance of the convection terms with respect to the viscous diffusion terms. Dean (1928a) and Adler (1934) showed that the resistance of low Reynolds number flow in coiled circular pipes of moderate curvature can be expressed as a power series expansion of the squared Dean number, defined as

$$De = \frac{1}{\rho} \frac{1}{R_c} \frac{\partial p}{\partial \phi} \frac{a^3}{\nu^2} \left(\frac{a}{R_c}\right)^{\frac{1}{2}} \tag{3.27}$$

, a denoting the pipe radius. If the pressure gradient is

is normalized in the same way as in chapter 2, this definition can be elaborated to

$$De = \frac{V^2}{aRe'}\frac{a^3}{\nu^2}\left(\frac{a}{R_c}\right)^{\frac{1}{2}} = Re'\left(\frac{a}{R_c}\right)^{\frac{1}{2}} \quad \text{with} \quad Re' = \frac{Va}{\nu} \tag{3.28}$$

So the resistance parameter in coiled circular pipes is similar to the convection parameter in the present equations. Therefore the quantity $Re\sqrt{\varepsilon}$ will be referred to as the Dean number.
Of all parameters in the system (also the curvature ratio ε and the channel aspect ratio d/B play a part), the Dean number is the most important one for the velocity redistribution (De Vriend, 1978a). Therefore, considerations will be limited to the influence of this parameter. The channel geometry is kept constant and, for convenience, the geometrical parameters are taken the same as those of a rather sharply curved flume in the Laboratory of Fluid Mechanics of the Delft University of Technology (De Vriend, 1979b; see also chapter 8): $\varepsilon = 0.04$ and $d/B = 0.1$.
The results of a series of computations for this geometry and with Dean numbers ranging from 0 to 50, give rise to the following observations.

a. Main velocity distribution (figure 3 a-b).
As becomes evident from figure 3, the main velocity distribution in fully developed curved flow is strongly dependent on the Dean number, i.e. on the convective transport of momentum by the secondary flow. For De = 0 the horizontal distribution of the main velocity is skewed inwards, so that the maximum lies close to the inner sidewall; the vertical distribution is practically parabolic then. As De increases, however, the skewness is gradually inverted and the velocity maximum moves towards the outer wall; along with this the velocity at the surface is gradually reduced and at higher Dean numbers the velocity maximum even lies below the surface.

b. Boundary shear stress (figure 3c).
The shear stresses at the fixed boundaries, which are proportional to the normal velocity gradients, are influenced by the Dean number through the main velocity redistribution. Figure 3c shows that the tangential shear stress at the inner wall and at the bottom near the inner wall is almost independent of De: the horizontal and the vertical deformations of the main velocity distribution are counteracting here. Further outwards at the bottom and at the outer wall, however, the horizontal and vertical deformations are acting in the same sense and the shear stress increases strongly with the Dean number (see also Falcón, 1979).

c. Longitudinal pressure gradient (figure 4).
As was stated before, the longitudinal pressure gradient in the axis, $\frac{\partial p}{\partial \phi}$, can easily be shown to be a constant if the flow is independent on ϕ. This constant, denoted by $-\iota$, is related to the tangential shear stress at the fixed boundaries: integrating equation (3.13) multiplied by r^2 over the cross-section yields, after some elaboration,

$$\frac{B}{d}\,\iota = \int_{-B/2d}^{B/2d} r^2 \left.\frac{\partial u}{\partial \zeta}\right|_{\zeta=-1} d\xi + \int_{-1}^{0} r^2 \left.\frac{\partial u}{\partial \xi}\right|_{\xi=-\frac{B}{2d}} d\zeta - \int_{-1}^{0} r^2 \left.\frac{\partial u}{\partial \xi}\right|_{\xi=\frac{B}{2d}} d\zeta \qquad (3.29)$$

Since for increasing De the main velocity gradients at the fixed boundaries remain almost constant or increase, the longitudinal slope factor ι may be expected to increase with De. Figure 4 shows that the ratio of ι and the longitudinal pressure gradient in the equivalent straight channel flow increases with De, indeed.

d. Secondary flow (figure 5).
The source term in the stream function equation for the secondary flow (3.24) is $\frac{\partial}{\partial \zeta}(u^2)$, so that the secondary flow will be rather sensitive to the deformations of the main velocity distribution. Figure 3 shows that for increasing De this source term tends to

decrease in the inner half of the bend and near the surface (where it can become even negative), whereas it increases in the outer half and near the bottom. Hence the maximum of the source term, which lies close to the inner wall and about half-way the vertical for De = 0, gradually moves outwards and downwards as De increases; the depth-averaged value, $u^2(\zeta = 0)$ gradually decreases all over the cross-section.

As a consequence of this behaviour of the source term, the stream function tends to decrease for increasing De (figures 5a-b) and the centre of circulation, i.e. the point where the maximum of ψ occurs, moves downwards and outwards, the latter until De $\simeq$ 25. Then the outward moving tendency is compensated by an inward one, which is caused by the fact (not shown by figure 3) that the downward displacement of the vertical maximum of $\frac{\partial}{\partial \zeta}(u^2)$ is stronger near the outer wall than near the inner wall. For the same reason the centre of circulation moves inwards again for De > 25 (figure 5 a-b and 5 d-e).

The decreasing tendency of the maximum of the stream function, $\hat{\psi}$, is stronger for higher Dean numbers. Consequently, for small De the quantity De$\hat{\psi}$, which can be considered as a measure of the secondary flow intensity*), is almost linear with De, but as the Dean number becomes higher, a reduction occurs and for De > 40 (in square pipes even for De > 20) the secondary flow intensity decreases again (figure 5c).

e. Transverse pressure distribution (figure 6).

Figure 6 shows the influence of the Dean number on the transverse pressure distribution. The deformation of the horizontal distribution of the pressure shown in figure 6a (from concave for De = 0 to convex for higher De) can be explained from the redistribution

---

*) Re$\hat{\psi}$ is a more appropriate expression for this intensity, but as ε is kept constant, De$\hat{\psi}$ can also be used.

of u^2, on the basis of equation (3.3) truncated to the two most important terms

$$\frac{\partial p}{\partial \xi} = \varepsilon^2 Re \frac{u^2}{r} \tag{3.30}$$

In addition, for all Dean numbers considered p is almost constant along the vertical (figure 6b), i.e. the pressure is practically hydrostatic. Hence it is concluded that, for the Dean numbers considered here, the transverse pressure distribution is hardly influenced by the secondary flow, but completely dominated by the centripetal acceleration of the main flow.
Figure 6a shows that the difference between the values of $p/\varepsilon^2 Re$ at the outer and at the inner wall hardly depends on De. According to the definition (see also equation 2.29)

$$p + \rho g z = \frac{\rho V^2}{\varepsilon Re} p = \frac{\rho \nu^2}{d^2} \frac{Re}{\varepsilon} p \tag{3.31}$$

, this implies that for given ρ, ν and d the transverse pressure drop is closely proportional to De^2. This is confirmed by figure 6c, where an exponent of 1.96 is found. The same figure shows that the transverse pressure drop in the shallow channel considered (d/B = 0.1) is about 5 times as large as in a square pipe (d/B = 0.5) under the same conditions. Apparently, the mean transverse pressure gradients are almost the same in either case.

f. Total energy (figure 7).
Figure 7 gives the transverse distribution of the total energy, normalized by

$$e = \frac{\varepsilon Re}{\rho V^2} (p + \rho g z + \frac{1}{2} \rho v_{tot}^2) = p + \varepsilon Re \frac{u^2 + \varepsilon^2 (v^2 + w^2)}{2} \tag{3.32}$$

From this figure and the transverse pressure distribution given in figure 6 it becomes evident that u^2 plays a predominant part in e. Consequently, the energy tends to concentrate more and more near the outer wall as De increases and the vertical distribution tends to flatten.

The foregoing considerations show that most of the phenomena to be observed when the Dean number is raised gradually from 0 to about 50 can be explained from the deformation of the main velocity distribution. Explaining this deformation, however, requires some further analysis.

3.6. Analysis of the main velocity redistribution

Regarding the longitudinal momentum equations for fully-developed curved laminar flow

$$De^2 \{- \frac{1}{r} \frac{\partial \psi}{\partial \zeta} (\frac{\partial u}{\partial \xi} + \frac{\varepsilon}{r} u) + \frac{1}{r} \frac{\partial \psi}{\partial \xi} \frac{\partial u}{\partial \zeta}\} =$$

$$\frac{1}{r} + \frac{\partial^2 u}{\partial \zeta^2} + \frac{\partial^2 u}{\partial \xi^2} + \frac{\varepsilon}{r} \frac{\partial u}{\partial \xi} - \frac{\varepsilon^2}{r^2} u \qquad (3.33)$$

and for the equivalent fully-developed straight channel flow

$$0 = 1_0 + \frac{\partial^2 u}{\partial \zeta^2} + \frac{\partial^2 u}{\partial \xi^2} \qquad (3.34)$$

, three sources of difference between the main velocity distributions in these flows can be distinguished, viz.:

- the factor $\frac{1}{r}$ in the pressure gradient term of (3.33),
- the extra diffusion terms due to the main flow curvature,
- the secondary flow convection terms.

The combination of the first two sources gives rise to the "potential flow" effect, which is to be observed in the zero Dean number solution (see, for instance, figure 3): outside

the sidewall boundary layers the main velocity distribution is almost similar to the one in a potential vortex (u proportional to $\frac{1}{r}$; see also De Vriend, 1973a & 1973b).
The "inversion" of this main velocity distribution to an outward skewed distribution with the velocity maximum at some distance below the surface must be attributed to convection of main flow momentum by the secondary flow. It will be analysed hereafter, both mathematically (what is the influence of the various terms in the momentum equations?) and physically (what is the physical explanation of the observed phenomena?). Thereby a distinction will be made between low, intermediate and high Dean number flow, each of which allows for a specific mathematical approach.

3.6.1. Low Dean number flow

For low Dean numbers the influence of convection can be considered as a perturbation of the zero Dean number solution (cf. Dean (1928a) and Adler (1934) for circular pipes, Itō (1951), Cuming (1952) and De Vriend (1973a & 1973b) for rectangular channels). Accordingly, the dependent variables in the system of equations describing the flow can be written as power series expansions of De^2. So, for instance,

$$u = \sum_{k=0}^{\infty} De^{2k} u_k \quad ; \quad \iota = \sum_{k=0}^{\infty} De^{2k} \iota_k \quad ; \quad \psi = \sum_{k=0}^{\infty} De^{2k} \psi_k \tag{3.35}$$

If lateral diffusion is neglected (far from the sidewalls), the first order perturbation function u_1 of the zero Dean number solution u_0 can be written as (De Vriend, 1978a; see also De Vriend, 1973a)

$$u_1 = \frac{\iota_1}{\iota_0} u_0 + u_1' \tag{3.36}$$

with $$u_1' = \overline{u_1'}\,\frac{3}{2}(1-\zeta^2) + \frac{\bar{\psi}_0}{r}\left(\frac{\partial \bar{u}_0}{\partial \xi} + \frac{\varepsilon}{r}\bar{u}_0\right) f_1(\zeta) +$$

$$+ \frac{\bar{u}_0}{r}\frac{\partial \bar{\psi}_0}{\partial \xi} f_2(\zeta) \qquad (3.37)$$

and $$\overline{u_1'} = -\frac{6656}{7315}\frac{\bar{\psi}_0}{r}\left(\frac{\partial \bar{u}_0}{\partial \xi} + \frac{\varepsilon}{r}\bar{u}_0\right) - \frac{3328}{7315}\frac{\bar{u}_0}{r}\frac{\partial \bar{\psi}_0}{\partial \xi} \qquad (3.38)$$

, the overbars denoting depth-averaged values. The functions f_1 and f_2, which are polynomials in ζ, are represented in figure 8a-b.

The two constituents of $\overline{u_1'}$ are negative close to the inner wall and positive close to the outer wall, whereas they almost vanish in the central region.

Hence the depth-averaged velocity will be reduced near the inner wall and increased near the outer wall. Although this influence is of a local kind*), it agrees qualitatively with the results of the shallow channel computations by the complete model (figure 3).

The second and the third term in expression (3.37) for u_1' indicate how the vertical distribution of u is influenced by convection due to the radial and the vertical velocity component. As long as $\frac{1}{r}\frac{\partial}{\partial \xi}(r\bar{u}_0)$ is positive, the radial velocity component causes a flattening of the main velocity profile, whereas a positive vertical velocity gives rise to more oblique profiles of u, but to a much lower extent.

A physical interpretation of these results can be found by considering the main flow isovels and the streamlines of the secondary flow for the zero Dean number solution, as shown in figure 8c for the inner wall region. Everywhere in

---

*) Even if lateral diffusion is taken into account, this local character remains (De Vriend, 1973a & 1973b).

this region u_0 appears to increase along the streamlines of the secondary flow.
So in any point the longitudinal momentum of the fluid conveyed by the secondary flow is smaller than the longitudinal momentum in the undisturbed flow.
As a consequence, an overall decrease of the main velocity with respect to u_0 occurs here. The opposite holds for the outer wall region, where the fluid conveyed by the secondary flow has a momentum surplus and an overall increase of the main velocity occurs.
The explanation for the vertical redistribution of the velocity is essentially the same, but requires a more quantitative reasoning. The inclinations α_i and α_s of the isovels and the streamlines in figure 8c follow from

$$\tan \alpha_i = - \frac{\partial u_0}{\partial \xi} \Big/ \frac{\partial u_0}{\partial \zeta} \qquad \text{and} \qquad \tan \alpha_s = - \frac{\partial \psi_0}{\partial \xi} \Big/ \frac{\partial \psi_0}{\partial \zeta} \tag{3.39}$$

Hence it can easily be derived that

$$v_0 \frac{\partial u_0}{\partial \xi} + w_0 \frac{\partial u_0}{\partial \zeta} = \sqrt{v_0^2 + w_0^2} \sqrt{\left(\frac{\partial u_0}{\partial \xi}\right)^2 + \left(\frac{\partial u_0}{\partial \zeta}\right)^2} \sin(\alpha_s - \alpha_i) \tag{3.40}$$

So if the term $\varepsilon \frac{u_0 v_0}{r}$ is neglected *), the magnitude of the convection terms in the longitudinal momentum equation is proportional to the local strength of the secondary flow, the local main velocity gradient and the sine of the angle of intersection between the main flow isovels and the secondary flow streamlines. According to figure 8, the

---

*) If this term, originating from the divergence of the coordinate system, is taken into account, the same reasoning holds for lines of constant ru_0 rather than for the isovels.

streamlines intersect the isovels at much smaller angles near the bottom than near the surface and also the secondary flow intensity is somewhat smaller in the lower parts of the cross-section. In the wall region the main velocity gradient is of the same order of magnitude throughout the vertical, so that the effect of the secondary flow will be relatively stronger in the upper part of the vertical. Consequently, the shape of the main velocity profile becomes flatter near the surface*). The redistribution of the main velocity works out as a deformation of the main flow isovels in the direction of the secondary flow. Essentially the same phenomenon is found in turbulent flow in straight non-circular conduits, where a secondary flow occurs, as well. The deformation of the main flow isovels can be explained in the same way then (see, for instance: Prandtl, 1952, Schlichting, 1951, and Reynolds, 1974).

3.6.2. Intermediate Dean number flow

At small Dean numbers only small and local perturbations of the zero Dean number velocity occur, as was shown in the foregoing. As the Dean number increases, however, the perturbations grow stronger and the lateral interaction grows more and more important, until the influence of convection is felt throughout the cross-section, whether this is shallow or not.
This difference between low and intermediate Dean number flow is reflected in the mathematical approach: for small De perturbation techniques are applicable, but for higher De these methods fail (see also chapter 4). The similarity of the velocity profiles, however, which is strongly present in low Dean number flow, persists up to much higher Dean numbers, especially if the channel is shallow. This is readily shown by figure 9, where $\bar{u}/\bar{u}|_{\xi=0}$ and $u/\bar{u}$ appear to be hardly dependent on ζ and ξ,

---

*) If the convection terms would be constant along the vertical, the perturbation of u_0 would be parabolic, so that the shape of the main velocity profile would not be effected.

respectively, even at Dean numbers giving rise to velocity redistributions throughout the cross-section*).
When adopting similarity approximations for the main and the secondary flow,

$$u(\xi,\zeta) = \bar{u}(\xi)\, f(\zeta) \qquad \text{and} \qquad \psi(\xi,\zeta) = \bar{\psi}(\xi)\, g(\zeta) \tag{3.41}$$

, the horizontal and the vertical redistributions of u are described by

$$De^2 \overline{g \frac{\partial f}{\partial \zeta}} \{\frac{\bar{\psi}}{r} (\frac{\partial \bar{u}}{\partial \xi} + \frac{\varepsilon}{r} \bar{u}) + \frac{\bar{u}}{r} \frac{\partial \bar{\psi}}{\partial \xi}\} =$$

$$\frac{1}{r} \frac{\partial^2 \bar{u}}{\partial \xi^2} + \frac{\varepsilon}{r} \frac{\partial \bar{u}}{\partial \xi} - \frac{\varepsilon^2}{r^2} \bar{u} - \bar{u} \frac{\partial f}{\partial \zeta}\Big|_{\zeta=1} \tag{3.42}$$

and

$$De^2 \{- \frac{\bar{\psi}}{r} (\frac{\partial \bar{u}}{\partial \xi} + \frac{\varepsilon}{r} \bar{u}) \frac{\partial g}{\partial \zeta} f + \frac{\bar{u}}{r} \frac{\partial \bar{\psi}}{\partial \zeta} g \frac{\partial f}{\partial \zeta}\} =$$

$$\frac{1}{r} + \bar{u} \frac{\partial^2 f}{\partial \zeta^2} + \frac{\partial}{\partial \xi} (\frac{1}{r} \frac{\partial r\bar{u}}{\partial \xi}) f \tag{3.43}$$

, respectively. For given $\bar{\psi}$, f and g**), $\bar{u}$ and $\imath$ can be solved from (3.42) and the integral conditon of continuity (3.16). Figure 10 shows the approximation of $\bar{u}$ obtained in this way to be good, except for the outer wall region at relatively high De. The same holds for equation 3.43), from which f can be solved if $\bar{\psi}$, $\bar{u}$ and g are given**) (see figure 11).

---

*) Only at relatively high De considerable deviations occur locally near the outer wall.

**) To be taken from the solution obtained for the same case by the complete model (see par. 3.5).

Hence it is concluded that equations (3.42) and (3.43) can be used for the analysis of the main velocity redistribution*).

In the depth-averaged longitudinal momentum equation (3.42) the following (groups of) terms can be distinguished in addition to the longitudinal slope term:

- the radial convection terms $De^2 \overline{g \frac{\partial f}{\partial \zeta}} \frac{\bar{\psi}}{r} \left(\frac{\partial \bar{u}}{\partial \xi} + \frac{\varepsilon}{r} \bar{u}\right)$

- the vertical convection term $De^2 \overline{g \frac{\partial f}{\partial \zeta}} \frac{\bar{u}}{r} \frac{\partial \bar{\psi}}{\partial \xi}$

- the lateral diffusion terms $\frac{\partial^2 \bar{u}}{\partial \xi^2} + \frac{\varepsilon}{r} \frac{\partial \bar{u}}{\partial \xi} - \frac{\varepsilon^2}{r^2} \bar{u}$

- the bed shear stress term $- \bar{u} \left.\frac{\partial f}{\partial \zeta}\right|_{\zeta=-1}$

The influence of each of these terms or groups of terms on $\bar{u}$ is shown in figure 12, which gives rise to the following observations (see also De Vriend, 1978a):

. if the vertical convection term is neglected, the depth-averaged velocity distribution hardly differs from its zero Dean number limit (see figure 12a);

. if the radial convection terms are neglected, lateral interaction is almost absent, especially in the central region (see figure 12c);

. the lateral influencing due to the radial convection terms is exclusively outward (figure 12c);

---

*) Introducing parts of the complete solution into the diffusion terms is not sufficient to make the equation represent the essential features of the velocity redistribution; the correct representation of these features is due to the convection terms, as becomes evident if they are omitted.

. neglecting the lateral diffusion terms away from the sidewalls has hardly any influence on $\bar{u}$ (see figure 12a);
. the direct influence of the boundary conditions at the sidewalls (full-slip or no-slip) is restricted to the sidewall regions (see figure 12b);
. neglecting the bed shear stress gives rise to much less uniform and at higher De much stronglier skewed distributions of $\bar{u}$ (see figure 12a).

Hence it is concluded that the vertical convection term is the main cause of the local decrease of $\bar{u}$ near the inner wall and the local increase near the outer wall, whereas radial convection provides for an outward lateral interaction. Consequently, the region influenced by the local velocity reduction near the inner wall is extended outwards until it covers the greater part of the cross-section and the region influenced by the local velocity increase near the outer wall is compressed against the wall (see figures 12a and b, the influence of neglecting the radial convection terms). If the bed shear stress were absent, this combined effect of vertical and radial convection would lead to an almost linear increase of $\bar{u}$ with ξ in the central region (see Appendix A). The bed shear stress, however, tends to attenuate the non-uniformities in $\bar{u}$ and consequently the distribution of $\bar{u}$ is deflected towards an almost horizontal asymptote, as is shown in Appendix A.

In equation (3.43) for the vertical distribution of the main velocity the (groups of) terms to be distinguished in addition to the longitudinal slope term are:

- the radial convection terms $\quad -De^2 \frac{\bar{\psi}}{r}\left(\frac{\partial \bar{u}}{\partial \xi} + \frac{\varepsilon}{r}\bar{u}\right)\frac{\partial g}{\partial \zeta} f$

- the vertical convection terms $\quad De^2 \frac{\bar{u}}{r}\frac{\partial \bar{\psi}}{\partial \xi} g \frac{\partial f}{\partial \zeta}$

- the lateral diffusion terms $\quad \left(\frac{\partial^2 \bar{u}}{\partial \xi^2} + \frac{\varepsilon}{r}\frac{\partial \bar{u}}{\partial \xi} - \frac{\varepsilon^2}{r^2}\bar{u}\right) f$

- the vertical diffusion term $\quad \bar{u}\frac{\partial^2 f}{\partial \zeta^2}$

The analysis of the influence of each of these terms or groups of terms (shown in figure 13) leads to the following conclusions (see De Vriend, 1978a):

- near the inner wall the vertical convection term causes a decrease of f near the bottom and an increase near the surface, whereas near the outer wall the reverse occurs;
- the radial convection term gives rise to a (considerably stronger) increase of f near the bottom and a decrease near the surface in the inner wall region, whereas it causes the reverse effect in the outer wall region;
- in the central region of the cross-section (i.e. away from the sidewalls) the influence of the vertical convection term is small, but the radial convection term is quite important; it gives rise to similar deformations of f as in the inner wall region;
- the influence of lateral diffusion and of the no-slip conditions at the sidewalls on f is rather small.

The physical explanation of the local deformations of the velocity distribution near the sidewalls is the same as for low Dean number flow (section 3.6.1). Away from the sidewalls the vertical velocities are small and the convective transport of momentum is mainly horizontal, outward in the upper half of the vertical and inward in the lower half. The net outward transport of momentum, combined with the bottom shear stress as a damping factor, causes a retarded outward expansion of the low velocity region near the inner wall until the greater part of the cross-section in influenced.
Near the outer wall, however, the net outward momentum transport compresses the local velocity peak against the wall, where it is partly damped by viscous forces. As a consequence of these effects, the main velocity distribution tends to be skewed outwards in the greater part of the cross-section. The local horizontal convection combined with this outward skewed velocity distribution gives rise to the flattening of the main velocity profile in a vertical, the fluid conveyed from further inwards

causing a momentum deficit in the upper half of the vertical and the fluid conveyed from further outwards causing a surplus in the lower half.

3.6.3. High Dean number flow

As was stated in par. 3.4., the flow at higher (effective) Dean numbers (De > 60) is not quite relevant to the present investigations. Therefore reference is made here to the the theoretical and experimental work reported in the literature (see also De Vriend, 1978a): Joseph et al. (1975) and Cheng et al. (1976) for the mathematical prediction of flow at rather high Dean numbers; Smith (1976) for an theoretical discussion on the limit case of very high Dean numbers, where the main velocity gradients and the secondary flow are concentrated in rather thin layers along the fixed walls and an inviscid core occurs; Mori et al. (1971) for experimental evidence.

3.7. Reverse secondary circulation

A most striking phenomenon to be observed at the end of the intermediate Dean number range (De = 50 - 60) is the abrupt transition of the single-vortex pattern of the secondary flow into a double-vortex pattern: a second, counterrotating vortex develops near the surface in the outer wall region. For square pipes this phenomenon can be shown by the present mathematical model and it was also reported by Cheng et al. (1970), Joseph et al. (1975) and Cheng et al. (1976). The latter showed the second vortex to occur at sufficiently high Dean numbers in shallow channels, as well. Since a similar reverse circulation has often been observed in experiments on turbulent flow in curved channels (Yen, 1965; Rao, 1975; Choudhary et al., 1977; De Vriend et al., 1977; De Vriend, 1979b), it is worthwhile to try and find at least a qualitative explanation of this phenomenon.

This explanation can be found in the mutual influencing of the main and the secondary flow. At sufficiently high Dean numbers the secondary flow convection gives rise to negative vertical derivatives of the main velocity near the surface (cf. par. 3.5). Consequently, the source term in the secondary flow equation, $\frac{\partial}{\partial \zeta}(u^2)$, becomes negative there and hence the stream function of the secondary flow tends to become negative there. The corresponding reverse secondary circulation, however, tends to destroy itself as long as the main velocity shows an outward increase: the momentum surplus caused by the fluid conveyed from further outwards tends to make the velocity derivative and the source term in the secondary flow equation positive, again. In the outer wall region, however, the main velocity sharply decreases towards the outer wall. Hence the reverse circulation tends to intensify itself, its convective effect giving rise to a further reduction of the main velocity at the surface. This also explains the abruptness of the transition from the single-vortex to the double-vortex pattern: once the reverse circulation comes into existence near the outer wall, it intensifies itself as far as viscous forces permit.
The foregoing suggests the development of the additional vortex to be a matter of hydrodynamic instability. On closer investigation, the underlying mechanism appears to be essentially the same as for the so-called Görtler-vortices in the boundary layer along a concave wall (Görtler, 1940; see also Schlichting, 1951), for the instability of laminar flow in an infinitely deep narrow curved channel (Dean, 1928b) and for the so-called Taylor-vortices between two concentric rotating cylinders (Taylor, 1923; see also Schlichting, 1951). Each of these phenomena is characterized by a dimensionless number of the same nature as the Dean number.

3.8. Discussion

In the foregoing it has been shown that the secondary circulation in curved channel flow gives rise to a redistribution of the main velocity and hence to a redistribution and an overall increase of

the boundary shear stress. In rectangular channels the inner wall region appeared to play a most important part in this redistribution process: the transverse transport of momentum by the secondary flow gives rise to a local reduction of the main velocity there, which may influence the main velocity distribution in the greater part of the cross-section, especially if the Dean number is not small and the bend is long.
Regarding this influence of the inner wall, a mathematical model of the flow in curved rectangular channels should account for the sidewall regions, even if the channel is shallow (cf. par. 4.3). Therefore, in case of shallow rectangular channels, computations limited to the central region (Van Bendegom, 1947; Engelund, 1974; De Vriend, 1976 & 1977; Falcón, 1979) are doomed to fail.
In case of shallow channels with gently sloping banks, however, the sidewalls, if present at all, are much less important. Instead of being caused by the lateral diffusion in combination with the no-slip conditions at the sidewalls, the radial variations of the main velocity are mainly due to the transverse variation of the depth of flow then and consequently they are spread over a much wider region. Hence the vertical velocity component, which is the main cause of the velocity reduction near the inner wall in rectangular channels, is not concentrated in a pronounced peak near the sidewalls, but is spread out more evenly. This provides the possibility to make flow computations without accounting for sidewall regions or lateral diffusion (Kalkwijk et al., 1980; see also chapter 8).

3.9. Summary of conclusions

The conclusions to be drawn from the present chapter can be summarized in three groups, concerning the flow pattern, the mechanism of main velocity redistribution and the mathematical description of the flow, respectively.

1. The flow pattern.
Fully-developed laminar flow in curved (rectangular) channel is

strongly dependent on the Dean number Re/ε, characterizing the importance of the convective effect of the secondary flow on the main flow. For De increasing from 0 to about 60,

- the main velocity maximum shifts from the inner to the outer wall;
- the vertical distribution of the main velocity becomes flatter and for higher De the maximum even lies below the surface;
- the centre of circulation of the secondary flow gradually moves down;
- the centre of circulation of the secondary flow moves outwards up to a certain Dean number and then shifts inwards again;
- the secondary flow intensity increases, reaches a maximum at about the same Dean number (depending on the channel aspect ratio) and decreases again;
- on approaching the end of the Dean number range considered (De > about 50), suddenly a counterrotating secondary circulation develops near the surface in the outer bend;
- the longitudinal wall shear stress increases, especially in the outer bend;
- the longitudinal pressure gradient strongly increases in comparison with the one in the equivalent straight channel flow;
- the transverse pressure gradient is closely proportional to De^2, irrespective of the channel aspect ratio;
- the shape of the transverse pressure distribution changes from concave to convex;
- the vertical distribution of the pressure remains closely hydrostatic;
- the total flow energy concentrates near the outer wall.

Starting from the deformations of the main velocity distribution, all other phenomena can be explained satisfactorily.

2. The mechanism of main velocity distribution.

The transverse redistribution of the main velocity for De increasing from zero on is due to the convective transport of main flow momentum by the secondary flow. For shallow rectangular channels, the mechanism of this convective redistribution can be summarized as follows:

- near the inner wall, the momentum of the undisturbed main flow in-

creases along the streamlines of the secondary flow; convection of momentum along these streamlines gives rise to an overall reduction of u, which is strongest in the upper part of the cross-section; consequently, $\bar{u}$ is reduced throughout the inner wall region and the vertical distribution function $u/\bar{u}$ grows smaller in the upper half and larger in the lower half of the vertical;

- near the outer wall, the momentum of the undisturbed main flow decreases along the streamlines of the secondary flow, so that convection causes an increase of $\bar{u}$ and a skewing of the vertical distribution function $u/\bar{u}$;
- in the central part of the cross-section, the secondary flow, and hence the convective transport of main flow momentum, is almost horizontal, outward in the upper half of the vertical and inward in the lower half; in combination with the bottom shear stress as a damping factor, the resulting net outward transport of momentum causes a retarded outward expansion of the low velocity region near the inner wall and a compression of the high velocity region near the outer wall; as a consequence, the depth-averaged main velocity distribution tends to be skewed outwards and the vertical profile of the main velocity tends to be flattened in the greater part of the cross-section.

For De=0, the main velocity distribution is skewed inwards, due to the 'potential flow effect'. At low Dean numbers, the effects of secondary flow convection are small and they are confined to the sidewall regions. At intermediate Dean numbers, the effects of secondary flow convection in the sidewall regions grow stronger and there is a horizontal interaction that extends these effects over the whole cross-section. In high Dean number flow, a strong mutual interaction between the main and the secondary flow occurs, giving rise to 'hydrodynamic instability' in the form of a reverse secondary circulation near the outer wall.

3. The mathematical description of the flow.

The investigations of the complete Navier-Stokes model describing fully-developed steady laminar flow in curved rectangular ducts

have led to the following general conclusions:

- though maybe not the most efficient and powerful one, the present solution procedure for the complete Navier-Stokes equations, solving a fourth-order equation for the stream function of the secondary flow, yields good results at low and intermediate Dean numbers; for Dean numbers higher than about 60, as the reverse secondary circulation develops near the outer wall, the iterative solution procedure becomes ill-convergent;
- the group of terms representing the transverse inertia of the secondary flow is the only one that can be omitted from the system of equations without introducing important errors;
- the lateral diffusion terms are of minor importance in the central part of a shallow cross-section, but in the sidewall regions they cannot be disregarded;
- the secondary flow convection terms in the main flow equation cannot be disregarded, not even in a first approximation, unless the Dean number is very small; in a shallow channel, the vertical convection term causes mainly local deformations of the main velocity distribution, whereas the radial convection term is mainly responsible for lateral interaction;
- the bottom shear stress tends to make the transverse distribution of $\bar{u}$ more uniform; hence it attenuates the outwards skewing effect of secondary flow convection.

Further details on the effects of the various terms in the main flow equation are summarized in the following scheme.

	region of the cross-section					
	inner wall		central		outer wall	
	$\bar{u}$	f	$\bar{u}$	f	$\bar{u}$	f
vertical convection			unimportant			
radial convection						
vertical diffusion	viscous damping		retar-dation	visc. damp.	viscous damping	
radial diffusion	viscous damping		unimportant		viscous damping	

Legenda:

 important decrease

 slight decrease

 important increase

 slight increase

 important skewing

 slight skewing

 important flattening

 slight flattening

 outward skewing

4. Simplified computation methods for shallow channels

4.1. Relevance and approach

Even in the relatively simple case of steady fully-developed laminar curved flow the solution of the complete Navier-Stokes equations requires a considerable computational effort. In the mathematical model of the flow and the bed topography in curved alluvial rivers, however, the much more complicated problem of developing turbulent flow has to be solved once in everey time step made in the computation of the bottom configuration (see chapter 1). Hence fully three-dimensional flow computations would give rise to unacceptably high computer costs, so that considerable simplifications of the mathematical system are needed. The literature provides little information at this point. On the one hand there is a considerable amount of recent literature on the solution of the complete or almost-complete system of equations (fully-developed laminar flow: see also chapter 3; developing laminar flow: Patankar et al. (1974), Humphrey et al. (1977), Ghia et al. (1977); developing turbulent flow: Patankar et al. (1975), Pratap (1975), Pratap et al. (1975), Leschziner et al. (1978 & 1979)), on the other hand there is a long series of publications in which quite elementary perturbation techniques are applied (laminar flow: Boussinesq (1868), Dean (1928), Itō (1951), De Vriend (1973a & 1973b) and many others; turbulent flow: Ananyan (1956), Rozovskii (1961), Engelund (1964), Ikeda (1975), De Vriend (1976 & 1977), Falcón (1979) and many others). The wide range of possible simplifications between these two extremes, however, is paid hardly any attention in the literature. Therefore the most important of these simplifications will be investigated here.

A considerable reduction of computer time would be attained if it would be possible to simplify the calculations in a cross-section without loosing too much accuracy. Therefore the simplification of the mathematical model of fully-developed laminar flow (see chapter 3) will be studied first, with the complete model as a reference. Two types of simplifications

will be considered in this respect, viz. omitting unimportant terms from the differential equations and applying approximative computation methods, such as successive approximations and similarity solutions.

4.2. Simplification of the differential equations

4.2.1. Simplification of the longitudinal momentum equation

As suggested already by par. 3.6, none of the (groups of) terms distinguished in the longitudinal momentum equation is negligible throughout the cross-section.

- The vertical convection term plays a most important part near the sidewalls and especially its effect near the inner wall is indispensable for a proper description of the flow, even in the central region of the cross-section. If the cross-section is rectangular, the vertical convection term in the central region is negligible, but neglecting this term is not quite profitable since it means hardly a simplification of the mathematical problem.
  In addition, vertical convection is important where considerable vertical velocities occur and in the final model, dealing with a more or less arbitrary cross-sectional shape, these vertical velocities can be considerable in any part of the cross-section.
- The radial convection terms can be neglected neither near the sidewalls, where they have a local effect similar to the one of vertical convection, nor in the central region, where they give rise to a most important lateral interaction.
- The vertical diffusion term is indispensable throughout the cross-section.
- The lateral diffusion terms are only important near the sidewalls and even there the role is limited to damping sharp radial velocity variations and matching the velocity distribution with the no-slip conditions at the walls. This relative unimportance of lateral diffusion is readily illustrated by replacing the no-slip conditions at the sidewalls by full-slip conditions

(see figure 12b): the velocities near the sidewalls are influenced considerably, especially at higher Dean numbers, but the shape of the transverse velocity distribution away from the walls remains almost the same. This suggests that there must be possibilities for simplifications in the lateral diffusion terms, especially when bearing in mind that a detailed prediction of the flow close to a vertical sidewall is not likely to be quite important in the mathematical model to be developed.
On the other hand it should be noted that simplifications are only profitable if the second-order radial derivatives can be eliminated from the equation*).
If the lateral diffusion terms are simply neglected, however, additional measures should be taken in order to prevent the occurrence of spurious positive or negative velocity peaks and steep radial velocity gradients (cf. figure 12b; see also De Vriend, 1978a). Besides, the no-slip conditions at the sidewalls should be dropped then, as well, and it is not clear what lateral condition should be used in combination with the remaining equation (which is first-order in ξ), nor where this condition should be imposed. Therefore the possitility of omitting the lateral diffusion terms is rejected here.

It should be noted that many terms due to the curvate of the coordinate system, i.e. terms with $\frac{\varepsilon}{r}$, can be neglected. As these terms are always of a lower order than the leading terms of the same type, however, this neglect is hardly profitable.

4.2.2. Simplification of the stream function equation of the secondary flow

Two drastic simplifications of the stream function equation (3.24) for the secondary flow will be investigated, viz. neglecting the

---

*) The depth-averaged equation becomes first-order then and allows for much simpler computation methods, especially in case of developing flow (De Vriend, 1976 & 1977, Kalkwijk et al. , 1980).

convection terms and neglecting all radial derivatives in the diffusion terms.

Neglecting the non-linear convection terms greatly reduces the computational work, since the solving operator of the remaining equation becomes independent of the intermediate results of the iteration procedure then. Figure 15 gives an impression of the influence of the convection terms at a rather high Dean number (De = 50). As far as the main velocity distribution is concerned, this influence is small and even the secondary flow pattern is hardly influenced, except for the outer wall region, where ψ becomes somewhat higher. Hence it is concluded that the convection terms in the stream function equation of the secondary flow are negligible, indeed.

Another simplification of the stream function equation that would save a great deal of computer time is the neglect of all radial derivatives in the diffusion terms. In combination with the neglect of the convection terms, this would reduce the stream function equation to*)

$$\frac{\partial^4 \psi}{\partial \zeta^4} = \frac{\partial u^2}{\partial \zeta} \tag{4.1}$$

Imposing the boundary conditions (3.18) and 3.20), the solution of this equation can be written as

$$\psi = \int_{-1}^{\zeta} d\zeta \int_{-1}^{\zeta} d\zeta \int_{-1}^{\zeta} u^2 d\zeta - (1 + \frac{3}{2}\zeta - \frac{1}{2}\zeta^3) *$$

$$* \int_{-1}^{0} d\zeta \int_{-1}^{\zeta} d\zeta \int_{-1}^{\zeta} u^2 d\zeta - \frac{1}{4}\zeta(1+\zeta)^2 \int_{-1}^{0} u^2 d\zeta \tag{4.2}$$

, which can easily be evaluated numerically. If u=0 at the

*) The expressions for the secondary flow commonly used in the literature (Boussinesq (1868), Rozovskii (1961) and many others) are based on essentially the same simplifications.

sidewalls, this solution can be shown to satisfy both the condition of impermeability ($\psi = 0$) and the no-slip condition ($\frac{\partial \psi}{\partial \xi} = 0$) at these walls.
In the central region of the cross-section the simplification of the stream function equation to (4.1) seems to be allowable, but for the sidewall regions this is not quite evident. Therefore expression (4.2) has been evaluated for the whole cross-section on the basis of a main velocity distribution obtained by the complete model. At higher Dean numbers, the resulting stream function shows considerable deviations from the solution of the complete equation, especially in the outer wall region (see figure 16 for De = 50). Besides, replacing equation (3.24) in the mathematical model by its truncated version (4.1) gives rise to ill-convergence of the iterative solution procedure at Dean numbers at which the solution of the complete model is still convergent. Hence it is concluded that even in the stream function equation of the secondary flow the lateral diffusion terms should be treated with caution and cannot simply by neglected.
As to the terms due to the divergence of the coordinate system the same can be stated as in par. 4.2.1.: neglecting these terms is hardly profitable as they are of lower order than the leading terms of the same type.

4.3. Successive approximation methods

In the literature on flow in river bends successive approximation methods are widely used to solve the often strongly simplified governing differential equations (cf. par. 4.1). These methods are based on the expansion of each depedent variable in the mathematical system in a power series of a small parameter δ. Starting from the solution for $\delta = 0$, the successive terms of these series are determined one by one, making use of the knowledge of the foregoing ones (Van Dyke, 1964; Nayfeh, 1973). In practice the series expansions, with the curvature ratio or the (effective) Dean number as a perturbation parameter, are usually cut off after one of two non-zero terms.
Without pretending generality, table 4.1 gives some of the most important examples of the use of perturbation techniques for the

mathematical description of flow in shallow channel bends*)
(see also par. 4.1).

Author	flow type	develop-ment	vali-dity	number of non-zero terms	
				main flow	sec.flow
Boussinesq (1868)	L	F-D	C	1	1
Ananyan (1965)	L/T	F-D	CS	2	1
Rozovskii (1961)	L/T	F-D	C/S	1/2	1
De Vriend (1973a & 1973b)	L	F-D	CS/C/S	2	1
De Vriend (1976 & 1977)	T	D	C	2	1

(L = laminar; T = turbulent; F-D = fully-developed; D = developing;
C = central region; S = sidewall region; CS = whole cross-section).

Table 4.1 Applications of perturbation methods in curved channel flow

4.3.1. Successive approximation in the central region of a shallow channel

As was stated before, the commonly applied simplified computation method for the undisturbed main velocity and the secondary flow in the central region of very shallow curved channels can be considered as a strongly truncated perturbation method. Turbulent flow versions of this mehtod, widely used in river engineering practice, have been published in a great variety (see, for instance; Van Bendegom, 1947; Rozovskii, 1961; Yen, 1965; Engelund, 1974; Ikeda, 1975; De Vriend, 1976 & 1977; Falcón, 1979). Therefore the applicability of the laminar flow counterpart of this method (see also Boussinesq, 1868 and De Vriend, 1973a & 1973b) will be subject to a closer investigation.

*) Except for the oldest one (Boussinesp, 1868), the numerous publications with only the basic approximations for the main velocity and the secondary flow are not mentioned in this table.

In addition to a seldomly mentioned Reynolds number limitation (the effective Reynolds number is, often implicitly, supposed to be of the order $O(\varepsilon^0)$), the basic assumption of these models is that the influence of the sidewalls is restricted to a region close to these walls. Hence in shallow channels there is a central region, where the horizontal derivatives of the main velocity and of the stream function of the secondary flow are much smaller than the vertical ones. Accordingly, these radial derivatives can be normalized by R_c instead of d, so that the normalized longitudinal momentum equation becomes

$$\varepsilon^2 Re^2 \{- \frac{1}{r} \frac{\partial \psi}{\partial \zeta} (\frac{\partial u}{\partial r} + \frac{1}{r} u) + \frac{1}{r} \frac{\partial \psi}{\partial r} \frac{\partial u}{\partial \zeta}\} =$$

$$\frac{1}{r} + \frac{\partial^2 u}{\partial \zeta^2} + \varepsilon^2 (\frac{\partial^2 u}{\partial r^2} + \frac{1}{r} \frac{\partial u}{\partial r} - \frac{u}{r^2}) \qquad (4.3)$$

and the integral condition of continuity can be written as

$$\int_{1-B/2R_c}^{1+B/2R_c} dr \int_{-1}^{0} u d\zeta = B/R_c \qquad (4.4)$$

If secondary flow inertia is neglected, the normalized stream function equation becomes

$$\frac{\partial u^2}{\partial \zeta} = \frac{\partial^4 \psi}{\partial \zeta^4} + 2\varepsilon^2 (\frac{\partial^4 \psi}{\partial r^2 \partial \zeta^2} - \frac{1}{r} \frac{\partial^3 \psi}{\partial r \partial \zeta^2}) +$$

$$+ \varepsilon^4 (\frac{\partial^4 \psi}{\partial r^3} - \frac{2}{r} \frac{\partial^3 \psi}{\partial r^3} + \frac{3}{r^2} \frac{\partial^2 \psi}{\partial r^2} - \frac{3}{r^3} \frac{\partial \psi}{\partial r}) \qquad (4.5)$$

For $Re^2 = O(\varepsilon^0)$, this system can be solved by successive approximations with ε^2 as a perturbation parameter. This implies that u, or rather

$u' = u/\iota^{*})$, ι and ψ are expanded in power series of ε^2

$$u' = \sum_{k=0}^{\infty} \varepsilon^{2k} u'_k \; ; \qquad \iota = \sum_{k=0}^{\infty} \varepsilon^{2k} \iota_k \; ; \qquad \psi = \sum_{k=0}^{\infty} \varepsilon^{2k} \psi_k \tag{4.6}$$

If these expansions are formally substituted into (4.3) through (4.5), these equations can be rewritten to the form

$$Eq = \sum_{k=0}^{\infty} \varepsilon^{2k} Eq_k = 0 \tag{4.7}$$

in which the expressions Eq_k can contain u'_i, ι_i and ψ_i $(i = 0,1,\ldots,k)$. Equation (4.7) must hold for a continuous range of ε^2, which implies that the expression Eq_k must be equal to zero. This yields a series of equations

$$Eq_k = 0 \tag{4.8}$$

from which the k-th order variables can be solved.
Thus the zero order approximation of the present system becomes

$$\frac{\partial^2 u'_0}{\partial \zeta^2} = \frac{1}{r}; \qquad \int_{1-B/2R_c}^{1+B/2R_c} dr \int_{-1}^{0} \iota_0 u'_0 \, d\zeta = \frac{B}{R_c} \; ; \qquad \frac{\partial^4 \psi_0}{\partial \zeta^4} = \iota_0^2 \frac{\partial u_0'^2}{\partial \zeta} \tag{4.9}$$

With the appropriate boundary conditions this yields

$$u'_0 = \frac{1-\zeta^2}{2r}; \qquad \iota_0 = \frac{3B}{R_c} \left(\ln \frac{1+B/2R_c}{1-B/2Rc}\right)^{-1};$$

$$\psi_0 = \frac{\iota_0^2}{r^2} \frac{\zeta^7 - 7\zeta^5 + 11\zeta^3 - 5\zeta}{840} \tag{4.10}$$

---

*) Equation (4.3) can be rewritten as an equation for u', in which the source term $\frac{1}{r}$ is independent of ι. Thus the three variables u', ι and ψ can be solved one by one from separate equation.

Similarly, the higher order systems (for k = 1,2,3...) become

$$\frac{\partial^2 u'_k}{\partial \zeta^2} = -\left(\frac{\partial^2 u}{\partial r^2} + \frac{1}{r}\frac{\partial u}{\partial r} - \frac{u}{r^2}\right)_{k-1} +$$

$$+ \mathrm{Re}^2 \left\{-\frac{1}{r}\frac{\partial \psi}{\partial \zeta}\left(\frac{\partial u}{\partial r} + \frac{u}{r}\right) + \frac{1}{r}\frac{\partial \psi}{\partial r}\frac{\partial u}{\partial \zeta}\right\}_{k-1} \qquad (4.11)$$

$$\int_{1-B/2R_c}^{1+B/2R_c} dr \int_{-1}^{0} \iota_k u'_0 d\zeta = \int_{1-B/2R_c}^{1+B/2R_c} dr \int_{-1}^{0} -\sum_{i=1}^{k} \iota_{k-i}\, u'_i \, d\zeta \qquad (4.12)$$

$$\frac{\partial^4 \psi_k}{\partial \zeta^4} = -\frac{\partial}{\partial \zeta}(u^2)_k + 2\left(\frac{\partial^4 \psi}{\partial r^2 \partial \zeta^2} - \frac{1}{r}\frac{\partial^3 \psi}{\partial r \partial \zeta^2}\right)_{k-1} +$$

$$+ \left(\frac{\partial^4 \psi}{\partial r^4} - \frac{2}{r}\frac{\partial^3 \psi}{\partial r^3} + \frac{3}{r^2}\frac{\partial^2 \psi}{\partial r^2} - \frac{3}{r^3}\frac{\partial \psi}{\partial r}\right)_{k-2} \qquad (4.13)$$
$$(k>1)$$

For successively increasing k, the quantities u'_k, ι_k and ψ_k can be solved from these systems with the relevant boundary conditions. Substitution of the results into (4.6) yields successive approximations of u, ι and ψ, respectively. Neither the zero order approximation (4.10), nor any higher order approximation of the solution of (4.3) through (4.5) satisfies the boundary conditions at the sidewalls, since the radial derivatives in the system are at least an order ε^2 smaller than the leading terms and occur only as known source terms in the higher order systems (4.11) through (4.13). This incompatibility with the boundary conditions is consistent with the assumption that the sidewalls have no influence on the flow in the central region. The only way to satisfy the sidewall conditions is to determine a local solution for the sidewall regions (Rozovskii, 1961; De Vriend, 1973a & 1973b).

The applicability of the above method to the central region of a shallow channel was investigated by solving the system (4.11)-(4.12) with fixed secondary flow ($\psi=\psi_0$) for a shallow channel ($d/B = 0.1$; $\varepsilon = 0.04$) and Reynolds numbers up to 50 (i.e. Dean numbers up to 10). The perturbation was carried out on computer, up to the tenth-order approximation.
As is shown in figure 17, the basic solution (4.10) agrees well with the zero Dean number solution of the complete model, especially if ι_0 is replaced by the "exact" value of ι. According to figure 18a the procedure converges only for small Dean numbers (at the inner wall the depth-averaged main velocity "explodes" for De as small as 7.5). Besides, the main velocity distribution obtained by this method shows no trace of the outward skewing tendency in the solution of the comple system (figure 18b), by lack of the local velocity reduction near the inner wall (cf. par. 3.6). On the contrary, as a consequence of the inward skewed basic velocity distribution (giving rise to negative radial derivatives and negative vertical velocities), $\bar{u}$ tends to be skewed further inwards as De increases.
Hence it must be concluded that successive approximations of this type are only applicable at very low Dean numbers. As soon as secondary flow convection becomes important, however, they are essentially wrong. This conclusion stands when local solutions near the sidewalls are included, even if the method of matched asymptotic expansions is used (De Vriend, 1973a & 1973b): the solution in the central region is fully-determined in itself, so it cannot be influenced by these local solutions.

4.3.2. Low Dean number perturbations

Successive approximations of the solution in the whole cross-section with De (or rather: De^2) as a perturbation parameter are widely applied to pipe flow problems (Dean, 1928; Adler, 1934; Itō, 1951; Cuming, 1952). The successive approximation of the solution for the whole cross-section of a shallow channel presented by De Vriend (1973a & 1973b) can be rewritten as a set of low Dean number perturbation series that is applicable to less shallow channels, as well.

Since the cross-section is treated as a whole, the influence of convection could be properly represented. Hence it is worthwhile to investigate to what extent (read: Dean number) this perturbation method is applicable here.
For simplicity, the secondary flow is considered as being known, so that the system to be solved consists of the longitudinal momentum equation (3.13) and the integral condition of continuity (3.16). Introducing the perturbation series

$$u' = u/\iota = \sum_{k=0}^{\infty} De^{2k} u'_k \tag{4.14}$$

, the zero order longitudinal momentum equation becomes

$$\frac{\partial^2 u'_0}{\partial \zeta^2} + \frac{\partial^2 u'_0}{\partial \xi^2} + \frac{\varepsilon}{r}\frac{\partial u'_0}{\partial \xi} - \frac{\varepsilon^2}{r^2} u'_0 = -\frac{1}{r} \tag{4.15}$$

and the higher order equations ($k > 0$) read

$$\frac{\partial^2 u'_k}{\partial \zeta^2} + \frac{\partial^2 u'_k}{\partial \xi^2} + \frac{\varepsilon}{r}\frac{\partial u'_k}{\partial \xi} - \frac{\varepsilon^2}{r^2} u'_k = +$$

$$-\frac{1}{r}\frac{\partial \psi}{\partial \zeta}\left(\frac{\partial u'}{\partial \xi} + \frac{\varepsilon}{r} u'\right)_{k-1} + \frac{1}{r}\frac{\partial \psi}{\partial \xi}\left(\frac{\partial u'}{\partial \zeta}\right)_{k-1} \tag{4.16}$$

From these equation u'_k can be solved for successively higher k, independently of ι. The m-th order approximation of ι is given by

$$\iota^{(m)} = \frac{B}{d} \int_{-B/2d}^{B/2d} d\xi \int_{-1}^{0} \sum_{k=0}^{m} u'_k d\zeta \tag{4.17}$$

As an example, u was computed for the shallow channel mentioned before ($\varepsilon = 0.04$; $\frac{d}{B} = 0.1$), with k ranging up to 10 and the imposed secondary flow corresponding with u_0.

Figure 19 shows the results for gradually increasing Dean numbers. The agreement with the results of the complete model is far better now, even the influence of secondary flow convection being properly represented (at De = 7.5), but convergence is just as poor as for the central region perturbation: the series expandion (4.14) is divergent for De $\geq$ 10. This implies that low Dean number perturbations are not applicable as a solution technique for the present problem.

4.3.3. Depth-averaged equation derived by successive approximations

Although the successive approximation method with ε or De as a perturbation parameter fails at the Dean numbers of interest, it could be used to derive approximations of the depth-averaged equations (cf. De Vriend, 1976 & 1977, for turbulent flow). According to figures 3a and 3b, the influence of the Dean number on the vertical distribution of the main velocity becomes important at considerably higher values of De than the influence on the radial distribution*). Hence a low Dean number perturbation is likely to be applicable to the vertical distribution of u up to Dean numbers higher than 10, at least if the depth-averaged main velocity distribution is appropriately represented. This implies that the depth-averaged longitudinal momentum equation should account for the secondary flow convection and should include the sidewall regions.
The procedure to be followed when deriving the depth-averaged system can be outlined as follows. According to par. 3.6.2, the similarity approximation (3.41) holds good for u and ψ, so that the low Dean number limit can be approximated by

*) This accords with several turbulent flow experiments in curved shallow channels (Rozovskii, 1961; Yen, 1965; De Vriend et al., 1977; Nouh et al., 1979), from which it was concluded that the vertical distribution of the main velocity in a curved channel section is approximately the same as in a straight section, even though the radial distribution shows considerable deformations.

$$u_0(\xi,\zeta) = \bar{u}_0(\xi)\, f_0(\zeta) \quad \text{and} \quad \psi_0(\xi,\zeta) = \bar{\psi}_0(\xi)\, g_0(\zeta) \tag{4.18}$$

The vertical distribution functions $f_0(\zeta)$ and $g_0(\zeta)$ can be determined far from the sidewalls, where lateral diffusion is negligible and the system of zero-order equations reduces to (4.9). Since $\bar{f} = 1$ and $\bar{g} = 1$ by definition, this leads to

$$f_0(\zeta) = \frac{3}{2}(1 - \zeta^2) \quad \text{and} \quad g_0(\zeta) = \frac{24}{19}(\zeta^7 - 7\zeta^5 + 11\zeta^3 - 5\zeta) \tag{4.19}$$

The first-order perturbation of u_0 follows from (cf. equation 4.11)

$$\frac{\partial^2 u_1}{\partial \zeta^2} + \frac{\partial^2 u_1}{\partial \xi^2} + \frac{\varepsilon}{r}\frac{\partial u_1}{\partial \xi} - \frac{\varepsilon^2}{r^2} u_1 = -\frac{1}{r} - \frac{1}{r}\frac{\partial \psi_0}{\partial \zeta}\left(\frac{\partial u_0}{\partial \xi} + \frac{\varepsilon}{r} u_0\right) +$$

$$+ \frac{1}{r}\frac{\partial \psi_0}{\partial \xi}\frac{\partial u_0}{\partial \zeta} \tag{4.20}$$

Now u_1 is approximated by

$$u_1(\xi,\zeta) = \bar{u}_{1,0}(\xi)\, f_0(\zeta) + \bar{u}_{1,1}(\xi)\, f_{1,1}(\zeta) + \bar{u}_{1,2}(\xi)\, f_{1,2}(\zeta) \tag{4.21}$$

, in which the three components represent the contributions of the longitudinal slope term, the radial convection term and the vertical convection term, respectively. The functions $f_{1,1}$ and $f_{1,2}$ are solved from the systems

$$\frac{\partial^2 f'_{1,1}}{\partial \zeta^2} = -f_0 \frac{\partial g_0}{\partial \zeta} \quad \text{with} \quad f'_{1,1}\Big|_{\zeta=-1} = 0; \quad \frac{\partial f'_{1,1}}{\partial \zeta}\Big|_{\zeta=0} = 0$$

$$\text{and } f_{1,1} = f'_{1,1}/\overline{f'_{1,1}} \tag{4.22}$$

$$\frac{\partial^2 f'_{1,2}}{\partial \zeta^2} = g_0 \frac{\partial f_0}{\partial \zeta} \quad \text{with} \quad f'_{1,2}\Big|_{\zeta=-1} = 0; \quad \frac{\partial f'_{1,2}}{\partial \zeta}\Big|_{\zeta=0} = 0$$

$$\text{and} \quad f_{1,2} = f'_{1,2} / \overline{f'_{1,2}} \tag{4.23}$$

, derived from (4.20) in the central region, the boundary conditions at the bottom and the surface and the definitions of $f_{1,1}$ and $f_{1,2}$. The solutions of (4.22) and (4.23) are polynomials in ζ.

Making use of the information on the vertical distribution functions provided by (4.19) and the solutions of (4.22) and (4.23), the longitudinal momentum equation (3.13) can be averaged over the depth of flow to yield

$$\frac{\partial^2 \bar{u}}{\partial \xi^2} + \frac{\varepsilon}{r} \frac{\partial \bar{u}}{\partial \xi} - \left(\frac{\varepsilon^2}{r^2} + 3\right) \bar{u} = -\frac{1}{r} + De^2 \left[\frac{128}{95} \left\{\frac{\bar{\psi}}{r} \left(\frac{\partial \bar{u}}{\partial \xi} + \frac{\varepsilon}{r} \bar{u}\right) + \right.\right.$$

$$\left.\left. + \frac{\bar{u}}{r} \frac{\partial \bar{\psi}}{\partial \xi}\right\} - \frac{79}{52} \bar{u}_{1,1} - \frac{1}{26} \bar{u}_{1,2}\right] \tag{4.24}$$

The quantities $\bar{u}_{1,1}$ and $\bar{u}_{1,2}$ follow from (4.20), averaged over the depth of flow:

$$\frac{\partial^2 \bar{u}_{1,1}}{\partial \xi^2} + \frac{\varepsilon}{r} \frac{\partial \bar{u}_{1,1}}{\partial \xi} - \left(\frac{\varepsilon^2}{r^2} + \frac{77}{52}\right) \bar{u}_{1,1} = \frac{128}{95} \frac{\bar{\psi}}{r} \left(\frac{\partial \bar{u}}{\partial \xi} + \frac{\varepsilon}{r} \bar{u}\right) \tag{4.25}$$

$$\frac{\partial^2 \bar{u}_{1,2}}{\partial \xi^2} + \frac{\varepsilon}{r} \frac{\partial \bar{u}_{1,2}}{\partial \xi} - \left(\frac{\varepsilon^2}{r^2} + \frac{77}{26}\right) \bar{u}_{1,2} = \frac{128}{95} \frac{\bar{u}}{r} \frac{\partial \bar{\psi}}{\partial \xi} \tag{4.26}$$

Similarly, the depth-averaged stream function of the secondary flow becomes

$$\frac{\partial^4\bar{\psi}}{\partial\xi^4} - 2\,\frac{\varepsilon}{r}\,\frac{\partial^3\bar{\psi}}{\partial\xi^3} + \left(3\,\frac{\varepsilon^2}{r^2} - \frac{240}{19}\right)\frac{\partial^2\bar{\psi}}{\partial\xi^2} - \left(3\,\frac{\varepsilon^3}{r^3} - \frac{240}{19}\,\frac{\varepsilon}{r}\right)\frac{\partial\bar{\psi}}{\partial\xi} +$$

$$+ \frac{5040}{19}\,\bar{\psi} = \bar{u}^2\, f^2(0) \qquad (4.27)$$

With the appropriate boundary conditions, the system (4.24) through (4.27) can be solved iteratively. The zero Dean number solution could be used as a first estimate.
The procedure of solving $\bar{u}$ from the depth-averaged longitudinal momentum equation (4.24) and the additional equations (4.25) and (4.26) will be called semi-implicit, part of the convection terms in (4.24) being incorporated in the solving operator and part of them being introduced as known source terms.
As an example, this semi-implicit computation was carried out for the same shallow channel as in the foregoing paragraphs ($d/B = 0.1$; $\varepsilon = 0.04$), with the secondary flow fixed at its zero-order approximation. According to figure 20 convergence is far better now: even for De = 50 the procedure converges. The agreement with the equivalent solution of the complete system, however, becomes rather poor as De increases.
If in (4.25) and (4.26) the lateral diffusion terms are neglected, these equations reduce to explicit expressions of $\bar{u}_{1,1}$ and $\bar{u}_{1,2}$ in terms of $\bar{u}$ and $\bar{\psi}$. Substituting these expressions into (4.24) yields a fully-implicit equation for $\bar{u}$, reading

$$\frac{\partial^2\bar{u}}{\partial\xi^2} + \frac{\varepsilon}{r}\,\frac{\partial\bar{u}}{\partial\xi} - \left(\frac{\varepsilon^2}{r^2} + 3\right)\bar{u} = -\frac{1}{r} + De^2\,\frac{78}{77}\,\frac{128}{95}\left\{2\,\frac{\bar{\psi}}{r}\left(\frac{\partial\bar{u}}{\partial\xi} + \frac{\varepsilon}{r}\,\bar{u}\right) +\right.$$

$$\left. + \frac{\bar{u}}{r}\,\frac{\partial\bar{\psi}}{\partial\xi}\right\} \qquad (4.28)$$

As this equation is fully-implicit in $\bar{u}$ (apart from the influence of $\bar{u}$ on $\bar{\psi}$), no convergence problems are encountered when solving it.
In spite of the partial neglect of lateral diffusion, the

solution (4.28) for the aforementioned shallow channel with fixed zero-order secondary flow (see figure 20) agrees better with the solution of the complete system than the results of the aforementioned semi-implicit procedure. Still, for De > 20, considerable differences occur here, as well. Convergence grows poorer if the secondary flow is correlated to the actual depth-averaged velocity instead of being fixed at its zero order approximation (see figure 21), but if the procedure converges (De $\leq$ 10 for the semi-implicit procedure; De $\leq$ 17.5 for the fully-implicit one), the solution agrees better with the one of the complete system.
The conclusion to be drawn from the foregoing is that the iterative solution of $\bar{u}$ and $\bar{\psi}$ from depth-averaged equations on the basis of low Dean number approximations for the vertical distribution function f and g are not suited for the present purpose. Convergence is not guaranteed over a sufficiently wide range of Dean numbers and even if the procedure converges, the deviations from the solution of the complete system may be unacceptably large.

4.4. Similarity solution

A logical continuation of the foregoing is to maintain the similarity hypothesis (3.41), which has been shown to hold rather good, but to leave the low Dean number approximations of f and g. The alternative is to solve these functions from differential equations to be derived from the longitudinal momentum equation (3.13) and the stream function equation (3.24). If lateral diffusion is neglected, the longitudinal momentum equation yields (cf. equation 3.43)

$$\frac{\partial^2 f'}{\partial \zeta^2} - De^2 \left(\frac{1}{r}\frac{\partial \bar{\psi}}{\partial \xi}\right)\Big|_{\xi=\xi_0} g \frac{\partial f'}{\partial \zeta} +$$

$$+ De^2 \left(\frac{\bar{\psi}}{r\bar{u}}\frac{\partial \bar{u}}{\partial \xi} + \frac{\varepsilon}{r^2}\bar{\psi}\right)\Big|_{\xi=\xi_0} \frac{\partial g}{\partial \zeta} f' = -1 \qquad (4.29)$$

, with $f'\big|_{\zeta=-1} = 0; \quad \frac{\partial f'}{\partial \zeta}\Big|_{\zeta=0} = 0; \quad f = f'/\overline{f'}$ (4.30)

and ξ_0 indicating the vertical in which f is detérmined (the channel axis, for instance). Similarly, the stream function equation with the lateral diffusion terms and the convection terms neglected leads to

$$\frac{\partial^4 g'}{\partial \zeta^4} = \frac{\partial f^2}{\partial \zeta} \tag{4.31}$$

with $g'\big|_{\zeta=-1} = 0; \ \frac{\partial g'}{\partial \zeta}\Big|_{\zeta=-1} = 0; \ g'\big|_{\zeta=0} = 0;$

$$\frac{\partial^2 g'}{\partial \zeta^2}\Big|_{\zeta=0} = 0; \ g = g'/\overline{g'} \tag{4.32}$$

The system (4.29) through (4.32) can be applied in an iterative solution procedure in combination with the depth-averaged system (cf. equation 3.42)

$$\frac{\partial^2 \bar{u}'}{\partial \xi^2} + \frac{\varepsilon}{r}\frac{\partial \bar{u}'}{\partial \xi} - \left(\frac{\varepsilon^2}{r^2} + \frac{\partial f}{\partial \zeta}\Big|_{\zeta=-1}\right)\bar{u} =$$

$$-\frac{1}{r} + De^2\,\overline{g\,\frac{\partial f}{\partial \zeta}}\left\{\frac{\bar{\psi}}{r}\left(\frac{\partial \bar{u}'}{\partial \xi} + \frac{\varepsilon}{r}\bar{u}'\right) + \frac{\bar{u}'}{r}\frac{\partial \bar{\psi}}{\partial \xi}\right\} \tag{4.33}$$

with $\bar{u}'\Big|_{\xi=\pm\frac{B}{2d}} = 0$ and $\bar{u} = \frac{B\bar{u}'}{d} \Big/ \int_{-B/2d}^{B/2d} \bar{u}'\,d\xi$ (4.34)

$$\frac{\partial^4 \bar{\psi}}{\partial \xi^4} - 2\,\frac{\varepsilon}{r}\,\frac{\partial^3 \bar{\psi}}{\partial \xi^3} + \left(3\,\frac{\varepsilon^2}{r^2} + 2\,\frac{\partial g}{\partial \zeta}\Big|_{\zeta=0}\right)\left(\frac{\partial^2 \bar{\psi}}{\partial \xi^2} - \frac{\varepsilon}{r}\frac{\partial \bar{\psi}}{\partial \xi}\right) +$$

$$+ \left(\frac{\partial^3 g}{\partial \zeta^3}\Big|_{\zeta=0} - \frac{\partial^3 g}{\partial \zeta^3}\Big|_{\zeta=-1}\right)\bar{\psi} = \bar{u}^2 f^2\Big|_{\zeta=0} \tag{4.35}$$

with $\bar{\psi}\big|_{\xi=\pm\frac{B}{2d}} = 0$ and $\frac{\partial\bar{\psi}}{\partial\xi}\big|_{\xi=\pm\frac{B}{2d}} = 0$ (4.36)

As was shown in par. 3.6.2, equation (4.29) yields satisfactory results of f at low and intermediate Dean numbers if $\bar{u}$, $\bar{\psi}$ and g resulting from the complete model are introduced as known functions. Similarly, $\bar{u}$ is appropriately described by (4.33) with $\bar{\psi}$, f and g as known functions, so that an iterative procedure based on (4.29) through (4.36) may be expected to give better results than the simplified models studied hitherto.
This iterative solution procedure was applied to the shallow "test-channel" ($\varepsilon = 0.04$; $\frac{d}{B} = 0.1$). Figure 22a shows that convergence is hardly a problem: when applying a damping rule of the form

$$\bar{u}^{(k)} = \alpha u^{(k-1)} + (1 - \alpha)\,\bar{u}^{(k)} \quad \text{with} \quad \alpha < 1 \tag{4.37}$$

, convergence can be attained up to the end of the intermediate Dean number range ($De < 50$). According to figures 22b through e, there is a good agreement between the results of the present system and the complete model; the influence of secondary flow convection is appropriately represented. Only near the sidewalls, especially near the outer wall, considerable deviations are found, but since the sidewall regions are of no direct interest to the final model, these deviations are acceptable as long as their influence does not extend to the other parts of the cross-section.
From the same point of view, even artifices suppressing the spurious velocity peak near the outer wall are acceptable as long as the velocity distribution further inwards is not disturbed. Thus the applicability of the present procedure can be extended up to the Dean numbers at which it becomes divergent.
Regarding all this, the iterative procedure solving (4.29) through (4.36) is thought to be suited as a simplified

computation method for fully-developed laminar flow in shallow channels. Though this similarity procedure is not as cheap as the simplified computation methods treated in the foregoing paragraphs, it still reduces computer costs considerably (say by a factor 5 to 10), especially if the channel is very shallow.

4.5. Discussion

The foregoing paragraphs lead to the conclusion that the commonly used simplified computation methods for curved shallow channel flow are not applicable to rectangular channels for a sufficiently wide range of (effective) Dean numbers, whereas the similarity hypothesis (3.41) appears to be a suitable basis for simplification of the mathematical model. Once again (see also par. 3.8) it should be stressed, however, that shallow channel approximations can apply to channels with gently sloping banks instead of vertical sidewalls, provided that the secondary flow convection terms are incorporated in the longitudinal momentum equation, even in the lowest order of approximation.

The similarity hypothesis holds good in fully-developed flow, but this does not imply that it will do so in developing flow, as well. Longitudinal accelerations, for instance, are known to give rise to deformations of the velocity profile (chlichting, 1951; De Vriend, 1976 & 1977), so that the similarity may be affected by the longitudinal accelerations occurring in developing curved channel flow. Therefore the applicability of the similarity hypothesis in developing flow computations will have to be verified.

There is no reason why the similarity hypothesis should no longer hold good if the flow is turbulent instead of laminar. Besides, similarity has been shown in various experiments on turbulent curved channel flow (Rozovskii, 1961; Yen, 1965; De Vriend et al., 1977 & 1978). So a simplification of the mathematical model on the basis of (3.41) is likely to be possible for turbulent flow, as well.

4.6. Summary of conclusions

The conclusions to be drawn from the investigations of simplified computation methods for curved shallow channel flow can be outlined as follows:

- in curved channels with a shallow rectangular cross-section, the sidewall regions can only be left out of consideration if secondary flow convection is of minor importance to the main velocity distribution, i.e. if the Dean number is very small ($De < 5$); consequently, the commonly applied computation methods for flow in river bends, on the basis of a shallow channel approximation, cannot be used for rectangular channel flow as soon as curvature effects are important; for the same reason, computation methods considering the central region and the sidewall region separately, such as the method of matched asymptotic expansions, will fail if the Dean number is not very small;
- if the cross-section is treated as a whole, the main and the secondary flow at Dean numbers smaller than about 10 can be approximated by a low Dean number expansion, with the influence of secondary flow convection excluded from the basic solution of u; in that case, successive approximations with De^2 as a perturbation parameter can be used to solve the mathematical system; for Dean numbers higher than 10, however, the effects of secondary flow convection must be incorporated even in a first approximation of the main velocity distribution;
- a compound solution procedure, solving the set of depth-averaged equations to be derived on the basis of low Dean number expansions for the vertical distributions of the velocity components, yields good results up to higher values of De (15 to 20) than complete low Dean number expansions; still, this range is not wide enough to cover the effective Dean number range that can be expected in river bends (De_0 up to 50);
- in shallow channels, the vertical distributions of the main and the secondary velocity components are closely self-similar in the larger part of each cross-section; this similarity can be used as a basis for an iterative computational procedure, in which the horizontal and the vertical distributions of the velocity components

are calculated alternately; this procedure yields satisfactory predictions of the flow in the larger part of a cross-section (for De > 20, spurious peaks in the velocities are introduced locally near the outer wall) and almost throughout the Dean number range considered (only if the interaction between the main and the secondary flow is so strong, that the aforementioned similarity is violated, the procedure yields erroneous results).

Though these conclusions are based on laminar flow computations, they will also apply to turbulent flow, provided that De is replaced by the effective Dean number De_0 (based on the overall mean turbulence viscosity instead of the molecular viscosity; see chapter 6) and the quantitative specifications mentioned herein are considered as global indications.

5. Computation of developing laminar flow in curved rectangular channels

5.1. Objective of the investigation

There are three important differences between fully-developed laminar flow in curved rectangular channels as considered in the foregoing and turbulent flow in shallow river bends as to be described by the final mathematical model, viz.

- streamwise variations of the flow, due to longitudinal variations of the channel curvature,
- turbulence, and
- the influence of the non-rectangular cross-sectional shape and its longitudinal variations.

In order to avoid too many complications at one time, these extensions of the model will be introduced one by one.

A rather logical continuation of the fully-developed laminar flow analysis is to consider developing laminar flow in shallow rectangular channels of varying curvature. Then the flow variations due to the longitudinal variation of the channel curvature form the only new aspect to be dealt with. This provides the possibility to establish a simplified computation procedure for developing flow without complications due to turbulence or cross-sectional geometry.

5.2. Main and secondary flow

Putting $\alpha \equiv 1$ since the flow is laminar and $h \equiv 1$ since the channel is rectangular, the normalized system (2.30) through (2.36) will be simplified on the basis of the experience gained from the investigation of fully-developed flow (chapters 3 and 4). The approximations of the main and the secondary flow that were made there will be transposed to the main and the secondary velocity components in developing flow, starting from the following definition:

> the horizontal velocity component in the direction of the streamlines of the depth-averaged flow field (called streamwise direction hereafter) is the horizontal component of the main velocity; the horizontal velocity component perpendicular to this streamwise direction is the horizontal component of the secondary flow.

This definition is based on the idea that the secondary flow causes no net outward or inward discharge. In the limit case of fully-developed flow, the main velocity becomes tangential and the horizontal component of the secondary flow becomes radial. The above definition allows for a vertical component of the main as well as the secondary flow. If the main and secondary constituents of the velocity components u, v and w are defined by

$$u = u_m + \varepsilon^2 u_s; \quad v = v_m + v_s; \quad w = w_m + w_s \tag{5.1}^{*)}$$

(the suffix m standing for main and s for secondary), then the vertical velocity components can be defined by splitting the equation of continuity into two parts:

$$\frac{1}{r}\frac{\partial u_m}{\partial \phi} + \frac{\partial v_m}{\partial \xi} + \frac{\varepsilon}{r} v_m + \frac{\partial w_m}{\partial \zeta} = 0 \tag{5.2}$$

and

$$\frac{\varepsilon^2}{r}\frac{\partial u_s}{\partial \phi} + \frac{\partial v_s}{\partial \xi} + \frac{\varepsilon}{r} v_s + \frac{\partial w_s}{\partial \zeta} = 0 \tag{5.3}$$

Averaging equation (5.2) over the depth of flow yields

$$\frac{1}{r}\frac{\partial \bar{u}}{\partial \phi} + \frac{\partial \bar{v}}{\partial \xi} + \frac{\varepsilon}{r}\bar{v} = 0 \tag{5.4}$$

and since the definition of main and secondary flow states

$$\frac{v_m}{u_m} = \frac{\bar{v}}{\bar{u}} \text{ and hence } \frac{u_m}{\bar{u}} = \frac{v_m}{\bar{v}} \tag{5.5}$$

---

*) The tangential component of the secondary flow must be of the order $0(\varepsilon^2)$, since both the secondary flow and the deviation of the main flow direction from the tangential direction are of the order $0(\varepsilon)$.

, equation (5.2) can be elaborated to

$$\frac{\partial w_m}{\partial \zeta} = - \frac{\bar{u}}{r} \frac{\partial}{\partial \phi} \left(\frac{u_m}{\bar{u}}\right) - \bar{v} \frac{\partial}{\partial \xi} \left(\frac{v_m}{\bar{v}}\right) \tag{5.6}$$

Obviously, the vertical component of the main velocity is caused by streamwise variations of the vertical distribution of the horizontal main velocity.

5.3. Simplification of the mathematical system

In the first instance, the mathematical system will be simplified by neglecting terms that are an order $O(\varepsilon^2)$ smaller than the leading terms of the same type and terms that have appeared negligible in fully-developed flow. In addition, the vertical distribution of the main velocity is assumed to vary only weakly in the streamwise direction, so that the convection terms due to w_m can be neglected in the momentum equations. The resulting equations read

$$\frac{1}{r} \frac{\partial u_m}{\partial \phi} + \frac{\partial v_m}{\partial \xi} + \frac{\varepsilon}{r} v_m + \frac{\partial w_m}{\partial \zeta} = 0 \tag{5.7}$$

$$\frac{\partial v_s}{\partial \xi} + \frac{\varepsilon}{r} v_s + \frac{\partial w_s}{\partial \zeta} = 0 \tag{5.8}$$

$$\varepsilon \mathrm{Re} \left(\frac{u_m}{r} \frac{\partial u_m}{\partial \phi} + v_m \frac{\partial u_m}{\partial \xi} + \frac{\varepsilon}{r} u_m v_m + v_s \frac{\partial u_m}{\partial \xi} + w_s \frac{\partial u_m}{\partial \zeta} + \frac{\varepsilon}{r} v_s u_m\right) =$$

$$- \frac{1}{r} \frac{\partial p}{\partial \phi} + \nabla^2 u_m \tag{5.9}$$

$$\varepsilon^3 \mathrm{Re} \left(\frac{u_m}{r} \frac{\partial v_m}{\partial \phi} + v_m \frac{\partial v_m}{\partial \xi} + \frac{u_m}{r} \frac{\partial v_s}{\partial \phi} + v_m \frac{\partial v_s}{\partial \xi} + v_s \frac{\partial v_m}{\partial \xi} + w_s \frac{\partial v_m}{\partial \zeta}\right) +$$

$$- \varepsilon^2 \mathrm{Re} \frac{u_m^2}{r} = - \frac{\partial p}{\partial \xi} + \varepsilon^2 (\nabla^2 v_m + \nabla^2 v_s) - 2 \frac{\varepsilon^3}{r^2} \frac{\partial u_m}{\partial \phi} \tag{5.10}$$

$$\varepsilon^3 Re \left(\frac{u_m}{r}\frac{\partial w_s}{\partial \phi} + v_m \frac{\partial w_s}{\partial \xi}\right) = -\frac{\partial p}{\partial \zeta} + \varepsilon^2 \nabla^2 w_s \qquad (5.11)$$

Two important groups of terms in these equations vanish in fully-developed flow, viz. the terms representing the streamwise inertia of the main and the secondary flow. It will be clear that the main flow inertia should be taken into account in bends of not very mild curvature, but the importance of the secondary flow inertia remains to be investigated.
To that end the rate of decay of the secondary flow in a straight channel beyond a bend is considered (see Appendix B). If the streamline curvature is assumed to be zero from the bend exit on, the distance needed for the secondary flow to be reduced to 10% of its original strength is given by

$$l_{0.1} = 0.14\ Re\ d \qquad (5.12)$$

So for the Reynolds numbers to be considered (up to a few hundreds; cf. chapter 3), this distance will range up to some 10-20 times the depth of flow. For shallow channels this implies that the length of attenuation of the secondary flow after an abrupt vanishing of its sources is of the same order of magnitude as the channel width. The streamline curvature, however, which is the main source of the secondary flow, also decays over a distance of this order of magnitude. Hence the streamwise inertia of the secondary flow cannot be disregarded when attention is focused on the computation of the secondary flow itself or of quantities in which it plays an important part.
The principal purpose of the present model is the computation of the main velocity distribution and the bottom shear stress. As will be shown in par. 5.6, the computational procedure to be used consists of two subsequent steps, viz. a main flow computation step and a bottom shear stress computation step. The neglect of the streamwise inertia of the secondary flow will be considered for either step.

In chapter 3 the main velocity distribution in fully-developed flow was shown to be influenced strongly by the secondary flow. Experiments on developing turbulent flow in curved channels, however, have shown this influence needs a rather long distance to establish (see De Vriend, 1976; De Vriend et al., 1977; De Vriend, 1979b). Besides, the main velocity in a straight reach beyond a bend needs a rather long distance to reach its straight channel distribution (Rozovskii, 1961; De Vriend, 1978b). As a consequence of this retarded response of the main flow, local errors in the secondary flow near the entrance and the exit of a bend will not give rise to important errors in the main velocity distribution. Hence neglecting the streamwise inertia of the secondary flow seems acceptable in the main flow computation step.

The radial and vertical momentum equations to be solved in the main flow computation step then become

$$\varepsilon^3 Re \left(\frac{u_m}{r}\frac{\partial v_m}{\partial \phi} + v_m \frac{\partial v_m}{\partial \xi} + v_s \frac{\partial v_m}{\partial \xi} + w_s \frac{\partial v_m}{\partial \zeta}\right) - \varepsilon^2 Re \frac{u_m^2}{r} =$$

$$- \frac{\partial p}{\partial \xi} + \varepsilon^2 (\nabla^2 v_m + \nabla^2 v_s) - 2 \frac{\varepsilon^3}{r^2} \frac{\partial u_m}{\partial \phi} \qquad (5.13)$$

$$0 = - \frac{\partial p}{\partial \zeta} + \varepsilon^2 \nabla^2 w_s \qquad (5.14)$$

The bottom shear stress, and especially its direction, is influenced much more directly by the secondary flow. Since the direction of the bottom shear stress is of predominant importance to the transverse bottom configuration in alluvial channel bends, the secondary flow inertia must certainly be accounted for in the bottom shear stress computation step.

5.4. Interpretation of the simplified equations

In spite of the simplifications, the momentum equations derived in the foregoing paragraph, especially the radial one, are not

very transparent.

A better insight into the structure of the equations is obtained by transforming them to stream-oriented coordinates. To that end a curvilinear coordinate system (n,s,ζ) is defined, in which s is the distance along the streamlines of the depth-averaged flow, normalized by R_c, and n the distance along the normal lines, normalized by d*). If the corresponding s- and n-wise velocity components are denoted by u_m and $v_m + v_s$, respectively, v_m is identically equal to zero by definition. The transformation of which no details will be given, leads to the following equations of continuity:

$$\frac{\partial u_m}{\partial s} - \frac{u_m}{r_n} + \frac{\partial w_m}{\partial \zeta} = 0 \tag{5.15}$$

$$\frac{\partial v_s}{\partial n} - \frac{\varepsilon}{r_s} v_s + \frac{\partial w_s}{\partial \zeta} = 0 \tag{5.16}$$

, where $1/r_s$ and $1/r_n$ are the local curvatures (normalized by R_c) of the streamlines and the normal lines, respectively**). The transformed momentum equations read

$$\varepsilon Re \left\{u_m \frac{\partial u_m}{\partial s} + v_s \left(\frac{\partial u_m}{\partial n} - \frac{\varepsilon}{r_s} u_m \right) + w_s \frac{\partial u_m}{\partial \zeta}\right\} = - \frac{\partial p}{\partial s} + \nabla_1^2 u_m \tag{5.17}$$

$$\varepsilon^3 Re\, u_m \frac{\partial v_s}{\partial s} + \varepsilon^2 Re \frac{u_m^2}{r_s} = - \frac{\partial p}{\partial n} + \varepsilon^2 \nabla_1^2 v_s + \varepsilon^2 \frac{\partial \tilde{\omega}_m}{\partial s} \tag{5.18}$$

---

*) s increases in the main flow direction, n from the left bank on (see also figure 23).

**) $1/r_s$ is taken positive when the normal lines converge and $1/r_n$ is taken positive when the streamlines converge.

$$\varepsilon^3 \mathrm{Re}\, u_m \frac{\partial w_s}{\partial s} = - \frac{\partial p}{\partial \zeta} + \varepsilon^2 \nabla_1^2 w_s \qquad (5.19)$$

in which $\nabla_1^2 = \frac{\partial^2}{\partial \zeta^2} + \frac{\partial^2}{\partial n^2} - \frac{\varepsilon}{r_s} \frac{\partial}{\partial n}$ and $\tilde{\omega}_m = - \frac{\partial u_m}{\partial n} + \frac{\varepsilon}{r_s} u_m$.

In this transformed system the main and the secondary flow are separated, in that the main flow is described by equations (5.15) and (5.17) and the secondary flow follows from equations (5.16), (5.18), and (5.19). The main flow momentum equation (5.17) accounts for the streamwise inertia of the main flow and for transverse convection and diffusion. The secondary flow equations (5.18) and (5.19) involve streamwise inertia and transverse diffusion terms and two types of source terms, viz. the usual centrifugal term (based on the local streamwise curvature now) and a term due to the streamwise variation of the main flow vorticity. As the former term is of the order $0(\varepsilon^2 \mathrm{Re})$ and the latter of the order $0(\varepsilon^2)$, the vorticity term is likely to be of minor importance as a source of secondary flow.

The main flow momentum equation (5.17) can be used to analyse the mechanism of the transverse redistribution of the main velocity under the influence of secondary flow convection. If lateral diffusion is disregarded and

$$u_m = \bar{u}_m (n,s)\, f(\zeta) \qquad (5.20)$$

, then equation (5.17) can be rewritten as

$$\varepsilon \mathrm{Re}\, \overline{f^2}\, \bar{u}_m \frac{\partial \bar{u}_m}{\partial s} + \varepsilon \mathrm{Re}\, \overline{v_s f} \frac{\partial \bar{u}_m}{\partial n} + \{\frac{\partial f}{\partial \zeta}\Big|_{\zeta=-1} - \frac{\varepsilon^2 \mathrm{Re}}{r_s} \overline{v_s f} +$$

$$+ \varepsilon \mathrm{Re}\, \overline{w_s \frac{\partial f}{\partial \zeta}}\} \bar{u}_m = - \frac{\partial \bar{p}}{\partial s} \qquad (5.21)$$

Along the characteristics

$$\frac{dn}{ds} = \overline{v_s f}/(\bar{u}_m \overline{f^2}) \tag{5.22}$$

this equation becomes

$$\varepsilon Re\ \overline{f^2}\ \bar{u}_m \frac{d\bar{u}_m}{ds} + \{\frac{\partial f}{\partial \zeta}\Big|_{\zeta=-1} + \varepsilon Re\ \overline{w_s \frac{\partial f}{\partial \zeta}}\}\ \bar{u}_m = -\frac{d\bar{p}}{ds} \tag{5.23}$$

(cf. Kalkwijk et al., 1980).
The quantity $\overline{v_s f}$ tends to be positive when the normal lines diverge (i.e. $1/r_s$ negative) and negative when they converge*). Hence the characteristics (5.22) will be directed outwards, at least at some distance downstream of a point where the streamline curvature changes sign.
The quantity in braces in equation (5.23) will be positive as long as w_s is not distinctly negative, i.e. away from the outer wall. Then the depth-averaged main velocity will show a retarded adaptation to its source $-\frac{d\bar{p}}{ds}$. Close to the outer wall, however, the damping factor in (5.23) can become negative and in that case the main velocity would tend to increase exponentially along the characteristics if it were not damped by lateral diffusion.
As a consequence of the outward characteristic direction and the damping character of equation (5.23) in the greater part of the cross-section, the influence of the local main velocity reduction in the inner wall region (due to secondary flow convection; see chapter 3) will gradually extend further outwards, growing weaker and weaker. Hence the main velocity redistribution in developing curved flow at a constant intermediate Dean number shows a striking resemblance with the deformation of the main

---

*) The streamwise inertia of the secondary flow keeps the sign of $\overline{v_s f}$ from being determined exclusively by the sign of the local streamline curvature.

velocity distribution in fully-developed flow at gradually increasing De (chapter 3). In the first part of the bend, where the secondary flow is still establishing, the potential flow effect will dominate (cf. low Dean number flow; see also figure 3), but on proceeding through the bend the influence of secondary flow convection becomes perceptible, first in the inner wall region, later on also in a gradually extending part of the central region.

5.5. Similarity approximation in the main flow computation step.

In chapters 3 and 4 the similarity approximation (3.41) was shown to hold good for fully-developed flow in shallow curved channels. A generalized form of this approximation is adopted for developing flow, at least in the main flow computation step (cf. par. 5.3). Accordingly, the main velocity components are given by

$$u_m = \bar{u}\, f(\zeta;\phi) \qquad \text{and} \qquad v_m = \bar{v}\, f(\zeta;\phi) \tag{5.24}$$

, i.e. the vertical distribution function f is assumed to be invariant in a cross-section, but it is allowed to vary weakly with ϕ, in such a way that its ϕ-derivatives are negligible with respect to the ϕ-derivatives of $\bar{u}$.
The equation of continuity (5.8) allows for the definition of a stream function for the secondary flow. Regarding (3.8) and (3.12) and adopting the same similarity approximation as for the main flow, this definition reads

$$v_s = -\frac{Re}{r}\frac{\partial \psi}{\partial \zeta} \qquad \text{and} \qquad w_s = \frac{Re}{r}\frac{\partial \psi}{\partial \xi} \qquad \text{with} \qquad \psi = \bar{\psi}\, g(\zeta;\phi) \tag{5.25}$$

Substituting (5.24) and (5.25) into the longitudinal momentum equation (5.9) and neglecting the derivatives of f and g with respect to ϕ leads to

$$\varepsilon Re\ f^2(\frac{\bar{u}}{r}\frac{\partial\bar{u}}{\partial\phi} + \bar{v}\frac{\partial\bar{u}}{\partial\xi} + \frac{\varepsilon}{r}\overline{vu}) + \varepsilon Re^2\ \{- f\frac{\partial g}{\partial\zeta}\frac{\bar{\psi}}{r}(\frac{\partial\bar{u}}{\partial\xi} + \frac{\varepsilon}{r}\bar{u}) +$$

$$+ g\frac{\partial f}{\partial\zeta}\frac{\bar{u}}{r}\frac{\partial\bar{\psi}}{\partial\xi}\} = -\frac{1}{r}\frac{\partial p}{\partial\phi} + \frac{\partial^2 f}{\partial\zeta^2}\bar{u} + f(\frac{\partial^2\bar{u}}{\partial\xi^2} + \frac{\varepsilon}{r}\frac{\partial\bar{u}}{\partial\xi}) \qquad (5.26)$$

Another conclusion to be drawn from the fully-developed flow investigations is that the pressure is almost hydrostatic. Hence the longitudinal pressure gradient can be assumed independent of ζ and (5.26) can be considered as an equation for f with a constant source term. If the quantitiy f^2 in the main flow convection terms is approximated by $\hat{f}f$, $\hat{f}$ denoting a known estimate of f, equation (5.26) becomes linear in f. As a consequence, the unknown variable f in this equation can be replaced by the quantity $f' = -f(\frac{1}{r}\frac{\partial p}{\partial\phi})^{-1}$. If, in addition, the vertical distribution functions are evaluated in the channel axis, where lateral diffusion is negligible, equation (5.26) can be replaced by

$$\bar{u}\frac{\partial^2 f'}{\partial\zeta^2} - De^2\frac{\bar{u}}{r}\frac{\partial\bar{\psi}}{\partial\xi}g\frac{\partial f'}{\partial\zeta} + \{De^2\frac{\bar{\psi}}{r}(\frac{\partial\bar{u}}{\partial\xi} + \frac{\varepsilon}{r}\bar{u})\frac{\partial g}{\partial\zeta} +$$

$$- \varepsilon Re\ (\frac{\bar{u}}{r}\frac{\partial\bar{u}}{\partial\phi} + \bar{v}\frac{\partial\bar{u}}{\partial\xi} + \frac{\varepsilon}{r}\overline{vu})\hat{f}\ \}\ f' = -1 \qquad (5.27)$$

and $f = f'/\overline{f'}$. If $\bar{u}$, $\bar{\psi}$ and $\bar{g}$ are known, f can be solved from this equation and conditions (4.30).
Averaging equation (5.26) over the depth of flow yields

$$\varepsilon Re\ \overline{f^2}\ (\frac{\bar{u}}{r}\frac{\partial\bar{u}}{\partial\phi} + \bar{v}\frac{\partial\bar{u}}{\partial\xi} + \frac{\varepsilon}{r}\overline{uv}) + De^2\ \overline{g\frac{\partial f}{\partial\zeta}}\{\frac{\bar{\psi}}{r}(\frac{\partial\bar{u}}{\partial\xi} + \frac{\varepsilon}{r}\bar{u}) +$$

$$+ \frac{\bar{u}}{r}\frac{\partial\bar{\psi}}{\partial\xi}\} = -\frac{1}{r}\frac{\partial\bar{p}}{\partial\phi} + \frac{\partial^2\bar{u}}{\partial\xi^2} + \frac{\varepsilon}{r}\frac{\partial\bar{u}}{\partial\xi} - \bar{u}\left.\frac{\partial f}{\partial\zeta}\right|_{\zeta=-1} \qquad (5.28)$$

Similarly, the depth-averaged version of the radial momentum equation (5.13) reads

$$\varepsilon^3 \mathrm{Re}\ \overline{f^2}\ (\frac{\bar{u}}{r}\frac{\partial \bar{v}}{\partial \phi} + \bar{v}\frac{\partial \bar{v}}{\partial \xi}) - \varepsilon^2\ \mathrm{Re}\ \overline{f^2}\ \frac{\bar{u}^2}{r} + \varepsilon^2 \mathrm{De}^2\ \overline{g\ \frac{\partial f}{\partial \zeta}}\ \{\frac{\bar{\psi}}{r}\frac{\partial \bar{v}}{\partial \xi} + \frac{\bar{v}}{r}\frac{\partial \bar{\psi}}{\partial \xi}\} =$$

$$-\frac{\partial \bar{p}}{\partial \xi} + \varepsilon^2\ \{\frac{\partial^2 \bar{v}}{\partial \xi^2} + \frac{\varepsilon}{r}\frac{\partial \bar{v}}{\partial \xi} - \bar{v}\left.\frac{\partial f}{\partial \zeta}\right|_{\zeta=-1} +$$

$$+ \mathrm{Re}\ \frac{\bar{\psi}}{r}\left.\frac{\partial^2 g}{\partial \zeta^2}\right|_{\zeta=-1}\} - 2\frac{\varepsilon^3}{r^2}\frac{\partial \bar{u}}{\partial \phi} \qquad (5.29)$$

Together with the depth-averaged equation of continuity and an appropriate set of boundary conditions, equations (5.28) and (5.29) can be used to determine the depth-averaged velocity and pressure fields.
The stream function equation for the secondary flow to be derived from the momentum equations (5.13) and (5.14) reads

$$\frac{1}{r}\ (\frac{\partial^4 \bar{\psi}}{\partial \xi^4} - 2\frac{\varepsilon}{r}\frac{\partial^3 \bar{\psi}}{\partial \xi^3})\ g + \frac{2}{r}\ (\frac{\partial^2 \bar{\psi}}{\partial \xi^2} - \frac{\varepsilon}{r}\frac{\partial \bar{\psi}}{\partial \xi})\ \frac{\partial^2 g}{\partial \zeta^2} + \frac{\bar{\psi}}{r}\frac{\partial^4 g}{\partial \zeta^4} =$$

$$\frac{1}{\mathrm{Re}}\ \{(\frac{\partial^2 \bar{v}}{\partial \xi^2} + \frac{\varepsilon}{r}\frac{\partial \bar{v}}{\partial \xi} - 2\frac{\varepsilon}{r^2}\frac{\partial \bar{u}}{\partial \phi})\ \frac{\partial f}{\partial \zeta} + \bar{v}\frac{\partial^3 f}{\partial \zeta^3}\} - \{\varepsilon(\frac{\bar{u}}{r}\frac{\partial \bar{v}}{\partial \phi} + \bar{v}\frac{\partial \bar{v}}{\partial \xi}) +$$

$$-\frac{\bar{u}^2}{r}\}\ \frac{\partial f^2}{\partial \zeta} + \varepsilon \mathrm{Re}\ \{\frac{\bar{\psi}}{r}\frac{\partial \bar{v}}{\partial \xi}\ (f\frac{\partial g}{\partial \zeta}) - \frac{\bar{v}}{r}\frac{\partial \bar{\psi}}{\partial \xi}\frac{\partial}{\partial \zeta}\ (g\frac{\partial f}{\partial \zeta})\} \qquad (5.30)$$

Making use of equations (5.4) and (5.27) and of the expressions for $1/r_s$ and $1/r_n$ derived by De Vriend (1978b)

$$\frac{1}{r_s} = \frac{1}{\bar{u}^3}\ \{\bar{u}(\varepsilon\frac{\bar{u}}{r}\frac{\partial \bar{v}}{\partial \phi} + \varepsilon\bar{v}\frac{\partial \bar{v}}{\partial \xi} - \frac{\bar{u}^2}{r}) - \varepsilon\bar{v}(\frac{\bar{u}}{r}\frac{\partial \bar{u}}{\partial \phi} + \bar{v}\frac{\partial \bar{u}}{\partial \xi} + \frac{\varepsilon}{r}\overline{\overline{vu}})\} \qquad (5.31)$$

$$\frac{1}{r_n} = \frac{1}{\bar{u}^3}\{\varepsilon\bar{v}(\varepsilon\frac{\bar{u}}{r}\frac{\partial\bar{v}}{\partial\phi} + \varepsilon\bar{v}\frac{\partial\bar{v}}{\partial\xi} - \frac{\bar{u}^2}{r}) + \bar{u}(\frac{\bar{u}}{r}\frac{\partial\bar{u}}{\partial\phi} + \bar{v}\frac{\partial\bar{u}}{\partial\xi} + \frac{\varepsilon}{r}\overline{\overline{uv}})\} \qquad (5.32)$$

, this equation can be elaborated to

$$\frac{1}{r}(\frac{\partial^4\bar{\psi}}{\partial\xi^4} - 2\frac{\varepsilon}{r}\frac{\partial^3\bar{\psi}}{\partial\xi^3})g + \frac{2}{r}(\frac{\partial^2\bar{\psi}}{\partial\xi^2} - \frac{\varepsilon}{r}\frac{\partial\bar{\psi}}{\partial\xi})\frac{\partial^2 g}{\partial\zeta^2} + \frac{\bar{\psi}}{r}\frac{\partial^4 g}{\partial\zeta^4} =$$

$$\frac{1}{Re}\frac{1}{r}\frac{\partial\bar{\omega}_m}{\partial\phi}\frac{\partial f}{\partial\zeta} - \frac{\bar{u}^2}{r_s}\frac{\partial f^2}{\partial\zeta} - \varepsilon Re(\frac{\bar{u}}{r_n} + 2\frac{\varepsilon}{r}\bar{v})\frac{\bar{\psi}}{r}\frac{\partial}{\partial\zeta}(f\frac{\partial g}{\partial\zeta}) \qquad (5.33)^*)$$

, where $\bar{\omega}_m$ denotes the vorticity of the depth-averaged flow. The streamwise variation of this main flow vorticity is likely to be of minor importance as a source of secondary flow and also the convection terms in (5.33) will be unimportant, except locally near the entrance and the exit of a bend. So in the main flow computation step these terms are likely to be negligible. If g is determined in the channel axis, the radial derivatives of ψ are negligible and equation (5.33) leads to the same system for g as in fully-developed flow (see equations (4.31) and (4.32)).
Regarding the aforementioned simplifications, averaging (5.33) over the depth of flow yields

$$\frac{\partial^4\bar{\psi}}{\partial\xi^4} - 2\frac{\varepsilon}{r}\frac{\partial^3\bar{\psi}}{\partial\xi^3} + 2(\frac{\partial^2\bar{\psi}}{\partial\xi^2} - \frac{\varepsilon}{r}\frac{\partial\bar{\psi}}{\partial\xi})\left.\frac{\partial g}{\partial\zeta}\right|_{\zeta=0} +$$

$$+ \bar{\psi}(\left.\frac{\partial^3 g}{\partial\zeta^3}\right|_{\zeta=0} - \left.\frac{\partial^3 g}{\partial\zeta^3}\right|_{\zeta=-1}) = -\frac{r\bar{u}^2}{r_s}\left.f^2\right|_{\zeta=0} \qquad (5.34)$$

, from which $\bar{\psi}$ can be solved if $\bar{u}$, g, f and $1/r_s$ are known. So if the similarity approximations (5.24) and (5.25) apply, the vertical and horizontal distributions of the main and the

---

*) Note that the source terms in this equations agree with the ones in equation (5.18).

secondary flow can be computed separately.

5.6. Solution procedure for the main flow computation step

The computational procedure of the mathematical model will be split into two subsequent steps, as was suggested in the foregoing. These two steps are:

- the main flow computation step, especially aiming at the depth-averaged velocity field, and
- the bottom shear stress computation step, especially aiming at the magnitude and the direction of the bottom shear stress.

The former step allows for a more or less approximative computation of the secondary flow and the vertical distribution of the main velocity, the latter one involves more accurate computations of these quantities, but no further adjustment of the depth-averaged velocity.

As was shown in par. 5.5, the main flow computation consists of four elements, viz. the computations of f, g, $\bar{\psi}$ and the depth-averaged flow. Each of these quantities, however, can only be computed if known estimates of one or more of the other ones are available. This implies that an iterative solution procedure must be drawn up, involving each of the above elements.

The following procedure is adopted:

1. Estimate f, g and $\bar{\psi}$, by taking the low Dean number limits of the vertical distribution functions (see equation 4.19), for instance, and setting $\bar{\psi} = 0$.
2. Determine $\bar{u}$, $\bar{v}$ and $\bar{p}$ on the basis of equations (5.4), (5.28) and (5.29), using one of the computation methods described in Appendix C.
3. Calculate the local streamline curvature using (5.31).
4. Solve $\bar{\psi}$ from equation (5.34) with boundary conditions (4.36).
5. Solve f from equation (5.27) with conditions (4.30).
6. Solve g from equation (4.31) with conditions (4.32).
7. Repeat the procedure from 2 on, until a termination criterion is satisfied.

If nessessary, convergence can be improved by applying damping

rules like (4.37) to each of the elements 2, 4, 5 and 6. Since the procedure is aiming at the depth-averaged flow, the termination criterion concerns $\bar{u}$.
It reads (cf. conditon 3.25)

$$\max \{|\bar{u}^{(n)} - \bar{u}^{(m-1)}|\} < \delta \qquad (\delta << 1) \tag{5.35}$$

5.7. The bottom shear stress computation step

A most important assumption underlying the main flow computation is the applicability of the similarity approximations (5.24) and (5.25). Longitudinal accelerations of the main flow, however, are known to give rise to deformations of the velocity profile (Schlichting, 1951; De Vriend, 1976 & 1977) and hence to changes in the relation between the bottom shear stress and the local depth-averaged velocity. Since, for the present uniformly shaped channel, the longitudinal accelerations must have a zero cross-sectional mean value, they must be distributed non-uniformly over a cross-section, so that they will affect approximation (5.24), which supposes f independent of ξ. Therefore this approximation is generalized in the bottom shear stress computation step, in that f is allowed to vary weakly with ξ as well as ϕ, in such a way that the ξ- and ϕ-wise derivatives of f are negligible compared with the ξ- and ϕ-wise derivatives of $\bar{u}$. So

$$u_m = \bar{u}\, f(\zeta, \xi, \phi) \quad \text{and} \quad v_m = \bar{v}\, f(\zeta; \xi, \phi) \tag{5.36}$$

This provides the possibility to correct f for the effect of not too strong longitudinal accelerations after having computed the depth-averaged flow*).
As solving equation (5.26) or (5.27) in all verticals of a cross-section appears to yield erroneous results, this correction

---

*) If the effect of the accelerations on the bottom shear stress gives rise to unacceptable changes of the depth-averaged flow, it should be accounted for in the main flow computation step, as well (see par. 5.8.1).

is introduced by solving the following modified version of equation (5.27) in all verticals:

$$\bar{u}\,\frac{\partial^2 f'}{\partial\zeta^2} - De^2\,\bar{u}\,\left(\frac{1}{r}\,\frac{\partial\bar{\psi}}{\partial\xi}\right)\Big|_{\xi=0} g\,\frac{\partial f'}{\partial\zeta} + \left[De^2\bar{u}\,\left\{\frac{\bar{\psi}}{r\bar{u}}\,\left(\frac{\partial\bar{u}}{\partial\xi} + \frac{\varepsilon}{r}\,\bar{u}\right)\right\}\Big|_{\xi=0}\frac{\partial g}{\partial\zeta} + \right.$$

$$\left. - \varepsilon Re\,\left(\frac{\bar{u}}{r}\,\frac{\partial\bar{u}}{\partial\phi} + \bar{v}\,\frac{\partial\bar{u}}{\partial\xi} + \frac{\varepsilon}{r}\,\overline{uv}\right)\tilde{f}\right] f' = -1 \qquad (5.37)$$

with conditions (4.30).

Once f is known, the relation between the longitudinal component of the bottom shear stress and the local depth-averaged velocity can be established.
After normalization by $\rho V^2/Re$, this component follows from

$$\tilde{\tau}_{\phi b} = \frac{\partial u}{\partial\zeta}\Big|_{\zeta=-1} = \bar{u}\,\frac{\partial f}{\partial\zeta}\Big|_{\zeta=-1} \qquad (5.38)$$

The radial component of the bottom shear stress, made dimensionless by the same factor as the longitudinal one, follows from

$$\tilde{\tau}_{rb} = \varepsilon\,\frac{\partial v}{\partial\zeta}\Big|_{\zeta=-1} = \varepsilon\bar{v}\,\frac{\partial f}{\partial\zeta}\Big|_{\zeta=-1} - \varepsilon Re\,\frac{\bar{\psi}}{r}\,\frac{\partial^2 g}{\partial\zeta^2}\Big|_{\zeta=-1} \qquad (5.39)$$

The secondary flow part of this component must be determined rather accurately, since it is this part that causes the transverse bottom slope in alluvial river bends.
In the main flow computation step the radial and vertical momentum equations were simplified at the following points:

a. the transverse inertia of the secondary flow is neglected on the basis of the results of the fully-developed flow investigations;
b. the streamwise inertia of the secondary flow is neglected; this is likely to give rise to important errors in the secondary flow part of $\tilde{\tau}_{rb}$ near the entrance and the exit of a bend;

c. the convective effect of the secondary flow on v_m is neglected; regarding equation (5.33), this seems to be unacceptable near the entrance and the exit of a bend;

d. only the streamline curvature is retained as a source of secondary flow; although the second source, due to the streamwise variation of the main flow vorticity, is of minor importance in a bend, it could be of some importance in a straight reach beyond a bend, where it decays much slowlier than the streamline curvature (De Vriend, 1978b);

e. the vertical distribution of the stream function is assumed independent of ξ; as the vertical distribution of the main velocity varies with ξ, this assumption introduces an error in regions where important streamwise accelerations of the main flow occur;

f. the vertical distribution of the stream function is assumed weakly dependent on ϕ, or, in general, on the longitudinal coordinate; this may introduce errors in the description of the secondary flow beyond a bend (see Appendix B); still this assumption will be maintained, since the bottom shear stress due to the secondary flow is much less sensitive to these errors than the secondary flow intensity (Appendix B).

Taking account of these arguments, the stream function equation to be derived from (5.10) and (5.11) can be elaborated to

$$\left(\frac{\partial^4\bar{\psi}}{\partial\xi^4} - 2\,\frac{\varepsilon}{r}\,\frac{\partial^3\bar{\psi}}{\partial\xi^3}\right) g + 2\left(\frac{\partial^2\bar{\psi}}{\partial\xi^2} - \frac{\varepsilon}{r}\,\frac{\partial\bar{\psi}}{\partial\xi}\right)\frac{\partial^2 g}{\partial\zeta^2} + \bar{\psi}\,\frac{\partial^4 g}{\partial\zeta^4} +$$

$$- \varepsilon\mathrm{Re}\left[\left(\frac{\bar{u}}{r}\,\frac{\partial\bar{\psi}}{\partial\phi} + \bar{v}\,\frac{\partial\bar{\psi}}{\partial\xi} - 3\,\frac{\varepsilon}{r}\,\bar{v}\,\bar{\psi} - \frac{\bar{u}}{r_n}\,\bar{\psi}\right)\frac{\partial}{\partial\zeta}\left(f\,\frac{\partial g}{\partial\zeta}\right) +\right.$$

$$+ \left\{\frac{\bar{u}}{r}\,\frac{\partial}{\partial\phi}\left(\frac{\partial^2\bar{\psi}}{\partial\xi^2} - 3\,\frac{\varepsilon}{r}\,\frac{\partial\bar{\psi}}{\partial\xi}\right) + \bar{v}\,\frac{\partial}{\partial\xi}\left(\frac{\partial^2\bar{\psi}}{\partial\xi^2} - 2\,\frac{\varepsilon}{r}\,\frac{\partial\bar{\psi}}{\partial\xi}\right) + \frac{\partial\bar{u}}{\partial\xi}\,\frac{1}{r}\,\frac{\partial^2\bar{\psi}}{\partial\xi\partial\phi} +\right.$$

$$\left.\left. + \frac{\partial\bar{v}}{\partial\xi}\left(\frac{\partial^2\bar{\psi}}{\partial\xi^2} - \frac{\varepsilon}{r}\,\frac{\partial\bar{\psi}}{\partial\xi}\right)\right\} fg\right] = \frac{1}{\mathrm{Re}}\,\frac{\partial\bar{\omega}_m}{\partial\phi}\,\frac{\partial f}{\partial\zeta} - \frac{r\bar{u}^2}{r_s}\,\frac{\partial f^2}{\partial\zeta} \qquad (5.40)$$

When attempting to compute g on the basis of this equation with $\bar{\psi}$ resulting from the main flow computation step or, in an iterative procedure, from the depth-averaged version of this equation, the streamwise inertia terms give rise to erroneous solutions or even ill-convergence near the exit of a bend (De Vriend, 1978b). On the other hand, it is shown in Appendix B that neither the equation including the streamwise derivatives of g nor the equation for g in which the streamwise inertia terms are neglected give rise to problems, at least in the simple case considered there.
Apparently, the streamwise inertia terms and the streamwise derivatives of g should be retained or neglected both. Regarding point f, the latter possibility is chosen.
In order to account for the radial variation of f, g is allowed to vary weakly with ξ (cf. assumption 5.36) and it is solved in all verticals from the truncated stream function equation

$$\frac{\partial^4 g'}{\partial \zeta^4} = \frac{1}{Re} \frac{\partial \bar{\omega}_m}{\partial \phi} \frac{\partial f}{\partial \zeta} - \frac{r\bar{u}^2}{r_s} \frac{\partial f^2}{\partial \zeta} \tag{5.41}$$

with conditions (4.32).
The depth-averaged stream function $\bar{\psi}$ follows from the depth-averaged version of (5.40), reading

$$\frac{\partial^4 \bar{\psi}}{\partial \xi^4} - 2\frac{\varepsilon}{r}\frac{\partial^3 \bar{\psi}}{\partial \xi^3} + 2\left(\frac{\partial^2 \bar{\psi}}{\partial \xi^2} - \frac{\varepsilon}{r}\frac{\partial \bar{\psi}}{\partial \xi}\right)\frac{\partial g}{\partial \zeta}\Big|_{\zeta=0} + \bar{\psi}\left(\frac{\partial^3 g}{\partial \zeta^3}\Big|_{\zeta=0} - \frac{\partial^3 g}{\partial \zeta^3}\Big|_{\zeta=-1}\right) +$$

$$- \varepsilon Re \left[\left(\frac{\bar{u}}{r}\frac{\partial \bar{\psi}}{\partial \phi} + \bar{v}\frac{\partial \psi}{\partial \xi} - 3\frac{\varepsilon}{r}\bar{v}\bar{\psi} - \frac{\bar{u}}{r_n}\bar{\psi}\right)\left(f\frac{\partial g}{\partial \zeta}\right)\Big|_{\zeta=0} +\right.$$

$$+ \left\{\frac{\bar{u}}{r}\frac{\partial}{\partial \phi}\left(\frac{\partial^2 \bar{\psi}}{\partial \xi^2} - 3\frac{\varepsilon}{r}\frac{\partial \bar{\psi}}{\partial \xi}\right) + \bar{v}\frac{\partial}{\partial \xi}\left(\frac{\partial^2 \bar{\psi}}{\partial \xi^2} - 2\frac{\varepsilon}{r}\frac{\partial \psi}{\partial \xi}\right) + \frac{\partial \bar{u}}{\partial \xi}\frac{1}{r}\frac{\partial^2 \bar{\psi}}{\partial \xi \partial \phi} +\right.$$

$$\left.\left. + \frac{\partial \bar{v}}{\partial \xi}\left(\frac{\partial^2 \bar{\psi}}{\partial \xi^2} - \frac{\varepsilon}{r}\frac{\partial \bar{\psi}}{\partial \xi}\right)\right\}\overline{fg}\right] = \frac{1}{Re}\frac{\partial \bar{\omega}_m}{\partial \phi} f\Big|_{\zeta=0} - \frac{r\bar{u}^2}{r_s} f^2\Big|_{\zeta=0} \tag{5.42}$$

, with the boundary conditions (4.36) and the inflow condition $\bar{\psi} = 0$, supposing the channel sections considered here to be preceeded by a long straight reach without secondary flow.

As long the influence of the streamwise main flow accelerations on f is not too strong, it is sufficient to correct f for this influence by solving equation (5.37) on the basis of the results for $\bar{u}$, $\bar{\psi}$ and g as obtained from the main flow computation step. As the equation for g is simplified in such a way that g is independent of $\bar{\psi}$, this implies that the four elements of the bottom shear stress computation step, concerning f, g, $\bar{\psi}$ and the shear stress components, respectively, have to be gone through only once.

5.8. Verification of the simplifying assumptions

The mathematical model of developing laminar flow derived in the foregoing is based on a number of simplifying assumptions. Apart from the ones that were also made for fully-developed flow, the most important of these assumption are:

- the simplification of the main flow convection terms in the main flow equations,
- the vertical similarity of the main velocity distribution in the main flow computation step,
- the neglect of the streamwise inertia of the secondary flow in the main flow computation step,
- the other simplifications of the stream function equation for the secondary flow in the main flow computation step and
- the partial neglect of the streamwise inertia of the secondary flow in the bed shear stress computation step.

It will be attempted to verify these assumptions one by one, either by estimating the magnitude of the neglected terms or by considering the effect of including these terms in the model. This verification will be carried out on the basis of computational results for the so-called LFM-flume (see chapter 9), which has a rather sharp 180° bend giving rise to rather strong curvature effects (De Vriend, 1979b & 1980b).

5.8.1. The simplification of the main flow convection terms

In the stream-oriented coordinate system described in par. 5.4, the complete main flow momentum equation contains the main flow convection terms

$$\varepsilon Re \left\{ u_m \frac{\partial u_m}{\partial s} + w_m \frac{\partial u_m}{\partial \zeta} \right\}$$

The simplifications of the main flow convection terms in the actual model, on the basis of the similarity hypothesis for the main flow, are equivalent to putting

$$u_m \frac{\partial u_m}{\partial s} + w_m \frac{\partial u_m}{\partial \zeta} \simeq \bar{u}_m \frac{\partial \bar{u}_m}{\partial s} f^2 \qquad (5.43)$$

Making use of equation (5.15) and the generalized similarity hypothesis for the main flow (cf. (5.20) and (5.36))

$$u_m = \bar{u}_m f(\zeta; n, s) \qquad (5.44)$$

, the vertical component of the main velocity can be expressed as

$$w_m = - \bar{u}_m \frac{\partial F}{\partial s} \quad \text{with} \quad F = \int_{-1}^{\zeta} f d\zeta \qquad (5.45)$$

Then approximation (5.43) can be elaborated to

$$f^2 \bar{u}_m \frac{\partial \bar{u}_m}{\partial s} + \bar{u}_m^2 \left(f \frac{\partial f}{\partial s} - \frac{\partial f}{\partial \zeta} \frac{\partial F}{\partial s} \right) \simeq f^2 \bar{u}_m \frac{\partial \bar{u}_m}{\partial s} \qquad (5,46)$$

Both terms in the left hand part of this approximation vary about zero, in such a way that the first term may become smaller than the second one.
If this occurs when all main flow convection terms are

unimportant, however, approximation (5.46) is still acceptable. Therefore this approximation is assumed to hold good if the range of variation of the first term is much larger than the range of variation of the second one.
Figure 24 gives a rough indication of the extrema of the two terms for the LFM-flume with De = 25. It shows that the range of variation of the first term in (5.46) is far the largest, indeed.

5.8.2. Vertical similarity of the main velocity distribution

In the main flow computation step the main velocity distribution is assumed strictly self-similar in a cross-section. As was shown in chapter 4, this similarity hypothesis holds rather good for fully-developed curved flow and it is likely to allow for a proper representation of the effects of diffusion and secondary flow convection in developing curved flow, as well. Longitudinal accelerations of the main flow, however, will give rise to deformations of the main velocity distribution (see par. 5.7). Hence the similarity approximations (5.24) and (5.25) in the main flow computation step will cause errors in the depth-averaged velocity field.
An indication of these errors in the results of the main flow computation for the LFM-flume (De = 25) is given in figure 25. The reference distributions in this figure are obtained from an extended version of the main flow computation step, with the generalized similarity approximation (5.36) instead of (5.24) and, correspondingly, equation (5.37) instead of (5.27). It becomes evident that, although the vertical distribution function f undergoes considerable deformations, especially near the entrance and the exit of the bend, the distribution of $\bar{u}$ is hardly affected. Hence it is concluded that the strict similarity approximation (5.24) is applicable in the main flow computation step.

5.8.3. The stream function equation for the secondary flow in the main flow computation step.

In the main flow computation step a strongly truncated version

of the stream function equation for the secondary flow is used (see par. 5.6). Both the streamwise inertia and all sources but the main flow curvature are neglected. Since the neglected terms vanish as the flow becomes fully-developed, these simplifications have to be verified for developing flow.
To that end a reference computation was made for the LFM-flume at De = 25, with the extensive stream function equation (see par. 5.7) in both computation steps.
Figure 27 shows that the main velocity distribution obtained in this way differs only slightly (less than 10%) from the distribution found by the procedure described in par. 5.6. The essential features of the main velocity redistribution in and beyond the bend, such as the outward shift of the velocity maximum and the flattening of the vertical distribution, are globally the same in either case.
Still this does not prove the truncated secondary flow equation applicable in the main flow computation step, since small differences in $\bar{u}$ could give rise to much larger differences in the secondary flow and the bottom shear stress. Figure 28 gives the bottom shear stress results from three different computations, with

. the truncated secondary flow equation in both computation steps,
. the truncated secondary flow equation in the main flow computation step and the extensive one in the bottom shear stress computation step and
. the extensive secondary flow equation in both computation steps,

respectively.
Taking the results of the last computation as a reference, the bottom shear stress resulting from the first one is up to 20% too small in the greater part of the bend (see figure 28a). In contrast with the expectation, however, the results of the second computation are hardly better or even worse. The same phenomenon can be observed in the direction of the bottom shear stress, though the differences are much larger here (locally up to 10^{o}, whereas the overall mean angle is about 20^{o}; see figures 28b and c): in the greater part of the bend the results of the second computation are hardly

better and sometimes even worse than the results of the first one. The differences between the bottom shear stress results from the three computations may have two causes, viz.:

. differences in the main bottom shear stress factor $\left.\frac{\partial f}{\partial \zeta}\right|_{\zeta=-1}$ and

. differences in the secondary flow.

According to figure 28d, the differences in the main bottom shear stress factor show the same tendency as the ones in the bottom shear stresses, but they are relatively small. Obviously, the greater part of the differences, especially in the direction of the shear stress, must be attributed to the secondary flow.

Figure 29 shows the secondary flow to be strongly influenced, indeed. In the first part of the bend, where the streamwise inertia of the secondary flow is important and the main velocity is hardly affected by secondary flow convection, the results of the two-step computation agree well with the ones of the extensive computation. As soon as secondary flow convection becomes important to $\bar{u}$, however, the two-step results lie much closer to the results of the truncated computation, except for the decay region beyond the bend (figure 29b). This illustrates that in the greater part of the bend the differences from the results of the extensive computation are only indirectly due to the truncation of the secondary flow equation: as all neglected terms are small there, including them has hardly any effect as long as u is kept the same. Including the effects of the truncation on u, however, has a much stronger effect, the principal source term in the depth-averaged secondary flow equation being proportional to $u^2\big|_{\zeta=0}$. Obviously, it is the interaction between the secondary flow and the main flow that gives rise to the strong influence of the simplifications in the secondary flow equation halfway the bend.

The conclusion to be drawn from the foregoing is that the two-step computation procedure suggested in par. 5.6 and 5.7 leads to important errors in the secondary flow and in the magnitude and the direction of the bottom shear stress. The extensive secondary flow equation described in par. 5.7 should be used throughout the computation rather than in an additional bottom shear stress computation step alone.

5.8.4. The partial neglect of the streamwise inertia in the secondary flow computation.

In the extensive secondary flow computation suggested in par. 5.7, streamwise inertia is included in $\bar{\psi}$ (equation 5.42), but not in g (equation 5.41). This partial neglect of the streamwise inertia was based on Appendix B, where the bottom shear stress due to the secondary flow in a straight reach beyond a bend is shown to be less sensitive to this simplification than the rate of decay of the secondary flow.
In order to verify this conclusion for the whole bend, the bottom shear stress computation step should be repeated with the streamwise inertia and the streamwise variation of g included in the secondary flow computation.
In that case the stream function equation to be derived from equations (5.10) and (5.11) becomes

$$\left(\frac{\partial^4\bar{\psi}}{\partial\xi^4} - 2\,\frac{\varepsilon}{r}\,\frac{\partial^3\bar{\psi}}{\partial\xi^3}\right)g + 2\left(\frac{\partial^2\bar{\psi}}{\partial\xi^2} - \frac{\varepsilon}{r}\,\frac{\partial\bar{\psi}}{\partial\xi}\right)\frac{\partial^2 g}{\partial\zeta^2} + \bar{\psi}\,\frac{\partial^4 g}{\partial\zeta^4} +$$

$$- \varepsilon\mathrm{Re}\left[\left(\frac{\bar{u}}{r}\,\frac{\partial\bar{\psi}}{\partial\phi} + \bar{v}\,\frac{\partial\bar{\psi}}{\partial\xi} - 3\,\frac{\varepsilon}{r}\,\bar{v}\,\bar{\psi} - \frac{\bar{u}}{r_n}\,\bar{\psi}\right)\frac{\partial}{\partial\zeta}\left(f\,\frac{\partial g}{\partial\zeta}\right) +\right.$$

$$+ \bar{\psi}\left(\frac{\bar{u}}{r}\,\frac{\partial}{\partial\phi} + \bar{v}\,\frac{\partial}{\partial\xi}\right)\frac{\partial}{\partial\zeta}\left(f\,\frac{\partial g}{\partial\zeta}\right) + \left(\frac{\partial^2\bar{\psi}}{\partial\xi^2} - \frac{\varepsilon}{r}\,\frac{\partial\bar{\psi}}{\partial\xi}\right)\left(\frac{\bar{u}}{r}\,\frac{\partial}{\partial\phi} + \bar{v}\,\frac{\partial}{\partial\xi}\right)fg +$$

$$+ \left\{\frac{\bar{u}}{r}\,\frac{\partial}{\partial\phi}\left(\frac{\partial^2\bar{\psi}}{\partial\xi^2} - 3\,\frac{\varepsilon}{r}\,\frac{\partial\bar{\psi}}{\partial\xi}\right) + \bar{v}\,\frac{\partial}{\partial\xi}\left(\frac{\partial^2\bar{\psi}}{\partial\xi^2} - 2\,\frac{\varepsilon}{r}\,\frac{\partial\bar{\psi}}{\partial\xi}\right) + \frac{\partial\bar{u}}{\partial\xi}\,\frac{1}{r}\,\frac{\partial^2\bar{\psi}}{\partial\xi\partial\phi} +\right.$$

$$\left.\left. + \frac{\partial\bar{v}}{\partial\xi}\left(\frac{\partial^2\bar{\psi}}{\partial\xi^2} - \frac{\varepsilon}{r}\,\frac{\partial\bar{\psi}}{\partial\xi}\right)\right\}fg + \frac{\partial\bar{\psi}}{\partial\xi}\left(\frac{\partial\bar{u}}{\partial\xi}\,\frac{1}{r}\,\frac{\partial}{\partial\phi} + \frac{\partial\bar{v}}{\partial\xi}\,\frac{\partial}{\partial\xi}\right)fg\right] =$$

$$\frac{1}{\mathrm{Re}}\,\frac{\partial\bar{\omega}_m}{\partial\phi}\,\frac{\partial f}{\partial\phi} - \frac{r\bar{u}^2}{r_s}\,\frac{\partial f^2}{\partial\zeta} \qquad (5.47)$$

For the computation of g all ξ-derivatives are neglected and only the most important streamwise inertia terms are retained. Then equation (5.47) reduces to

$$\bar{\psi}\,\frac{\partial^4 g}{\partial\zeta^4} - \varepsilon\mathrm{Re}\,\frac{\bar{u}}{r}\,\frac{\partial}{\partial\phi}\left\{\bar{\psi}\,\frac{\partial}{\partial\zeta}\left(f\,\frac{\partial g}{\partial\zeta}\right)\right\} = -\frac{r\bar{u}^2}{r_s}\,\frac{\partial f^2}{\partial\zeta} + \frac{1}{\mathrm{Re}}\,\frac{\partial\bar{\omega}_m}{\partial\phi}\,\frac{\partial f}{\partial\zeta} \tag{5.48}$$

Averaging (5.47) over the depth of flow yields the following equation for $\bar{\psi}$

$$\frac{\partial^4\bar{\psi}}{\partial\xi^4} - 2\,\frac{\varepsilon}{r}\,\frac{\partial^3\bar{\psi}}{\partial\xi^3} + 2\left(\frac{\partial^2\bar{\psi}}{\partial\xi^2} - \frac{\varepsilon}{r}\,\frac{\partial\bar{\psi}}{\partial\xi}\right)\left.\frac{\partial g}{\partial\zeta}\right|_{\zeta=0} + \bar{\psi}\left(\left.\frac{\partial^3 g}{\partial\zeta^3}\right|_{\zeta=0} - \left.\frac{\partial^3 g}{\partial\zeta^3}\right|_{\zeta=-1}\right) +$$

$$- \varepsilon\mathrm{Re}\left[\left(\frac{\bar{u}}{r}\,\frac{\partial\bar{\psi}}{\partial\phi} + \bar{v}\,\frac{\partial\bar{\psi}}{\partial\xi} - 3\,\frac{\varepsilon}{r}\,\bar{v}\,\bar{\psi} - \frac{\bar{u}}{r_n}\,\bar{\psi}\right) f\left.\frac{\partial g}{\partial\zeta}\right|_{\zeta=0} +\right.$$

$$+ \bar{\psi}\left(\frac{\bar{u}}{r}\,\frac{\partial}{\partial\phi} + \bar{v}\,\frac{\partial}{\partial\xi}\right) f\left.\frac{\partial g}{\partial\zeta}\right|_{\zeta=0} + \left(\frac{\partial^2\bar{\psi}}{\partial\xi^2} - \frac{\varepsilon}{r}\,\frac{\partial\bar{\psi}}{\partial\xi}\right)\left(\frac{\bar{u}}{r}\,\frac{\partial}{\partial\phi} + \bar{v}\,\frac{\partial}{\partial\xi}\right)\overline{fg}$$

$$+ \left\{\frac{\bar{u}}{r}\,\frac{\partial}{\partial\phi}\left(\frac{\partial^2\bar{\psi}}{\partial\xi^2} - 3\,\frac{\varepsilon}{r}\,\frac{\partial\bar{\psi}}{\partial\xi}\right) + \bar{v}\,\frac{\partial}{\partial\xi}\left(\frac{\partial^2\bar{\psi}}{\partial\xi^2} - 2\,\frac{\varepsilon}{r}\,\frac{\partial\bar{\psi}}{\partial\xi}\right) + \frac{\partial\bar{u}}{\partial\xi}\,\frac{1}{r}\,\frac{\partial^2\bar{\psi}}{\partial\xi\partial\phi} +\right.$$

$$\left. + \frac{\partial\bar{v}}{\partial\xi}\left(\frac{\partial^2\bar{\psi}}{\partial\xi^2} - \frac{\varepsilon}{r}\,\frac{\partial\bar{\psi}}{\partial\xi}\right)\right\}\overline{fg} + \frac{\partial\bar{\psi}}{\partial\xi}\left(\frac{\partial\bar{u}}{\partial\xi}\,\frac{1}{r}\,\frac{\partial}{\partial\phi} + \frac{\partial\bar{v}}{\partial\xi}\,\frac{\partial}{\partial\xi}\right)\left.\overline{fg}\right] =$$

$$\frac{1}{\mathrm{Re}}\,\frac{\partial\bar{\omega}_m}{\partial\phi}\left.f\right|_{\zeta=0} - \frac{r\bar{u}^2}{r_s}\left.f^2\right|_{\zeta=0} \tag{5.49}$$

For the sake of simplicity f and g are assumed independent of ξ and out of their ϕ-derivatives only the ones figuring in (5.48) are retained. Then the bottom shear stress computations for the LFM-flume (De=25) yield the results represented in figure 30.

As expected, the depth-averaged stream function of the secondary flow, shown in figure 30a, is somewhat more sensitive to the partial neglect of inertia than the direction of the bottom shear stress (figure 30b).
Apart from local deviations, especially in the inner wall region in the first part of the bend, the direction of the bottom shear stress is not affected very strongly. Therefore the present simplification is thought to be justified.

5.9. Qualitative comparison with measured data for turbulent flow

The experimental verification of the mathematical model described in the foregoing is somewhat problematic, as experimental information on developing laminar flow in curved shallow channels, if available at all, is rather concise (Asfari, 1968). The only possible way of verification is a qualitative one, viz. a comparison with equivalent turbulent flow experiments.
The data to be used for this qualitative verification stem from two series of experiments on turbulent flow in curved shallow channels, viz.

- experiments carried out in the Laboratory of Fluid Mechanics of the Delft University of Technology in a 1.70 m wide flume consisting of a 180° curved section with a radius of curvature of 4.25 m and two straight inflow and outflow sections of about 6 m effective length (see par. 9.2.4. and also De Vriend, 1976, 1977 and 1979b),
- experiments carried out at the "De Voorst"-branch of the Delft Hydraulics Laboratory in a 6.00 m wide flume consisting of a 32 m long straight inflow section and a curved section of about 90° with a radius of curvature of 50.00 m (see par. 9.2.1. and De Vriend et al., 1977).

These two flumes will be referred to as the LFM-flume and the DHL-flume, respectively. The flow conditions during the experiments chosen for the verification are summarized in the following table, in which Re_0 denotes the effective Reynolds number $13C/\sqrt{g}$ (see chapter 6) and $De_0 = Re_0\sqrt{\varepsilon}$.

flume	R_e (m)	B (m)	d (m)	Q (m^3/s)	C ($m^{\frac{1}{2}}/s$)	Re_0	De_0
LFM	4.25	1.70	0.17	0.19	30	125	25
DHL	50.00	6.00	025	0.61	50	212	15

In the mathematical simulation of these experiments the laminar Reynolds number was chosen equal to Re_0 (see also par. 7.8).
The verification of the model consists of a qualitative comparison of the measured and computed depth-averaged main velocity fields. Other quantities were not considered, either because they have not been measured (τ_b, α_τ) or because they are essentially different for the two types of flow (f, g and $\bar{\psi}$).
The computed depth-averaged velocity distribution agrees rather well with the measured data, in spite of the difference in flow type (figure 31).
Only close to the sidewalls the laminar velocities are somewhat smaller than the turbulent ones, as a consequence of lateral diffusion. Furthermore, the convective influence of the secondary flow in the first part of the bend seems to be considerably stronger for laminar flow, which can be explained in two ways:

- it is caused by an essential difference in behaviour between laminar and turbulent flow in the first part of the bend, as suggested by Asfari (1968); he carried out turbulent and laminar flow experiments in the same flume and concluded that the turbulent flow tended to shift inward in the first part of the bend before shifting gradually outwards, whereas the laminar flow appeared to start shifting outwards immediately after entering the bend;
- the turbulent Dean number gives no appropriate estimation of the laminar Dean number to be used in the mathematical simulation; when considering the depth-averaged velocity field in another LFM-experiment (C=60 $m^{\frac{1}{2}}/s$), for instance, the influence of secondary flow convection seems to be even smaller than for C=30 $m^{\frac{1}{2}}/s$ (De Vriend, 1976; see also par. 9.2.4), whereas the laminar simulation

with $De=De_0$ would suggest much stronger effects of convection (cf. chapter 3).

Either of these explanations will be discussed in chapter 7.

5.10 Discussion

It becomes evident from the foregoing that the two-step computational procedure described in par. 5.6 and 5.7 works well, provided that the streamwise inertia of the secondary flow intensity is accounted for in either computation step. Still this does not imply automatically that this procedure will also be suited for the computation of turbulent flow, where the mutual importance of the various groups of terms in the equations can be different. Therefore the verification of the simplifications described in par. 5.8 will have to be repeated for the turbulent flow model.

For the two cases of turbulent flow considered in par. 5.9, the simulation with the present laminar flow model yields a far better prediction of the depth-averaged main velocity redistribution than a simulation with a turbulent flow model disregarding secondary flow convection (De Vriend, 1976 & 1977; De Vriend et al., 1977). This illustrates, once again, that the main velocity redistribution in a bend is a matter of convection rather than of turbulence.

As was suggested in par. 5.9, the Dean number in a laminar simulation of turbulent flow in curved rectangular channels cannot simply be taken proportional to the effective Reynolds number $13C/\sqrt{g}$. The relation between De and the flow parameters for this kind of simulation needs further investigation.

5.11 Summary of conclusions

The definition of main and secondary flow given in par. 5.2 provides the possibility of separating the equations of continuity for these two flow constituents. Besides, a far-going separation between the momentum equations for the main and the secondary flow can be achieved. This separation, combined with similarity hypotheses for the main and the secondary velocity components, can be used as a basis of a simplified computation method for developing laminar flow in curved

shallow channels, with the following outlines:

- a main flow computation step, which is an iterative process of alternate computations of the depth-averaged main velocity field, the vertical distribution of the main velocity, the vertical distribution of the secondary flow and the depth-averaged stream function of the secondary flow; as this step is meant to determine the depth-averaged main velocity field, the other quantities are calculated only approximately, assuming strict similarity in every cross-section;
- a bottom shear stress computation step, in which the depth-averaged main velocity field is kept fixed and the vertical distribution of the main velocity as well as the vertical distribution and the depth-averaged stream function of the secondary flow are determined more accurately.

A closer investigation of the various elements of this computation method and of the possibility to introduce simplifications has shows that

- various basic concepts can be adopted for the computation of the main velocity field (see Appendix C); the most economic of these concepts are based on the direct calculation of the depth-averaged velocities and pressures using a forward marching technique; if the flow is mildly curved, it can be calculated with sufficient accuracy in one single sweep (parabolic procedure), which is quite efficient; even if repeated sweeps are needed, however, this approach (in its so-called partially-parabolic mode now) is still far more economic than a stream-function/vorticity method, for instance;
- the main velocity can have a non-zero vertical component; the convective influence of this component can be disregarded;
- the transverse similarity of the vertical distribution of the main velocity is affected by longitudinal accelerations of the main flow; this effect can be left out of consideration in the main flow computation step, but it can have a considerable influence on the magnitude and the direction of the bottom shear stress;
- the gradual growth and decay of the secondary flow cannot be left out of consideration in either computation step; in the one for the

main flow, however, the attendant deformations of the vertical distribution function g need not be accounted for, provided that all streamwise inertia terms are omitted from the equation for g; disregarding these deformations leads to a too rapid growth and decay of the secondary flow intensity, which is not allowable in the bottom shear stress computation step;
- though there is an additional source of secondary flow, related to the longitudinal variation of depth-averaged main flow vorticity, the streamline curvature is far the most important source of secondary circulation, such that the additional one can be disregarded.

By lack of experiments on laminar flow in curved shallow channels, the simplified mathematical model described herein could not be verified experimentally. A global comparison with the measured data from turbulent flow experiments has led to the conclusion that the deformations of the main velocity distributions show qualitatively the same features.

These deformations can be characterized as follows:
- as the flow enters a bend, the streamline curvature and the corresponding transverse pressure gradient develop rather quickly (over a distance O(B) around the bend entrance); the attendant longitudinal pressure gradients give rise to a longitudinal acceleration of the flow in the inner bend and a deceleration in the outer bend; as a consequence, the main velocity distribution is skewed inwards in the first part of the bend;
- on proceeding through the bend, the influence of secondary flow convection becomes perceptible; first, the local effects in the sidewall regions (decrease of $\bar{u}$ near the inner wall, increase near the outer wall; local deformations of $u/\bar{u}$) come into existence; subsequently, the horizontal interaction develops and causes a gradual and retarded outward extension of the region of reduced $\bar{u}$ near the inner wall, whereas the peak in $\bar{u}$ in the outer bend is compressed against the wall; if the bend is long enough, this process goes on until the outer wall region is reached and the main velocity distribution shows the features described in chapter 3;
- along with the transverse redistribution of $\bar{u}$, the vertical

distribution of the main velocity is gradually distorted; in the larger part of the cross-section, the vertical derivatives of the main velocity tend to become smaller near the surface and larger near the bottom; consequently, the bottom shear stress compared with the depth-averaged main velocity increases on proceeding through the bend;

- near the exit of a bend, a rapid decay of the transverse pressure gradient occurs (length scale B, again); the attendant longitudinal pressure gradients give rise to an additional outwards skewing of the main velocity distribution;
- if the bend is followed by a straight reach, the skewness of the main velocity distribution (or rather: the additional vorticity of the depth-averaged main flow) damps out gradually and without oscillations.

6. The modelling of turbulence

6.1. General

As was shown in chapter 2, the time-mean momentum equations for steady turbulent flow contain terms with the time-mean products of the velocity fluctuations, the so-called Reynolds stress terms. The Reynolds stresses, which are essentially due to turbulence, must be related to the mean flow in order to be able to describe this mean flow by the time-mean balance equations for mass and momentum (Launder et al., 1972; Hinze, 1975).
The equation (or system of equations) relating the Reynolds stresses to the mean flow is called turbulence model.
The literature gives a wide variety of such turbulence models, ranging from direct algebraic relations between the components of the Reynolds stress tensor and mean flow quantities to complicated systems of transport equations for turbulence properties (see Launder et al., 1972; Rodi, 1978b).
Since the present flow model is meant to be incorporated in a larger model for alluvial river bends (see chapter 1), in which it is to be activated frequently, it is necessary to reduce the expenses of the flow computations as far as possible. Therefore the simplest allowable turbulence model will be applied here. The rather good prediction of the depth-averaged main velocity in turbulent flow by the laminar flow model described in the foregoing chapter (see par. 5.9) suggests this turbulence model can be a fairly simple one.

6.2. Mixing length hypothesis

It is a rather common practice in turbulence modelling to assume an analogy between the turbulent diffusion of momentum, defined as the time-mean exchange of momentum due to turbulence, and the molecular one. On the analogy of the relation between the viscous stress tensor and the rate-of-strain tensor through the molecular viscosity η, the components of the Reynolds stress tensor are assumed proportional to the corresponding components of the rate-of-strain tensor, with the scalar A_t (eddy viscosity, turbulence viscosity) as a factor of

proportionality (see par. 2.2). The eddy viscosity A_t is assumed to depend on the mean properties of the flow only.
Although fundamental objections can be made against the eddy viscosity concept (Hinze, 1975), it appears to yields a satisfactory description of the mean flow properties in many cases of turbulent flow (see, for instance: Rodi, 1978b).
Since A_t depends on the mean flow, which in turn depends on A_t, the mathematical system describing the mean flow is not closed until either a relation between A_t and the mean flow properties has been established or additional differential equations have been formulated, from which such a relation can be derived. In general, these additional equations describe the production, transport and dissipation of turbulence properties (see Launder et al., 1972, and Rodi, 1978b).
A direct algebraic relation between A_t and certain mean flow properties is mathematically the simplest. Therefore a turbulence model of this type will be adopted here. A widely applied group of such models is based on Prandtl's mixing lengh hypothesis (Prandtl, 1925), which can be generalized to (Rodi, 1978b)

$$A_t = \rho L_m^2 \left[\left(\frac{\partial v_i}{\partial x_j} + \frac{\partial v_j}{\partial x_i} \right) \frac{\partial v_i}{\partial x_j} \right]^{1/2} \qquad (6.1)^*)$$

, in which v_i (i=1,2,3) denotes mean velocity component in the x_i-direction of the cartesian coordinate system (x_1,x_2,x_3). If the mixing length L_m can be prescribed or can be expressed explicitly in terms of mean flow quantities, (6.1) is a direct algebraic relation between A_t and the mean flow, but even this relation is fairly complicated in its general form. In the present flow case, however, the coordinate system can be chosen in such a way, that certain components of the velocity vector and the rate-of-strain tensor become predominant. Hence it must be possible to simplify (6.1) drastically.

---

*) The Einstein summation convention applies to the term in brackets.

6.3. Uniform rectilinear shear flow

In order to have an indication of how (6.1) could be simplified, the well-known case of uniform rectilinear shear flow is considered. In a cartesian coordinate system (x,y,z), with the x-axis in the flow direction and the z-axis vertically upward, there is only one non-zero component and relation (6.1) reduces to

$$A_t = \rho L_m^2 \left|\frac{\partial v_x}{\partial z}\right| \tag{6.2}$$

Then the normalized system of equations describing this flow reads (see par. 2.4)

$$0 = -\frac{\partial p}{\partial s} + \frac{\partial}{\partial \zeta}\left(\alpha \frac{\partial u}{\partial \zeta}\right) \tag{6.3}$$

$$\alpha = l_m^2 \left|\frac{\partial u}{\partial \zeta}\right| Re_0 \tag{6.4}$$

, in which l_m is the mixing length normalized by d and s is the normalized streamwise coordinate.
The vertical distribution of l_m in (6.4) determines the vertical distribution of u. It is rather usual to prescribe l_m in such a way, that the distributions of α and u are in good agreement with experiments.
In practice, $u(\zeta)$ can often be approximated by rather simple mathematical expressions, such as logarithmic or power law functions (see, for instance: Reynolds, 1974). According to Rozovskii (1961), the logarithmic profile is the best suited as a first approximation of the main velocity distribution in a bend. Therefore the mixing length distribution is chosen such, that it yields a logarithmic velocity profile in uniform flow. Hence

$$\alpha = -\kappa^2 \zeta (1+\zeta)^2 \left|\frac{\partial u}{\partial \zeta}\right| Re_0 \tag{6.5}$$

, where κ denotes Von Kármán's constant, and

$$u = (-\frac{1}{Re_0}\frac{\partial p}{\partial s})^{\frac{1}{2}} \ln\frac{1+\zeta}{1+\zeta^*} \tag{6.6}$$

, in which ζ^* is the level slightly above the bottom where u=0. Adopting Chézy's factor C as a characterization of the bottom resistance*), this level follows from (see also De Vriend, 1976)

$$\zeta^* = -1 + \exp(-1 - \frac{\kappa C}{\sqrt{g}}) \tag{6.7}$$

and the logarithmic velocity distribution becomes

$$u = \bar{u}\{1 + \frac{\sqrt{g}}{\kappa C} + \frac{\sqrt{g}}{\kappa C}\ln(1+\zeta)\} \tag{6.8}$$

Substitution of (6.8) into (6.5) yields

$$\alpha = -\frac{\kappa\sqrt{g}}{C}\zeta(1+\zeta)\,Re_0 \tag{6.9}$$

This parabolic distribution of the turbulence viscosity and the corresponding logarithmic distribution of the velocity seem to be in good agreement with various experiments reported in the literature (see, for instance, Vanoni, 1946, and Jobson et al, 1970; see also par. 6.6.1 and 6.6.2).
Regarding definition (2.26), the depth-averaged value of α must be equal to one here. Hence

---

*) In fact, the quantity $C/\sqrt{g}$ should be used to characterize the bottom roughness, since flow resistance has nothing to do with gravity, whereas Chezy's factor is proportional to $\sqrt{g}$.

$$Re_0 = \frac{6}{\kappa}\frac{C}{\sqrt{g}} \qquad \text{and} \qquad \alpha = -6\zeta(1+\zeta) \tag{6.10}$$

So the effective Reynolds number is proportional to the dimensionless bottom resistance factor $C/\sqrt{g}$. Similar results for Re_0 can be found in the literature (Engelund, 1964 & 1974, Rastogi et al., 1978), but the coefficient of proportionality is mostly somewhat different (see par. 6.6.1).

6.4. Fully-developed straight channel flow

In case of a straight rectangular channel of finite width, but without secondary circulations, the streamwise momentum equation for fully-developed flow becomes

$$0 = -\frac{\partial p}{\partial s} + \frac{\partial}{\partial \zeta}\left(\alpha \frac{\partial u}{\partial \zeta}\right) + \frac{\partial}{\partial \xi}\left(\alpha \frac{\partial u}{\partial \xi}\right) \tag{6.11}$$

and the corresponding version of the mixing length hypothesis (6.1) reads

$$\alpha = l_m^2 \left\{\left(\frac{\partial u}{\partial \zeta}\right)^2 + \left(\frac{\partial u}{\partial \xi}\right)^2\right\}^{\frac{1}{2}} Re_0 \tag{6.12}$$

, in which the distribution of $l_m(\xi,\zeta)$ must be given in order to solve the distribution of u from (6.11) and (6.12). The choice of l_m, however, introduces important uncertainties, so that the computational effort needed to solve the rather complicated system (3.9)-(3.10) may be unjustified. In that case either more sophisticated turbulence models have to be applied (see, for instance; Rastogi et al., 1978; Rodi, 1978b; Leschziner, 1978), or more crude, but simpler models can be used just as well. As the modelling of turbulence is not expected to be of primary importance to the present curved flow computations (cf. par. 5.9), it will be attempted to find a simpler mode than (6.12).

The channels to be considered are shallow, so that the vertical diffusion of momentum will be predominant in the greater part of the cross-section. Only at relatively small distances (order

of magnitude d) from the sidewalls the influence of horizontal diffusion will be perceptible. Although in curved rectangular channel flow an accurate description of the flow near the sidewalls, especially near the inner wall, may be needed in order to have a good prediction of the flow in the other parts of the cross-section (see chapters 3 and 4), the accurate description of the flow in the sidewall regions itself is not aimed at. Besides, in the actual applications of the mathematical model to alluvial channels, a vertical inner sidewall, if present at all, will be of minor importance because of the relatively small depth of flow in the inner bend; in that case the role of the vertical inner wall in the main velocity redistribution is taken over by the gently sloping bank there (Kalkwijk et al., 1980). Therefore it will be attempted to formulate a turbulance model based on the one for infinitely wide streams described in par. 6.3, i.e. with the turbulence viscosity based on the vertical exchange of momentum.
It is rather obvious in this respect to take the vertical distribution of the turbulence viscosity the same as in uniform flow, i.e.

$$\alpha \sim 6\zeta(1+\zeta) \tag{6.13}$$

It should be noted, however, that this distribution is derived from the more or less arbitrarily adopted logarithmic distribution of the velocity in uniform rectilinear shear flow. In a later stage, the vertical distribution of α will be subject to further investigations (see par. 6.2.2.).
In the shallow flows considered here, turbulence is mainly generated at the bottom. Therefore it is rather obvious to take the turbulence viscosity proportional to the bottom friction velocity. In case of uniform flow, the normalized bottom friction velocity u_τ equals $\sqrt{g}/C$, so that it seems logical to describe the normalized turbulence viscosity for channels of finite width by

$$\alpha = -6\,\frac{C}{\sqrt{g}}\,u_\tau\zeta(1+\zeta) \tag{6.14}$$

Although, in general, the quantity $Cu_\tau/\sqrt{g}$ is not equal to unity, it will be of the order O(1), so that the turbulence viscosity is appropriately normalized in this way.
For shallow rectangular channels it seems somewhat overdone to relate α to the local bottom friction velocity, since the only regions where the quantity $Cu_\tau/\sqrt{g}$ will deviate considerably from unity are the sidewalls regions and there a turbulence model based on the vertical exchange of momentum is likely to be wrong. Especially if longitudinal accelerations occur, such as in curved channels, the non-uniformity of these accelerations will influence the transverse distribution of the turbulence viscosity to a much higher extent than the non-uniformity of u_τ. In channels with large scale variations of the bed level, however, u_τ will vary much stronglier and expression (6.14) makes more sense. Therefore this expression will be applied to rectangular channels, as well.
Though the distribution of α according to (6.14) may be not quite correct in the sidewall regions, it tends to zero at the sidewalls, which corresponds with the physical idea that the mixing lenght and the turbulence viscosity should vanish at the fixed boundaries. On the other hand, this gives rise to problems when attempting to impose the no-slip conditions there (see also par. 6.3). Launder et al. (1974) suggest to cope with these problems by applying a "wall function technique", i.e. the distribution of the velocity close to a fixed boundary is given as a function of the distance to that boundary. For smooth walls the following "universal law of the wall" is often used (Rastogi et al., 1978; Rodi, 1978b):

$$V_{res} = \frac{V_\tau}{\kappa} \ln(Ey^+) \qquad (6.15)$$

, in which: V_{res} = resultant velocity parallel to the wall,
V_τ = resultant friction velocity for the wall,
E = roughness parameter ($\simeq$ 9 for smooth walls),

y^+ = $V_\tau \tilde{y}/\nu$ = dimensionless wall distance,

$\tilde{y}$ = wall distance,

ν = kinematic viscosity of the fluid.

Since in alluvial rivers the bottom uses to be rough, however, a rough wall equivalent of (6.15) or a generalized form holding good for smooth and for rough walls is needed. Therefore the following generalized wall function is adopted:

$$V_{res} = \frac{V_\tau}{\kappa} \{ \frac{\kappa C}{\sqrt{g}} + 1 + \ln \frac{\tilde{y}}{d} \} \qquad (6.16)$$

, which corresponds with the logarithmic velocity distribution (6.8).
Rewriting this expression into the form of (6.15) yields

$$V_{res} = \frac{V_\tau}{\kappa} \ln(E^* \frac{y}{d}) \quad \text{with} \quad E^* = \exp(1 + \frac{\kappa C}{\sqrt{g}}) \qquad (6.17)$$

In case of a smooth wall, the Chezy factor can be approximated by (Chow, 1959)

$$\frac{C}{\sqrt{g}} \simeq 2.5 \ln(3.7 \frac{V_\tau d}{\nu}) \qquad (6.18)$$

, so that

$$E^* \simeq 10 \frac{V_\tau d}{\nu} \qquad (6.19)$$

, which is almost in accordance with the value of 9 for E.
The rough wall approximation of the Chezy factor given by Chow (1959) reads

$$\frac{C}{\sqrt{g}} \simeq 2.5 \ln(12.2 \frac{d}{k}) \qquad (6.20)$$

, k denoting the Nikuradse sand roughness. In that case

$$E^* \simeq 33 \frac{d}{k} \tag{6.21}$$

, so that the wall function (6.17) can be elaborated to

$$V_{res} = \frac{V_\tau}{\kappa} \ln(33 \frac{\tilde{y}}{k}) \tag{6.22}$$

The dependence of V_{res} on the dimensionless wall distance y/k corresponds with the theory of turbulent boundary layers along rough flat plates (Hinze, 1975).

In order to have an indication of the performance of this turbulence model, it is applied to fully-developed flow in a straight shallow channel. Assuming the logarithmic distribution (6.8) to hold good for the velocity in any vertical, equations (6.11) and (6.14) can be elaborated to

$$0 = - \frac{\partial p}{\partial s} - 6 \frac{C}{\sqrt{g}} \zeta(1+\zeta) \{1 + \frac{\sqrt{g}}{\kappa C} + \frac{\sqrt{g}}{\kappa C} \ln(1+\zeta)\} \frac{\partial}{\partial \xi}(\bar{u} \frac{\partial \bar{u}}{\partial \xi}) +$$

$$- \frac{6}{\kappa} u_\tau \bar{u} \tag{6.23}$$

If the velocity has the same vertical distribution throughout the cross-section, the bed friction will be proportional to the depth-averaged velocity and for the logarithmic velocity distribution adopted here, the constant of proportionality is $\sqrt{g}/C$. Averaging (6.23) over the depth then yields

$$0 = - \frac{\partial \bar{p}}{\partial s} + (1 + \frac{1}{6} \frac{\sqrt{g}}{\kappa C}) \frac{\partial}{\partial \xi} (\bar{u} \frac{\partial \bar{u}}{\partial \xi}) - 6 \frac{\sqrt{g}}{\kappa C} \bar{u}^2 \tag{6.24}$$

The wall function approximations for $\bar{u}$ near the sidewalls are

$$\bar{u} = \frac{|\bar{u}_{\tau w}|}{\kappa} \{\frac{\kappa C}{\sqrt{g}} + 1 + \ln(\frac{B}{2d} + \xi)\} \quad \text{for} \quad \xi \leq -\frac{B}{2d} + \delta \tag{6.25}$$

$$\bar{u} = \frac{|\bar{u}_{\tau w}|}{\kappa} \{\frac{\kappa C}{\sqrt{g}} + 1 + \ln(\frac{B}{2d} - \xi)\} \quad \text{for} \quad \xi \geq \frac{B}{2d} - \delta \tag{6.26}$$

, where δ denotes the interval on which the approximation holds good and $\bar{u}_{\tau w}$ is the depth-averaged sidewall friction velocity.
The system (6.24) through (6.26) contains two unknown constants, viz. the longitudinal pressure gradient, which can be determined from the integral condition of continuity, and the sidewall friction velocity, which must be determined from an additional condition obtained by assuming that both equations (6.24) and the wall function approximation (6.25) or (6.26) hold good in the wall-nearest mesh of the computational grid. Further details of the solution procedure are given in Appendix D.

For three cases of fully-developed straight channel flow, the results of the aforementioned depth-averaged model were compared with measured data.
Figure 32a shows this comparison for a narrow, smooth-walled rectangular pipe (Tracy, 1965; height/width = 6.4; C = 60 $m^{\frac{1}{2}}/s$); in figure 32b the computational results are compared with measured data from a shallow rectangular open channel with artificially roughened bottom (Rodi, 1978b; depth/width $\simeq$ 1/30; C_{bottom} = 21 $m^{\frac{1}{2}}/s$); a comparison with measured data from a shallow rectangular pipe (Builtjes, 1981; height/width = 1/10; C = 60 $m^{\frac{1}{2}}/s$) is given in figure 32c. As was to be expected, only close to the sidewalls the computed depth-averaged velocities deviate from the measured ones; the measured velocities are somewhat higher there. An important part of this deviation, however, will be due to the secondary circulation caused by the transverse anisotropy of turbulence near the

sidewalls (Gessner et al., 1965; Tracy, 1965; Gerard, 1978). This circulation, which cannot be accounted for when applying a scalar turbulence viscosity, deflects the main flow isovels towards the corners formed by the bottom and the sidewalls, thus giving rise to higher depth-averaged velocities near the sidewalls.

In addition to this secondary circulation, there can be two other causes of deviations between measured and computed velocities, viz. the similarity can be shown by solving equation (6.11) for a given turbulence viscosity a and comparing the resulting distributions of the depth-averaged velocity and the bottom shear stress with the one obtained from the corresponding depth-averaged equation

$$0 = - \frac{\partial p}{\partial s} + \overline{a'f} \frac{\partial}{\partial \xi} \left(\bar{a} \frac{\partial \bar{u}}{\partial \xi} \right) - \bar{a}\bar{u} \left(a' \frac{\partial f}{\partial \zeta} \right) \Big|_{\zeta=-1} \tag{6.27}$$

, which is based on the similarity hypothesis

$$u(\xi,\zeta) = \bar{u}(\xi)\, f(\zeta); \qquad a(\xi,\zeta) = \bar{a}(\xi)\, a'(\zeta) \tag{6.28}$$

The comparison was made for three different distributions of a, viz.

1) the parabolic distribution (see also 6.13)

$$a = \min \{-6\zeta(1+\zeta),\ 6(\tfrac{B}{2d} + \xi)(1 - \tfrac{B}{2d} - \xi)\}$$

$$\text{for } \xi \leq - \frac{B}{2d} + 0.5$$

$$a = -6\zeta(1+\zeta) \quad \text{for} \quad - \frac{B}{2d} + 0.5 \leq \xi \leq \frac{B}{2d} - 0.5 \tag{6.29}$$

$$a = \min \{-6\zeta(1+\zeta),\ 6(\tfrac{B}{2d} - \xi)(1 - \tfrac{B}{2d} + \xi)\}$$

$$\text{for } \xi \geq \frac{B}{2d} - 0.5$$

2) a distribution corresponding with (6.14)

$$a = \bar{u}\ \{-6\zeta(1+\zeta)\} \tag{6.30}$$

3) the mixing length distribution (6.12) with (cf. Rodi, 1978b)

$$l_m = \min\ \{\kappa(1+\zeta),\ \ \kappa(\frac{B}{2d} + \xi),\ \ \kappa(\frac{B}{2d} - \xi),\ 0.1\} \tag{6.31}$$

In all depth-averaged computations a' was taken parabolic, according to (6.13), and f was taken logarithmic, according to (6.8).

Figure 33 shows that in the first two cases the depth-averaged velocities resulting from the depth-averaged computations agree rather well with the ones resulting from the fully two-dimensional computations, although the latter are uniform over a larger part of the cross-section. The mixing length model, however, leads to important differences between the results of the two computations: the depth-averaged computation leads to spuriously thick wall layers (figure 33c).

Rastogi et al. (1978) give a similar comparison between two-dimensional and depth-averaged computations with the so-called k-ε-model (see also Rodi, 1978b), where the turbulence viscosity is related to the turbulent kinetic energy and its rate of dissipation, both of which are solved from transport equations including convective transport, diffusion, production and dissipation/destruction. For a shallow channel with a very rough bottom ($C = 21\ m^{\frac{1}{2}}/s$) and smooth sidewalls, the results of the two computations appear to be in good agreement (figure 32b). It is not clear, however, whether this agreement is equally good if the bottom and the sidewalls are of the same roughness.

Figure 33 also gives a comparison between the bottom shear stress distributions resulting from the two-dimensional and the depth-averaged computations. The effect of depth-averaging appears to be rather small for the turbulence models 1) and 2), but it is much stronger for the mixing length model. Apart from that, it should

be noted that all distributions are likely to be in error near the sidewalls, because of the effect of the secondary circulation there (Leutheusser, 1963; Liggett et al., 1965).
It is concluded from the foregoing that depth-averaging of the momentum equation will not give rise to serious errors as long as simple turbulence models like 1) and 2) are applied, but that more sophisticated turbulence models can lead to erroneous results. For the two-dimensional versions of the turbulence models considered here, the distributions of the depth-averaged velocity and the bottom shear stress hardly differ, as is shown in figure 34. Similarly, figure 32b shows that the results of the depth-averaged versions of model 2) and the k-ε-model are in good agreement. So for all turbulence models considered it will be the aforementioned secondary circulation that is the main cause of the differences between the measured and the computed depth-averaged velocities represented in figure 32.

6.5. Turbulence model for curved channel flow

Compared with fully-developed straight channel flow, the flow in curved channels will be attended with extra strain-rates due to longitudinal accelerations, streamline curvature and the skewed velocity field. Although these extra strain-rates may have a considerable influence on the turbulence properties (Bradshaw, 1976; Hunt et al., 1979), this influence will be small for rather mildly curved shallow channels. Therefore this influence is left out of consideration here and, as in case of fully-developed straight channel flow, the turbulence model will be based on the assumption of predominant bottom friction. To that end expression (6.14) is generalized to

$$\alpha = \frac{C}{\sqrt{g}} \; U_\tau \alpha'(\zeta) \qquad (6.32)$$

, in which U_τ is the resultant normalized bottom friction velocity in the vertical considered and $\alpha'(\zeta)$ is a vertical distribution function, for the present the parabola $\alpha'(\zeta) = -6\zeta(1+\zeta)$.

The wall function approximation for the resultant velocity u_{res} parallel to the bottom is formulated as

$$u_{res}\Big|_{\zeta \leq -1+\delta} = \frac{U_\tau}{\kappa} \{\frac{\kappa C}{\sqrt{g}} + 1 + \ln(1+\zeta)\} \tag{6.33}$$

If the bottom is horizontal, this can be split into

$$u\Big|_{\zeta \leq -1+\delta} = \frac{u_\tau}{\kappa} \{\frac{\kappa C}{\sqrt{g}} + 1 + \ln(1+\zeta)\} \tag{6.34}$$

$$v\Big|_{\zeta \leq -1+\delta} = \frac{v_\tau}{\kappa} \{\frac{\kappa C}{\sqrt{g}} + 1 + \ln(1+\zeta)\} \tag{6.35}$$

, u_τ and εv_τ being the longitudinal and the transverse component of U_τ, respectively. These components of the bottom friction velocity are determined by the additional conditions arising from the assumption that the domains of validity of the wall function approximation and the system of differential equations overlap (see also Appendix E).
The wall function approximations near the sidewalls can be treated in a similar way, to yield

$$u\Big|_{\xi \leq -B/2d+\delta_l} = \frac{u_{\tau l}}{\kappa} \{\frac{\kappa C}{\sqrt{g}} + 1 + \ln(\frac{B}{2d} + \xi)\} \tag{6.36}$$

$$w\Big|_{\xi \leq -B/2d+\delta_l} = \frac{w_{\tau l}}{\kappa} \{\frac{\kappa C}{\sqrt{g}} + 1 + \ln(\frac{B}{2d} + \xi)\} \tag{6.37}$$

$$u\Big|_{\xi \geq B/2d-\delta_r} = -\frac{u_{\tau r}}{\kappa} \{\frac{\kappa C}{\sqrt{g}} + 1 + \ln(\frac{B}{2d} - \xi)\} \tag{6.38}$$

$$w\Big|_{\xi \geq B/2d-\delta_r} = -\frac{w_{\tau r}}{\kappa} \{\frac{\kappa C}{\sqrt{g}} + 1 + \ln(\frac{B}{2d} - \xi)\} \tag{6.39}$$

, where $u_{\tau l}$ and $\varepsilon w_{\tau l}$ are the longitudinal and the vertical

of the friction velocity at the left wall and $u_{\tau r}$ and $\varepsilon w_{\tau r}$ are the corresponding components at the right wall.
Averaging (6.36) and (6.38) over the depth of flow yields the following generalization of (6.25) and (6.26):

$$\bar{u}\Big|_{\xi \leq -B/2d+\delta_l} = \frac{\bar{u}_{\tau l}}{\kappa} \{\frac{\kappa C}{\sqrt{g}} + 1 + \ln(\frac{B}{2d} + \xi)\} \tag{6.40}$$

$$\bar{u}\Big|_{\xi \geq B/2d-\delta_r} = - \frac{\bar{u}_{\tau r}}{\kappa} \{\frac{\kappa C}{\sqrt{g}} + 1 + \ln(\frac{B}{2d} - \xi)\} \tag{6.41}$$

The depth-averaged wall friction velocities $\bar{u}_{\tau l}$ and $\bar{u}_{\tau r}$ are determined from overlap conditions, in a similar way as in the case of straight channel flow discussed before.
The wall function approximations used for the velocities parallel to the fixed boundaries have implications for the velocities normal to these boundaries, as well. The distribution of the vertical velocity component w near the bottom, for instance, is determined by the equation of continuity and the wall function approximations (6.34) and (6.35), yielding

$$w\Big|_{\zeta \leq -1+\delta} = - \frac{1}{\kappa} (\frac{\partial v_\tau}{\partial \xi} + \frac{\varepsilon}{r} v_\tau + \frac{1}{r} \frac{\partial u_\tau}{\partial \phi})(1+\zeta) \{\frac{\kappa C}{\sqrt{g}} + \ln(1+\zeta)\} \tag{6.42}$$

Similarly, the radial velocity component near the sidewalls is given by

$$v\Big|_{\xi \leq -B/2d+\delta_l} \simeq - \frac{1}{\kappa} (\frac{1}{r} \frac{\partial u_{\tau l}}{\partial \phi} + \frac{\partial w_{\tau l}}{\partial \zeta})(\frac{B}{2d} + \xi) \{\frac{\kappa C}{\sqrt{g}} + \ln(\frac{B}{2d} + \xi)\} \tag{6.43}$$

$$v\Big|_{\xi \geq B/2d-\delta_r} \simeq - \frac{1}{\kappa} (\frac{1}{r} \frac{\partial u_{\tau r}}{\partial \phi} + \frac{\partial w_{\tau r}}{\partial \zeta})(\frac{B}{2d} - \xi) \{\frac{\kappa C}{\sqrt{g}} + \ln(\frac{B}{2d} - \xi)\} \tag{6.44}$$

The shear stresses at the fixed boundaries are related to the wall friction velocities through the definition

$$u_{\tau_{res}} = |\tau_{res}|^{\frac{1}{2}} \operatorname{sign}(\tau_{res}) \qquad (6.45)^{*})$$

On the other hand, the shear stress components are related to the corresponding component of the rate of strain through the Boussinesq-hypothesis. The bottom shear stress components $\tau_{b\phi}$ and $\varepsilon\tau_{b\xi}$, for instance, follow from

$$\tau_{b\phi} = \lim_{\zeta\downarrow -1} \frac{\alpha}{Re_0} \frac{\partial u}{\partial \zeta} \quad ; \quad \tau_{b\xi} = \lim_{\zeta\downarrow -1} \frac{\alpha}{Re_0} \frac{\partial v}{\partial \zeta} \qquad (6.46)$$

Making use of (6.32), (6.34) and (6.35), these expressions can be elaborated to

$$\tau_{b\phi} = U_\tau u_\tau; \quad \tau_{b\xi} = U_\tau v_\tau \text{ , whence } \tau_{b_{res}} = U_\tau^2 \text{ (for } U_\tau > 0) \qquad (6.47)$$

, which is consistent with (6.45)
Similarly, the shear stresses at the sidewalls are give by

$$\tau_{l\phi} = \lim_{\xi\downarrow -B/2d} \frac{\alpha}{Re_0} \frac{\partial u}{\partial \xi} = |U_{\tau l}| u_{\tau l};$$

$$\tau_{l\zeta} = \lim_{\xi\downarrow -B/2d} \frac{\alpha}{Re_0} \frac{\partial w}{\partial \xi} = |U_{\tau l}| w_{\tau l} \qquad (6.48)$$

$$\tau_{r\phi} = \lim_{\xi\uparrow B/2d} \frac{\alpha}{Re_0} \frac{\partial u}{\partial \xi} = |U_{\tau r}| u_{\tau r};$$

$$\tau_{r\zeta} = \lim_{\xi\uparrow B/2d} \frac{\alpha}{Re_0} \frac{\partial w}{\partial \xi} = |U_{\tau r}| w_{\tau r} \qquad (6.49)$$

Both (6.48) and (6.49) are consistent with (6.45).

6.6. Sensitivity analysis for the turbulence model

The turbulence model described in the foregoing is based

---

*) Here τ denotes the shear stress normalized by ρV^2.

on a considerable number of hypotheses and assumptions. Although the verification of the two basic hypotheses, the Boussinesq hypothesis and the mixing length hypothesis, would be most interesting for the present complicated flow case, their applicability is left out of consideration here (see, for instance: Bradshaw, 1976 and Hunt et al., 1979). The various assumptions concerning the distribution of the turbulence viscosity, however, will be subject to a closer investigation and the influence of the overall mean value and the vertical and horizontal distributions of the turbulence viscosity on various aspects of the flow will be analysed. For this analysis the differential equations and solution procedures described in chapter 7 will be utilized.

6.6.1. Influence of the overall mean value of the turbulence viscosity

As was stated in par. 6.3, the parabolic distribution of the turbulence viscosity in uniform rectilinear shear flow corresponds with an effective Reynolds number

$$Re_0 = \frac{6}{\kappa} \frac{C}{\sqrt{g}} \tag{6.50}$$

and the overall mean value of the turbulence viscosity is then given by

$$\bar{A}_0 \approx 0.067\ \rho v_* d \tag{6.51}$$

, where $v_* = V\sqrt{g}/C$ is the bottom friction velocity. In the literature somewhat different values of the constant of proportionality in (6.51) are suggested: Engelund (1964) gives a value of 0.077 and Rastogi et al. (1978) use 0.0765 in their depth-averaged version of the k-ε-model. These values, however, are based on experimental data for uniform flow in closed channels, so they will only hold good if the influence of the water surface on the turbulence is negligible. A comparison of the turbulence characteristics measured in uniform open channel

flow (Nakagawa et al., 1975) with those for a closed channel (Laufer, 1951) shows that the water surface influences turbulence, indeed (see also Rodi, 1978b)*).

Until recently, the turbulence viscosity used to be determined experimentally from the vertical distributions of the turbulence-averaged velocity v_0 and the shear stress τ_{sz} in uniform flow, making use of the definition

$$A_t = \frac{\tau_{sz}}{\frac{\partial v_0}{\partial z}} \tag{6.52}$$

In uniform open channel flow τ_{sz} varies linearly from its maximum at the bottom to zero at the surface. Adopting Chezy's law, this yields

$$A_t = -\frac{g}{C^2}\frac{\bar{v}_0^2}{d}\frac{z}{\frac{\partial v_0}{\partial z}} \tag{6.53}$$

The vertical distribution of v_0, and hence the vertical derivative of v_0 in (6.52), is mostly approximated by fitting a certain type of curve (logarithmic, for instance) to the measured data.

As will be shown in par. 6.6.2, the distribution of the velocity in the upper parts of the vertical is hardly influenced by the distribution of the turbulence viscosity there. Inversely, this implies that the turbulence viscosity distribution in this region will be quite sensitive to the distribution curve adopted as an approximation of the measured velocities. Hence the depth-averaged turbulence viscosity will also be strongly dependent on

---

*) This could explain the velocity reduction near the water surface often observed in open channel flow, even if the channel is straight and shallow (see, for instance: De Vriend et al., 1977 & 1978, or De Vriend, 1979b & 1980b).

this approximation and therefore the aforementioned method of experimental determination of A_t can be expected to yield a wide variety of depth-averaged values.
Rozovskii (1961) gives a review of the experimental values of $\bar{A}_t$ obtained in this way. Grouped according to the approximation of the measured velocity distribution:

- the Boussinesq-Basin parabola, with A_t constant in a vertical and a finite slip-velocity at the bottom (cf. Engelund, 1964), which leads to values of the constant of proportionality in (6.46) between 0.065 and 0.071 (Engelund: 0.077);
- the elliptic distribution (Karaushev, 1946), yielding values of the constant that depend on C:

$$\frac{\bar{A}_t}{\rho v_* d} = (1.9 + 0.7 \frac{C}{\sqrt{g}})^{-1} \quad \text{for} \quad 3 < \frac{C}{\sqrt{g}} < 21 \qquad (6.54)$$

  , so that for C = 60 $m^{\frac{1}{2}}/s$ a value of 0.065 is found;
- the logarithmic distribution, for which the constant equals $\kappa/6$, as was shown in the foregoing; for κ=0.4, this yields a value of 0.067, but for higher values of κ (Rastogi et al. (1978) use 0.42; Rodi (1978b) suggests 0.435; Rozovskii (1961) suggests values as large as 0.5), the constant increases in proportion;
- the power law distribution; the 1/7th-power law, for instance, yields a value of $1.15\sqrt{g}/C$ for the constant, i.e. 0.060 for C = 60 $m^{\frac{1}{2}}/s$.

Another class of experiments from which A_t can be determined concerns the dispersion of suspended matter in uniform straight channel flow.
This indirect determination of A_t is based on the so-called Reynolds-analogy (see Hinze, 1975), which states that in turbulent flow the transport processes for mass and momentum are analoguous. At the experiments reported by Jobson et al., (1970), dye was injected at the free surface of fully-developed straight channel flow. From the rate of dispersion of this dye the transfer coefficient was derived. The observed values of this coefficient differ

only a few per cent from those predicted by equation (6.51). Similar experiments on heat transfer in an open channel (Ueda et al., 1977) suggest about 10% smaller values of the transfer coefficient.

In addition, experiments were made with suspensions of fine-grained sand (Vanoni, 1944; Jobson et al., 1970; Coleman, 1970), but then the dispersion process is complicated by the different densities of the fluid and the suspended particles. Hence the values of $\bar{A}_t$ obtained from these experiments are not quite reliable.

Recent advances in measuring techniques (hot film, laser-doppler anemometry) allow for the turbulent velocity fluctuations to be measured. Hence A_t can be determined from turbulence quantities, using, for instance, the basic relation of the k-ε-model (Launder et al., 1972, 1978b)

$$A_t = c_\mu \frac{k_t^2}{\varepsilon_t} \tag{6.55}$$

, in which k_t denotes the local turbulent kinetic energy, ε_t the rate of energy dissipation and c_μ a known constant of proportionality.

Equation (6.55) was used to derive A_t from the measured distributions of k_t and ε_t in uniform open channel flow presented by Nakagawa et al. (1975).

The resulting values of A_t are so widely scattered, however, that it is impossible to fit a reliable distribution curve to the measured data (see figure 35). The mean value of A_t lies between 0.06 and 0.07, but regarding the large scatter in the data, a more exact figure cannot be given. This shows that determining A_t from turbulence data requires much higher measuring accuracies in order to provide reliable information.

The foregoing leads to the conclusion that a great deal of uncertainty exists about the value of the constant of proportionality in (6.51), even for uniform rectilinear shear flow.

For curved channel flow this uncertainty is even stronger, as it is hardly known how turbulence is affected by the extra strain rates due to longitudinal accelerations, streamline curvature and the skewed velocity field (see Bradshaw, 1976). Therefore it is worthwhile to investigate the sensitivity of a mathematical model as described in chapter 7 to the overall mean turbulence viscosity. The overall mean turbulence viscosity is incorporated in the effective Reynolds number, which can be generalized to

$$Re_0 = \frac{\gamma}{\kappa}\frac{C}{\sqrt{g}} \quad \text{and hence} \quad \bar{A}_0 = \frac{\kappa}{\gamma}\rho v_* d \tag{6.56}$$

The influence of the constant γ is to be investigated now. As the mixing length close to the bottom will be proportional to the bottom distance (Prandtl, 1925; Schlichting, 1951).

$$\ell_m = \kappa(1+\zeta) \tag{6.57}$$

the vertical distribution of the turbulence viscosity near the bottom must be (see (6.4))

$$\alpha = \gamma(1+\zeta) \tag{6.58}$$

Therefore the generalization of Re_0 and A_0 to (6.56) is combined with a correction of the parabolic distribution of α in order to satisfy (6.57) and (6.58):

$$\alpha = -\frac{C}{\sqrt{g}} U_\tau \zeta\,(1+\zeta)\,\{12(1+\zeta) - \gamma(1+2\zeta)\} \tag{6.59}$$

For γ=6 this reduces to the parabola $-6\zeta(1+\zeta)$, for smaller γ the distribution is slightly deformated, the maximum shifting somewhat upwards and increasing slightly (figure 36a). Figure 36 shows how a variation of γ between 0.4 and 6.0 (i.e. a variation of κ/γ between 1.0 and 0.067) influences

various aspects of curved channel flow. The vertical distribution of the main velocity and the stream function of the secondary flow (figure 36b) are hardly affected and no more is the main bed shear stress factor k_m^2 ($= \tau_b C^2/(g\bar{U}^2)$), as is shown by figure 36c. The secondary bed shear stress factor $k_m k_s$, however, increases considerably as γ decreases (figure 36d) and the intensity of the fully-developed secondary flow, $\hat{\psi}Re_0/\bar{u}$, as well as the secondary flow convection factor $\overline{uv}_s/\bar{u}^2$ in fully-developed curved flow decrease fairly strongly with decreasing γ (figures 36e and 36f). These results lead to the conclusion that quantities related to the main flow are hardly influenced by γ, whereas quantities related to the secondary flow are much more sensitive to this factor.

6.6.2. Influence of the vertical distribution of the turbulence viscosity

As was shown in par. 6.3, a purely logarithmic velocity distribution will correspond with a parabolic distribution of the turbulence viscosity, at least in uniform rectilinear shear flow. If turbulence is described by the k-ε-model, however, as was done with success in various fully three-dimensional computations of turbulent flow in curved channels (Pratap, 1975; Pratap et al., 1975; Leschziner et al., 1978 and 1979), a quite different turbulence viscosity distribution is found (see figure 37): near the bottom it closely agrees with the parabola but in the upper half of the vertical a remains almost constant rather than descreasing to zero at the surface. Nonetheless, the resulting velocity distribution hardly differs from the logarithmic one, not even in the upper half of the vertical (figure 37). Hence it is concluded that the distribution of the turbulence viscosity in the upper half of the vertical is rather unimportant to the prediction of uniform rectilinear shear flow. Inversely, the turbulence viscosity distribution will be quite sensitive to changes in the velocity distribution, so that it is rather difficult to determine A_t from velocity measurements (see par. 6.6.1). This explains why some experiments reported in the literature seem to provide evidence in favour of the parabolic

distribution (Vanoni, 1944; Jobson et al., 1970), whereas others seem to corroborate the more uniform distribution according to the k-ε-model (Coleman, 1970). On the basis of physical arguments, some reduction of the turbulence viscosity is to be expected near the water surface (cf. Rodi, 1978b), but there is not enough experimental evidence to quantify this reduction (see Nakagawa et al., 1975, and the elaboration of their data represented in figure 34).
In view of this doubt about the vertical distribution of the turbulence viscosity, even in the rather simple case of uniform rectilinear shear flow, the influence of this distribution on curved flow needs to be established. To that end, three different distributions are considered, each of them with the same slope at the bottom (cf. expression 6.58) and with $\gamma=5$:
1) the modified parabolic distribution (6.59):

$$\alpha' = -\zeta(1+\zeta)(7+2\zeta) \tag{6.60}$$

2) an approximation of the k-ε-distribution shown in figure 37:

$$\begin{aligned} \alpha' &= \frac{1}{9}(1+\zeta)(8\zeta^2-35\zeta+2) \quad \text{for} \quad \zeta \leq -0.5 \\ \alpha' &= \frac{43}{36} \quad \text{for} \quad \zeta \geq -0.5 \end{aligned} \tag{6.61}$$

3) a uniform distribution in the upper part of the vertical combined with a linearly decreasing part near the bottom

$$\begin{aligned} \alpha' &= 5(1+\zeta) \quad \text{for} \quad \zeta \leq -0.775 \\ \alpha' &= 1.127 \quad \text{for} \quad \zeta \geq -0.775 \end{aligned} \tag{6.62}$$

The vertical distribution functions f, g and $\frac{\partial g}{\partial \zeta}$ and the most important constants in the depth-averaged equations are represented in figures 38 and 39 for each of these distributions. Figures 38a through 38d show that the vertical distributions

of the main and secondary velocity components are influenced only slightly by the distribution of a. The coefficients in the depth-averaged main flow equations (7.25) and (7.26) represented in figures 39a through 39d, are hardly influenced, either, and no more is the secondary bed shear stress factor $k_m k_s$ (figure 39g). The coefficients in the depth-averaged stream function equation (7.39), however, are influenced to a considerably higher extent, as is shown by figures 39e and 39f as well as by the secondary flow intensity in fully-developed curved flow represented in figure 39h.
The same must be stated as regards the secondary flow convection factor $\overline{uv}_s/\bar{u}^2$, which is shown in figure 39i.
The only quantity for which the differences exceed 15% is the factor $\overline{ga^r}_{\zeta\zeta}$ (figure 39f), figuring in a group of higher order terms in the depth-averaged stream function equation (7.39).
In order to establish the influence of the great difference between the values of this factor for the distributions (6.60) and (6.61), the complete turbulent flow model described in chapter 7 was applied to the LFM-flume (see chapter 9) with either distribution of a'. A comparison of the results shown in figure 40 makes clear that, although the flume is rather sharply curved, the depth-averaged main velocity is hardly influenced and that the influence on the depth-averaged stream function of the secondary flow nowhere exceeds 10%.
The foregoing leads to the conclusion that the distribution of the turbulence viscosity in the upper part of the vertical hardly influences the main flow, whereas its influence on the secondary flow is rather small.
The secondary flow intensity and the convective effect of the secondary flow on the main flow tend to increase as the turbulence viscosity becomes more uniform in the upper part of the vertical.

6.6.3. Influence of the horizontal distribution of the turbulence viscosity

The turbulence viscosity in the present model is related more or less arbitrarily to the local bottom friction velocity. As was stated in

par. 6.2 and 6.3, this will be approximately correct in the central region of straight or mildly curved shallow channels, where the velocity gradients, and hence the exchange of momentum due to turbulence, are mainly vertical. Near the sidewalls and in sharply curved flow, however, where important extra strain rates occur, this turbulence model will give rise to errors in the predicted velocities. In general, the extra strain rates due to the sidewalls tend to increase the local turbulence viscosity (cf. figures 33b and 33c). This effect is felt mainly in $\bar{a}$, as the vertical distribution of a remains practically unaltered.
In straight channel flow, the effect of local errors in $\bar{a}$ near the sidewalls will be restricted to the sidewall regions. In curved channels, however, in which there is an important transverse exchange of momentum throughout the cross-section, this effect could extend over a much larger region. Therefore, the influence of the horizontal distribution of the turbulence viscosity in the sidewall regions was subject to a seperate investigation.
To that end, the depth-averaged main velocity in the LFM-flume was computed with three different, more or less arbitrary distributions of $\bar{a}$ viz.

1) the present model ($\bar{a} \sim U_\tau$)

2) $\bar{a}$ corresponding with the parabolic distribution (6.29)

3) $\bar{a}$ = 1 with linear wall layers, i.e.

$$\bar{a} = \min \{1,\ 6(\frac{B}{2d} + \xi),\ 6(\frac{B}{2d} - \xi)\} \qquad (6.63)$$

Figure 41 shows that there are considerable differences between the resulting distributions of $\bar{u}$, but that they are restricted to the regions close to the sidewalls. Hence it is concluded that, especially near the sidewalls, the horizontal distribution of the turbulence viscosity needs special attention if local errors have to be avoided. If a detailed description of the velocity in the sidewalls regions is not wanted, however,

the accurate modelling of turbulence is rather unimportant there, either.

6.7. Discussion

The foregoing paragraphs make clear that, although various more or less fundamental objections can be made against the simple turbulence model presented in par. 6.5, this model seems acceptable for the present purpose as long as the Boussinesq hypothesis holds good. The assumed overall mean value of the turbulence viscosity was shown to have a rather strong effect on the secondary flow and the secondary bed shear stress (par. 6.6.1), whereas its horizontal distribution in the sidewall regions appeared to be rather important to the depth-averaged main velocity distribution there (par. 6.6.3). The assumed vertical distribution of the turbulence viscosity, however, appeared to be much less critical, provided that near the bottom the linear distribution (6.58) is approached. Therefore future research on eddy viscosity models for turbulent flow in curved shallow channels should be concentrated on the first two aspects.

It should be noted that adopting the Boussinesq hypothesis implies that the prediction of various phenomena, such as the secondary flow due to the anisotropy of turbulence and the sharp velocity reduction near the water surface found in many experiments, is excluded in advance. For the prediction of the depth-averaged main velocity this will be of minor importance, as excellent predictions, even for sharply curved flows, have been obtained on the basis of the Boussinesq hypothesis (Pratap, 1975; Leschziner et al., 1978 & 1979). The predictions of the secondary flow and the vertical distribution of the main flow, however, can be influenced much stronglier by this hypothesis. In straight rectangular channels, the secondary circulation in the sidewall regions caused by the anisotropy of turbulence there (see par. 6.4) cannot be predicted and neither can the corresponding deformation of distributions of the main velocity (increase in the corners, reduction near the surface) and the bottom shear stress (increase near the sidewalls). Though in bends the source of this circulation exists as well, the circulation itself

is mostly dominated by the secondary flow due to curvature (see Shukry, 1949). The latter can be appropriately predicted by a model based on the Boussinesq hypothesis, so that the deformations of the velocity and the bottom shear stress distributions in a bend are likely to be described better than in a straight channel. Furthermore, the presence of turbulence anisotropy as a source of secondary flow can explain why in experiments (De Vriend et al., 1977; De Vriend, 1979b & 1981b) a reverse secondary circulation is found in the upper part of the outer wall region at considerably smaller effective Dean numbers than in the mathematical predictions, either laminar (see par. 3.7) or turbulent (De Vriend et al., 1980a). It is in the upper part of the outer wall region that the two types of secondary flow are counteracting, in such a way that the reverse circulation comes sooner into existence.

Another phenomenon that cannot be predicted when making use of the Boussinesq hypothesis is the velocity reduction near the surface, which was observed in many experiments, both in straight and in curved channels (Chow, 1959; De Vriend et al., 1977 & 1978; De Vriend, 1979b & 1980b).

It is mostly attributed to the aforementioned secondary circulation due to the anisotropy of turbulence (Rouse, 1961; Gessner et al., 1965; Gerard, 1978), but if this were the only cause, the velocity in a shallow straight channel should hardly be reduced at the surface in the central part of the cross-section, the secondary flow being concentrated near the sidewalls (see also: Tracy, 1965). This is in conflict, however, with observations in a very shallow open channel (De Vriend et al., 1977 & 1978), where considerable velocity reductions at the surface were found everywhere in the flume. On the other hand the secondary flow due to curvature can also give rise to main velocity reductions in the upper part of the vertical (see chapter 3), but these are usually much smaller and spread over a much thicker layer than the reductions meant here, for which no satisfactory explanation could be given so far.

7. Computation of turbulent flow in curved rectangular channels

7.1. Objective and approach

Having formulated a (tentative) turbulence model (see chapter 6), the most logical continuation of the mathematical modelling would be to describe fully-developed turbulent flow in curved rectangular channels. On the analogy of chapters 3 and 4, an extensive mathematical model, solving the complete system of turbulence-averaged equations, could be used as a basis and as a reference for simplified computation methods. In contrast with laminar flow, however, even a model solving the complete system of equations for turbulent flow can only be approximative, because of the approximative character of the turbulence model. In addition, the performance of such a model can hardly be tested, by lack of experimental data or more sophisticated mathematical models that could serve as a reference. Consequently, an extensive model of fully-developed turbulent flow is not likely to provide sufficient reliable information to make it worth developing here. Instead of deriving a simplified computational procedure from a model of fully-developed turbulent flow, the basic simplifications that appeared to hold good for laminar flow (see chapter 4) will be supposed applicable to turbulent flow, as well. Apart from neglecting the transverse inertia of the secondary flow, this implies in the first place that a similarity hypothesis is made for the velocity distribution in a cross-section. Several experiments on turbulent flow in curved shallow channels (Rozovskii, 1961; De Vriend et al., 1977 & 1978) seem to justify this hypothesis, but others (Yen, 1965; Siebert et al., 1975; De Vriend, 1979b) make clear that, especially near the sidewalls, caution should be exercised as soon as the effects of curvature become important. Besides, it was shown in par. 6.4 that for some turbulence models the similarity hypothesis can give rise to considerable computational errors in the sidewalls regions. For the turbulence model described in par. 6.5, however, these errors appeared to be of minor importance. In order to avoid complications due to a non-uniform shape of the cross-section, the computational procedure will be outlined here for

rectangular channels with a rigid-lid approximation for the water surface. The most important simplifying assumptions will be verified in the same way as it was done for laminar flow in chapter 5. Besides, a global comparison with measured data will be made in order to test the turbulence model.

7.2. Simplification of the mathematical system

The system of balance equations for mass and momentum, given in chapter 2, will be simplified using the experience gained in the development of the laminar flow model (see chapter 5). Firstly, the flow is split up into a main and a secondary part, according to the definition in par. 5.2, so that the equations of continuity for the main and the secondary flow can be separated.
In addition, all terms that are an order $0(\varepsilon^2)$ smaller than the leading terms of the same type in the same equation are disregarded, and so are the transverse inertia terms in the secondary flow equations, which have proved negligible in the laminar flow case (chapter 3).
The resulting system of equations reads

$$\frac{1}{r}\frac{\partial u_m}{\partial \phi} + \frac{\partial v_m}{\partial \xi} + \frac{\varepsilon}{r} v_m = 0 \tag{7.1}$$

$$\frac{\partial v_s}{\partial \xi} + \frac{\varepsilon}{r} v_s + \frac{\partial w_s}{\partial \zeta} = 0 \tag{7.2}$$

$$\varepsilon Re_0 \left(\frac{u_m}{r}\frac{\partial u_m}{\partial \phi} + v_m \frac{\partial u_m}{\partial \xi} + \frac{\varepsilon}{r} v_m u_m + v_s \frac{\partial u_m}{\partial \xi} + w_s \frac{\partial u_m}{\partial \zeta} + \frac{\varepsilon}{r} v_s u_m\right) =$$

$$-\frac{1}{r}\frac{\partial p}{\partial \phi} + \alpha \nabla^2 u_m + \frac{\partial \alpha}{\partial \xi}\left(\frac{\partial u_m}{\partial \xi} - \frac{\varepsilon}{r} u_m\right) + \frac{\partial \alpha}{\partial \zeta}\frac{\partial u_m}{\partial \zeta} \tag{7.3}$$

$$\varepsilon^3 Re_0 \left(\frac{u_m}{r}\frac{\partial v_m}{\partial \phi} + v_m \frac{\partial v_m}{\partial \xi} + v_s \frac{\partial v_m}{\partial \xi} + w_s \frac{\partial v_m}{\partial \zeta} + \frac{u_m}{r}\frac{\partial v_s}{\partial \phi} + v_m \frac{\partial v_s}{\partial \xi}\right) +$$

$$- \varepsilon^2 Re_0 \frac{u_m^2}{r} = - \frac{\partial p}{\partial \xi} + \varepsilon^2 \alpha \left(\nabla^2 v_m + \nabla^2 v_s - 2 \frac{\varepsilon}{r^2}\frac{\partial u_m}{\partial \phi}\right) +$$

$$+ \frac{\varepsilon^2}{r}\frac{\partial \alpha}{\partial \phi}\left(\frac{\partial u_m}{\partial \xi} - \frac{\varepsilon}{r} u_m\right) + 2\varepsilon^2 \frac{\partial \alpha}{\partial \xi}\left(\frac{\partial v_m}{\partial \xi} + \frac{\partial v_s}{\partial \xi}\right) +$$

$$+ \varepsilon^2 \frac{\partial \alpha}{\partial \zeta}\left(\frac{\partial v_m}{\partial \zeta} + \frac{\partial v_s}{\partial \zeta} + \frac{\partial w_s}{\partial \xi}\right) \qquad (7.4)$$

$$\varepsilon^3 Re_0 \left(\frac{u_m}{r}\frac{\partial w_s}{\partial \phi} + v_m \frac{\partial w_s}{\partial \xi}\right) = - \frac{\partial p}{\partial \zeta} + \varepsilon^2 \alpha \nabla^2 w_s + \frac{\varepsilon^2}{r}\frac{\partial \alpha}{\partial \phi}\frac{\partial u_m}{\partial \zeta} +$$

$$+ \varepsilon^2 \frac{\partial \alpha}{\partial \xi}\left(\frac{\partial v_m}{\partial \zeta} + \frac{\partial v_s}{\partial \zeta} + \frac{\partial w_s}{\partial \xi}\right) + 2\varepsilon^2 \frac{\partial \alpha}{\partial \zeta}\frac{\partial w_s}{\partial \zeta} \qquad (7.5)$$

, in which $\nabla^2 = \frac{\partial^2}{\partial \zeta^2} + \frac{\partial^2}{\partial \xi^2} + \frac{\varepsilon}{r}\frac{\partial}{\partial \xi}$

7.3. Interpretation of the simplified equations

In order to gain some more insight into the system (7.1) through (7.5) and to facilitate its physical interpretation, it is transformed to the stream-oriented coordinate system (n,s,ζ) represented in figure 23. The transformation, which is quite similar to the one applied to the laminar flow equations in par. 5.4, leads to

$$\frac{\partial u_m}{\partial s} - \frac{u_m}{r_n} + \frac{\partial w_m}{\partial \zeta} = 0 \qquad (7.6)$$

$$\frac{\partial v_s}{\partial n} - \frac{\varepsilon}{r_s} v_s + \frac{\partial w_s}{\partial \zeta} = 0 \qquad (7.7)$$

$$\varepsilon Re_0 \{u_m \frac{\partial u_m}{\partial s} + v_s (\frac{\partial u_m}{\partial n} - \frac{\varepsilon}{r_s} u_m) + w_s \frac{\partial u_m}{\partial \zeta}\} =$$

$$- \frac{\partial p}{\partial s} + a\nabla_1^2 u_m + \frac{\partial a}{\partial n} (\frac{\partial u_m}{\partial n} + \frac{\varepsilon}{r_s} u_m) + \frac{\partial a}{\partial \zeta} \frac{\partial u_m}{\partial \zeta} \qquad (7.8)$$

$$\varepsilon^3 Re_0 u_m \frac{\partial v_s}{\partial s} + \varepsilon^2 Re_0 \frac{u_m^2}{r_s} = - \frac{\partial p}{\partial n} + \varepsilon^2 a (\nabla_1^2 v_s + \frac{\partial \tilde{\omega}_m}{\partial s}) +$$

$$+ 2\varepsilon^2 \frac{\partial a}{\partial n} (\frac{\partial v_s}{\partial n} - \frac{u_m}{r_n}) + \varepsilon^2 \frac{\partial a}{\partial \zeta} (\frac{\partial v_s}{\partial \zeta} + \frac{\partial w_s}{\partial n}) +$$

$$+ \varepsilon^2 \frac{\partial a}{\partial s} (- \tilde{\omega}_m + 2 \frac{\varepsilon}{r_s} u_m) \qquad (7.9)$$

$$\varepsilon^3 Re_0 u_m \frac{\partial w_s}{\partial s} = - \frac{\partial p}{\partial \zeta} + \varepsilon^2 a \nabla_1^2 w_s + \varepsilon^2 \frac{\partial a}{\partial n} (\frac{\partial v_s}{\partial \zeta} + \frac{\partial w_s}{\partial n}) +$$

$$+ 2\varepsilon^2 \frac{\partial a}{\partial \zeta} \frac{\partial w_s}{\partial \zeta} + \varepsilon^2 \frac{\partial a}{\partial s} \frac{\partial u_m}{\partial \zeta} \qquad (7.10)$$

, in which $\nabla_1^2 = \frac{\partial^2}{\partial \zeta^2} + \frac{\partial^2}{\partial n^2} - \frac{\varepsilon}{r_s} \frac{\partial}{\partial n}$ and $\tilde{\omega}_m = - \frac{\partial u_m}{\partial n} + \frac{\varepsilon}{r_s} u_m$.

Apart from the additional terms arising from the spatial variations of the turbulence viscosity, these equations are very similar to the laminar flow equations (5.15) through (5.19). The only important differences are the spatial variations of a and the replacement of Re by Re_0. Once again, this suggests that, apart from quantitative differences, the convective redistribution of the main velocity in turbulent flow through curved channels is characterized by Re_0 rather than Re. This becomes even more evident when analysing the mechanism of the main velocity redistribution under the influence of secondary flow convection. Supposing lateral diffusion to be of minor importance (cf. chapter 4) and

adopting the similarity hypothesis (5.20) for the main flow, the streamwise momentum equation (7.8) can be averaged over the depth of flow to yield

$$\varepsilon Re_0 \overline{f^2}\, \bar{u}_m \frac{\partial \bar{u}_m}{\partial s} + \varepsilon Re_0 \overline{v_s f} \frac{\partial \bar{u}_m}{\partial n} + \{(a \frac{\partial f}{\partial \zeta})\Big|_{\zeta=-1} - \frac{\varepsilon^2 Re_0}{r_s} \overline{v_s f} + \varepsilon Re_0 \overline{w_s \frac{\partial f}{\partial \zeta}}\} \bar{u}_m = - \frac{\partial \bar{p}}{\partial s} \tag{7.11}$$

Together with the truncated transverse momentum equation

$$\varepsilon^2 Re_0 \frac{\bar{u}_m^2}{r_s} \overline{f^2} = - \frac{\partial \bar{p}}{\partial n} \tag{7.12}$$

this equation can be reduced to

$$\varepsilon Re_0 \overline{f^2}\, \bar{u}_m \frac{d\bar{u}_m}{ds} + \{(a \frac{\partial f}{\partial \zeta})\Big|_{\zeta=-1} + \varepsilon Re_0 \overline{w_s \frac{\partial f}{\partial \zeta}}\} \bar{u}_m = - \frac{d\bar{p}}{ds} \tag{7.13}$$

holding along the characteristics

$$\frac{dn}{ds} = \overline{v_s f} / (\bar{u}_m \overline{f^2}) \tag{7.14}$$

Equations (7.13) and (7.14) and their laminar flow counterparts (5.23) and (5.22) are very much alike. Apart from the replacement of Re by Re_0, all differences are due to the spatial variations of a. For the turbulence model given in par. 6.5, this implies, for instance, that far from the sidewalls in a very shallow and mildly curved channel (cf. Rozovskii, 1961 and De Vriend, 1973 & 1977)

$$\overline{f^2} = 1 + \frac{g}{\kappa^2 C^2} \qquad \text{rather than } \frac{6}{5} \tag{7.15}$$

$$\left(a\,\frac{\partial f}{\partial \zeta}\right)\Big|_{\zeta=-1} = \bar{u}_m\,\frac{\gamma}{\kappa}\,\frac{\sqrt{g}}{C} \qquad \text{rather than 3} \qquad (7.16)$$

$$\overline{v_s f} \simeq -\frac{\bar{u}_m}{r_s}\,\frac{\sqrt{g}}{\kappa C}\left(5 - 15.6\,\frac{\sqrt{g}}{\kappa C} + 37.5\,\frac{g}{\kappa^2 C^2}\right) \qquad \text{rather than}$$

$$-\frac{\bar{u}_m^2}{r_s}\,\frac{2}{175}\,\mathrm{Re} \qquad (7.17)$$

In spite of these quantitative differences, however, the main and secondary flow patterns are globally the same for either case, so that the mechanism of the main velocity redistribution will be essentially the same, as well. In the first part of a bend downstream of a straight channel section, the depth-averaged main velocity distribution will be skewed inwards as a consequence of the longitudinal pressure gradients*). Once the secondary circulation comes into existence, $\bar{u}_m$ undergoes a local reduction near the inner wall, which is caused by the combined convective effects of v_s and w_s. When proceeding through the bend, the region influenced by this velocity reduction is gradually extended outwards by transverse convection, whereas the magnitude of the reduction becomes smaller as the distance to the inner wall increases. This leads to a gradual "inversion" of the depth-averaged velocity distribution from skewed inwards in the first part of the bend to almost uniform or even skewed outwards in the last part of it.

7.4. Main flow computation step

On the basis of the experience gained for laminar flow (chapter 5), the computational procedure for turbulent flow in curved shallow channels is split up into two subsequent steps, viz. a main flow computation step and a bottom shear stress computation step. The former aims at the calculation of the depth-averaged

*) cf. the "potential flow" effect in laminar flow (see par. 3.6).

main velocity, the latter is meant for a more accurate determination of the vertical distribution of the main velocity, the secondary flow and the magnitude and direction of the bottom shear stress. The most important difference between the two steps is the similarity hypothesis, which is applied in a rather rigorous form ((5.24) and (5.25)) in the main flow computation step and in a more generalized form (see (5.36)) in the bottom shear stress computation step.
The outlines of the main flow computation step are the same as in the laminar flow model: the depth-averaged main velocity and pressure fields, the secondary flow intensity and the vertical distributions of the main and the secondary flow are computed alternately in an iterative procedure. In the following the computation of each of these quantities will be discussed in further detail and the iterative solution procedure will be summarized.

7.4.1. Vertical distribution of the main velocity

Adopting the similarity approximations (5.24) and (5.25) for the main and the secondary flow and expression (6.32) for the turbulence viscosity, the longitudinal momentum equation (7.3) can be elaborated to

$$\bar{u}\,\frac{CU_\tau}{\sqrt{g}}\,a'\,\frac{\partial^2 f}{\partial\zeta^2} + \{\bar{u}\,\frac{CU_\tau}{\sqrt{g}}\,\frac{\partial a'}{\partial\zeta} - \varepsilon Re_0^2\,\frac{\bar{u}}{r}\,\frac{\partial\bar{\psi}}{\partial\xi}\,g\}\,\frac{\partial f}{\partial\zeta} +$$

$$- \varepsilon Re_0\,(\frac{\bar{u}}{r}\,\frac{\partial\bar{u}}{\partial\phi} + \bar{v}\,\frac{\partial\bar{u}}{\partial\xi} + \frac{\varepsilon}{r}\,\overline{\bar{u}\bar{v}})\,f^2 +$$

$$+ \Big[\,\varepsilon Re_0^2\,\frac{\bar{\psi}}{r}\,(\frac{\partial\bar{u}}{\partial\xi} + \frac{\varepsilon}{r}\,\bar{u})\,\frac{\partial g}{\partial\zeta} + \{\frac{CU_\tau}{\sqrt{g}}\,(\frac{\partial^2\bar{u}}{\partial\xi^2} + \frac{\varepsilon}{r}\,\frac{\partial\bar{u}}{\partial\xi}) +$$

$$+ \frac{C}{\sqrt{g}}\,\frac{\partial U_\tau}{\partial\xi}\,(\frac{\partial\bar{u}}{\partial\xi} - \frac{\varepsilon}{r}\,\bar{u})\}\,a'\Big]f = \frac{1}{r}\,\frac{\partial p}{\partial\phi} \qquad (7.18)^*)$$

*) As in this equation terms being an order $O(\varepsilon^2)$ smaller than the leading terms of the same type have been neglected, U_τ can be replaced by u_τ.

This equation becomes linear in f if the main flow inertia term is linearized by

$$f^2 \simeq \tilde{f}\, f \tag{7.19}$$

, $\tilde{f}$ denoting an estimate of f (for example: the distribution found in the foregoing iteration step). If $\bar{u}$, $U_\tau(u_\tau)$, $\bar{v}$, $\bar{\psi}$, $\tilde{f}$, g and the longitudinal pressure gradient are known, equation (7.18) can be considered as an ordinary second-order linear differential equation in ζ, from which $f(\zeta)$ can be solved if an appropriate set of boundary conditons is given.
The boundary conditions that are relevant here are the shear stress condition at the surface (see (2.36)) and the wall function approximation (6.33) near the bottom. They yield

$$a' \frac{\partial f}{\partial \zeta} = 0 \qquad \text{at} \qquad \zeta = 0 \tag{7.20}$$

and

$$f = k_m \{1 + \frac{\sqrt{g}}{\kappa C} + \frac{\sqrt{g}}{\kappa C} \ln(1+\zeta)\} \tag{7.21}$$

on the bottom-nearest mesh of the computational grid. The constant k_m in (7.21) is related to the ratio of the bottom friction velocity and the depth-averaged velocity through

$$k_m = \frac{C}{\sqrt{g}} \frac{u_\tau}{\bar{u}} = \frac{C}{\sqrt{g}} \frac{v_{\tau m}}{\bar{v}} \tag{7.22}$$

It is determined from the additional condition provided by assuming that both the longitudinal momentum equation (7.18) and the wall function approximation (7.21) hold good on the bottom-nearest mesh. For further details reference is made to Appendix E.
Making use of (7.22), which for known k_m expresses u_τ and v_τ

in terms of $\bar{u}$ and $\bar{v}$, respectively, equation (7.18) can be reformulated as

$$\tilde{k}_m \bar{u}^2 a' \frac{\partial^2 f}{\partial \zeta^2} + \{\tilde{k}_m \bar{u}^2 \frac{\partial a'}{\partial \zeta} - \varepsilon Re_0^2 \frac{\bar{u}}{r} \frac{\partial \bar{\psi}}{\partial \xi} g\} \frac{\partial f}{\partial \zeta} +$$

$$- \varepsilon Re_0 (\frac{\bar{u}}{r} \frac{\partial \bar{u}}{\partial \phi} + v \frac{\partial \bar{u}}{\partial \xi} + \frac{\varepsilon}{r} \overline{\bar{u}\bar{v}}) \tilde{f} f + \{\varepsilon Re_0^2 \frac{\bar{\psi}}{r} (\frac{\partial \bar{u}}{\partial \xi} + \frac{\varepsilon}{r} \bar{u}) \frac{\partial g}{\partial \zeta} +$$

$$+ \tilde{k}_m (\bar{u} \frac{\partial^2 \bar{u}}{\partial \xi^2} + \frac{\partial \bar{u}}{\partial \xi} \frac{\partial \bar{u}}{\partial \xi}) a'\} f = \frac{1}{r} \frac{\partial p}{\partial \phi} \qquad (7.23)$$

, where $\tilde{k}_m$ denotes a known estimate of k_m. Equation (7.23) is the one that is actually solved in the model.
Once the constant k_m is known, the components of the bottom shear stress due to the main flow follow from (7.22) and the definitions of u_τ and v_τ. Hence

$$\tau_{b\phi_m} = \frac{g}{C^2} k_m^2 \bar{u}^2 \qquad \text{and} \qquad \tau_{b\xi_m} = \frac{g}{C^2} k_m^2 \bar{u} \bar{v} \qquad (7.24)$$

7.4.2. Depth-averaged main velocity field

Making use of the similarity approximations (5.24) and (5.25), the tangential and radial momentum equations (7.3) and (7.4) can be averaged over the depth of flow, to yield

$$\varepsilon Re_0 \overline{f^2} (\frac{\bar{u}}{r} \frac{\partial \bar{u}}{\partial \phi} + \bar{v} \frac{\partial \bar{u}}{\partial \xi} + \frac{\varepsilon}{r} \overline{\bar{u}\bar{v}}) + \varepsilon Re_0^2 \{- \overline{f \frac{\partial g}{\partial \zeta}} \frac{\bar{\psi}}{r} (\frac{\partial \bar{u}}{\partial \xi} + \frac{\varepsilon}{r} \bar{u}) +$$

$$+ \overline{g \frac{\partial f}{\partial \zeta}} \frac{\bar{u}}{r} \frac{\partial \bar{\psi}}{\partial \xi}\} = - \frac{1}{r} \frac{\partial \bar{p}}{\partial \phi} - k_m \bar{u}^2 (a' \frac{\partial f}{\partial \zeta})\Big|_{\zeta=-1} +$$

$$+ k_m \overline{a' f} (\bar{u} \frac{\partial^2 \bar{u}}{\partial \xi^2} + \frac{\partial \bar{u}}{\partial \xi} \frac{\partial \bar{u}}{\partial \xi}) \qquad (7.25)$$

and

$$\varepsilon^3 Re_0 \overline{f^2} \left(\frac{\bar{u}}{r}\frac{\partial \bar{v}}{\partial \phi} + \bar{v}\frac{\partial \bar{v}}{\partial \xi}\right) - \varepsilon^2 Re_0 \overline{f^2}\frac{\bar{u}^2}{r} + \varepsilon^3 Re_0^2 \left(-\overline{f\frac{\partial g}{\partial \zeta}}\frac{\bar{\psi}}{r}\frac{\partial \bar{v}}{\partial \xi} + \right.$$

$$\left. + \overline{g\frac{\partial f}{\partial \zeta}}\frac{\bar{v}}{r}\frac{\partial \bar{\psi}}{\partial \xi}\right) = -\frac{\partial \bar{p}}{\partial \xi} - \varepsilon^2 k_m \overline{\bar{u}\bar{v}} \left(a'\frac{\partial f}{\partial \zeta}\right)\Big|_{\zeta=-1} + \varepsilon^2 k_m \overline{a'f}\left\{\bar{u}\frac{\partial^2 \bar{v}}{\partial \xi^2} + \right.$$

$$\left. + \frac{\partial \bar{u}}{\partial \xi}\frac{\partial \bar{v}}{\partial \xi} + 5\frac{\varepsilon}{r}\bar{u}\frac{\partial \bar{v}}{\partial \xi} - \frac{\varepsilon}{r}\bar{v}\frac{\partial \bar{u}}{\partial \xi}\right\} + \text{other terms} \qquad (7.26)$$

, in which the "other terms" are of the order $0(\varepsilon^2, \varepsilon^3 Re_0^2)$ and concern the secondary flow. These terms are disregarded in the main flow computation.
For the logarithmic distribution (7.21) of f near the bottom, the factor $\left(a'\frac{\partial f}{\partial \zeta}\right)\Big|_{\zeta=-1}$ in these equations becomes

$$\left(a'\frac{\partial f}{\partial \zeta}\right)\Big|_{\zeta=-1} = k_m \gamma \frac{\sqrt{g}}{\kappa C} = k_m Re_0 \frac{g}{C^2} \qquad (7.27)$$

Equations (7,25) and (7.26) and the depth-averaged equation of continuity

$$\frac{1}{r}\frac{\partial \bar{u}}{\partial \phi} + \frac{\partial \bar{v}}{\partial \xi} + \frac{\varepsilon}{r}\bar{v} = 0 \qquad (7.28)$$

form a system of three partial differential equations, from which the three unknowns $\bar{u}$, $\bar{v}$ and $\bar{p}$ can be solved if an appropriate set of boundary conditions is given.
The treatment of $\bar{u}$ and $\bar{v}$ in the vicinity of the sidewalls was discussed in par. 6.5. Appendix F gives further details of these sidewalls approximations and their incorporation in the model.

The inflow and outflow conditions to be imposed depend on the method of solution (stream function/vorticity, parabolic, partially-parabolic; see Appendix C), but in any case the distribution of the longitudinal velocity at the inflow boundary must be given. Though any distribution that satisfies the sidewall conditions can be imposed, the velocity distribution in the equivalent fully-developed straight channel is chosen here, i.e. the inflow section is assumed to be preceded by an infinitely long straight channel of the same cross-sectional configuration and with the same roughnesses of bottom and sidewalls. The computation of this fully-developed straight channel flow is described in Appendix D.

Like in the laminar flow model, the computation of the depth-averaged main velocity and pressure fields is the most difficult and time-consuming part of the solution procedure. In order to find an efficient computation method, a turbulent flow transcription has been made of the methods discussed in Appendix C, viz. the stream function/vorticity method, the parabolic and partially-parabolic modes of Spalding's method and the 'simple-channel' method.
For the stream function/vorticity method the problem of convergence, which was already encountered in the laminar flow case (De Vriend, 1978b), becomes acute in case of turbulent flow: convergence turns out to be very poor then and hence the computations are very expensive or even fail. This deterioration of convergence must probably be attributed to the extra degree of freedom in the sidewall conditions of $\bar{u}$, which depend on the solution in the other parts of the cross-section instead of giving a strict prescription of $\bar{u}$.
The other three methods are indentical in their treatment of the longitudinal momentum equation. Since the sidewall boundary conditions related to this equation form the only essential difference between the laminar and turbulent flow versions of these models, their relative efficiencies in case of turbulent flow are almost the same as indicated in Appendix C. Hence the parabolic mode of

Spalding's method is by far the most efficient, but also the most simplified. The efficiencies and the accuracies of the partially-parabolic Spalding-method and the simple-channel method are not far apart. In order to be able to compare results of parabolic and partially-parabolic computations, the two modes of Spalding's method will be applied henceforth.

7.4.3. Vertical distribution of the secondary flow

As in the laminar flor model, a stream function of the secondary flow is defined by (5.25). The turbulent flow version of the stream function equation is obtained by eliminating the pressure from the transverse and vertical momentum equations (7.4) and (7.5) (see also De Vriend, 1979b). The resulting equation is rather complicated and needs some further simplification in order to be manageable.

On the basis of the experience gained from the laminar flow model (chapter 5), the stream function equation is simplified at the following points:

- the transverse inertia of the secondary flow is disregarded,
- the vertical distribution function g is assumed independent of ξ,
- the vertical distribution function is assumed weakly dependent on ϕ, i.e. the ϕ-derivatives of g are disregarded in the stream function equation.

In addition, only the leading terms in the equation are retained, so even the terms with $\frac{\varepsilon}{r}$ are omitted. Then the stream function equation becomes (cf. equation (5.40)):

$$a\left(\frac{\partial^4\bar{\psi}}{\partial\xi^4}\,g + 2\,\frac{\partial^2\bar{\psi}}{\partial\xi^2}\,\frac{\partial^2 g}{\partial\zeta^2} + \bar{\psi}\,\frac{\partial^4 g}{\partial\zeta^4}\right) + 2\,\frac{\partial a}{\partial\xi}\left(\frac{\partial^3\bar{\psi}}{\partial\xi^3}\,g + \frac{\partial\bar{\psi}}{\partial\xi}\,\frac{\partial^2 g}{\partial\zeta^2}\right) +$$

$$+ 2\,\frac{\partial a}{\partial\zeta}\left(\frac{\partial^2\bar{\psi}}{\partial\xi^2}\,\frac{\partial g}{\partial\zeta} + \bar{\psi}\,\frac{\partial^3 g}{\partial\zeta^3}\right) + 4\,\frac{\partial^2 a}{\partial\xi\partial\zeta}\,\frac{\partial\bar{\psi}}{\partial\xi}\,\frac{\partial g}{\partial\zeta} + \left(\frac{\partial^2 a}{\partial\xi^2} - \frac{\partial^2 a}{\partial\zeta^2}\right)\left(\frac{\partial^2\bar{\psi}}{\partial\xi^2}\,g - \bar{\psi}\,\frac{\partial^2 g}{\partial\zeta^2}\right) +$$

$$- \varepsilon Re_0\left[\left(\frac{\bar{u}}{r}\,\frac{\partial\bar{\psi}}{\partial\phi} + \bar{v}\,\frac{\partial\bar{\psi}}{\partial\xi} + \frac{\partial\bar{v}}{\partial\xi}\,\bar{\psi} - \frac{\bar{v}}{\bar{u}}\,\frac{\partial\bar{u}}{\partial\xi}\,\bar{\psi}\right)\frac{\partial}{\partial\zeta}\left(f\,\frac{\partial g}{\partial\zeta}\right) +\right.$$

$$+ \{(\frac{\bar{u}}{r}\frac{\partial}{\partial\phi} + \bar{v}\frac{\partial}{\partial\xi})\frac{\partial^2\bar{\psi}}{\partial\xi^2} + (\frac{\partial\bar{u}}{\partial\xi}\frac{1}{r}\frac{\partial}{\partial\phi} + \frac{\partial\bar{v}}{\partial\xi}\frac{\partial}{\partial\xi})\frac{\partial\bar{\psi}}{\partial\xi}\} fg \Big| =$$

$$- \frac{r\bar{u}^2}{r_s}\frac{\partial f^2}{\partial\zeta} + \frac{r}{Re_0}\{(\frac{a}{r}\frac{\partial\bar{\omega}_m}{\partial\phi} - \frac{\bar{\omega}_m}{r}\frac{\partial a}{\partial\phi})\frac{\partial f}{\partial\zeta} + (\frac{\partial a}{\partial\zeta}\frac{1}{r}\frac{\partial\bar{\omega}_m}{\partial\phi} - \frac{\bar{\omega}_m}{r}\frac{\partial^2 a}{\partial\phi\partial\zeta})f\} \qquad (7.29)$$

For given $\bar{u}$, $\bar{\psi}$, a and f, this equation could be used to determine g. As was shown for the laminar flow model, however, the inconsistency of retaining the streamwise inertia terms for $\bar{\psi}$ and omitting them for g gives rise to computational trouble. Therefore, the streamwise inertia terms for $\bar{\psi}$ and g are disregarded here (see also par. 5.7).
Since g has been assumed independent of ξ, it can be determined in the channel axis, where the ξ-derivatives of $\bar{\psi}$ are negligible. In addition, the terms with $\bar{\omega}_m$ are assumed to be of minor importance as a source of secondary flow, at least in the main flow computation step. Then equation (7.29) reduces to

$$\bar{\psi}\frac{\partial^2}{\partial\zeta^2}(a\frac{\partial^2 g}{\partial\zeta^2}) = -\frac{r\bar{u}^2}{r_s}\frac{\partial f^2}{\partial\zeta} \qquad (7.30)$$

It should be pointed out that in the actual model g is not solved from this equation, but from

$$\frac{\partial^2}{\partial\zeta^2}(a'\frac{\partial^2 g}{\partial\zeta^2}) = c\frac{\partial f^2}{\partial\zeta} \qquad (7.31)$$

in which c is adjusted in such a way, that $\bar{g} = 1$ in each iteration step of the main flow computation (see also Appendix G).

The boundary conditions at the surface are the same as for laminar flow, viz.

$$g = 0 \quad \text{and} \quad a'\frac{\partial^2 g}{\partial\zeta^2} = 0 \quad \text{at} \quad \zeta = 0 \qquad (7.32)$$

The conditions at the bottom are replaced by the wall function approximations given in par. 6.5. If $\xi v_{\tau s}$ denotes the part of the transverse component of the bottom friction velocity due to the secondary flow, the components of this friction velocity can be written as (see also (7.22))

$$v_\tau = k_m \frac{\sqrt{g}}{C} \bar{v} + v_{\tau s} \qquad \text{and} \qquad u_\tau = k_m \frac{\sqrt{g}}{C} \bar{u} \tag{7.33}$$

Then the wall function approximations for the secondary flow can be derived from (6.34), (6.35) and (6.42), in combination with the depth-averaged equation of continuity (7.28), to yield

$$v_s = \frac{v_{\tau s}}{\kappa} \{\frac{\kappa C}{\sqrt{g}} + 1 + \ln(1+\zeta)\} \qquad \text{for} \quad \zeta \leq \zeta_1 \tag{7.34}$$

$$w = -\frac{1}{\kappa} (\frac{\partial v_{\tau s}}{\partial \xi} + \frac{\varepsilon}{r} v_{\tau s})(1+\zeta) \{\frac{\kappa C}{\sqrt{g}} + \ln(1+\zeta)\} \qquad \text{for} \quad \zeta \leq \zeta_1 \tag{7.35}$$

The wall function approximation for ψ to be derived from these expressions reads

$$\psi = -\frac{r v_{\tau s}}{\kappa Re_0} (1+\zeta) \{\frac{\kappa C}{\sqrt{g}} + \ln(1+\zeta)\} \qquad \text{for} \quad \zeta \leq \zeta_1 \tag{7.36}$$

Hence the wall function for g can be written as

$$g = k_s (1+\zeta) \{1 + \frac{\sqrt{g}}{\kappa C} \ln(1+\zeta)\} \qquad \text{for} \quad \zeta \leq \zeta_1 \tag{7.37}$$

, in which the constant k_s is related to the ratio of $v_{\tau s}$ and $\bar{\psi}$ through

$$k_s = -\frac{C}{\sqrt{g}} \frac{r v_{\tau s}}{\bar{\psi} Re_0} \tag{7.38}$$

It is determined by assuming that both equation (7.30) and wall function (7.37) hold good on the bottom-nearest mesh of the computational grid. Appendix G gives further details of the solution procedure.

7.4.4. Depth-averaged stream function of the secondary flow

For $a = k_m \bar{u}\, a'$ (cf. equation (6.32)) the depth-averaged version of equation (7.29) can be elaborated to (see De Vriend, 1979a)

$$\overline{a'g}\left(\bar{u}\frac{\partial^4\bar{\psi}}{\partial\xi^4} + 2\frac{\partial\bar{u}}{\partial\xi}\frac{\partial^3\bar{\psi}}{\partial\xi^3} + \frac{\partial^2\bar{u}}{\partial\xi^2}\frac{\partial^2\bar{\psi}}{\partial\xi^2}\right) + \left(a'\frac{\partial g}{\partial\zeta}\right)\Big|_{\zeta=0}\left(2\bar{u}\frac{\partial^2\bar{\psi}}{\partial\xi^2} + \right.$$

$$\left. + 2\frac{\partial\bar{u}}{\partial\xi}\frac{\partial\bar{\psi}}{\partial\xi} - \frac{\partial^2\bar{u}}{\partial\xi^2}\bar{\psi}\right) - \overline{g\frac{\partial^2 a'}{\partial\zeta^2}}\left(\bar{u}\frac{\partial^2\bar{\psi}}{\partial\xi^2} + 2\frac{\partial\bar{u}}{\partial\xi}\frac{\partial\bar{\psi}}{\partial\xi} + \frac{\partial^2\bar{u}}{\partial\xi^2}\bar{\psi}\right) +$$

$$+ cf^2\Big|_{\zeta=0}\bar{u}\,\bar{\psi} - \frac{\varepsilon Re_0}{k_m}\left[\left\{\left(\frac{\bar{u}}{r}\frac{\partial}{\partial\phi} + \bar{v}\frac{\partial}{\partial\xi}\right)\frac{\partial^2\bar{\psi}}{\partial\xi^2} + \left(\frac{\partial\bar{u}}{\partial\xi}\frac{1}{r}\frac{\partial}{\partial\phi} + \frac{\partial\bar{v}}{\partial\xi}\frac{\partial}{\partial\xi}\right)\frac{\partial\bar{\psi}}{\partial\xi}\right\}\right.$$

$$\left.\overline{fg} + \left(\frac{\bar{u}}{r}\frac{\partial\bar{\psi}}{\partial\phi} + \bar{v}\frac{\partial\bar{\psi}}{\partial\xi} + \frac{\partial\bar{v}}{\partial\xi}\bar{\psi} - \frac{\bar{v}}{\bar{u}}\frac{\partial\bar{u}}{\partial\xi}\bar{\psi}\right)\left(f\frac{\partial g}{\partial\zeta}\right)\Big|_{\zeta=0}\right] =$$

$$-\frac{r\bar{u}^2}{k_m r_s}f^2\Big|_{\zeta=0} + \frac{r}{Re_0}\left(\frac{\bar{u}}{r}\frac{\partial\bar{\omega}_m}{\partial\phi} - \frac{\bar{\omega}_m}{r}\frac{\partial\bar{u}}{\partial\phi}\right)(a'f)\Big|_{\zeta=0} \qquad (7.39)$$

In the main flow computation step the source term with $\bar{\omega}_m$ is disregarded.

In order to solve $\bar{\psi}$ from this equation, boundary conditions must be given at the inflow boundary and at the sidewalls. The inflow condition for $\bar{\psi}$ corresponding with the assumption of fully-developed straight channel flow at the inflow boundary reads

$$\bar{\psi}_{inflow} = 0 \qquad (7.40)$$

The sidewall conditions are provided by the wall function approximations (6.37), (6.39), (6.43) and (6.44). The functions (6.43) and (6.44) can be split up into two parts, one for v_m and one for v_s. Near the left wall, for instance, this leads to

$$v_m = -\frac{1}{\kappa r}\frac{\partial u_{\tau 1}}{\partial \phi}\left(\frac{B}{2d}+\xi\right)\left\{\frac{\kappa C}{\sqrt{g}}+\ln\left(\frac{B}{2d}+\xi\right)\right\} \quad \text{for} \quad \xi \leq \xi_1 \tag{7.41}$$

$$v_s = -\frac{1}{\kappa}\frac{\partial w_{\tau 1}}{\partial \zeta}\left(\frac{B}{2d}+\xi\right)\left\{\frac{\kappa C}{\sqrt{g}}+\ln\left(\frac{B}{2d}+\xi\right)\right\} \quad \text{for} \quad \xi \leq \xi_1 \tag{7.42}$$

Hence the wall function approximations for $\bar{\psi}$ become

$$\bar{\psi} = \frac{\bar{r w}_{\tau 1}}{\kappa Re_0}\left(\frac{B}{2d}+\xi\right)\left\{\frac{\kappa C}{\sqrt{g}}+\ln\left(\frac{B}{2d}+\xi\right)\right\} \quad \text{for} \quad \xi \leq \xi_1 \tag{7.43}$$

near the left wall and

$$\bar{\psi} = -\frac{\bar{r w}_{\tau r}}{\kappa Re_0}\left(\frac{B}{2d}-\xi\right)\left\{\frac{\kappa C}{\sqrt{g}}+\ln\left(\frac{B}{2d}-\xi\right)\right\} \quad \text{for} \quad \xi \geq \xi_n \tag{7.44}$$

near the right wall. The quantities $w_{\tau 1}$ and $w_{\tau r}$ in these expressions are determined by assuming both equation (7.39) and approximations (7.43) and (7.44) to hold good on the wall-nearest meshes of the computational grid.
The procudure followed thereby is described in Appendix H.

7.4.5. Iterative solution procedure

The outlines of the iterative solution procedure applied in the main flow computation step are essentially the same as in the laminar flow model (see par. 5.6):

1a. Estimate the vertical distribution functions f and g by taking, for instance, the logarithmic distribution for f

$$f = 1 + \frac{\sqrt{g}}{\kappa C} + \frac{\sqrt{g}}{\kappa C}\ln(1+\zeta) \tag{7.45}$$

and solving g from equation (7.31) or evaluating the analytical solution corresponding with (7.45) (see also De Vriend, 1976 & 1977)

$$g = c_1 \{- 2\zeta F_1 - \frac{\sqrt{g}}{\kappa C} \zeta F_2 + 2(1 - \frac{g}{\kappa^2 C^2})(1+\zeta) \ln(1+\zeta) + \frac{\sqrt{g}}{\kappa C} (1+\zeta) \ln^2(1+\zeta)\} \qquad (7.46)$$

$$\text{with } c_1 = \frac{8}{2 - 5 \frac{\sqrt{g}}{\kappa C} + 4 \frac{g}{\kappa^2 C^2}}$$

$$F_1 = \int_{-1+\zeta^*}^{\zeta} \frac{\ln(1+\zeta)}{\zeta} d\zeta \qquad (\zeta^* = e^{-1 - \frac{\kappa C}{\sqrt{g}}})$$

$$F_2 = \int_{-1+\zeta^*}^{\zeta} \frac{\ln^2(1+\zeta)}{\zeta} d\zeta$$

1b. Estimate the depth-averaged stream function of the secondary flow by taking $\bar{\psi} \equiv 0$, for instance.

2. Determine $\bar{u}$, $\bar{v}$ and $\bar{p}$ on the basis of equations (7.25), (7.26) and (7.28), using one of the computation methods described in Appendix C, except for the stream function/vorticity method (see also Appendix F').

3. Calculate the local streamline curvatures using (5.31) and (5.32).

4. Solve $\bar{\psi}$ from equation (7.39) as indicated in Appendix H.

5. Solve f from equation (7.23) as indicated in Appendix E.

6. Solve g from equation (7.31) as indicated in Appendix G.

7. Repeat the procedure from 2 on, until a termination criterion such as (5.35) is satisfied.

In order to speed up convergence, underrelaxation rules such as (4.37) can be applied in any of the elements 2, 4, 5 and 6.

7.5. Bottom shear stress computation step

The normalized bottom shear stress components $\tau_{b\phi}$ and $\varepsilon\tau_{b\xi}$ are given by (see also (7.24) and (7.38))

$$\tau_{b\phi} = \frac{g}{C^2} k_m^2 \bar{u}^2 \quad \text{and} \quad \tau_{b\xi} = \frac{g}{C^2} k_m^2 \overline{\bar{u}\bar{v}} - \frac{g}{C^2} k_m k_s \, Re_0 \, \bar{u} \frac{\bar{\psi}}{r} \tag{7.47}$$

These expressions are evaluated using the depth-averaged main velocities resulting from the main flow computation step. The friction constants k_m and k_s are determined from extended calculations of f and g, in which the effect of longitudinal accelerations of the main flow is taken into account. The depth-averaged stream function of the secondary flow is adjusted to the improved distributions of f and g.

Longitudinal accelerations of the main flow give rise to deformations of the vertical distribution of the main velocity (Schlichting, 1951; De Vriend, 1976 & 1977: see also par. 5.7) and hence to changes in the bottom friction constant k_m. As the longitudinal accelerations will be distributed non-uniformly over a cross-section, however, they can only be accounted for if f is allowed to vary with ξ. Therefore, the generalized similarity hypothesis (6.36) is adopted, i.e. f is allowed to vary with ξ in such a way, that the ξ-derivatives of f in the differential equations are negligible with respect to the ξ-derivatives of $\bar{u}$.
Strictly speaking, f would then be described by equation (7.23) in every vertical of the cross-section. When solving f from this equation, however, the results near the sidewalls are obviously erroneous. Apparently, the longitudinal momentum equation should be solved there as a whole rather than being split up into an equation for $\bar{u}$ and one for f. As this would imply an unacceptable complication of the model, the main flow accelerations are accounted for in a different way. In view of the fact that the similarity hypothesis holds good for fully-developed straight and curved flows (cf. par. 4.4 and par. 6.4), the effect

of the main flow accelerations is introduced by solving

$$\tilde{k}_m \bar{u}^2 \frac{\partial}{\partial \zeta}(\alpha' \frac{\partial f}{\partial \zeta}) - \varepsilon Re_0^2 \bar{u}^2 (\frac{1}{r\bar{u}} \frac{\partial \bar{\psi}}{\partial \xi})\Big|_{\xi=0} g \frac{\partial f}{\partial \zeta} +$$

$$+ \varepsilon Re_0^2 \bar{u}^2 \{\frac{\bar{\psi}}{\bar{u}^2 r}(\frac{\partial \bar{u}}{\partial \xi} + \frac{\varepsilon}{r}\bar{u})\}\Big|_{\xi=0} \frac{\partial g}{\partial \zeta} f - \varepsilon Re_0 (\frac{\bar{u}}{r}\frac{\partial \bar{u}}{\partial \phi} +$$

$$+ \bar{v}\frac{\partial \bar{u}}{\partial \xi} + \frac{\varepsilon}{r}\overline{\bar{u}\bar{v}}) \tilde{\gamma} f = \frac{1}{r}\frac{\partial \bar{p}}{\partial \phi} \qquad (7.48)$$

The transverse diffusion in the channel axis is disregarded in this equation, which is acceptable if the disturbances of f due to the main flow accelerations are small.

The direction of the bottom shear stress is given by

$$\tan \alpha_\tau = \frac{\bar{v}}{\bar{u}} - \frac{k_s}{k_m} Re_0 \frac{\bar{\psi}}{\bar{u}r} \qquad (7.49)$$

Apart from the entrance and exit regions of a bend, where $\bar{v}$ can be important, this direction is determined mainly by the secondary flow. As the direction of the bottom shear stress is of great importance to the transverse bottom configuration in alluvial channel bends, the secondary flow part of (7.49) has to be determined rather accurately. Therefore the secondary flow computation will be reconsidered on the basis of the simplifications made in the main flow computation step:

a. in view of the results of the fully-developed laminar flow investigations, it seems justifiable to disregard the transverse inertia of the secondary flow even here;
b. in addition to the streamline curvature, the streamwise variation of the main flow vorticity should be retained as a source of secondary flow; in a bend this source

will be of minor importance, but in a straight reach beyond a bend it decays much slowlier than the streamline curvature, so that it can be of some importance there;

c. as f is allowed to vary weakly with ξ, g should be so, as well, since f and $\frac{\partial f}{\partial \zeta}$ figure in the source terms of the equation for g;

d. in order to have an accurate description of the transverse bottom shear stress in regions with important streamwise variations of the secondary flow intensity, the vertical distribution function g is allowed to vary with ϕ and the ϕ-derivatives of g are retained in the streamwise inertia terms of the stream function equation for the secondary flow (see Appendix I).

In view of these arguments, the following equations for g and $\bar{\psi}$ are solved in the bottom shear stress computation step (see also par. 5.7 and Appendix I):

$$\frac{\partial^2}{\partial\zeta^2}\left(a'\frac{\partial^2 g}{\partial\zeta^2}\right) - \frac{\varepsilon \mathrm{Re}_0}{k_m \bar{\psi}}\frac{1}{r}\frac{\partial^2}{\partial\phi\partial\zeta}\left(\bar{\psi} f \frac{\partial g}{\partial\zeta}\right) = -\frac{r\bar{u}}{k_m \bar{\psi} r_s}\frac{\partial f^2}{\partial\zeta} +$$

$$+ \frac{1}{\mathrm{Re}_0}\frac{1}{\bar{u}\bar{\psi}}\left(\frac{\bar{u}}{r}\frac{\partial\bar{\omega}_m}{\partial\phi} - \frac{\bar{\omega}_m}{r}\frac{\partial\bar{u}}{\partial\phi}\right)\frac{\partial}{\partial\zeta}(a'f) \qquad (7.50)$$

$$\overline{a'g}\left(\bar{u}\frac{\partial^4\bar{\psi}}{\partial\xi^4} + 2\frac{\partial\bar{u}}{\partial\xi}\frac{\partial^3\bar{\psi}}{\partial\xi^3} + \frac{\partial^2\bar{u}}{\partial\xi^2}\frac{\partial^2\bar{\psi}}{\partial\xi^2}\right) + \left(a'\frac{\partial g}{\partial\zeta}\right)\Big|_{\zeta=0}\left(2\bar{u}\frac{\partial^2\bar{\psi}}{\partial\xi^2} +\right.$$

$$\left. + 2\frac{\partial\bar{u}}{\partial\xi}\frac{\partial\bar{\psi}}{\partial\xi} - \frac{\partial^2\bar{u}}{\partial\xi^2}\bar{\psi}\right) - \overline{g\frac{\partial^2 a'}{\partial\zeta^2}}\left(\bar{u}\frac{\partial^2\bar{\psi}}{\partial\xi^2} + 2\frac{\partial\bar{u}}{\partial\xi}\frac{\partial\bar{\psi}}{\partial\xi} + \frac{\partial^2\bar{u}}{\partial\xi^2}\bar{\psi}\right) +$$

$$+ \left\{\frac{\partial}{\partial\zeta}\left(a'\frac{\partial^2 g}{\partial\zeta^2}\right)\Big|_{\zeta=0} - \frac{\partial}{\partial\zeta}\left(a'\frac{\partial^2 g}{\partial\zeta^2}\right)\Big|_{\zeta=-1}\right\}\bar{u}\bar{\psi} - \frac{\varepsilon \mathrm{Re}_0}{k_m}\left[\left\{\left(\frac{\bar{u}}{r}\frac{\partial}{\partial\phi} +\right.\right.\right.$$

$$\left.\left.\left. + \bar{v}\frac{\partial}{\partial\xi}\right)\frac{\partial^2\bar{\psi}}{\partial\xi^2} + \left(\frac{\partial\bar{u}}{\partial\xi}\frac{1}{r}\frac{\partial}{\partial\phi} + \frac{\partial\bar{v}}{\partial\xi}\frac{\partial}{\partial\xi}\right)\frac{\partial\bar{\psi}}{\partial\xi}\right\}\overline{fg} +\right.$$

$$\left. + \left(\frac{\bar{u}}{r}\frac{\partial\bar{\psi}}{\partial\phi} + \bar{v}\frac{\partial\bar{\psi}}{\partial\xi} + \frac{\partial\bar{v}}{\partial\xi}\bar{\psi} - \frac{\bar{v}}{\bar{u}}\frac{\partial\bar{u}}{\partial\xi}\bar{\psi}\right)\left(f\frac{\partial f}{\partial\zeta}\right)\Big|_{\zeta=0}\right.$$

$$+ \frac{\bar{u}\bar{\psi}}{r} \frac{\partial}{\partial \phi} \{(f \frac{\partial g}{\partial \zeta})\Big|_{\zeta=0}\}\Big] = - \frac{r\bar{u}^2}{k_m r_s} f^2\Big|_{\zeta=0} + \frac{r}{Re_0} (\frac{\bar{u}}{r} \frac{\partial \bar{\omega}_m}{\partial \phi} +$$

$$- \frac{\bar{\omega}_m}{r} \frac{\partial \bar{u}}{\partial \phi}) (a' f)\Big|_{\zeta=0} \qquad (7.51)$$

Appendix G describes how g is solved from equation (7.50). The procedure to determine $\bar{\psi}$ from equation (7.51) is the same as in the main flow computation step (equation (7.39) and Appendix H).

7.6. Verification of the simplifying assumptions

Before proceeding to the overall verification of the model by comparing its results with measured data (see par. 7.7 and chapter 9), the influence of the most important simplifying assumptions will be investigated. In addition to the ones deduced from the fully-developed curved flow investigations, these assumptions are

- the application of the similarity hypothesis to the main flow convection terms in the main flow equations;
- the neglect of the influence of longitudinal accelerations on the vertical distribution of the main velocity in the main flow computation step;
- the simplifications of the stream function equation for the secondary flow in the main flow computation step.

These simplifications will be verified one by one, either by estimating the magnitude of the disregarded terms or by considering the effect of including these terms in the model. The verification will be made for the LFM-flume (see chapter 9), which has a rather sharp 180^o bend giving rise to rather strong curvature effects, thus providing a severe test of the model.

7.6.1. The simplification of the main flow convection terms

If the complete main flow momentum equation would be formulated in terms of the stream-oriented coordinates (n,s,ζ) described

in paragraphs 5.4 and 7.3 and shown in figure 23, it would contain the following main flow convection terms

$$\varepsilon Re_0 \left(u_m \frac{\partial u_m}{\partial s} + w_m \frac{\partial u_m}{\partial \zeta}\right) \tag{7.52}$$

In the model, these terms are simplified to

$$\varepsilon Re_0 \bar{u}_m \frac{\partial \bar{u}_m}{\partial s} f^2 \tag{7.53}$$

on the basis of the similarity hypothesis for the main velocity. As was shown in par. 5.4, this simplification is allowable if

$$f^2 \bar{u}_m \frac{\partial \bar{u}_m}{\partial s} + \bar{u}_m^2 \left(f \frac{\partial f}{\partial s} - \frac{\partial f}{\partial \zeta} \frac{\partial F}{\partial s}\right) \simeq f^2 \bar{u}_m \frac{\partial \bar{u}_m}{\partial s}$$

$$\text{with } F = \int_{-1}^{\zeta} f d\zeta \tag{7.54}$$

, i.e. if the range of variation of the first term in (7.54) is much larger than the range of variation of the second term. According to figure 42, this is true for the greather part of the LFM-flume. Only locally near the bend exit the range of variation of the second term amounts about 25% of the first one. Therefore the simplification of (7.52) to (7.53) is thought to be acceptable.

7.6.2 The influence of longitudinal accelerations of the main flow

In the main flow computation step the vertical distribution of the main velocity is assumed self-similar throughout a cross-section. As was stated in par. 7.5, the longitudinal accelerations of the main flow in a bend will influence the distribution function f in such a way, that this similarity, and hence the relation

between the bottom shear stress and the depth-averaged velocity, is violated. Consequently, the depth-averaged main velocity will be affected and it is important to assess the effect of the strictly applied similarity hypothesis on the results of the main flow computation step.

An indication of the influence of the longitudinal accelerations on the vertical distribution functions f and g in the LFM-flume is given by figure 43, representing the results of the main flow computation step and the bottom shear stress computation step*). The vertical distribution functions appear to be almost invariable in a cross-section, except for the entrance and exit regions of the bend, where slight variations occur (figures 43a and 43b). The bottom shear stress factors k_m and k_s and the constant c are represented in figure 43c.

The main bottom shear stress factor k_m is influenced only slightly, whereas k_s and c vary somewhat stronglier, especially near the entrance and near the exit of the bend.

The effect of the variations in f and g due to the longitudinal accelerations on the distribution of the depth-averaged main velocity can be shown by comparing the results of the main flow computation step with the ones of an additional depth-averaged flow computation following the bottom shear stress computation step. Figure 44a shows that this effect is of minor importance to the depth-averaged main velocity. Besides, even its influence on the secondary flow intensity is rather small and of a local kind, as is shown by figure 44b.

The magnitude of the bottom shear stress (figure 45a), which is dominated by the main component, i.e. by k_m and $\bar{u}$ (see equation (7.47)), is hardly influenced.

The direction, however, in which the secondary flow, and hence k_s and $\bar{\psi}$, are more important (see equation (7.49)), is influenced to a higher extent, as is shown in figure 45b: locally the effect of the longitudinal accelerations amounts 20% of the overall mean

---

*) With g determined from the simplified equation (7.31) rather than from the extended equation (7.50).

value of α_τ in the bend.
The conclusion to be drawn from the foregoing is that the effect of the streamwise accelerations of the main flow on the vertical distribution functions can be disregarded when computing the depth-averaged main flow, but that it should be taken into account in the bottom shear stress computation.

7.6.3. The simplifications in the secondary flow computation

In the main flow computation step the streamwise inertia of the secondary flow is partly accounted for, insofar that horizontal derivatives of g are left out of consideration and that g is solved from a strongly truncated equation without streamwise inertia terms (equation (7.31)). The only streamwise inertia terms retained are the ones concerning $\bar{\psi}$ in the depth-averaged stream function equation (7.39).
The latter terms are relatively easy to include in the model, as they hardly give rise to extra computational effort. The other terms, however, would involve important computational effort when included in the model. Therefore it is worthwhile to investigate the effects of the two groups of streamwise inertia terms separately.
Figure 46 gives a comparison between the depth-averaged main velocity distributions, the secondary flow intensities and the directions of the bottom shear stress in the LFM-flume for three different models, with

a) all streamwise inertia terms of the secondary flow included,
b) only the inertia terms of $\bar{\psi}$ in the depth-averaged stream function equation retained,
c) all streamwise inertia terms of the secondary flow disregarded.

According to figure 46a, the main velocity distribution in the bend is hardly influenced by the secondary flow inertia. In the downstream straight reach, however, the inertia terms have a somewhat stronger effect, in that the distribution of $\bar{u}$ tends to be more oblique. This effect is not represented by including only the inertia terms for $\bar{\psi}$ in the depth-averaged stream function equation. Still the differences between the three models are so

small (less than 5%), that each one is thought acceptable for the main flow computation step.

Figures 46b and c show that the growth and decay of the secondary flow intensity are so slow, that the influence of streamwise inertia is considerable throughout the flume: in the bend the secondary flow does not reach the intensity it would have if the streamwise inertia were absent and in the downstream straight reach the intensity decays much slowlier. The remainder of the secondary flow in this straight reach gives rise to the aforementioned additional deformation of the depth-averaged main velocity distribution (figure 46a).

It becomes evident from figures 46b and c that including only the streamwise inertia terms for $\bar{\psi}$ in the depth-averaged stream function equation accounts for only a small part of the inertia effects in the secondary flow intensity. The same can be stated as to the direction of the bottom shear stress, though the effect of including $\bar{\psi}$-inertia is somewhat stronger there (see figure 46d). Obviously, all streamwise inertia terms of the secondary flow must be taken into account in the bottom shear stress computation step.

It is concluded from the foregoing that the streamwise inertia of the secondary flow can be disregarded when computing the depth-averaged main flow, whereas it has to be incorporated in the bottom shear stress computation step. In contrast with the laminar flow case (see par. 5.8.4), all streamwise inertia terms, both for $\bar{\psi}$ and for g, must be included, both in the equation for $\bar{\psi}$ and in the one for g.

7.7. Preliminary comparison with measured data

The present turbulent flow model will be compared extensively with measured data in chapter 9. Still a preliminary comparison is made here for the same cases as in par. 5.9, in order to have a global indication of the performance of the turbulent flow model as compared with the laminar flow model described in chapter 5 and with the old turbulent flow model, in which secondary flow convection is disregarded (De Vriend, 1976 & 1977).

Figure 47 shows the depth-averaged velocity distributions for the

mildly curved DHL-flume*) and for the rather sharply curved LFM-flume (see par. 9.2.1 and 9.2.4, respectively). The present turbulent flow model yields obviously better predictions of $\bar{u}$ than the old one, but the improvement compared with the laminar flow model is less evident. For the DHL-flume the turbulent model predictions are better than the laminar ones, indeed (figure 47a), but for the LFM-flume, especially in the second half of the bend and in the downstream straight reach, they are certainly not (figure 47b). There the turbulent flow model tends to underestimate the obliqueness of the depth-averaged velocity distribution.

7.8. Discussion

It was shown in the foregoing that the two-step procedure for the computation of turbulent flow in curved shallow channels (see par. 7.4 and par. 7.5) works rather wall, provided that the streamwise inertia of the secondary flow is properly incorporated in the bottom shear stress computation step. In contrast with the laminar flow case, the depth-averaged main velocity distribution is hardly influenced if only the streamwise inertia terms for $\bar{\psi}$ in the depth-averaged stream function equation are accounted for. If also the streamwise variations of g and the inertia terms in the equation for g are included, however, the influence of secondary flow inertia is much stronger than in case of laminar flow (cf. figures 30 and 45). The preliminary experimental verification of the turbulent flow model described in the present chapter shows that the predictions are not quite satisfactory in case of a rather sharply curved flume with a rough bottom.
In general, the effect of secondary flow convection seems to be underestimated. This can have various causes, such as

*) With the overall mean value of the secondary flow intensity adjusted to the measured one (see also par. 9.2 .2).

- the secondary flow intensity and/or the vertical velocity component are predicted inappropriately (cf. De Vriend et al., 1977),
- the distribution of $\bar{u}$ in the sidewall regions is not correct (see also chapter 6),
- the predicted secondary flow convection factor $f \frac{\partial g}{\partial \zeta}$ is in error,
- the similarity hyptohesis does not hold good for sharp bends (cf. De Vriend, 1979b; see also par. 7.1).

These possible shortcomings of the model will receive further attention in chapter 9.

According to figure 47b, the laminar flow model gives results that agree better with the measured data in the downstream half of the LFM-flume than the results from the turbulent flow model. As was stated before, this does not imply that in the present stage a laminar simulation of turbulent flow in curved channels is preferable before a turbulent flow computation.
There are considerable qualitative and quantitative differences between the laminar and turbulent flow models and under other conditions (higher Re_0, for instance) the laminar model will lead to obviously incorrect predictions.
Equations (7.13) through (7.17) give an impression of the quantitative differences between the models for laminar and for turbulent flow in the limit case of extremely shallow channels of mild curvature. For a proper simulation of turbulent flow by the laminar model, Re must be chosen such, that the characteristics (7.14) coincide and the ratios of the terms in equation (7.13) are the same. This implies that, for $\bar{u}_m \simeq 1$, the following conditions must be fulfilled:

$$\frac{\frac{\sqrt{g}}{\kappa C}\left(5 - 15.6\,\frac{\sqrt{g}}{\kappa C} + 37.5\,\frac{g}{\kappa^2 C^2}\right)}{1 + \frac{g}{\kappa^2 C^2}} = \frac{\frac{2}{175}\,\mathrm{Re}}{\frac{6}{5}} \tag{7.55}$$

$$\frac{\varepsilon \mathrm{Re}_0\left(1 + \frac{g}{\kappa^2 C^2}\right)}{\mathrm{Re}_0\,\frac{g}{C^2}} = \frac{\varepsilon \mathrm{Re}\,\frac{6}{5}}{3} \tag{7.56}$$

$$\frac{\varepsilon Re_0 \frac{\sqrt{g}}{\kappa C}\left(5 - 15.6 \frac{\sqrt{g}}{\kappa C} + 37.5 \frac{g}{\kappa^2 C^2}\right)}{Re_0 \frac{g}{C^2}} = \frac{\varepsilon Re^2 \frac{2}{175}}{3} \qquad (7.57)$$

If condition (7.55) is fulfilled, the direction of the characteristics is represented correctly; condition (7.56) accounts for the main flow inertia and condition (7.57) for the secondary flow convection. The conditions are interdependent, in that fulfilling two of them is sufficient. This is only possible, however, for specific values of C and Re, viz. for $C/\sqrt{g} \simeq 7.0$ (see figure 48), which is unrealistically small for alluvial rivers. Moreover, figure 48 shows that the values of Re corresponding with each of the three conditions (7.55) through (7.57) are far apart, especially at higher values of $C/\sqrt{g}$. This implies that, whatever value is chosen for Re, at least one of the essential phenomena (main flow inertia, local effect of secondary flow convection, transverse interaction due to secondary flow convection) is improperly represented. Only in extreme cases (negligible secondary flow convection, fully-developed curved flow) two out of the three conditions are not relevant and the simulation can be "exact".
Finally, figure 48 shows that laminar simulation of turbulent flow on the basis of the mean turbulence viscosity, i.e. $Re = Re_0$ (see par. 5.9) implies that main flow inertia is underestimated and that the effects of secondary flow convection are mostly overestimated. This corresponds with Asfari's (1968) observation (see also figure 47) that in the first part of the bend the tendency of the flow to shift outwards is stronger for laminar flow than for turbulent flow.

7.9. Summary of conclusions

The investigations described in the present chapter have made clear that, apart from the obvious differences in the diffusive transport of mean flow momentum, laminar and turbulent flow in curved shallow channels show a striking resemblance, both physically and mathematically.

The mathematical approaches of the two flow modes are quite similar, based on the same definition of main and secondary flow and the same similarity hypothesis and using the same two-step computation method (see chapter 5). The only essential difference lies in the variable turbulence viscosity in case of turbulent flow and the treatment of the fixed boundaries.
Also the investigation of the various elements of the turbulent flow model leads to the same conclusions as in the laminar flow case. The only difference is, that the stream-function/vorticity method for the computation of the depth-averaged main flow is not only expensive, but even ill-convergent in case of turbulent flow.
In spite of the different mechanism of diffusive momentum transport, the main velocity redistribution in curved turbulent flow shows essentially the same features as in laminar flow, this redistribution being mainly a matter of convection and the flow pattern being globally the same.
Still there are quantitative difference between the two flow modes:

- the intensity of the 'undisturbed' secondary flow (i.e. fully-developed secondary flow that is not influenced by the vicinity of sidewalls) lies between 1.5 and 2.5 times εV instead of $\frac{Re}{75}\,\varepsilon V$;
- the adaptation of the secondary flow intensity to an abrupt change in its source proceeds according to a damping exponential function with a characteristic length of about $1.3C/\sqrt{g}$ times the depth of flow rather than about 0.06 Red;
- the rate of outward extension of the influence of secondary flow convection on the main flow, characterized by the transverse celerity of a disturbance in $\bar{u}$, lies between 0.60 and 0.85 times εV*), instead of about 0.01 ReεV;
- the rate at which disturbances in the main velocity distribution

---

*) This celerity holds good for a given secondary flow intensity; the dependence of the secondary flow on the main velocity, however, tends to increase it, up to twice the indicated value if the secondary flow is determined by the local main flow properties alone.

damp out beyond a bend is characterized by a length scale of about $0.5C^2/g$ times the depth of flow, instead of about 3.5 Red. As a consequence, laminar flow cannot be used as a quantitative model of turbulent flow, not even in curved channels.

8. Computation of turbulent flow in curved shallow channels of arbitrary cross-sectional shape

8.1. Objective and approach

The next step on the way to a mathematical model of steady flow in curved river channels is the extension to channels of arbitrary cross-sectional shape. In order to be able to simulate the flow in curved alluvial channels, this shape is allowed to vary along the channel. The channel width, however, is kept constant for the time being.

In view of the important role of the sidewall regions in curved rectangular channel flow, it may seem rather inefficient to develop a mathematical model of the flow in natural river bends as an extension of the rectangular channel model. The banks of natural river channels are usually mildly sloping, especially the convex bank in a bend, which was shown to be the most important for the main velocity redistribution (see chapter 3). In a channel with mildly sloping banks the transverse variations of the main velocity are mainly due to variations in the depth of flow rather than to the no-slip conditions at the banks in combination with lateral diffusion. Consequently, the transverse gradients of $\bar{u}$, and hence the vertical component of the secondary flow, are spead out more evenly than in a rectangular channel. Then it is possible to disregard lateral diffusion completely and to simplify the model drastically (Kalkwijk et al., 1980).

Still, extending the rectangular channel model to arbitrary cross-sections is relevant, firstly because artificially steepened banks do occur in engineering practice (steeply sloping or vertical bank protections; quay-walls) and secondly because many laboratory experiments on flow in curved alluvial channels have been be carried out in flumes with fixed vertical or steep banks*).

---

*) If the banks are left free, the channel will start meandering, so that the horizontal geometry varies with time (Parker, 1976; see also Callander, 1978).

There are various ways to deal with the arbitrary shape of the cross-section in a mathematical model:

- finite-difference formulation of the flow equations on a rectangular grid, with the channel bed approximated by grid-lines;
- finite-difference formulation on a rectangular grid with the channel bed intersecting the grid-lines;
- finite-difference formulation on an orthogonal curvilinear grid fitted to the channel geometry;
- finite-difference formulation on a non-orthogonal grid, such that it is equivalent to transforming the cross-section to a rectangle;
- finite-element formulation with the elements fitted to the channel geometry.

In the first method, the bottom discretization is likely to introduce important errors. Of the other methods, the one based on the transformation of the vertical seems a logical extension of the rectangular channel method. Therefore this one will be applied here.

8.2. Mathematical formulation

The mathematical system describing the flow has to be generalized to channels of arbitrary cross-sectional shape. The basic differential equations, representing the conservation of mass and momentum, are the same as in case of rectangular channels; equations (2.4) and (2.11) through (2.13) still hold good. The boundary conditions, however, need some generalization. Firstly, the bottom level is allowed to vary with R and ϕ, so that the boundary conditions at the bottom and the banks can be formulated as

$$v_R = 0; \quad v_\phi = 0; \quad v_z = 0 \quad \text{at } z = z_b(R,\phi) \quad \text{and} \quad \text{at } R = R_c \pm \frac{B}{2} \qquad (8.1)^*)$$

*) In the actual model, these conditions are to be replaced by wall function approximations (see par. 8.3).

, in which z_b is a given function of R and ϕ. It should be noted that, even in case of sloping banks, the lateral bounds of the flow are assumed to be formed by vertical sidewalls of small height, since a zero depth of flow can give rise to computational problems.
Secondly, even in case of the "rigid-lid" approximation the water surface is not necessarily horizontal or parallel to the cross-sectional mean bottom. Therefore this approximation (cf. conditions (2.14) and (2.15)) is generalized to

$$v_z = v_R \frac{\partial z_s}{\partial R} + v_\phi \frac{1}{R} \frac{\partial z_s}{\partial \phi} \quad \text{at} \quad z = z_s(R,\phi) \tag{8.2}$$

$$(A_t + \eta)\left(\frac{\partial v_\phi}{\partial z} + \frac{1}{R}\frac{\partial v_z}{\partial \phi}\right) = 0 \quad \text{and} \quad (A_t + \eta)\left(\frac{\partial v_R}{\partial z} + \frac{\partial v_z}{\partial R}\right) = 0$$

$$\text{at } z=z_s \tag{8.3}$$

, where z_s is considered as a known function of R and ϕ*). The Froude number is still assumed so small, that derivatives of z_s can be disregarded in the mathematical system.
The integral condition of continuity (2.17) is generalized to

$$\int_{R_c-B/2}^{R_c+B/2} dR \int_{z_b}^{z_s} v_\phi dz = Q \tag{8.4}$$

The normalization of the differential equations (2.4) and (2.11) through (2.13) is the same as in par. 2.4 (see equations (2.30) through (2.33)).
The normalized boundary conditions read

$$v = 0; \quad u = 0; \quad w = 0 \quad \text{at} \quad \zeta = \zeta_b \quad \text{and} \quad \text{at} \quad \xi = \pm \frac{B}{2d} \tag{8.5}$$

*) In general, z_s will be a simple function of R and ϕ, such as a plane having the overall longitudinal channel slope.

$$w = \frac{u}{r}\frac{\partial \zeta_s}{\partial \phi} + v\frac{\partial \zeta_s}{\partial \xi} \qquad \text{at} \qquad \zeta = \zeta_s \tag{8.6}$$

$$\alpha\left(\frac{\partial u}{\partial \zeta} + \frac{\varepsilon^2}{r}\frac{\partial w}{\partial \phi}\right) = 0 \qquad \text{and} \qquad \alpha\left(\frac{\partial v}{\partial \zeta} + \frac{\partial w}{\partial \xi}\right) = 0 \quad \text{at} \quad \zeta = \zeta_s \tag{8.7}$$

with $\zeta_b = z_b/d$ and $\zeta_s = z_s/d$.
Normalizing the integral condition of continuity (8.4) yields

$$\int_{-B/2d}^{B/2d} d\xi \int_{\zeta_b}^{\zeta_s} u\,d\zeta = \frac{B}{d} \tag{8.8}$$

Finally, the normalized depth of flow h is defined by

$$h = \frac{z_s - z_b}{d} = \zeta_s - \zeta_b \tag{8.9}$$

It should be stressed that the normalization applies only to channels with a smoothly varying bottom level, i.e. without steps in the bottom. Otherwise, the bottom configuration can give rise to velocity gradients and "secondary" velocity components of which the order of magnitude cannot be characterized by the curvature parameter d/R_0 (see also De Vriend, 1976).

8.3. Transformation of the vertical

In accordance with par. 8.1, the model for arbitrarily shaped cross-sections is based upon a finite-difference formulation of the mathematical system on a non-orthogonal computational grid, chosen in such a way that the surface, the bottom and the vertical sidewalls (see par. 8.2) are described by grid lines. This can be achieved by discretizing the system on a rectangular grid after the coordinate transformation

$$z = \frac{\zeta-\zeta_s}{h}; \quad \xi' = \xi; \quad \phi' = \phi \tag{8.10}$$

As illustrated in figure 49, the vertical coordinate z is constant along the surface (z=0) and along the bottom (z=-1) and the vertical sidewalls remain at $\xi' = \pm$ B/2d. So (8.10) transforms the arbitrary shape of the cross-section in the (ξ,ϕ,ζ)-system into a rectangle of height 1 and width B/d in the (ξ',ϕ',z)-system.
The system of normalized differential equations and boundary conditions described in par. 8.2 is reformulated in terms of ξ', ϕ' and z, maintaining the original velocity components u, v and w and the pressure p as dependent variables. This transformation, details of which are given in Appendix J, leads to the following differential equations:

$$\frac{1}{r}\frac{\partial u}{\partial \phi'} + \frac{\partial v}{\partial \xi'} + \frac{\varepsilon}{r} v + \frac{1}{h}\frac{\partial w}{\partial z} - T_{s'}\frac{\partial u}{\partial z} - T_{\xi'}\frac{\partial v}{\partial z} = 0 \tag{8.11}$$

$$\varepsilon Re_0 \left\{\frac{u}{r}\frac{\partial u}{\partial \phi'} + v\frac{\partial u}{\partial \xi'} + \frac{w}{h}\frac{\partial u}{\partial z} - (uT_{s'} + vT_{\xi'})\frac{\partial u}{\partial z} + \frac{\varepsilon}{r}uv\right\} =$$

$$- \frac{1}{r}\frac{\partial p}{\partial \phi'} + T_{s'}\frac{\partial p}{\partial z} + \alpha\left(\nabla_2^2 u - \frac{\varepsilon^2}{r^2}u + 2\frac{\varepsilon^3}{r^2}\frac{\partial v}{\partial \phi'} - 2\frac{\varepsilon^3}{r}T_{s'}\frac{\partial v}{\partial z}\right) +$$

$$+ 2\frac{\varepsilon^2}{r}\frac{\partial \alpha}{\partial \phi'}\left(\frac{1}{r}\frac{\partial u}{\partial \phi'} + \frac{\varepsilon}{r}v - T_{s'}\frac{\partial u}{\partial z}\right) + \frac{\partial \alpha}{\partial \xi'}\left(\frac{\partial u}{\partial \xi'} - \frac{\varepsilon}{r}u + \frac{\varepsilon^2}{r}\frac{\partial v}{\partial \phi'} +\right.$$

$$\left. - T_{\xi'}\frac{\partial u}{\partial z} - \varepsilon^2 T_{s'}\frac{\partial v}{\partial z}\right) + \frac{1}{h}\frac{\partial \alpha}{\partial z}\left\{\frac{1}{h}\frac{\partial u}{\partial z} + \frac{\varepsilon^2}{r}\frac{\partial w}{\partial \phi'} +\right.$$

$$\left. - \varepsilon^2 h T_{s'}\left(\frac{1}{r}\frac{\partial u}{\partial \phi'} + \frac{\varepsilon}{r}v - \frac{\partial v}{\partial \xi'}\right) - hT_{\xi'}\left(\frac{\partial u}{\partial \xi'} - \frac{\varepsilon}{r}u + \frac{\varepsilon^2}{r}\frac{\partial v}{\partial \phi'}\right) +\right.$$

$$\left. + h(T_{\xi'}^2 + \varepsilon^2 T_{s'}^2)\frac{\partial u}{\partial z}\right\} \tag{8.12}$$

$$\varepsilon^3 Re_0 \left\{\frac{u}{r}\frac{\partial v}{\partial \phi'} + v\frac{\partial v}{\partial \xi'} + \frac{w}{h}\frac{\partial v}{\partial z} - (uT_{s'} + vT_{\xi'})\frac{\partial v}{\partial z}\right\} - \varepsilon^2 Re_0 \frac{u^2}{r} =$$

$$- \frac{\partial p}{\partial \xi'} + T_{\xi'} \frac{\partial p}{\partial z} + \varepsilon^2 a \left(\nabla_2^2 v - \frac{\varepsilon^2}{r^2} v - 2 \frac{\varepsilon}{r^2} \frac{\partial u}{\partial \phi'} + 2 \frac{\varepsilon}{r} T_{s'} \frac{\partial u}{\partial z}\right) +$$

$$+ \frac{\varepsilon^2}{r} \frac{\partial a}{\partial \phi'} \left(\frac{\partial u}{\partial \xi'} - \frac{\varepsilon}{r} u + \frac{\varepsilon^2}{r} \frac{\partial v}{\partial \phi'} - T_{\xi'} \frac{\partial u}{\partial z} - \varepsilon^2 T_{s'} \frac{\partial v}{\partial z}\right) +$$

$$+ 2\varepsilon^2 \frac{\partial a}{\partial \xi'} \left(\frac{\partial v}{\partial \xi'} - T_{\xi'} \frac{\partial v}{\partial z}\right) + \frac{\varepsilon^2}{h} \frac{\partial a}{\partial z} \left\{\frac{1}{h} \frac{\partial v}{\partial z} + \frac{\partial w}{\partial \xi'} - h T_{s'} \left(\frac{\partial u}{\partial \xi'} + \right.\right.$$

$$\left. - \frac{\varepsilon}{r} u + \frac{\varepsilon^2}{r} \frac{\partial v}{\partial \phi'}\right) - h T_{\xi'} \left(- \frac{1}{r} \frac{\partial u}{\partial \phi'} - \frac{\varepsilon}{r} v + \frac{\partial v}{\partial \xi'}\right) +$$

$$\left. + h\left(T_{\xi'}^2 + \varepsilon^2 T_{s'}^2\right) \frac{\partial v}{\partial z}\right\} \tag{8.13}$$

$$\varepsilon^3 Re_0 \left\{\frac{1}{r} \frac{\partial w}{\partial \phi'} + v \frac{\partial w}{\partial \xi'} + \frac{w}{h} \frac{\partial w}{\partial z} - \left(u T_{s'} + v T_{\xi'}\right) \frac{\partial w}{\partial z}\right\} =$$

$$- \frac{1}{h} \frac{\partial p}{\partial z} + \varepsilon^2 a \nabla_2^2 w + \frac{\varepsilon^2}{r} \frac{\partial a}{\partial \phi'} \left(\frac{1}{h} \frac{\partial u}{\partial z} + \frac{\varepsilon^2}{r} \frac{\partial w}{\partial \phi'} - \varepsilon^2 T_{s'} \frac{\partial w}{\partial z}\right) +$$

$$+ \varepsilon^2 \frac{\partial a}{\partial \xi'} \left(\frac{1}{h} \frac{\partial v}{\partial z} + \frac{\partial w}{\partial \xi'} - T_{\xi'} \frac{\partial w}{\partial z}\right) + \frac{\varepsilon^2}{h} \frac{\partial a}{\partial z} \left\{\frac{2}{h} \frac{\partial w}{\partial z} - h T_{s'} \left(\frac{1}{h} \frac{\partial u}{\partial z} + \right.\right.$$

$$\left. + \frac{\varepsilon^2}{r} \frac{\partial w}{\partial \phi'}\right) - h T_{\xi'} \left(\frac{1}{h} \frac{\partial v}{\partial z} + \frac{\partial w}{\partial \xi'}\right) + h\left(T_{\xi'}^2 + \varepsilon^2 T_{s'}^2\right) \frac{\partial w}{\partial z}\right\} \tag{8.14}$$

, in which

$$\nabla_2^2 = \frac{\varepsilon^2}{r^2} \frac{\partial^2}{\partial \phi'^2} + \frac{\partial^2}{\partial \xi'^2} + \frac{\varepsilon}{r} \frac{\partial}{\partial \xi'} + \frac{1}{h^2} \frac{\partial^2}{\partial z^2} - 2\varepsilon^2 T_{s'} \frac{1}{r} \frac{\partial^2}{\partial \phi \, \partial z} +$$

$$- 2T_{\xi'} \frac{\partial^2}{\partial \xi' \partial z} + \left(T_{\xi'}^2 + \varepsilon^2 T_{s'}^2\right) \frac{\partial^2}{\partial z^2} - \left(T_{\xi'\xi'} + \frac{\varepsilon}{r} T_{\xi'} + \varepsilon^2 T_{s's'}\right) \frac{\partial}{\partial z} \tag{8.15}$$

$$T_{s'} = \frac{1+z}{h} \frac{1}{r} \frac{\partial \zeta_s}{\partial \phi'} - \frac{z}{h} \frac{1}{r} \frac{\partial \zeta_b}{\partial \phi'} \tag{8.16}$$

$$T_{\xi'} = \frac{1+z}{h}\frac{\partial \zeta_s}{\partial \xi'} - \frac{z}{h}\frac{\partial \zeta_b}{\partial \xi'} \tag{8.17}$$

$$T_{s's'} = \frac{1+z}{h}\{\frac{1}{r^2}\frac{\partial^2 \zeta_s}{\partial \phi'^2} - \frac{2}{h}\frac{1}{r}\frac{\partial \zeta_s}{\partial \phi'}(\frac{1}{r}\frac{\partial \zeta_s}{\partial \phi'} - \frac{1}{r}\frac{\partial \zeta_b}{\partial \phi'})\} +$$

$$- \frac{z}{h}\{\frac{1}{r^2}\frac{\partial^2 \zeta_b}{\partial \phi'^2} - \frac{2}{h}\frac{1}{r}\frac{\partial \zeta_b}{\partial \phi'}(\frac{1}{r}\frac{\partial \zeta_s}{\partial \phi} - \frac{1}{r}\frac{\partial \zeta_b}{\partial \phi'})\} \tag{8.18}$$

$$T_{\xi'\xi'} = \frac{1+z}{h}\{\frac{\partial^2 \zeta_s}{\partial \xi'^2} - \frac{2}{h}\frac{\partial \zeta_s}{\partial \xi'}(\frac{\partial \zeta_s}{\partial \xi'} - \frac{\partial \zeta_b}{\partial \xi'})\} +$$

$$- \frac{z}{h}\{\frac{\partial^2 \zeta_b}{\partial \xi'^2} - \frac{2}{h}\frac{\partial \zeta_b}{\partial \xi'}(\frac{\partial \zeta_s}{\partial \xi'} - \frac{\partial \zeta_b}{\partial \xi'})\} \tag{8.19}$$

The transformed boundary conditions become:

$$u = 0; \quad v = 0; \quad w = 0 \quad \text{at} \quad z = -1 \quad \text{and at} \quad \xi' = \pm \frac{B}{2d} \tag{8.20}$$

$$w = \frac{u}{r}\frac{\partial \zeta_s}{\partial \phi'} + v\frac{\partial \zeta_s}{\partial \xi'} \qquad \text{at} \quad z = 0 \tag{8.21}$$

$$\alpha(\frac{1}{h}\frac{\partial u}{\partial z} + \frac{\varepsilon^2}{r}\frac{\partial w}{\partial \phi'} - \varepsilon^2 T_{s'}\frac{\partial w}{\partial z}) = 0 \qquad \text{at} \quad z = 0 \tag{8.22}$$

$$\alpha(\frac{1}{h}\frac{\partial v}{\partial z} + \varepsilon^2\frac{\partial w}{\partial \xi'} - T_{\xi'}\frac{\partial w}{\partial z}) = 0 \qquad \text{at} \quad z = 0 \tag{8.23}$$

$$\int_{-B/2d}^{B/2d} h\,d\xi' \int_{-1}^{0} u\,dz = \frac{B}{d} \tag{8.24}$$

The differential equations and boundary conditions in the transformed system have the same structure as in the (ξ,ϕ,ζ)-system, but there are additional terms (with $T_{s'}$, $T_{\xi'}$, $T_{s's'}$

and $T_{\xi',\xi'}$) that account for the non-orthogonality of the transformation. For $\zeta_s \equiv 0$ and $\zeta_b \equiv -1$, i.e. $h \equiv 1$, these terms vanish and the equations become identical to the ones in the (ξ,ϕ,ζ)-system.

8.4. Turbulence model

The turbulence model applied in the rectangular channel computations, as described in the foregoing, is based on the assumption that the turbulence viscosity in a vertical is determined solely by the flow conditions in that vertical, i.e. lateral influencing is disregarded. In rectangular channels, this give rise to errors in the velocity predictions near the sidewalls, but, in spite of the important role of the sidewall regions in curved rectangular channel flow, these errors are only of local importance (see chapter 7).
The role of the sidewall regions will be less important in channels with sloping banks, so that the basic idea of the aforementioned turbulence model will also hold good for arbitrarily shaped channels, at least if the bottom level varies smoothly (see also Lundgren et al., 1964). Therefore the turbulence viscosity is related to the mean flow by

$$A_t = \rho \frac{\kappa}{\gamma} V_\tau (z_s - z_b) \alpha'\left(\frac{z}{z_z - z_b}\right) \tag{8.25}$$

, or, in the normalized system,

$$\frac{A_t}{\rho V d} = \frac{\kappa}{\gamma} U_\tau h\alpha'(z) \tag{8.26}$$

According to (7.22), the normalized resultant bottom friction velocity U_τ is related to the local value of the normalized resultant depth-averaged main velocity $\bar{U}$ through

$$U_\tau = k_m \frac{\sqrt{g}}{C} \bar{U} \tag{8.27}$$

In uniform rectilinear shear flow, the value of Chezy's factor for a hydraulically rough bottom is usually assumed to vary with the bottom roughness height k and with the depth of flow (Chow, 1959). According to the White-Colebrook formula, C can then be given by (see also (6.29))

$$\frac{C}{\sqrt{g}} = 2.5 \ln (12.2 \frac{z_s - z_b}{k}) \tag{8.28}$$

In alluvial river bends, not only the depth of flow, but also the bottom roughness, and especially the height of the bed forms, will show spatial variations. For convenience, these variations are isolated by splitting C into two parts

$$C = C_0 + C' \tag{8.29}$$

, in such a way that

$$\frac{C_0}{\sqrt{g}} = 2.5 \ln(12.2 \frac{d}{k_0}) \quad \text{and} \quad \frac{C'}{\sqrt{g}} = 2.5 \ln \frac{h}{k'} \tag{8.30}$$

, k_0 denoting a representative bottom roughness and k' being defined by $k' = k/k_0$.

If the effective Reynolds number Re_0 is defined by

$$Re_0 = \frac{\gamma}{\kappa} \frac{C_0}{\sqrt{g}} \tag{8.31}$$

(cf. definition (6.56)), expression (8.26) can be elaborated to

$$a = k_m \frac{C_0}{C} \bar{U} \, h a'(z) \tag{8.32}$$

, which for $C_0 \equiv C$ and $h \equiv 1$ changes into the expression used in the rectangular channel model.

On the assumption that considerable differences in h and k can occur, but that the variations are always gradual, the correction C' is incorporated in the model, but its derivatives are disregarded.

As the turbulence viscosity goes to zero at the fixed boundaries of the flow, the velocity gradients should go to infinity there in order to have a finite shear stress. Therefore, at these boundaries the "wall-function" technique, discussed in chapter 6, is applied instead of the boundary conditions (8.20). The wall function approximation for the resultant normalized velocity $U_{//}$ parallel to such a boundary reads

$$U_{//} = \frac{U_\tau}{\kappa} \left(\frac{\kappa C}{\sqrt{g}} + 1 + \ln\chi\right) \tag{8.33}$$

, in which χ denotes the wall distance normalized by d. Correspondingly, the normalized velocity $U_\perp$ perpendicular to that boundary is given by

$$U_\perp = \frac{1}{\kappa} \operatorname{div}(\vec{U}_\tau)\ \chi\ \left(\frac{\kappa C}{\sqrt{g}} + \ln\chi\right) \tag{8.34}$$

The wall functions (8.33) and (8.34) have to be translated to functions for u, v and w. In shallow channels without steep bottom slopes, the wall functions for the horizontal velocity components near the bottom can be approximated by

$$u \simeq \frac{u_\tau}{\kappa} \left\{\frac{\kappa C}{\sqrt{g}} + 1 + \ln(1+z)\right\} \tag{8.35}$$

$$v \simeq \frac{v_\tau}{\kappa} \left\{\frac{\kappa C}{\sqrt{g}} + 1 + \ln(1+z)\right\} \tag{8.36}$$

Then the wall function for the vertical velocity component can be derived from the equation of continuity (8.11), to yield

$$w \simeq -\frac{h}{\kappa}\left(\frac{1}{r}\frac{\partial u_\tau}{\partial \phi'} + \frac{\partial v_\tau}{\partial \xi'} + \frac{\varepsilon}{r} v_\tau\right)(1+z)\left\{\frac{\kappa C}{\sqrt{g}} + \ln(1+z)\right\} +$$

$$+ \frac{1}{\kappa}\left(\frac{u_\tau}{r}\frac{\partial \zeta_b}{\partial \phi'} + v_\tau \frac{\partial \zeta_b}{\partial \xi'}\right)\left\{\frac{\kappa C}{\sqrt{g}} + 1 + \ln(1+z)\right\} \qquad (8.37)$$

The wall function approximations near the vertical sidewalls are similar to the ones in case of a rectangular channel (see par. 6.5):

$$u \simeq \frac{u_{\tau l}}{\kappa}\left\{\frac{\kappa C_w}{\sqrt{g}} + 1 + \ln\left(\frac{B}{2d} + \xi'\right)\right\} \qquad (8.38)$$

$$w \simeq \frac{w_{\tau l}}{\kappa}\left\{\frac{\kappa C_w}{\sqrt{g}} + 1 + \ln\left(\frac{B}{2d} + \xi'\right)\right\} \qquad (8.39)$$

$$v \simeq -\frac{1}{\kappa}\left(\frac{1}{r}\frac{\partial u_{\tau l}}{\partial \phi'} + \frac{1}{h}\frac{\partial w_{\tau l}}{\partial z}\right)\left(\frac{B}{2d} + \xi'\right)\left\{\frac{\kappa C_w}{\sqrt{g}} + \ln\left(\frac{B}{2d} + \xi'\right)\right\} \qquad (8.40)$$

at the left wall and

$$u \simeq -\frac{u_{\tau r}}{\kappa}\left\{\frac{\kappa C_w}{\sqrt{g}} + 1 + \ln\left(\frac{B}{2d} - \xi'\right)\right\} \qquad (8.41)$$

$$w \simeq -\frac{w_{\tau r}}{\kappa}\left\{\frac{\kappa C_w}{\sqrt{g}} + 1 + \ln\left(\frac{B}{2d} - \xi'\right)\right\} \qquad (8.42)$$

$$v \simeq -\frac{1}{\kappa}\left(\frac{1}{r}\frac{\partial u_{\tau r}}{\partial \phi'} + \frac{1}{h}\frac{\partial w_{\tau r}}{\partial z}\right)\left(\frac{B}{2d} - \xi'\right)\left\{\frac{\kappa C_w}{\sqrt{g}} + \ln\left(\frac{B}{2d} - \xi'\right)\right\} \qquad (8.43)$$

at the right wall. Since the Chezy-factor of the bottom is allowed to vary with ξ' and ϕ', the Chezy-factor of the sidewalls in (8.38) through (8.43) is denoted by C_w. Moreover, this provides the possibility to give different roughnesses to the sidewalls and the bottom.

If the channel is formed by a bottom without steeply sloping

parts and two vertical sidewalls, the wall function approximations (8.35) through (8.43) are sufficient to replace the fixed-boundary conditions (8.20). If important parts of the bed are steeply sloping, however, such as in case of steep banks, these conditions will not hold good there. But then the vertical transformation in combination with the vertical and horizontal similarity hypothesis that will be made hereafter is not relevant there, either. For the moment, however, this imperfection of the model is accepted and the bottom functions (8.35) through (8.37) are applied to the steeply sloping parts, anyway.
The numerical treatment of the wall functions is essentially the same as in the rectangular channel model (see chapter 7 and Appendices E through H), and so is the determination of the boundary shear stresses from the friction velocities.

8.5. Simplification

The transformed system of differential equations and boundary conditions described in the foregoing will be simplified before being solved. Firstly, the simplifications that were made in the rectangular channel model (separation of main and secondary flow; neglect of terms in the momentum equations; similarity hypothesis) will be introduced here, as well. In addition, however, a number of simplifications will be based on a limitation of the model to moderate Froude number flow in channels with a length scale of the bottom level variations that is much larger than the depth of flow. This limitation is consistent with the shallow channel approximation and it applies to most alluvial rivers.

8.5.1. Main and secondary flow

The separation of the main and the secondary flow is somewhat more complicated than in case of a rectangular channel, as the bottom configuration can give rise to a considerable vertical component of the main velocity. The separation is based on the definition of the main and the secondary flow given in par. 5.2. This implies that the vertical component of the main velocity follows from the equation of continuity for the main flow

$$\frac{1}{r}\frac{\partial u_m}{\partial \phi'} + \frac{\partial v_m}{\partial \xi'} + \frac{\varepsilon}{r} v_m - T_{s'}\frac{\partial u_m}{\partial z} - T_{\xi'}\frac{\partial v_m}{\partial z} + \frac{1}{h}\frac{\partial w_m}{\partial z} = 0 \qquad (8.44)$$

Similarly, the vertical component of the secondary flow follows from the equation of continuity of the secondary flow. If terms being an order $0(\varepsilon^2)$ smaller than the leading terms in this equation are disregarded, it reads

$$\frac{\partial v_s}{\partial \xi'} + \frac{\varepsilon}{r} v_s - T_{\xi'}\frac{\partial v_s}{\partial z} + \frac{1}{h}\frac{\partial w_s}{\partial z} = 0 \qquad (8.45)$$

The additional transformation terms with $T_{s'}$ and $T_{\xi'}$, accounting for the spatial variations of the bottom and surface levels, give rise to additional vertical velocities. In the momentum equations, these velocities should be accounted for, as will be shown hereafter.

8.5.2. Simplification of the momentum equations

In addition to the terms that figure in the rectangular channel model, the momentum equations (8.12) through (8.14) contain a considerable number of terms arising from the non-uniformity of the water surface elevation and the bed level. On the assumption that the bed configuration is such, that the terms of the former group remain of the same order of magnitude as in case of rectangular channel flow, these terms are simplified in the same way as in the rectangular channel model. This implies, that all terms being an order $0(\varepsilon^2)$ smaller than the leading terms of the same type are omitted and that the terms representing the transverse inertia of the secondary flow are also disregarded. On the other hand, it would be convenient if some of the additional terms could be disregarded, as well. Therefore these terms will be subject to a closer investigation here.
The transverse configuration of the water surface in a bend is described appropriately by

$$\frac{\partial z_s}{\partial R} = \frac{\overline{v_\phi^2}}{R} \text{ or, in the normalized system: } \frac{\partial \zeta_s}{\partial \xi'} = \frac{V^2}{gd}\frac{\varepsilon}{r}\overline{u^2} \qquad (8.46)$$

(Yen et al., 1971; De Vriend, 1976 & 1977; De Vriend et al., 1977 & 1978; De Vriend, 1979). So the (normalized) slope of the order of magnitude $O(\varepsilon Fr^2)$ in which Fr denotes the Froude number $V/\sqrt{(gd)}$. In the channels to be considered, not only ε, but also Fr^2 will be much smaller than unity, so that the transverse surface slope will be very small. The same holds good for the second derivative of ζ_s with respect to ξ' (see also chapter 9). Therefore the terms with first and second derivatives of ζ_s with respect to ξ' are omitted from the momentum equations.

As was stated before (see, for instance, par. 8.4), considerations are limited to channels with a smoothly varying bed level. If L denotes the length scale of the transverse variations of this level, the order of magnitude of the first and second derivatives of ζ_b with respect to ξ' is given by

$$\frac{\partial \zeta_b}{\partial \xi'} = O\left(\frac{d}{L}\right) \qquad \text{and} \qquad \frac{\partial^2 \zeta_b}{\partial \xi'^2} = O\left(\frac{d^2}{L^2}\right) \qquad (8.47)$$

The limitation of the model to smoothly varying bed levels is formalized to taking $d^2/L^2 << 1$ and omitting all terms of the order $O(d^2/L^2)$ from the momentum equations.

In general, the limitation to small Froude numbers and especially the one to small bottom slopes will be more restrictive than the limitation to small values of ε. For most of the natural rivers to be considered, the square of the Froude number can become larger than ε, which seldomly exceeds 0.05 (cf. par. 3.4; see also: Jansen, 1979). The length scale of the transverse bed level variations is related to the channel width rather than to the radius of curvature of the axis, and as B/R_0 is seldomly larger than 0.5 (Leopold et al., 1964), the ratio d/L will be larger than ε. Still Fr^2 and d/L are supposed small

enough to justify the aforementioned simplifications of the momentum equations.

If these simplifications are justified, the additional terms that are an order $O(\varepsilon^2)$ smaller than the leading terms of the same type can certainly be disregarded. Then the simplified momentum equations become

$$\varepsilon Re_0 \{\frac{u_m}{r}\frac{\partial u_m}{\partial \phi'} + v_m \frac{\partial u_m}{\partial \xi'} + \frac{\varepsilon}{r} v_m u_m + (\frac{w_m}{h} - u_m T_{s'} - v_m T_{\xi'}) \frac{\partial u_m}{\partial z} +$$

$$+ v_s \frac{\partial u_m}{\partial \xi'} + \frac{\varepsilon}{r} v_s u_m + (\frac{w_s}{h} - v_s T_{\xi'}) \frac{\partial u_m}{\partial z}\} = -\frac{1}{r}\frac{\partial p}{\partial \phi'} +$$

$$+ (T_{s'} \frac{\partial p}{\partial z}) + a\nabla_3^2 u_m + \frac{\partial a}{\partial \xi'}(\frac{\partial u_m}{\partial \xi'} - \frac{\varepsilon}{r} u_m - T_{\xi'} \frac{\partial u_m}{\partial z}) +$$

$$+ \frac{1}{h}\frac{\partial a}{\partial z}(\frac{1}{h}\frac{\partial u_m}{\partial z} - hT_{\xi'} \frac{\partial u_m}{\partial \xi'}) \qquad (8.48)^*)$$

$$\varepsilon^3 Re_0 \{\frac{u_m}{r}\frac{\partial v_m}{\partial \phi'} + v_m \frac{\partial v_m}{\partial \xi'} + (\frac{w_m}{h} - u_m T_{s'} - v_m T_{\xi'}) \frac{\partial v_m}{\partial z}\} +$$

$$- \varepsilon^2 Re_0 \frac{u_m^2}{r} + \varepsilon^3 Re_0 \{v_s \frac{\partial v_m}{\partial \xi'} + (\frac{w_s}{h} - v_s T_{\xi'}) \frac{\partial u_m}{\partial z} + \frac{u_m}{r}\frac{\partial v_s}{\partial \phi'} +$$

$$+ v_m \frac{\partial v_s}{\partial \xi'} + (\frac{w_m}{h} - u_m T_{s'} - v_m T_{\xi'}) \frac{\partial v_s}{\partial z}\} = -\frac{\partial p}{\partial \xi'} + T_{\xi'} \frac{\partial p}{\partial z} +$$

$$+ \varepsilon^2 a (\nabla_3^2 v_m - 2\frac{\varepsilon}{r^2}\frac{\partial u_m}{\partial \phi'} + \nabla_3^2 v_s) + \frac{\varepsilon^2}{r}\frac{\partial a}{\partial \phi'}(\frac{\partial u_m}{\partial \xi'} - \frac{\varepsilon}{r} u_m - T_{\xi'} \frac{\partial u_m}{\partial z}) +$$

---

*) According to the vertical momentum equation (8.14), the vertical derivative of the total pressure is of the order of magnitude $O(\varepsilon^2, \varepsilon^3 Re_0)$, so that it can also be omitted from this equation.

$$+ 2\varepsilon^2 \frac{\partial a}{\partial \xi'} \left(\frac{\partial v_m}{\partial \xi'} - T_{\xi'} \frac{\partial v_m}{\partial z} + \frac{\partial v_s}{\partial \xi'} - T_{\xi'} \frac{\partial v_s}{\partial z}\right) + \frac{\varepsilon^2}{h} \frac{\partial a}{\partial z} \left\{\frac{1}{h} \frac{\partial v_m}{\partial z} +\right.$$

$$+ \frac{\partial w_m}{\partial \xi'} - hT_{s'} \frac{\partial u_m}{\partial \xi'} - hT_{\xi'} \left(\frac{\partial v_m}{\partial \xi'} - \frac{1}{r} \frac{\partial u_m}{\partial \phi'}\right) + \frac{1}{h} \frac{\partial v_s}{\partial z} + \frac{\partial w_s}{\partial \xi'} +$$

$$\left. - hT_{\xi'} \frac{\partial v_s}{\partial \xi'}\right\} \tag{8.49}$$

$$\varepsilon^3 Re_0 \left\{ \frac{u_m}{r} \frac{\partial w_m}{\partial \phi'} + v_m \frac{\partial w_m}{\partial \xi'} + \left(\frac{w_m}{h} - u_m T_{s'} - v_m T_{\xi'}\right) \frac{\partial w_m}{\partial z} + v_s \frac{\partial w_m}{\partial \xi'} +\right.$$

$$+ \left(\frac{w_s}{h} - v_s T_{\xi'}\right) \frac{\partial w_m}{\partial z} + \frac{u_m}{r} \frac{\partial w_s}{\partial \phi'} + v_m \frac{\partial w_s}{\partial \xi'} + \left(\frac{w_m}{h} - u_m T_{s'} +\right.$$

$$\left.\left. - v_m T_{\xi'}\right) \frac{\partial w_s}{\partial z}\right\} = - \frac{1}{h} \frac{\partial p}{\partial z} + \varepsilon^2 a \left(\nabla_3^2 w_m + \nabla_3^2 w_s\right) + \frac{\varepsilon^2}{r} \frac{\partial a}{\partial \phi'} \frac{1}{h} \frac{\partial u_m}{\partial z} +$$

$$+ \varepsilon^2 \frac{\partial a}{\partial \xi'} \left(\frac{1}{h} \frac{\partial v_m}{\partial z} + \frac{\partial w_m}{\partial \xi'} - T_{\xi'} \frac{\partial w_m}{\partial z} + \frac{1}{h} \frac{\partial v_s}{\partial z} + \frac{\partial w_s}{\partial \xi'} - T_{\xi'} \frac{\partial w_s}{\partial z}\right) +$$

$$+ \frac{\varepsilon^2}{h} \frac{\partial a}{\partial z} \left\{\frac{2}{h} \frac{\partial w_m}{\partial z} - T_{s'} \frac{\partial u_m}{\partial z} - hT_{\xi'} \left(\frac{1}{h} \frac{\partial v_m}{\partial z} + \frac{\partial w_m}{\partial \xi'}\right) + \frac{2}{h} \frac{\partial w_s}{\partial z} +\right.$$

$$\left. - hT_{\xi'} \left(\frac{1}{h} \frac{\partial v_s}{\partial z} + \frac{\partial w_s}{\partial \xi'}\right)\right\} \tag{8.50}$$

, in which $\nabla_3^2 = \frac{\partial^2}{\partial \xi'^2} + \frac{\varepsilon}{r} \frac{\partial}{\partial \xi'} + \frac{1}{h^2} \frac{\partial^2}{\partial z^2} - 2T_{\xi'} \frac{\partial^2}{\partial \xi' \partial z}$

8.5.3. Simplification of the boundary conditions

The boundary conditions at the surface, (8.21) through (8.23), are simplified by omitting terms that are an order $0(\varepsilon^2)$ smaller than the leading terms. Furthermore, these conditions are split up into a main and a secondary flow part, so that

$$w_m = \frac{u_m}{r} \frac{\partial \zeta_s}{\partial \phi'} + v_m \frac{\partial \zeta_s}{\partial \xi'} \quad \text{and} \quad w_s = v_s \frac{\partial \zeta_s}{\partial \xi'} \quad \text{at} \quad z = 0 \tag{8.51}$$

$$\frac{a}{h}\frac{\partial u_m}{\partial z} = 0;\ \frac{a}{h}\frac{\partial v_m}{\partial z} = 0 \quad \text{and} \quad \frac{a}{h}\frac{\partial v_s}{\partial z} = 0 \quad \text{at} \quad z = 0 \tag{8.52}$$

Splitting the kinematical condition (8.21) into a main and a secondary flow part as in (8.51) is consistent with splitting the equation of continuity (8.11) into equations (8.44) and (8.45). If equation (8.44) is averaged over the depth of flow, the resulting equation and condition (8.51) can be combined to the depth-averaged equation of continuity

$$\frac{1}{r}\frac{\partial \bar{u}}{\partial \phi'} + \frac{\partial \bar{v}}{\partial \xi'} + \frac{\varepsilon}{r}\bar{v} + \frac{1}{h}\left(\frac{\bar{u}}{r}\frac{\partial h}{\partial \phi'} + \bar{v}\frac{\partial h}{\partial \xi'}\right) = 0 \tag{8.53}$$

Integrating equation (8.45) over the depth of flow yields the secondary flow part of condition (8.51).
The boundary conditions at the fixed boundaries are replaced by the wall function approximations (8.35) through (8.43), each of which is split up into a main and a secondary flow part.
The integral condition of continuity (8.24) concerns the main flow by definition, so

$$\int_{-B/2d}^{B/2d} h\,d\xi' \int_{-1}^{0} u_m\,dz = \frac{B}{d} \tag{8.54}$$

8.5.4. Interpretation of the simplified system

In order to facilitate the physical interpretation of the simplified system, the equations of continuity and the main flow momentum equation are transformed to the stream-oriented coordinate system (n', s', z), which in turn is obtained by vertical transformation of the system (n, s, ζ) represented in figure 23 (see also par. 5.4 and par. 7.3).
The transformed equations of continuity read

$$\frac{\partial u_m}{\partial s'} - \frac{u_m}{r_n} + \frac{1}{h}\frac{\partial w_m}{\partial z} - T_{s'}\frac{\partial u_m}{\partial z} = 0 \quad \text{with} \quad T_{s'} = \frac{1+z}{h}\frac{\partial \zeta_s}{\partial s'} - \frac{z}{h}\frac{\partial \zeta_b}{\partial s'} \tag{8.55}$$

$$\frac{\partial v_s}{\partial n} - \frac{\varepsilon}{r_s} v_s + \frac{1}{h} \frac{\partial w_s}{\partial z} - T_{n'} \frac{\partial v_s}{\partial z} = 0 \quad \text{with} \quad T_{n'} = \frac{1+z}{h} \frac{\partial \zeta_s}{\partial n'} - \frac{z}{h} \frac{\partial \zeta_b}{\partial n'} \tag{8.56}$$

These equations show, once again, that the spatical variations of the bottom and water surface levels give rise to additional vertical velocities, both for the main and for the secondary flow.
Transformation of the main flow momentum equation (8.48) yields

$$\varepsilon Re_0 \{u_m \frac{\partial u_m}{\partial s'} + (\frac{w_m}{h} - u_m T_{s'}) \frac{\partial u_m}{\partial z} + v_s \frac{\partial u_m}{\partial n'} - \frac{\varepsilon}{r_s} v_s u_m +$$

$$+ (\frac{w_s}{h} - v_s T_{n'}) \frac{\partial u_m}{\partial z}\} = - \frac{\partial p}{\partial s'} + \alpha \nabla_4^2 u_m + \frac{\partial \alpha}{\partial n'} (\frac{\partial u_m}{\partial n'} + \frac{\varepsilon}{r_s} u_m +$$

$$- T_{n'} \frac{\partial u_m}{\partial z}) + \frac{1}{h} \frac{\partial \alpha}{\partial z} (\frac{1}{h} \frac{\partial u_m}{\partial z} - h T_{n'} \frac{\partial u_m}{\partial n'}) \tag{8.57}$$

, in which $\nabla_4^2 = \frac{\partial^2}{\partial n'^2} - \frac{\varepsilon}{r_s} \frac{\partial}{\partial n'} + \frac{1}{h^2} \frac{\partial^2}{\partial z^2} - 2T_{n'} \frac{\partial^2}{\partial n' \partial z}$.

So the spatial variations of ζ_s and ζ_b, and the additional vertical velocities they induce, give rise to additional convection and diffusion of main flow momentum.
The transformed versions of the transverse and vertical momentum equations are still complicated, as a consequence of the additional terms due to these spatial variations; the corresponding vertical velocities give rise to additional sources of secondary flow, which are much less important than the main flow curvature.

The mechanism of the main velocity redistribution under the influence of the secondary flow can be analysed in a similar way as in par. 7.3.
Adopting the similarity hypothesis (5.20) for the main flow, the vertical component of the main velocity can be derived from equation (8.55) and its depth-averaged version

$$\frac{\partial \bar{u}_m}{\partial s} - \frac{\bar{u}_m}{r_n} + \frac{\bar{u}_m}{h} \frac{\partial h}{\partial s'} = 0 \tag{8.58}$$

After some elaboration, this yields (see also par. 8.6.1).

$$w_m = \bar{u}_m \frac{\partial h}{\partial s'} zf + \bar{u}_m \frac{\partial \zeta_s}{\partial s'} f \tag{8.59}$$

Consequently

$$\frac{w_m}{h} - \bar{u}_m T_{s'} = 0 \tag{8.60}$$

So the additional main flow convection terms in (8.57) drop out if the similarity hypothesis holds good for u_m.
The equation of continuity for the secondary flow (8.56) is approximately satisfied if the stream function ψ' is defined by

$$v_s = \frac{1}{hr_s} \frac{\partial \psi'}{\partial z} \quad \text{and} \quad w_s = -\frac{1}{r_s} \frac{\partial \psi'}{\partial n'} + T_{n'} \frac{1}{r_s} \frac{\partial \psi'}{\partial z} \tag{8.61}$$

So the vertical component of the secondary flow consists of two parts, one of which is also encountered in rectangular channel flow; the other one is due to the transverse non-uniformity of the cross-section. It can be shown from (8.56) and (8.61) that

$$\frac{w_s}{h} - v_s T_{n'} = -\frac{1}{hr_s} \frac{\partial \psi'}{\partial n'} \tag{8.62}$$

, i.e. the additional secondary flow convection terms in (8.57) compensate one another if (8.61) holds good.
Taking account of these results and disregarding lateral diffusion in the central part of a shallow channel with a smooth bottom configuration, the longitudinal momentum equation can be reduced to

$$\varepsilon Re_0 \{u_m \frac{\partial u_m}{\partial s'} + \frac{1}{hr_s} \frac{\partial \psi'}{\partial z} (\frac{\partial u_m}{\partial n'} - \frac{\varepsilon}{r_s} u_m) - \frac{1}{hr_s} \frac{\partial \psi'}{\partial n'} \frac{\partial u_m}{\partial z}\}$$

$$= - \frac{\partial p}{\partial s'} + \frac{1}{h^2} \frac{\partial}{\partial z} (a \frac{\partial u_m}{\partial z}) \qquad (8.63)$$

Averaging (8.63) over the depth of flow yields

$$\varepsilon Re_0 \overline{f^2}\, \bar{u}_m \frac{\partial \bar{u}_m}{\partial s'} + \frac{\varepsilon Re_0}{hr_s} \overline{f \frac{\partial \psi'}{\partial z}} \frac{\partial \bar{u}_m}{\partial n'} + \{\frac{1}{h^2} (a \frac{\partial f}{\partial z})\Big|_{z=-1} +$$

$$- \frac{\varepsilon^2 Re_0}{hr_s^2} \overline{f \frac{\partial \psi'}{\partial z}} - \frac{\varepsilon Re_0}{hr_s} \overline{\frac{\partial \psi'}{\partial n'} \frac{\partial f}{\partial z}}\} \bar{u}_m = - \frac{\partial \bar{p}}{\partial s'} \qquad (8.64)$$

Together with the truncated transverse momentum equation

$$\varepsilon^2 Re_0 \frac{\bar{u}_m^2}{r_s} \overline{f^2} = - \frac{\partial \bar{p}}{\partial n'} \qquad (8.65)$$

this equation can be reduced to

$$\varepsilon Re_0 \overline{f^2}\, \bar{u}_m \frac{d\bar{u}_m}{ds} + \{\frac{1}{h^2} (a \frac{\partial f}{\partial z})\Big|_{z=-1} - \frac{\varepsilon^2 Re_0}{hr_s^2} \overline{\frac{\partial f}{\partial z} \frac{\partial \psi'}{\partial n'}}\} \bar{u}_m = - \frac{d\bar{p}}{ds'} \qquad (8.66)$$

holding along the characteristics

$$\frac{dn'}{ds'} = (\frac{1}{hr_s} \overline{f \frac{\partial \psi'}{\partial z}}) / (\bar{u}_m \overline{f^2}) \qquad (8.67)$$

Apart from the factors $\frac{1}{h}$, these equations correspond with equations (7.13) and (7.14). Apparently, the mechanism of the transverse redistribution of the main velocity under the convective influence of a given secondary circulation is

essentially the same as in rectangular channels (cf. par. 7.3). This does not imply, however, that the main velocity redistribution processes in rectangular and in arbitrarily shaped channels are quantitatively comparable, since the secondary circulation, and especially the horizontal distribution of the vertical velocity component, will be quite different in either case.

As becomes evident from definitions (5.25) and (8.61) for the stream function of the secondary flow, the vertical velocity component is related to the transverse variation of the stream function, which in turn is related to the depth-averaged main velocity. Consequently, the vertical velocities in rectangular channels are concentrated near the sidewalls, where the greather part of the transverse variations of $\bar{u}_m$ and ψ' occurs. In natural rivers with mildly sloping banks, however, the transverse variations of $\bar{u}_m$ and ψ' are spread over a much wider region and so are the vertical velocities. Hence the local convective effects of the vertical velocity on the distribution of $\bar{u}_m$ and also the outward influencing due to the horizontal component of the secondary flow are quite different from the ones in a rectangular channel (cf. par. 5.4 and par. 7.3).

This is readily illustrated by the case of fully developed secondary flow in shallow channels with mildly sloping banks and without vertical sidewalls.

Then the secondary flow can be approximated by (see also Rozovskii, 1961 and De Vriend, 1976)

$$\psi' = h^2 \bar{u}_m g'(z); \quad v_s = \frac{h\bar{u}_m}{r_s} \frac{\partial g'}{\partial z}; \quad w_s = -\frac{g'}{r_s} \frac{\partial (h^2 u_m)}{\partial n'} + \frac{h\bar{u}_m}{r_s} \frac{\partial h}{\partial n'} z \frac{\partial g'}{\partial z} \tag{8.68}$$

, in which $g'(z)$ is a given distribution function. Substituting (8.68) into (8.64) yields, after some elaboration

$$\varepsilon Re_0 \overline{f^2}\, \bar{u}_m \frac{\partial \bar{u}_m}{\partial s'} + 2\varepsilon Re_0 \overline{f \frac{\partial g'}{\partial z}} \frac{h\bar{u}_m}{r_s} \frac{\partial \bar{u}_m}{\partial n'} +$$

$$+ \frac{\bar{u}_m^2}{h} \{(\alpha' \frac{\partial f}{\partial z})\Big|_{z=-1} - \varepsilon^2 Re_0 \overline{f \frac{\partial g'}{\partial z}} \frac{h^2}{r_s^2} +$$

$$+ 2\varepsilon Re_0 \overline{f \frac{\partial g'}{\partial z}} \frac{h}{r_s} \frac{\partial h}{\partial n'}\} = - \frac{\partial \bar{p}}{\partial s'} \qquad (8.69)$$

Together with equation (8.65), this equation can be reduced to

$$\varepsilon Re_0 \overline{f^2} \frac{d}{ds'} (\frac{\bar{u}_m^2}{2}) + \frac{\bar{u}_m^2}{h} \{(\alpha' \frac{\partial f}{\partial z})\Big|_{z=-1} + \varepsilon Re_0 \overline{f \frac{\partial g'}{\partial z}} \frac{\partial}{\partial n'}(\frac{h^2}{r_s})\} =$$

$$- \frac{d\bar{p}}{ds'} \qquad (8.70)$$

, which holds along the characteristics

$$\frac{dn'}{ds'} = 2 \frac{h}{r_s} \overline{f \frac{\partial g'}{\partial z}} / \overline{f^2} \qquad (8.71)$$

(cf. Kalkwijk et al., 1980)*). The influence of the transverse variation of the depth of flow is clearly shown by equation (8.70). In rectangular channels, the term with h^2/r_s in this equation vanishes and, apart from a smaller term with $1/r_s^2$, the usual energy equation along a streamline in turbulent shear flow is obtained (Rouse, 1970). If there are transverse variations of h, however, the term with h^2/r_s in (8.70) is

*) As a consequence of the direct relation between ψ' and $\bar{u}_m$ assumed in (8.68), the system (8.70) through (8.71) is different from (8.66) and (8.67). Only if there is no direct relation between ψ' and $\bar{u}_m$, the latter equations form a characteristic system.

always positive on the point bar in the inner part of a bend and negative on the outer bank. This implies that these variations of h give rise to an additional *) redistribution of the total flow energy in the normal plane. Along the characteristics in the inner part of a bend they tend to reduce the energy, in the outer part they tend to enhance it. In gently curved channels with mildly sloping banks this additional energy redistribution can be the most important effect of secondary flow convection (Kalkwijk et al., 1980).

8.6. Main flow computation step

The solution procedure for the arbitrary channel model is essentially the same as for rectangular channels (see par. 7.4 and par. 7.5). It consists of two parts, viz. a main flow computation step, aiming at the calculation of the depth-averaged main velocity distribution, and a bottom shear stress computation step, meant for a more accurate determination of the vertical distribution of the main flow, the secondary flow and the bottom shear stress. In the main flow computation step, the vertical distribution of the main velocity, the depth-averaged main velocity and pressure fields, the vertical distribution of the secondary flow and the depth-averaged stream function of the secondary flow are calculated alternately in an iterative procedure.

8.6.1. Similarity hypothesis

In the main flow computation step, a strict version of the similarity hypothesis is applied to the main and the secondary flow. For the main flow, this implies that

$$u_m = \bar{u}\, f(z) \qquad \text{and} \qquad v_m = \bar{v}\, f(z) \tag{8.72}$$

---

*) In addition to the redistribution arising from the deviation of the characteristic direction (8.71) from the longitudinal direction of the channel.

Then the equation of continuity for the main flow (8.44) can be rewritten as

$$(\frac{1}{r}\frac{\partial \bar{u}}{\partial \phi'} + \frac{\partial \bar{v}}{\partial \xi'} + \frac{\varepsilon}{r}\bar{v})f + \frac{1}{h}\frac{\partial w_m}{\partial z} - (\bar{u}T_{s'} + \bar{v}T_{\xi'})\frac{\partial f}{\partial z} = 0 \qquad (8.73)$$

Averaging over the depth of flow yields

$$\frac{1}{r}\frac{\partial \bar{u}}{\partial \phi'} + \frac{\partial \bar{v}}{\partial \xi'} + \frac{\varepsilon}{r}\bar{v} + \frac{1}{h}(\frac{\bar{u}}{r}\frac{\partial h}{\partial \phi'} + \bar{v}\frac{\partial h}{\partial \xi'}) = 0 \qquad (8.74)$$

and combining (8.73) and (8.74) leads to

$$\frac{1}{h}\frac{\partial w_m}{\partial z} = \frac{1}{h}(\frac{\bar{u}}{r}\frac{\partial h}{\partial \phi'} + \bar{v}\frac{\partial h}{\partial \xi'})(f + z\frac{\partial f}{\partial z}) + \frac{1}{h}(\frac{\bar{u}}{r}\frac{\partial \zeta_s}{\partial \phi} + \bar{v}\frac{\partial \zeta_s}{\partial \xi'})\frac{\partial f}{\partial z} \qquad (8.75)$$

The vertical velocity component can be solved from this equation and condition (8.51) at the surface, to yield

$$w_m = (\frac{\bar{u}}{r}\frac{\partial h}{\partial \phi'} + \bar{v}\frac{\partial h}{\partial \xi'})zf + (\frac{\bar{u}}{r}\frac{\partial \zeta_s}{\partial \phi} + \bar{v}\frac{\partial \zeta_s}{\partial \xi'})f \qquad (8.76)$$

Near the bottom, this expression corresponds with the wall function approximation (8.37), as can be shown by rewriting (8.76) to

$$w_m = -h(\frac{1}{r}\frac{\partial \bar{u}}{\partial \phi'} + \frac{\partial \bar{v}}{\partial \xi'} + \frac{\varepsilon}{r}\bar{v})(1+z)f + (\frac{\bar{u}}{r}\frac{\partial \zeta_b}{\partial \phi} + \bar{v}\frac{\partial \zeta_b}{\partial \xi'})f \qquad (8.77)^{*)}$$

*) In addition to (8.76) and (8.77), there is another way to express w_m, viz.

$$w_m = (\frac{\bar{u}}{r}\frac{\partial \zeta_s}{\partial \phi'} + \bar{v}\frac{\partial \zeta_s}{\partial \xi'})(1+z)f - (\frac{\bar{u}}{r}\frac{\partial \zeta_b}{\partial \phi'} + \bar{v}\frac{\partial \zeta_b}{\partial \xi'})zf \qquad (8.77')$$

So w_m consists of two parts, both varying linearly with z. The first one, arising from the spatial variations of the water level, vanishes at the bottom, the second one, arising from the bottom level variations, equals zero at the surface.

Substituting the wall function approximations (8.35) and (8.36) into this expression leads to condition (8.37).

The equation of continuity of the secondary flow (8.56) is satisfied by defining the stream function of the secondary flow as (see also definitions (5.25) and (8.61))

$$v_s = -\frac{Re_0}{hr}\frac{\partial\psi}{\partial z} \quad \text{and} \quad w_s = \frac{Re_0}{r}\left(\frac{\partial\psi}{\partial\xi'} - T_{\xi'}\frac{\partial\psi}{\partial z}\right) \tag{8.78}$$

Then the similarity hypothesis for the secondary flow comes to

$$\psi = \bar{\psi}g(z); \quad v_s = -\frac{Re_0}{hr}\bar{\psi}\frac{\partial g}{\partial z}; \quad w_s = \frac{Re_0}{r}\left(\frac{\partial\bar{\psi}}{\partial\xi'}g - T_{\xi'}\bar{\psi}\frac{\partial g}{\partial z}\right) \tag{8.79}$$

The above definition of ψ is consistent with definition (5.25) for rectangular channels. In the untransformed cross-section the lines of constant ψ are the streamlines of the secondary flow.

8.6.2. Vertical distribution of the main velocity

Making use of the similarity hypotheses (8.72) and (8.79) and of expression (8.32) for a, with $\bar{u}$ as an approximation of $\bar{U}$, the longitudinal momentum equation (8.48) can be rewritten as an equation for f:

$$\tilde{k}_m\frac{C_0}{C}\frac{\bar{u}^2}{h}a'\frac{\partial^2 f}{\partial z^2} + \left(\tilde{k}_m\frac{C_0}{C}\frac{\bar{u}^2}{h}\frac{\partial a'}{\partial z} - 3\tilde{k}_m\frac{C_0}{C}\bar{u}\frac{\partial\bar{u}}{\partial\xi'}\frac{\partial h}{\partial\xi'}za' + \right.$$

$$\left. - \varepsilon Re_0^2\frac{\bar{u}}{hr}\frac{\partial\bar{\psi}}{\partial\xi'}g\right)\frac{\partial f}{\partial z} - \varepsilon Re_0\left(\frac{\bar{u}}{r}\frac{\partial\bar{u}}{\partial\phi'} + \bar{v}\frac{\partial\bar{u}}{\partial\xi'} + \frac{\varepsilon}{r}\overline{uv}\right)\frac{\partial f}{\partial}f +$$

$$+ \left\{\tilde{k}_m\frac{C_0}{C}\left(h\bar{u}\frac{\partial^2\bar{u}}{\partial\xi'^2} + h\frac{\partial\bar{u}}{\partial\xi'}\frac{\partial\bar{u}}{\partial\xi'} + \bar{u}\frac{\partial\bar{u}}{\partial\xi'}\frac{\partial h}{\partial\xi'}\right)a' + \right.$$

$$\left. - \tilde{k}_m\frac{C_0}{C}\bar{u}\frac{\partial\bar{u}}{\partial\xi'}\frac{\partial h}{\partial\xi'}z\frac{\partial a'}{\partial z} + \varepsilon Re_0^2\frac{\bar{\psi}}{hr}\left(\frac{\partial\bar{u}}{\partial\xi'} + \frac{\varepsilon}{r}\bar{u}\right)\frac{\partial g}{\partial z}\right\}f = \frac{1}{r}\frac{\partial\bar{p}}{\partial\phi'} \tag{8.80}$$

, in which k_m and $\hat{f}$ are known estimates of k_m and f, respectively.
The boundary condition at the surface, to be derived from (8.52), reads

$$a' \frac{\partial f}{\partial z} = 0 \qquad \text{at} \qquad z = 0 \tag{8.81}$$

and the wall function approximation (8.35) near the bottom leads to the following wall function approximation for f

$$f = k_m \{1 + \frac{\sqrt{g}}{\kappa C} + \frac{\sqrt{g}}{\kappa C} \ln(1+z)\} \tag{8.82}$$

The vertical distribution function f is solved from the system (8.80) through (8.82) with the lateral diffusion terms disregarded. From a mathematical point of view, this system is quite similar to the one for rectangular channel flow, (7.18) through (7.21). Therefore the same solution procedure can be applied as in the rectangular channel model (see par. 7.4.1 and Appendix E).
Once the constant k_m is known, the component of the bottom shear stress due to the main flow follows from expressions (7.24).

8.6.3. Depth-averaged main velocity field

The depth-averaged longitudinal and transverse momentum equations become

$$\varepsilon Re_0 \overline{f^2} \left(\frac{\bar{u}}{r} \frac{\partial \bar{u}}{\partial \phi'} + \bar{v} \frac{\partial \bar{u}}{\partial \xi'} + \frac{\varepsilon}{r} \overline{uv}\right) - \varepsilon Re_0^2 \overline{f \frac{\partial q}{\partial z}} \left\{\frac{\bar{\psi}}{hr} \left(\frac{\partial \bar{u}}{\partial \xi'} + \frac{\varepsilon}{r} \bar{u}\right) +\right.$$

$$\left. + \frac{\bar{u}}{hr} \frac{\partial \bar{\psi}}{\partial \xi'}\right\} = - \frac{1}{r} \frac{\partial \bar{p}}{\partial \phi'} - k_m \frac{C_0}{C} \frac{\bar{u}^2}{h} \left(a' \frac{\partial f}{\partial z}\right)\Big|_{z=-1} + k_m \frac{C_0}{C} \overline{a'f} \left(h\bar{u} \frac{\partial^2 \bar{u}}{\partial \xi'^2} +\right.$$

$$\left. + h \frac{\partial \bar{u}}{\partial \xi'} \frac{\partial \bar{u}}{\partial \xi'} + 4\bar{u} \frac{\partial \bar{u}}{\partial \xi'} \frac{\partial h}{\partial \xi'}\right) + k_m \frac{C_0}{C} \overline{zf \frac{\partial a'}{\partial z}} 2\bar{u} \frac{\partial \bar{u}}{\partial \xi'} \frac{\partial h}{\partial \xi'} \tag{8.83}$$

$$\varepsilon^3 \mathrm{Re}_0 \overline{f^2} \left(\frac{\bar{u}}{r}\frac{\partial \bar{v}}{\partial \phi'} + \bar{v}\frac{\partial \bar{v}}{\partial \xi'}\right) - \varepsilon^2 \mathrm{Re}_0 \overline{f^2}\frac{\bar{u}^2}{r} - \varepsilon^3 \mathrm{Re}_0^2 \overline{f\frac{\partial g}{\partial z}}\left(\frac{\bar{\psi}}{hr}\frac{\partial \bar{v}}{\partial \xi'} +\right.$$

$$\left. + \frac{\bar{v}}{hr}\frac{\partial \bar{\psi}}{\partial \xi'}\right) = -\frac{\partial \bar{p}}{\partial \xi'} - \varepsilon^2 k_m \frac{C_0}{C}\frac{\bar{u}\bar{v}}{h}\left(a'\frac{\partial f}{\partial z}\right)\Big|_{z=-1} + \varepsilon^2 k_m \frac{C_0}{C}\overline{a'f}\left\{h\bar{u}\frac{\partial^2 \bar{v}}{\partial \xi'^2} +\right.$$

$$+ h\frac{\partial \bar{u}}{\partial \xi'}\frac{\partial \bar{v}}{\partial \xi'} + 4\bar{u}\frac{\partial \bar{v}}{\partial \xi'}\frac{\partial h}{\partial \xi'} + \frac{\bar{u}}{r}\frac{\partial \bar{u}}{\partial \phi'}\frac{\partial h}{\partial \xi'} + \frac{\varepsilon}{r}\left(h\bar{u}\frac{\partial \bar{v}}{\partial \xi'} - 3h\frac{u}{r}\frac{\partial \bar{u}}{\partial \phi'} +\right.$$

$$\left. - h\bar{v}\frac{\partial \bar{u}}{\partial \xi'}\right\} + \varepsilon^2 k_m \frac{C_0}{C}\overline{zf\frac{\partial a'}{\partial z}}\, 2\bar{v}\frac{\partial \bar{u}}{\partial \xi'}\frac{\partial h}{\partial \xi'} +$$

$$+ \text{other terms } 0(\varepsilon^3 \mathrm{Re}_0, \varepsilon^2) \qquad (8.84)$$

The "other" terms in (8.84) concern the secondary flow. They are disregarded in the main flow computation, which is allowable since all terms in equation (8.84), except for the pressure gradient term and the centrifugal term, are an order $0(\varepsilon^2)$ smaller than the corresponding ones in equation (8.83). From this point of view even most of the terms retained in (8.84) could be disregarded, but they are retained because of the symmetry with equation (8.83) (see also par. 5.5 and par. 7.4.2). The depth-averaged main velocity and pressure fields can be solved from equations (8.83) and (8.84), the depth-averaged equation of continuity (8.74) and an appropriate set of boundary conditions. The boundary conditions at the sidewalls are replaced by the depth-averaged versions of the wall function approximations (8.38), (8.40), (8.41) and (8.43):

$$\bar{u} \approx \frac{\bar{u}_{\tau 1}}{\kappa}\left\{\frac{\kappa C_w}{\sqrt{g}} + 1 + \ln\left(\frac{B}{2d} + \xi'\right)\right. \qquad (8.85)$$

$$\bar{v} \approx -\frac{1}{\kappa}\frac{1}{hr}\frac{\partial h\bar{u}_{\tau 1}}{\partial \phi'}\left(\frac{B}{2d} + \xi'\right)\left\{\frac{\kappa C_w}{\sqrt{g}} + \ln\left(\frac{B}{2d} + \xi'\right)\right\} \qquad (8.86)$$

near the inner wall and

$$\bar{u} \simeq - \frac{\bar{u}_{\tau r}}{\kappa} \{\frac{\kappa C_w}{\sqrt{g}} + 1 + \ln(\frac{B}{2d} - \xi')\} \tag{8.87}$$

$$\bar{v} \simeq - \frac{1}{\kappa} \frac{1}{h_r} \frac{\partial h \bar{u}_{\tau r}}{\partial \phi'} (\frac{B}{2d} - \xi') \{\frac{\kappa C_w}{\sqrt{g}} + \ln(\frac{B}{2d} - \xi')\} \tag{8.88}$$

near the outer wall. The mathematical treatment of these approximations is the same as in the rectangular channel case (see Appendix F).
In addition to the conditions at the sidewalls, the depth-averaged main velocity at the inflow boundary must be prescribed. Though any distribution can be imposed, the one used in the test computations of the present model is the depth-averaged velocity distribution in the equivalent fully-developed straight channel flow, i.e. the inflow section is assumed to be preceded by an infinitely long straight channel with the same cross-sectional configuration and the same boundary roughness as in the inflow section.
The computation method used to solve the depth-averaged main flow system is the same as in the rectangular channel model, viz. the partially-parabolic (and occasionally the parabolic) mode of Spalding's method (see Appendix C).

8.6.4. Vertical distribution of the secondary flow

Making use of definition (8.78), a stream function equation for the secondary flow can be derived from the transverse and vertical momentum equations (8.49) and (8.50) by eliminating the pressure. This leads to an extensive and complicated equation (see De Vriend, 1981b), which is simplified further before being used. After introducing the strict similarity hypotheses (8.72) and (8.79), only the leading terms are retained, i.e. even terms of the order $O(\varepsilon, d/L)$ are disregarded. The resulting equation reads

$$k_m \frac{C_0}{C} \left[a' g \left(\bar{u} \frac{\partial^4 \bar{\psi}}{\partial \xi'^4} + 2 \frac{\partial \bar{u}}{\partial \xi'} \frac{\partial^3 \bar{\psi}}{\partial \xi'^3} + \frac{\partial^2 \bar{u}}{\partial \xi'^2} \frac{\partial^2 \psi}{\partial \xi'^2} \right) + \right.$$

$$+ a' \frac{\partial^2 g}{\partial z^2} \frac{1}{h^2} \left(2\bar{u} \frac{\partial^2 \bar{\psi}}{\partial \xi'^2} + 2 \frac{\partial \bar{u}}{\partial \xi'} \frac{\partial \bar{\psi}}{\partial \xi'} - \frac{\partial^2 \bar{u}}{\partial \xi'^2} \bar{\psi} \right) + \frac{\partial^2 a'}{\partial z^2} g \frac{1}{h^2} \left(-\bar{u} \frac{\partial^2 \bar{\psi}}{\partial \xi'^2} \right) +$$

$$\left. + \frac{\partial a'}{\partial z} \frac{\partial g}{\partial z} \frac{1}{h^2} \left(2\bar{u} \frac{\partial^2 \bar{\psi}}{\partial \xi'^2} + 4 \frac{\partial \bar{u}}{\partial \xi'} \frac{\partial \bar{\psi}}{\partial \xi'} \right) + \frac{\partial^2}{\partial z^2} \left(a' \frac{\partial^2 g}{\partial z^2} \right) \frac{\bar{u}\bar{\psi}}{h^4} \right] +$$

$$- \varepsilon \mathrm{Re}_0 \left[\frac{1}{h} \left(\frac{\bar{u}}{r} \frac{\partial}{\partial \phi'} + \bar{v} \frac{\partial}{\partial \xi'} \right) \frac{\partial^2 \bar{\psi}}{\partial \xi'^2} fg + \frac{1}{h} \left(\frac{\partial \bar{u}}{\partial \xi'} \frac{1}{r} \frac{\partial}{\partial \phi'} + \right. \right.$$

$$\left. \left. + \frac{\partial \bar{v}}{\partial \xi'} \frac{\partial}{\partial \xi'} \right) \frac{\partial \bar{\psi}}{\partial \xi'} fg + \frac{1}{h^3} \left(\frac{\bar{u}}{r} \frac{\partial \bar{\psi}}{\partial \phi'} + \bar{v} \frac{\partial \bar{\psi}}{\partial \xi'} + \bar{\psi} \frac{\partial \bar{v}}{\partial \xi'} \right) \frac{\partial}{\partial z} \left(f \frac{\partial g}{\partial z} \right) \right] =$$

$$- \frac{r\bar{u}^2}{h^2 r_s} \frac{\partial f^2}{\partial z} \qquad (8.89)$$

, in which only the major source term is retained.
Equation (8.89) could be used to determine g. As in the cases of laminar and turbulent flow in rectangular channels, however, numerical problems must be expected when including the streamwise inertia terms for $\bar{\psi}$ and not the ones for g in the equation for g. Therefore, both groups of terms are omitted from this equation in the main flow computation step. In addition, it has become evident from the rectangular channel computation that the vertical distribution functions should be determined in a region where lateral diffusion is negligible. Therefore, all ξ'-derivatives in equation (8.89) are omitted, so that it reduces to

$$\frac{\partial^2}{\partial z^2} \left(a' \frac{\partial^2 g}{\partial z^2} \right) = c \frac{\partial f^2}{\partial z} \qquad (8.90)$$

, in which c is theoretically equal to $-Ch^2 r\bar{u}/(k_m C_0 \bar{\psi} r_s)$. In the

actual computation, however, c is adjusted in such a way that $\bar{g} = 1$ in each iteration step.
The boundary conditions at the surface are

$$g = 0 \quad \text{and} \quad a' \frac{\partial^2 g}{\partial z^2} = 0 \quad \text{at} \quad z = 0 \tag{8.91}$$

and the wall function approximation near the bottom can be written as

$$g = k_s (1+z) \{1 + \frac{\sqrt{g}}{\kappa C} \ln(1+z)\} \tag{8.92}$$

, in which k_s is given by

$$k_s = - \frac{C}{\sqrt{g}} \frac{h r v_{\tau s}}{\bar{\psi} Re_0} \tag{8.93}$$

, $v_{\tau s}$ denoting the part of the transverse bottom friction velocity that is due to the secondary flow.
From a mathematical point of view, the system (8.90) through (8.92) is identical to the rectangular channel system (7.31), (7.32) and (7.37). Therefore, the solution procedure is the same, as well (see Appendix G).

8.6.5. Depth-averaged stream function of the secondary flow

Averaging equation (8.89) over the depth of flow yields

$$\overline{a'g} (\bar{u} \frac{\partial^4 \bar{\psi}}{\partial \xi'^4} + 2 \frac{\partial \bar{u}}{\partial \xi'} \frac{\partial^2 \bar{\psi}}{\partial \xi'^3} + \frac{\partial^2 \bar{u}}{\partial \xi'^2} \frac{\partial^2 \bar{\psi}}{\partial \xi'^2}) + (a' \frac{\partial g}{\partial z})\Big|_{z=0} \frac{1}{h^2} (2\bar{u} \frac{\partial^2 \bar{\psi}}{\partial \xi'^2} +$$

$$+ 2 \frac{\partial \bar{u}}{\partial \xi'} \frac{\partial \bar{\psi}}{\partial \xi'} - \frac{\partial^2 \bar{u}}{\partial \xi'^2} \bar{\psi}) - \overline{g \frac{\partial^2 a'}{\partial z^2}} \frac{1}{h^2} (\bar{u} \frac{\partial^2 \bar{\psi}}{\partial \xi'^2} - 2 \frac{\partial \bar{u}}{\partial \xi} \frac{\partial \bar{\psi}}{\partial \xi'} + \frac{\partial^2 \bar{u}}{\partial \xi'^2} \bar{\psi}) +$$

$$+ c f^2\Big|_{z=0} \frac{\bar{u}\bar{\psi}}{h^4} - \frac{\varepsilon Re_0 C}{k_m C_0} \left[\frac{\overline{fg}}{h} \{(\frac{u}{r} \frac{\partial}{\partial \phi'} + \bar{v} \frac{\partial}{\partial \xi'}) \frac{\partial^2 \bar{\psi}}{\partial \xi'^2} + (\frac{\partial \bar{u}}{\partial \xi'} \frac{1}{r} \frac{\partial}{\partial \phi'} +$$

$$+ \frac{\partial \bar{v}}{\partial \xi'} \frac{\partial}{\partial \xi'}\Big) \frac{\partial \bar{\psi}}{\partial \xi'}\Big\} + \Big\{\frac{\bar{u}}{r} \frac{\partial \bar{\psi}}{\partial \phi'} + \bar{v} \frac{\partial \bar{\psi}}{\partial \xi'} + \Big(\frac{\partial \bar{v}}{\partial \xi'} - \frac{\bar{v}}{\bar{u}} \frac{\partial \bar{u}}{\partial \xi'}\Big) \bar{\psi}\Big\} \Big(f \frac{\partial g}{\partial z}\Big)\Big|_{z=0}\Big] =$$

$$- \frac{C r \bar{u}^2}{k_m C_0 h^2 r_s} f^2\Big|_{z=0} \tag{8.94}$$

The inflow condition for $\bar{\psi}$ is the same as the rectangular channel model, i.e. condition (7.40).
The sidewall conditions are replaced by wall function approximations to be derived from (8.38) through (8.43):

$$\bar{\psi} = \frac{r \bar{w}_{\tau sl}}{\kappa Re_0} \Big(\frac{B}{2d} + \xi'\Big) \Big\{\frac{\kappa C_w}{\sqrt{g}} + \ln\Big(\frac{B}{2d} + \xi'\Big)\Big\} \tag{8.95}$$

near the left wall and

$$\bar{\psi} = - \frac{r \bar{w}_{\tau sr}}{\kappa Re_0} \Big(\frac{B}{2d} - \xi'\Big) \Big\{\frac{\kappa C_w}{\sqrt{g}} + \ln\Big(\frac{B}{2d} - \xi'\Big)\Big\} \tag{8.96}$$

near the right wall. The quantities $\bar{w}_{\tau sl}$ and $\bar{w}_{\tau sr}$ in these expressions denote depth-averaged wall friction velocities due to the secondary flow. Together with $\bar{\psi}$, these two constants are solved from equation (8.95) and conditions (7.40), (8.95) and (8.96) in the same way as described in Appendix H.

8.6.6. Iterative solution procedure

The iterative solution procedure applied in the main flow computation step is quite similar to the one in the rectangular channel models described in par. 5.6 and par. 7.4.5. In summary:

1a. Estimate the vertical distribution functions f and g (cf. expressions (7.45) and (7.46)).

1b. Estimate the depth-averaged stream function of the secondary flow by taking $\bar{\psi} \equiv 0$, for instance.

2. Solve the depth-averaged main velocity components $\bar{u}$ and $\bar{v}$ and

the pressure $\bar{p}$ as described in par. 8.6.3.

3. Calculate the local streamline curvature using (5.31).
4. Determine $\bar{\psi}$ as described in par. 8.6.5.
5. Determine f as described in par. 8.6.2.
6. Determine g as described in par. 8.6.4.
7. Repeat the procedure until a termination criterion is satisfied.

8.7. Bottom shear stress computation step

The normalized bottom shear stress components $\tau_{b\phi}$ and $\tau_{b\xi}$*) follow from expressions (7.47), evaluated using the depth-averaged main velocities resulting from the main flow computation step and k_m, k_s and $\bar{\psi}$ as resulting from an additional bottom shear stress computation step. In this additional step, the depth-averaged main velocity is kept fixed and the vertical distribution of the main flow as well as the secondary flow are solved from more extensive equations than in the main flow computation step.

8.7.1. Vertical distribution of the main velocity

As a consequence of the bed level variations, the streamwise accelerations of the main flow, and hence their effect on the vertical distribution of the main velocity, must be expected to be stronger in a natural channel than in a rectangular one. In the vertical distribution of the main velocity resulting from the main flow computation step, however, this effect is not accounted for. Though this may be allowable when computing the main flow, it is certainly not when computing the bottom shear stress, as was shown before (par. 5.8.2 and par. 7.6.2). Therefore, the vertical distribution of the main velocity is corrected for the streamwise main flow accelerations in the bottom shear stress computation step.

In accordance with the rectangular channel model (par. 7.5), this is done by generalizing the similarity hypothesis for the main velocity to

*) In fact, these are the horizontal components of the shear stress along the bed (cf. Falcón, 1979).

$$u_m = \bar{u}\, f(z;\xi',\phi') \quad \text{and} \quad v_m = \bar{v}\, f(z;\xi',\phi') \tag{8.97}$$

, i.e. by allowing f to depend weakly on ξ' and ϕ', in such a way, that its transverse and longitudinal derivatives can be disregarded in the main flow equations.
In principle, f could be solved from equation (8.80) in each vertical of the cross-section, but it became clear in par. 7.5, that this yields erroneous results in the sidewall regions. On the other hand, the strict similarity hypothesis works well in case of fully-developed flow in straight or curved rectangular channels (see chapters 3 and 6). Therefore, the streamwise main flow accelerations are assumed to be the only factor that disturbs similarity. In addition, the disturbances are assumed small, so that f can be solved from the same equation as in the main flow computation step, with a correction term for the main flow accelerations:

$$\frac{\partial}{\partial z}\left(a' \frac{\partial f}{\partial z}\right) - \varepsilon \mathrm{Re}_0^2 \left(\frac{C}{\tilde{k}_m C_0} \frac{1}{\bar{u}r} \frac{\partial \bar{\psi}}{\partial \xi'}\right)\Big|_{\xi_0} g \frac{\partial f}{\partial z} +$$

$$+ \varepsilon \mathrm{Re}_0^2 \left\{\frac{C}{\tilde{k}_m C_0} \frac{\bar{\psi}}{\bar{u}r} \left(\frac{\partial \bar{u}}{\partial \xi'} + \frac{\varepsilon}{r}\bar{u}\right)\right\}\Big|_{\xi_0} \frac{\partial g}{\partial z} f +$$

$$- \varepsilon \mathrm{Re}_0 \frac{C}{\tilde{k}_m C_0} \frac{h}{\bar{u}^2} \left(\frac{\bar{u}}{r} \frac{\partial \bar{u}}{\partial \phi'} + \bar{v} \frac{\partial \bar{u}}{\partial \xi'} + \frac{\varepsilon}{r} \overline{\overline{uv}}\right) = \frac{C}{\tilde{k}_m C_0} \frac{h}{\bar{u}^2 r} \frac{\partial p}{\partial \phi'} \tag{8.98}$$ *)

8.7.2. Vertical distribution of the secondary flow.

In appendix I it was shown that, in regions with important streamwise variations of the secondary flow intensity, the similarity hypothesis for the secondary flow is no longer

---

*) The lateral diffusion terms are disregarded when calculating f, both in the main flow computation step and in the bottom shear stress computation step.

applicable, not even in a generalized form similar to (8.97). In that case, the vertical distribution function g must be assumed to vary with ϕ' as well as z, in such a way that also the ϕ'-derivatives of g are retained in the streamwise inertia terms of the secondary flow equation. Then this equation becomes

$$\frac{\partial^2}{\partial z^2}\left(a' \frac{\partial^2 g}{\partial z^2}\right) - \varepsilon Re_0 \frac{h^3 \bar{u} C}{k_m \bar{\psi} r C_0} \frac{\partial}{\partial \phi'}\left\{\frac{\bar{\psi}}{h^2 \bar{u}} \frac{\partial}{\partial z}\left(f \frac{\partial g}{\partial z}\right)\right\} =$$

$$- \frac{h r \bar{u} C}{k_m r_s \bar{\psi} C_0} \frac{\partial f^2}{\partial z} \qquad (8.99)^{*)}$$

This equation is solved in each vertical of a cross-section, in order to account for the transverse variation of f discussed in par. 8.7.2.
The solution procedure is the same as the one in the rectangular channel model (see Appendix G).

8.7.3. Depth-averaged stream function of the secondary flow

The depth-averaged stream function equation for the secondary flow is brought into agreement with equation (8.99) by including the ϕ'-derivatives of g in the streamwise inertia terms. Then the equation reads (see also De Vriend, 1981b)

$$\overline{a'g}\left(\bar{u} \frac{\partial^4 \bar{\psi}}{\partial \xi'^4} + 2 \frac{\partial \bar{u}}{\partial \xi'} \frac{\partial^3 \bar{\psi}}{\partial \xi'^3} + \frac{\partial^2 \bar{u}}{\partial \xi'^2} \frac{\partial^2 \bar{\psi}}{\partial \xi'^2}\right) + \left(a' \frac{\partial g}{\partial z}\right)\Big|_{z=0} \frac{1}{h^2}\left(2\bar{u} \frac{\partial^2 \bar{\psi}}{\partial \xi'^2} +\right.$$

$$\left. + 2 \frac{\partial \bar{u}}{\partial \xi} \frac{\partial \bar{\psi}}{\partial \xi'} - \frac{\partial^2 \bar{u}}{\partial \xi'^2} \bar{\psi}\right) - \overline{g \frac{\partial^2 a'}{\partial z^2}} \frac{1}{h^2}\left(\bar{u} \frac{\partial^2 \bar{\psi}}{\partial \xi'^2} - 2 \frac{\partial \bar{u}}{\partial \xi} \frac{\partial \bar{\psi}}{\partial \xi} +\right.$$

*) As terms of the order $O(\varepsilon Re_0, d/L)$ have been disregarded in this equation, accounting for minor source terms of the order $O(1/Re_0)$ seems irrelevant (cf. equation 7.50).

$$+ \frac{\partial^2 \bar{u}}{\partial \xi'^2} \bar{\psi}) + \overline{\frac{\partial^2}{\partial z^2} (a' \frac{\partial^2 g}{\partial z^2})} \frac{\bar{u}\bar{\psi}}{h^4} - \frac{\varepsilon Re_0 C}{k_m C_0} \left[\overline{\frac{fg}{h^2}} (\frac{\bar{u}}{r} \frac{\partial}{\partial \phi'} + \bar{v} \frac{\partial}{\partial \xi'}) (h \frac{\partial^2 \bar{\psi}}{\partial \xi'^2}) + \right.$$

$$+ \overline{\frac{fg}{h}} (\frac{\partial \bar{u}}{\partial \xi'} \frac{1}{r} \frac{\partial}{\partial \phi'} + \frac{\partial \bar{v}}{\partial \xi'} \frac{\partial}{\partial \xi'}) (\frac{\partial \bar{\psi}}{\partial \xi'}) + \overline{zg \frac{\partial f}{\partial z}} \frac{\bar{u}}{h^2 r} \frac{\partial h}{\partial \phi'} \frac{\partial^2 \bar{\psi}}{\partial \xi'^2} +$$

$$\left. + \frac{\bar{u}}{h} (\frac{\bar{u}}{r} \frac{\partial}{\partial \phi} + \bar{v} \frac{\partial}{\partial \xi'}) \{\frac{\bar{\psi}}{h^2 \bar{u}} (f \frac{\partial g}{\partial z}) \Big|_{z=0}\} \right] = - \frac{Cr \bar{u}^2}{k_m C_0 h^2 r_s} f^2 \Big|_{z=0} \qquad (8.100)$$

The quantity $\bar{\psi}$ is solved from this equation and the relevant boundary conditions (see par. 8.6.5) in the same way as described in Appendix H.

8.8. Verification of the simplifying assumptions

The mathematical model for arbitrarily shaped channels described in the foregoing paragraphs is a generalization of the rectangular channel model described in chapter 7. The two models are based on the same basic assumptions, most of which were verified in chapter 7. Though the flow in curved non-rectangular channels will differ from the one in rectangular channels, the conclusions drawn from this verification are assumed to apply here, as well. This implies that the model will only be applicable to channels in which the transverse configuration of the cross-section varies gradually along the channel, which is consistent with the simplifications of the transformed equations (see par. 8.5).
An aspect of the model that needs specific verification for non-rectangular channels is the turbulence model. As was shown in chapter 6, this turbulence model works rather well for rectangular channels. In case of mildly sloping banks, where turbulent diffusion of momentum is mainly vertical, it is not likely to give rise to problems, either. It is not clear, however, whether it also applies to channels with steeply sloping banks.
An opportunity to test the turbulence model at this point is provided by a series of experiments in straight symmetric air-

channels, recently carried out by TNO-Holland (Builtjes, 1980). The cross-sectional shape of these channels was varied by giving the sidewalls different slopes (vertical, 2:3 and 1:4). In each case the longitudinal velocities in the fully-developed flow region were measured, for smooth walls and in the second case also for rough walls. The experiments were simulated using the present model in order to verify the turbulence model.
According to figures 32c and 50, the model yields rather good predictions for the rectangular channel as well as in case of mildly sloping banks. If the banks are steeply sloping, however, the predictions are less satisfactory, spurious velocity peaks occurring above the banks then. This suggest that the turbulence viscosity on steeply sloping banks is underestimated.
Expression (8.32) is based on the assumption that the turbulence viscosity is not influenced by lateral interaction. This is only true if transverse variations of the turbulence properties are absent. In case of steeply sloping banks, however, strong transverse variations of the turbulence properties occur. Consequently, turbulence generated in the central parts of the channel will tend to diffuse over the banks and hence the turbulence viscosity on the banks will be larger than predicted by (8.32).
An alternative expression for α, consistent with the rectangular channel model and leading to a slower decay of α on the banks, reads

$$\alpha = \bar{u}\ \alpha'(z) \tag{8.101}$$

According to figure 50, however, this leads to an overcompensation of the errors caused by (8.32), especially in case of mildly sloping banks.
Lateral diffusion of turbulence can be accounted for by determining the turbulence properties from transport equations including convection, diffusion, production and dissipation terms (Launder et al., 1972). In the present case, the simplest and most direct way to do so is to solve $\bar{\alpha}$ from a transport equation in which only lateral diffusion, production and dis-

sipation are retained. A heuristic form of this equation reads (cf. Nee et al., 1969)

$$D^2 \frac{\partial}{\partial \xi'} \left(\bar{a} \frac{\partial \bar{a}}{\partial \xi'} \right) - \bar{a}^2 = - \bar{a} \, k_m \frac{C_0}{C} \bar{u} h \qquad (8.102)$$

The boundary conditions are based on the assumption that $\bar{a}$ goes linearly to zero on the two wall-nearest meshes of the computational grid.

The constant D in equation (8.102) determines the rate of lateral diffusion.

For D=0, equation (8.102) reduces to (8.32) and for D>0 lateral diffusion gives rise to lateral spreading of disturbances in $\bar{a}$. In uniform rectilinear shear flow, the region over which such a disturbance is spread has a characteristic width of $2D$ times the depth of flow scale.

Figures 32c and 50 show the results of fully-developed straight channel flow computations based on (8.102), with D=0.5 and D=1.0. For the rectangular channel (figure 32c), the results for D=1.0 are not too good, but the ones for D=0.5 agree even better with the measured data than the results obtained with (8.32). Also in case of steeply sloping banks (figure 50), equation (8.102) leads to better predictions: the velocity peaks near the banks are reduced (smooth wall case) or even vanish (rough wall case) and the agreement with the measured data grows better, especially for D=0.5. In case of mildly sloping banks, however, the predictions tend to grow worse as D increases.

Although equation (8.102) is not based on a physically consistent approach of lateral diffusion of turbulence properties*), it is this equation, with D=0.5, that will be incorporated in the model

---

*) From a physical point of view it seems more appropriate, for instance, to use hD in (8.102) rather than D, so that the chacteristic width of the lateral spreading becomes $2D$ times the local depth of flow. When doing so, however, the velocity predictions hardly differ from the ones based on (8.32).

when it is applied to non-rectangular channels with steep transverse bottom slopes.

8.9. Discussion

The greater part of the simplifications underlying the non-rectangular channel model described in the foregoing has not been verified explicitly.

As was stated in par. 8.8, the simplifying assumptions corresponding with the ones in the rectangular channel model are likely to hold good as long as the transverse bottom configuration changes gradually in the streamwise direction. In addition to these assumptions, however, a number of terms due to the spatial variations of the bottom level was omitted on the basis of rather global order-of-magnitude considerations. Actually, these specific non-rectangular channel simplifications should be verified, as well.

The verification of the simplifying assumptions in the rectangular channel model was made by considering the effects of the simplifications on the solution for a specific, rather sharply curved channel. As the effective Dean number is the most important parameter in this case and the model works well for $De_0 = 0$, the simplifications that are approved for rather high De_0 will certainly by applicable to lower Dean number flow.

In non-rectangular channels, however, the flow will also be strongly dependent on the bottom configuration. Hence a rather sharply curved flume with a rather pronounced bottom configuration should be considered for the verification of the simplifying assumptions. In rather sharply curved flumes like the FLM-flume, however, the configuration of an alluvial bed will mostly be so pronounced that the present model will certainly not apply to it (see Sutmuller, 1981).

It is not clear what combination of channel curvature and bed configuration should be taken instead. Therefore, the verification of the specific non-rectangular channel simplifications will not be made here. Instead, the results of the non-rectangular channel computations described in chapter 9 will be verified at this point if they give occasion to it.

For specific classes of non-rectangular channel flow, the model allows for further simplifications (cf. the case of mildly curved channels with gently sloping banks referred to before). Especially in the main flow computation step considerable simplifications will often be possible.
A most important reduction of computer expenses is attained when applying the parabolic rather than the partially-parabolic mode of the solution procedure for the depth-averaged main velocity field. As will be illustrated in chapter 9, this is possible when the configuration of the channel, including its curvature, shows only gradual longitudinal variations.
Another time-saving simplification is to disregard lateral interaction in the stream function equation for the secondary flow. The fourth-order partial differential equation (8.100) then reduces to a first-order ordinary differential equation of the form (see Appendix K)

$$\frac{\partial \Psi}{\partial s} + c_1 \frac{\Psi}{h} = c_2 \frac{r}{h r_s} \qquad \text{with} \qquad \Psi = \frac{\bar{\psi}}{h^2 \bar{u}} \left(-f \frac{\partial g}{\partial z}\right)\Big|_{z=0} \tag{8.103}$$

, which is much easier to be solved. This simplification will be applicable in case of gently sloping banks, on which the main velocity and the secondary flow intensity decay to zero along with the depth of flow.
If, in addition, the bed topography and the channel curvature change only gradually along the channel, even the streamwise inertia term in (8.103) can be omitted, so that in any vertical the secondary flow is determined completely by the local properties of the main velocity.
In case of mildly sloping banks not only the lateral influencing in ψ, but also the effect of lateral diffusion on $\bar{u}$ can be disregarded. As a consequence, the main flow equations become first-order in ξ and ϕ (cf. par. 8.5.4) and are easier to be solved than the parabolic partial differential equations in the complete system.

Nonetheless, the simplified main flow equations require some caution as regards the lateral boundary conditions for $\bar{u}$. If the lateral diffusion terms are retained, two boundary conditions are needed for $\bar{u}$ in every cross-section and it is rather obvious that these are provided by the condition of no-slip at the fixed boundaries. If the lateral diffusion terms are omitted, however, the no-slip conditions are no longer relevant, either. Still it seems as though the system requires one lateral boundary condition for $\bar{u}$, the longitudinal momentum equation being first-order in ξ. On closer investigation, however, the characteristics of the simplified system turn out not to interest the lateral bounds of flow (see par. 8.5.4 and expressions (8.67) and (8.71)). This implies that lateral boundary conditions cannot be imposed and that the solution of the system is determined uniquely by the inflow and outflow conditions. It also implies that the numerical solution procedure must be devised such, that no lateral boundary conditions are required*) (cf. Kalkwijk et al., 1980).

In alluvial channel bends the inner bank will often be mildly sloping as a consequence of the point bar in the inner bend. The outer bank, however, will mostly be much steeper, if not protected artificially. In such cases, the aforementioned simplifications for mildly sloping banks will hold good for the inner bank region and the central part of the cross-section, but not for the outer bank region.
Still this does not imply that the simplifications for mildly sloping banks cannot be applied then. As was shown extensively in chapter 3 and in par. 8.5.4, the lateral interaction in $\bar{u}$ caused by secondary flow convection is exclusively outward. As a consequence, local effects of convection in the inner part of the bend are extended outwards and local effects in the outer part are compressed against the outer boundary. The same holds good for the influence of errors:

*) In a finite-difference procedure, this can be attained by discretizing the longitudinal momentum equation with all convection terms, including the ones due to the secondary flow, in the conservative form.

the influence of errors in $\bar{u}$ made in the inner part of the bend will extend over the whole cross-section and the influence of errors made in the outer part will be restricted to this outer part. On the other hand, an accurate description of the flow over the steep outer bank is not wanted in many cases, so that errors in $\bar{u}$ and $\bar{\psi}$ are acceptable as long as their influence is restricted to the outer bank region. This provides the possibility to simplify the model even in case of a steep outer bank.
When applying the simplified model for mildly curved channels with gently sloping banks to a channel with a steep outer bank, however, the main velocity on the outer bank will tend to grow exponentially (Kalkwijk et al., 1980; see also equation (8.70), where the damping factor, i.e. the term in braces, can become negative for strongly negative $\partial h^2/\partial n'$)*). The influence of this erroneous growth of $\bar{u}$ extends over the whole cross-section, not through secondary flow convection, but through the integral condition of continuity. Therefore, measures must be taken to prevent this exponential growth, such as omitting or modifying the responsible term in the equation as soon as the depth of flow decays steeply.
Although this approach needs some further investigation, it can be attractive as it leads to highly economic flow computations for a class of curved channel problems that is often encountered, both in river engineering practice and in hydraulic research (mobile-bed experiments in curved flumes).

8.10 Summary of conclusion

The conclusions to be drawn from the present chapter can be summarized as follows.

In case of non-rectangular channels with not too abrupt variations of the bed level, the cross-section can be transformed to a rectangle, in such a way that the similarity hypothesis applies to the velocity

---

*) In the complete model, this growing tendency is suppressed by lateral diffusion (see also chapter 4).

components in the transformed channel. Though the transformation introduces additional terms with the derivatives of the depth of flow, the system of equations remains essentially the same as for rectangular channel flow. Hence this system can be solved using the same procedure as in case of a rectangular channel.
In spite of this similarity between the models for rectangular and non-rectangular channels, there are some differences in the modelling of turbulence. The direct algebraic relation between the turbulence viscosity and the local main flow properties, which holds good for rectangular channels, can also be applied to non-rectangular channels with mildly sloping banks. If the banks are steep, however, a lateral interaction must be introduced into the turbulence model. This can be achieved by solving the turbulence viscosity from a diffusion-type equation.

Both the main and the secondary flow in non-rectangular channels are influenced by the spatial variations of the depth of flow. These variations give rise to additional vertical velocities, often dominating the ones arising from the same causes as in rectangular channel flow.
The convection terms in the main flow equation due to the additional vertical component of the main velocity are compensated by the other additional main flow convection terms, so that they drop out of the mathematical system. In the convective effect of the secondary flow, however, the depth variations will often play a predominant part, as they give rise to an additional transverse redistribution of the main flow energy and the main velocity that is often much stronger than the one in a rectangular channel.

9. Verification of the model

9.1. Objective and approach

In this chapter, the turbulent flow model described in the foregoing will be tested by comparing its results with measured data and with computational results from a fully three-dimensional model. It will be attempted to indicate the shortcomings of the model and to analyse why they occur and how they can be eliminated. The measured data are taken from experiments in various curved flumes, viz.:

1) the DHL-flume, at the "De Voorst"-branch of the Delft Hydraulics Laboratory; in this large flume, with a rather gentle bend ($B/R_c = 0.12$) of almost 90^o (see figure 51), experiments have been made with a rectangular cross-section (De Vriend et al., 1977) and with a fixed bottom of more or less the same shape as in a natural river (De Vriend et al., 1978);
2) the IIHR-flume, at the Iowa Institute of Hydraulic Research, containing two opposite and rather sharp bends ($B/R_c = 0.25$) of 90^o each (see figure 58); two of the experiments made in this flume will be considered: one with a shallow trapezoidal cross-section (Yen, 1965) and another one with a fixed bottom configuration corresponding with the equilibrium configuration during a mobile-bed experiment in the same flume (Yen, 1967);
3) the LFM-flume, in the Laboratory of Fluid Mechanics of the Delft University of Technology; two rectangular channel experiments in this sharply curved ($B/R_c = 0.4$) U-shaped flume (see figure 63) will be considered, one with a smooth bottom (De Vriend, 1979b) and one with a rough bottom (De Vriend, 1981b);
4) the IHHE-flume, at the Institute of Hydrology and Hydraulic Engineering of the Academy of Sciences of the USSR; in this very sharply curved ($B/R_c = 1.0$) U-shaped flume with a horizontal bottom and vertical sidewalls (see figure 70), Rozovskii (1961) made extensive flow measurements.

Recently, one of Rozoviskii's experiments was simulated on computer using a fully three-dimensional mathematical model (Leschziner et al., 1978). A similar model was used to simulate two of the rectangular channel experiments in the LFM-flume and the DHL-flume (De Vriend et al., 1981). The results of these fully three-dimensional computations will be used to verify some important aspects of the flow on which no measured data are available.

9.2. Verification for rectangular channels

9.2.1. Simulation of the flat bed experiments in the DHL-flume

The rectangular channel experiments in the DHL-flume (De Vriend et al., 1977) concern velocity and water level measurements for two discharges (0.61 and 0.30 m^3/s), with a depth of flow of 0.25 m near the outflow boundary in either case. The magnitude and the direction of the horizontal velocity component were measured in the nodal points of a three-dimensional measuring grid covering the whole flume. The water surface elevation was measured in selected verticals in this grid.
The two flow cases have been simulated numerically using the parabolic as well as the partially-parabolic model, on the computational grid indicated in figure 51. It consists of 25 cross-sections, from the inflow section 24 m before the bend entrance to the outflow section at 82.5°, with 29 verticals in each cross-section and 21 points in a vertical. When measured along the channel axis, the distance between two adjacent cross-sections is 4.00 m. The distance between the verticals in a cross-section ranges from 0.2d near the sidewalls to 2.0d in the central region. The interval between the grid points in the lower half of a vertical increases exponentially from 0.003d near the bottom to 0.1 d at half depth; in the upper half the vertical spacing is 0.1 d.

Figures 52 through 55 show the results of the simulation. The depth-averaged main velocity distribution (figure 52a) is predicted rather well. Only in the bend the velocity reduction in the inner wall region and the velocity increase near the outer wall are inappropriately represented. It seems as though the effects of secondary flow convection are underestimated.

The results of the parabolic model shown in figure 52a are quite similar to the ones of the partially-parabolic model, systematic differences occurring only near the bend entrance and close to the sidewalls in the bend. There the effects of secondary flow convection are even weaker than according to the partially-parabolic model. Figure 52a also gives the results of the parabolic and partially parabolic modes of the fully three-dimensional model for this case*). The results agree well with the measured data, even near the sidewalls in the bend. Apart from that, the (small) differences between the parabolic and the partially-parabolic model results are similar to the ones for the present model.

Figure 52b shows the measured and the calculated vertical distributions of the main velocity**). According to the present model, there is hardly any deformation of the main velocity profile. The measured data, however, show that such deformations do occur, even when disregarding the highest grid points where the measurements could be influenced by the vicinity of the water surface (Wessels, 1980). Once again, the model seems to underestimate the effects of secondary flow convection. The deformations of the main velocity profile are represented much better by the fully three-dimensional model, even though its prediction of f in the straight channel section is not too good.

The measured and the computed results for the secondary flow are compared in figure 53. Although the measured data are rather inaccurate (De Vriend, 1978c), it can be concluded from figure 53a, that the present model underestimates the secondary flow intensity i_s***) considerably (by 25 to 50%), but that the distance needed for the secondary flow to establish is correctly represented. In addition, the magnitude and the longitudinal

---

*) In these fully three-dimensional computations the measured inflow distribution had to be introduced, but by mistake this was done in reverse. This explains the differences between the model predictions and the measured data in the first part of the flume.

**) The results from the corresponding parabolic models are hardly deviant. Therefore they are not represented.

***) Defined as $\frac{1}{2}\int_{-1}^{0}|v_s|d\zeta$

distribution of the secondary flow intensity appear to be predicted rather well by the fully three-dimensional model.

The transverse distributions of the secondary flow intensity resulting from the two models shows significant and systematic differences, not only in magnitude, but also in shape (figure 53b). The sidewall layers according to the present model are rather thin and the secondary flow intensity is almost constant in the other parts of the cross-section. According to the fully three-dimensional model, however, the sidewall regions are much thicker and $\hat{\psi}Re_0$ is almost constant in a much smaller part of the cross-section *). As far as the measured data provide reliable information at this point, they seem to agree best with the tree-dimensional model, especially beyond the first part of the bend. The differences between the parabolic and the partially-parabolic model predictions are small, again. The parabolic models yield transverse distributions that tend to be more uniform than the ones resulting from the corresponding partially-parabolic ones.

The calculated pressure distributions are compared with the measured water surface configuration in figure 54. As far as the scatter in the measured data permits, it can be concluded that the model predictions are rather good at this point, although the transverse pressure drop seems slightly underestimated. The differences between the two models and between the parabolic and partially-parabolic modes of either model are rather small. Only near the bend entrance the parabolic mode of the fully three-dimensional model yields significantly different results (figure 54b)**).

Measured data on the magnitude and the direction of the bottom shear stress are not available for the DHL-flume. Still the two models are compared at these points, which are of primary importance to bottom

---

*) The tendency of the secondary flow intensity to increase towards the inner side of the bend is also represented by the present model, since the intensity should be compared with $\hat{\psi}Re_0/r$ rather than with $\hat{\psi}Re_0$.

**) The results obtained by the parabolic mode of the present model closely agree with the results from the partially-parabolic one, probably because the bend entrance is treated in a slightly different way as in the parabolic fully 3-D model.

level predictions in curved alluvial channels.
Figures 55a and 55b show that the differences in the depth-averaged velocity predictions are amplified in the magnitude of the bottom shear stress. As a consequence, the differences between the shear stresses predicted by the two models locally amount 25%. Besides, the overall mean value of the bottom shear stress predicted by the present model is somewhat larger (about 10%) than the one resulting from the fully three-dimensional model. Finally it should be noted that according to either model the bottom shear stress in the bend is hardly larger than in the straight reach upstream.
The deviation angle of the bottom shear stress vector from the longitudinal direction is represented by figures 55c and 55d. Here it is the secondary flow intensity that dominates the differences between the two models and consequently the transverse distributions of α_τ in figure 55c show a striking resemblance to the ones of i_s in figure 53b: the sidewall layers in the distributions obtained by the present model are much thinner and the overall mean value of α_τ is too small. The latter difference is also observed in figure 55d, which shows that, apart from local differences near the bend entrance, the length needed for α_τ to reach its final value in the bend is about the same for either model.

9.2.2. Evaluation and analysis

The foregoing comparison with measured data and with the fully three-dimensional model leads to the conclusion that, even for the mildly curved and shallow DHL-flume, the present model produces significant errors at the following points:

- the reduction of the depth-averaged main velocity in the inner bend and the increase in the outer bend are too small and occur in a too narrow region;
- the deformation of the vertical distribution of the main velocity along the bend is underestimated;
- the fully-developed secondary flow intensity is underestimated;
- the sidewall layers in the transverse distribution of the secondary flow intensity are too thin, so that the vertical component of the secondary flow is concentrated too strongly near the sidewalls;

. the magnitude of the bottom shear stress in the inner bend is overestimated;
. the deviation of the bottom shear stress vector from the longitudinal direction is underestimated and its transverse distribution is too uniform, with too thin wall layers.

From a river engineering point of view, only the last two shortcomings are serious, but as they are related directly to the main velocity and the secondary flow, respectively, the other points are relevant, as well.

The nature of the errors in the main velocity predictions suggests that they must be attributed to an underestimation of the effects of secondary flow convection, caused not only by the underestimation of the secondary flow intensity, but also by the errors in the transverse distribution of i_s. The latter errors cause the vertical velocity component to be concentrated too strongly near the sidewalls. As a consequence, the convective reduction and increase of $\bar{u}$ occur in too thin layers along the inner and the outer wall, respectively. In the inner wall region, this hampers the outward extension of the region with reduced $\bar{u}$ by the transverse component of the secondary flow.

On the other hand, the secondary flow intensity is related to the depth-averaged main velocity through the source of secondary flow (which is proportional to $\bar{u}^2$). Hence too thin wall layers in $\bar{u}$ will give rise to too thin wall layers in i_s, i.e. to vertical velocities that are concentrated too strongly along the sidewalls.

Especially in the inner wall region, this mutual interaction between the main and the secondary flow could cause errors in the transverse distributions of $\bar{u}$ and i_s (either too thick or too thin wall layers) to persist or even to enhance themselves, once they have come into existence. If that holds true, the fair agreement between the results of the fully three-dimensional computations and the measured data could be a coincidence, as the inflow distribution imposed in these computations has too thick sidewall layers, which have not yet been extinguished at the bend entrance. In that case, the present model could also yield good predictions if the velocity distribution at the bend entrance were taken the same as in the fully three-dimensional computations.

Figure 56, however, shows that this is not quite true. The computations

represented in this figure differ at two points from the ones described in par. 9.2.1, viz.:

. the inflow boundary is situated at 8 m before the bend entrance; two cases are compared, one with the inflow velocity identical to the fully three-dimensional model and the other one with the usual inflow condition;

. in view of the discussion hereafter, the turbulence model is adjusted in such a way (γ=7; a' according to the 'k-ε-approximation'), that the overall mean secondary flow intensity corresponds better with the measured data*).

The results obtained by the present model are far better now, at least in the inner wall region, but it becomes evident from figure 96, that this must be attributed to the latter difference rather than to the former one: the results of the two computations approach one another on proceeding through the bend.

On the other hand, the overall mean secondary flow intensity is overestimated in these computations, whereas it is not in the fully three-dimensional one. This implies that the present model still underestimates the convective reduction of $\bar{u}$ in the inner wall region. Besides, the predicted distributions of $\bar{u}$ and i_s in the outer wall region remain rather poor, whereas they are not in the fully three-dimensional model (cf. par. 4.4).

Hence it is concluded that other differences between the present model and the fully three-dimensional one must play a part here. In the following, the effects of the most prominent differences will be subject to a closer investigation.

In the secondary flow computation, not only $\bar{u}$, but also f and the turbulence viscosity play a part. This becomes evident from the stream function equation for the secondary flow given in the foregoing chapters and it can also be shown by the following approximative reasoning (see also Kalkwijk et al., 1980).

Making use of the approximation

$$\frac{\partial \bar{p}}{\partial \xi} = - \varepsilon^2 Re_0 \frac{\overline{u^2}}{r_s} - \varepsilon^2 \left(a \frac{\partial v_s}{\partial \zeta} \right) \Big|_{\zeta=-1} \qquad (9.1)$$

*) The intensity turns out to be somewhat overestimated now (see figure 56b).

, the transverse momentum equation in a vertical far from the sidewalls in a long uniform bend can be written as

$$\frac{\partial}{\partial\zeta}\left(a\,\frac{\partial v_s}{\partial\zeta}\right) + \left(a\,\frac{\partial v_s}{\partial\zeta}\right)\Big|_{\zeta=-1} = Re_0\,\frac{\bar{u}^2}{r_s}\,(f^2 - \overline{f^2}) \qquad (9.2)$$

In order to find out what role $\bar{a}$, a', $\bar{u}$ and f play in the secondary flow computation, this computation is carried out in a number of verticals in two cross-sections of the DHL-flume, assuming all lateral and longitudinal influencing to be absent and introducing the values of the above quantities as obtained from the present and from the fully three-dimensional model.
Figure 57a shows the distributions of $\bar{a}(\xi)$ and $a'(\zeta)$ resulting from the two models. Away from the sidewalls, the transverse distribution of the depth-averaged turbulence viscosity is rather uniform, so that the quantity is described reasonably well by the expression

$$\bar{a} = k_m \bar{u} \qquad (9.3)$$

used in the present model. Near the sidewalls, however, high peaks occur in the fully three-dimensional model predictions of $\bar{a}$. These peaks, which are likely to be caused by the production of turbulence energy due to the transverse main velocity gradients, are not represented by the present model. The vertical distributions of the turbulence viscosity "resulting" from the two models show important differences, especially in the upper half of the vertical. As was to be expected from a model applying the k-ε turbelence model, the fully three-dimensional computations lead to a distribution function $a'(\zeta)$ that agrees better which the 'k-ε-approximation' than with the parabolic distribution applied in the present model. In addition, it should be noted that close to the sidewalls $a'(\zeta)$ is almost uniform in the greater part of the vertical.
The contributions of $\bar{u}$ and f to the source of secondary flow are represented in figure 57b. For $\bar{u} \equiv 1$, the source term in

the depth-averaged stream function equation for the secondary flow is dominated by $f^2|_{\zeta=0}$. In the main flow computation step of the present model, this is a constant in each cross-section. The corresponding result of the fully three-dimensional model, however, shows somewhat lower values near the sidewalls, with sidewall layer thicknesses of about 2d. These sidewall layers are found not only in the bend, but also at the bend entrance, where the secondary flow is still very weak. Hence they must be attributed to the sidewall influence rather than to the convective influence of the secondary flow. This hypothesis is supported by the vertical distributions of the quantity $f^2 - \overline{f^2}$ shown in the same figure. These distributions show globally the same features in the bend and at the bend entrance, i.e. the influence of secondary flow convection is rather small. Near the sidewalls, however, the distributions differ considerably from the ones in the central part of the cross-section and in both cross-sections considered the differences are of the same kind, so most likely they are due to sidewall effects.

When considering $u^2|_{\zeta=0}$, the sidewall layers in the transverse distribution are much thicker, as a consequence of the contribution of $\bar{u}^2$. This contribution also leads to differences between the two cross-sections: at the bank entrance the inner wall layer tends to be the thinner one, in the last part of the bend the outer wall layer is the thinnest.

The local secondary flow computation mentioned before is carried out in a number of verticals in either cross-section, with various combinations of $\bar{a}$, a', $\bar{u}$ and f derived from the two models. The results are shown in figure 57c*). According to the present model, the quantity $\hat{\psi}Re_0/\bar{u}^2$ is constant in a cross-section, if all lateral and longitudinal interaction is ignored. In the central part of the cross-section, this constant closely agrees

*) The results of the complete models for the secondary flow intensity at the bend entrance have been scaled up by about a factor 5 in order to let them correspond with the results of the computations per vertical.

with the results of the complete model, which implies that the secondary flow intensity is underestimated by about 25%. On the other hand, introducing the results for $a'(\zeta)$ and $f(\zeta)$ from the fully three-dimensional model and taking $\bar{a} \equiv 1$*) yields much better values for i_s in the central part of the cross-section, though this quantity is still underestimated by about 5%. When calculating i_s in the same way for $\gamma = 6$, $\bar{u} = 1$, $\bar{a} = 1$, $f(\zeta)$ logarithmic and $a'(\zeta)$ parabolic and comparing the result with the one form the analytical solution for this case (see par. 7.4.5), however, the difference is almost the same. Apparently, this error must be attributed to the numerical solution procedure.

Hence it must be concluded that the greater part of the underestimation of i_s by the present model is caused either by the assumed distribution of $a'(\zeta)$ or by errors in the source of the secondary flow, $f^2 - \overline{f^2}$. If for the latter the results of the fully three-dimensional computations are introduced, however, the values of i_s in the central part of the cross-section grow hardly better, so that it must be $a'(\zeta)$ that causes the trouble at this point. In chapter 6 it was already shown, that replacing the parabolic distribution for a' by the so-called 'k-ε-approximation' leads to higher secondary flow intensities. Figure 56c shows that introducing this approximation into the present computations has the same effect, such that it provides a satisfactory explanation of the underestimation of i_s.

Apart from the secondary flow intensity in the central region, the computation per vertical can also give an indication of the reason why the quantity $\hat{\psi}Re_0/\bar{u}^2$ tends to decay near the sidewalls. As was stated before, the main flow computation step of the present model yields a constant value of this quantity in each cross-section. When the vertical distributions of the main velocity resulting from the fully three-dimensional computations are introduced, however, this quantity becomes smaller near the sidewalls,

*) In order to let the computations correspond with the ones based on the present model.

irrespective of the distribution of a' that is assumed. At the bend entrance, this reduction is restricted to a rather narrow (< d) region near the walls, but in the last part of the bend it extends further inwards (up to about 3d from the walls). Obviously, it is the deformation of f that causes the sidewall layers in the transverse distribution of $\hat{\psi}Re_0/\bar{u}^2$. In view of the distribution of $f^2 - \overline{f^2}$ shown in figure 57b, the reduction close to the sidewalls must be attributed to direct sidewall effects on f*), whereas somewhat further away from the walls it is caused by deformations of f due to secondary flow convection.

As regards the measures to be taken in order to improve the description of the secondary flow by the present model, the remedy for the underestimation of the secondary flow intensity is rather simple: apply the 'k-ε-approximation'

$$a' = -\frac{16}{3}(1+\zeta)(1+5\zeta+4\zeta^2) + \frac{\gamma}{9}(1+\zeta)(10+41\zeta+40\zeta^2) \quad \text{for} \quad \zeta \leq -\frac{1}{2}$$

$$a' = \frac{4}{3} - \frac{\gamma}{36} \quad \text{for} \quad \zeta \geq -\frac{1}{2} \tag{9.4}$$

instead of the parabolic distribution (6.59), in spite of the theoretical objections that can be made against it (Ueda et al., 1977; Rodi, 1978b).

The thin sidewall layers in the transverse distribution of i_s, however, do not allow for such a simple remedy. With the present set-up of the model, it seems hardly possible to account for the deformations of f due to direct sidewall effects. As these deformations are restricted to rather thin layers along the walls, however, the reduction of the secondary flow intensity due to these deformations could be introduced artificially, for instance by letting the source term in the depth-averaged stream function equation for the secondary flow decay linearly

---

*) Close to the sidewalls, the velocity is determined by the shear layer along the wall rather than by the one along the bottom, so that u is almost uniform in the greater part of a vertical there.

to zero over a distance 2d adjacent to the wall.
As was stated in par. 7.5, accounting for the convective influence of the secondary flow on f by solving equation (7.23) in all verticals of the computationad grid leads to erroneous results, especially near the sidewalls. In view of the aforementioned artifice, however, the verticals at a distance smaller than 2d from the sidewalls can be left out of consideration. In the remaining verticals, lateral diffusion is likely to be rather unimportant, so that it is possible to account for the convective influence of the secondary flow on f in these verticals by solving

$$\tilde{k}_m \bar{u}^2 \frac{\partial}{\partial \zeta}\left(a' \frac{\partial f}{\partial \zeta}\right) - \varepsilon Re_0^2 \frac{\bar{u}}{r} \frac{\partial \bar{\psi}}{\partial \xi} g \frac{\partial f}{\partial \zeta} + \varepsilon Re_0^2 \frac{\bar{\psi}}{r}\left(\frac{\partial \bar{u}}{\partial \xi} + \frac{\varepsilon}{r} \bar{u}\right) \frac{\partial g}{\partial \zeta} f +$$

$$- \varepsilon Re_0 \left(\frac{\bar{u}}{r} \frac{\partial \bar{u}}{\partial \phi} + \bar{v} \frac{\partial \bar{u}}{\partial \xi} + \frac{\varepsilon}{r} \overline{\bar{u}\bar{v}}\right) \tilde{f} f = \frac{1}{r} \frac{\partial p}{\partial \phi} \qquad (9.5)$$

This approach was tested out using the results of the fully three-dimensional computations. Figure 57d shows that in the central region of the cross-section the predictions of the vertical distribution of the main velocity are rather good, especially for the 'k-ε-approximation' of a'. In this region, however, the effects of secondary flow convection are rather small and even the predictions by the present model are rather good there. Near the sidewalls, where the secondary flow has a much stronger influence on f, this influence is overestimated. In the inner wall region, the main velocity near the surface is reduced too far and near the outer wall the vertical distribution is too oblique, such that $f^2|_{\zeta=0}$ shows a peak where, according to the fully three-dimensional model, a slight decrease should occur.
Hence it must be concluded that the improvement of the model attained by accounting for the convective influence of the secondary flow on f in each separate vertical is not likely to justify the high expenses it entails. This implies that in the regions of a rectangular cross-section where the convective interaction between the main and the secondary flow

is important, the computation of the flow, and especially of the magnitude and the direction of the bottom shear stress, cannot be simplified so far, that it becomes economically more attractive than fully three-dimensional computations. As a consequence, the flow in curved rectangular channels that are not quite shallow and mildly curved has to be computed using a fully three-dimensional model in order to have a proper prediction of the bottom shear stress.

9.2.3. Simulation of a flat bed experiment in the IIHR-flume

In spite of the imperfections that came forward in the foregoing paragraphs, the present model has been used to simulate one of the experiments in the IHHR-flume (Yen, 1965). This flume contains two opposite 90^{o} bends with a short straight reach in between (see figure 58), which makes it especially suited for testing the growth and decay of the secondary flow. Besides, out of the flumes mentioned in par. 9.1, this is the only one in which extensive bottom shear stress measurements have been made. This provides the possibility to test the model at its most important point.
One flow case has been selected from the series of experiments made in this flume, viz. 'Run 3' (Yen, 1965), with a mean depth of flow of 0.512 ft (0.16 m) and a mean velocity of 2.27 fps (0.69 m/s). The measured data for this case concern the magnitude and the direction of the horizontal velocity component, the water surface elevation and the bottom shear stress, in the straight reach between the bends and in the second bend.
In the mathematical simulation, the shallow trapezoidal cross-section of the channel (d/B = 0.08; sidewalls 1:1) was approximated by a rectangle with $B = B_{bottom} + d \simeq 6.5$ ft (1.99 m). The Chezy-factor was taken 127 $ft^{\frac{1}{2}}/s$ (70 $m^{\frac{1}{2}}/s$), which corresponds with the longitudinal slope of the channel ($7.2 * 10^{-4}$) in the experiment. Though measured data are avalaible for the second part of the flume only, the numerical simulation covered the whole flume in order to have proper inflow conditions for the second part. The computational grid used in the simulation is indicated in figure 58. It consists of 25 cross-section, from the inflow section 7 ft

ahead of the first bend to the outflow section 7 ft downstream of the second bend, with 22 (horizontal) x 20 (vertical) meshes in each cross-section.
On the basis of the experience gained from the DHL-flume (see par. 9.2.2), the overall mean turbulence viscosity was assumed to correspond with $\gamma=7$ and for the vertical distribution of the turbulence viscosity the 'k-ε-approximation' was adopted. For the rest, the model was identical to the one used to simulate the DHL-experiments (par. 9.2.1).

The results of the simulation are represented in figure 59 through 62. Figure 59a shows, that the prediction of the depth-averaged main velocity distribution goes wrong at the same point as for the DHL-flume: the influence of secondary flow convection is concentrated too much along the sidewalls. Near the inner wall, $\bar{u}$ is reduced far too strongly and over too narrow a region, whereas near the outer wall a much too pronounced peak in $\bar{u}$ occurs. The thickness of the layer near the inner wall in which $\bar{u}$ is influenced by the too strong reduction ranges from less than d in the first part of the bend to about 4d in the second part. The spurious peak in $\bar{u}$ near the outer wall extends over a distance of about d. In the central part of the cross-section, situated between these two layers, the distribution of $\bar{u}$ is predicted reasonably well.
The measured vertical distributions of the main velocity represented in figure 59b (see Yen, 1965, for more extensive data) show a rather strong transverse non-uniformity. Near the inner wall, the velocity in the upper part of the vertical is reduced much further than in the central region and near the outer wall. In addition, the deformations of f generated in the first bend persist in the first part of the second bend, expecially near the right wall (which is the inner wall in the first bend). Neither this memory-effect nor the transverse non-uniformity in the deformations is represented by the present model.
A deformation that is represented, though too strongly by lack of inertia, is the increase of f in the upper half of the vertical in the greater part of the second bend. This deformation contrasts

with the one in a single bend, where f shows rather a decrease in the upper part of the vertical (cf. chapter 3 and par. 9.2.4). The explanation can be found in the transverse distribution of $\bar{u}$ combined with the sense of rotation of the secondary circulation. In the last part of the first bend and especially in the straight reach between the two bends, the depth-averaged main velocity is skewed towards the left wall, so that the counterclockwise secondary circulation there gives rise to a reduction of f in the upper part of the vertical (cf. chapter 3). In the first part of the second bend, the skewness of $\bar{u}$ persists and is even enhanced by the non-uniform longitudinal pressure gradient near the bend entrance. The secondary flow, however, becomes clockwise at the entrance of the second bend and hence it causes an increase of f near the surface.

According to figures 60a and 60b, the 'measured' secondary flow intensity in the channel axis *), is about 30% smaller than the calculated one. In contrast with the experience for the DHL-flume (par. 9.2.2), γ=6 would have done better here. Apart from the accuracy of the 'measured' data, however, it should be pointed out that the present flume is narrower and sharplier curved than the DHL-flume (d/B = 0.079 vs. 0.042; d/R_c = 0.018 vs. 0.005). Consequently, the transverse non-uniformity in the deformations of the main velocity profile will be stronger and the sidewall-layers in the transverse distribution of the secondary flow intensity will be thicker (cf. par. 9.2.2). In the last part of the DHL-flume these sidewall layers extended over about 5d from the walls (see figure 53), so that it seems reasonable to suppose that in the IIHR-flume the sidewall layers in i_s interact. This becomes even more plausible when taking into account that in the outer wall regions of both flumes a reverse secondary circulation occurs (cf. par. 3.7 and De Vriend et al., 1977), which drastically reduces the secondary flow intensity there. Roughly speaking,

*) The 'measured' secondary flow intensity represented in figure 60a is derived from the outward, inward and net radial discharges in the channel axis as given in Yen's thesis (see De Vriend, 1979a, for further details).

the reverse circulation extends to about 1.5 d from the outer wall, so that the effective width for the secondary flow is reduced relatively more in the IIHR-flume.

Apart from the overall magnitude of the secondary flow, its growth and decay and the shape of its vertical distribution are described reasonably well, as is shown by figure 60b. Only near the surface systematic differences between the measured and the calculated vertical distributions are found. The measured data mostly show a finite gradient of v_s at the surface, whereas in the mathematical model this gradient equals zero. This suggests that the turbulence viscosity should go to zero at the surface, rather than being constant in the upper part of the vertical (cf. Ueda et al., 1977; see also par. 9.2.2).

Figure 61 shows that the calculated transverse pressure distribution is in good agreement with the measured water surface configuration. The deformation of the transverse distribution of $\bar{u}$ is reflected in the shape of the surface; in the first part of the bend, where $\bar{u}$ and hence $\frac{\partial \bar{p}}{\partial \xi}$ and $\frac{\partial \zeta_s}{\partial \xi}$ have their maximum, it is concave, whereas it is convex in the last part of the bend, where the maxima have shifted to the outer wall. In addition, it becomes evident from figure 61 that the distance needed for the transverse slope of the surface to establish and to decay is much smaller than the one of the depth-averaged main flow vorticity*) or the secondary flow intensity.

The agreement between the measured and the calculated bottom shear stress distributions in figures 62a and 62b is not quite good. Firstly, the errors in $\bar{u}$ are reflected in an intensified degree, since τ_b is related to $\bar{u}^2$. In addition, however, the predicted longitudinal variations of $\tau_b/\bar{u}^2$ are far too strong. As became evident from figure 59b, both the measured and the calculated vertical distributions of the main velocity become more oblique in the first part of the second bend. According to the mathematical model, these more oblique profiles correspond with a reduction of

*) $\bar{\omega}_m$ can be considered as a measure for the deviation of the transverse distribution of $\bar{u}$ from the free vortex distribution (cf. De Vriend, 1976 & 1979c).

$\tau_b/\bar{u}^2$, as is readily illustrated by figure 62b. The measured data, however, hardly show a decreasing tendency of $\tau_b/\bar{u}^2$, in spite of the small, but still significant deformation of the measured velocity profiles. On the other hand, it should be noted that the bottom shear stress in the IIHR-experiment was measured using a Preston tube, which is not quite suited for this purpose in skewed flow, i.e. especially in the last part of the bend (Nishi et al., 1974). Therefore, it seems rather risky to draw conclusions from figure 62b.

The predicted direction of the bottom shear stress (figures 62c and 62d) agrees well with the measured data in the central part of the cross-section, although there is a slight over-estimation in the bend. The measured and the calculated transverse distributions of α_τ, however, show significant differences (figure 62d). It seems as though, especially in the last part of the bend, the central region, if present at all, is rather narrow and the sidewall layers cover the greater part of the cross-section. This would be in accordance with the aforementioned suggestion, that the sidewall layers in the transverse distribution of the secondary flow intensity interact.

In summary, it can be concluded that the present mathematical model works not too well for the IIHR-flume, expecially when attention is focused on the bottom shear stress. The main velocity and, to a higher extent, the magnitude of the bottom shear stress are only reliable in the central part of the cross-section, and even there errors up to 10% (in $\bar{u}$) and 20% (in τ_b) are not exceptional. The predictions of the secondary flow and the direction of the bottom shear stress are even worse, the sidewall layers in the transverse distributions of these quantities covering the larger part of the cross-section.

9.2.4. Simulation of the LFM-experiments

In view of the conclusions drawn from the simulation of the IIHR-experiment described in the foregoing paragraph, it seems as though it makes no sense to simulate the flat bed experiments in the even sharplier curved and narrower LFM-flume. Still there are some arguments to do so:

. it would be interesting to know how the tendencies to be observed in the differences between the results of the DHL-flume and the ones for the IIHR-flume pursue in the LFM-flume;
. the flumes considered so far comprised bends of at most 90°, whereas the LFM-flume comprises a 180° bend, so that the flow is likely to get nearer to its fully-developed curved stage;
. the two flat bed experiments in the LFM-flume provide the possibility to consider the influence of the bottom roughness;
. the fully three-dimensional model used to simulate the DHL-experiments was also applied to the LFM-flume in order to test its performance for a rather sharply curved and narrow flume (De Vriend et al., 1981); the results of this model can be used as a reference if an analysis of the present model results appears necessary (cf. par. 9.2.2).

Therefore the LFM-experiments have still been simulated, in spite of the poor predictions to be expected.

The geometry of the flume is shown in figure 63. It is 1.70 m wide and consists of a straight inflow section (effective length 6.00 m), a 180° bend (radius of curvature of the axis 4.25 m) and a straight outflow section (effective length 6.00 m). The bottom is horizontal and the water level is adjusted by a tail gate.
In the smooth bed experiment, the bottom and the sidewall were plastered with mortar ($k \simeq 10^{-3}$), in the rough bed experiment the bottom was covered with a single layer of gravel of 3 to 5 cm diameter, set in a layer of mortar, so that the Nikuradse roughness was about 0.03 m. In both experiments the discharge was 0.19 m^3/s and the depth of flow was about 0.17 m*), so that the values of Chezy's factor for the smooth and the rough bottom were about 60 $m^{\frac{1}{2}}/s$ and about 30 $m^{\frac{1}{2}}/s$.
In either case, the magnitude and the direction of the horizontal velocity vector and also the water surface elevations were measured (see De Vriend, 1979b and 1981b, for further details).

*) Especially in the rough bottom case, the backwater effect was rather strong, with the depth of flow ranging from 0.14 to 0.20 m.

The computational grid used in the simulation for this flume is indicated in figure 63. It consists of 25 almost equidistant cross-sections (6 in either straight reach, 2 at the transitions and 11 in the bend), 21 non-equidistant verticals in each cross-section and 20 points per vertical, distributed in the same way as for the other two flumes.
The model used for the simulation was identical to the ones used before, except for the turbulence model. In order to have a reasonable prediction of the secondary flow intensity, the turbulence model was adjusted by taking $\gamma=6$ and $\alpha'(\zeta)$ parabolic. It should be stressed, however, that this deviation from the foregoing model is not based on physical arguments. It is rather an artifice, meant to compensate for the reduction of the secondary flow intensity by lateral constraint.

9.2.4.1. Smooth-bottom simulation

The results of the smooth-bottom simulation are shown in figures 64 through 67.
The depth-averaged main velocity distributions in figure 64a show that the model describes even the main velocity in this channel rather poorly. Although the predictions are certainly better than the ones obtained from a shallow water computation without secondary flow convection (De Vriend, 1976 & 1977), the local effects of this convection are too strong near the sidewalls and extend insufficiently far into the central part of the cross-section. Consequently, the predicted distribution of $\bar{u}$ in the central part keeps 'free-vortex' features ($\bar{u} \sim \frac{1}{r}$) throughout the bend, rather than shifting gradually from the 'free-vortex' distribution in the first part of the bend to a more uniform distribution in the last part. This implies that at this point the present model works hardly better than a model without secondary flow convection. In the central part of the straight reach beyond the bend, however, the 'forced-vortex'-like distribution ($\bar{u} \sim r$) is described reasonably well, though the values of $\bar{u}$ are somewhat too high because of the errors in the sidewall regions. So there the present model yields considerably better results than a model without secondary flow convection.

Figure 64a also shows, that the results of the fully three-dimensional computations are in fair agreement with the measured data, except for the effect of the reverse secondary circulation in the outer wall region (a local reduction of $\bar{u}$, see also chapter 3).

Figure 64b gives the measured and the calculated vertical distribution of the main velocity in the channel axis and at a distance d from the sidewalls. Apart from the rather sharp reduction of the measured velocities near the surface, which is possibly due to measuring errors (Wessels, 1980), the measured data show significant deformations of f, both in a cross-section and along the channel. In the inner bend, the reduction of f in the upper half of the vertical is so strong, that the main velocity maximum occurs in the lower half. Further outwards, the effects of secondary flow convection are not so strong, but still considerable.

Since the transverse non-uniformity of f due to the secondary flow is not incorporated in the present model*), it is not reproduced. The predicted deformation of f along the channel axis is too weak, but qualitatively correct: on proceeding through the bend, the main velocity reduction in the upper part of the vertical gradually becomes stronger, so that the velocity maximum is shifted to a point below the surface. In spite of the quantitative underestimation of the deformations (due to the underestimation of $\frac{1}{r}\frac{\partial}{\partial \xi}(r\bar{u})$; see equation (7.23) and figure 64a), the predicted distributions of f in the channel axis agree rather well with the measured data. Only downstream of the bend considerable differences are found, since the calculated deformation rapidly decays there, whereas the measured one persists much longer. This too rapid decay of the deformation is likely to be caused by the combined action of a too rapid decay of the secondary flow intensity (see figure 65a) and the absence of a memory effect in f (the inertia term with $f\frac{\partial f}{\partial s}$ has been disregarded; see also par. 7.6.1 and De Vriend, 1979b).

The fully three-dimensional model gives a rather good description of the deformations of f, although it tends to underestimate them near the sidewalls. In addition, the effects of the reverse secondary

*) Including the effect of secondary flow convection by solving (7.23) in each vertical leads to erroneous results (see par. 7.5).

circulation in the outer wall region are not reproduced. Especially in the first part of the bend this gives rise to considerable errors near the outer wall.

Finally, it should be pointed out that the supposed inaccuracy of the measured data near the surface makes it impossible to draw conclusions as to the most suitable vertical distribution of the turbulence viscosity in the upper half of the vertical (parabolic or uniform).

Figure 65a, representing the distribution of the secondary flow intensity in various longitudinal sections, suggests that, apart from a region close to the outer wall, the secondary flow intensity is predicted fairly well by the present model*). Only the rate of decay beyond the bend seems somewhat overestimated. When considering figure 65b, however, this appears to be a rather optimistic interpretation. The shape of the longitudinal distribution of i_s may be reproduced fairly well, the transverse distribution definitely shows essential differences from the measured data. Firstly, the reverse secondary circulation observed near the surface in the outer wall region (see figure 65c) causes a considerable reduction of i_s there. Since such a circulation does not occur in the model predictions, this reduction is not represented. In addition to local effects, however, the reverse circulation gives rise to a reduction of the 'effective' channel width for the secondary flow by about 2d, i.e. 20%. Consequently, the sidewall layers in the transverse distribution of i_s cover the entire cross-section, especially in the second half of the bend (cf. par. 9.2.1 and par. 9.2.3). So in this part of the bend there is no longer question of two sidewall regions and a central region in between **), but the sidewall layers interact and the lateral constraint, caused directly or indirectly by the sidewalls (cf. par. 9.2.2), influences i_s

---

*) Both the measured and the calculated values of i_s are considerably smaller than the intensity in a very shallow channel with a logarithmic main velocity distribution ($i_s \simeq 1.67\ \bar{u}/r_s$).

**) In contrast, the transverse distribution of $\bar{u}$ clearly shows this three-partite character throughout the flume.

throughout the cross-section. According to the present model, however, the sidewall layers in the transverse distribution of the secondary flow intensity are separated by a distinct central region, so that they cannot interact and lateral constraint occurs only close to the sidewalls.

On the other hand, the sidewall layers in the measured distribution of i_s are thinner in the first half of the bend (cf. par. 9.2.1), so that their interaction, if present at all, is weaker than in the second half. Consequently, the model predictions of the secondary flow intensity in the first half of the bend shows the same features as in the shallower channels considered before: the intensity far from the sidewalls is underestimated considerably and the sidewall layers are far too thin. Hence it is concluded that the agreement of the predicted and the measured secondary flow intensities in the second half of the bend partly emanates from the mutual compensation of two errors: i_s tends to be underestimated by the choice of the turbulence model and it tends to be overestimated by lack of lateral constraint.

The increasing lateral constraint is not the only cause of the gradual decay of the secondary flow intensity in the second half of the bend, since such a decay, though somewhat weaker, is also predicted by the present model. It is caused by the deformation of the main velocity profiles, giving rise to lower values of f near the surface and hence to a decrease of the source of the secondary flow (cf. the depth-averaged stream function equation for the secondary flow (7.39)). This also explains why the secondary flow intensity is smaller than the one in a very shallow channel with a logarithmic main velocity distribution (De Vriend, 1976 & 1977).

The fully three-dimensional model tends to overestimate i_s, especially in the outer half of the cross-section and in the second half of the bend, i.e. in the regions where the influence of the reverse secondary circulation near the outer wall is felt. This reverse circulation is not reproduced by the model (see the discussion in par. 9.2.5). Correspondingly, the rate of decay of i_s in the second half of the bend is somewhat underestimated. Apart from this all, the predicted decay of the secondary flow intensity beyond the bend is somewhat too strong.

The present simplified model gives a rather good description of the

vertical distribution of the secondary flow in the central region of the first half of the bend (figure 65c). In the second half and near the inner wall, however, the deformations of f have a considerable influence on $\frac{\partial q}{\partial \zeta}$ and as these deformations are inappropriately reproduced by the model, the predicted vertical distributions of the secondary flow show considerable errors there. The reverse secondary circulation occurring in the upper part of the vertical near the outer wall cannot be reproduced by the present model, so that the vertical distribution of v_s is completely wrong there. The fully three-dimensional model gives a better description of the deformations of $\frac{\partial q}{\partial \zeta}$ near the inner wall and in the second half of the bend, but it yields no reverse secondary circulation near the outer wall.

As usual, the calculated transverse pressure distribution is in rather good agreement with the measured water surface configuration (see figure 66), though the transverse pressure drop tends to be slightly underestimated, both by the present model and by the fully three-dimensional one. Differences in shape between the measured and the calculated distributions can easily be traced back to differences in the depth-averaged main velocity (cf. figure 64a).

In view of the good predictions of the main velocity by the fully three-dimensional model, it seems allowable to use the magnitude of the bottom shear stress calculated by this model as a reference for the simplified model. The differences between the transverse distributions of τ_b in figure 67a show the same features as the differences in $\bar{u}^2$ (cf. figure 64a). The gradual deformation of the main velocity profile along the bend is reflected in the gradual increase of the bottom shear stress factors resulting from either model (figure 67b). The direction of the bottom shear stress (figures 67c and 67d) varies along the channel in a similar way as the secondary flow intensity (see figure 65a). In the first part of the bend $|\alpha_\tau|$ grows until it reaches its maximum about half-way; in the second half of the bend and in the downstream straight reach it gradually decreases again. As a consequence of the deformation of the main velocity profile, the maximum of $|\alpha_\tau|$ is considerably smaller than it would be in a very shallow channel with a logarithmic main velocity distribution, where (De Vriend, 1976 & 1977)

$$\alpha_\tau = \text{atan}\ \{\frac{2\varepsilon}{\kappa^2 r_s}\ (1 - \frac{\sqrt{g}}{\kappa C})\} \qquad (9.6)$$

In the present case, this corresponds with $\alpha_\tau \simeq 23^o$.
Apart from some anomalies in the results of the fully three-dimensional model near the entrance and the exit of the bend, the two models differ in almost the same way as in the secondary flow intensity, at least in the channel axis (figure 67c). Most probably, the peaks near the sidewalls in the transverse distribution of α_τ resulting from the simplified model (figure 67d) are spurious, the one near the inner wall being caused by the too strong reduction of $\bar{u}$ and the one near the outer wall arising from the spurious peak in i_s near this wall. The transverse distribution resulting from the fully three-dimensional model does not show these peaks, but in view of the errors in i_s (figure 65b), this distribution is still unreliable as a reference for the simplified model. This is the more so, as the treatment of the transverse velocity component near the bottom in this model (logarithmic distribution of v_r on the bottom-nearest mesh of the computational grid) gives rise to an underestimation of the transverse bottom shear stress when applying a coarse computational grid*).

9.2.4.2. Rough-bottom simulation

The results of the rough-bottom simulation are compared with the measured data in figures 68 through 69. In the same figures, some of the smooth-bottom data are plotted once again, in order to show the effects of the bottom roughness.
In general, the conclusions on the performance of the simplified model in the simulation of the smooth bottom experiments in the LFM-flume apply to the rough bottom case, as well. Therefore,

*) For the horizontal component of the secondary flow, which is a most important constituent of v_r, the logarithmic distribution only holds good as an approximation very close to the bottom (cf. the transverse velocity profiles in figure 65c).

attention will be focused here on the systematic differences between the two cases and their representation by the model.
The most important difference between the two flow cases is the much smaller characteristic length of longitudinal variations in case of a rough bottom*), which means that rough-bottom flow adapts much faster to longitudinal variations of the channel geometry (such as the curvature). This difference is reflected in two aspects of the depth-averaged main velocity distributions plotted in figure 68a. Firstly, the transition from the 'free-vortex' distribution in the first part of the bend to an outward skewed distribution in the last part occurs much more abruptly in case of a rough bottom (between 45° and 90° rather than from 45° to 135°). This leads to considerable differences between the smooth and rough bottom distributions half-way the bend. Secondly, the skewness of the main velocity distribution immediately downstream of the bend damps out more rapidly with a rough bottom.
The model leads to a rather good reproduction of the latter phenomenon, but the former one is represented poorly as a consequence of the too strong concentration of the effects of secondary flow convection in the sidewall regions.
In addition to these differences, figure 68a clearly shows that the influence of secondary flow convection of $\bar{u}$ is not distinctly weaker for the rough bottom than for the smooth one. Obviously, the effective Dean number is not quite appropriate as a measure for this influence (see also par. 7.8).
Apart from the points close to the water surface, the 'undisturbed' vertical distribution of the main velocity for the rough bottom (figure 68b) is considerably more oblique than the one for the smooth bottom. In the bend, however, the distributions are more alike, whence it is concluded that the deformations of f in the

*) In case of steady shallow water flow without secondary flow effects, the characteristic length varies in proportion with C^2 (see De Vriend, 1979c).

bend are stronger in the rough bottom case. On the other hand, however, these deformation tend to decay faster beyond the bend. As was stated before, the model in its present form does not account for the transverse non-uniformity of f, but it should reproduce the deformations along the channel axis. In contrast with the measured data and the smooth bottom predictions, however, the predicted rough bottom distributions show only a weak deformation along the bend. Probably, this is mainly a consequence of the erroneous prediction of $\bar{u}$ (see figure 68a), which amounts to underestimating $\frac{1}{r}\frac{\partial}{\partial \xi}(r\bar{u})$ in the greater part of the bend and hence to underestimating the effect of radial convection (cf. the main flow equations in chapter 7).

In spite of the considerably larger scatter in the measured secondary flow intensities for the rough bottom (figures 69a and 69b), some conclusions can be drawn from a comparison with the smooth channel data.

Firstly, there are significant differences between the longitudinal distributions of i_s (figure 69a). In the first part of the bend, the intensity grows faster*) and reaches a higher maximum, whereas the gradual decay in the second half of the bend is considerably weaker, if present at all (near the bend exit, i_s shows rather a slight increase). On the other hand, the decay in the straight reach beyond the bend is considerably stronger, again.

Secondly, the outer sidewall layer in the transverse distribution of i_s is somewhat thinner in case of a rough bottom, though the reverse secondary circulation occurs, again. As a consequence, the cross-sectional maximum of i_s is higher and lies further outwards. Probably, the smaller lateral constraint that attends this thinner sidewall layer explains part of the smaller decrease of the

*) In contrast with the dept-averaged main velocity, the characteristic length of the longitudinal variations of i_s is proportional to C instead of C^2 (see Appendix I). Hence the growth of i_s is still faster for the rough bottom, but the differences are not as large as in the variation of the transverse distribution of $\bar{u}$ (see figure 68a).

secondary flow intensity in the second half of the bend. Neither the longitudinal nor the transverse distribution of the secondary flow intensity is reproduced quite correctly by the model. Apart from a considerable underestimation of i_s in the central part of the cross-section ($\gamma = 7$ and the 'k-ε-approximation' for $a'(\zeta)$ would have done better here, again), the considerable differences between the measured data for the smooth and the rough bottom are hardly found in the model results. The rate of growth of i_s in the first part of the bend is hardly larger and further on in the bend the two intensities hardly differ; the increase of i_s near the bend exit in the rough bottom case is not reproduced. On the other hand, the rate of decay in the second half of the bend is smaller for the rough bottom*) and the decay beyond the bend is considerably stronger, indeed.
The calculated transverse distributions of the secondary flow intensity hardly differ from the ones for the smooth bottom. The sidewall layers are still too thin, the reverse secondary circulation is not reproduced and the significant differences between the measured distributions for the smooth and the rough bottom are not found in the model results.
On comparing the measured vertical distributions of the transverse velocity component for the two flow cases (see figure 69c), the rough bottom distribution shows significantly smaller deformations in the bend, at least in the central part of the cross-section and in the outer wall region. The model predictions for the rough bottom correspond rather well with the measured data at this point. Only in the outer wall region, where the reverse secondary circulation occurs, quite deviant distri-

*) The cause of this smaller decay, however, is different from the one in the measured data. Here it is the smaller deformation of f, whereas in the measured data it is rather the smaller lateral constraint, the deformation of the measured f being even stronger than in the smooth bottom case (see figure 68b).

butions are found. As far as the rather concise and scattered measured data in the decay region beyond the bend allow for a conclusion, it seems as though the model exaggerates the deformation of $\frac{\partial q}{\partial \zeta}$ there (cf. Appendix I).
In summary, the foregoing leads to the conclusion that the smaller characteristic length of longitudinal variations is the only effect of roughening the bottom that is appropriately incorporated in the model.

9.2.5. Simulation of one of the IHHE-experiments

In spite of the rather negative conclusions as regards the performance of the present simplified model in case of sharply curved channels, it would be interesting to simulate one of the experiments in the sharply curved IHHE-flume (Rozovskii, 1961, see figure 70), because of the following reasons:

- Rozovskii's 'experiment no. 1' was simulated numerically with a fully three-dimensional model*) (Leschziner et al., 1978); this provides another possibility to compare the present model with a more extensive one;
- Rozovskii states that his secondary flow predictions, which are quite similar to the present ones, are rather good, especially for 'experiment no. 1' (see also De Vriend, 1976 & 1977);
- the simulation provides the possibility of testing the mathematical performance of the model (i.e. the convergence of the iteration procedures) under extreme conditions (cf. par. 4.4).

Therefore, it has been attempted to simulate Rozovskii's 'experiment no.1'.

The plan view of the IHHE-flume is shown in figure 70. It was 0.80 m wide and consisted of a 180° bend with a mean radius

*) Quite similar to the one used to simulate the experiments in the DHL-flume (par. 9.2.1) and in the LFM-flume (par. 9.2.4.1).

of curvature of 0.80 m, preceded and followed by straight reaches of which 0.80 m long parts are included in the simulation. In 'experiment no. 1' the discharge was 0.0123 m^3/s, with a depth of flow of about 0.06 m. Various computational grids and underrelaxation factors have been attempted, but in all cases the simulation failed because of ill-convergence of the iteration procedure for the main flow computation. Apparently, the effects of secondary flow convection were too strong to guarantee convergence of the similarity solution forming the basis of the model (cf. fully-developed laminar flow (par. 4.4), for which the similarity solution converges up to De = 40).

In spite of this failure of the main flow computation, it can be interesting to consider the results of the IHHE-experiments in the light of the conclusions drawn from the foregoing paragraphs.
One of the conclusions Rozovskii draws from his experiments is that the secondary flow in shallow curved channels with a smooth bottom is readily approximated by a theoretical expression based on a logarithmic distribution of the main velocity and a parabolic distribution of the turbulence viscosity (cf. expressions (6.8) and (6.14), respectively).

$$v_s = \frac{\bar{u}}{\kappa^2 r} \left| 2F_1(\zeta) + \frac{\sqrt{g}}{\kappa C} F_2(\zeta) - 2\left(1 - \frac{\sqrt{g}}{\kappa C}\right) \right| \qquad (9.7)$$

with $F_1(\zeta) = \int_{-1}^{\zeta} \frac{\ln(1+\zeta)}{\zeta} d\zeta$ and $F_2(\zeta) = \int_{-1}^{\zeta} \frac{\ln^2(1+\zeta)}{\zeta} d\zeta$.

Under the same conditions, the present model would yield a quite similar expression for fully-developed secondary flow (see also: De Vriend, 1976 & 1977):

$$v_s = \frac{\bar{u}}{\kappa^2 r}\left|2F_1(\zeta) + \frac{\sqrt{g}}{\kappa C}F_2(\zeta) - 2\left(1 - \frac{\sqrt{g}}{\kappa C}\right)\left\{1 + \frac{\sqrt{g}}{\kappa C} + \right.\right.$$

$$\left.\left. + \frac{\sqrt{g}}{\kappa C}\ln(1+\zeta)\right\}\right| \qquad (9.8)$$

The only difference between the two results arises from Rozovskii's assumption that the secondary flow slips along the bottom. Taking $\bar{\psi}Re_0$ as a measure for the secondary flow intensity, expression (9.7) yields

$$\bar{\psi}Re_0 = -\int_{-1}^{0} d\zeta \int_{-1}^{\zeta} v_s d\zeta = \frac{\bar{u}}{r}\frac{1}{4\kappa^2}\left(1 - \frac{1}{2}\frac{\sqrt{g}}{\kappa C}\right) \qquad (9.9)$$

and (9.8) leads to

$$\bar{\psi}Re_0 = \frac{\bar{u}}{r}\frac{1}{4\kappa^2}\left(1 - \frac{5}{2}\frac{\sqrt{g}}{\kappa C} + 2\frac{g}{\kappa^2 C^2}\right) \qquad (9.10)$$

For $C = 60\ m^{\frac{1}{2}}/s$ and $\kappa = 0.5$, as Rozovskii suggests, the intensity according to (9.9) amounts $0.95\ \frac{\bar{u}}{r}$, whereas (9.10) yields $0.76\ \frac{\bar{u}}{r}$.

As expected, Rozovskii's theory with its full-slip condition at the bottom yields significantly higher secondary flow intensities, even for a smooth bottom. So if expression (9.7) provides a good approximation of the secondary flow in Rozovskii's smooth bottom experiments, as this author states, expression (9.8) does not so. Still some caution should be exercised in concluding that (9.7) is preferable to the present model with its no-slip condition at the bottom. Firstly, neither the IHHE-experiments nor any of the experiments discussed before have yielded transverse velocity data so close to the bottom that they provide direct experimental evidence in favour of either distribution. Secondly, expression (9.7) in combination with the logarithmic main velocity distribution leads to infinite values of v_s/u at the bottom, i.e.

to a deviation angle of 90^{o} for the velocity vector at the bottom. As this is in contrast with numerous experimental observations, Rozovskii suggests to use the expression

$$\tan \alpha_v \simeq 11 \div 12 \frac{d}{R} \tag{9.11}$$

This corresponds rather with (9.8), which yields (De Vriend, 1976 & 1977)

$$\tan \alpha_v = \frac{2}{\kappa^2} \left(1 - \frac{\sqrt{g}}{\kappa C}\right) \frac{d}{R} \tag{9.12}$$

For $\kappa = 0.4$ and $C = 60\ m^{\frac{1}{2}}/s$, the constant of proportionality in this expression equals 10.9, but it should be pointed out that this value decreases rapidly for higher values of κ (for $\kappa = 0.5$, for instance, the constant becomes 7.2). The supposed variation of Von Karman's constant in a bend, however, will be considered later.

A third reason for caution in drawing conclusions from the IHHE-experiments in point of the applicability of (9.7) or (9.8) as an expression for v_s lies in the conditions on which these expressions are based, viz.:

- the main velocity distribution shows only minor deviations from the logarithmic distribution (6.8),
- the secondary flow is fully-developed and it is not influenced by lateral constraint.

Rozovskii states that the former condition is fulfilled in his shallow channel experiments (such as 'experiment no. 1'), provided that Von Karman's constant is raised to 0.5. On closer examination of the results of these experiments, however, the main velocity profile shows considerable deformations from vertical to vertical, not only in a cross-section, but also along the channel axis. These deformations are similar to the ones observed in the experiments discussed in the foregoing paragraphs (reduction near the surface, maximum below the surface, steeper gradients near the bottom). Obviously, they

are due to secondary flow convection and it seems an over-simplification to account for them by raising κ, even though this has globally the same effect on f as weak secondary flow convection (cf. Nouh, 1978)*).

In view of the observations in the LFM-experiments (par. 9.2.4), the second of the aforementioned conditions is not likely to be fulfilled in the IHHE-flume, either. Even though the flow in 'experiment no. 1' is somewhat shallower than in the LFM-flume ($\frac{d}{B}$ = 0.075 instead of 0.1), so that there may be a region where lateral constraint is negligible **), the secondary flow is not likely to reach its 'undisturbed' fully-developed stage anywhere in the flume***). Rozovskii recognizes that, even in the channel axis, the first part of the bend is needed for the secondary flow to develop, whereas in the second half of the bend a gradual decay of the intensity occurs. On the basis of the conclusions drawn from the experiments discussed before, the growth and decay regions must be expected to interact in the sharply curved IHHE-flume.

In view of these arguments it is concluded that experiments in sharply curved channels like the LFM-flume or the IHHE-flume cannot be used to verify ' undisturbed' secondary flow models like (9.7) or (9.8) (see also: Yen, 1965 & 1972; Engelund, 1974, Kikkawa et al., 1973; Ikeda, 1975 and many others).

---

*) A more legitimate reason for raising κ in a bend would be to account for an effect of curvature on turbulence, but then a more advanced turbulence model is preferable (cf. Rodi, 1978b).

**) In spite of the reverse secondary circulation near the outer wall, which was also observed in the IHHE-experiments.

***) If the bend would be infinitely long instead of 180°, the fully-developed secondary flow intensity would be smaller than the 'undisturbed' one as a consequence of main flow deformations and lateral constraint (cf. chapter 3).

9.2.6. On the mathematical prediction of the reverse secondary circulation

In all experiments considered in the foregoing, a reverse secondary circulation was observed in the upper part of the outer wall region. It is rather obvious that the present simplified model, with its predominant similarity approximation, does not reproduce this circulation. At the first glance, however, it seems surprising that the fully three-dimensional simulations (see also: Leschziner, 1978) yield no reverse circulation, either. Since the place and the shape of the additional vortex agree well with the ones in fully-developed laminar flow in curved rectangular ducts (cf. chapter 3), it seems obvious to suppose that they have essentially the same cause, viz. secondary flow convection. In that case the fully three-dimensional models used for the simulation ought to reproduce the second vortex in sharply curved flows with a strong convective interaction between the main and the secondary flow (cf. the full Navier-Stokes models of fully-developed curved laminar flow, mentioned in chapter 3). Since the reverse circulation can be important to river morphology (bank erosion, meandering), it is worthwhile to investigate where the three-dimensional models fail in this respect.

In principle, the reverse circulation can be suppressed by numerical effects; it can exist in the solution of the differential equations underlying the model, whereas discretization effects, such as artificial viscosity, suppress it in the actual model. As far as the simulation of the experiments in the DHL-flume and in the LFM-flume are concerned, this possibility is not excluded, since the computational grids were rather coarse, especially in the vertical, and grid-independence was tested only globally (only two grids were considered in either case; see De Vriend et al., 1981). In the simulation of the IHHE-experiment, however, a finer grid was chosen on the basis of grid-independence tests (Leschziner et al., 1978). Still the reverse circulation was not reproduced, not even for this sharply curved flume, in which the interaction between the main and the secondary flow must be strong (see also Rozovskii's measured data). Hence it is concluded that the absence of the reverse circulation from the

fully three-dimensional model predictions must have a physical background rather than a numerical one.

Another indication for a more complicated mechanism of the second vortex formation in turbulent flow is provided by the DHL-experiments (see De Vriend et al., 1977). Even in this mildly curved flume, in which the convective effects of the secondary flow were not quite strong, a distinct reverse circulation was found. Obviously, it is not the convective interaction alone that causes this circulation. This is the more probable as the additional vortex develops in the first part of the bend (see, for instance, De Vriend, 1979b), i.e. in a region where the flow is far from fully-developed and the influence of secondary flow convection is still establishing.

A secondary flow phenomenon that is typical for turbulent flow in non-circular ducts and cannot be described by models based on a scalar turbulence viscosity such as the ones discussed herein, is the secondary flow due to the anisotropy of turbulence (see, for instance, Gessner et al., (1965) and also par. 6.4 and 6.7). Although in shallow rectangular channels this secondary motion can involve a larger number of cells, the four principle ones are lying two by two along the sidewalls, in such a way that the flow along the bottom and along the sidewalls moves away from the corner and the flow at the surface moves away from the wall. This implies that, if this secondary flow would persist in a bend, the upper vortex near the outer wall would have the same sense of rotation as the observed reverse circulation, whereas the upper vortex near the inner wall would rather agree with the 'normal' secondary flow.

The secondary flow due to the anisotropy of turbulence cannot be the only cause of the reverse circulation. Firstly, the latter represents only one of the four principal cells of the former and the other three cells are not found as such in a bend. Secondly, the reverse circulation in a bend is considerably stronger than the circulation in the corresponding cell in a straight channel. In the DHL-flume, the reverse circulation was distinctly perceptible in the bend, but not in the upstream straight reach, and

similar observations were made in the LFM-experiments.
In view of these arguments, the most plausible explanation of the observed reverse circulation in a bend is the combined action of turbulence anisotropy and secondary flow convection. As became evident in chapter 3, a reverse circulation near the surface in the outer wall region of a rectangular channel bend tends to intensify itself through its convective interaction with the main flow, i.e. convection acts in a destabilizing manner there. In the other three corners, however, convection has a stabilizing effect. So upon entering a bend, three out of the four principal vortices of the secondary motion in fully-developed straight channel flow will vanish (cf. Shukry, 1949), either suppressed by the secondary flow due to curvature (lower inner wall) or incorporated in it (upper inner wall and lower outer wall). Only the one near the upper outer wall will persist and even grow stronger.
On the basis of this analysis, it is concluded that the reverse secondary circulation in turbulent flow through curved channels can only be described properly by a fully three-dimensional model in which the concept of a scalar turbulence viscosity is abandoned (Reece, 1977; see also Launder et al., 1972 and Rodi, 1978b) or at least modified in such a way, that the secondary flow due to turbulence anisotropy can be reproduced (Tatchell, 1975).

9.2.7. Discussion and conclusions

The main conclusion to be drawn from the verification of the present model for rectangular channels is that in developing curved flow the basic hypothesis of the model, the similarity hypothesis, fails as soon as the convective interaction between the main and the secondary flow becomes important. Obviously, the effect of secondary flow convection on the vertical distribution of the main velocity is not less important than the effect on the depth-averaged main velocity. If one is neglected, the other one cannot be reproduced correctly. This implies that

the deformations of the main velocity throughout the cross-section should be incorporated even in a simplified model. Hence such models become so expensive, that it must be doubted whether they are more economic than fully three-dimensional parabolic or partially-parabolic models*).

The negative conclusion on the applicability of the similarity hypothesis in developing turbulent flow in curved rectangular channels is in striking contrast with the positive conclusion for fully-developed laminar flow (see par. 4.4). At first sight, it is not clear whether this must be attributed to turbulence or rather to the developing character of the flow. A closer examination of the model results for developing laminar flow could provide more information at this point.

According to figure 48, the laminar flow simulation of the rough bottom experiments in the LFM-flume (Re = 125; C = 30 $m^{\frac{1}{2}}/s$; see figure 31) should represent the effects of secondary flow convection rather well, though it underestimates the main flow inertia. Therefore it makes sense to compare the results of this simulation with the ones from the turbulent flow model. When doing so, the laminar flow model appears to show the same shortcomings as the turbulent one in the first half of the bend: the effects of secondary flow convection on $\bar{u}$ are too strong and restricted to too narrow regions along the sidewalls. Since the main flow inertia is smaller, however, the laminar flow in the last part of the bend gets nearer to its fully-developed curved stage than the turbulent one. In this part of the bend, the local overestimation of the effects of secondary flow convection has vanished**). It seems as though the transverse distribution

---

*) Elliptic models are much more expensive (Rodi, 1978a), but the foregoing has made clear that longitudinal diffusion can readily be disregarded for the present type of flow.

**) Except for the peak in the outer wall region, which is also found in the similarity solution for fully-developed laminar flow.

of the depth-averaged main velocity tends to agree better with the measured data as the flow approaches its fully-developed curved stage. This suggests that the poorer performance of the model for developing turbulent flow must primarily be attributed to the developing character of the flow.

In addition to the general conclusion concerning the applicability of the similarity hypothesis, the foregoing verification yields a series of conclusions as to the performance of the model in predicting specific aspects of turbulent flow in curved channels of shallow rectangular cross-section. These conclusions can be summarized as follows.

- In bends with a limited angle of rotation, in which the flow does not reach its fully-developed curved stage, the predicted effects of secondary flow convection on the depth-averaged main velocity are concentrated too much along the sidewalls. Consequently, the depth-averaged main velocity distribution is described rather poorly for not too mildly curved channels, i.e. as soon as secondary flow convection becomes important. On the other hand, the outward skewing of the main velocity distribution at the bend exit and the gradual decay of the skewness in a straight reach downstream of the bend are described reasonably well.
- The cross-sectional non-uniformity of the deformations of the main velocity profile in a bend is hardly reproduced, since the most important cause of these deformations, secondary flow convection, is not appropriately incorporated. This avenges itself as soon as this convection grows important, not only in the vertical profile of the main velocity, but also in its depth-averaged distribution and in the secondary flow.
- The magnitude of the 'undisturbed' secondary flow intensity is reproduced appropriately, if the overall mean value and the vertical distribution of the turbulence viscosity are chosen correctly. Its growth and decay in the central part of a shallow, mildly curved channel is also described reasonably well. The transverse distribution of the secondary flow intensity, however, is essentially wrong, especially in thick layers along the side-

walls.

- The vertical distribution of the secondary flow reflects the errors in the main velocity profile. If the latter is correct, however, the former is also rather good, except for the outer wall region, where the reverse secondary circulation is not reproduced.
- The transverse pressure distribution is in fair agreement with the measured data. Small deviations are readily explained from errors in the transverse distribution of the main velocity.
- The magnitude of the bottom shear stress is closely related to the main velocity distribution. As the errors in the latter are even intensified in the former, the model predictions at this point become rather poor as soon as secondary flow convection grows important.
- The direction of the bottom shear stress highly depends on the secondary flow, so that it is properly described in the central part of shallow, mildly curved channels only.
- Only the most important effect of roughening the bottom, the smaller length scale of longitudinal variations, is reproduced in a satisfactory fashion.

In addition, it should be pointed out that the verification has provided no evidence for the turbulence model to be too simple for this type of flow.

The verification has given more insight into the quantitative aspects of developing turbulent flow in curved rectangular channels. Firstly, it has made clear that the main flow needs quite a long distance to become fully-developed, especially in case of a smooth bottom. The horizontal and vertical deformations of the main velocity take place so slowly, that even a 180^{o} bend is often not sufficient to reach the fully-developed stage (cf. Muramoto, 1965 & 1967). Even apart from these gradual deformations of the main velocity distribution, the secondary circulation has been shown to need a considerable distance to reach its full strength, as well. Besides, the interaction of the sidewall layers tends to reduce the secondary flow intensity in not too shallow channels, even in the central part of the cross-section, and a similar effect is observed if the

channel is not too mildly curved, so that the secondary flow convection causes considerable deformations of the main velocity vertical. Roughly speaking, 'undisturbed' secondary flow occurs only in long bends (say $\phi_{tot}/\varepsilon > 5C/\sqrt{g}$; Appendix I) of mild curvature (say $R_c/B > 5$) in shallow channels (say $B/d > 15$) at a sufficiently large distance from the sidewalls (say > 5d).

9.3. Verification for non-rectangular channels

9.3.1. Simulation of the non-rectangular channel experiments in the DHL-flume

In addition to the flat bed experiments discussed in par. 9.2.1., a similar series of experiments has been carried out in the DHL-flume with a fixed non-rectangular cross-section (De Vriend et al., 1978). To that end, the flat bottom of the original flume (see figure 51) was replaced by the bottom indicated in figure 71, i.e. with a configuration as can be expected in natural river bends. In the straight inflow section the bottom was made parabolic, such that

$$z_b = -0.84 \frac{y'}{B}\left(1 - \frac{y'}{B}\right) + 0.20 \text{ m} \quad \text{with} \quad y' = R - R_c + \frac{B}{2} \qquad (9.13)^*)$$

In the greater part of the bend, viz. beyond the cross-section at 27.5°, the bottom consisted of a point bar in the inner bend and a scour hole in the outer bend. The bottom level was given by

$$z_b = 1.625 \frac{y'}{B}\left(1.4 \frac{y'}{B} - 0.8\right) + 0.20 \text{ m} \quad \text{for} \quad y' \leq 0.4B \qquad (9.14)^*)$$

$$= 0.7\left(1 - \frac{y'}{B}\right)^2 + 0.20 \text{ m} \quad \text{for} \quad y' \geq 0.4B$$

---

*) Datum = bottom level in the straight reach of the original channel.

In the transition zone, between 0^o and 27^o, a gradual transition between (9.13) and (9.14) was attained by taking

$$z_b(\phi) = z_b(0^o) + (\frac{\phi}{27.5})^2 \{3 - 2 \frac{\phi}{27.5}\}\{z_b(27.5^o) - z_b(0^o)\} \qquad (9.15)$$

, in which the polar coordinate ϕ is expressed in degrees and $\phi = 0$ at the bend entrance.
For the bottom level described by (9.13) through (9.15) and a horizontal water surface lying more than 0.20 m above datum, the cross-sectional area is constant along the whole flume:

$$A_{cr} = 0.84 + 6(z_s - 0.20) \ m^2 \qquad (9.16)$$

In this non-rectangular channel, velocity and water surface measurements were made, in the same way as in the rectangular channel and under almost the same conditions. The water level was adjusted at about 0.25 m above datum (so $A_{cr} = 1.14 \ m^2$ vs. $1.50 \ m^2$ in the rectangular channel) and the two discharges ($Q = 0.45 \ m^3/s$ and $0.23 \ m^3/s$) were chosen such, that the overall mean velocities agreed with the ones in the rectangular channel case.

The numerical simulation of these experiments was carried out on a computational grid consisting of 25 cross-sections, 28 verticals in each cross-section and 20 steps in each vertical (cf. par. 9.2.1). In the mathematical model, the turbulence viscosity was chosen in conformity with the conclusions from par. 9.2.2, i.e. with $\gamma=7$ and the 'k-ε-approximation' for $a'(z)$. The results of the simulation and the measured data are shown in figures 72 through 74. In addition, the results of a simulation with a strongly simplified model by Kalkwijk et al. (1980) are shown in the same figures (see also Appendix K).
According to figure 72a, the depth-averaged main velocity is predicted fairly well. Only close to the outer wall and in the

transition zone, between the bend entrance and the cross-section at 27.5^{o}, the results of the computation show slight, but systematic deviations from the measured data. Figure 72a also shows that the strongly simplified model yields good predictions of $\bar{u}$, as well, and that it makes hardly any difference whether the depth-averaged turbulence viscosity is calculated from equation (8.102) or is taken directly proportional to $\bar{u}h$ in accordance with (8.32). This suggests that lateral diffusion is of minor importance here.

In the central part of the channel and in the inner bend, the deformations of the measured main velocity profiles are rather small (see figure 72b). Only near the outer bank somewhat stronger deformations of f are found, especially in the last part of the bend. As was stated before, only the deformations in the channel axis are incorporated in the present model, so that the ones in the outer bend are not reproduced. The predicted deformations in the channel axis show the same features as the measured ones, except for the transition zone, where too strong deformations are predicted. All deformations are so small, however, that they hardly provide a verification of the model at this point. Even the 'undisturbed' logarithmic distribution gives a rather good description of the main velocity profile here.

Both the measured and the calculated longitudinal distributions of the secondary flow intensity show a striking peak at the end of the transition zone (see figure 73a), which corresponds with the one in the longitudinal distribution of the source term $h\bar{u}/r_s$ shown in the same figure. The latter peak must be attributed mainly to the curvature of the streamlines, which tend to follow the deepest part of the channel. In the first half of the transition zone, this deepest part is almost straight (see figure 71a), but in the second half it is curved sharplier than the channel walls.

The overall magnitude of the secondary flow intensity is predicted reasonably well by the present model, but the decay of i_s beyond the transition zone is somewhat too strong in the channel axis and too weak in the outer bend. The same conclusions can be drawn

from the transverse distributions of i_s shown in figure 73b. In the transition zone, the measured secondary flow intensity reaches its maximum further outwards (13.8^o) or at about the same place (27.5^o) as the one predicted by the present model. Further downstream, however, the measured data show a considerable reduction of i_s in the outer bend: the peak in the deepest part of the channel is cut off, so that the maximum becomes somewhat smaller and lies further inwards.

The explanation of this phenomenon is the same as in the corresponding rectangular channel case (see par. 9.2.2): the deformations of the main velocity profile in the outer bend, or rather in the region with negative w_s, give rise to a reduction of the source of secondary flow and hence to smaller secondary flow intensities.

Figures 73a and 73b also make clear that the strongly simplified model underestimates the secondary flow intensity considerably, especially in the outer bend. Probably, this is the combined result of various errors. Firstly, the secondary flow in this model is based on a turbulence viscosity with $\gamma=6$ and purely parabolic $a'(\zeta)$, which yields too small values of i_s (cf. par. 9.2.2). Secondly, the secondary flow intensity is taken proportional to the local channel curvature 1/r rather than to the streamline curvature $-1/r_s$, which explains why the secondary flow intensity predicted by this model shows no peak at the end of the transition zone. Thirdly, errors in the longitudinal distribution of i_s are introduced by supposing the secondary flow to be determined by local main flow properties only. Hence the gradual growth of the secondary flow intensity in the first part of the bend is not reproduced and neither would be the gradual decay in an eventual straight reach beyond the bend.

Still this does not imply that the strongly simplified model must be rejected for the computation of the secondary flow. According to figure 73b, the shape of the transverse distribution of i_s is almost the same as the one resulting from the present model, which suggests that the role of lateral diffusion is unimportant here. In other words; on accepting the errors made by the present model, lateral

diffusion can be left out of consideration, as well. Besides, the greater part of the aforementioned errors can be eliminated by rather simple modifications of the model, as is shown in Appendix K.

Figure 73c shows that the predictions of the vertical distribution of the secondary flow are in good agreement with the measured data throughout the flume. The differences between the present model and the strongly simplified one (see expression (9.8)) are so small, that it is not possible to decide in favour of any of the two models at this point.

The transverse pressure distribution resulting from the present model gives a rather good description of the transverse configuration of the water surface in the second half of the bend (see figures 74a and 74b). In the first half, however, the transverse pressure drop is underestimated considerably*). On the other hand, the longitudinal distribution of this quantity shows the same features as the measured data, viz. a gradual increase in the transition zone and a slight decrease beyond it, both reflecting the longitudinal variation of the streamline curvature.

The overall magnitude of the transverse pressure drop predicted by the strongly simplified model is in better agreement with the measured data in the first half of the bend, but in the second half it is too large. Since the model uses the local curvature of the longitudinal coordinate lines (1/r) instead of the streamline curvature, the gradual growth and decay of the transverse pressure drop in the first half of the bend is not reproduced.

The conclusion to be drawn from the foregoing is that the present model yields satisfactory predictions of the main flow (and hence

---

*) Possibly, this is a consequence of an imperfection in the computational procedure, since the transverse pressure drop estimated by integrating the quantity u^2/r_s resulting from the model is larger than the one calculated by the model itself (0.194 vs. 0.158 at 27.5° in figure 74b).

of the magnitude of the bottom shear stress) in the mildly curved non-rectangular channel considered here. The predictions of the secondary flow (and hence of the direction of the bottom shear stress) are also reasonably good, although the secondary flow intensity in the outer bend is overestimated, since the model takes no account of the deformations of the main velocity profile there.
It has also become evident, however, that for the present channel the effort made to account for lateral diffusion and for the deformations of the main velocity profiles due to longitudinal accelerations is superfluous, since the strongly simplified model, in which these effects are disregarded, yields satisfactory results, as well. As is shown in Appendix K, some minor modifications enable this model to yield even secondary flow predictions of the same quality as the present one.

9.3.2. Simulation of the non-rectangular channel experiment in the IIHR-flume.

In the S-shaped flume described in par. 9.2.3 (see also figure 58), C.L. Yen (1967) carried out a series of movable bed experiments. To that end, the sloping sidewalls of the flume were replaced by vertical ones, in such a way that the channel width became 7 ft 8 in (2.34 m). After one of the experiments, the large scale configuration of the equilibrium bed (i.e. with the ripples and dunes smoothed out) was copied in mortar, to yield a fixed non-rectangular channel of 'natural' configuration (see figure 75a).
In Yen's report, this bottom configuration is given for the second half of the flume only. For the numerical computation, however, the bottom configuration is needed for the whole flume. Therefore, the channel geometry in the first bend is assumed to be similar to the one in the second bend and the bottom is taken horizontal in the upstream straight reach, with a smooth transition to the bend. The resulting bottom configuration is shown in figure 75b.
In this non-rectangular channel, extensive measurements were taken of the water surface configuration, the magnitude and the direction of the horizontal velocity vector, the bottom shear stress and the

longitudinal component of the turbulence intensity. Hence these experiments are suited for testing the present model in case of a non-rectangular channel with vertical sidewalls and alternating bends of rather strong curvature. Therefore, it was attempted to simulate C.L. Yen's Run 1 (d = 0.13 m; Q = 0.103 m^3/s with the present model.

The computational grid used in the simulation is similar to the one described in par. 9.2.3, but in the bends the number of cross-sections is 12 instead of 8, in order to have a more uniform longitudinal step size.
On the basis of the experience gained from the simulation of the flat bed experiment (par. 9.2.3), the turbulence viscosity in the mathematical model was slightly modified, with γ=6 instead of 7 and the k-ε-approximation of $\alpha'(z)$ maintained.
The depth-averaged main velocity distribution resulting from a first simulation *) is shown in figure 76. It seems as though the solution in the second bend has not quite converged, since spurious oscillations are found in $\bar{u}$ there. In the first bend, however, these oscillations are absent and the solution seems reliable. Therefore, the calculated distributions of $\bar{u}$ in the second bend have been smoothed and the distributions in the corresponding cross-sections of the first bend have been plotted, as well.
None of these distributions, however, is in good agreement with the measured data. The pronounced outward shift of the measured flow is not reproduced by the model, not even in the first bend, although the inflow distribution was taken uniform instead of skewed inwards**).
The dubious results for the second bend and the poor agreement with measured data make further comparisons with these data useless before the solution procedure has been improved. Even after this

*) i.e. with the same model as used to simulate the non-rectangular channel experiments in the DHL-flume (see par. 9.3.1).

**) In the experiments, the inflow distribution was adjusted in such a way, that the main velocity distribution at the bend entrances were globally similar.

has been done, however, the model can give rise to problems in this case. In the sidewall regions it will show the same shortcomings as in a rectangular channel, viz. too strong local effects of secondary flow convection and too little horizontal interaction, both in the main and in the secondary flow.
It should be noted that the strongly simplified model does not work for this case, either, unless it is modified essentially. The model in its present form accounts for the influence of secondary flow convection, but only as far as it is due to the transverse variation of the depth of flow. This approximation gives rise to problems for C.L. Yen's flume, whether the vertical sidewalls are considered as very steep banks or as slipping walls. In the former case, the depth of flow decreases very sharply on approaching the walls. As a consequence, the energy head and $\bar{u}$ increase exponentially along the outer wall of a bend (see Kalkwijk et al., 1980).
If the walls are assumed slipping, the depth of flow can increase or decrease throughout a cross-section, so that the vertical velocity component can be positive everywhere*). In that case, secondary flow convection reduces the energy head throughout the cross-section, whereas it ought to produce only a redistribution of the flow energy. Besides, the reduction of the energy head and the main velocity is strongest where the vertical velocity has its maximum, i.e. near the outer wall. Hence the convective effect of this secondary flow leads to an inwards shift of the main flow, whereas the opposite occurs in reality (see also De Vriend, 1976 & 1977).

9.3.3. Discussion and conclusions

It has become evident from the foregoing, that for a model of curved channel flow a proper description of the vertical component of the secondary flow is indispensable as soon as the convective influence of the secondary flow on the main flow becomes important. In rectangular channels, this vertical velocity component is concentrated

*) The vertical velocity component due to the transverse variation of the depth is positive when the depth increases towards the outer wall.

for the greater part in peaks near the sidewalls, where lateral diffusion is greatly important. The verification of the rectangular channel model has made clear that this sidewall peak in the vertical component of the secondary flow is described rather poorly by the present model. As a consequence, the rectangular channel model yields rather poor predictions of the main velocity redistribution due to secondary flow convection.

In non-rectangular channels, the transverse variation of the water depth also contributes to the vertical component of the secondary flow. If the bottom is sloping not too steeply, this contribution to w_s is hardly influenced by lateral diffusion and it is described well by the present model. This explains why the model works rather well for channels with mildly sloping banks, the contribution by the transverse variations of the water depth being predominant then. In that case, however, it is not necessary to incorporate lateral diffusion, so that the present model is too complicated (and expensive) then.

These considerations lead to the conclusion that the effort made in the present model to account for lateral diffusion and for the inversion of the secondary flow near vertical sidewalls is not quite effective. Even though the model yields rather good predictions of the 'undisturbed' main flow (i.e. not influenced by secondary flow convection; cf. the straight channel flow computations discussed in chapters 6 and 8), main velocity distributions with considerable influence of secondary flow convection are predicted rather poorly as soon as there are regions with important lateral diffusion. As was shown in par. 9.2.2, the most important cause of this failure lies in the three-dimensional interaction between the main and the secondary flow in the sidewall regions. Therefore, depth-averaged models with more sophisticated turbulence models are not likely to work much better than the present one. The best remedy is to make fully three-dimensional computations, either with a rather simple turbulence model like the present one or with a more extensive model like the one used in the fully three-dimensional computations for the DHL-flume and the LFM-flume.

This does not imply that depth-averaged models cannot be applied

at all. Most of the large natural rivers have mildly sloping banks, so that a strongly simplified model without lateral diffusion is applicable. On the other hand, most of the laboratory flumes used in curved flow research are provided with vertical sidewalls, which excludes the application of depth-averaged flow models. Only in case of an alluvial bottom, a modified version of the strongly simplified model can be applicable (see par. 8.9).

10. Conclusions and recommendations

As was stated in the Introduction, the present investigations had a twofold purpose, viz. to improve the insight into the flow phenomena in a river bend and to develop a simplified mathematical model yielding appropriate predictions of these phenomena. In this chapter, the most important conclusions will be resumed and their practical implications will be examined. Furthermore, recommendations for the practical utilization of the mathematical model and suggestions for further research will be given.

The present investigations have contributed to a better understanding of the essential features of flow in curved channels, both from a physical and a mathematical point of view. The physical and mathematical analysis of fully-developed curved laminar flow has proved to be suited for this purpose. In addition, the physical interpretation of the mathematical systems describing developing laminar and turbulent flow in curved channels has appeared very useful and the comparison of the results of various mathematical models with measured data and the analysis of the differences have been elucidative, as well.
This part of the work has yielded a large number of conclusions, the most important of which can be resumed as follows.

- The convective influence of the secondary flow in a bend can give rise to an important redistribution of the main flow. In rectangular channels, it is this effect that causes the main flow to shift gradually outwards on proceeding through a bend.
- The flow in curved channels with steep banks or vertical sidewalls is more complicated than the one in channels with mildly sloping banks where the depth of flow gradually decreases to zero. In the former case, the inner wall region, and hence lateral diffusion, plays a most important part in the redistribution of the main velocity and the secondary flow near the outer wall tends to form a small additional counterrotating cell.
- In curved channel flow, lateral interaction is much stronger than in a straight channel. Hence the influence of vertical sidewalls or steeps banks is present in a considerably larger part of the cross-section. A central region with negligible sidewall effects will be found only

for high channel aspect ratios. This is particularly true for the secondary flow, where the sidewall layers in not very shallow channels ($B/d < 15$) interact and reduce the maximum intensity.

The most conspicuous practical implications of these conclusions can be outlined as follows.

- The commonly used simplified computation methods for curved channel flow, disregarding sidewall effects and secondary flow convection, only hold good for very mildly curved flow ($d/R_c < 0.1 \frac{g}{C^2}$). In other cases, secondary flow convection should be taken into account. If, in addition, the channel has steep banks (slope > about 15^o), and especially if it is rectangular, the sidewall regions cannot be left out of consideration, either.
- Curved flow experiments in rather narrow flumes ($B/d < 15$) with vertical sidewalls or steep banks, which are rather common laboratory practice, are not quite suited to investigate the nature of flow in large natural river bends; the flow phenomena in such flumes are more complicated, which involves the unnecessary risk of misinterpretation.
- Hydraulic scale models of alluvial rivers are usually distorted, i.e. the vertical length scale factor is smaller than the horizontal one, in order to have a correct reproduction of the bottom friction. Apart from other scale effects, the narrowing of the channel due to this distortion can affect the secondary flow, especially if the channel aspect ratio becomes smaller than about 15.

The present investigations, however, have also raised the need of further investigations. The bottom shear stress, for instance, which plays a most important part in the interaction between the flow and the bed topography in alluvial channel bends, has hardly been investigated experimentally, at least in a reliable way. Also a proper understanding of the characteristics of turbulence in a bend, and how it influences the mean flow, is still lacking. In both cases, modern measuring techniques, such as laser-doppler anemometry, seem to offer important new prospects.

The development of a simplified mathematical model has not led to completely satisfactory results. Even though it has been approved for

fully-developed flow in straight as well as in curved shallow channels, the similarity hypothesis for the main and the secondary velocity components has appeared not very successful for developing curved flow with a strong interaction between the main flow and the secondary circulation. Since this hypothesis forms the basis of the simplifications in the mathematical model, this model shows important shortcomings in case of sharply curved channels with steep banks or vertical sidewall.

On the other hand, it should be pointed out that large natural rivers are mostly rather mildly curved ($R_c/B > 4$ to 5) and have a shallow cross-section ($B/d > 15$). For such channels, the model yields rather good predictions of the main flow and a reasonable description of the secondary circulation, even in case of vertical sidewalls. Moreover, the (expensive) refinements incorporated in the bottom shear stress computation step can be omitted for these channels. This applies in particular to channels with mildly sloping banks where the water depth gradually decreases to zero. Then the present model yields good predictions, both of the main and the secondary flow, but it appears unnecessarily complicated and expensive, since a drastically simplified and much more economic model yields results of the same quality then (see Appendix K).

In summary, the following recommendations for the practical use of mathematical models of curved channel can be given:

- if the channel is shallow ($B/d > 15$) and mildly curved ($R_c/B > 5$), without steep bottom slopes and with mildly sloping banks (slope < about 15^o) where the water depth gradually decreases to zero, the aforementioned strongly simplified model can be applied;
- in similar channels with steep banks and/or steep transverse bottom slopes, a simplified version of the present model, without refinements in the bottom shear stress computation step, will be applicable;
- in narrow and sharply curved channels with steeply sloping banks or vertical sidewalls, fully three-dimensional models have to be applied; such models are also indispensable if an accurate description of the main and the secondary flow near the outer bank is needed, such as, for instance, in a study of waste-water disposal in the outer bend or of bank erosion in freely meandering channels.

The most important points at which the mathematical modelling needs further extension are:

- the modelling of flow in non-rectangular channels with a steeply sloping or vertical outer bank (cf. par. 9.3.2); though this channel configuration is rather rare in large natural rivers, most of the laboratory experiments with a movable bed have been carried out in channels with vertical sidewalls; it would be inexpedient not to use the information gathered from such laborious experiments; it seems advisable not only to improve the present model at this point, but also to extend the strongly simplified model in such a way, that this kind of channels can be dealt with, without errors near the outer wall spoiling the predictions throughout the flume;
- generalization of the strongly simplified model to more arbitrary channel configurations (variable curvature, variable width), in order to extend its applicability to practical problems;
- extension of fully three-dimensional models to non-rectangular channels of arbitrary cross-sectional shape; as was stated before, such computations are sometimes indispensable in order to have reliable flow predictions; so far, however, they have only been reported for rectangular channels.

The strongly simplified model seems to offer good prospects for the mathematical prediction of the flow in large natural rivers and for incorporation in a larger model describing the bed formation in alluvial river bends. Measured data to verify this strongly simplified model, however, are hardly available. Hence there is a distinct need of velocity measurements in shallow, mildly curved laboratory flumes with mildly sloping banks and a bottom configuration as in natural rivers, preferably with a single bend and a long straight outflow section or with two or more consecutive bends.

In addition to these laboratory experiments, prototype measurements in large river bends are needed. So far, such measurements have concerned the main flow only, or at best the secondary flow is measured in a few single cross-sections, mostly in a rather primitive way. Recent advances in prototype measuring technique (acoustic or electromagnetic velocity measurements) provide the possibility of measuring

two or even three velocity components simultaneously. Adapting these techniques for measurements from a vessel and executing an extensive measuring programme in a large natural river bend would provide most valuable information, that can be of great use to the verification of mathematical models.

In summary, it can be stated that, though there is much work left to be done, the mathematical modelling of flow in curved shallow channels has come to the point where the flow models can be incorporated in a mathematical model of the bed formation in alluvial river bends.

ACKNOWLEDGEMENTS

The present investigations have been carried out in the Laboratory of Fluid Mechanics of the Delft University of Technology, Dept. of Civil Engineering. They form part of the river bend investigation project of the River Research Group in the joint hydraulics research programme T.O.W. (Toegepast Onderzoek Waterstaat), in which Rijkswaterstaat, the Delft Hydraulics Laboratory and the Delft University of Technology participate. By order of this organization, the experiments in the 'DHL-flume' have been carried out and elaborated at the 'De Voorst'-branch of the Delft Hydraulics Laboratory and the fully three-dimensional computations for the 'DHL-flume' and the 'LFM-flume' have been executed by CHAM Ltd., London and elaborated by the Delft Hydraulics Laboratory. The author is greatly indebted to T.O.W. for permitting him to incorporate the results in this thesis.
The kind of cooperation of the collegues in T.O.W., expecially F.G. Koch, C. Flokstra and J.J.M. van Haperen, is gratefully acknowledged.
Finally, the author wishes to thank E.O.F. Calle for developing some of the basic elements of the computer codes, D.C. Post and A.M. den Toom for conducting the experiments in the 'LFM-flume' and elaborating the results, W.F.J. Ritter and his staff for drawing the figures and Mrs. J. Theuns and Mrs. S.E.J. Oosterman for the laborious typing work.

REFERENCES

1. ADLER, M., 1934, Strömung in gekrümmten Rohren, ZAMM, 14, H.5,p.257
2. ALLEN, J., 1978, L. van Bendegom: a neglected innovator in meander studies, Can. Soc. of Petr. Geol., Memoir 5, p.199
3. ANANYAN, A.K., 1965, Fluid flow in bends of conduits, Israel Progr. for Scientific Transl., Jerusalem (orig. publ. in Russian, 1957)
4. ANANYAN, A.K., 1967, An approximate theory of secondary flows at the bend of the river course, Proc. XII-th IAHR-Congress, Fort Collins, Colorado, paper A52
5. ASFARI, A.F., 1968, Secondary flows in river bends, Unpublished thesis, London University
6. BENDEGOM, L. VAN, 1943, Spiral flow, Rijkswaterstaat, Studiedienst Bovenrivieren, Nota 43.5 (in Dutch)
7. BENDEGOM, L. VAN, 1947, Some considerations on river morphology and river improvement, De Ingenieur, 59, no.4, p. B1-11 (in Dutch) (Englisch transl.: Nat. Res. Council of Canada, Techn. Tr. 1054, 1963)
8. BEYERHAUS, E., 1922, Die Wirkungen einer Krümmung in offenen Wasserläufen auf Bewegungsvorgang und Bettgestaltung, Z.f.d.Bauwesen, 72, H.4-6, p.156
9. BLUE, F.L. Jr., HERBERT, J.K. and LANCEFIELD, R.L., 1934, Flow around a river bend investigated, Civil Engng., 4, no.5, p.258
10. BIRD, R.B., STEWART, W.E. and LIGHTFOOT, E.N., 1960, Transport phenomena, Wiley, New York/Toppan, Tokyo
11. BÖSS, P., 1934, Anwendung der Potentialtheorie auf die Bewegung des Wassers in gekrümmten Kanal- oder Flussstrecken, Der Bauingenieur, 15, H.25/26, p.251
12. BÖSS, P., 1938, Die Berechnung der Wasserbewegung in gekrümmten Flussstrecken mittels der Potentialtheorie und ihre Ueberprüfung durch Modellversuche, In: 'Wasser- und Geschiebebewegung in gekrümmten Flussstrecken', H. Wittmann und P. Böss, Springer, Berlin
13. BOUSSINESQ, J., 1868, Mémoire sur l'influence de frottement dans les mouvements réguliers des fluides; XII- Essai sur le mouvement permanent d'un liquide dans un canal horizontal à axe circulaire, J. de Math. Pures et Appl., 2ème Série, Tome XIII, p.413
14. BRADSHAW, P., 1976, Complex turbulent flows, In: 'Theoretical and Applied Mechanics', W.T. Koiter (ed.), North-Holland Publ. Comp., Amsterdam
15. BUILTJES, P.J.H., 1981, Velocity distributions in channels with various bottom profiles, TNO, Afd. Maatsch. Techn., Rept. 81-01462 (in Dutch)
16. CALLANDER, R.A., 1978, River Meandering, Ann. Rev. Fluid Mech., 10, p.129
17. CHENG, K.C. and AKIYAMA, M., 1970, Laminar forced convection heat transfer in curved rectangular channels, Int. J. Heat Mass Transfer, 13, p.471
18. CHENG, K.C., LIN, R.-C. and OU, J.-W., 1976, Fully developed laminar flow in curved rectangular channels, Trans. ASME, J. Fluids Engng., 98, series I, no.1, p.41
19. CHOUDHARY, U.K., 1979, Pattern of longitudinal velocity distribution in curved channels, J. Inst. Engrs., India, Civil Eng. Div., 59, p.231
20. CHOUDHARY, U.K. and NARASIMHAN, S., 1977, Flow in 180° open channel rigid boundary bends, Proc. ASCE, J. Hydr. Div., 103, HY6, p.651

21. CHOW, V.-T., 1959, Open channel hydraulics, McGraw-Hill, New York
22. DEAN, W.R., 1927, Note on the motion of fluid in a curved pipe, Phil. Mag., S7, 4, no.20, p.208
23. DEAN, W.R., 1928a, The stream-line motion of fluid in a curved pipe, Phil. Mag., S7, 5, no.30, p.673
24. DEAN, W.R., 1928b, Fluid motion in a curved channel, Proc. Royal Soc., A121, no.787, p.402
25. EINSTEIN, H.A. and HARDER, J.A., 1954, Velocity distribution and the boundary layer at channel bends, Trans. AGU, 35, no.1, p.144
26. ENGELUND, F., 1964, A practical approach to self-preserving turbulent flow, Acta Polytechn. Scand., Ci 27
27. ENGELUND, F., 1974, Flow and bed topography in channel bends, Proc. ASCE, Jnl. Hydr. Div., 100, HY11, p.1631
28. EUSTICE, J., 1911, Experiments on streamline motion in curved pipes, Proc. Royal Soc., A85, p.119
29. FALCON, M.A., 1979, Analysis of flow in alluvial channel bends, Ph.D. thesis, University of Iowa, Iowa (USA)
30. FARGUE, L., 1908, La forme du lit des rivières a fond mobile, Gauthier-Villars, Paris
31. FOX, J.A. and BALL, D.J., 1968, The analysis of secondary flow in bends in open channels, Proc. Inst. Civil Engrs., 39, p.467
32. FRANCIS, J.R.D. and ASFARI, A.F., 1971, Velocity distributions in wide curved open-channel flows, J. Hydr. Res., 9, no.1, p.73
33. GERARD, R., 1978, Secondary flow in noncircular conduits, Proc. ASCE, J. Hydr. Div., 104, HY5, p.755
34. GESSNER, F.B. and JONES, J.B., 1965, On some aspects of fully-developed turbulent flow in rectangular channels, J. Fluid Mech., 23, pt.4, p.689
35. GHIA, K.G. and SOKHEY, J.S., 1977, Laminar incompressible viscous flow in curved ducts of regular cross-section, Trans. ASME, J. Fluid Engng., 99, series I, p.640
36. GÖRTLER, H., 1941, Ueber eine dreidimensionale Instabilität laminarer Grenzschichten an konkaven Wänden, ZAMM, 21, p.250
37. GOSMAN, A.D. and PUN, W.M., 1973, Calculation of recirculating flow, Imp. College, London, Heat-Transfer Report no. HTS/74/2
38. GÖTZ, W., 1975, Sekundärströmungen in aufeinander folgenden Gerinnekrümmungen, Univ. Fredericiana, Karlruhe, Mitt. Theodor-Rehbock-Flussbaulaboratorium, Heft 163
39. HARRINGTON, R.A., KOUWEN, N. and FARQUHAR, G.J., 1978, Behaviour of a hydrodynamic finite element model, Proc. Second Int. Conf. on Finite Elements in Water Resources, Imp. College, London
40. HINDERKS, A., 1927, Nebenströmungen in gekrümmten Kanälen, VDI Zeitschrift, 71, no.51, p.1779
41. HINZE, J.O., 1975, Turbulence, McGraw-Hill, New York
42. HOWARD, J.H.G., PRATAP, V.S. and SPALDING, D.B., 1975, Measurements of the turbulent flow in a rectangular curved duct, Imp. College, London, Mech. Engng. Dept., Report HTS/75/18
43. HUMPHREY, J.A.C., TAYLOR, A.M.K. and WHITELAW, J.H., 1977, Laminar flow in a square duct of strong curvature, J. Fluid Mech., 83, pt.3, p.509
44. HUNT, I.A. and JOUBERT, P.N., 1979, Effect of small streamline curvature on turbulent duct flow, J. Fluid Mech., 91, pt.4, p.633
45. IKEDA, S., 1975, On secondary flow and bed profile in alluvial curved open channel, Proc. XVI-th IAHR-Congress, Sao Paulo, Brasil, paper B14

46. ITO, H., 1951, Theory on laminar flow through curved pipes of elliptic and rectangular cross-section, Rep. Inst. High Speed Mech., Tohoku University, Japan, 1, p.1
47. JANSEN, P.Ph. (ed.), 1980, Principles of River Engineering, Pitman Publishing Ltd, London
48. JOBSON, H.E. and SAYRE, W.W., 1970, Vertical transfer in open channel flow, Proc. ASCE, J. Hydr. Div., 96, HY3, p.703
49. JOSEPH, B., SMITH, E.P. and ADLER, R.J., 1975, Numerical treatment of laminar flow in helically coiled tubes of square cross-section, AIChE Journal, 21, no.5, p.965
50. KALKWIJK, J.P.Th. and DE VRIEND, H.J., 1980, Flow in rivers with arbitrary alignment, IAHR-Symp. on River Engng., Belgrado, paper D13
51. KALKWIJK, J.P.Th. and DE VRIEND, H.J., 1980, Computation of the flow in shallow river bends, J. Hydr. Res., 18, no.4, p.327 (also: Comm. on Hydraulics, Delft Univ. of Techn., Rept. 80-1)
52. KARAUSHEV, A.V., 1946, Distribution of velocities and coefficients of turbulent exchange along the vertical, GCI Proc., 56, no.2 (ref. from Rozovskii, 1961)
53. KIKKAWA, H., IKEDA, S., OKKAWA, H. and KAWAMURA, Y., 1973, Secondary flow in a bend of turbulent stream, Proc. JSCE, 219, p.107 (see also: Trans. JSCE, 5(1973), p.100)
54. KUIPERS, J. and VREUGDENHIL, C.B., 1973, Calculation of two-dimensional horizontal flow, Delft Hydraulics Laboratory, Rept. S163, part I
55. LANDAU, L.D. and LIFSCHITZ, E.M., 1975, Fluid Mechanics, Pergamon Press, Oxford
56. LAUFER, J., Investigations of turbulent flow in a two-dimensional channel, NACA Report 1053
57. LAUNDER, B.E. and SPALDING, D.B., 1972, Mathematical models of turbulence, Academic Press, London
58. LAUNDER, B.E. and SPALDING, D.B., 1974, The numerical calculation of turbulent flows, Comp. Meth. in Appl. Mech. and Engng., 3, p.269
59. LEOPOLD, L.B., WOLMAN, M.G. and MILLER, J.P., 1964, Fluvial processes in geomorphology, San Francisco
60. LESCHZINER, M., 1978, Einführung in numerische Verfahren zur Lösung der partiellen Differentialgleichungen, In: 'Numerische Berechnung turbulenter Strömungen in Forschung und Praxis', Hochschulkursus Univ. Karlsruhe, Vorl. 7
61. LESCHZINER, M. and RODI, W., 1979, Calculation of strongly curved open channel flow, Proc. ASCE, J. Hydr. Div., 105, HY10, p.1297 (also: Univ. Karlsruhe, Report SFB80/T/126, May 1978)
62. LEUTHEUSSER, H.J., 1963, Turbulent flow in rectangular ducts, Proc. ASCE, J. Hydr. Div., 89, HY3, p.1
63. LIGGETT, J.A., CHIU, C.-L. and MIAO, L.S., 1965, Secondary currents in a corner, Proc. ASCE, J. Hydr. Div., 91, HY6, p.99
64. LOMAX, H. and STEGER, J.L., 1975, Relaxation methods in fluid mechanics, Ann. Rev. of Fluid Mech., 7, p.63
65. LUNDGREN, H. and JONSSON, G., 1964, Shear and velocity distribution in shallow channels, Proc. ASCE, J. Hydr. Div., 90, HY1, p.1
66. McGUIRK, J., 1978, Numerische Verfahren für dreidimensionale Strömungen, In: 'Numerische Berechnung turbulenter Strömungen in Forschung und Praxis', Hochschulkursus Univ. Karlsruhe, Vorl. 9
67. MORI, Y. and NAKAYAMA, W., 1965, Study on forced convective heat transfer in curved pipes (1st report, laminar region), Int. J. Heat and Mass Transfer, 8, p.67

68. MORI, Y. and NAKAYAMA, W., 1967, Study on forced convective heat transfer in curved pipes, Int. J. Heat Mass Transfer, 10, p.37
69. MORI, Y., UCHIDA, U. and UKON, T., 1971, Forced convective heat transfer in a curved channel with a square corss-section, Int. J. Heat Mass Transfer, 14, p.1787
70. MURAMOTO, Y., 1965, Flow through curved open channels; Part I- On Characteristics of upper layer in fully developed region, Bull. Dis. Prev. Res. Inst., 14, pt.2, p.1
71. MURAMOTO, Y., 1967, Secondary flows in curved open channels, Proc. XII-th IAHR-Congress, Fort Collins, Colorado, paper A53
72. NAKAGAWA, H., NEZU, I. and UEDA, H., Turbulence of open channel flow over smooth and rough beds, Proc. JSCE, 241, p.155
73. NAYFEH, A.H., 1973, Perturbation methods, Wiley, New York
74. NEE, V.W. and KOVASZNAY, L.S.G., 1969, Simple phenomenological theory of turbulent shear flows, Physics of Fluids, 12, no.3, p.473
75. NIEMEYER, G., 1969, Efficient simulation of nonlinear steady flow, Proc. ASCE, J. Hydr. Div., 105, HY3, p.185
76. NISHI, M., SENOO, Y. and TERAZONO, M., 1974, Measurement of local wall friction force exerted by skewed turbulent boundary layers by means of an improved Preston tube, Bull. JSME, 17, no.113, p.1447
77. NOUH, M.A., 1978, Stochastic prediction of shear stress distributions at the bed of open channel bends, Ph.D. thesis, Univ. of Ottawa, Can.
78. NOUH, M.A. and TOWNSEND, R.D., 1979, Shear stress distribution in stable channel bends, Proc. ASCE, J. Hydr. Div., 105, HY10, p.1233
79. PARKER, G., 1976, On the cause and characteristic scales of meandering and braiding rivers, J. Fluid Mech., 76, pt.3, p.457
80. PATANKAR, S.V., 1975, Numerical prediction of three-dimensional flows, In: 'Studies in convection; theory, measurement and applications', B.E. Launder (ed.), Academic Press, London
81. PATANKAR, S.V., PRATAP, V.S. and SPALDING, D.B., 1974, Prediction of laminar flow and heat transfer in helically coiled pipes, J. Fluid Mech., 62, pt.3, p.539
82. PATANKAR, S.V., PRATAP, V.S. and SPALDING, D.B., 1975, Prediction of turbulent flow in curved pipes, J. Fluid Mech., 67, pt.3, p.583
83. PATANKAR, S.V. and SPALDING, D.B., 1972, A calculation procedure for heat, mass and momentum transfer in three-dimensional parabolic flows, Int. J. Heat Mass Transfer, 15, p.1787
84. PRAAGMAN, N., 1979, Numerical solution of the shallow water equations by a finite element method, Doct. thesis, Delft Univ. of Techn.
85. PRANDTL, L., 1925, Ueber die ausgebildete Turbulenz, ZAMM, 5, p.136
86. PRANDTL, L., 1952, Essentials of Fluid Dynamics, Blackie, London
87. PRATAP, V.S., 1975, Flow and heat transfer in curved ducts, Imp. Coll., London, Dept. Mech. Engng., Ph.D. thesis HTS/75/25
88. PRATAP, V.S. and SPALDING, D.B., 1975, Numerical computations of the flow in curved ducts, Aeron. Quart., 26, pt.3, p.219
89. PRATAP, V.S. and SPALDING, D.B., 1967, Fluid flow and heat transfer in three-dimensional duct flows, Int. J. Heat Mass Transfer, 19, p.1183
90. RAO, K.V., 1975, Secondary flow in a curved channel as revealed by a laser Doppler anemometer, Proc. LDA-Symp., Copenhagen, p.710
91. RASTOGI, K. and RODI, W., 1978, Predictions of heat and mass transfer in open channels, Proc. ASCE, J. Hydr. Div., 104, HY3, p.397
92. REECE, G.J., A generalized Reynolds-stress model of turbulence, Ph.D. thesis, Univ. of London
93. REYNOLDS, A.J., 1974, Turbulent flows in engineering, Wiley, London

94. ROACHE, P.J., 1972, Computational fluid dynamics, Hermosa Publishers, Albuquerque, New Mexico
95. RODI, W. (ed.), 1978a, Numerische Berechnung turbulenter Strömungen in Forschung und Praxis, Hochschulkursus Univ. Karlsruhe
96. RODI, W., 1978b, Turbulence models and their application in hydraulics; a state of the art review, Univ. Karlsruhe, Rept. SFB80/T/127
97. ROUSE, H., 1961, Fluid mechanics for hydraulic engineers, McGraw-Hill, New York
98. ROUSE, H., 1965, Advanced mechanics of fluids, Wiley, New York
99. ROUSE, H., 1970, Work-energy equation for the streamline, Proc. ASCE, J. Hydr. Div., 96, HY5, p.1179
100. ROZOVSKII, I.L., 1961, Flow of water in bends of open channels, Israel Progr. for Scientific Transl., Jerusalem (orig. publ. 1957)
101. SCHLICHTING, H., 1951, Boundary layer theory, Braun, Karlsruhe (English edition: McGraw-Hill, New York, 1968)
102. SHUKRY, A., 1949, Flow around bends in an open flume, Proc. ASCE, 6, p.713 (also: Trans. ASCE, 115(1950), p.751)
103. SIEBERT, W. and GÖTZ, W., 1975, A study on the deformation of secondary flow in models of rectangular meandering channels, Proc. XVI-th IAHR-Congress, Sao Paulo, Brasil, paper B19
104. SMITH, F.T., 1976, Steady motion within a curved pipe, Proc. Royal Soc., A347, p.345
105. SUTMULLER, A.M. and GLERUM, H.L., 1980, Description and evaluation of measurements in a curved channel model with a sand bottom, Delft Univ. of Techn., Dept. of Civil Engng., River Engng. Group, Rept. 14.71.01.01.01.
106. TATCHELL, D.G., 1975, Convection processes in confined three-dimensional boundary layers, Ph.D. thesis, University of London
107. TAYLOR, G.I., 1923, Stability of a viscous liquid contained between two rotating cylinders, Phil. Trans., A223, p.289
108. TAYLOR, G.I., 1929, The criterion for turbulence in curved pipes, Proc. Royal Soc., A124, p.243
109. THOMSON, J., 1876, On the origin of windings of rivers in alluvial plains, with remarks on the flow of water in bends in pipes, Proc. Royal Soc., A25, p.5
110. THOMSON, J., 1877, Experimental demonstration in respect to the origin of windings in rivers in alluvial plains and the mode of flow of water around bends in pipes, Proc. Royal Soc., A26, p.356
111. THOMSON, J., 1879, On the flow of water round river bends, Proc. Inst. Mech. Engrs., p.456
112. TRACY, H.J., 1965, Turbulent flow in a three-dimensional channel, Proc. ASCE, Jnl. Hydr. Div., 91, HY6, p.9
113. UEDA, H., MÖLLER, R., KOMORI, S. and MIZUSHINA, T., 1977, Eddy diffusivity near the free surface of open channel flow, Int. J. Heat Mass Transfer, 20, no.11, p.1127
114. VAN DYKE, M., 1975, Perturbation methods in fluid mechanics, Stanford Parabolic Press (1st ed. Academic Press, New York, 1964)
115. VANONI, V.A., 1941, Velocity distribution in open channels, Civil Engng., 11, no.6, p.356
116. VANONI, V.A., 1944, Transportation of suspended sediment by water, Proc. ASCE, 70, no.6, p.793 (also: Trans. ASCE, 111, p.67)
117. VRIEND, H.J. DE, 1973a, Theory of viscous flow in curved shallow channels, Comm. on Hydraulics, Delft Univ. of Techn., Rept. 72-1
118. VRIEND, H.J. DE, 1973b, Theory of viscous flow in wide curved open channels, Proc. Int. Symp. River Mech., Bangkok, Thailand, paper A17

119. VRIEND, H.J. DE, 1976, A mathematical model of steady flow in curved shallow channels, Comm. on Hydraulics, Delft Univ. of Techn., Rept. 76-1
120. VRIEND, H.J. DE, 1977, A mathematical model of steady flow in curved shallow channels, J. Hydr, Res., 15, no. 1, p.37
121. VRIEND, H.J. DE, 1978a, Fully developed laminar flow in curved ducts, Delft Univ. of Techn., Dept. of Civil Engng., Lab. of Fluid Mech., Internal Rept. 2-78
122. VRIEND, H.J. DE, 1978b, Developing laminar flow in curved rectangular channels, Delft Univ. of Techn., Dept. of Civil Engng., Lab. of Fluid Mech., Internal Rept. 6-78
123. VRIEND, H.J. DE, 1978c, Accuracy of measurements in a curved open channel, Delft Hydr. Lab./Delft Univ. of Techn., TOW-report R657-VII/M1415-III
124. VRIEND, H.J. DE, 1979a, Steady turbulent flow in curved rectangular channels, Delft Univ. of Techn., Dept. of Civil Engng., Lab. of Fluid Mech., Internal Rept. 5-79
125. VRIEND, H.J. DE, 1979b, Flow measurements in a curved rectangular channel, Delft Univ. of Techn., Dept. of Civil Engng., Lab. of Fluid Mech., Internal Rept. 9-79
126. VRIEND, H.J. DE, 1979c, Streamline curvature and bed resistance in shallow water flow, Delft Univ. of Techn., Dept. of Civil Engng., Lab. of Fluid Mech., Internal Report 1-79
127. VRIEND, H.J. DE, 1981a, Steady turbulent flow in curved shallow channels of non-rectangular cross-section, Delft Univ. of Techn., Dept. of Civil Engng., Lab. of Fluid Mech., Internal Rept. (to appear)
128. VRIEND, H.J. DE, 1981b, Flow measurements in a curved rectangular channel; Part II- rough bottom, Delft Univ. of Techn., Dept. of Civil Engng., Lab. of Fluid Mech., Internal Rept. (to appear)
129. VRIEND, H.J. DE, 1981c, Velocity redistribution in curved rectangular channels, to appear in the J. of Fluid Mech.
130. VRIEND, H.J. DE and KOCH, F.G., 1977, Flow of water in a curved open channel with a fixed plane bed, Delft Hydr. Lab./Delft Univ. of Techn., TOW-rept. R657-V/M1415-I
131. VRIEND, H.J. DE and KOCH, F.G., 1978, Flow of water in a curved open channel with a fixed uneven bed, Delft Hydr. Lab./Delft Univ. of Techn., TOW-rept. R657-VI/M1415-II
132. VRIEND, H.J. DE and KOCH, F.G., 1981, Fully three-dimensional computations of steady turbulent flow in curved rectangular channels, TOW-rept. R657-X/R1631
133. WESSELS, A.C.E., 1980, The micropropeller, Delft Hydr. Lab., Res. Rept. S73 part II (in Dutch)
134. WHITE, C.M., 1929, Streamline flow through curved pipes, Proc. Royal Soc., A123, p.645
135. YEN, B.C., 1965, Characteristics of subcritical flow in a meandering channel, Rept. Inst. Hydr. Res., Univ. of Iowa
136. YEN, B.C., 1967, Some aspects of flow in meandering channels, Proc. XII-th IAHR-Congress, Fort Collins, Colorado, paper A57
137. YEN, B.C., 1972, Spiral motion of developed flow in wide curved open channels, In: 'Sedimentation', H.W. Shen (ed.), Univ. of California, Berkeley, California
138. YEN, C.L., 1967, Bed configuration and characteristics of subcritical flow in a meandering channel, Ph. D. thesis, Univ. of Iowa

139. YEN, C.L., 1970, Bed topography effect on flow in a meander, Proc. ASCE, J. Hydr. Div., 96, HY1, p.57
140. YEN, C.L. and YEN, B.C., 1971, Water surface configuration in channel bends, Proc. ASCE, J. Hydr. Div., 97, HY2, p.303
141. ZIMMERMANN, C., 1974, Sohlausbildung, Reibungsfaktoren und Sediment-transport in gleichförmich gekrümmten und geraden Gerinnen, Dissertation, Univ. Karlsruhe

Samenvatting

Als bijdrage in de ontwikkeling van een wiskundig model van de stroming en de bodemligging in rivierbochten, wordt een fysische en wiskundige analyse gemaakt van permanente stroming in gekromde waterlopen en wordt een berekeningsmethode voor deze stroming ontwikkeld.
Na de formulering en de normalisatie van het stelsel differentiaalvergelijkingen dat de stroming in zijn algemeenheid beschrijft (hoofdstuk 2), volgt een analyse van volledig ontwikkelde laminaire stroming in gekromde rechthoekige leidingen, gebaseerd op berekeningen met de volledige Navier-Stokes vergelijkingen voor dit geval (hoofdstuk 3). Deze analyse leidt tot de conclusie, dat de convectie van impulsie in dwarsrichting, die het gevolg is van de secundaire stroming, kan leiden tot aanzienlijke vervormingen van de hoofdsnelheidsverdeling: het maximum van de hoofdsnelheid krijgt daardoor de neiging zich te verplaatsen van de binnen- naar de buitenbocht en van de waterspiegel naar beneden. Het blijkt dat de mate van vervorming toeneemt met het Deangetal, gedefiniëerd als het produkt van het Reynoldsgetal en de wortel uit de diepte-straal-verhouding. Bovendien blijkt dat andere kromingseffekten, zoals de 'bochtweerstand', kunnen worden verklaard uit deze herverdeling van de hoofdsnelheid.
In hoofdstuk 3 wordt verder aangetoond, dat in gekromde rechthoekige kanalen met name het binnenwandgebied een belangrijke rol speelt in het herverdelingsproces van de hoofdstroom. Daardoor zijn de gebruikelijke 'ondiep-water-benaderingen', waarin de wandgebieden buiten beschouwing blijven, niet toepasbaar voor de stroming in niet al te flauw gekromde rechthoekige kanalen, zelfs al zijn deze ondiep. Dit wordt nader geïllustreerd en uitgewerkt in hoofdstuk 4, waar ook een aantal andere vereenvoudigde berekeningswijzen voor volledig ontwikkelde laminaire stroming in ondiepe, rechthoekige, gekromde leidingen wordt onderzocht. Een rekenmethode op basis van gelijkvormigheidsveronderstellingen voor hoofd- en secundaire stroming blijkt daarbij goed te voldoen.
In hoofdstuk 5 worden hoofd- en secundaire stroming in zich ontwik-

kelende bochtstroming eenduidig gedefiniëerd en worden de gelijkvormigheidsveronderstellingen uit hoofdstuk 4 toegepast op de hoofd- en secundaire snelheidsverdelingen. Op basis hiervan wordt, naar analogie van de eerder genoemde rekenmethode voor volledig ontwikkelde bochtstroming, een rekenmodel opgezet voor zich ontwikkelende laminaire stroming in bochtige kanalen met rechthoekige dwarsdoorsnede. Enkele van de belangrijkste vereenvoudigende veronderstellingen, die aan dit model ten grondslag liggen, worden via een gevoeligheidsonderzoek getoetst, hetgeen leidt tot de conclusie dat de berekening van het over de diepte gemiddelde hoofdsnelheidsveld beter losgekoppeld kan worden van de berekening van de grootte en de richting van de bodemschuifspanning, aangezien de laatste hogere eisen stelt aan de beschrijving van de hoofdsnelheidsvertikaal en de secundaire stroming. Tenslotte leidt een globale en kwalitatieve toetsing van het model aan in turbulente stroming gemeten verdelingen van de over de diepte gemiddelde hoofdsnelheid tot bemoedigende resultaten.

Om de volgende stap naar een rekenmodel van de stroming in een rivierbocht te kunnen maken, moet een adekwaat turbulentiemodel geformuleerd worden. Ervan uitgaande dat dit model zo eenvoudig mogelijk moet zijn, wordt in hoofdstuk 6 een turbulentiemodel ontwikkeld op basis van een mengweghypothese. Bij toetsing aan metingen in rechte kanalen met ondiepe, rechthoekige dwarsdoorsnede blijkt dit model goed te voldoen. Verder wordt in dit hoofdstuk met behulp van een gevoeligheidsanalyse de invloed van de belangrijkste veronderstellingen in het turbulentiemodel nagegaan. Daaruit blijkt, dat de intensiteit van de secundaire stroming in een bocht erg gevoelig is voor het gemiddelde van de turbulentieviscositeit en voor de vertikale verdeling van deze grootheid.

Met behulp van dit turbulentiemodel en naar analogie van het rekenmodel voor zich ontwikkelende laminaire stroming, wordt in hoofdstuk 7 een vereenvoudigd wiskundig model ontwikkeld van turbulente stroming in bochtige kanalen met ondiepe rechthoekige dwarsdoorsnede. Evenals in hoofdstuk 5, worden de belangrijkste vereenvoudigende veronderstellingen getoetst via een gevoeligheids-

onderzoek. Een eerste globale vergelijking met laboratoriummetingen geeft aanleiding tot gematigd optimisme ten aanzien van de werking van het model.

Als (voorlopig) laatste stap naar een wiskundig model van de stroming in een rivierbocht wordt, voortbouwend op hoofdstuk 7, het model gegeneraliseerd naar waterlopen met min of meer willekeurig gevormde, ondiepe dwarsdoorsnede. Dit wordt bereikt door de dwarsdoorsnede te transformeren tot een rechthoek. Hoewel dit aanleiding geeft tot extra termen in de differentiaalvergelijkingen, verandert de aard van het wiskundige stelsel niet en kan wezenlijk dezelfde oplossingsprocedure als in hoofdstuk 7 gehanteerd worden. Bij toetsing aan metingen in rechte kanalen met trapeziumvormige dwarsdoorsnede blijkt echter, dat het turbulentiemodel wel enige aanpassing behoeft. Dit kan eenvoudig worden opgevangen door het introduceren van laterale diffusie in de turbulentieviscositeit.

In hoofdstuk 9 wordt het ontwikkelde model getoetst aan verscheidene laboratoriumexperimenten en aan de resultaten van een volledig driedimensionale wiskundige simulatie van twee van deze experimenten. Voor ondiepe en flauw gekromde waterlopen blijkt het model goed te werken, maar het vertoont ernstige gebreken bij minder ondiepe en scherper gekromde stroming. Uit een analyse van deze gebreken blijkt, dat de gelijkvormigheidshypothesen die aan het model ten grondslag liggen niet opgaan voor zich ontwikkelende gekromde stroming met een sterke interaktie tussen hoofd- en secundaire stroming. Dit ondanks het feit, dat deze hypothesen wel voldoen in volledig ontwikkelde gekromde stroming, ook bij hogere Deangetallen. Het opheffen van dit bezwaar, zoal mogelijk, maakt het rekenmodel zo duur, dat voor dergelijke gevallen evengoed volledig driedimensionale berekeningen gemaakt kunnen worden.

Anderzijds kan het model drastisch worden vereenvoudigd in geval van ondiepe, flauw gekromde rivieren met flauw hellende oevers. Aangezien vele rivieren aan deze eisen voldoen, c.q. als zodanig geschematiseerd kunnen worden, is een dergelijk sterk vereenvoudigd en goedkoop model zeer aantrekkelijk als onderdeel van een wiskundig model van de stroming en de bodemligging in bochtige alluviale rivieren.

In hoofdstuk 10, tenslotte, worden de belangrijkste conclusies nog eens geresumeerd en worden enige praktische implicaties genoemd. Verder worden aanbevelingen gedaan voor de praktische toepassing van de vereenvoudigde wiskundige modellen en wordt de behoefte aan verder onderzoek geformuleerd.

STEADY FLOW IN SHALLOW CHANNEL BENDS

Part II : Figures and Appendices

Proefschrift

ter verkrijging van de graad van doctor in
de technische wetenschappen aan de
Technische Hogeschool Delft,
op gezag van de rector magnificus
prof. ir. B.P.Th. Veltman,
voor een commissie aangewezen door het
college van dekanen te verdedigen op
woensdag 17 juni 1981 te 14.00 uur

door

Hubrecht Johannis de Vriend
civiel ingenieur,

geboren te Oudelande

Dit proefschrift is goedgekeurd door de promotor
prof. dr. ir. J.P.Th. Kalkwijk

Met dank aan Hil en Jet

CONTENTS (PART II)

LIST OF FIGURES

Appendix A. Combined effect of secondary flow convection and bottom shear stress on the main velocity distribution in fully-developed laminar flow

As was stated in par. 3.6, the combination of horizontal secondary flow convection and bottom shear stress causes a retarded outward expansion of the low velocity region near the inner wall. This phenomenon can be illustrated by the following simplified example for the central region.
Taking $\bar{\psi}$ as a constant, neglecting radial diffusion and putting $r = 1$ for simplicity, the longitudinal momentum equation (3.42) reduces to

$$k_1 \frac{\partial \bar{u}}{\partial \xi} = 1 - k_2 \bar{u} \quad \text{with} \quad k_1 = De^2 \overline{g \frac{\partial f}{\partial \zeta}} \bar{\psi} \quad \text{and} \quad k_2 = \left.\frac{\partial f}{\partial \zeta}\right|_{\zeta=-1} \tag{A.1}$$

This first order differential equation requires only one boundary condition.
As it holds only for the central region, the no-slip conditions $\bar{u} = 0$ at the sidewalls are not relevant. The fact that the highest order term in the equation is due to secondary flow convection, which causes an exclusively outward influencing of the depth-averaged main velocity, suggests to formulate the boundary condition as

$$\bar{u} = \bar{u}_0 \quad \text{at} \quad \xi = \xi_0 \tag{A.2}$$

, where ξ_0 globally indicates the edge of the inner wall layer.
Then the solution of equation (A.1) reads

$$\bar{u} = \frac{1}{k_2} + \left(\bar{u}_0 - \frac{1}{k_2}\right) e^{-\frac{k_2}{k_1}(\xi - \xi_0)} \tag{A.3}$$

If there is no convection (De = 0), this reduces to

$$\bar{u} = \frac{1}{k_2} \tag{A.4}$$

If convection occurs (De > 0), the velocity near the inner wall is reduced and $\bar{u}_0$ becomes smaller than ι/k_2, so that $\bar{u}$ gradually increases with ξ to its asymptote ι/k_2. The higher the Dean number becomes, the greater the difference between u_0 and ι/k_2 and the smaller k_2/k_1, so the slowier the approach of $\bar{u}$ to its asymptote. If the bed shear stress is neglected, however, so if $k_2/k_1 \downarrow 0$,

$$\bar{u} = \bar{u}_0 + \frac{\iota}{k_1} (\xi - \xi_0) \qquad (A.5)$$

So by lack of the damping effect of the bed shear stress, the depth-averaged velocity in the central region keeps growing linearly with ξ instead of approaching a horizontal asymptote. This tendency is clearly shown by the mean velocity curves for zero bottom shear stress in figure 12.

Appendix B. Decay of the secondary circulation in laminar flow beyond a bend

Laminar flow in a straight channel with a fully-developed main velocity distribution that is not influenced by the secondary flow is described by the normalized system

$$\frac{\partial v}{\partial \xi} + \frac{\partial w}{\partial \zeta} = 0 \tag{B.1}$$

$$0 = -\frac{\partial p}{\partial s} + \frac{\partial^2 u}{\partial \zeta^2} + \frac{\partial^2 u}{\partial \xi^2} \tag{B.2}$$

$$\varepsilon^3 \mathrm{Re}\ u \frac{\partial v}{\partial s} = -\frac{\partial p}{\partial \xi} + \varepsilon^2 \left(\frac{\partial^2 v}{\partial \zeta^2} + \frac{\partial^2 v}{\partial \xi^2}\right) \tag{B.3}$$

$$\varepsilon^3 \mathrm{Re}\ u \frac{\partial w}{\partial s} = -\frac{\partial p}{\partial \zeta} + \varepsilon^2 \left(\frac{\partial^2 w}{\partial \zeta^2} + \frac{\partial^2 w}{\partial \xi^2}\right) \tag{B.4}$$

$$\int_{-B/2d}^{B/2d} d\xi \int_{-1}^{0} u\, d\zeta = \frac{B}{d} \tag{B.5}$$

$$u = 0; \quad v = 0; \quad w = 0 \quad \text{at} \quad \zeta = -1 \quad \text{and at} \quad \xi = \pm \frac{B}{2d} \tag{B.6}$$

$$\frac{\partial u}{\partial \zeta} = 0; \quad \frac{\partial v}{\partial \zeta} = 0; \quad w = 0 \quad \text{at} \quad \zeta = 0 \tag{B.7}$$

$$v = v_0; \quad w = w_0 \quad \text{at} \quad s = 0 \tag{B.8}$$

Longitudinal diffusion is neglected here, as it affects the results only slightly, as was shown by Ananyan (1965), who used the turbulent flow version of this system including the longitudinal diffusion terms to describe the decay of the secondary circulation in turbulent flow. Around the axis of a shallow channel the vertical velocity component will be much smaller than the radial one. So if considerations are limited to the region around the channel axis, w can be put equal to zero. In addition, horizontal diffusion is neglected and for simplicity u is introduced as a known function , viz.

$$\bar{u} = 1 \quad \text{and} \quad f(\zeta) = \frac{3}{2}\,(1 - \zeta^2) \tag{B. 9}$$

Then the equations concerning the secondary flow in the system (B.1) through (B.8) reduce to

$$\varepsilon^3 \mathrm{Re} f \frac{\partial v}{\partial s} = -\frac{\partial \mathcal{P}}{\partial \xi} + \varepsilon^2 \frac{\partial^2 v}{\partial \zeta^2} \tag{B.10}$$

$$\frac{\partial \mathcal{P}}{\partial \zeta} = 0 \tag{B.11}$$

$$v\Big|_{\zeta=-1} = 0; \quad \frac{\partial v}{\partial \zeta}\Big|_{\zeta=0} = 0; \quad v\Big|_{s=0} = v_0 \tag{B.12}$$

The transverse pressure slope is considered as a constant, which can be determined from the integral condition of continuity

$$\int_{-1}^{0} v \, d\zeta = 0 \tag{B.13}$$

Defining a new longitudinal coordinate σ by

$$\sigma = \frac{s}{\varepsilon \mathrm{Re}} \tag{B.14}$$

and assuming the secondary flow at the inflow boundary to be

$$v_0 = \tilde{v}_0 \, g'(\zeta) \quad \text{with} \quad g'(\zeta) = \frac{24}{19}\,(-7\zeta^6 + 35\zeta^4 - 33\zeta^2 + 5) \tag{B.15}$$

, these equations can be rewritten as

$$f \frac{\partial v}{\partial \sigma} = -\frac{1}{\varepsilon^2} \frac{1}{\tilde{v}_0} \frac{\partial p}{\partial \xi} + \frac{\partial^2 v}{\partial \zeta^2} \quad \text{with} \quad v = v/\tilde{v}_0 \tag{B.16}$$

$$v\Big|_{\zeta=-1} = 0; \quad \frac{\partial v}{\partial \zeta}\Big|_{\zeta=0} = 0; \qquad v\Big|_{s=0} = g'(\zeta) \tag{B.17}$$

$$\int_{-1}^{0} v \, d\zeta = 0 \tag{B.18}$$

The solution of this system is represented in figure B.1. As was to be expected, the secondary circulation gradually damps out, near the bottom somewhat faster than near the surface. The point where the secondary flow has been reduced to 10% of its initial value lies at $\sigma \approx 0.14$, i.e. at a distance of about 0.14 Re times the depth of flow from the entrance of the straight reach considered.
This result agrees rather well with the results of fully three-dimensional computations of laminar flow in a square pipe (Humphrey et al. (1977)): for Re $\approx$ 200*) the secondary velocities had been reduced to about 25% of their original magnitude at $\sigma \approx 0.06$ and to about 7% at $\sigma \approx 0.2$.

In various recent analyses of turbulent flow in river bends (De Vriend (1979a), Falcón (1979), Nouh et al. (1979)), the vertical distribution of v is taken strictly self-laminar. The foregoing shows that this is not exactly correct for the present laminar flow case, but it is interesting to assess the effect of this approximation. Suppose

$$v = \tilde{v}\, g'(\zeta) \tag{B.19}$$

with $g'(\zeta)$ according to (B.15). Then the transverse momentum equation becomes

$$fg' \frac{\partial \tilde{v}}{\partial \sigma} = -\frac{1}{\varepsilon^2}\frac{\partial p}{\partial \xi} + \tilde{v}\frac{\partial^2 g'}{\partial \zeta^2} \tag{B.20}$$

At each level ζ, however, this equation yields a different solution of $\tilde{v}$, approximation (B.19) being not exactly true for the solution of (B.16) through (B.18). Therefore (B.20) must be reduced to an appropriate one-dimensional equation, which can be done in various ways.
De Vriend(1979a) takes the difference between the two equations obtained by evaluating (B.20) at the bottom and at the surface. This yields

$$(fg')\Big|_{\zeta=0} \frac{\partial \tilde{v}}{\partial \sigma} \tilde{v} \left(\frac{\partial^2 g'}{\partial \zeta^2}\Big|_{\zeta=0} - \frac{\partial^2 g'}{\partial \zeta^2}\Big|_{\zeta=-1}\right) \tag{B.21}$$

*) Based on the hydraulic radius of the pipe.

and hence, regarding (B.9) and (B.15),

$$\tilde{v} = \tilde{v}_0 e^{-28\sigma} \tag{B.22}$$

According to this expression the 10% intensity is reached at $\sigma \simeq 0.08$. Falcón (1979) uses the moment-of-momentum equation about $\zeta = -\frac{1}{2}$ rather than the momentum equation (B.20):

$$fg' \left(\zeta + \tfrac{1}{2}\right) \frac{\partial \tilde{v}}{\partial \sigma} = -\frac{1}{\varepsilon^2} \frac{\partial p}{\partial \xi} \left(\zeta + \tfrac{1}{2}\right) + \tilde{v} \frac{\partial^2 g'}{\partial \zeta^2} \left(\zeta + \tfrac{1}{2}\right) \tag{B.23}$$

and takes the dept-average. Then the pressure gradient term vanishes and the solution of the resulting equation reads

$$\tilde{v} = \tilde{v}_0 \, e^{-24.47\sigma} \tag{B.24}$$

, so that the 10% intensity is reached at $\sigma \simeq 0.09$.
Nouh et al. (1979) simply neglect the transverse pressure gradient and evaluate (B.20) at the level $\zeta = -0.9$. This yields here

$$\tilde{v} = \tilde{v}_0 \, e^{-192.6\sigma} \tag{B.25}$$

, i.e. 90% reduction of the secondary flow at $\sigma \simeq 0.012$.
So the errors introduced by strict application of the similarity approximation (B.19) are considerable: the rate of decay of the secondary flow is overestimated in the first two cases by a factor 1.5 - 2, in the last case by a factor 12.

The bottom shear stress due to the secondary flow is proportional to the vertical derivative of v at the bottom. Since v = 0 there, this derivative can be approximated by

$$\left.\frac{\partial v}{\partial \zeta}\right|_{\zeta=-1} \simeq 20 \left. v \right|_{\zeta=-0.9} - 5 \left. v \right|_{\zeta=-0.8} \tag{B.26}$$

According to figure B.1, v decays faster near the bottom than near the surface (90% reduction at $\sigma \simeq 0.10$), so that the bottom shear stress due to the secondary flow will decay faster than the secondary flow intensity.

If v is approximated by (B.19), however, its vertical derivative at the bottom decays at the same rate as $\tilde{v}$, i.e. 90^{o} reduction at $\sigma \simeq 0.08$. This implies that with the similarity approximation (B.19) the decay of the bottom shear stress due to the secondary flow is predicted much better than the decay of the secondary flow intensity.

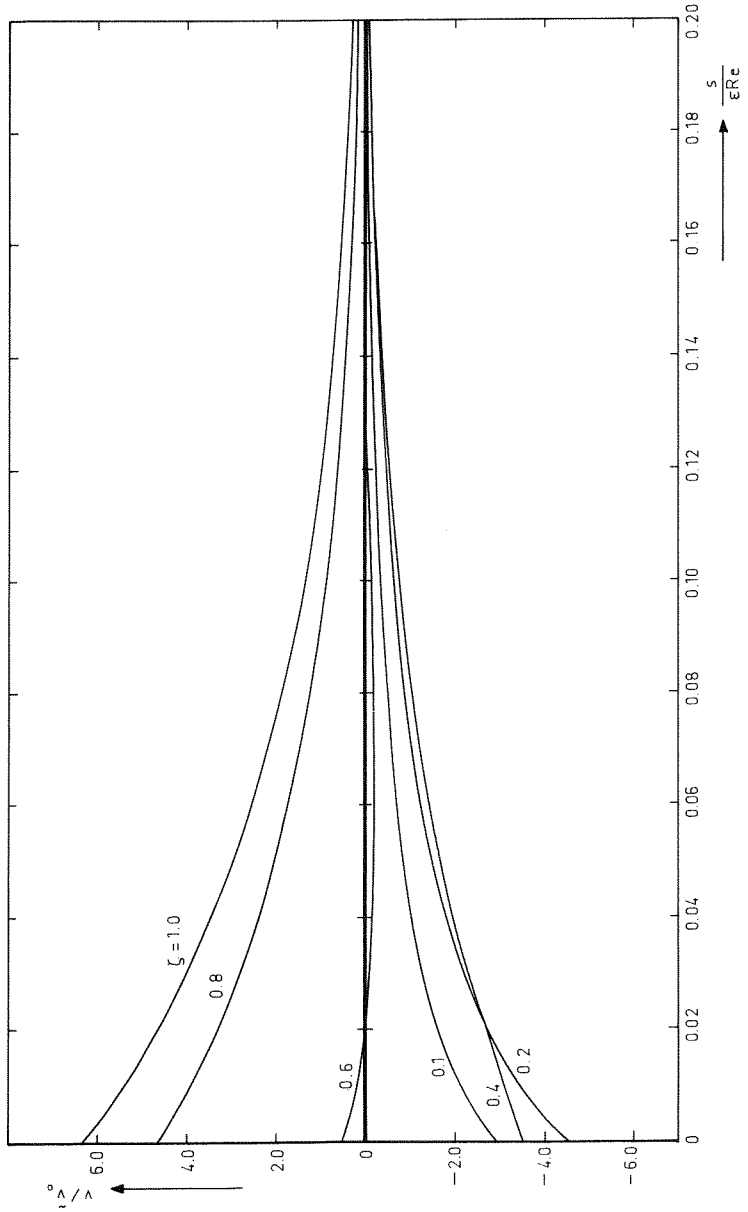

Figure B.1. Decay of laminar secondary flow in a straight reach

Appendix C. Computation methods for the depth-averaged velocity in laminar flow

C.1. Mathematical formulation of the problem

As was shown in chapter 5, the depth-averaged laminar flow in a bend of a shallow rectangular channel is described by the equations

$$\frac{1}{r}\frac{\partial \bar{u}}{\partial \phi} + \frac{\partial \bar{v}}{\partial \xi} + \frac{\varepsilon}{r}\bar{v} = 0 \qquad (C.1)$$

$$\varepsilon \mathrm{Re}\ \overline{f^2}\left(\frac{\bar{u}}{r}\frac{\partial \bar{u}}{\partial \phi} + \bar{v}\frac{\partial \bar{u}}{\partial \xi} + \frac{\varepsilon}{r}\overline{uv}\right) + \mathrm{De}^2\ \overline{g\frac{\partial f}{\partial \zeta}}\left\{\frac{\bar{\psi}}{r}\left(\frac{\partial \bar{u}}{\partial \xi} + \frac{\varepsilon}{r}\bar{u}\right) + \frac{\bar{u}}{r}\frac{\partial \bar{\psi}}{\partial \xi}\right\} =$$

$$-\frac{1}{r}\frac{\partial \bar{p}}{\partial \phi} + \frac{\partial^2 \bar{u}}{\partial \xi^2} + \frac{\varepsilon}{r}\frac{\partial \bar{u}}{\partial \xi} - \bar{u}\left.\frac{\partial f}{\partial \zeta}\right|_{\zeta=-1} \qquad (C.2)$$

$$\varepsilon^3 \mathrm{Re}\ \overline{f^2}\left(\frac{\bar{u}}{r}\frac{\partial \bar{v}}{\partial \xi} + \bar{v}\frac{\partial \bar{v}}{\partial \xi}\right) - \varepsilon^2 \mathrm{Re}\ \overline{f^2}\frac{\bar{u}^2}{r} + \varepsilon^2 \mathrm{De}^2\ \overline{g\frac{\partial f}{\partial \zeta}}\left\{\frac{\bar{\psi}}{r}\frac{\partial \bar{v}}{\partial \xi} + \frac{\bar{v}}{r}\frac{\partial \bar{\psi}}{\partial \xi}\right\} =$$

$$-\frac{\partial \bar{p}}{\partial \xi} + \varepsilon^2\left\{\frac{\partial^2 \bar{v}}{\partial \xi^2} + \frac{\varepsilon}{r}\frac{\partial \bar{v}}{\partial \xi} - \bar{v}\left.\frac{\partial f}{\partial \zeta}\right|_{\zeta=-1} - 2\frac{\varepsilon}{r^2}\frac{\partial \bar{u}}{\partial \phi} + \mathrm{Re}\ \frac{\bar{\psi}}{r}\left.\frac{\partial^2 g}{\partial \zeta^2}\right|_{\zeta=-1}\right\} \qquad (C.3)$$

The quantities f, g and $\bar{\psi}$ are known, $\bar{u}$, $\bar{v}$ and $\bar{p}$ have to be solved from this system with an appropriate set of boundary conditions. The boundary conditions at the sidewalls stem from the impermeability of these walls and the no-slip conditions there. Hence

$$\bar{u} = 0 \quad \text{and} \quad \bar{v} = 0 \quad \text{at} \quad \xi = \pm\frac{B}{2d} \qquad (C.4)$$

The inflow conditions are based on the assumption that the inflow section $s = 0$ is preceded by a very long straight reach, so that the velocity and pressure distributions for fully-developed straight channel flow can be imposed there. This implies that

$$\bar{u} = \bar{u}_0(\xi); \quad \bar{v} = 0 \quad \text{and} \quad \bar{p} = \text{constant} \quad \text{for} \quad s = 0 \qquad (C.5)$$

, in which $\bar{u}_0(\xi)$ denotes the depth-averaged velocity distribution in fully-developed straight channel flow and the constant can be chosen

arbitrarily, only the derivatives of $\bar{p}$ being important. The quantity $\bar{u}_0(\xi)$ is solved from the longitudinal momentum equation

$$0 = -\frac{\partial \bar{p}}{\partial s} + \frac{\partial^2 \bar{u}_0}{\partial \xi^2} - \bar{u}_0 \left.\frac{\partial f}{\partial \zeta}\right|_{\zeta=-1} \tag{C.6}$$

and the integral condition of continuity

$$\int_{-B/2d}^{B/2d} \bar{u}_0 d\xi = \frac{B}{d} \tag{C.7}$$

For parabolically distributed f, this yields

$$\bar{u}_0 = \frac{i}{3}\left(1 - \frac{\cosh\ \xi\sqrt{3}}{\cosh\ \hat{\xi}\sqrt{3}}\right) \quad \text{and} \quad i_0 = \frac{3}{1 - \frac{2}{\sqrt{3}}\frac{d}{B}\tanh\ \hat{\xi}\sqrt{3}} \tag{C.8}$$

with $\hat{\xi} = B/2d$.
It should be noted that the choice of this inflow distribution is rather arbitrary; it can be replaced by any other one.
The two-dimensional flow problem described by the system (C.1) through (C.5) can be solved in various ways, some of which will be discussed hereafther.

C.2. The stream-function/vorticity method.

The stream-function/vorticity concept is widely used for the computation of two-dimensional incompressible laminar flows (Roache (1972)). Instead of solving the velocity components $\bar{u}$ and $\bar{v}$ and the total pressure $\bar{p}$ directly from the depth-averaged system (C.1) through (C.5), this system is reformulated in terms of the stream function Φ, defined by

$$\bar{u} = \frac{\partial \Phi}{\partial \xi}; \quad v = -\frac{1}{r}\frac{\partial \Phi}{\partial \phi} \tag{C.9}$$

and the depth-averaged main flow vorticity $\bar{\omega}_m$ (for simplicity the suffix m will be omitted hereafter). The equation of continuity (C.1) is automatically satisfied by definition (C.9) and if terms being an order $O(\varepsilon^2)$ smaller than the leading terms of the same type are neglected,

the momentum equations (C.2) and (C.3) can be replaced by the vorticity transport equation

$$\varepsilon Re\ \overline{f^2}\ (\frac{\bar{u}}{r}\frac{\partial\bar{\omega}}{\partial\phi} + \bar{v}\frac{\partial\bar{\omega}}{\partial\xi}) + \varepsilon Re^2\ \overline{g\frac{\partial f}{\partial\zeta}}\{\frac{\bar{\psi}}{r}\frac{\partial\bar{\omega}}{\partial\xi} + 2\frac{\bar{\omega}}{r}\frac{\partial\bar{\psi}}{\partial\xi} - \frac{\bar{u}}{r}(\frac{\partial^2\bar{\psi}}{\partial\xi^2} - \frac{\varepsilon}{r}\frac{\partial\bar{\psi}}{\partial\xi})\} =$$

$$\frac{\partial^2\bar{\omega}}{\partial\xi^2} + \frac{\varepsilon}{r}\frac{\partial\bar{\omega}}{\partial\xi} - \bar{\omega}\left.\frac{\partial\hat{f}}{\partial\zeta}\right|_{\zeta=-1} \qquad (C.10)$$

In addition, the expression for the depth-averaged vorticity

$$\bar{\omega} = \frac{\varepsilon^2}{r}\frac{\partial\bar{v}}{\partial\phi} - \frac{\partial\bar{u}}{\partial\xi} - \frac{\varepsilon}{r}\bar{u} \qquad (C.11)$$

can be combined with definition (C.9) to

$$\frac{\partial^2\Phi}{\partial\xi^2} + \frac{\varepsilon}{r}\frac{\partial\Phi}{\partial\xi} + \frac{\varepsilon^2}{r^2}\frac{\partial^2\Phi}{\partial\phi^2} = -\bar{\omega} \qquad (C.12)$$

Now Φ and $\bar{\omega}$ are determined by solving equations (C.10) and (C.12) simultaneously. Once these quantites are known, $\bar{u}$ and $\bar{v}$ are evaluated using (C.9) and subsequently the pressure is solved from a combination of equations (C.2) and (C.3).

The advantage of this procedure is that the number of equations to be solved simultaneously is reduced from three to two (cf. chapter 3).

On the other hand, the boundary conditions for $\bar{\omega}$ cannot be formulated explicitly, which may give rise to

For the present channel flow, however, this problem can be coped with in a rather elegant way, as will be shown hereafter.

In view of equation (C.12), boundary conditions for Φ must be given at the sidewalls and at the inflow and outflow boundaries. According to equation (C.10), $\bar{\omega}$ must be given at the inflow boundary and at the sidewalls. The sidewall conditions (C.4), however, only lead to conditions for Φ:

$$\Phi = \text{constant} \qquad \text{and} \quad \frac{\partial\Phi}{\partial\xi} = 0 \qquad \text{at} \qquad \xi = \pm\frac{B}{2d} \qquad (C.13)$$

Since equation (C.12) is second-order in ξ, only two out of these four

conditions can be imposed on Φ; the other two must be reformulated in terms of $\bar{\omega}$.

A rather obvious choice is to take Φ constant along the sidewalls. The integral condition of continuity requires the difference between the right and left wall values of Φ to be equal to B/d, but apart from that, the constants can be chosen arbitrarily, only the derivatives of Φ being of interest. Therefore, the sidewall conditions of Φ are taken

$$\Phi = 0 \quad \text{at} \quad \xi = -\frac{B}{2d} \quad \text{and} \quad \Phi = \frac{B}{d} \quad \text{at} \quad \xi = \frac{B}{2d} \tag{C.14}$$

Equation (C.12) combined with conditions (C.13) leads to

$$\bar{\omega} = -\frac{\partial^2 \Phi}{\partial \xi^2} \quad \text{at} \quad \xi = \pm \frac{B}{2d} \tag{C.15}$$

, which provides the sidewall boundary conditions for $\bar{\omega}$ if the distribution of Φ can be estimated. A great variety of finite-difference approximations of conditions (C.15) was applied with success in the numerical simulation (of a wide range of) laminar flow problems (Roache (1972)). Since these boundary conditions will vary during the iteration process, however, they may give rise to ill-convergence. Therefore, a more direct approach is chosen, making use of the specific features of the present flow case (a simple channel with predominant longitudinal flow). As terms being an order $O(\varepsilon^2)$ smaller than the leading terms of the same type in the same equation are neglected, expression (C.11) can be simplified to

$$\bar{\omega} = -\frac{\partial \bar{u}}{\partial \xi} - \frac{\varepsilon}{r}\bar{u} \tag{C.16}$$

Hence, $\bar{u}$ being equal to zero at the left wall,

$$\bar{u} = -\frac{1}{r}\int_{-B/2d}^{\xi} r\bar{\omega}\,d\xi \tag{C.17}$$

As $\bar{u} = 0$ at the right wall, as well, this yields the integral condition

$$\int_{-B/2d}^{B/2d} r\bar{\omega}\,d\xi = 0 \tag{C.18}$$

In addition, the integral condition of continuity leads to

$$\int_{-B/2d}^{B/2d} \frac{d\xi}{r} \int_{-B/2d}^{\xi} r\bar{\omega} d\xi = -\frac{B}{d} \tag{C.19}$$

Conditions (C.18) and (C.19), which are invariant throughout the iteration process, can be applied instead of boundary conditions at the sidewalls. As the vorticity transport equation (C.10) is linear in $\bar{\omega}$, this can be done without too many complications (De Vriend (1978b)).
The inflow conditions for Φ and $\bar{\omega}$ follows directly from the given inflow velocity distribution. In general:

$$\Phi = \int_{-B/2d}^{\xi} \bar{u}_0 d\xi \qquad \text{and} \qquad \bar{\omega} = -\frac{\partial \bar{u}_0}{\partial \xi} \quad \text{at} \quad s = 0 \tag{C.20}$$

From a physical point of view it is not quite obvious to prescribe the velocity distribution at the outflow boundary; it would be preferable to have a free boundary there, exerting no influence on the flow further upstream. Therefore the boundary condition for Φ at the outflow boundary is made as "weak" as possible:

$$\frac{\partial^2 \Phi}{\partial s^2} = 0 \qquad \text{at} \qquad s = s_{\text{outflow}} \tag{C.21}$$

In summary, the stream function and the vorticity of the depth-averaged main flow are solved from equations (C.10) and (C.12) with conditions (C.14) and (C.18) through (C.21). For further details of the iterative solution procedure: see De Vriend (1978b).

C.3. Spalding's method

A family of essentially different, quite powerful computational methods came forward in the early seventies and will be indicated by the name of Spalding's method, referring to the main author. The methods have been applied with success to a great variety of flow problems,

two- and three-dimensional, laminar and turbulent (see Rodi (1978a)). The essential feature of all computational procedures belonging to this family is that the velocity components are solved from the momentum equations with estimated pressure gradients and the pressure field is corrected in such a way that the equation of continuity is satisfied. Three groups of methods can be distinguished (Rodi (1978)), dealing with

- "parabolic" flows, in which only downstream influencing occurs, i.e. the velocity components and the pressure are not influenced by the flow conditions further downstream (Patankar et al. (1972)),
- "partially-parabolic" flows, in which upstream influencing occurs only through the pressure[x]) (Pratap et al. (1976))., and
- "elliptic" flows, in which upstream influencing occurs both through the pressure and through longitudinal diffusion (Gosman et al. (1973), Patankar (1975)).

The character of the differential equations, and hence the solution procedure to be applied, is essentially different for each group: parabolic flows allow for a much simpler and more economical procedure than partially-parabolic flows, which in turn are easier to be computed than elliptic flows.

In case of curved channel flow, the parabolic flow approximation applies to gentle bends only (McGuirk (1978)). In sharper bends the pressure will give rise to considerable upstream influencing, especially near the transition between channel sections of different curvature. This is readily illustrated by the water surface configuration in curved open channels of not very mild curvature: the transverse slope of the water surface starts to develop before the bend entrance and to decay before the exit of the bend is reached (cf. the visualization of the potential flow solution for a bend by Böss (1938) and the results of turbulent flow experiments by Rozovskii (1961) and De Vriend (1979b)). On the other hand, the elliptic flow approximation is only needed if

---

[x]) The stream function/vorticity system described in section C.2 corresponds more or less with this partially-parabolic flow approximation: longitudinal diffusion is neglected, but the second derivative with respect to ϕ in equation (C.12) is retained, so that part of the upstream influencing is represented.

longitudinal diffusion is important, i.e. if flow separation occurs. In the momentum equations (C.2) and (C.3), however, longitudinal diffusion is neglected, so that the elliptic procedures are not relevant here.

Hence the partially-parabolic flow approximation is the most suited for the present model, but in addition it will be investigated to what extent the much more economical parabolic procedure is applicable. Therefore, slightly modified two-dimensional versions of the parabolic and partially-parabolic procedures described in the original publications (Patankar et al. (1972) and Pratap et al. (1976), respectively) were developed.

The main outlines of these procedures will be given hereafter.

First the momentum equations are rewritten in the conservative form

$$\frac{1}{r}\frac{\partial}{\partial\phi}(U\bar{u}) + \frac{1}{r}\frac{\partial}{\partial\xi}(rV\bar{u}) + \frac{\varepsilon}{r}V\bar{u} = -\frac{1}{r}\frac{\partial\bar{p}}{\partial\phi} + \frac{1}{r}\frac{\partial}{\partial\xi}(r\frac{\partial\bar{u}}{\partial\xi}) - \bar{u}\left.\frac{\partial f}{\partial\zeta}\right|_{\zeta=-1} \qquad (C.22)$$

$$\frac{\varepsilon}{r}\frac{\partial}{\partial\phi}(U\bar{v}) + \frac{\varepsilon}{r}\frac{\partial}{\partial\xi}(rV\bar{v}) - \frac{U}{\varepsilon r}\bar{u} = -\frac{1}{\varepsilon^2}\frac{\partial\bar{p}}{\partial\xi} + \frac{1}{r}\frac{\partial}{\partial\xi}(r\frac{\partial\bar{v}}{\partial\xi}) +$$

$$-\bar{v}\left.\frac{\partial f}{\partial\zeta}\right|_{\zeta=-1} - 2\frac{\varepsilon}{r^2}\frac{\partial\bar{u}}{\partial\phi} + \mathrm{Re}\,\frac{\bar{\psi}}{r}\left.\frac{\partial^2 g}{\partial\zeta^2}\right|_{\zeta=-1} \qquad (C.23)$$

with $$U = \varepsilon\mathrm{Re}\,\overline{f^2}\,\bar{u} \qquad (C.24)$$

and $$V = \varepsilon\mathrm{Re}\,\overline{f^2}\,\bar{v} + \mathrm{De}^2\,\overline{g\frac{\partial f}{\partial\zeta}}\frac{\bar{\psi}}{r} \qquad (C.25)$$

Subsequently, the system is discretized. The quantities $\bar{u}$, $\bar{v}$ and $\bar{p}$ are defined on a staggered gird as indicated in figure C.1. Discretized versions of (C.1), (C.22) and (C.23) are obtained by formal integration of these equations over the elements indicated in figure C.1 as "p-element", "$\bar{u}$-element" and "$\bar{v}$-element", respectively. If in the integrated equations a quantity is not defined in the centre of the element face where it is needed, the nearest upstream value is used. The first derivatives with respect to ξ remaining from the lateral

diffusion terms are evaluated using finite-difference approximations (see also Leschziner (1978)).

In general, the velocities calculated from the momentum equations will not exactly satisfy the equation of continuity (C.1). Therefore the pressure field, and hence the velocities, are corrected to guarantee the conservation of mass.

This pressure correction consists of two parts, viz. the correction of the cross-sectional mean value of the longitudinal pressure gradient, in order to satisfy the integral condition of continuity, and the correction of the transverse pressure distribution, in order to satisfy the conservation of mass in each cell of the computational grid.

The local pressure correction is the only point at which the parabolic and the partially-parabolic procedures essentially differ. A most important feature of the parabolic procedure is the "uncoupling" of the longitudinal and the transverse pressure gradients. In the present model this uncoupling is realized as follows. Let the pressure $\bar{p}_j$ in cross-section j be known, then the transverse distribution $\bar{p}'_{j+1} = \bar{p}_{j+1} - \bar{\bar{p}}_{j+1}$ (double overbars denoting the cross-sectional mean value) is estimated on the basis of the truncated radial momentum equation

$$\frac{\partial \bar{p}}{\partial \xi} = \varepsilon^2 \mathrm{Re}\, \frac{\bar{u}^2}{r} \tag{C.26}$$

or, in the later iteration steps of the partially-parabolic procedure, on the basis of the pressure distribution found in the foregoing iteration step. Then the longitudinal pressure gradient in (C.1) can be estimated by

$$\frac{\partial \bar{p}}{\partial \phi} = \frac{\partial \bar{p}'}{\partial \phi} + \frac{\partial \bar{\bar{p}}}{\partial \phi} \tag{C.27}$$

, in which the first component is approximately known, whereas the second one remains to be adjusted in such a way that the integral condition of continuity is satisfied. Subsequently, $\bar{v}$ is solved from (C.2) with the estimated transverse pressure distribution and $\bar{p}'$ and $\bar{v}$ are corrected in order to satisfy local continuity. In

the partially-parabolic procedure the same steps are made, but the last one, the local pressure correction, involves $\bar{p}$, $\bar{u}$ and $\bar{v}$ rather than $\bar{p}'$ and $\bar{v}$, so that the "uncoupling" is only partial. Consequently, the partially-parabolic procedure requires a number of sweeps through the flow field, whereas parabolic flow can be computed in a single sweep.

The algorithms of the parabolic and partially-parabolic procedures incorporated in the present model can be summarized follows.

1. Compute the velocity distribution $\bar{u}_0$ and the longitudinal pressure gradient i_0 for fully developed flow in the equivalent straight channel (cf. C.8).
2. Estimate the cross-sectional mean values of the pressure by integrating

$$\frac{\partial \bar{\bar{p}}}{\partial s} = - i_0 \qquad \text{(C.28)}$$

along the channel axis.

3. Start marching downstream from cross-section to cross-section and carry out the following operations in each subsequent cross-section j.
4. Estimate the velocity components by

$$u_j = \bar{u}_{j-1} \quad \text{and} \quad \bar{v}_{j-\frac{1}{2}} = \bar{v}_{j-1\frac{1}{2}} \qquad (\bar{v}_{-\frac{1}{2}} = 0) \qquad \text{(C.29)}$$

5. Estimate the transverse distribution of the pressure $\bar{p}_{j-\frac{1}{2}}$ as described before (equation C.26).
6. Solve $\bar{u}_j$ and $\bar{\bar{p}}_{j+\frac{1}{2}}$ from the longitudinal momentum equation (C.22) and the integral condition of continuity*).
7. Solve $\bar{v}_{j-\frac{1}{2}}$ from the transverse momentum equation (C.23).

---

*) In contrast with the methods described in the original publications, this is done at once i.e. the transverse distribution $\bar{u}_j/\bar{\bar{u}}_j$ is solved from (C.22) with unit longitudinal slope and $p_{j+\frac{1}{2}}$ is adjusted in such a way, that the integral condition of continuity ($\bar{\bar{u}}_j = 1$) is satisfied.

8. Ensure continuity in each cell between the cross-sections j and j-1 by correcting either $\bar{p}_{j-\frac{1}{2}} - \bar{\bar{p}}_{j-\frac{1}{2}}$ and $\bar{v}_{j-\frac{1}{2}}$ (parabolic mode) or $\bar{p}_{j-\frac{1}{2}}$, $\bar{v}_{j-\frac{1}{2}}$, $\bar{u}_j$ and $\bar{u}_{j-1}$ (partially-parabolic mode).
9. After the whole flow domain has been swept through, the computation is stopped (parabolic mode) or the marching procedure 3 through 8 is repeated until a termination criterion is satisfied (partially-parabolic mode),

There are various ways to improve this procedure and to speed up its convergence (Pratap (1975)). The non-linearity of equation (C.22), for instance, can best be accounted for by repeating step 6 several times before proceeding to 7. This repetition is more effective if the main velocities are underrelaxated (see also par. 3.3.). In addition, convergence is improved by underrelaxating the pressure correction:

$$\bar{p} = \tilde{\bar{p}} + \alpha d\bar{p} \qquad (C.30)$$

, in which $\tilde{\bar{p}}$ is the pressure before correction, $d\bar{p}$ is the calculated pressure correction and α is a constant between 0 and 1 (here $\alpha = 0.5$). Finally, the rate at which the influence of downstream events travels upstream (one cell per sweep) can be increased by applying a weighted part of the pressure correction in section $j-\frac{1}{2}$ to the pressure further upstream

$$(\bar{p}_{j-\frac{1}{2}-k})_{\text{new}} = (\bar{p}_{j-\frac{1}{2}-k})_{\text{old}} + \beta_k d\bar{p}_{j-\frac{1}{2}} \qquad \text{for} \qquad 0 < k < j-\tfrac{1}{2} \qquad (C.31)$$

The weighing factor β_k decreases as j-k increases. For further details of this additional pressure correction reference is made to the original publication (Pratap (1975)).

C.4. The simple-channel method

Apart from the specific simple-channel modifications, the computational methods described in the foregoing sections are applicable to geometrically more complicated flow situations, as well (Roache (1972); Rodi (1978a)). For simple channels with predominant longitudinal

velocity, however, a more specific procedure can be drawn up. For convenience, the same staggered computational grid and the same discretization will be used as in Spalding's model. Also $\bar{u}$ and $\bar{p}$ are determined in the same way as described in section C.3. The transverse velocity component, however, is now solved from the equation of continuity rather than from the transverse pressure distribution. This approach is likely to allow for important simplifications of the transverse momentum equation, in which the pressure gradient term and the centrifugal term dominate the other terms by far.

The algorithm of the parabolic and partially-parabolic modes (cf. section C.3) of this simple-channel method is almost the same as for the equivalent modes of Spalding's mehtod. Only steps 7 and 8, concerning the transverse velocity and the pressure correction, are replaced by

7. Solve $v_{j-\frac{1}{2}}$ from the equation of continuity (C.1).
8. Solve $\bar{p}_{j-\frac{1}{2}} - \bar{\bar{p}}_{j-\frac{1}{2}}$ from the transverse momentum equation (C.23) or a simplified version of it.

In the parabolic mode of the method, the marching procedure is carried out only once, in the partially-parabolic mode it is repeated until a termination criterion is satisfied.

Out of the three ways to speed up convergence indicated in section C.3, only the first two are applied here: repetition of step 6 and under-relaxation of the pressure. The latter is realized by putting

$$\bar{p}^{(k)} = \alpha \tilde{\bar{p}}^{(k)} + (1 - \alpha)\bar{p}^{(k-1)} \quad \text{with} \quad 0 < \alpha \leq 1 \quad \text{(here: } \alpha = 0.5\text{)} \qquad \text{(C.32)}$$

, in which $\tilde{\bar{p}}^{(k)}$ is the pressure resulting from the k-th iteration step.

C.5. Comparison of the methods

In addition to the three computational methods described in the foregoing, there are many other ways to solve the depth-averaged flow problem. The wide variety of computational methods for spatially two-dimensional unsteady flow, for instance, offers good prospects

when considering time as an iteration parameter (Lomax et al. (1975); see also Kuipers et al. (1973) for applications of a finite-difference procedure and Harrington et al. (1978) and Niemeyer (1979) for finite-element procedures to be applied in this way).
Investigating all these possibilities, however, would go beyond the present scope. Therefore only the methods given in sections C.2 through C.4 will be compared with one another, keeping in mind that they are not the only possible ones. The comparison is made by computing the depth-averaged flow in the LFM-flume (see chapter 8), for given f, g and $\bar{\psi}$ and on comparable computational grids.
The results of these computations are shown in figure C.2. The depth-averaged main velocity distributions obtained by the partially-parabolic mode of Spalding's method and by the simple-channel method almost coincide. The stream function/vorticity method yields somewhat deviant distributions, in that the local effects of secondary flow convection seem to be somewhat stronger. As was to be expected for this rather sharp bend, the results of the parabolic mode of Spalding's method deviate considerably from the ones of the partially-parabolic mode.
The computer costs greatly differ for the various methods considered here, as is readily illustrated by the following table, showing the time needed for comparable calculations on an IBM 370/158 computer.

	sweeps	iterations*)	time(s)
stream function/vorticity	50	1	330
Spalding partially-parabolic	10	5	70
simple-channel	10	5	60
Spalding parabolic	1	5	13

*) Number of intermediate iterations in the main velocity computation in a cross-section.

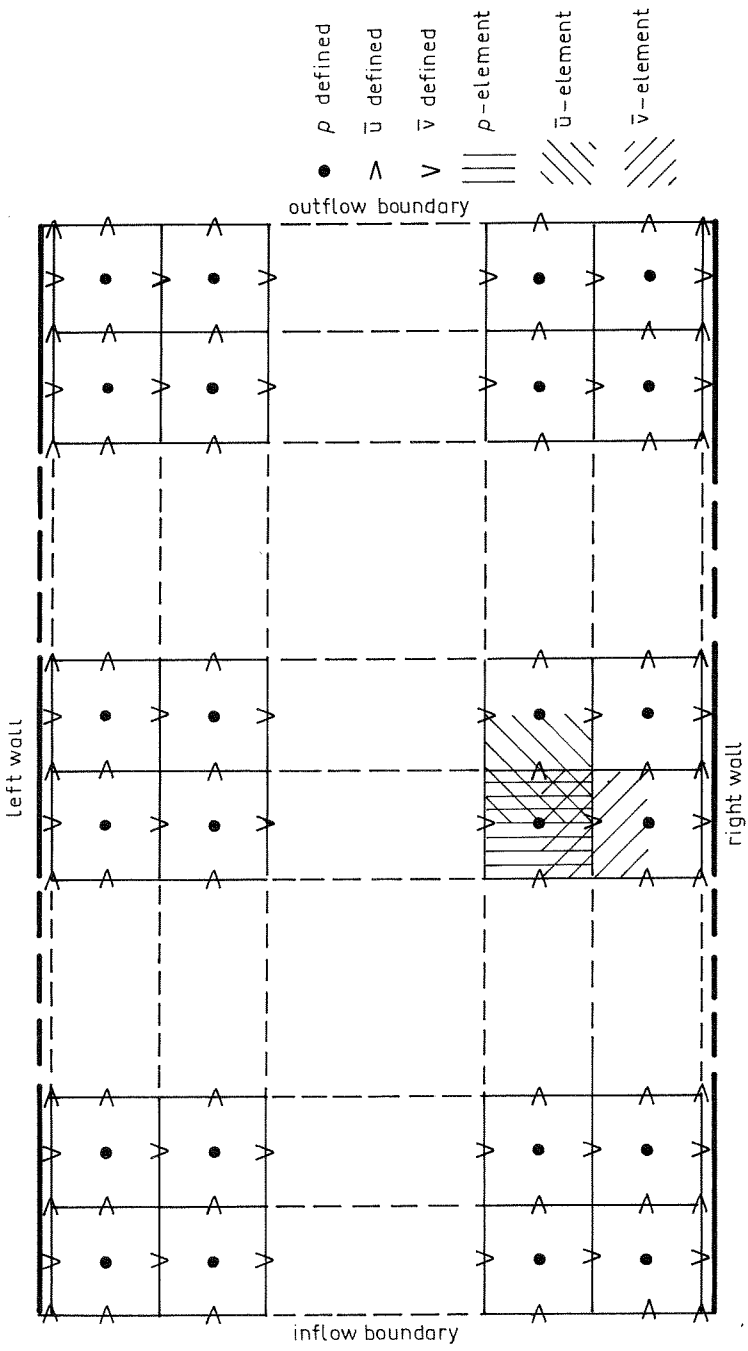

Figure C.1. Computational grid for Spalding's method

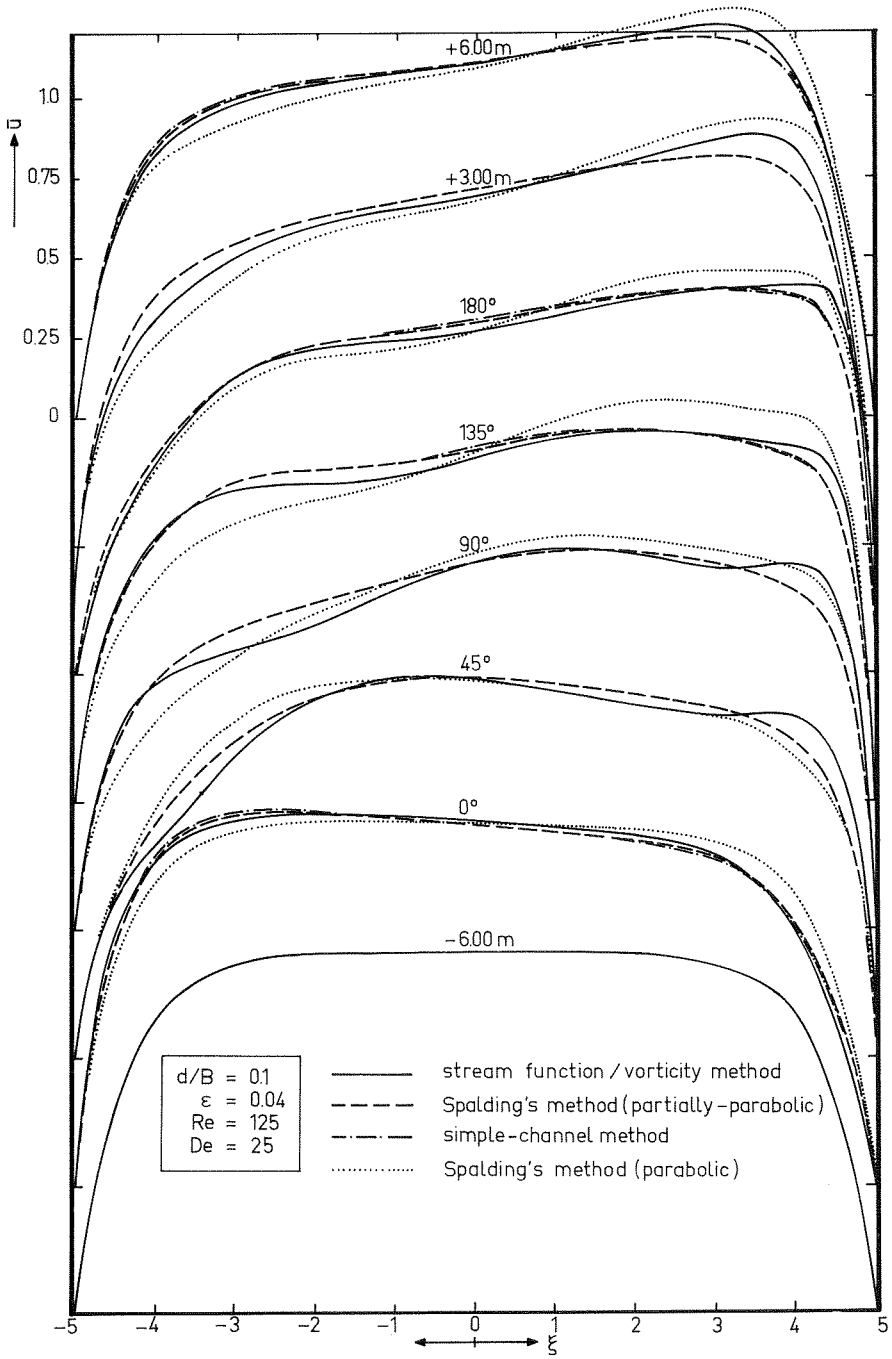

Figure C.2. Comparison of computation methods for the depth-averaged main velocity

Appendix D. Computation of fully-developed turbulent flow in straight shallow channels

Fully developed turbulent flow in straight shallow channels, with a logarithmic distribution for the velocity and a parabolic one for the turbulence viscosity in any vertical of the cross-section, can be described by the depth-averaged system derived in chapter 6:

$$0 = -\frac{\partial \bar{p}}{\partial s} + (1 + \frac{1}{6}\frac{\sqrt{g}}{\kappa C})\frac{\partial}{\partial \xi}(\bar{u}\frac{\partial \bar{u}}{\partial \xi}) - 6\frac{\sqrt{g}}{\kappa C}\bar{u}^2 \qquad (D.1)$$

with

$$\bar{u} = \frac{|\bar{u}_{\tau w}|}{\kappa}\{\frac{\kappa C}{\sqrt{g}} + 1 + \ln(\frac{B}{2d} + \xi)\} \quad \text{for} \quad \xi \leq -\frac{B}{2d} + \delta \qquad (D.2)$$

$$\bar{u} = \frac{|\bar{u}_{\tau w}|}{\kappa}\{\frac{\kappa C}{\sqrt{g}} + 1 + \ln(\frac{B}{2d} - \xi)\} \quad \text{for} \quad \xi \leq \frac{B}{2d} - \delta \qquad (D.3)$$

and the integral condition of continuity

$$\int_{-B/2d}^{B/2d} \bar{u}\,d\xi = \frac{B}{d} \qquad (D.4)$$

The pressure gradient in (D.1) can be determined from this integral condition of continuity; the depth-averaged wall friction velocity in (D.2) and (D.3) can be determined by assuming both equation (D.1) and the wall function approximation (D.2) or (D.3) to hold good in the wall-nearest mesh of the computational grid.
Integrating (D.1) from the grid point 0 at the left wall ($\xi = -B/2d$) to the grid point 1 at $\xi = -B/2d + \Delta\xi$, for instance, yields

$$0 = -\frac{\partial \bar{p}}{\partial s}\Delta\xi + (1 + \frac{1}{6}\frac{\sqrt{g}}{\kappa C})(\bar{u}\frac{\partial \bar{u}}{\partial \xi})_1 - Re_0\bar{\tau}_w - 6\frac{\sqrt{g}}{\kappa C}(\bar{u}^2)_{\frac{1}{2}}\Delta\xi \qquad (D.5)$$

, in which $(\bar{u}^2)_{\frac{1}{2}}$ stands for the value of $\bar{u}^2$ halfway the mesh.

On the other hand, the normalized sidewall shear stress τ_w is related to u by

$$\tau_w = \lim_{\xi \downarrow B/2d} \left(\frac{a}{Re_0} \frac{\partial u}{\partial \xi}\right) \tag{D.6}$$

Assuming the vertical distributions of u and a to be the same near the wall as in the other parts of the cross-section, the depth-averaged wall shear stress becomes

$$\bar{\tau}_w = \left(1 + \frac{1}{6} \frac{\sqrt{g}}{\kappa C}\right) \lim_{\xi \downarrow -B/2d} \left(\frac{\bar{a}}{Re_0} \frac{\partial \bar{u}}{\partial \xi}\right) \tag{D.7}$$

In uniform flow, the shear stress at the bottom follows from

$$\tau_b = \lim_{\zeta \downarrow -1} \left(\frac{a}{Re_0} \frac{\partial u}{\partial \zeta}\right) = \frac{g}{C^2} \bar{u}^2 \tag{D.8}$$

Accordingly, the limit of the depth-averaged shear stress at the left wall is supposed to be given by

$$\bar{\tau}_w = \left(1 + \frac{1}{6} \frac{\sqrt{g}}{\kappa C}\right) \frac{g}{C^2} \left(1 + \frac{\sqrt{g}}{\kappa C} + \frac{\sqrt{g}}{\kappa C} \ln \frac{\Delta \xi}{2}\right)^{-2} \left(\bar{u}^2\right)_{\frac{1}{2}} = \frac{K}{Re_0} \left(\bar{u}^2\right)_{\frac{1}{2}} \tag{D.9}$$

If, in addition, the second term in (D.5) is discretized using

$$\left(\bar{u} \frac{\partial \bar{u}}{\partial \xi}\right)_1 \simeq \frac{\left(\bar{u}^2\right)_{1\frac{1}{2}} - \left(\bar{u}^2\right)_{\frac{1}{2}}}{\xi_2 - \xi_0} \tag{D.10}$$

, in which the suffix 2 indicates the second grid point from the wall, the discretized version of (D.1) for the wall-nearest mesh can be written as

$$0 = - \frac{\partial \bar{p}}{\partial s} + \left(1 + \frac{1}{6} \frac{\sqrt{g}}{\kappa C}\right) \frac{\left(\bar{u}^2\right)_{1\frac{1}{2}} - \left(\bar{u}^2\right)_{\frac{1}{2}}}{(\xi_1 - \xi_0)(\xi_2 - \xi_0)} - \left(6 \frac{\sqrt{g}}{\kappa C} + \frac{K}{\xi_1 - \xi_0}\right) \left(\bar{u}^2\right)_{\frac{1}{2}} \tag{D.11}$$

Similarly, the equation near the outer wall can be discretized for the mesh $\xi_{n-1} \leq \xi \leq \xi_n$, to yield

$$0 = -\frac{\partial \bar{p}}{\partial s} + \left(1 + \frac{1}{6}\frac{\sqrt{g}}{\kappa C}\right)\frac{(\bar{u}^2)_{n-1\frac{1}{2}} - (\bar{u}^2)_{n-\frac{1}{2}}}{(\xi_n - \xi_{n-1})(\xi_n - \xi_{n-2})} +$$

$$- \left(6\frac{\sqrt{g}}{\kappa C} + \frac{K}{\xi_n - \xi_{n-1}}\right)(\bar{u}^2)_{n-\frac{1}{2}} \qquad (D.12)$$

The discretized version of (D.1) for the other meshes reads

$$0 = -\frac{\partial \bar{p}}{\partial s} + \left(1 + \frac{1}{6}\frac{\sqrt{g}}{\kappa C}\right)\left[\frac{(\bar{u}^2)_{i+\frac{1}{2}} - (\bar{u}^2)_{i-\frac{1}{2}}}{(\xi_i - \xi_{i-1})(\xi_{i+1} - \xi_{i-1})} - \frac{(\bar{u}^2)_{i-\frac{1}{2}} - (\bar{u}^2)_{i-1\frac{1}{2}}}{(\xi_i - \xi_{i-1})(\xi_i - \xi_{1-2})}\right] +$$

$$- 6\frac{\sqrt{g}}{\kappa C}(\bar{u}^2)_{i-\frac{1}{2}} \qquad (D.13)$$

for i = 2, 3, ..., n-1. Equations (D.11), (D.12) and (D.13) form a system of n linear equations with n unknowns $(\bar{u}^2)_{i-\frac{1}{2}}$ (i = 1, 2, ..., n), which can be solved if the source vector is known. All elements of this source vector, however, are equal to the longitudinal pressure gradient, which is an unknown constant. Therefore a new variable is introduced: $\bar{u}'^2$, defined as

$$\bar{u}'^2 = -\bar{u}^2 / \frac{\partial \bar{p}}{\partial s} \qquad (D.14)$$

If the system (D.11) through (D.13) is rewritten in terms of $\bar{u}'^2$, all elements of the source vector become equal to -1 and $\bar{u}'^2$ can be solved.
Subsequently, the longitudinal pressure gradient and hence $\bar{u}^2$ and $\bar{u}$ can be determined using (D.4):

$$\left(-\frac{\partial \bar{p}}{\partial s}\right)^{\frac{1}{2}} = \frac{B/d}{\int_{-B/2d}^{B/2d} \bar{u}'\,d\xi} \qquad (D.15)$$

Appendix E. Computation of the vertical distribution of the main velocity in turbulent flow

If the depth-averaged velocity field ($\bar{u}$, $\bar{v}$), the depth-averaged stream function of the secondary flow $\bar{\psi}$ and the vertical distribution functions $\mathcal{F}$ and g are known, equation (7.23) is a linear ordinary second-order differential equation in ζ with f as an unknown. It can be written as

$$a_1 \frac{\partial}{\partial \zeta}\left(\alpha' \frac{\partial f}{\partial \zeta}\right) + a_2 \alpha' f + a_3 \mathcal{F} f + a_4 \frac{\partial g}{\partial \zeta} f + a_5 g \frac{\partial f}{\partial \zeta} = \frac{1}{r}\frac{\partial p}{\partial \phi} \qquad (E.1)$$

, in which a_1 through a_5 are known functions of ξ and ϕ. The boundary condition at the surface reads (see 7.20)

$$\alpha' \frac{\partial f}{\partial \zeta} = 0 \quad \text{at} \quad \zeta = 0 \qquad (E.2)$$

and near the bottom $f(\zeta)$ is approximated by the wall function

$$f = k_m \left\{1 + \frac{\sqrt{g}}{\kappa C} + \frac{\sqrt{g}}{\kappa C} \ln(1+\zeta)\right\} \qquad (E.3)$$

, in which k_m is an unknown constant that is to be determined by letting both equation (E.1) and the wall function (E.3) hold good on the lowest mesh of the computational grid.
For $\alpha'(0) \neq 0$, condition (E.2) reduces to the symmetry condition $\left.\frac{\partial f}{\partial \zeta}\right|_{\zeta=0} = 0$, which can be treated as usual. For $\alpha'(0) = 0$, however, condition (E.2) is satisfied for any finite value of $\left.\frac{\partial f}{\partial \zeta}\right|_{\zeta=0}$. Still the problem is not ill-posed then, since in that case equation (E.1) becomes first-order at the surface, so that it can be treated as a compound boundary condition there.
Formal integration of equation (E.1) over the lowest mesh of the computatinal grid ($-1 \leq \zeta \leq \zeta_1$) yields, after substitution of (E.3) and some elaboration

$$a_1 \left(\alpha' \frac{\partial f}{\partial \zeta}\right)\Big|_{\zeta=\zeta_1} - a_1 k_m \frac{\sqrt{g}}{\kappa C}\gamma + a_2 k_m c_1 \gamma + a_3 \tilde{k}_m k_m c_2 +$$

$$+ (a_4 - a_5)\, k_m k_s c_2 + a_5 k_m k_s c_3 = \frac{1}{r}\frac{\partial p}{\partial \phi}(1+\zeta_1) \qquad (E.4)$$

with $$c_1 = \int_{-1}^{\zeta_1} -\zeta(1+\zeta)\left\{1 + \frac{\sqrt{g}}{\kappa C} + \frac{\sqrt{g}}{\kappa C}\ln(1+\zeta)\right\} d\zeta$$

$$c_2 = \int_{-1}^{\zeta_1} \left\{1 + \frac{\sqrt{g}}{\kappa C} + \frac{\sqrt{g}}{\kappa C}\ln(1+\zeta)\right\}^2 d\zeta$$

$$c_3 = (1+\zeta_1)\left\{1 + \frac{\sqrt{g}}{\kappa C}\ln(1+\zeta_1)\right\}\left\{1 + \frac{\sqrt{g}}{\kappa C} + \frac{\sqrt{g}}{\kappa C}\ln(1+\zeta_1)\right\}$$

and k_s denoting the secondary flow counterpart of k_m (see par. 7.4). If the first term is discretized, using (E.3) to express $f(\zeta_1)$ in terms of k_m, equation (E.4) and the discretized versions of equation (E.1) in all nodal points above $\zeta = \zeta_1$ form a system of linear algebraic equations from which k_m and $f(\zeta)$ can be solved. Since the longitudinal pressure gradient depends on f, introducing the latest value of $\frac{1}{r}\frac{\partial p}{\partial \phi}$ as a known quantity into (E.4) implies that during the iteration process $\bar{f}$ differs (slightly) from unity. As it is thought important to satisfy the condition $\bar{f} = 1$ in each iteration step (conservation of mass), the following procedure is applied instead.

The mathematical system (E.1) through (E.4) is reformulated in terms of $f' = f/(-\frac{1}{r}\frac{\partial p}{\partial \phi})$ and $k'_m = k_m/(-\frac{1}{r}\frac{\partial p}{\partial \phi})$. This yields

$$a_1 \frac{\partial}{\partial \zeta}\left(\alpha' \frac{\partial f'}{\partial \zeta}\right) + a_2 \alpha' f' + a_3 \tilde{f} f' + a_4 \frac{\partial g}{\partial \zeta} f' + a_5 g \frac{\partial f'}{\partial \zeta} = -1 \qquad (E.5)$$

with $$\alpha' \frac{\partial f'}{\partial \zeta} = 0 \quad \text{at} \quad \zeta = 0 \qquad (E.6)$$

and $$f' = k'_m \left\{1 + \frac{\sqrt{g}}{\kappa C} + \frac{\sqrt{g}}{\kappa C}\ln(1+\zeta)\right\} \quad \text{for} \quad \zeta \leq \zeta_1 \qquad (E.7)$$

. so that on the lowest mesh of the computational grid

$$a_1 \left(\alpha' \frac{\partial f'}{\partial \zeta}\right)\Big|_{\zeta=\zeta_1} - a_1 k'_m \frac{\sqrt{g}}{\kappa C} \gamma + a_2 k'_m c_1 \gamma + a_3 \tilde{k}_m k'_m c_2 +$$

$$+ (a_4 - a_5)\, k'_m k_s c_2 + a_5 k'_m k_s c_3 = -(1+\zeta_1) \qquad \text{(E.8)}$$

This system can be solved for k'_m and $f'(\zeta)$ in the same way as (E.1) through (E.4). Once these quantities are known, the condition $\bar{f} = 1$ is satisfied by putting

$$f = f'/\overline{f'} \qquad \text{and} \qquad k_m = k'_m/\overline{f'} \qquad \text{(E.9)}$$

Appendix F. Solution of the depth-averaged longitudinal momentum equation in case of turbulent flow

The depth-averaged longitudinal momentum equation (7.25) can be rewritten in the conservative form

$$\frac{1}{r}\frac{\partial(U\bar{u})}{\partial\phi} + \frac{\partial(V\bar{u})}{\partial\xi} + 2\frac{\varepsilon}{r}V\bar{u} = -\frac{1}{r}\frac{\partial\bar{p}}{\partial\phi} - a_1\tilde{u}\bar{u} + a_2\frac{\partial}{\partial\xi}(\tilde{u}\frac{\partial\bar{u}}{\partial\xi}) \qquad (F.1)$$

in which: $U = \varepsilon Re_0 \overline{f^2}\,\tilde{u}$

$$V = \varepsilon Re_0 \overline{f^2}\,\bar{v} + \varepsilon Re_0^2\, g\,\overline{\frac{\partial f}{\partial\zeta}}\frac{\bar{\psi}}{r}$$

, $\tilde{u}$ is a known estimate of $\bar{u}$ and a_1 and a_2 are constants. The boundary conditions at the sidewalls are replaced by the wall function approximations (6.40) and (6.41), which are assumend to hold good on the wall-nearest meshes of the computational grid. Hence

$$\bar{u} = \frac{\bar{u}_{\tau l}}{\kappa}\{\frac{\kappa C}{\sqrt{g}} + 1 + \ln(\frac{B}{2d} + \xi)\} \qquad \text{for} \quad \xi \leq -\frac{B}{2d} + \Delta\xi \qquad (F.2)$$

$$\bar{u} = -\frac{\bar{u}_{\tau r}}{\kappa}\{\frac{\kappa C}{\sqrt{g}} + 1 + \ln(\frac{B}{2d} - \xi)\} \qquad \text{for} \quad \xi \geq \frac{B}{2d} - \Delta\xi \qquad (F.3)$$

The depth-averaged longitudinal velocity component $\bar{u}$, the cross-sectional mean value of the longitudinal pressure gradient and the depth-averaged sidewall friction velocities $\bar{u}_{\tau l}$ and $\bar{u}_{\tau r}$ are solved from (F.1) through (F.3), the given inflow distribution of $\bar{u}$ and the integral condition continuity

$$\int_{-B/2d}^{B/2d} \bar{u}\,d\xi = \frac{B}{d} \qquad (F.4)$$

Starting from the inflow boundary, $\bar{u}$ is solved for the subsequent

cross-sections of the computational grid, estimating U, V, $\tilde{u}$ and the transverse distribution of $\bar{p}$ and adjusting the cross-sectional mean value of the longitudinal pressure gradient in such a way, that (F.4) is satisfied.

The system is discretized on the space-staggered grid represented in figure C.1. The discretized version of equation (F.1) is obtained by formal integration of the equation over a mesh around each $\bar{u}$-point, using upstream values of U and V if necessary (cf. Leschziner, 1978). When doing so for a mesh adjacent to the left wall, the lateral diffusion term becomes

$$a_2 \{(r\tilde{u} \frac{\partial \bar{u}}{\partial \xi} - \frac{1}{2} \varepsilon \tilde{u}\bar{u})\Big|_{\Delta\xi} - (r\tilde{u} \frac{\partial \bar{u}}{\partial \xi} - \frac{1}{2} \varepsilon \tilde{u}\bar{u})\Big|_{wall}\}\Delta\phi \qquad (F.5)$$

, which can be reduced to

$$a_2 \{(r\tilde{u} \frac{\partial \bar{u}}{\partial \xi} - \frac{1}{2} \varepsilon \tilde{u}\bar{u})\Big|_{\Delta\xi}\}\Delta\phi - Re_0 \, \bar{\tau}_{1\phi} r_{wall} \Delta\phi \qquad (F.6)$$

The sidewall shear stress $\tau_{1\phi}$ is related to the wall friction velocity $u_{\tau 1}$ through (6.48), whence

$$\bar{\tau}_{1\phi} \simeq \bar{u}^2_{\tau 1} \qquad (F.7)$$

In addition, the wall function approximation (F.2) gives a relation between $\bar{u}_{\tau 1}$ and the depth-averaged longitudinal velocity $\bar{u}|_{\xi_1}$ in the $\bar{u}$-point next to the left wall:

$$\bar{u}_{\tau 1} = \frac{\sqrt{g}}{C} \bar{u}|_{\xi_1} \{1 + \frac{\sqrt{g}}{\kappa C} + \frac{\sqrt{g}}{\kappa C} \ln(\frac{B}{2d} + \xi_1)\}^{-1} \qquad (F.8)$$

Using (F.7) and (F.8), the quantity $\bar{\tau}_{1\phi}$ in (F.6) can be expressed in terms of $\bar{u}|_{\xi_1}$. As the discretized version of (F.1) must be linear in $\bar{u}$, the following substitution is made in (F.6):

$$\bar{\tau}_{1\phi} = \tilde{u}_{\tau 1} \frac{\sqrt{g}}{C} \bar{u}|_{\xi_1} \{1 + \frac{\sqrt{g}}{\kappa C} + \frac{\sqrt{g}}{\kappa C} \ln(\frac{B}{2d} + \xi_1)\}^{-1} \qquad (F.9)$$

, $\tilde{u}_{\tau 1}$ denoting a known estimate of $\bar{u}_{\tau 1}$.
A similar procedure is followed near the outer wall. In addition, the derivatives $\frac{\partial \bar{u}}{\partial \xi}$, remaining in the lateral diffusion terms after the formal integration, are discretized. If n is the number of $\bar{u}$-points in a cross-section, equation (F.1) is thus replaced by n linear equations with n unknown $(\bar{u}|_{\xi 1} \ldots, \bar{u}|_{\xi_n})$.

The system of n linear equations in a cross-section can be formalized to

$$A.\bar{u} = S_1 \frac{\partial \bar{\bar{p}}}{\partial \phi} + S_2 \qquad (F.10)$$

, in which A is an n × n coefficient-matrix and S_1 and S_2 are known source vectors. Now $\bar{u}$ is split up into two parts, $\bar{u}_1$ and $\bar{u}_2$, in such a way that

$$\bar{u} = \frac{\partial \bar{\bar{p}}}{\partial \phi} \bar{u}_1 + \bar{u}_2 \qquad (F.11)$$

and

$$A.\bar{u}_1 = S_1 \; ; \qquad A.\bar{u}_2 = S_2 \qquad (F.12)$$

Equations (F.12) can be solved for $\bar{u}_1$ and $\bar{u}_2$. Once these quantities are known, the pressure gradient in (F.11) can be chosen such, that the integral conditon of continuity (F.4) is satisfied:

$$\frac{\partial \bar{\bar{p}}}{\partial \phi} = \{\frac{B}{d} - \int_{-B/2d}^{B/2d} \bar{u}_2 d\xi\} \; / \; \int_{-B/2d}^{B/2d} \bar{u}_1 d\xi \qquad (F.13)$$

Appendix G. Computation of the vertical distribution of the secondary flow in case of turbulent flow

The vertical distribution function g of the stream function of the secondary circulation in case of turbulent flow is solved from equation (7.31)

$$\frac{\partial^2}{\partial\zeta^2}\left(a' \frac{\partial^2 g}{\partial\zeta^2}\right) = c \frac{\partial f^2}{\partial\zeta} \qquad (G.1)$$

, in which the constant c is adjusted in such way, that $\bar{g} = 1$ in each iteration step of the main flow computation. From the point of view of convergence, fulfilling this conditon is preferable to evaluating

$$c = - \frac{\bar{ru}}{k_m r_s} \frac{1}{\bar{\psi}} \qquad (G.2)$$

on the basis of the most recent values of k_m, $\bar{u}/r_s$ and $\bar{\psi}$. The boundary conditions to be satisfied at the surface are

$$g = 0 \quad \text{and} \quad a' \frac{\partial^2 g}{\partial\zeta^2} = 0 \quad \text{at} \quad \zeta = 0 \qquad (G.3)$$

and the wall function approximation near the bottom reads

$$g = k_s (1+\zeta) \{1 + \frac{\sqrt{g}}{\kappa C} \ln(1+\zeta)\} \quad \text{for} \quad \zeta \leq \zeta_1 \qquad (G.4)$$

The bottom friction constant k_s follows from the assumption that equation (G.1) and wall function (G.4) both hold good on the bottom-nearst mesh of the computational grid.
The procedure used to solve g and k_s from (G.1), (G.3) and (G.4) is based on repeated vertical integration of (G.1). Formal integration of (G.1) from the bottom to an arbitrary level ζ yields

$$\frac{\partial}{\partial\zeta}\left(a'\frac{\partial^2 g}{\partial\zeta^2}\right) - \left\{\frac{\partial}{\partial\zeta}\left(a'\frac{\partial^2 g}{\partial\zeta^2}\right)\right\}\Big|_{\zeta=-1} = cf^2 \tag{G.5}$$

From (G.4) it follows that

$$\left\{\frac{\partial}{\partial\zeta}\left(a'\frac{\partial^2 g}{\partial\zeta^2}\right)\right\}\Big|_{\zeta=-1} = k_s\frac{\sqrt{g}}{\kappa C}\left\{\frac{\partial}{\partial\zeta}\left(\frac{a'}{1+\zeta}\right)\right\}\Big|_{\zeta=-1} = k_s c_1 \tag{G.6}$$

, which defines c_1 as a known constant.
Integrating (G.5) form the surface to the level ζ yields, in view of the dynamic condition at the surface,

$$a'\frac{\partial^2 g}{\partial\zeta^2} = c\int_0^\zeta f^2 d\zeta + k_s c_1\zeta \tag{G.7}$$

There are two possibilities for the distribution of a' near the surface, one with $a' = 0$ and $\frac{\partial a'}{\partial\zeta} \neq 0$ at $\zeta = 0$ and one with $a' \neq 0$ and $\frac{\partial a'}{\partial\zeta} = 0$ at $\zeta = 0$. In the latter case there are no problems when dividing (G.7) by a', in the former case it would imply division by zero. Expanding the first two terms of (G.7) in a Taylor series about $\zeta = 0$. however, shows that

$$\left.\frac{\partial^2 g}{\partial\zeta^2}\right|_{\zeta=0} = \left(c\,f^2\big|_{\zeta=0} + k_s c_1\right)\Big/\left.\frac{\partial a'}{\partial\zeta}\right|_{\zeta=0} \tag{G.8}$$

So in either case (G.7) can be divided by a', to yield

$$\frac{\partial^2 g}{\partial\zeta^2} = \frac{c}{a'}\int_0^\zeta f^2 d\zeta + k_s c_1\frac{\zeta}{a'} \tag{G.9}$$

Vertical integration of (G.9) from $\zeta = \zeta_1$ to an arbitrary level ζ leads to

$$\frac{\partial g}{\partial\zeta} = c\int_{\zeta_1}^\zeta \frac{d\zeta}{a'}\int_0^\zeta f^2 d\zeta + k_s c_1\int_{\zeta_1}^\zeta \frac{\zeta}{a'}\,d\zeta + c_2 \tag{G.10}$$

The constant of integration c_2 is determined by applying the wall function approximation to $\frac{\partial g}{\partial \zeta}$ at ζ_1, as well. Hence

$$\left.\frac{\partial g}{\partial \zeta}\right|_{\zeta=\zeta_1} = k_s \{1 + \frac{\sqrt{g}}{\kappa C} + \frac{\sqrt{g}}{\kappa C} \ln(1+\zeta_1)\} \tag{G.11}$$

so that

$$c_2 = k_s c_2' \quad \text{with} \quad c_2' = 1 + \frac{\sqrt{g}}{\kappa c} + \frac{\sqrt{g}}{\kappa C} \ln(1+\zeta_1) \tag{G.12}$$

Integrating (G.10) from ζ_1 to ζ then yields

$$g = c \int_{\zeta_1}^{\zeta} d\zeta \int_{\zeta_1}^{\zeta} \frac{d\zeta}{a'} \int_0^{\zeta} f^2 d\zeta + k_s c_1 \int_{\zeta_1}^{\zeta} d\zeta \int_{\zeta_1}^{\zeta} \frac{\zeta}{a'} d\zeta +$$

$$+ k_s c_2' (\zeta-\zeta_1) + c_3 \tag{G.13}$$

, in which the constant of integration c_3 follows from (G.4) at $\zeta = \zeta_1$:

$$c_3 = k_s c_3' \quad \text{with} \quad c_3' = (1+\zeta_1) \{1 + \frac{\sqrt{g}}{\kappa C} \ln(1+\zeta_1)\} \tag{G.14}$$

Now there are two conditions left to determine k_s and c, viz. the kinematic condition at the surface, $g\big|_{\zeta=0} = 0$, and the condtion $\bar{g} = 1$. For the sake of brevity, expression (G.13) is rewritten as

$$g = c g_1 + k_s g_2 \tag{G.15}$$

$$\text{with} \quad g_1 = \int_{\zeta_1}^{\zeta} d\zeta \int_{\zeta_1}^{\zeta} \frac{d\zeta}{a'} \int_0^{\zeta} f^2 d\zeta \tag{G.16}$$

$$\text{and} \quad g_2 = c_1 \int_{\zeta_1}^{\zeta} d\zeta \int_{\zeta_1}^{\zeta} \frac{\zeta}{a'} d\zeta + c_2' (\zeta-\zeta_1) + c_3' \tag{G.17}$$

Then the surface conditon leads to

$$k_s = - c g_1|_{\zeta=0} / g_2|_{\zeta=0} \tag{G.18}$$

and the condition $\bar{g} = 1$ gives

$$c = \{\bar{g}_1 - \frac{g_1|_{\zeta=0}}{g_2|_{\zeta=0}} \bar{g}_2\}^{-1} \tag{G.19}$$

So the vertical distribution function g follows from

$$g = \{g_1 - \frac{g_1|_{\zeta=0}}{g_2|_{\zeta=0}} g_2\} / \{\bar{g}_1 - \frac{g_1|_{\zeta=0}}{g_2|_{\zeta=0}} \bar{g}_2\} \tag{G.20}$$

In the bottom shear stress computation step g is solved from a more extensive equation including ϕ-derivatives of g (equation (7.50); see also Appendix I). This partial differential equation cannot be solved using the repeated integration procedure described in the foregoing. Introducing an implicit finite-difference formulation for the ϕ-derivatives leads to an equation of the form

$$\frac{\partial^2}{\partial \zeta^2} (a' \frac{\partial^2 g}{\partial \zeta^2}) - a_1(\xi,\phi) \frac{\partial}{\partial \zeta} (f \frac{\partial g}{\partial \zeta}) = c' S(\xi,\phi,\zeta) \tag{G.21}$$

, where the coefficient a_1 and the factor S in the source term are known and the constant c' is determined from the condition $\bar{g} = 1$. For the solution of this equation a special procedure has to be devised.

In the actual model, equation (G.21) is based on an implicit second-order discretization of the ϕ-derivatives as in the Crank-Nicholson scheme (see Roache, 1972), but for the sake of simplicity the procedure will be explained here as if first-order backward differencing were applied. In either case the essential points of the procedure are the same.

With the first-order scheme, equation (7.50) can be eleborated to

$$\frac{\partial^2}{\partial\zeta^2}\left(a'\,\frac{\partial^2 g}{\partial\zeta^2}\right) - \frac{\varepsilon Re_0}{k_m r\Delta\phi}\,\frac{\partial}{\partial\zeta}\left(f\,\frac{\partial g}{\partial\zeta}\right) = c'\left[-\frac{\varepsilon Re_0}{k_m r\Delta\phi}\,\bar{u}\,\tilde{\psi}\,\frac{\partial}{\partial\zeta}\left(\tilde{f}\,\frac{\partial\tilde{g}}{\partial\zeta}\right) + \right.$$

$$\left. - \frac{\bar{ru}^2}{r_s}\,\frac{\partial f^2}{\partial\zeta} + \frac{k_m}{Re_0}\left(\frac{\bar{u}}{r}\,\frac{\partial\bar{\omega}_m}{\partial\phi} - \frac{\bar{\omega}_m}{r}\,\frac{\partial\bar{u}}{\partial\phi}\right)\frac{\partial}{\partial\zeta}\,(a'f)\right] \qquad (G.22)$$

Integrating this equation from the bottom to an arbitrary level ζ yields, in the same way as for equation (G.1),

$$\frac{\partial}{\partial\zeta}\left(a'\,\frac{\partial^2 g}{\partial\zeta^2}\right) - \frac{\varepsilon Re_0}{k_m r\Delta\phi}\,f\,\frac{\partial g}{\partial\zeta} = k_s c_1 + c'\left[-\frac{\varepsilon Re_0}{k_m r\Delta\phi}\,\bar{u}\,\tilde{\psi}\,\tilde{f}\,\frac{\partial\tilde{g}}{\partial\zeta} + \right.$$

$$\left. - \frac{\bar{ru}^2}{r_s}\,f^2 + \frac{k_m}{Re_0}\left(\frac{\bar{u}}{r}\,\frac{\partial\bar{\omega}_m}{\partial\phi} - \frac{\bar{\omega}_m}{r}\,\frac{\partial\bar{u}}{\partial\phi}\right)a'f\right] \qquad (G.23)$$

, in which the constant c_1 is given by (G.6).
Now g is split up into two parts according to (G.15), so that the functions g_1 and g_2 can be solved from

$$\frac{\partial}{\partial\zeta}\left(a'\,\frac{\partial^2 g_1}{\partial\zeta^2}\right) - \frac{\varepsilon Re_0}{k_m r\Delta\phi}\,f\,\frac{\partial g_1}{\partial\zeta} = \left[\ldots\ldots\right] \qquad (G.24)$$

$$\frac{\partial}{\partial\zeta}\left(a'\,\frac{\partial^2 g_2}{\partial\zeta^2}\right) - \frac{\varepsilon Re_0}{k_m r\Delta\phi}\,f\,\frac{\partial g_2}{\partial\zeta} = c_1 \qquad (G.25)$$

with the surface conditions

$$a'\,\frac{\partial^2 g_1}{\partial\zeta^2} = 0 \quad \text{and} \quad a'\,\frac{\partial^2 g_2}{\partial\zeta^2} = 0 \quad \text{at} \quad \zeta = 0 \qquad (G.26)$$

and the wall function approximations

$$g_1 = 0 \quad \text{and} \quad g_2 = (1+\zeta)\left\{1 + \frac{\sqrt{g}}{\kappa C}\ln(1+\zeta)\right\} \quad \text{for} \quad \zeta \le \zeta_1 \qquad (G.27)$$

$$\frac{\partial g_1}{\partial \zeta} = 0 \quad \text{and} \quad \frac{\partial g_2}{\partial \zeta} = 1 + \frac{\sqrt{g}}{\kappa C} + \frac{\sqrt{g}}{\kappa C} \ln(1+\zeta) \qquad \text{for} \quad \zeta \leq \zeta_1 \tag{G.28}$$

When considered as two systems for $\frac{\partial g_1}{\partial \zeta}$ and $\frac{\partial g_2}{\partial \zeta}$, equations (G.24) through (G.28) can be solved in a similar way as the equation for f (see Appendix E).

Subsequently, g_1 and g_2 can be determined by integrating their vertical derivatives along the vertical, starting at the level $\zeta = \zeta_1$ and taking account of approximations (G.27).

Once the functions g_1 and g_2 are known, the constants k_s and c' can be determined as described before (see expressions (G.18) through (G.20)).

Appendix H. Computation of the depth-averaged stream function of the secondary flow in case of turbulent flow

The depth-averaged stream function equation for the secondary flow (7.39) is first-order in ϕ and fourth-order in ξ. It is solved using an implicit forward marching technique, i.e. starting from the upstream boundary $\bar{\psi}$ is solved implicity in each subsequent cross-section. The equation in ξ to be solved there can be written as

$$k_m \overline{a'g} \frac{\partial^2}{\partial \xi^2} (\bar{u} \frac{\partial^2 \bar{\psi}}{\partial \xi^2}) + a_1 \frac{\partial}{\partial \xi} (\bar{u} \frac{\partial \bar{\psi}}{\partial \xi}) + a_2 \bar{\psi} \frac{\partial^2 \bar{u}}{\partial \xi^2} + a_3 \frac{\partial^2}{\partial \xi^2} (\overline{u\psi}) +$$

$$+ a_4 \overline{u\psi} + a_5 \frac{\partial}{\partial \xi} (\bar{v} \frac{\partial^2 \bar{\psi}}{\partial \xi^2}) + a_6 \frac{\partial}{\partial \xi} (\overline{v\psi}) = S \qquad (H.1)$$

, in which a_1 through a_6 are known functions of ξ. The source term S contains the source terms of equation (7.39) and the known terms arising from the streamwise discretization.
Equation (H.1) must be solved in combination with the wall function approximations (7.43) and (7.44), in which the wall friction velocities $\bar{w}_{\tau l}$ and $\bar{w}_{\tau r}$ depend on the solution of (H.1). This problem is treated in a similar way as in the main velocity computation described in Appendix F.
Formal integration of (H.1) over the wall-nearest mesh of the computational grid yields for the left wall

$$k_m a'g \frac{\partial}{\partial \xi} (\bar{u} \frac{\partial^2 \bar{\psi}}{\partial \xi^2}) \Big|_{\xi=\xi_1} - k_m a'g \frac{\partial}{\partial \xi} (\bar{u} \frac{\partial^2 \bar{\psi}}{\partial \xi^2}) \Big|_{wall} + \text{other terms} =$$

$$\int_{-B/2d}^{\xi} S d\xi \qquad (H.2)$$

All terms in the left hand part of this equation, except the second one, can be evaluated in terms of the nodal values $\bar{\psi}_1$, $\bar{\psi}_2$,...

using the wall function (7.43) and standard finite difference schemes. The second term can be elaborated to

$$k_m \overline{a'g} \frac{\partial}{\partial \xi} \left(\bar{u} \frac{\partial^2 \bar{\psi}}{\partial \xi^2} \right) \Bigg|_{wall} = \frac{a'g}{a'f} \frac{\bar{r}\bar{w}_{\tau 1}}{\bar{u}_{\tau 1} Re_0} k_m \overline{a'^2} \frac{\partial}{\partial \xi} \left(\bar{u} \frac{\partial \bar{u}}{\partial \xi} \right) \Bigg|_{wall}$$

$$= - \frac{\overline{a'g}}{\overline{a'f}} \frac{\bar{r}\bar{w}_{\tau 1}}{\bar{u}_{\tau_1}} \bar{\tau}_{1\phi} \qquad \text{(H.3)}$$

, in which $\bar{\tau}_{1\phi}$ and $\bar{u}_{\tau 1}$ are known from the main flow computation. The quantity $\bar{w}_{\tau 1}$ is related to $\bar{\psi}_1$ through

$$\bar{w}_{\tau 1} = \kappa Re_0 \frac{\bar{\psi}_1}{r} \left[\left(\frac{B}{2d} + \xi_1 \right) \left\{ \frac{\kappa C}{\sqrt{g}} + \ln \left(\frac{B}{2d} + \xi_1 \right) \right\} \right]^{-1} \qquad \text{(H.4)}$$

Thus equation (H.2) is expressed in terms of $\bar{\psi}_1$, $\bar{\psi}_2$, ... On the mesh adjacent to the right wall a similar procedure is followed to express the equation corresponding with (H.2) in terms of $\bar{\psi}_n$, $\bar{\psi}_{n-1}$, ... On the other meshes of the computational grid equation (H.1) is discretized using standard methods. In this way the problem is reduced to solving n linear equations with n unknowns.

Appendix I. Decay of the secondary circulation in turbulent flow beyond a bend

As became evident from par. 5.8.4 and Appendix B, the accurate computation of the growth and decay of the secondary circulation in laminar flow requires special attention. In regions with a strong growth or decay of the secondary flow, a strict application of the similarity hypothesis (5.25) leads to considerable errors in the secondary flow intensity and, to a less extent, in the transverse component of the bottom shear stress. These errors are caused by the vertical non-uniformity of the rate of adaptation of the secondary flow to a streamwise variation of its sources: near the bottom the secondary flow tends to adapt faster to such a variation than near the surface. As this phenomenon is likely to occur in turbulent flow, as well, the laminar flow investigations described in Appendix B will also be made for turbulent flow.

In order to reduce the problem to the essentials, considerations are limited to the case of decaying secondary flow along a straight streamline*) in shallow channel flow. The main velocity is given, with $\bar{u} \equiv 1$ and $\bar{v} \equiv 0$, and in the transverse momentum equation all ξ-derivatives are disregarded, except for the transverse pressure gradient. The vertical distribution of the pressure is assumed hydrostatic. Then the transverse momentum equation (7.4) reduces to

$$\varepsilon^3 Re_0 \, u_m \frac{\partial v_s}{\partial s} = - \frac{\partial p}{\partial \xi} + \varepsilon^2 \frac{\partial}{\partial \zeta} \left(a \frac{\partial v_s}{\partial \zeta} \right) \tag{I.1}$$

and the stream function equation for the secondary flow becomes

$$\varepsilon Re_0 \frac{\partial}{\partial \zeta} \left(u_m \frac{\partial^2 \psi}{\partial s \partial \zeta} \right) = \frac{\partial^2}{\partial \zeta^2} \left(a \frac{\partial^2 \psi}{\partial \zeta^2} \right) \tag{I.2}$$

---

*) Actually: in a vertical plane through a straight streamline.

For $u_m = \bar{u}\, f(\zeta)$ and $a = \bar{u} a'(\zeta)$, these equation can be elaborated to

$$\varepsilon^3 Re_0 \, f \frac{\partial v_s}{\partial s} = - \frac{\partial p}{\partial \xi} + \varepsilon^2 \frac{\partial}{\partial \zeta} \left(a' \frac{\partial v_s}{\partial \zeta} \right) \tag{I.3}$$

and

$$\frac{\partial^2}{\partial \zeta^2} \left(a' \frac{\partial^2 \psi}{\partial \zeta^2} \right) - \varepsilon Re_0 \frac{\partial^2}{\partial s \partial \zeta} \left(f \frac{\partial \psi}{\partial \zeta} \right) = 0 \tag{I.4}$$

At the upstream end of the streamline plane considered, the secondary flow is given:

$$v_s \Big|_{s=0} = v_0 \qquad \text{and} \qquad \psi \Big|_{s=0} = \psi_0 \tag{I.5}$$

The dynamic condition at the surface reads

$$a' \frac{\partial v_s}{\partial \zeta} \Big|_{\zeta=0} = 0 \quad \text{and} \quad a' \frac{\partial^2 \psi}{\partial \zeta^2} \Big|_{\zeta=0} = 0 \tag{I.6}$$

The boundary condition at the bottom is replaced by the wall function approximation

$$v_s = \frac{v_{\tau s}}{\kappa} \left\{ \frac{\kappa C}{\sqrt{g}} + 1 + \ln(1+\zeta) \right\} \quad \text{and}$$

$$\psi = - \frac{r v_{\tau s}}{\kappa Re_0} (1+\zeta) \left\{ \frac{\kappa C}{\sqrt{g}} + \ln(1+\zeta) \right\} \tag{I.7}$$

The condition of zero net transverse velocity leads to

$$\int_{-1}^{0} v_s \, d\zeta = 0 \qquad \text{and} \qquad \psi \Big|_{\zeta=0} = 0 \tag{I.8}$$

The secondary flow can be determined either from equation (I.3) and the v_s-formulation of conditons (I.5) through (I.8) or from

equation (I.4) and the ψ-formulation of these conditions. The v_s-mode of the system was considered earlier by Ananyan (1965) and Rozovskii (1961). The former showed that, at least for $\alpha' \equiv 1$ and $u \equiv 1$, horizontal diffusion is of minor importance here. The latter solved the system for $\frac{\partial p}{\partial \xi} = 0$, parabolic α' and logarithmic u, which led to a rather good description of the decay of the secondary flow in a straight reach beyond a rather sharp bend in a shallow rectangular channel.
Figure I.1 shows the results of the numerical solution of the ψ-mode of the system, with α' according to (6.59) and the corresponding f for uniform rectilinear shear flow. At the inflow boundary the stream function is taken

$$\psi_0 = \frac{1}{Re_0} g(\zeta) \tag{I.9}$$

, in which $g(\zeta)$ is the vertical distribution function found from (7.31) for the given distributions of α' and f.
According to figure I.1.a, the quantity $Re_0\hat{\Psi}$, which can be taken as a measure of the secondary flow intensity*), decays almost exponentially with the normalized distance to the inflow boundary $\sigma = s/\varepsilon Re_0$. Consequently, the decay of the secondary flow intensity can be characterized by a relaxation lenght λ, defined by

$$Re\hat{\Psi} = Re_0\hat{\Psi}_0 e^{-\sigma/\lambda} \tag{I.10}$$

For $8 \leq C/\sqrt{g} \leq 24$ and $4 \leq \lambda \leq 6$, the values of λ lie between 0.076 and 0.082. This implies that the length needed for the secondary flow to be reduced 10% of its original intensity is given by

$$l_{0.1} \simeq 0.18\ Re_0 d \tag{I.11}$$

---

*) According to definition (5.25) : $\int_{-1}^{0} |v_s| d\zeta = 2Re_0 \frac{\hat{\Psi}}{r}$

This corresponds rather well with the results obtained by Rozovskii (1961)

$$\lambda \simeq 0.083 \quad \text{and} \quad l_{0.1} \simeq 0.19\ Re_0 d \tag{I.12}$$

Besides, (I.11) shows a strong resemblance to its laminar flow counterpart (5.12).
In addition to the decay of its intensity, the secondary flow undergoes a deformation of its vertical distribution, as shown in figure I.1.b.
This deformation can be explained from the tendency of the secondary flow to be reduced faster near the bottom then near the surface (see figure I.1c).
This tendency also explains why shortly after a transition between two subsequent opposite bends the secondary flow breaks up into two counter-rotating cells, the upper one being a remainder of the upstream bend and the lower one corresponding with the downstream bend already (cf. Rozovskii, 1961; Yen, 1965; Götz, 1975).
Another consequence of the faster reduction of the secondary flow near the bottom is that the transverse component of the bottom shear stress decays faster than the secondary flow intensity (see figure I.1.d). Near the inflow section $s = 0$ the rate of decay of $\tau_{b\xi}$ is about twice the one of $\hat{\psi}$, further downstream the decay rates are almost equal.

Though equations (I.3) and (I.4) are relatively simple for the case considered here, solving the complete three-dimensional stream function equation for the secondary flow would become far too expensive for the present mathematical model of curved channel flow. Therefore the possibility of simplified computations will be investigated here.
The basic assumption underlying all simplified computation methods for the growth and decay of the secondary flow in and beyond channels bends (Rozovskii, 1961; Nouh et al., 1979; Falcón, 1979; De Vriend, 1979a) is the similarity hypothesis

$$v_s = - \tilde{v}_s \frac{\partial g}{\partial \zeta} \qquad \text{and} \qquad \psi = \bar{\psi}\, g(\zeta) \tag{I.13}$$

If (I.13) holds good, equations (I.3) and (I.4) reduce to

$$f \frac{\partial g}{\partial \zeta} \frac{\partial \tilde{v}_s}{\partial \sigma} = \frac{1}{\varepsilon^2} \frac{\partial p}{\partial \xi} + \tilde{v}_s \frac{\partial}{\partial \zeta} \left(a' \frac{\partial^2 g}{\partial \zeta^2}\right) \tag{I.14}$$

$$\frac{\partial}{\partial \zeta} \left(f \frac{\partial g}{\partial \zeta}\right) \frac{\partial \bar{\psi}}{\partial \sigma} - \bar{\psi} \frac{\partial^2}{\partial \zeta^2} \left(a' \frac{\partial^2 g}{\partial \zeta^2}\right) = 0 \tag{I.15}$$

If g is known, the quantities $\tilde{v}_s$ and $\bar{\psi}$ can be solved from these equations and the relevant inflow conditions. Doing so at different levels ζ, however, leads to different results, since approximation (I.13) is not exactly true for the solution of the complete parabolic system (I.3) through (I.8). Hence simplifications of this type resolve themselves into replacing (I.14) or (I.15) by an appropriate one-dimensional equation.
Rozovskii (1961) states that the transverse pressure gradient in (I.14) is approximately equal to zero and can be disregarded. Then equation (I.14) can be rewritten into the form

$$\frac{\partial v_s}{\partial \sigma} = - \tilde{v}_s F(\zeta) \qquad \text{with} \qquad F(\zeta) = \frac{\partial}{\partial \zeta} \left(a' \frac{\partial^2 g}{\partial \zeta^2}\right) / \left(- f \frac{\partial g}{\partial \zeta}\right) \tag{I.16}$$

Averaging this equation over the depth of flow and taking $\bar{F} = 12$ yields

$$\tilde{v}_s = \tilde{v}_s \Big|_{\sigma=0} e^{-12\sigma} \tag{I.17}$$

and hence λ and $l_{0.1}$ according to (I.12).
Nouh et al. (1979) also neglect the transverse pressure gradient and solve (I.16) at the level $\zeta = - 0.9$, which yields

$$\tilde{v}_s = \tilde{v}_s \Big|_{\sigma=0} e^{-15.6\sigma} \tag{I.18}$$

This corresponds with $\lambda = 0.064$ and $l_{0.1} = 0.15\ Re_0 d$. It should be noted, however, that entirely different values of λ are found when solving (I.16) at other levels than $\zeta = -0.9$, as the function $F(\zeta)$ in this equation varies strongly along the vertical (see Rozovskii, 1961). Falcón (1979) considers the moment-of-momentum equation

$$(\tfrac{1}{2} + \zeta)\, f\, \frac{\partial g}{\partial \zeta}\, \frac{\partial \tilde{v}_s}{\partial \sigma} = \frac{\tfrac{1}{2} + \zeta}{\varepsilon^2}\, \frac{\partial p}{\partial \xi} + \tilde{v}_s\, (\tfrac{1}{2} + \zeta)\, \frac{\partial}{\partial \zeta}\, (a'\, \frac{\partial^2 g}{\partial \zeta^2}) \qquad \text{(I.19)}$$

instead of (I.14). Taking the depth-average of (I.19) yields

$$\overline{(\tfrac{1}{2} + \zeta)\, f\, \frac{\partial g}{\partial \zeta}}\, \frac{\partial \tilde{v}_s}{\partial \sigma} = -\, \tilde{v}_s\, \{\overline{a'\, \frac{\partial^2 g}{\partial \zeta^2}} - a'\, \frac{\partial^2 g}{\partial \zeta^2}\Big|_{\zeta=-1}\} \qquad \text{(I.20)}$$

For $C = 50\ m^{\frac{1}{2}}/s$, parabolic a', logarithmic f and corresponding g (see expression (7.46)), this leads to

$$\tilde{v}_s = \tilde{v}_s\Big|_{s=0}\, e^{-21.0\sigma} \qquad \text{(I.21)}$$

, whence $\lambda = 0.048$ and $l_{0.1} = 0.11\ Re_0 d$.

The equation for the depth-averaged stream function of the secondary flow in the main flow computation step of the present model (see par. 7.4.4) corresponds with the depth-average of equation (I.15), which is equivalent to the difference between the versions of (I.14) at the surface and near the bottom. So

$$f\, \frac{\partial g}{\partial \zeta}\Big|_{\zeta=0}\, \frac{\partial \tilde{v}_s}{\partial \sigma} = \tilde{v}_s\, \left[\frac{\partial}{\partial \zeta}\, (a'\, \frac{\partial^2 g}{\partial \zeta^2})\Big|_{\zeta=0} - \frac{\partial}{\partial \zeta}\, (a'\, \frac{\partial^2 g}{\partial \zeta^2})\Big|_{\zeta=\zeta^*}\right] \qquad \text{(I.22)}$$

with $\zeta^* = -1 + \exp\,(-\frac{\kappa C}{\sqrt{g}} - 1)$. For the example considered in the foregoing, the solution of this equation becomes

$$\tilde{v}_s = \tilde{v}_s\Big|_{s=0} e^{-61.8\sigma} \qquad (I.23)$$

and, correspondingly, $\lambda = 0.016$ and $l_{0.1} = 0.04\ Re_0 d$.
Compared with the results from the complete parabolic equation (see (I.10) and (I.11)), the last result is very poor. Besides, it is quite sensitive to the choice of the level ζ^*). Therefore, this approach must be rejected for the bottom shear stress computation step of the present turbulent flow model.
In contrast with the laminar flow case (see Appendix B), the methods disregarding the transverse pressure gradient (Rozovskii, Nouh et al.) lead to rather good predictions of the decay of the secondary flow intensity here. On the other hand, the results from Falcón's moment-of-momentum equation are somewhat poorer.
None of the methods based on the strict application of the similarity hypothesis is to predict the difference in decay rate between the secondary flow intensity and the transverse component of the bottom shear stress. In the example represented in figure I.1.d, for instance, application of the similarity hypothesis would lead to errors in the transverse bottom shear stress up to 50% (i.e. up to 10% of the value in the inflow section). So if the transverse bottom shear stress must be determined accurately, the similarity hypothesis should not be applied in its strict form (I.13), but the vertical deformations of the secondary flow profile must be taken into account.
Besides, the break-up of the secondary circulation near the transition between two subsequent opposite bends cannot be described, unless the vertical distribution of the secondary flow is allowed to vary with s as well as with ζ. Therefore the similarity hypothesis (I.13) is generalized to

$$v_s = -\tilde{v}_s \frac{\partial g}{\partial \zeta} \quad \text{and} \quad \psi = \bar{\psi}\, g(\zeta, s) \qquad (I.24)$$

The corresponding solution procedure is devised such, that it

is also applicable to the complete model of turbulent curved channel flow. If, for explanatory reasons, a simple first-order discretization is applied to the s-derivative, equation (I.4) can be rewritten as

$$\frac{\partial^2}{\partial\zeta^2}\left(a'\,\frac{\partial^2\psi}{\partial\zeta^2}\right) - \frac{1}{\Delta\sigma}\frac{\partial}{\partial\zeta}\left(f\,\frac{\partial\psi}{\partial\zeta}\right) = -\frac{1}{\Delta\sigma}\frac{\partial}{\partial\zeta}\left(\tilde{f}\,\frac{\partial\tilde{\psi}}{\partial\zeta}\right) \tag{I.25}$$

, where $\tilde{f}$ and $\tilde{\psi}$ are quantities at a distance $\Delta\sigma$ upstream of the section considered. Substituting (I.24) into this equation leads to

$$\bar{\psi}\left[\frac{\partial^2}{\partial\zeta^2}\left(a'\,\frac{\partial^2 g}{\partial\zeta^2}\right) - \frac{1}{\Delta\sigma}\frac{\partial}{\partial\zeta}\left(f\,\frac{\partial g}{\partial\zeta}\right)\right] = -\frac{\bar{\tilde{\psi}}}{\Delta\sigma}\frac{\partial}{\partial\zeta}\left(\tilde{f}\,\frac{\partial\tilde{g}}{\partial\zeta}\right) \tag{I.26}$$

and averaging over the depth of flow yields

$$\bar{\psi}\left[\overline{\frac{\partial^2}{\partial\zeta^2}\left(a'\,\frac{\partial^2 g}{\partial\zeta^2}\right)} - \frac{1}{\Delta\sigma}\,f\,\frac{\partial g}{\partial\zeta}\bigg|_{\zeta=0}\right] = -\frac{\bar{\tilde{\psi}}}{\Delta\sigma}\,\tilde{f}\,\frac{\partial\tilde{g}}{\partial\zeta}\bigg|_{\zeta=0} \tag{I.27}$$

In addition, equation (I.26) can be rewritten to the following equation for g:

$$\frac{\partial^2}{\partial\zeta^2}\left(a'\,\frac{\partial^2 g}{\partial\zeta^2}\right) - \frac{1}{\Delta\sigma}\frac{\partial}{\partial\zeta}\left(f\,\frac{\partial g}{\partial\zeta}\right) = -\frac{c'}{\Delta\sigma}\,\frac{\partial}{\partial\zeta}\left(\tilde{f}\,\frac{\partial\tilde{g}}{\partial\zeta}\right) \tag{I.28}$$

, in which the constant c', theorethically equal to $\bar{\tilde{\psi}}/\bar{\psi}$, is considered as an unknown, to be determined from the condition $\bar{g} = 1$. The solution procedure for equation (I.28) with the relevant boundary conditions is described in Appendix G. Once g is known, $\bar{\psi}$ can be determined from (I.27).
If g and $\bar{\psi}$ are solved alternately in all verticals of the computational grid, the solution of (I.27) and (I.28) is identical to the solution of equation (I.4) for the same streamwise discretization. In the complete model for turbulent curved channel flow, however, g is solved in the entire flow field before

solving $\bar{\psi}$. Therefore a similar iterative procedure is applied to equations (I.27) and (I.28):

. estimate g by taking the fully-developed curved flow distribution,

. calculate $\bar{\psi}$ from equation (I.27),

. calculate g from equation (I.28),

et cetera. If all sources of secondary flow are absent, this procedure can be shown to lead to the "exact" solution in two iteration steps. If there are sources of secondary flow (main flow curvature), it takes more iteration steps, but still convergence is quite rapid.

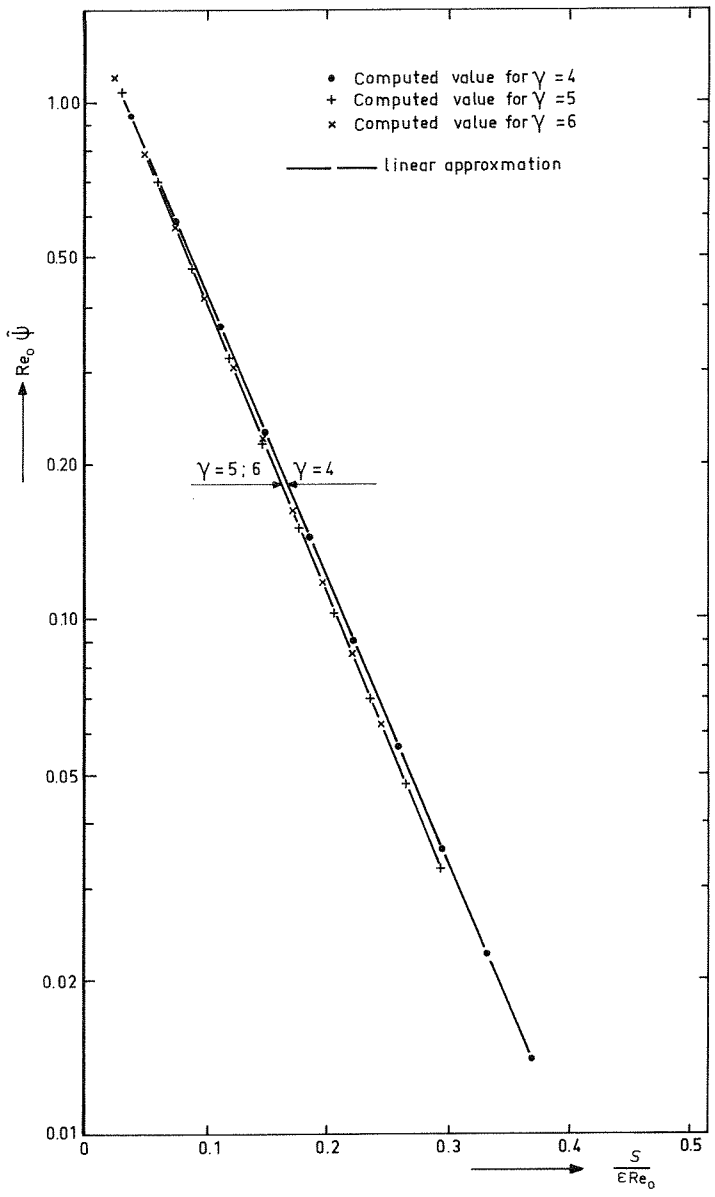

Figure I.1. Decay of the secondary flow beyond a bend
(a) Secondary flow intensity for C=50 $m^{\frac{1}{2}}/s$

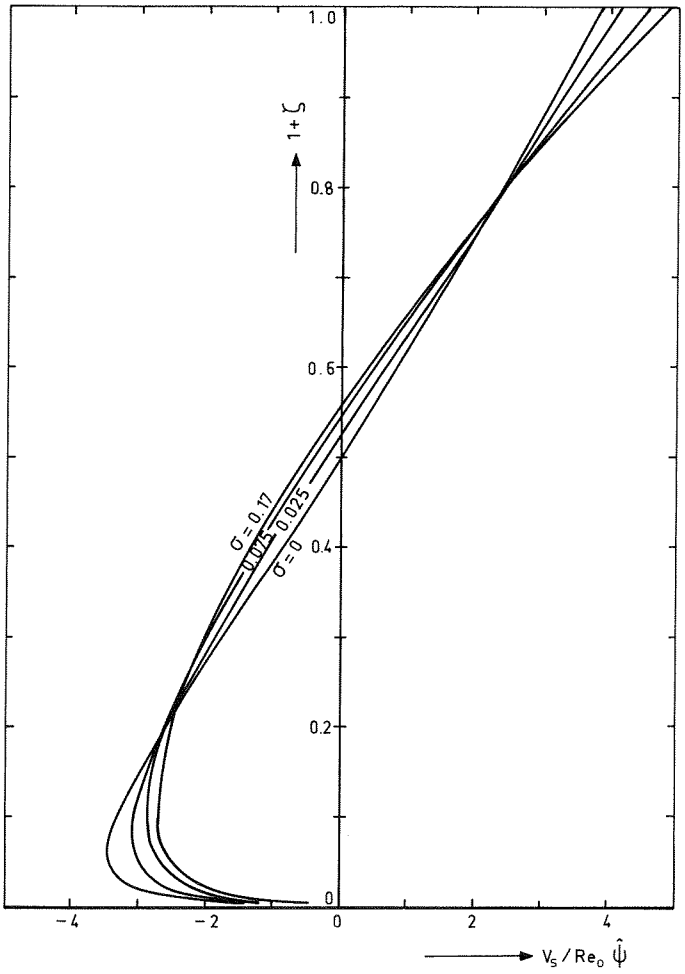

Figure I.1. Decay of the secondary flow beyond a bend
(b) Vertical distribution (γ=6; C=50 $m^{\frac{1}{2}}/s$)

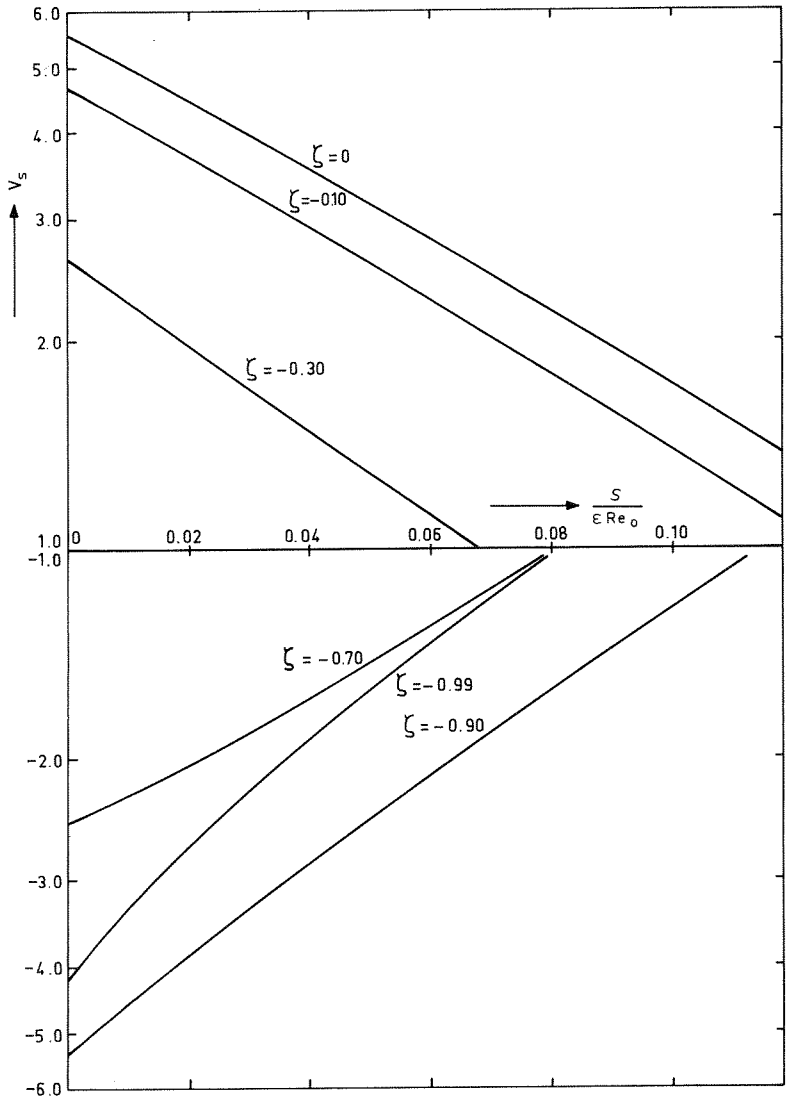

Figure I.1. Decay of the secondary flow beyond a bend
(c) Transverse velocity component (γ=5; C=50 $m^{\frac{1}{2}}/s$)

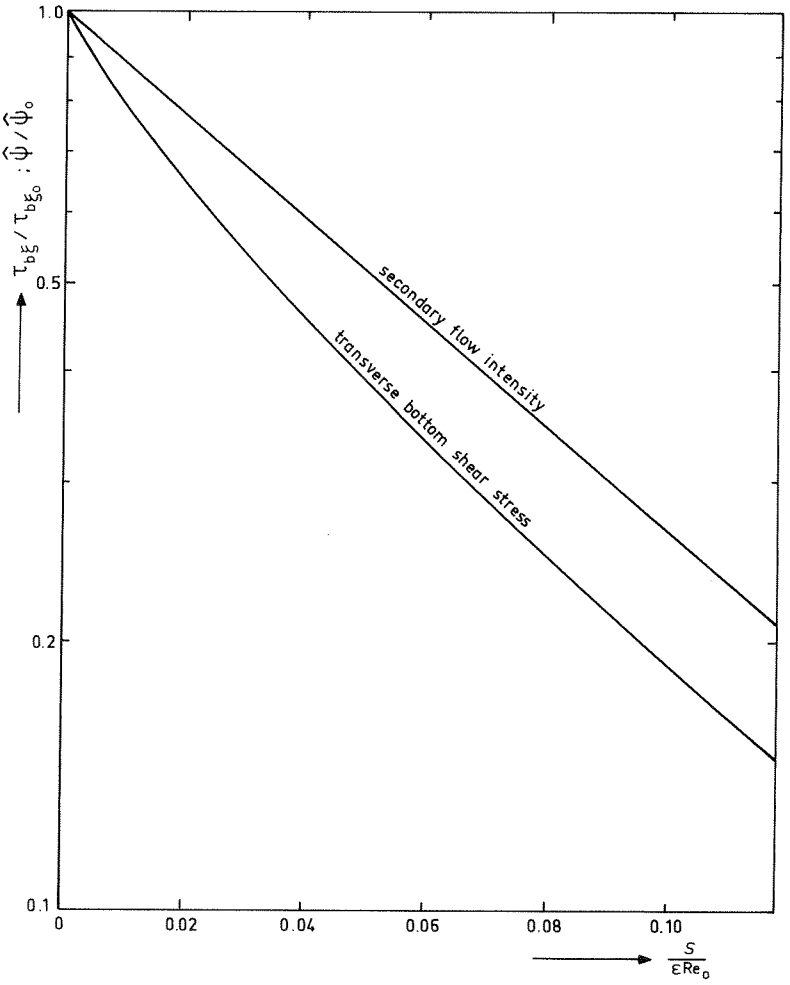

Figure I.1. Decay of the secondary flow beyond a bend
(d) Transverse bottom shear stress (γ=5; C=50 $m^{\frac{1}{2}}/s$)

Appendix J. Transformation of the vertical

The transformation from the cylindrical coordinate system (ξ,ϕ,ζ) to the non-orthogonal channel-fitted system (ξ',ϕ',z) is described by

$$\xi' = \xi; \quad \phi' = \phi; \quad z = \frac{\zeta-\zeta_s}{h} \tag{J.1}$$

Hence the elements of the transformation matrix are

$$\frac{\partial\xi'}{\partial\xi} = 1; \quad \frac{\partial\xi'}{\partial\phi} = 0; \quad \frac{\partial\xi'}{\partial\zeta} = 0 \tag{J.2}$$

$$\frac{\partial\phi'}{\partial\xi} = 0; \quad \frac{\partial\phi'}{\partial\phi} = 1; \quad \frac{\partial\phi'}{\partial\zeta} = 0 \tag{J.3}$$

$$\frac{\partial z}{\partial\xi} = -\frac{1}{h}\frac{\partial\zeta_s}{\partial\xi} - \frac{\zeta-\zeta_s}{h^2}\frac{\partial h}{\partial\xi} = -\frac{1+z}{h}\frac{\partial\zeta_s}{\partial\xi'} + \frac{z}{h}\frac{\partial\zeta_b}{\partial\xi'} \tag{J.4a}$$

$$\frac{\partial z}{\partial\phi} = -\frac{1}{h}\frac{\partial\zeta_s}{\partial\phi} - \frac{\zeta-\zeta_s}{h^2}\frac{\partial h}{\partial\phi} = -\frac{1+z}{h}\frac{\partial\zeta_s}{\partial\phi'} + \frac{z}{h}\frac{\partial\zeta_b}{\partial\phi'} \tag{J.4b}$$

$$\frac{\partial z}{\partial\zeta} = \frac{1}{h} \tag{J.4c}$$

The first and second derivatives occurring in the flow equations can then be elaborated to

$$\frac{\partial}{\partial\xi} = \frac{\partial}{\partial\xi'} - T_{\xi'}\frac{\partial}{\partial z} \qquad \text{with} \qquad T_{\xi'} = \frac{1+z}{h}\frac{\partial\zeta_s}{\partial\xi'} - \frac{z}{h}\frac{\partial\zeta_b}{\partial\xi'} \tag{J.5}$$

$$\frac{\partial}{\partial\phi} = \frac{\partial}{\partial\phi'} - T_{\phi'}\frac{\partial}{\partial z} \qquad \text{with} \qquad T_{\phi'} = \frac{1+z}{h}\frac{\partial\zeta_s}{\partial\phi'} - \frac{z}{h}\frac{\partial\zeta_b}{\partial\phi'} \tag{J.6}$$

$$\frac{\partial}{\partial\zeta} = \frac{1}{h}\frac{\partial}{\partial z} \tag{J.7}$$

$$\frac{\partial^2}{\partial \xi^2} = \frac{\partial^2}{\partial \xi'^2} - 2T_{\xi'} \frac{\partial^2}{\partial \xi' \partial z} + T_{\xi'}^2 \frac{\partial^2}{\partial z^2} - T_{\xi'\xi'} \frac{\partial}{\partial z} \tag{J.8}$$

$$\text{with} \quad T_{\xi'\xi'} = \frac{1+z}{h} \{\frac{\partial^2 \zeta_s}{\partial \xi'^2} - \frac{2}{h} \frac{\partial \zeta_s}{\partial \xi'} (\frac{\partial \zeta_s}{\partial \xi'} - \frac{\partial \zeta_b}{\partial \xi'})\} +$$

$$- \frac{z}{h} \{\frac{\partial^2 \zeta_b}{\partial \xi'^2} - \frac{2}{h} \frac{\partial \zeta_b}{\partial \xi'} (\frac{\partial \zeta_s}{\partial \xi'} - \frac{\partial \zeta_b}{\partial \xi'})\} \tag{J.9}$$

$$\frac{\partial^2}{\partial \phi^2} = \frac{\partial^2}{\partial \phi'^2} - 2T_{\phi'} \frac{\partial^2}{\partial \phi' \partial z} + T_{\phi'}^2 \frac{\partial^2}{\partial z^2} - T_{\phi'\phi'} \frac{\partial}{\partial z} \tag{J.10}$$

$$\text{with} \quad T_{\phi'\phi'} = \frac{1+z}{h} \{\frac{\partial^2 \zeta_s}{\partial \phi'^2} - \frac{2}{h} \frac{\partial \zeta_s}{\partial \phi'} (\frac{\partial \zeta_s}{\partial \phi'} - \frac{\partial \zeta_b}{\partial \phi'})\} +$$

$$- \frac{z}{h} \{\frac{\partial^2 \zeta_b}{\partial \phi'^2} - \frac{2}{h} \frac{\partial \zeta_b}{\partial \phi'} (\frac{\partial \zeta_s}{\partial \phi'} - \frac{\partial \zeta_b}{\partial \phi'})\} \tag{J.11}$$

$$\frac{\partial^2}{\partial \zeta^2} = \frac{1}{h^2} \frac{\partial^2}{\partial z^2} \tag{J.12}$$

The flow equations are transformed from the (ξ,ϕ,ζ)-system to the (ξ',ϕ',z)-system by substituting (J.5) through (J.12).

Appendix K. Strongly simplified model

Apart from the computational procedure, the strongly simplified model described by Kalkwijk et al. (1980) differs from the present one at the following essential points:

- lateral diffusion is disregarded;
- the secondary flow intensity depends on the local properties of the main flow only;
- the vertical distributions of the main and the secondary flow are strictly self-similar throughout the channel;
- the streamline curvature is approximated by the local curvature of the longitudinal coordinate lines 1/r;
- the transverse pressure distribution is determined by the centripetal accelaration only;
- as far as the convective influence of the secondary flow is concerned, the model accounts only for the influence of that part of the vertical velocity component that is caused by the transverse variation of the water depth.

In the notation utilized in chapter 8, the depth-averaged system of equations then reads (cf. equations (8.74), (8.83), (8.84) and (8.94), respectively),

$$\frac{1}{r}\frac{\partial \bar{u}}{\partial \phi'} + \frac{\partial \bar{v}}{\partial \xi'} + \frac{\varepsilon}{r}\bar{v} + \frac{1}{h}\left(\frac{\bar{u}}{r}\frac{\partial h}{\partial \phi'} + \bar{v}\frac{\partial h}{\partial \xi'}\right) = 0 \tag{K.1}$$

$$\varepsilon Re_0 \overline{f^2}\left(\frac{\bar{u}}{r}\frac{\partial \bar{u}}{\partial \phi'} + \bar{v}\frac{\partial \bar{u}}{\partial \xi'} + \frac{\varepsilon}{r}\overline{\overline{uv}}\right) - \varepsilon Re_0^2 \overline{f\frac{\partial g}{\partial z}}\frac{\overline{\overline{\psi u}}}{h^3}\frac{\partial}{\partial \xi}\left(\frac{h^2}{r}\right) =$$

$$-\frac{1}{r}\frac{\partial \bar{p}}{\partial \phi'} - \frac{C_0}{C}\frac{\bar{u}^2}{h}\left(a'\frac{\partial f}{\partial z}\right)\Big|_{z=-1} \tag{K.2}$$

$$\varepsilon^2 Re_0 \overline{f^2}\frac{\bar{u}^2}{r} = \frac{\partial \bar{p}}{\partial \xi'} \tag{K.3}$$

$$\bar{\psi} = \frac{C}{C_0}\frac{h^2\bar{u}}{c} \tag{K.4}$$

The vertical distribution functions and the constant c are taken the same as in 'undisturbed' fully-developed curved channel flow. For a purely parabolic vertical distribution of the turbulence viscosity, this means that f and g correspond with expressions (7.45) and (7.46), respectively. The constant c then follows from

$$c = \frac{48}{2 - 5\frac{\sqrt{g}}{\kappa C} + 4\frac{g}{\kappa^2 C^2}} \left(\frac{\kappa C}{\sqrt{g}} + 2 + \frac{\sqrt{g}}{\kappa C}\right) \tag{K.5}$$

and the constants in equations (K.2) and (K.3) become

$$\overline{f^2} = 1 + \frac{g}{\kappa^2 C^2} \simeq 1 \tag{K.6}$$

$$\alpha' \left.\frac{\partial f}{\partial z}\right|_{z=-1} = 6\frac{\sqrt{g}}{\kappa C} \tag{K.7}$$

$$-\overline{f\frac{\partial g}{\partial z}} = \left(5\frac{\sqrt{g}}{\kappa C} - 15.6\frac{g}{\kappa^2 C^2} + 37.5\frac{g\sqrt{g}}{\kappa^3 C^3}\right)\frac{\kappa c\sqrt{g}}{6C} = k_{sn}\frac{\kappa c\sqrt{g}}{6C} \tag{K.8}$$

Then the depth-averaged momentum equations (K.2) and (K.3) can be rewritten as

$$\varepsilon\left(\frac{\bar{u}}{r}\frac{\partial \bar{u}}{\partial \phi'} + \bar{v}\frac{\partial \bar{u}}{\partial \xi'} + \frac{\varepsilon}{r}\overline{\overline{uv}}\right) + \varepsilon k_{sn}\frac{\bar{u}^2}{h}\frac{\partial}{\partial \xi'}\left(\frac{h^2}{r}\right) =$$

$$-\frac{1}{Re_0 r}\frac{\partial \bar{p}}{\partial \phi'} - \frac{g}{C^2}\frac{\bar{u}^2}{h} \tag{K.9}$$

$$\frac{\partial \bar{p}}{\partial \xi'} = \varepsilon^2 Re_0 \frac{\bar{u}^2}{r} \tag{K.10}$$

If equations (K.1), (K.9) and (K.10) allow for a forward-marching solution technique (cf. the parabolic mode of Spalding's method discussed in Appendix C), the numerical

solution procedure is rather simple and quite economic. Hence a flow model based on these equations would be attractive as a part of an overall mathematical model of the flow and the bed topography in curved alluvial rivers. The aforementioned authors have shown that their model gives good predictions of the main velocity distribution in gently curved channels comprising not too long bends*)and having a shallow non-rectangular cross-section with mildly sloping banks**). The predictions of the secondary flow, however, are not too good, because of the following reasons (see par. 9.3.1):

- the purely parabolic turbulence viscosity leads to an underestimation of the secondary flow intensity;
- the gradual growth and decay of the secondary flow beyond the entrance and the exit of a bend is not incorporated in the model;
- the secondary flow intensity is based on r instead of r_s, so that the influence of variations of the latter is represented incorrectly.

Since the direction of the bottom shear stress and hence the transverse configuration of an alluvial channel is closely related to the secondary flow, the flow model should be modified at these points in order to be applicable in the alluvial channel model.

As was shown in par. 9.2.2, a slight modification of the turbulence model (γ=7 and the 'k-ε-approximation for $\alpha'(z)$) is sufficient to deal with the underestimation of the secondary flow intensity. Figure K.1 shows how this modification influences the secondary flow intensity and the convection factor k_{sn} in the depth-averaged main flow equation. Both quantities turn out to increase considerably.

---

*) The model degenarates as the flow approaches its fully-developed curved stage.

**) In order to have negligible lateral diffusion and a zero transverse velocity at the lateral bounds of the flow. Besides, it is a necessary condition for the contribution of $\frac{\partial h}{\partial \xi_T}$ to be predominant in w_s.

In addition, figure K.1 makes clear that there is a considerable discrepancy between expression (K.8) for k_{sn} and the results of the numerical computation for γ=6 and parabolic $a'(z)$, especially for lower values of C. Probably, this is caused by a different treatment of the velocity profiles near the bottom. In the analytical solution, expressions (7.45) and (7.46) are extrapolated to the bottom when determining c and $f\frac{\partial g}{\partial z}$, whereas in the numerical computation of k_{sn} both f and g are assumed logarithmic near the bottom. The errors introduced in the former case are the severest, especially for the lower values of C.

Although it entails no essential difficulties, the computation of the streamline curvature on the basis of (5.31) is rather laborious. Therefore, it will be attempted to simplify this computation.
The most drastic simplification, applied in the parabolic mode of the present model and in the strongly simplified model, is to use r instead of r_s. For rectangular channels, this is a rather good approximation, but for non-rectangular channels with the cross-sectional shape varying along the channel it is too crude. Therefore, it will be attempted to simplify (5.31) in a less far-reaching way.
The equivalent of (5.31) before normalization reads (see De Vriend, 1978b):

$$\frac{1}{R_s} = \frac{1}{\bar{v}_{tot}^3}\left\{\bar{v}_\phi\left(\frac{\bar{v}_\phi}{R}\frac{\partial \bar{v}_R}{\partial \phi} + \bar{v}_R\frac{\partial \bar{v}_R}{\partial R} - \frac{\bar{v}_\phi^2}{R}\right) + \right.$$

$$\left. - \bar{v}_R\left(\frac{\bar{v}_\phi^2}{R}\frac{\partial \bar{v}_\phi}{\partial \phi} + \bar{v}_R\frac{\partial \bar{v}_\phi}{\partial R} + \frac{\bar{v}_R\bar{v}_\phi}{R}\right)\right\} \qquad (K.11)$$

In case of shallow, gently curved rivers with mildly sloping banks, the order of magnitude of each term in this expression can be estimated on the basis of the following arguments:
. the length scale of the transverse variations of the main flow can be taken equal to the length scale L_t of the

transverse bed level variations; on the banks, $d \ll L_t \ll R_c$, whereas in the central region and in the inner bend $L_t \simeq R_c$;

. the longitudinal variations of the main flow and the bed level in a bend have a length scale of R_c;

. the order of magnitude of the transverse component of the main velocity is determined by the longitudinal variation of the streamwise velocity component and the depth of flow, i.e. $v_R = O(Vd/R_c)$.

Hence expression (K.11) can be normalized as

$$\frac{1}{r_s} = \frac{1}{(\bar{u}^2+\varepsilon^2\bar{v}^2)^{3/2}} \{ \bar{u} \, (\varepsilon \frac{\bar{u}}{r} \frac{\partial \bar{v}}{\partial \phi} + \frac{\varepsilon^2 R_c}{L_t} \bar{v} \frac{\partial \bar{v}}{\partial \eta} - \frac{\bar{u}^2}{r}) +$$

$$- \varepsilon \bar{v} \, (\frac{\bar{u}}{r} \frac{\partial \bar{u}}{\partial \phi} + \frac{\varepsilon R_c}{L_t} \bar{v} \frac{\partial \bar{u}}{\partial \eta} + \frac{\varepsilon}{r} \overline{uv}) \} \qquad (K.12)$$

, in which η denotes the transverse coordinate y after normalization by L_t. Making use of the depth-averaged equation of continuity, this expression can be elaborated to

$$\frac{1}{r_s} = -\frac{1}{r} + \varepsilon(\frac{1}{\bar{u}r} \frac{\partial \bar{v}}{\partial \phi} + \frac{\bar{v}}{\bar{h}ur} \frac{\partial h}{\partial \phi}) + O(\varepsilon \frac{d}{L_t}, \varepsilon^2) \qquad (K.13)$$

The term $O(\varepsilon)$ in this expression accounts for the gradual response of the streamline curvature to an abrupt transition in the channel curvature (through the term with $\frac{\partial \bar{v}}{\partial \phi}$) and for the effect of longitudinal variations of the cross-sectional shape (through the term with $\frac{\partial h}{\partial \phi}$). When truncated after the term $O(\varepsilon)$, expression (K.13) gives a good approximation of the streamline curvature in the kind of channels considered here (see figure K.2). Moreover, the influence of the depth-variation term turns out to be so small, that its effect cannot be drawn in figure K.2. Hence this term can also be omitted, so that the approximative expression for the streamline curvature reduces to

$$\frac{1}{r_s} = -\frac{1}{r} + \frac{\varepsilon}{\bar{u}r}\frac{\partial}{\partial\phi} \qquad (K.14)$$

It should be pointed out, that both (5.31) and (K.14) only yield good results if the term with $\frac{\partial v}{\partial \phi}$ can be calculated with sufficient accuracy, especially near points where the channel curvature changes abruptly. In partially-parabolic models or other iterative procedures in which the flow field is swept through several times, this is no problem, since $\frac{\partial v}{\partial \phi}$ can be discretized using central differences. In forward-marching solution procedures like in a parabolic model, however, only the velocities upstream of the cross-section considered are known, so that upstream difference schemes have to be utilized. If the longitudinal step size is rather large, this will give rise to considerable errors near an abrupt change of r, irrespective as to whether (5.31) or (K.14) is applied (see figure K.2). Hence, including the effects of local streamline curvature into a parabolic model implies the use of a rather small longitudinal step size, at least near the channel transitions.

As was shown in Appendix I, the gradual adaptation of the secondary flow intensity to an abrupt change in its source approximately proceeds according to a damping exponential function, at least if all lateral influencing is absent. This suggests to calculate the secondary flow intensity in the present channels, in which direct lateral influencing is of minor importance, from an equation of the form

$$a_1(\xi,s)\frac{\partial\hat{\Psi}}{\partial s} + a_2(\xi,s)\hat{\Psi} = a_3(\xi,s) \qquad (K.15)$$

, in which a_1, a_2 and a_3 are known functions of ξ and s. In view of equation (8.100), equation (K.15) should read

$$\varepsilon Re_0 \frac{\partial\Psi}{\partial s} + k_m \frac{C_0}{C} a_2' \frac{\Psi}{h} = -a_3' \frac{r}{hr_s} \quad \text{with } \Psi = \frac{\bar{\psi}}{h^2\bar{u}}\left(-f\frac{\partial g}{\partial z}\right)\Big|_{z=0} \qquad (K.16)$$

, in which a_2' and a_3' are constants.
For γ=7 and the vertical distribution of the turbulence viscosity according to the 'k-ε-approximation', the constant a_2' lies between 13.6 and 12.3 as C varies from 25 $m^{\frac{1}{2}}/s$ to 75 $m^{\frac{1}{2}}/s$ (cf. Appendix I, where the values of $\lambda=1/a_2'$ were shown to lie between 0.076 and 0.082 for $4 \leq \gamma \leq 6$ and parabolic turbulence viscosity).
In addition, the 'undisturbed' value of Ψ (for h=1, r_s=-r, k_m=1 and C=C_0) is equal to a_3'/a_2'. On the other hand, the intensity of 'undisturbed' secondary flow is given by

$$i_s = a_4 \frac{h\bar{u}}{r} \tag{K.17}$$

, in which a_4 is a constant, given in figure K.1. The corresponding expression for Ψ reads

$$\Psi = a_4(- f \frac{\partial g}{\partial z})\Big|_{z=0}/\hat{g} \tag{K.18}$$

, so that the constant a_3' follows from

$$a_3' = a_2' a_4 (-f \frac{\partial g}{\partial z})\Big|_{z=0}/\hat{g} \tag{K.19}$$

For γ=7 and a'(z) according to the 'k-ε-approximation', a_3' varies between 93 and 113 as C goes from 25 $m^{\frac{1}{2}}/s$ to 75$m^{\frac{1}{2}}/s$.
If the vertical distribution functions f and g and the constants a_2' and a_3' are assumed to be invariable in developing curved channels of the type considered here, equation (K.16) can be approximated by

$$\varepsilon Re_0 \frac{\partial \Psi}{\partial s} + 13 \frac{C_0}{C} \frac{\Psi}{h} = - 100 \frac{r}{h r_s} \tag{K.20}$$

The secondary flow intensity in developing curved flow through gently curved channels with mildly sloping banks can be computed from this equation and the relation

$$i_s = a_5 \Psi \frac{h\bar{u}}{r} \qquad (K.21)$$

, in which $a_5 \simeq 0.33 - 0.35 \frac{\sqrt{g}}{\kappa C}$.

In order to have an impression of the accuracy of this approximation, the secondary flow intensity in the non-rectangular channel experiments in the DHL-flume has been calculated using (K.20) and (K.21). In figure K.3, the results are compared with the ones from equation (8.100) for the same main velocity field and with the local approximation

$$i_s = -\frac{100}{13} a_5 \frac{C}{C_0} \frac{h\bar{u}}{r_s} \qquad (K.22)$$

This leads to the conclusion that the suggested approximative computation method for the secondary flow intensity amounts a considerable improvement in comparison with the local approximation (K.22), and the more in comparison with the one based on r instead of r_s , used in the original version of the strongly simplified model.

Incorporating this secondary flow computation into the strongly simplified model would imply a drastic change of the computation method, the direct correlation between i_s and $\bar{u}$ being absent then. The model in its original version, however, has been shown to yield satisfactory main flow predictions, so that such a complication seems unneccesary for the computation of the main flow. Rather should the secondary flow computation from (K.20) and (K.21) be applied in an additional computation step for the secondary flow and the bottom shear stress.

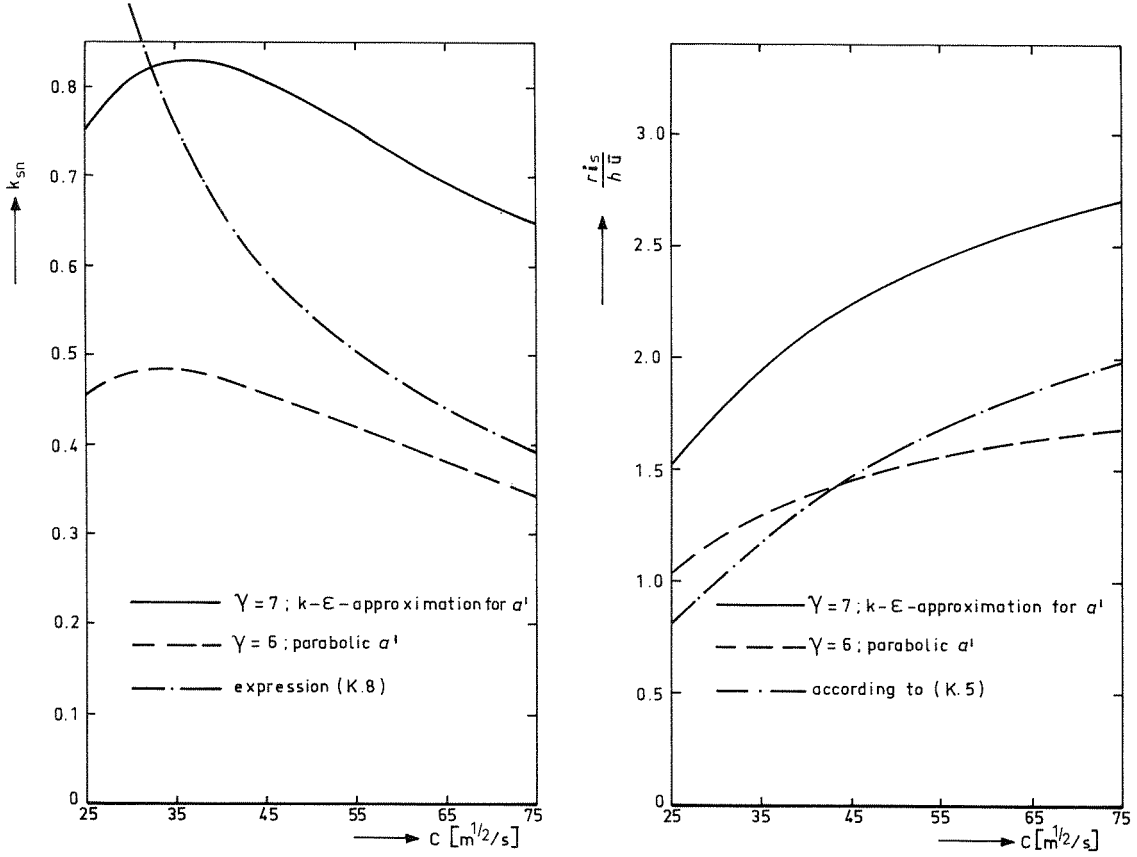

Figure K.1. Convection factor and intensity of the 'undisturbed' secondary flow

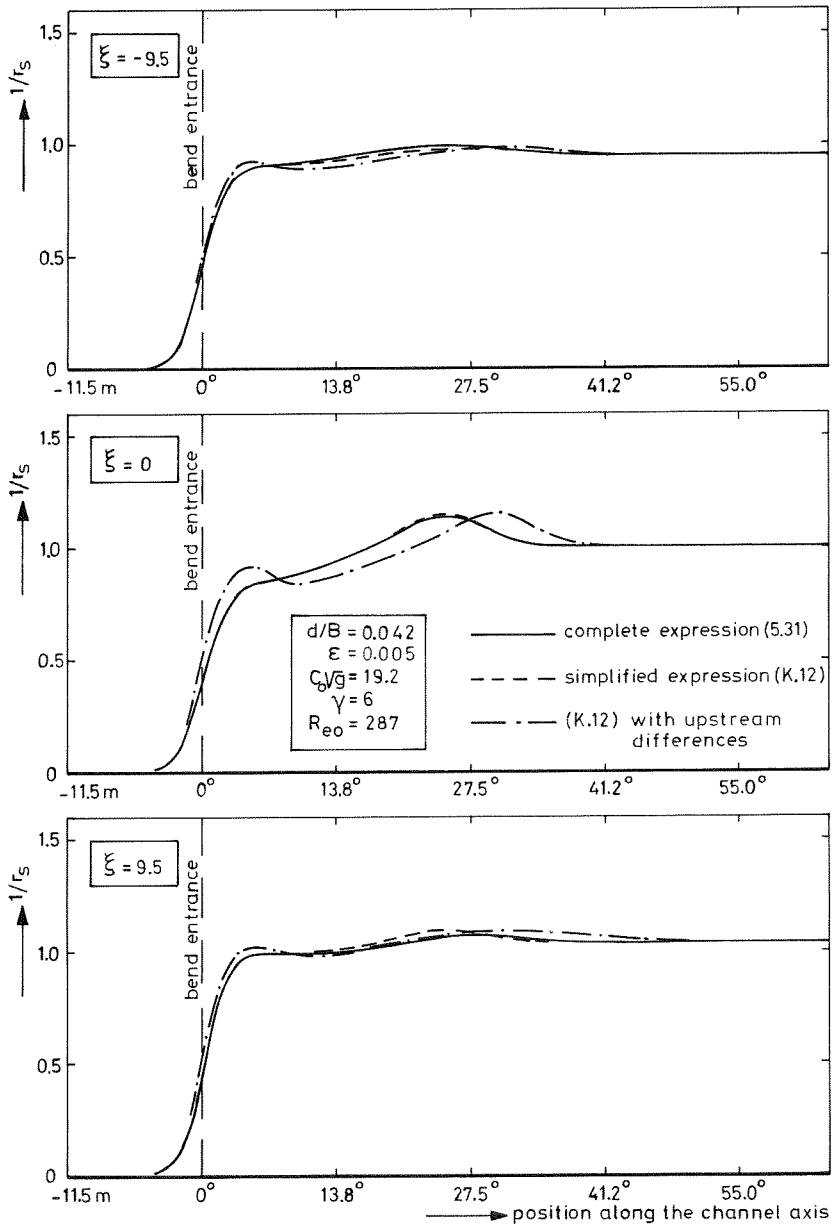

Figure K.2. Approximative computation of the streamline curvature (DHL-flume with non-rectangular cross-section)

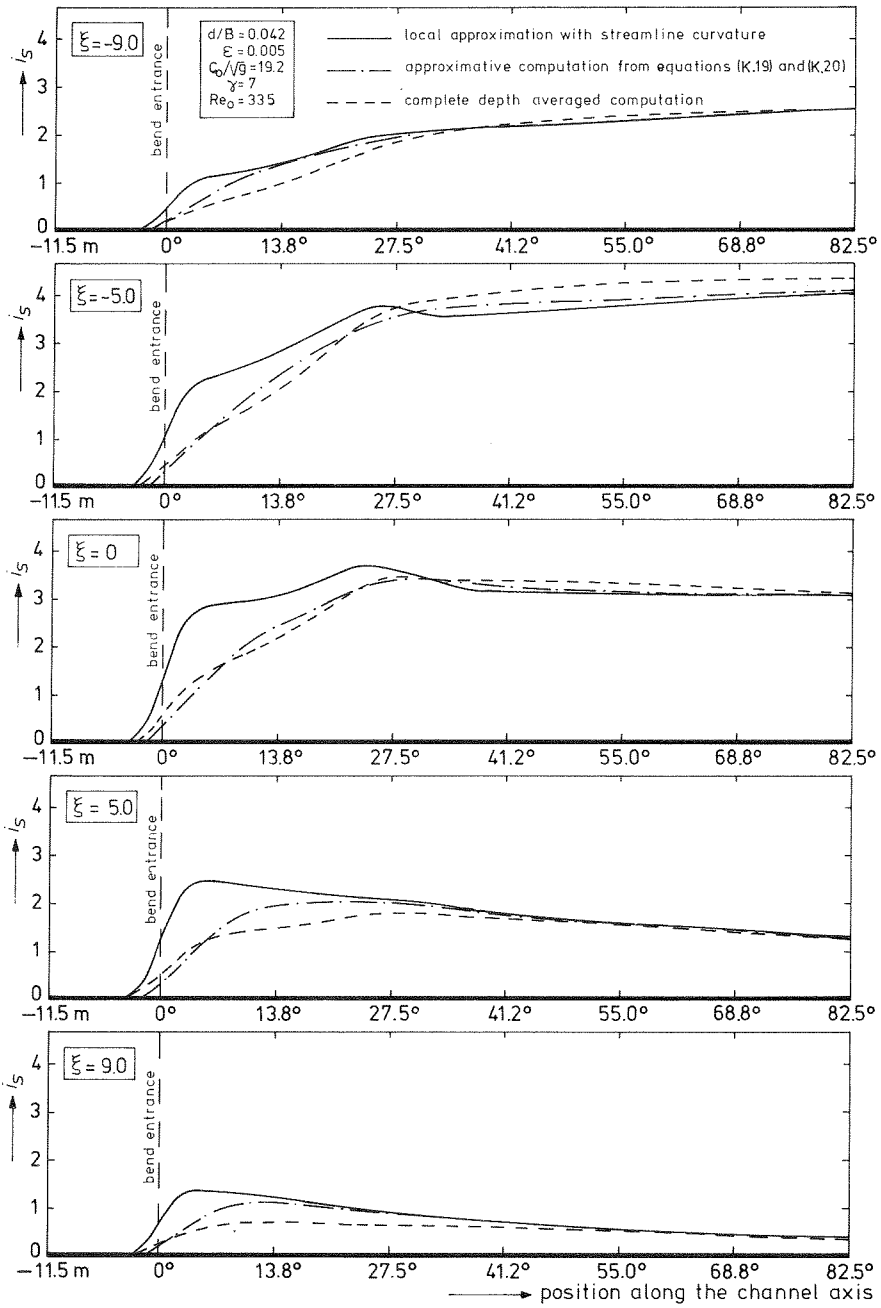

Figure K.3. Approximative computation of the secondary flow intensity (DHL-flume with non-rectangular cross-section)

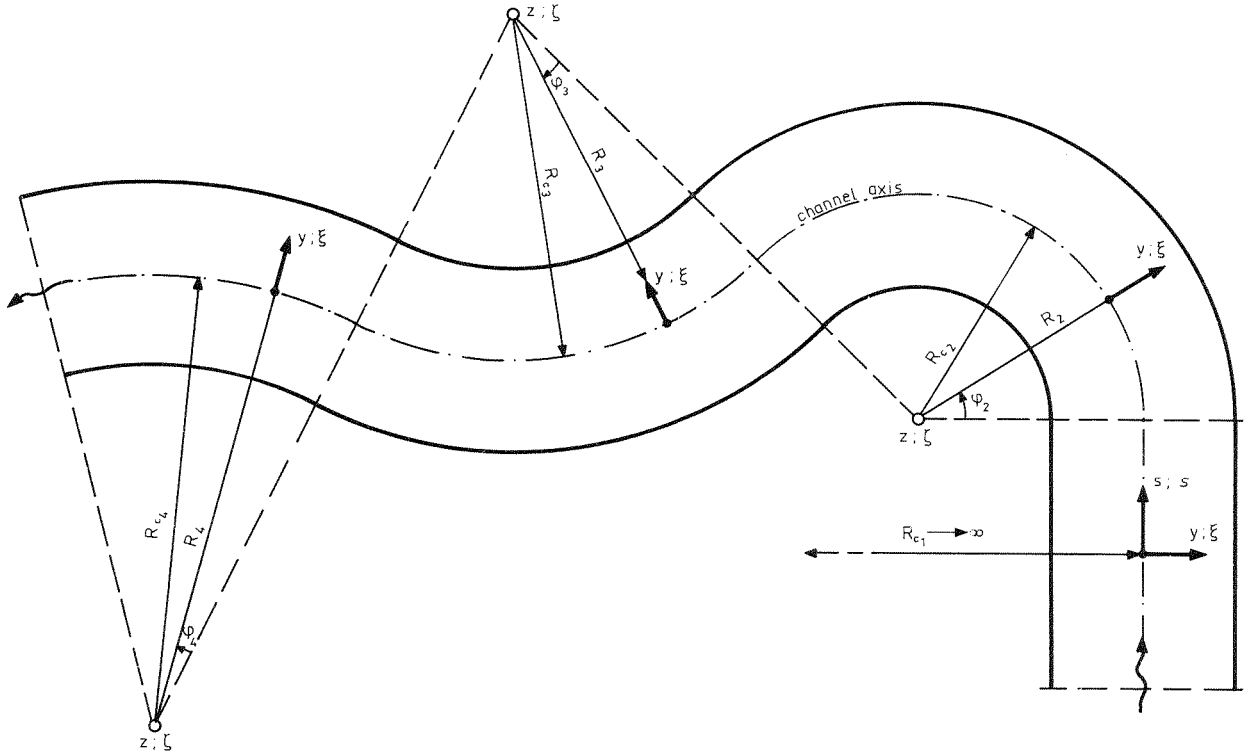

Figure 1. Combined cylindrical coordinate system

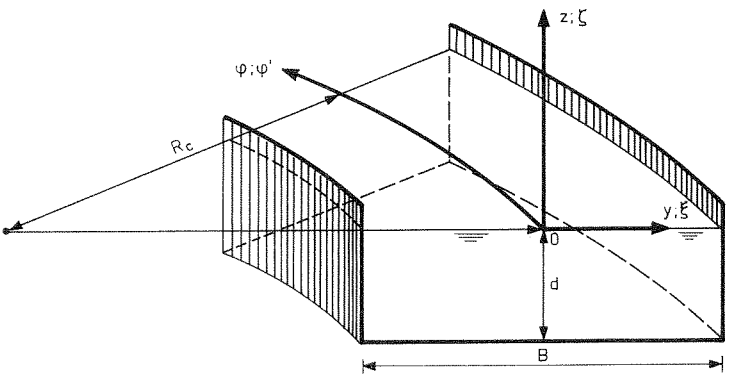

Figure 2. Definition sketch

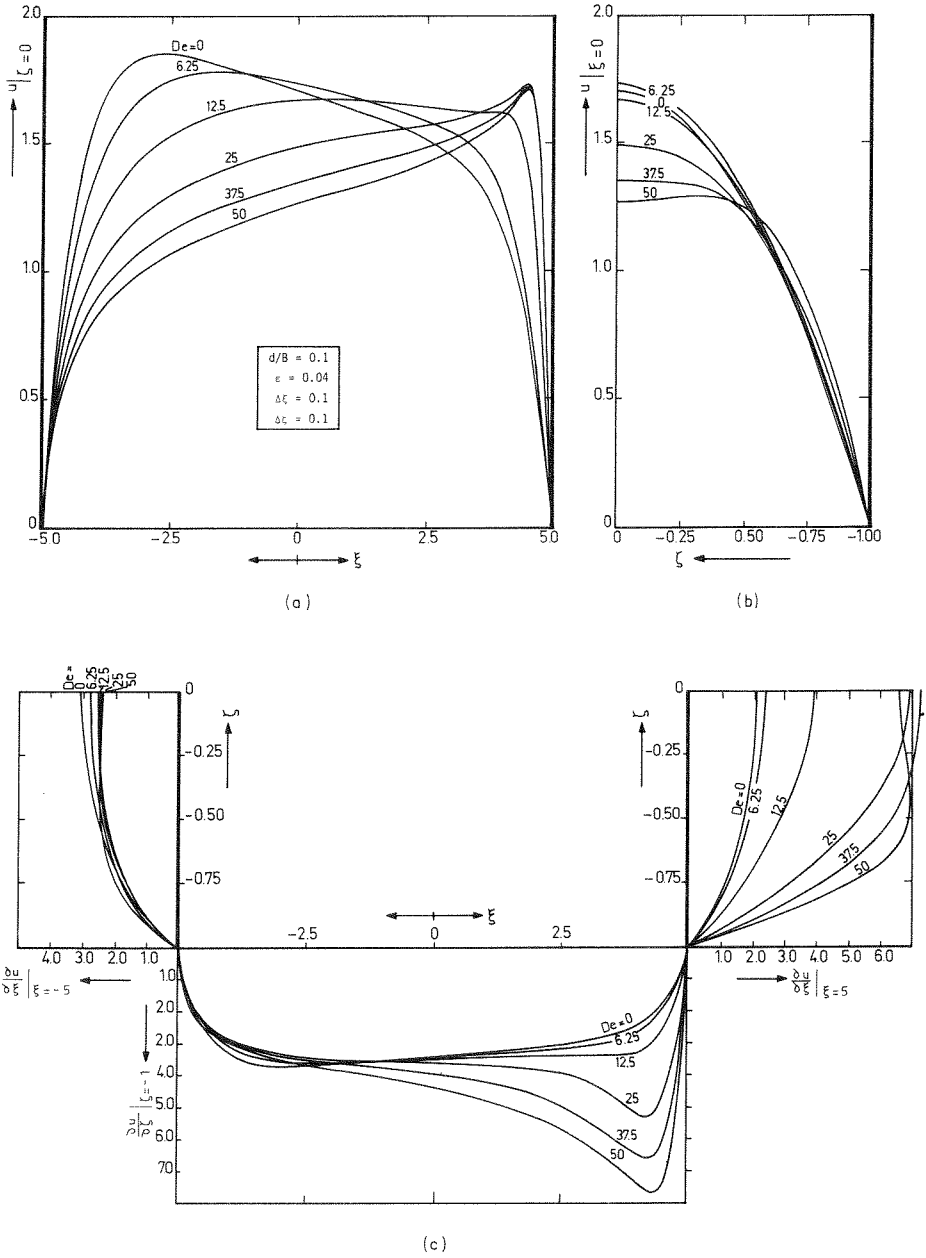

Figure 3. Influence of the Dean number on the main flow
(a) Main velocity at the surface (b) Main velocity in the axis
(c) Main velocity gradients normal to the fixed boundaries

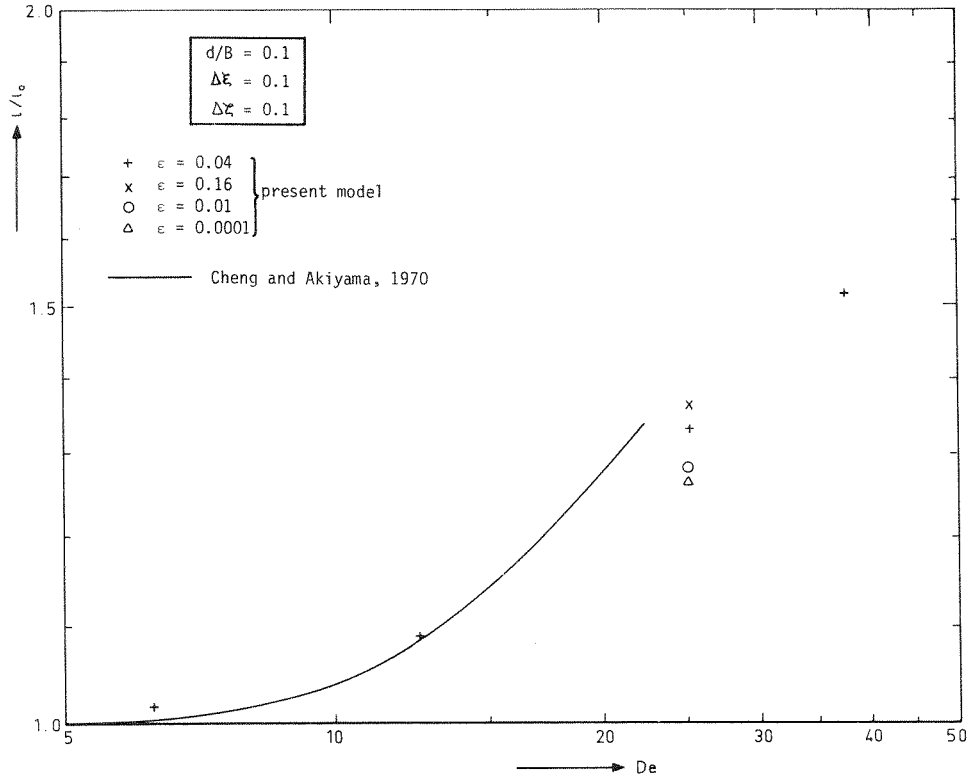

Figure 4. Influence of the Dean number on the longitudinal slope factor

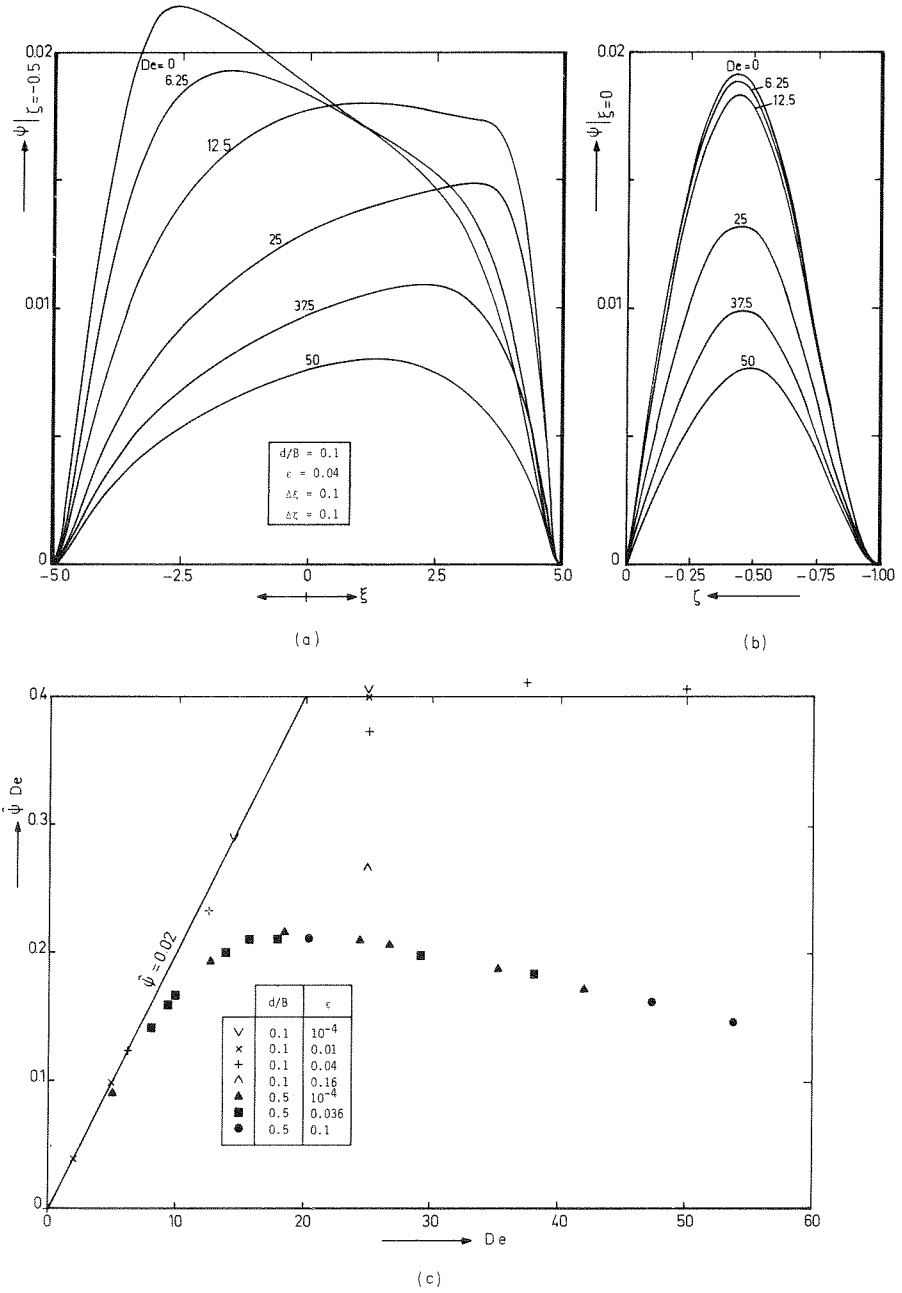

Figure 5. Influence of the Dean number on the secondary flow
(a) Stream function at half depth (b) Stream function in the axis
(c) Maximum of the stream function compared with values for a square pipe

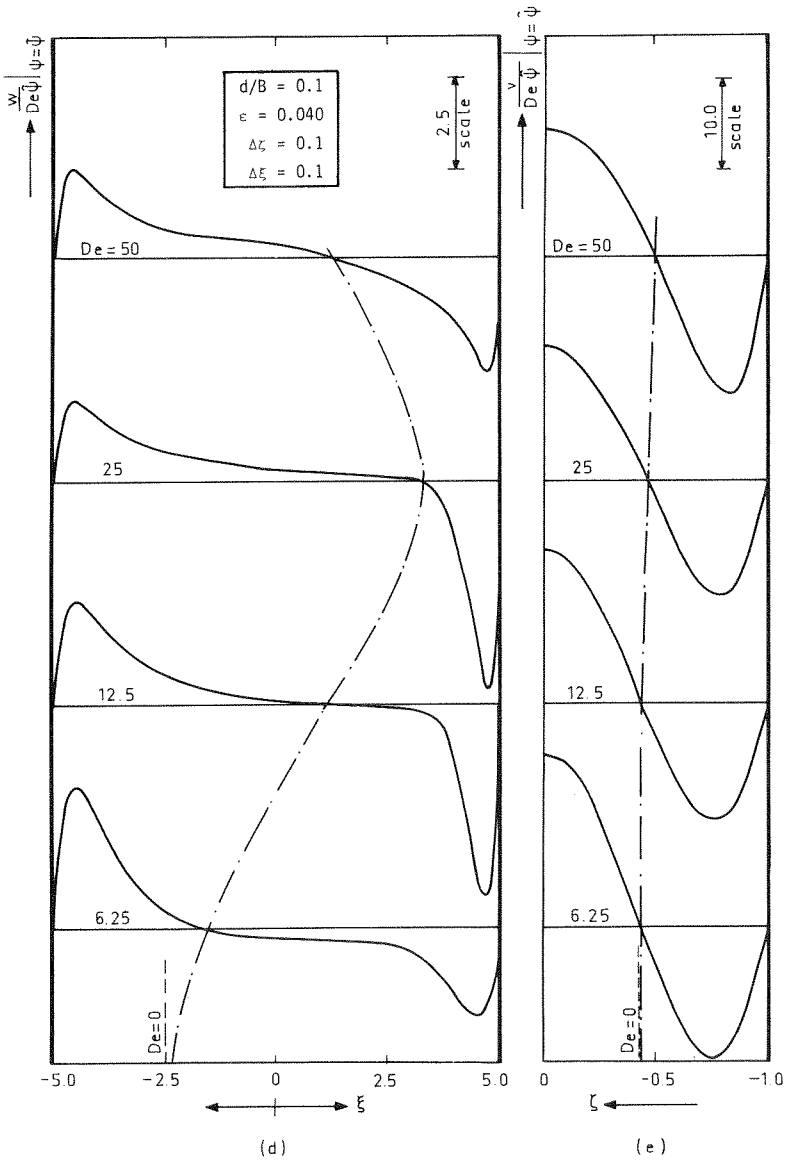

Figure 5. Influence of the Dean number on the secondary flow
(d) Vertical velocity (e) Radial velocity

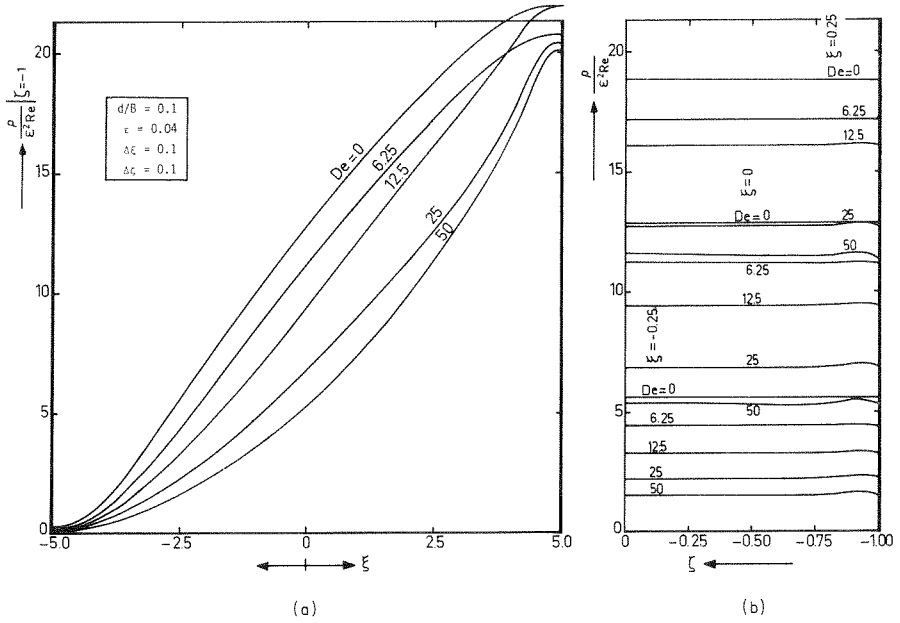

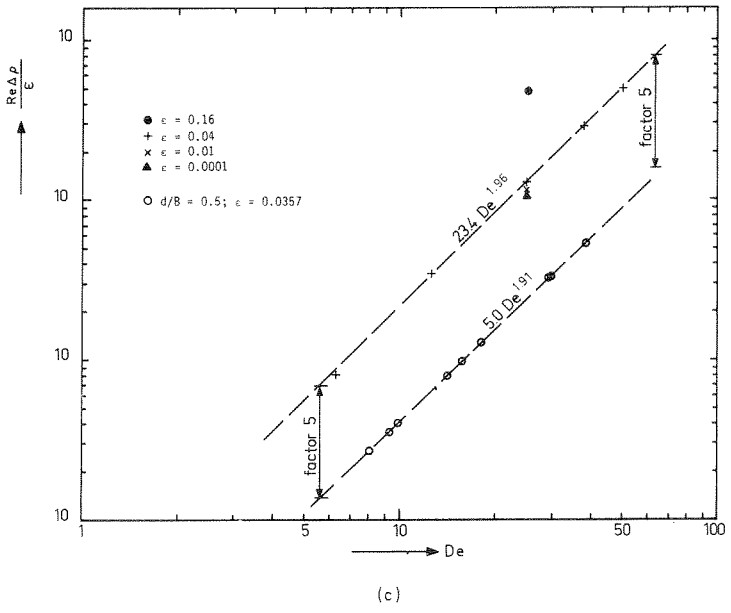

Figure 6. Influence of the Dean number on the transverse pressure distribution (a) Total pressure at the bottom (b) Vertical distributions of the total pressure (c) Transverse pressure drop

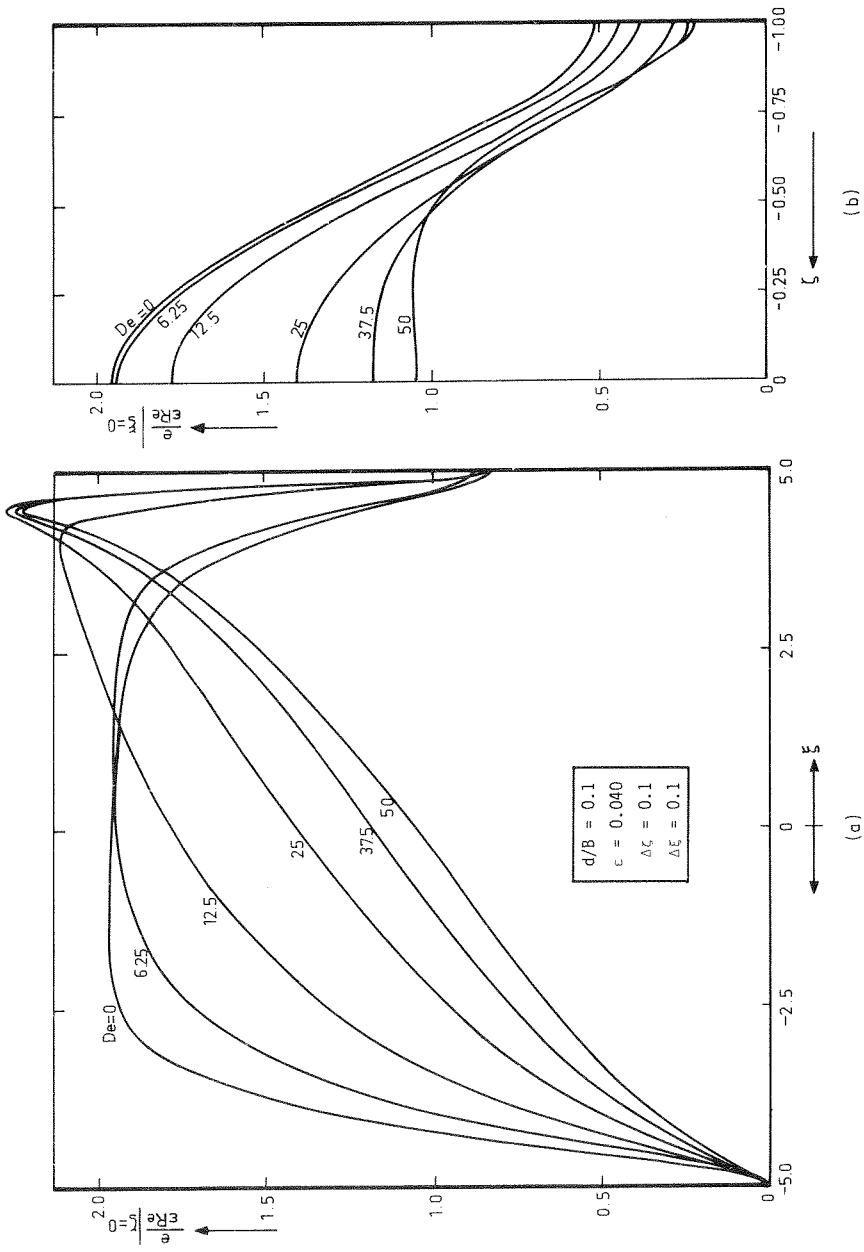

Figure 7. Influence of the Dean number on the total energy
(a) Total energy at the surface (b) Total energy in the axis

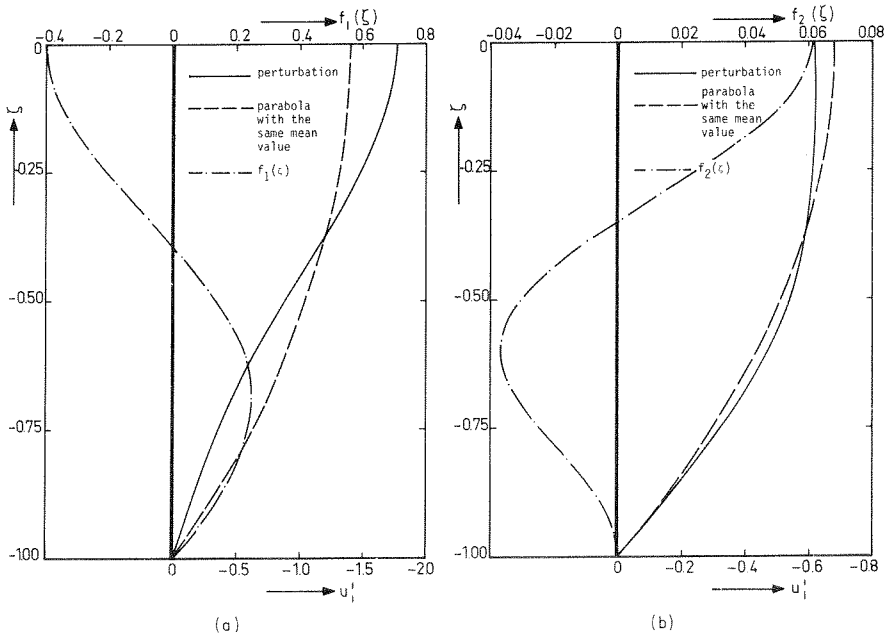

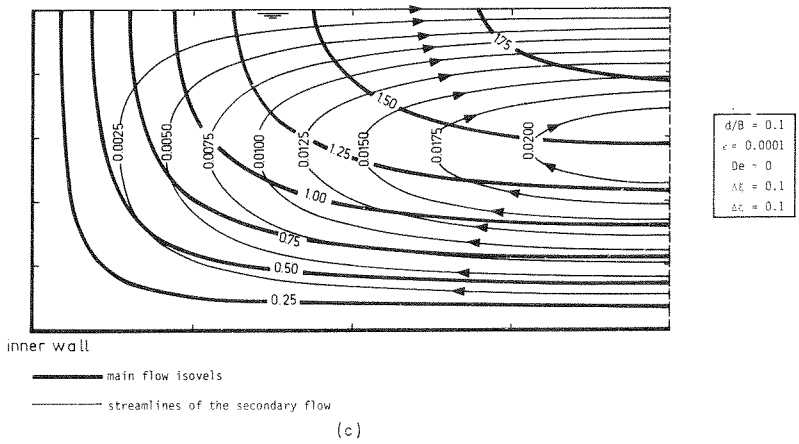

Figure 8. Perturbation of the main velocity due to secondary flow convection (a) Perturbation due to radial convection (b) Perturbation due to vertical convection (c) Main flow isovels and streamlines of the secondary flow

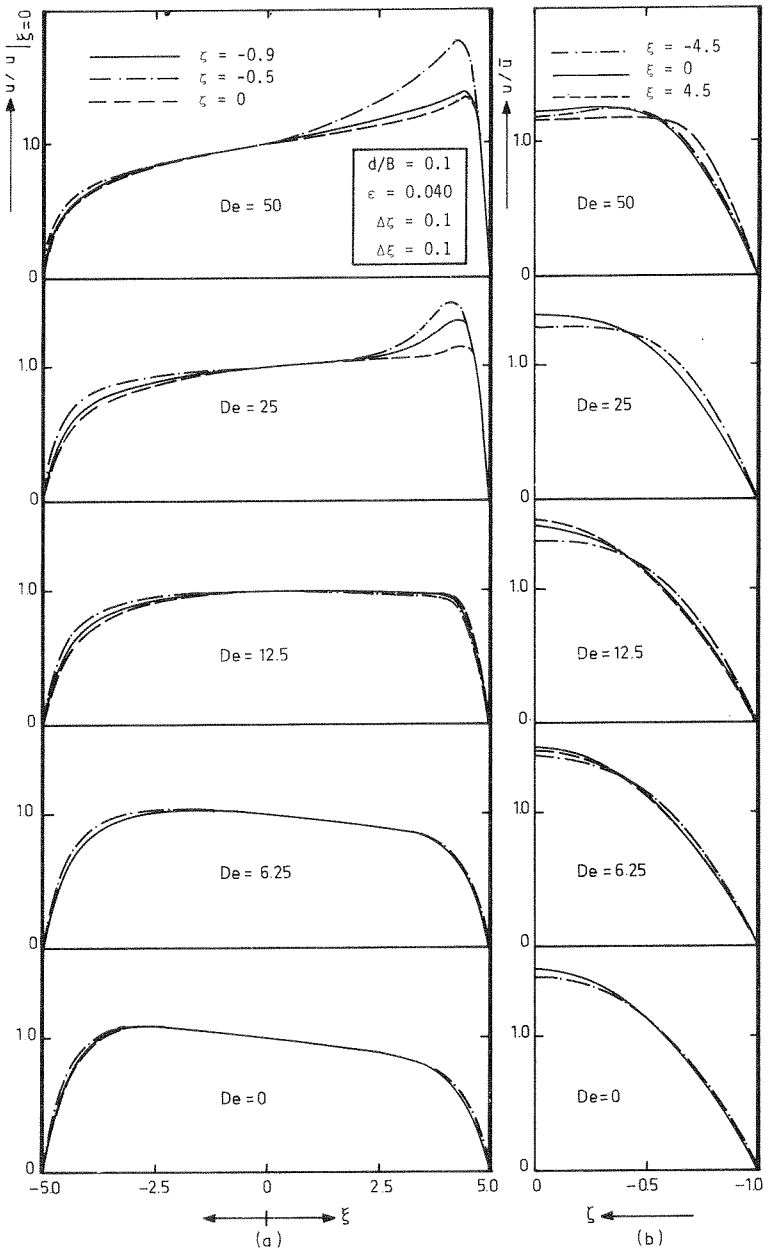

Figure 9. Similarity of the main velocity distribution
(a) Vertical similarity (b) Radial similarity

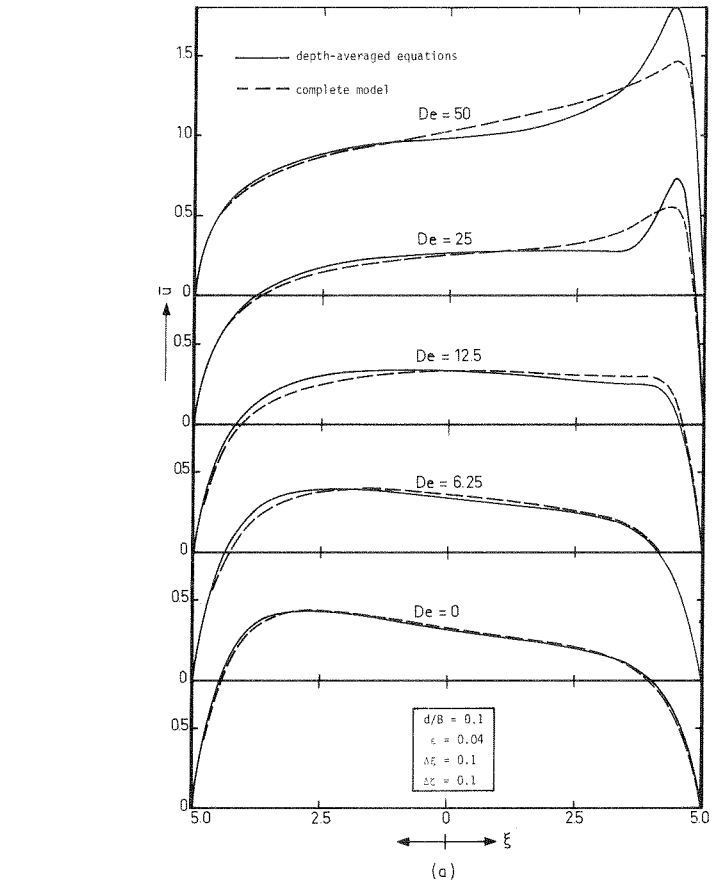

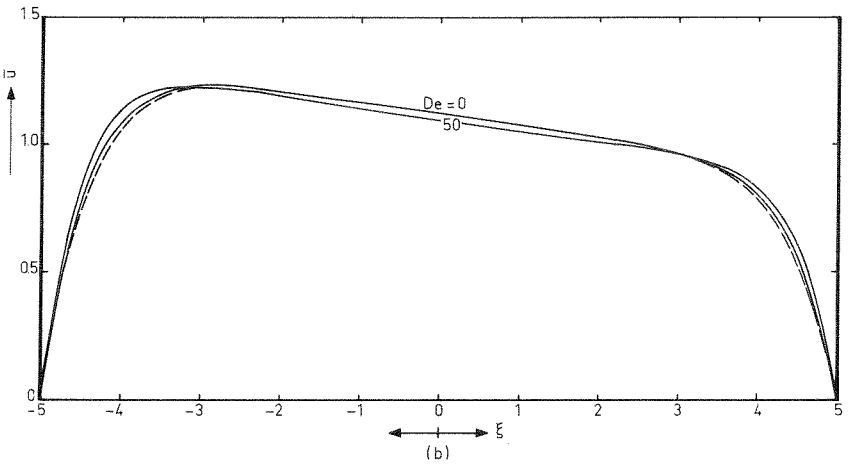

Figure 10. Separate computation of the depth-averaged main velocity
(a) Complete equation (b) Secondary flow convection terms disregarded

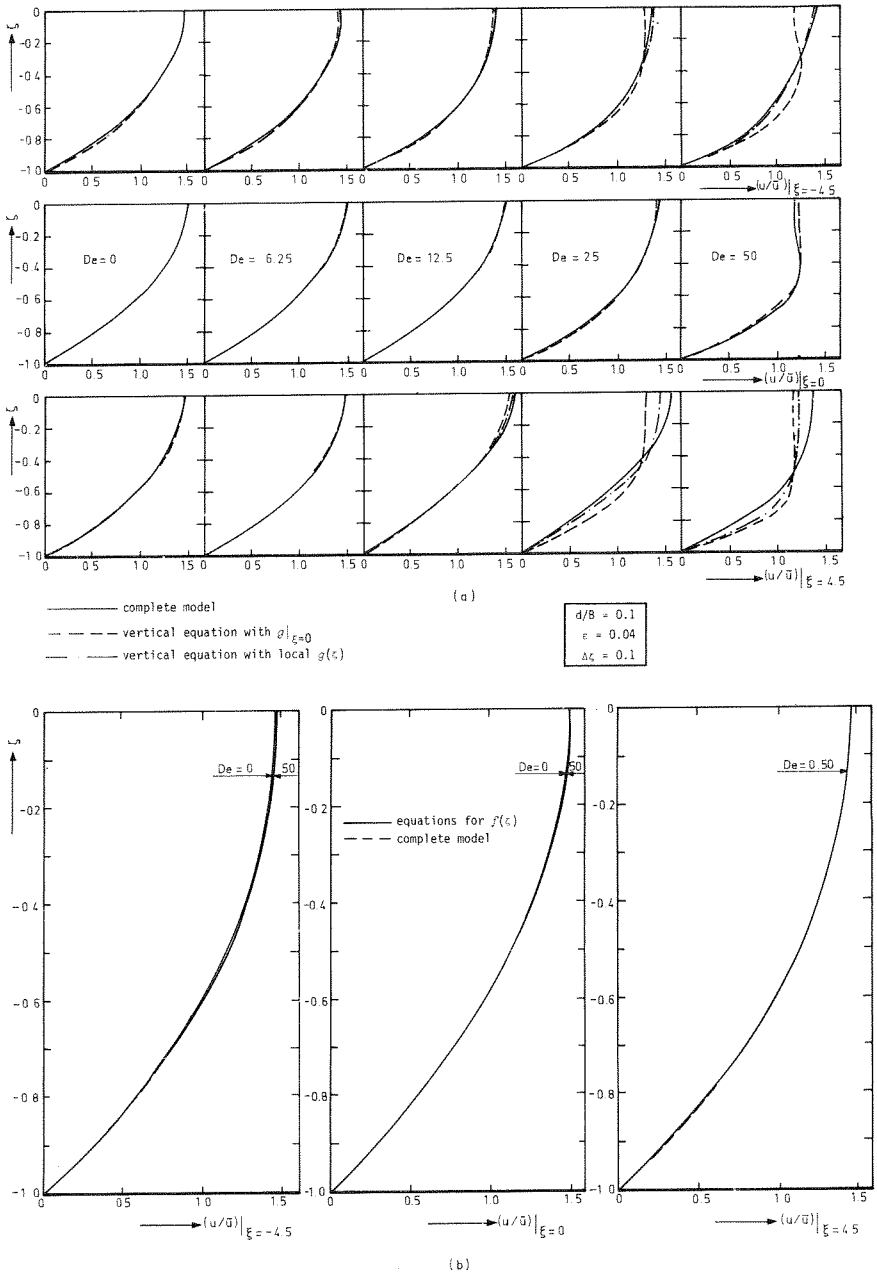

Figure 11. Separate computation of the vertical distribution of the main velocity
(a) Complete equation (b) Secondary flow convection terms disregarded

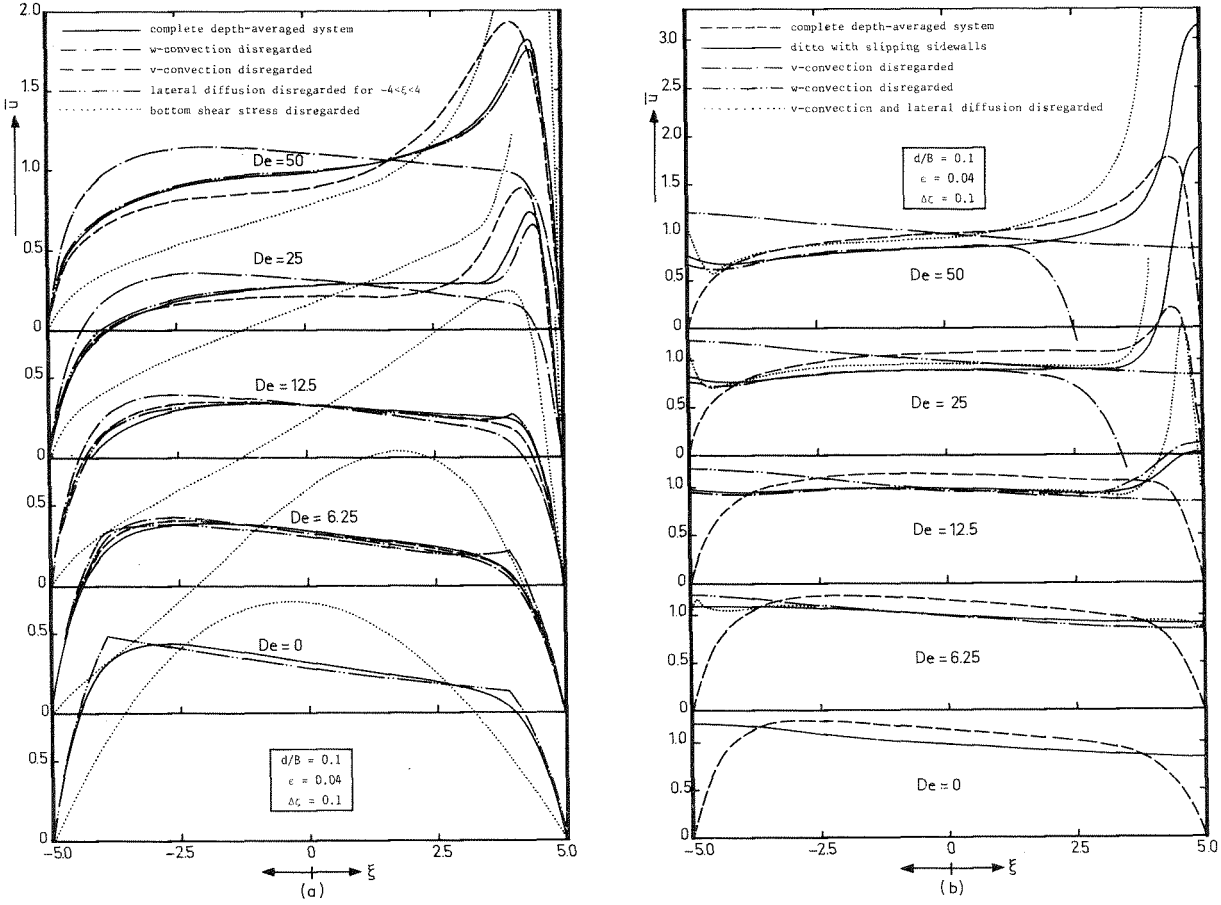

Figure 12. Analysis of the depth-averaged main velocity redistribution

(a) Influence of the secondary velocity components, lateral diffusion and the bottom shear stress

(b) Influence of the secondary velocity components in case of slipping sidewalls

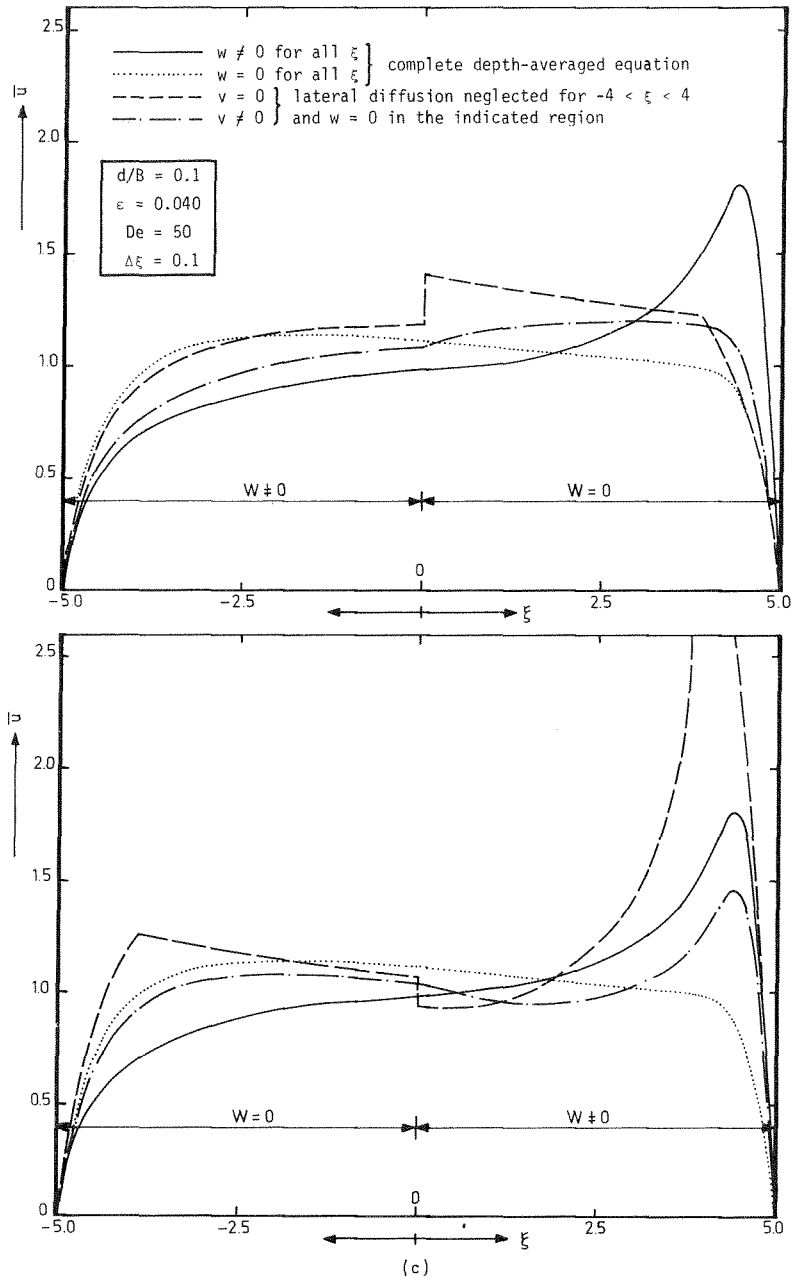

(c)

Figure 12. Analysis of the depth-averaged main velocity redistribution
(c) Retardation effect of radial convection

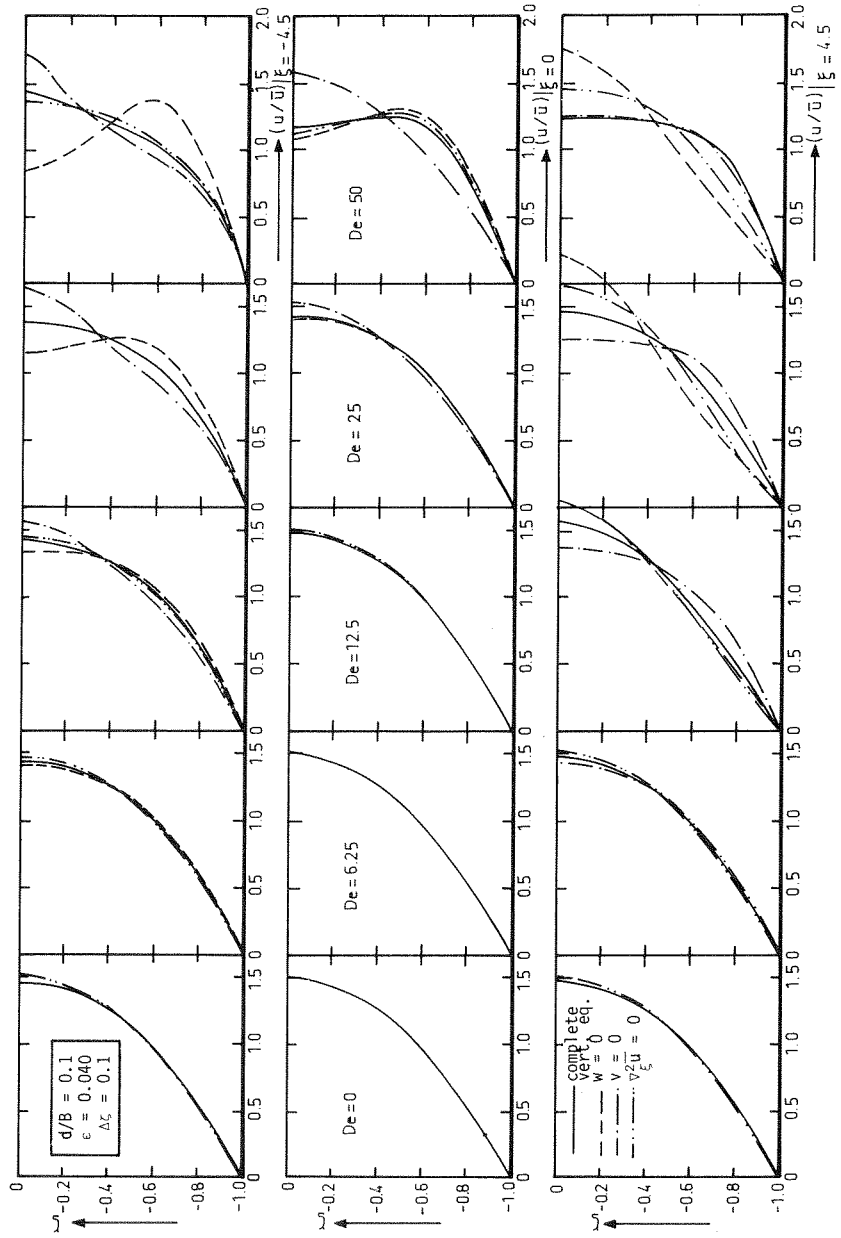

Figure 13. Analysis of the vertical redistribution of the main velocity

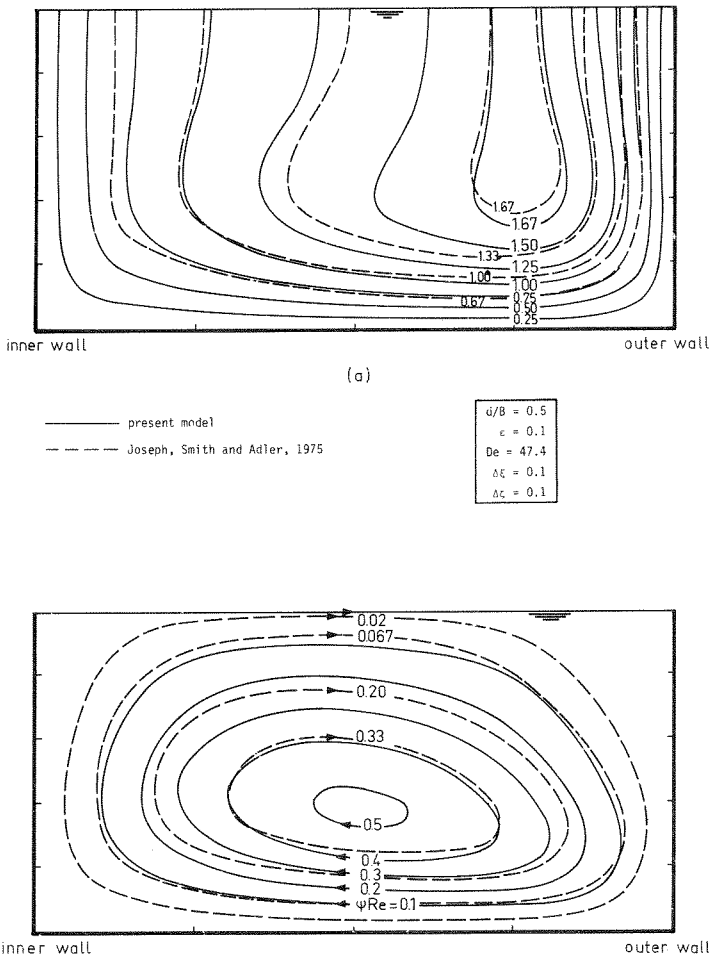

Figure 14. Transition to double helical flow pattern in a square pipe
(a) Main flow isovels for De=47.4
(b) Streamlines of the secondary flow for De=47.4

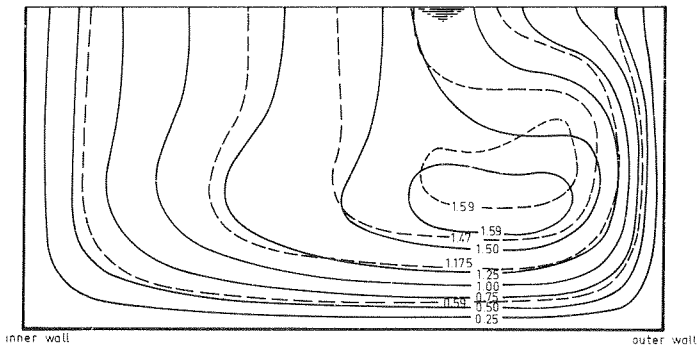

(c)

——— present model

— — — — Joseph, Smith and Adler, 1975

d/B = 0.5
ε = 0.1
De = 53.8
Δξ = 0.1
Δς = 0.1

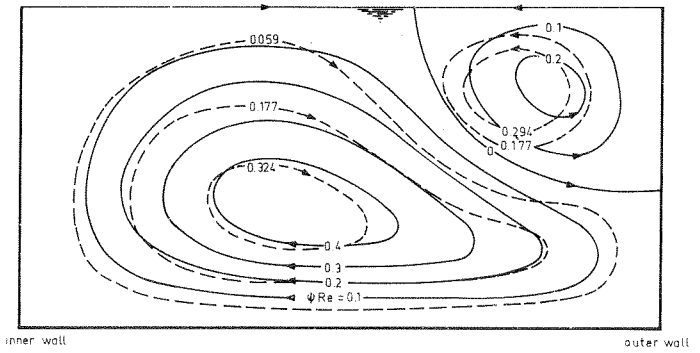

(d)

Figure 14. Transition to double helical flow pattern in a square pipe

(c) Main flow isovels for De=53.8

(d) Streamlines of the secondary flow for De=53.8

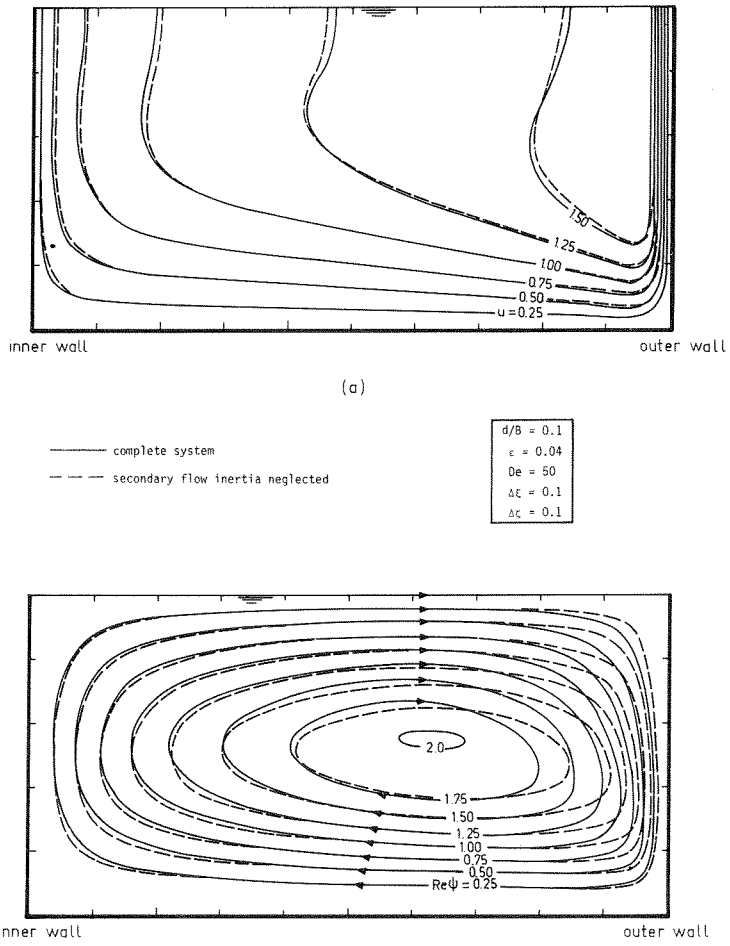

Figure 15. Influence of the convection terms in the stream function equation of the secondary flow
(a) Main flow isovels (b) Streamlines of the secondary flow

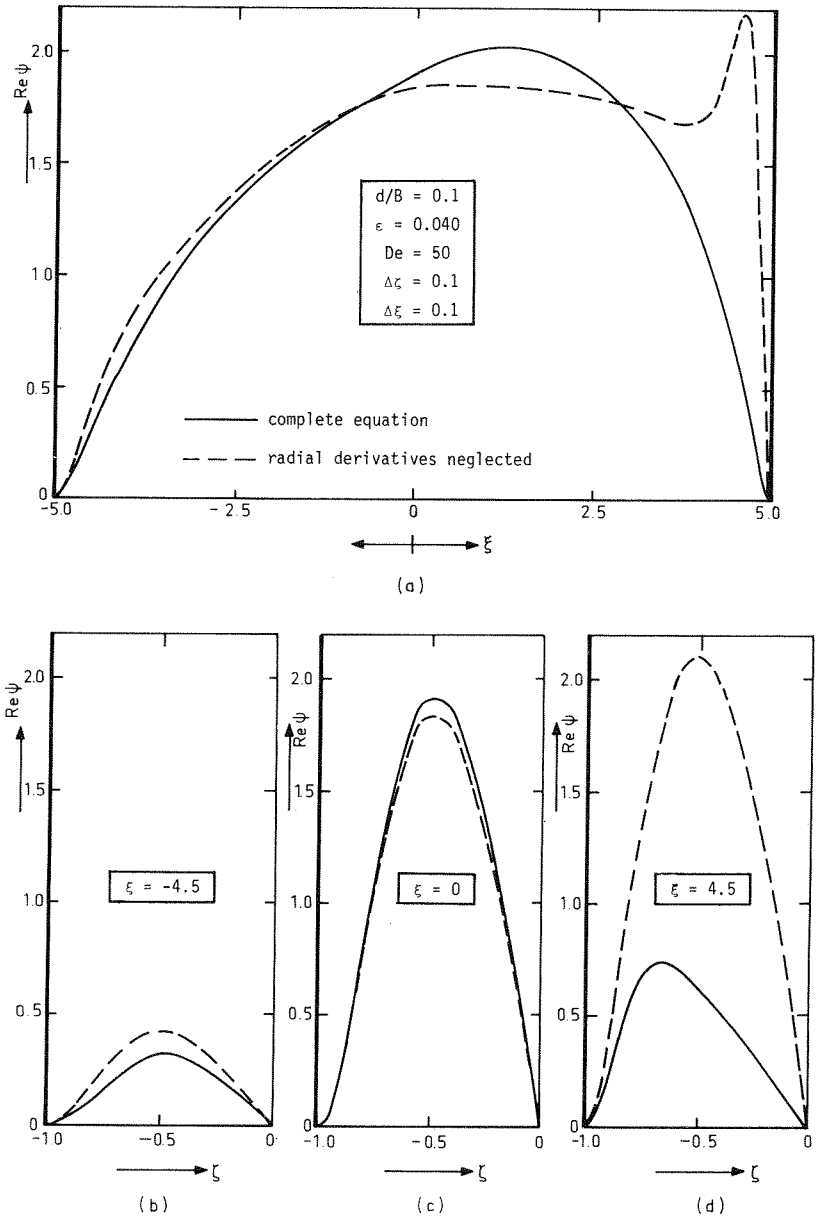

Figure 16. Influence of the radial diffusion terms in the stream function equation of the secondary flow

(a) Stream function at half depth (b)-(d) Stream function profiles

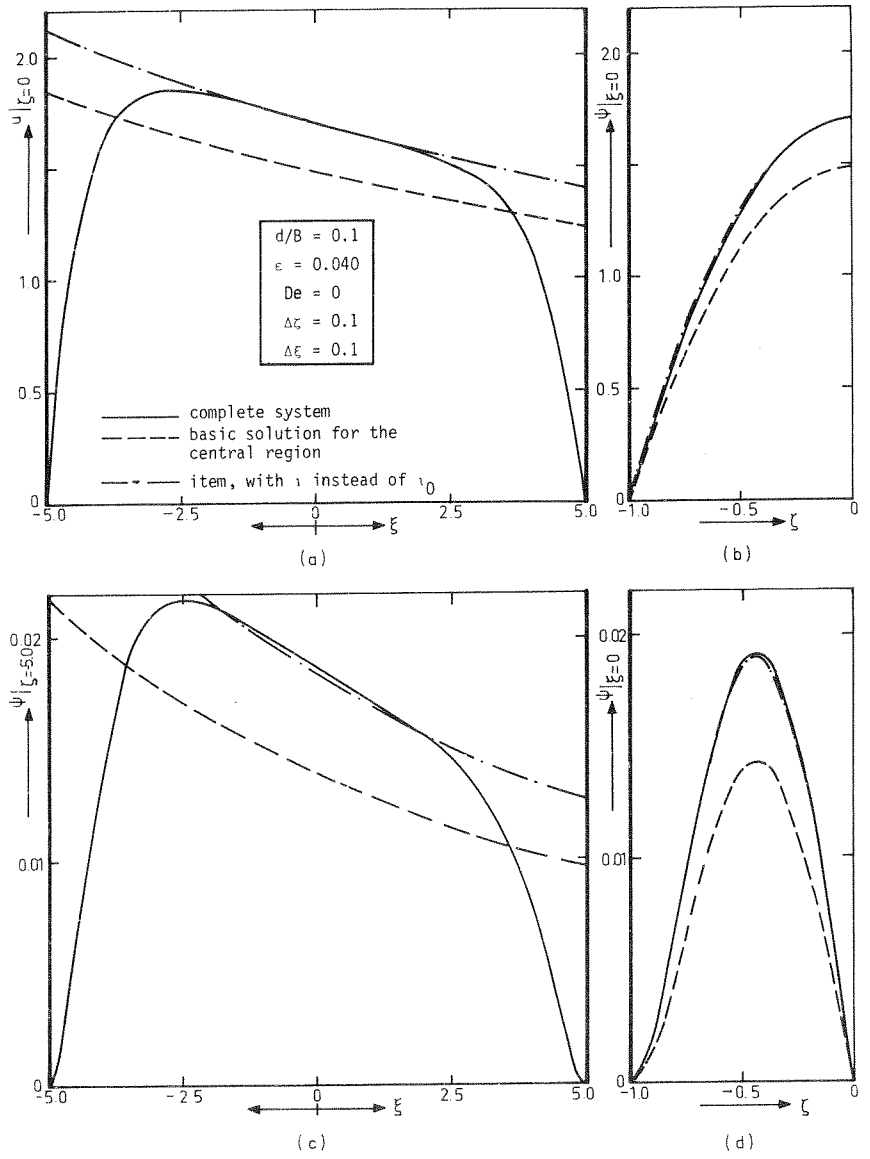

Figure 17. Basic solution for the central region of a shallow channel
(a) Main velocity at $\zeta=0$ (b) Main velocity at $\xi=0$
(c) Stream function at $\zeta=0$ (d) Stream function at $\xi=0$

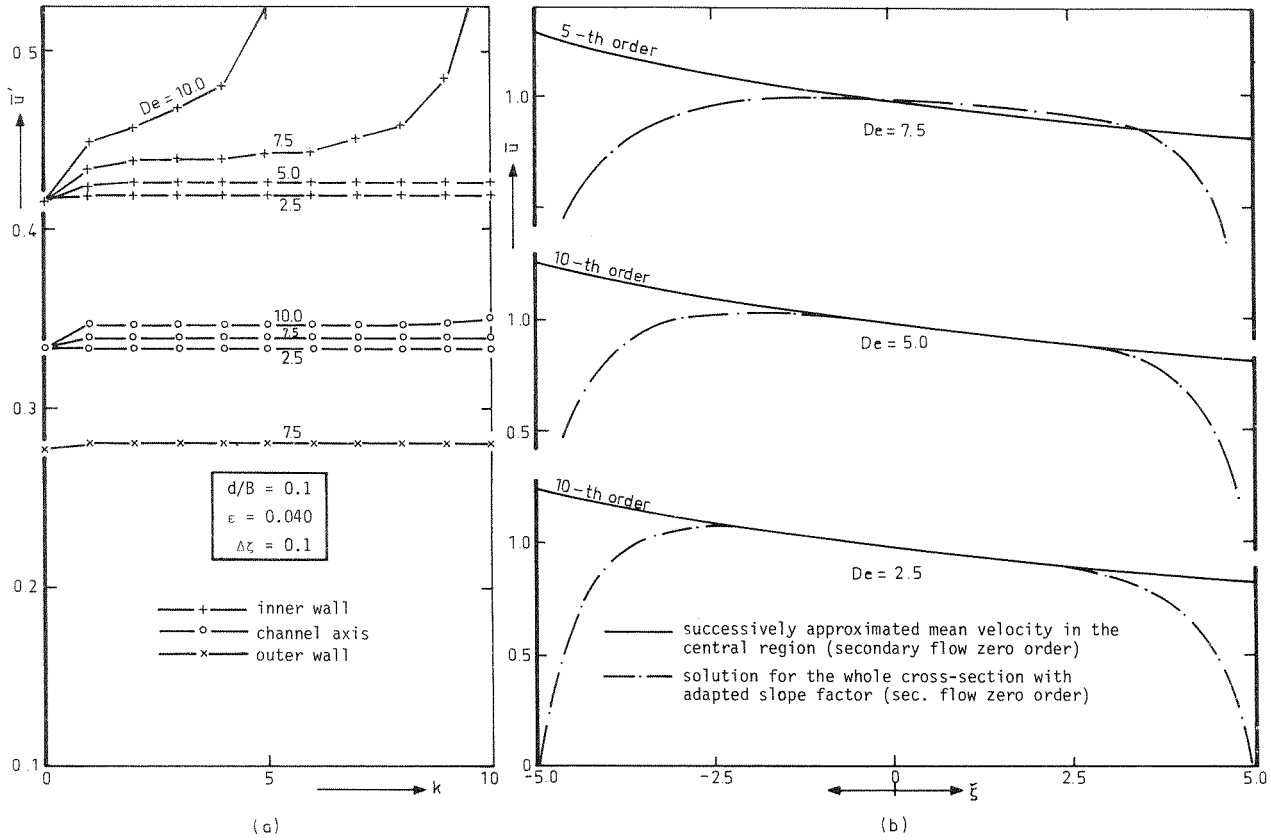

Figure 18. Successive approximation of the main velocity in the central region of a shallow channel
(a) Convergence (b) Depth-averaged main velocity distribution

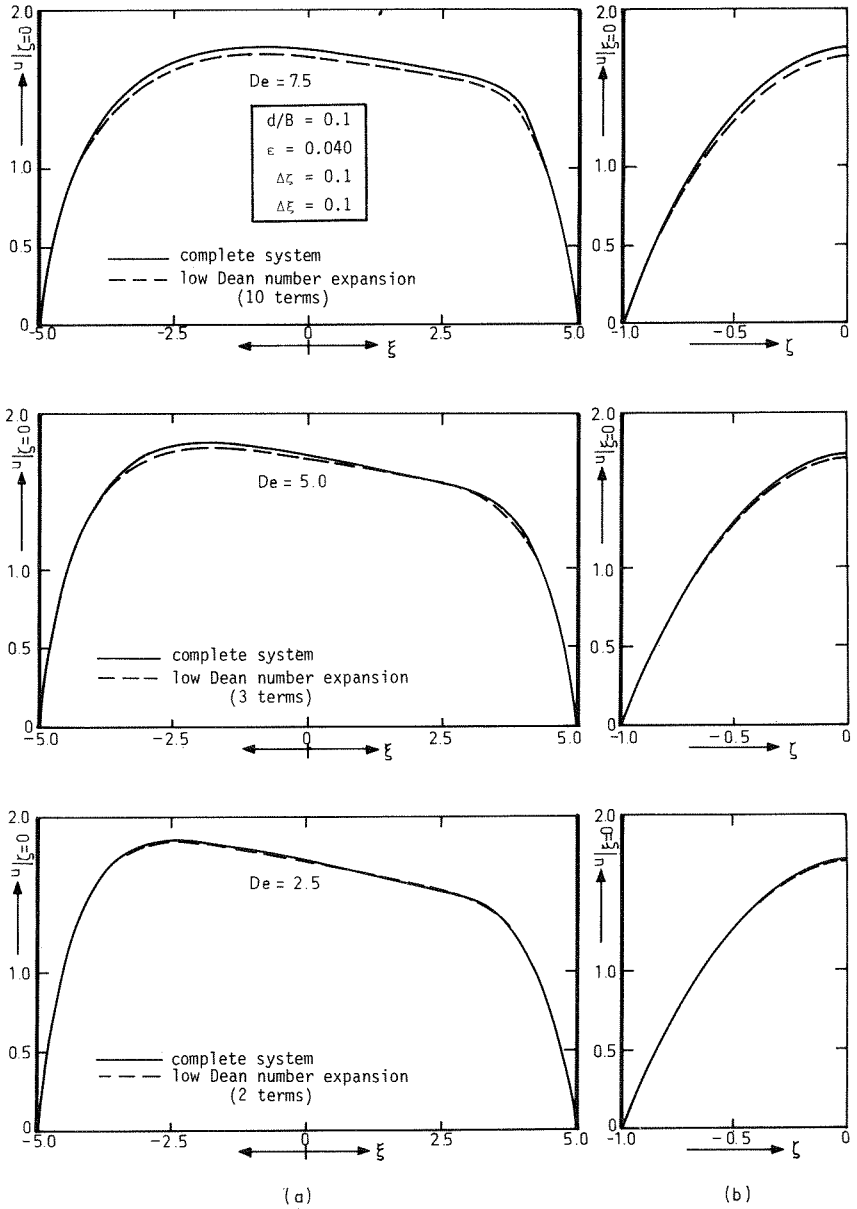

Figure 19. Successive approximation of the main velocity by low Dean number perturbations in the whole cross-section
(a) Main velocity at the surface (b) Main velocity in the axis

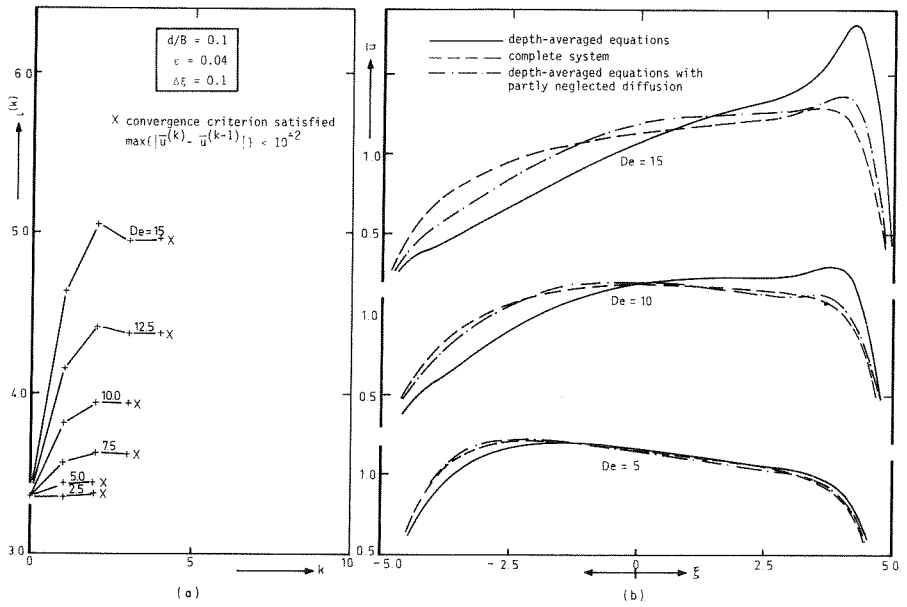

Figure 20. Solution of $\bar{u}$ from the semi-implicit depth-averaged equation (zero-order approximation of the secondary flow)
(a) Convergence (b) Depth-averaged velocity distribution

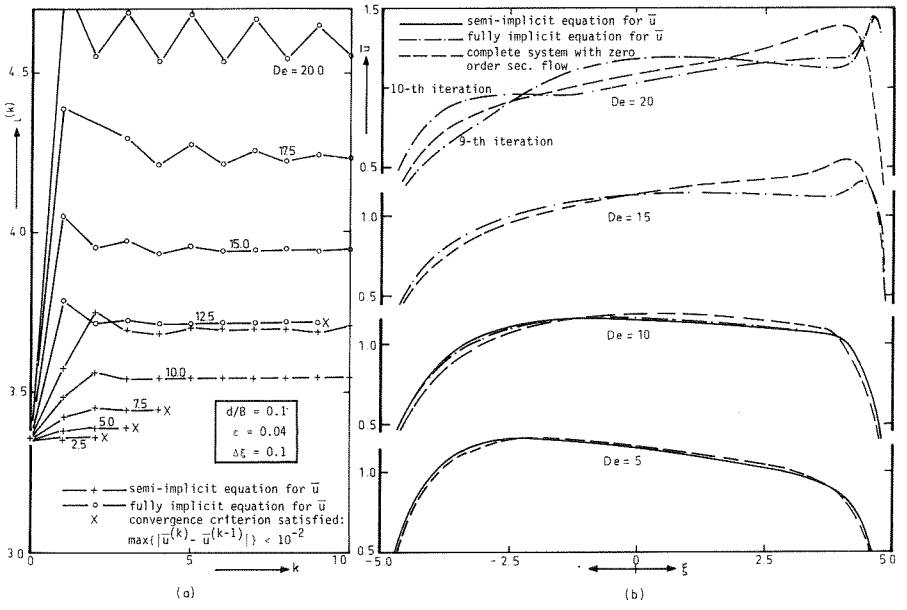

Figure 21. Solution of the depth-averaged system derived from the low Dean number expansion
(a) Convergence (b) Depth-averaged velocity distribution

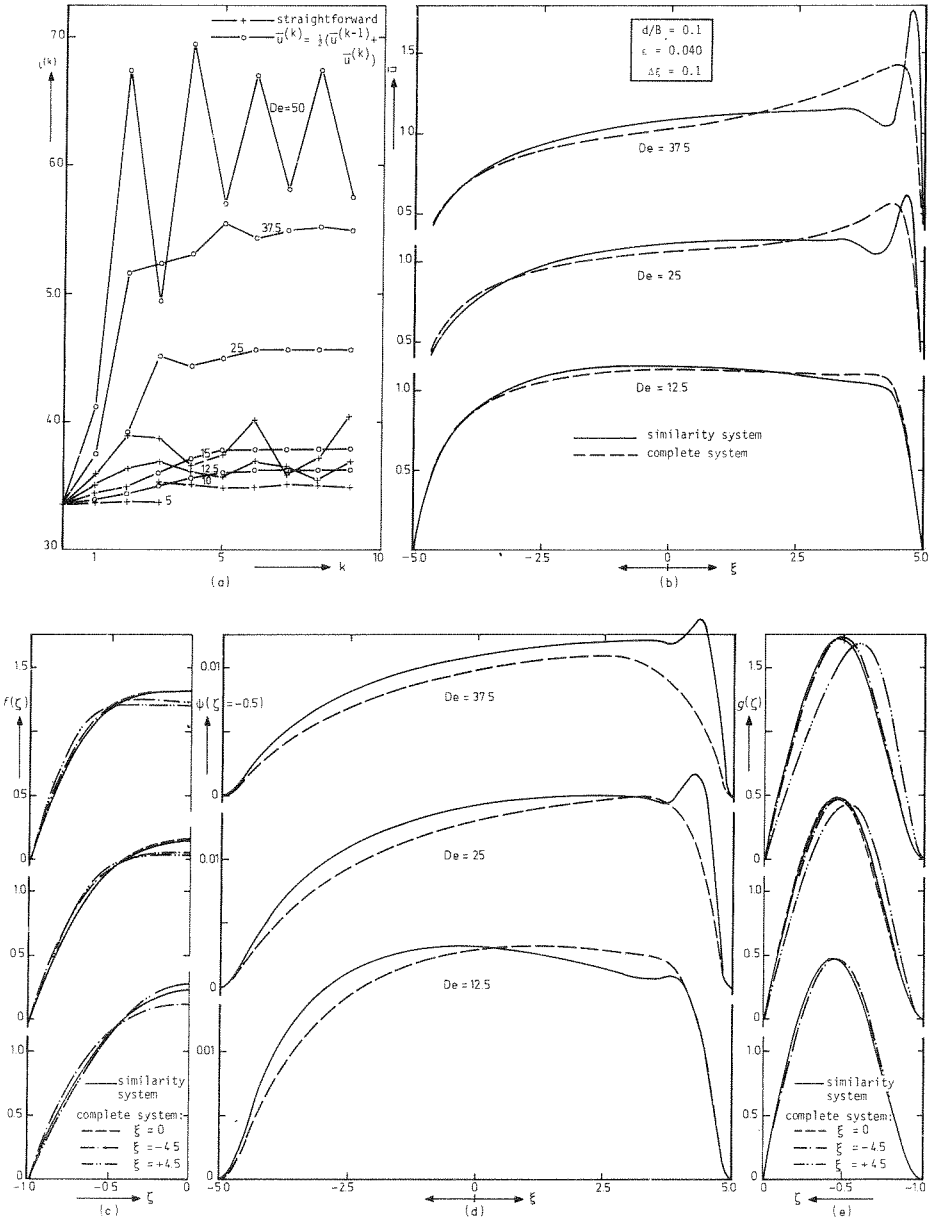

Figure 22. Similarity solution

(a) Convergence (b) Depth-averaged velocity distribution

(c) Vertical distribution of the main velocity (d) Stream function at half depth (e) Vertical distribution of ψ

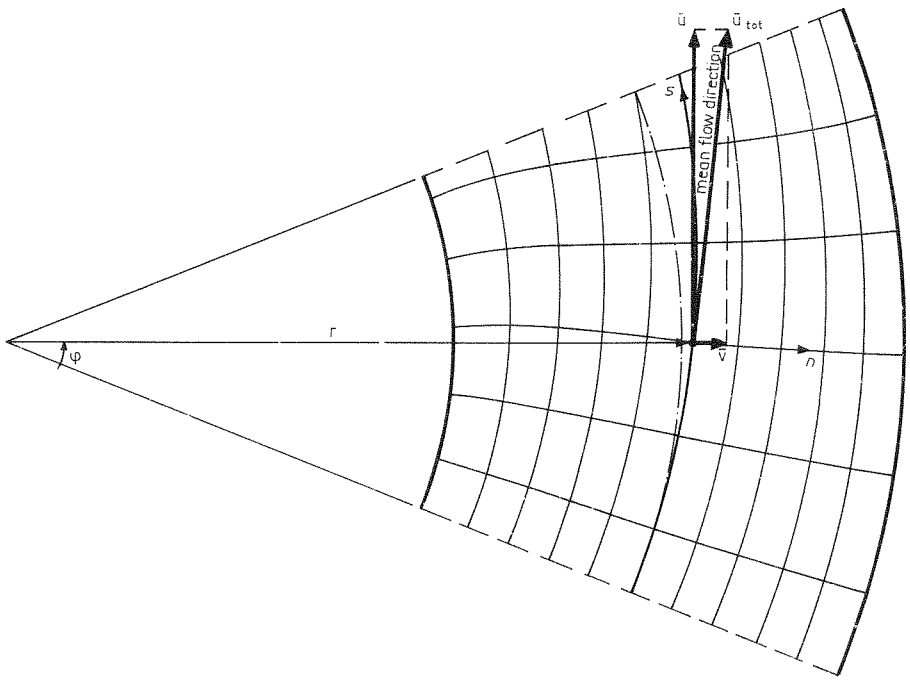

Figure 23. Stream-oriented coordinates

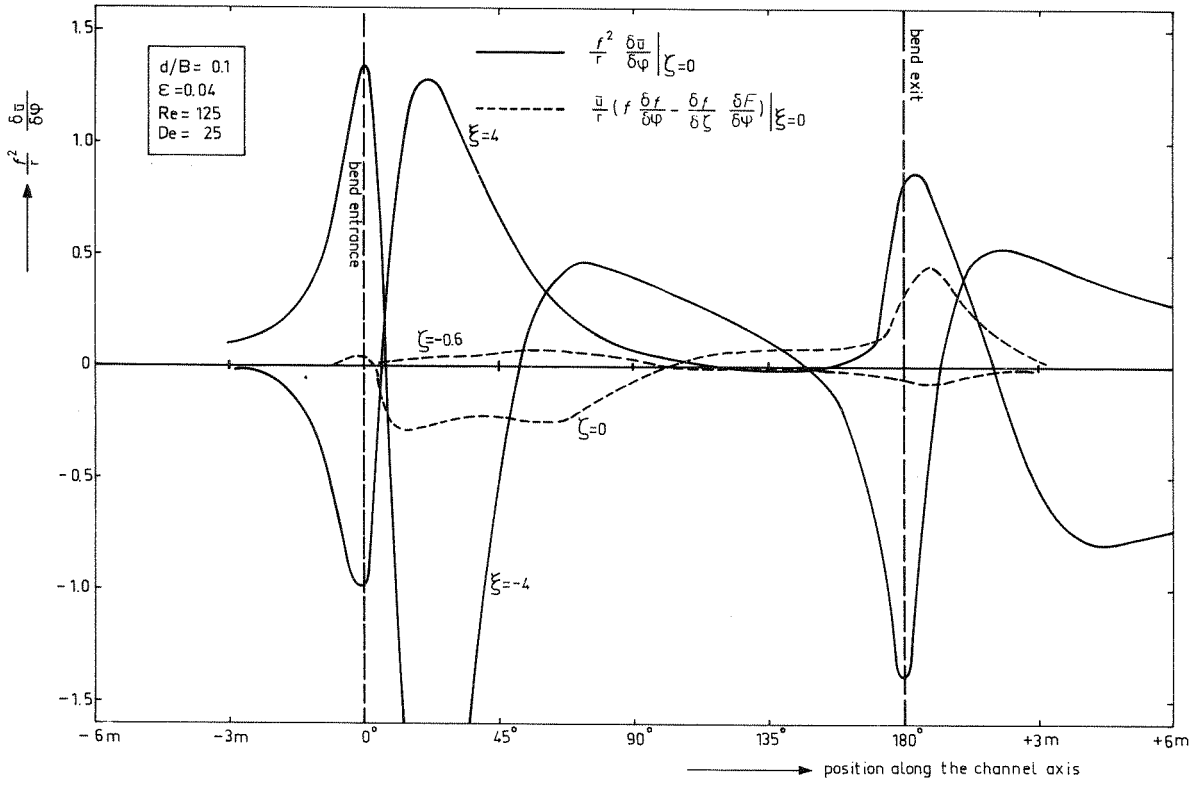

Figure 24. Applicability of the simplification of the main flow convection terms

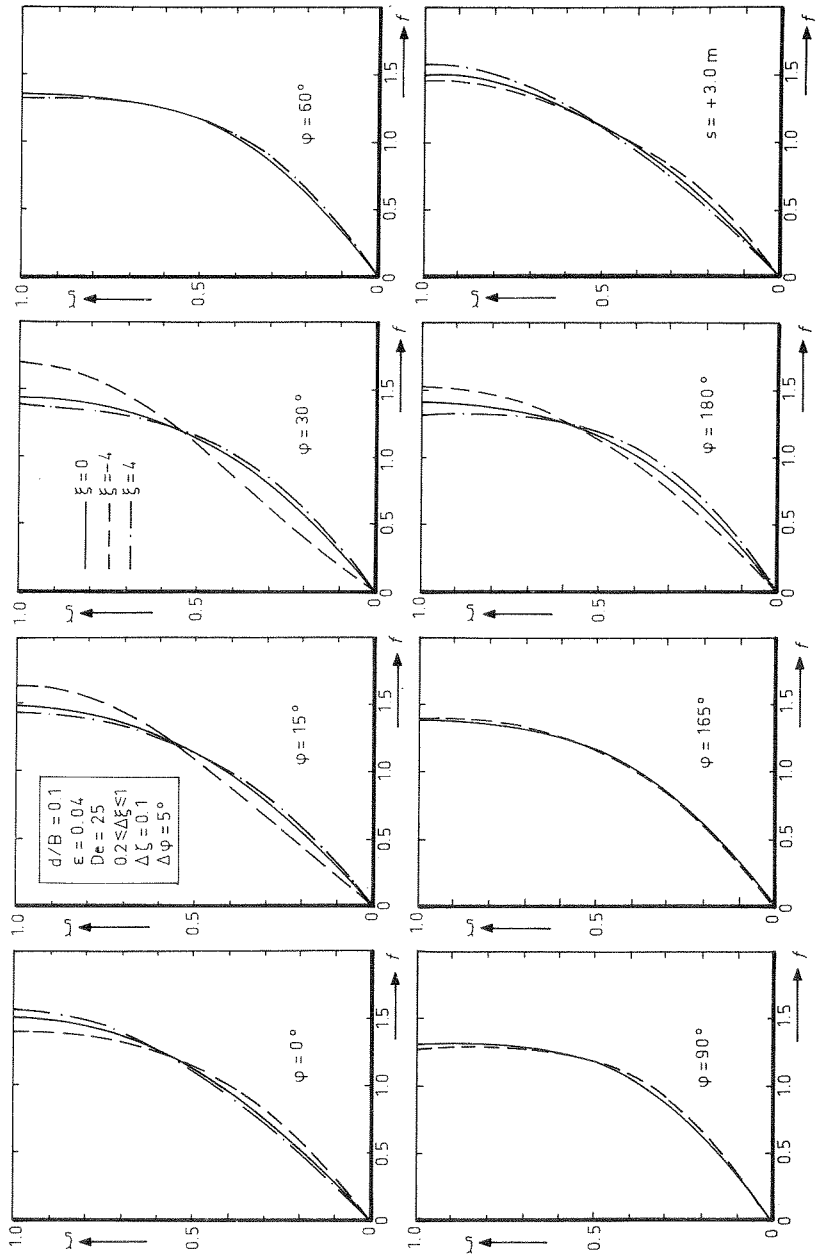

Figure 25. Influence of the streamwise accelerations on the main velocity distribution
(a) Vertical distribution of the main velocity

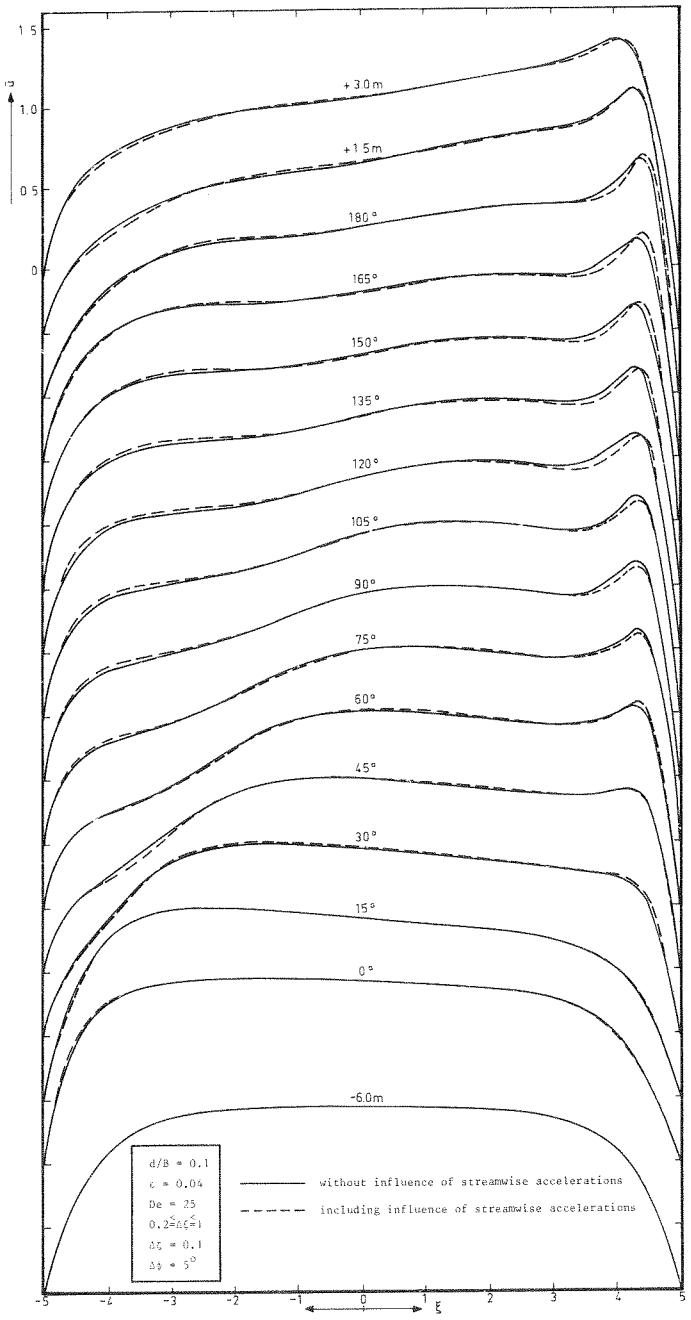

Figure 25. Influence of the streamwise accelerations on the main velocity distribution

(b) Depth-averaged main velocity

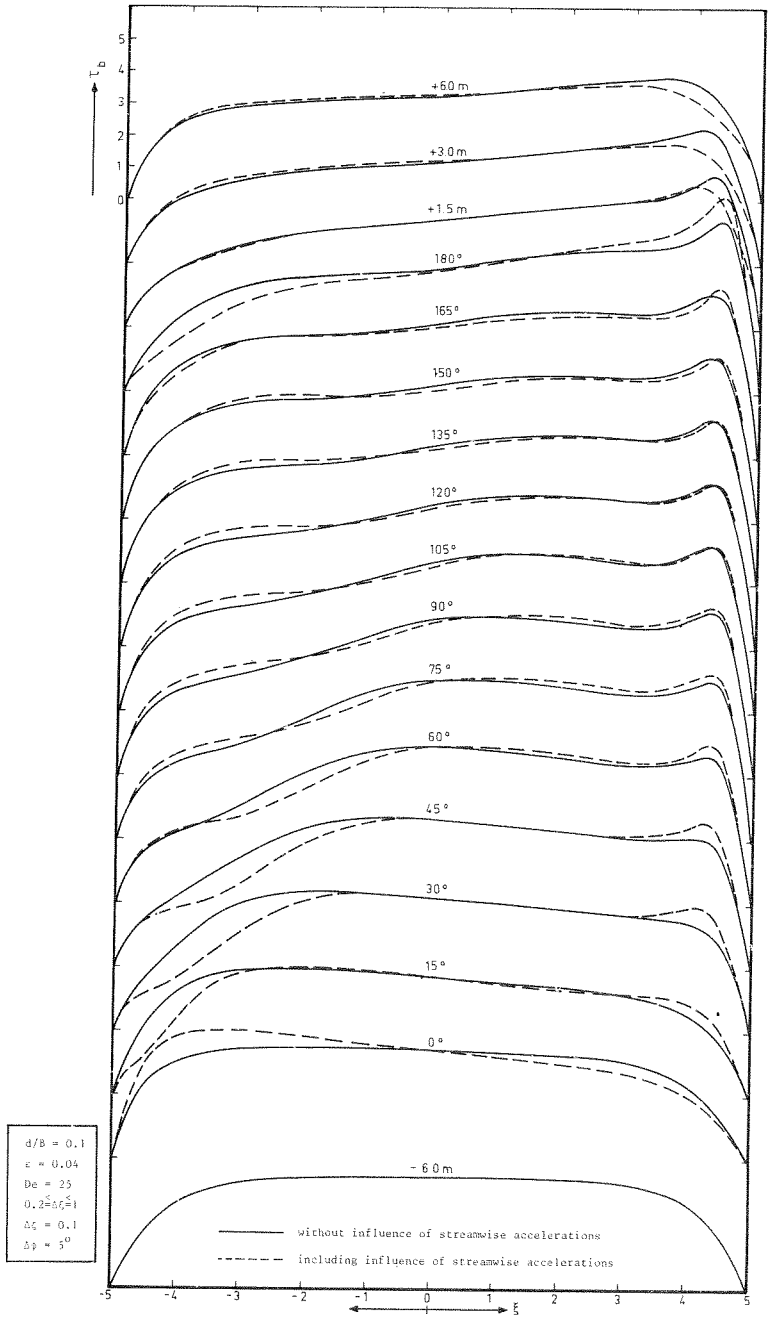

Figure 26. Influence of the streamwise accelerations on the bottom shear stress

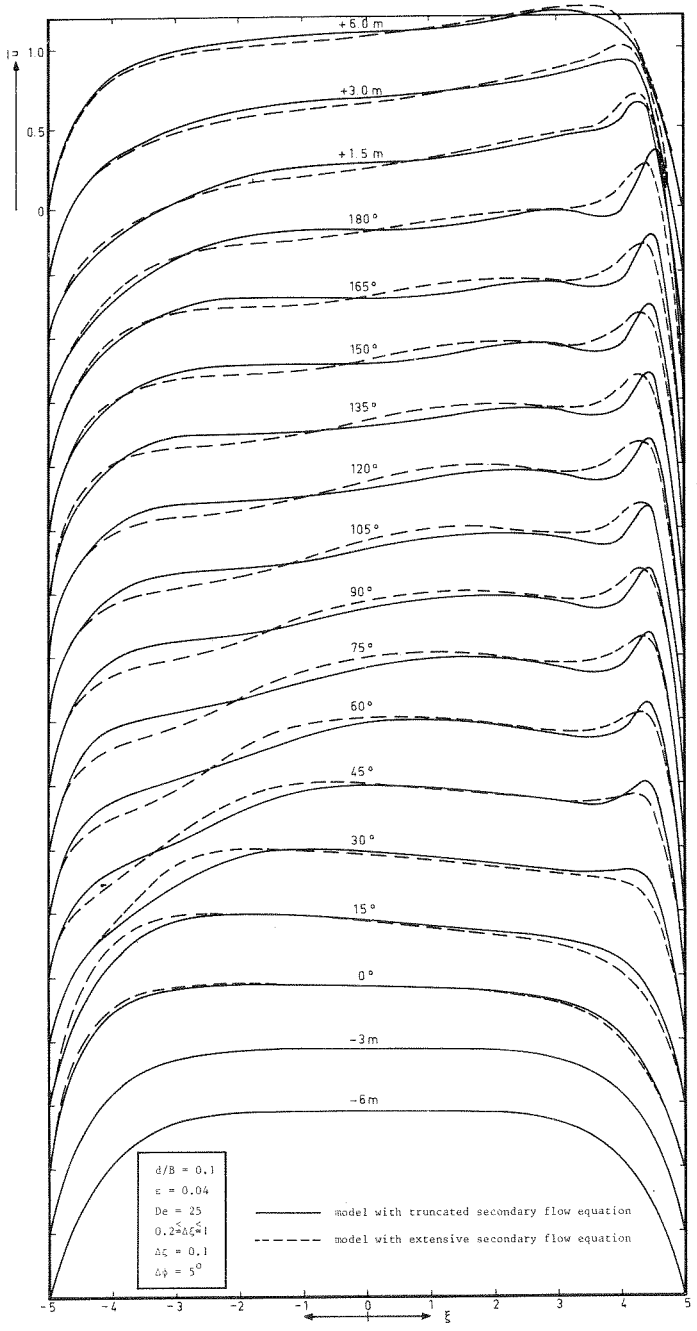

Figure 27. Influence of the simplifications of the secondary flow equation on the main velocity distribution

(a) Depth-averaged main velocity

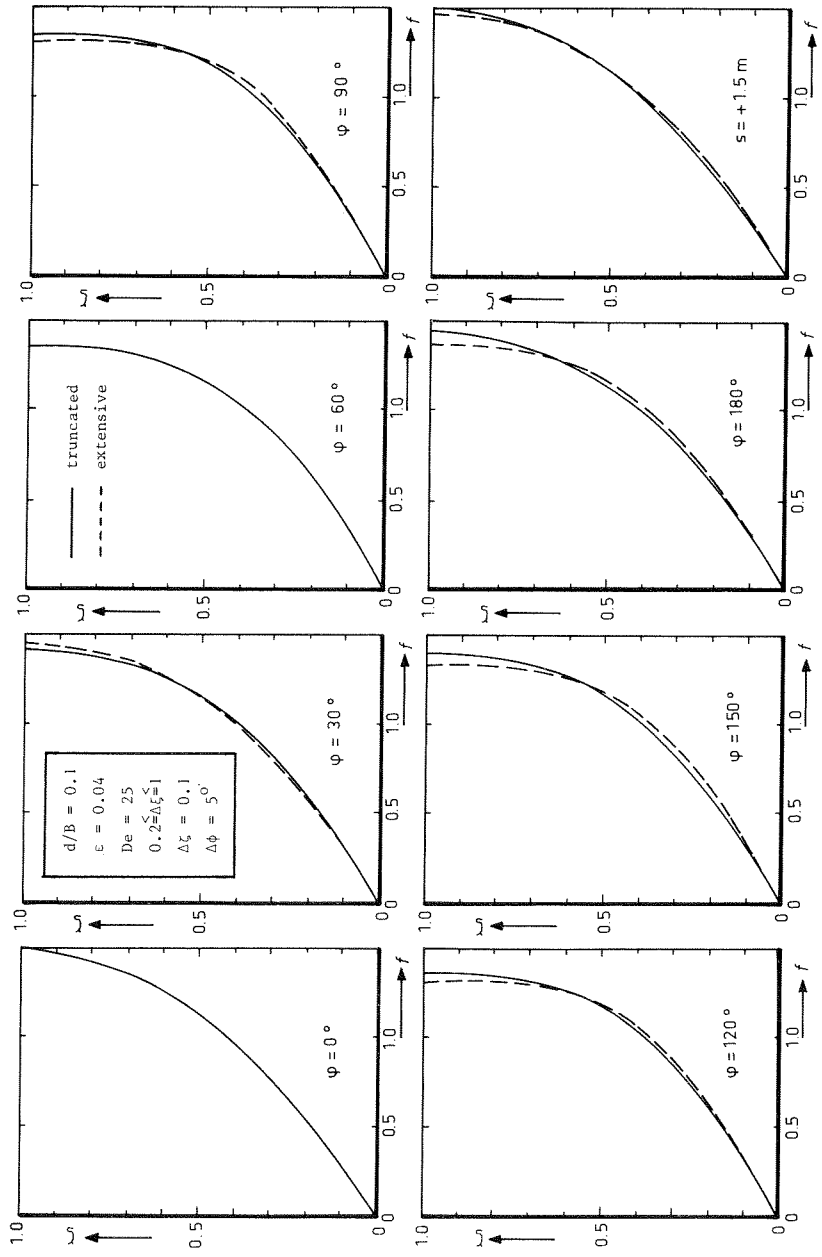

Figure 27. Influence of the simplifications of the secondary flow equation on the main velocity distribution
(b) Vertical distribution of the main velocity

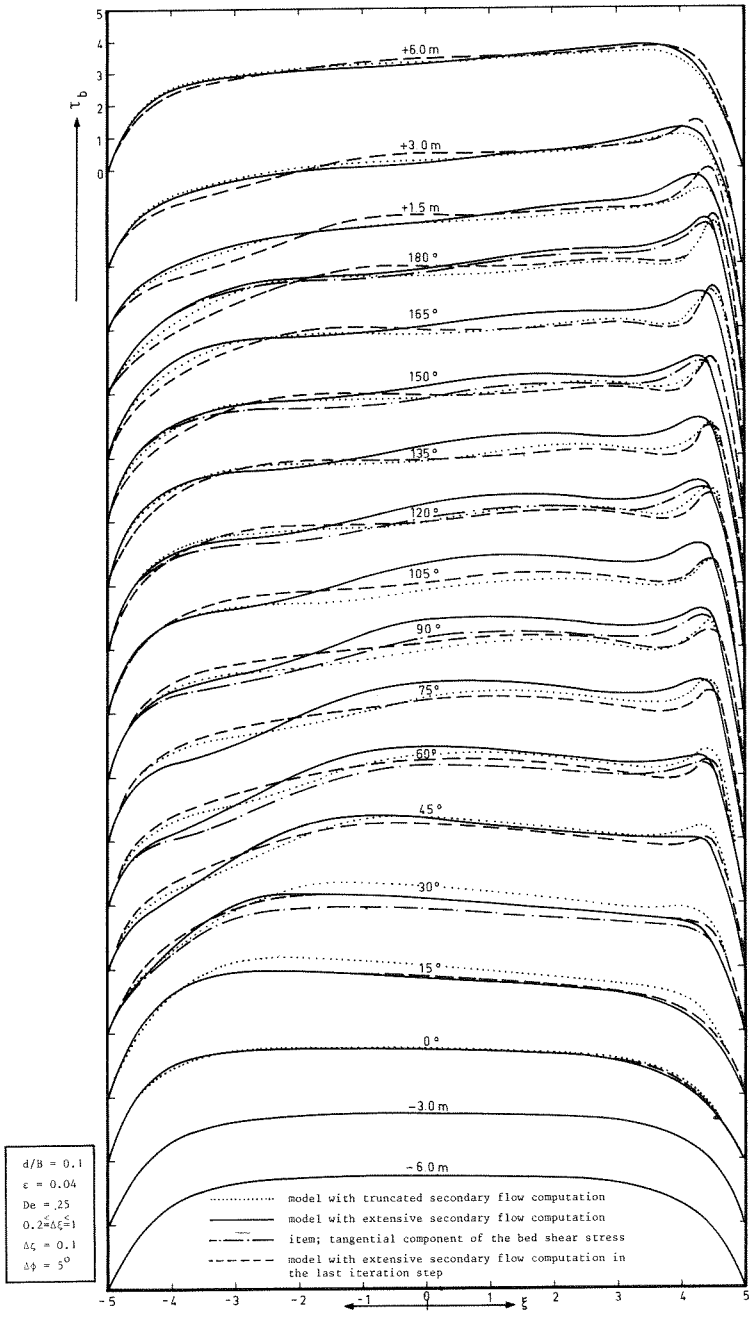

Figure 28. Influence of the simplifications of the secondary flow equation on the bottom shear stress
(a) Magnitude of the bottom shear stress

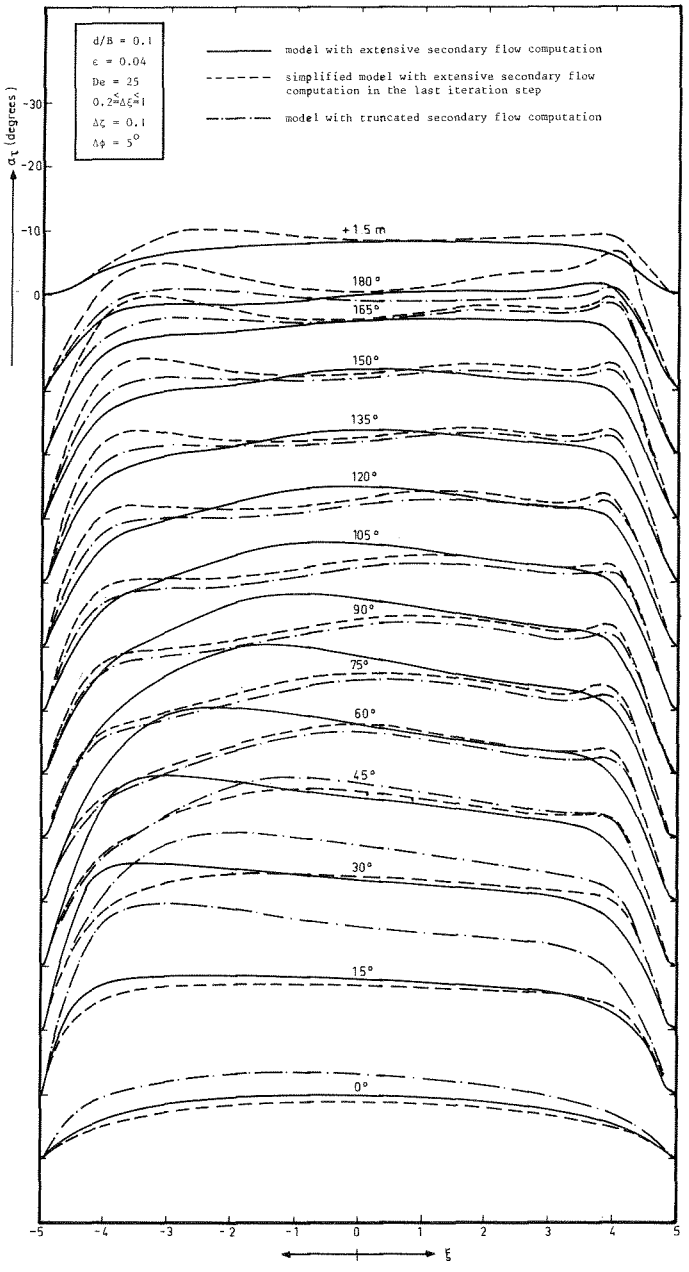

Figure 28. Influence of the simplifications of the secondary flow equation on the bottom shear stress
(b) Direction of the bottom shear stress

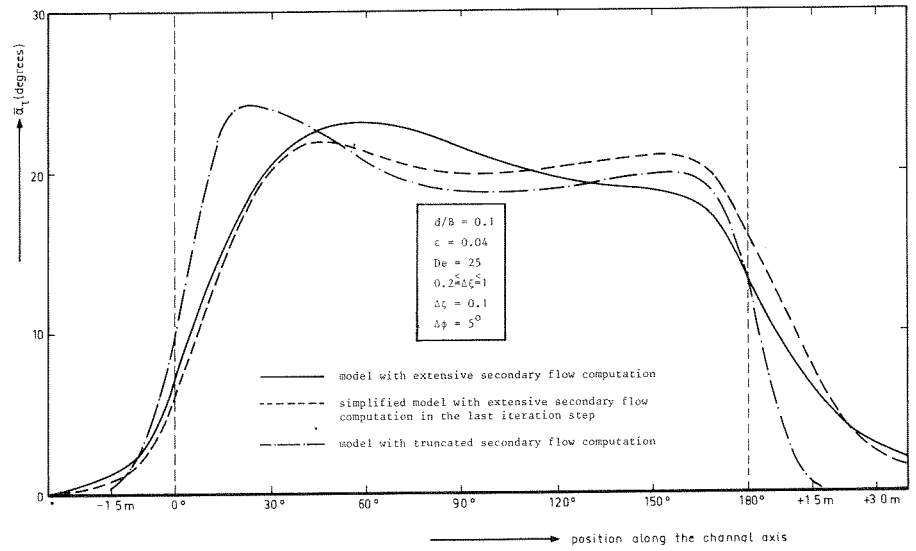

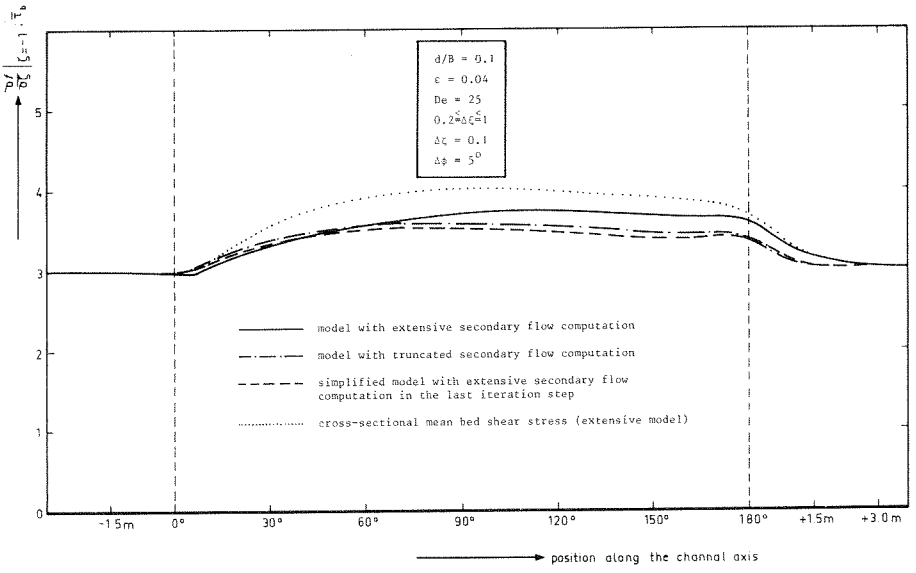

Figure 28. Influence of the simplifications of the secondary flow equation on the bottom shear stress

(c) Cross-sectional mean direction of the bottom shear stress

(d) Bottom shear stress factor of the main flow

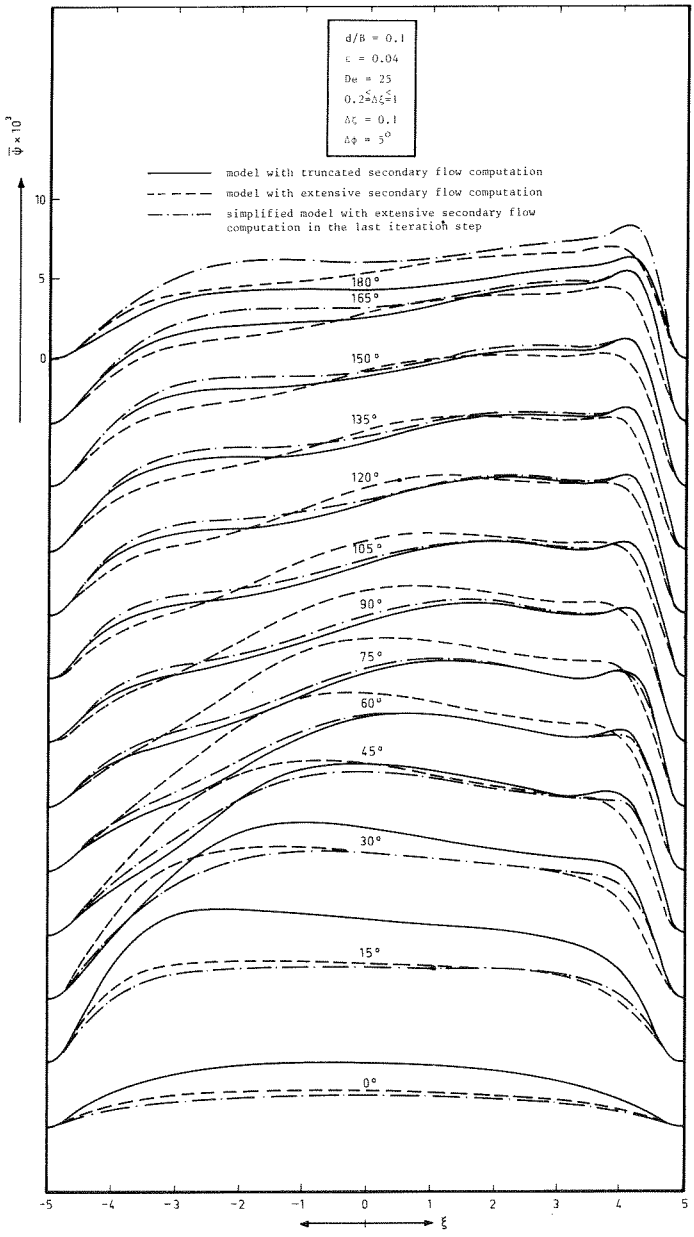

Figure 29. Influence of the simplifications of the secondary flow equation on the secondary flow

(a) Depth-averaged stream function

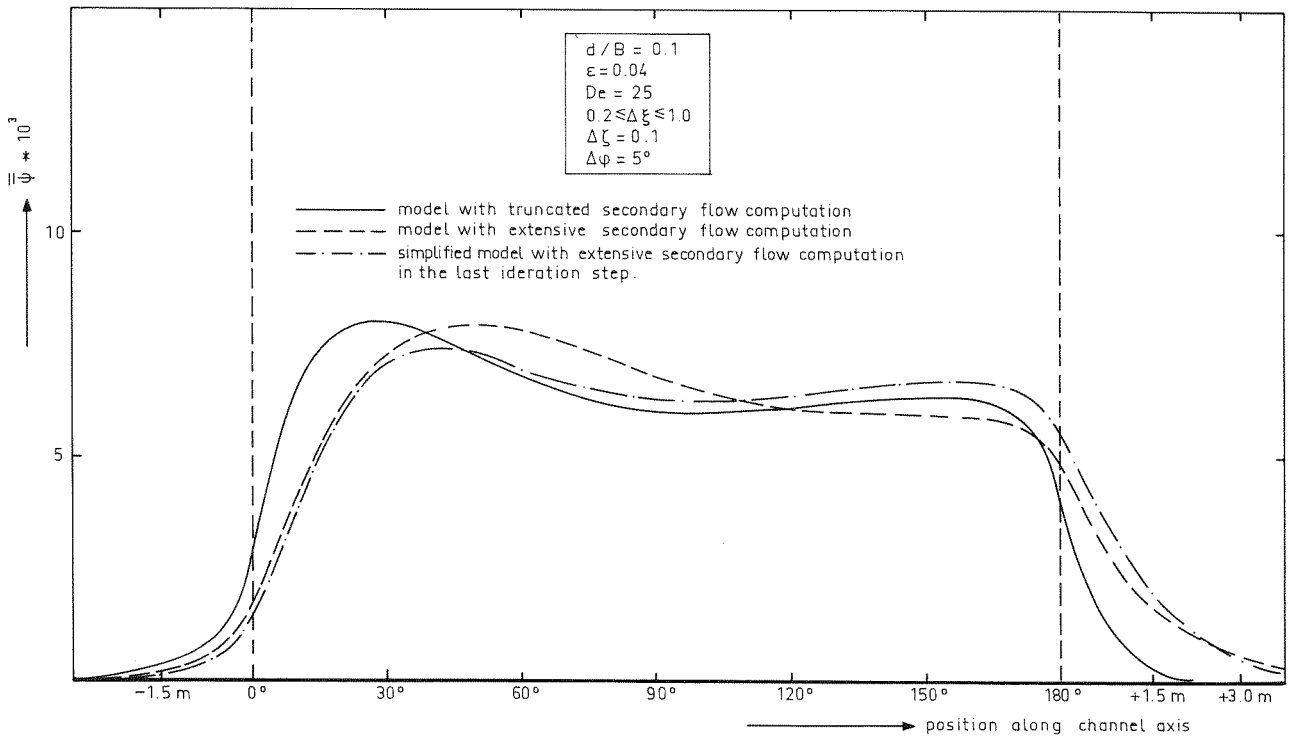

Figure 29. Influence of the simplifications of the secondary flow equation on the secondary flow
(b) Cross-sectional mean value of the stream function

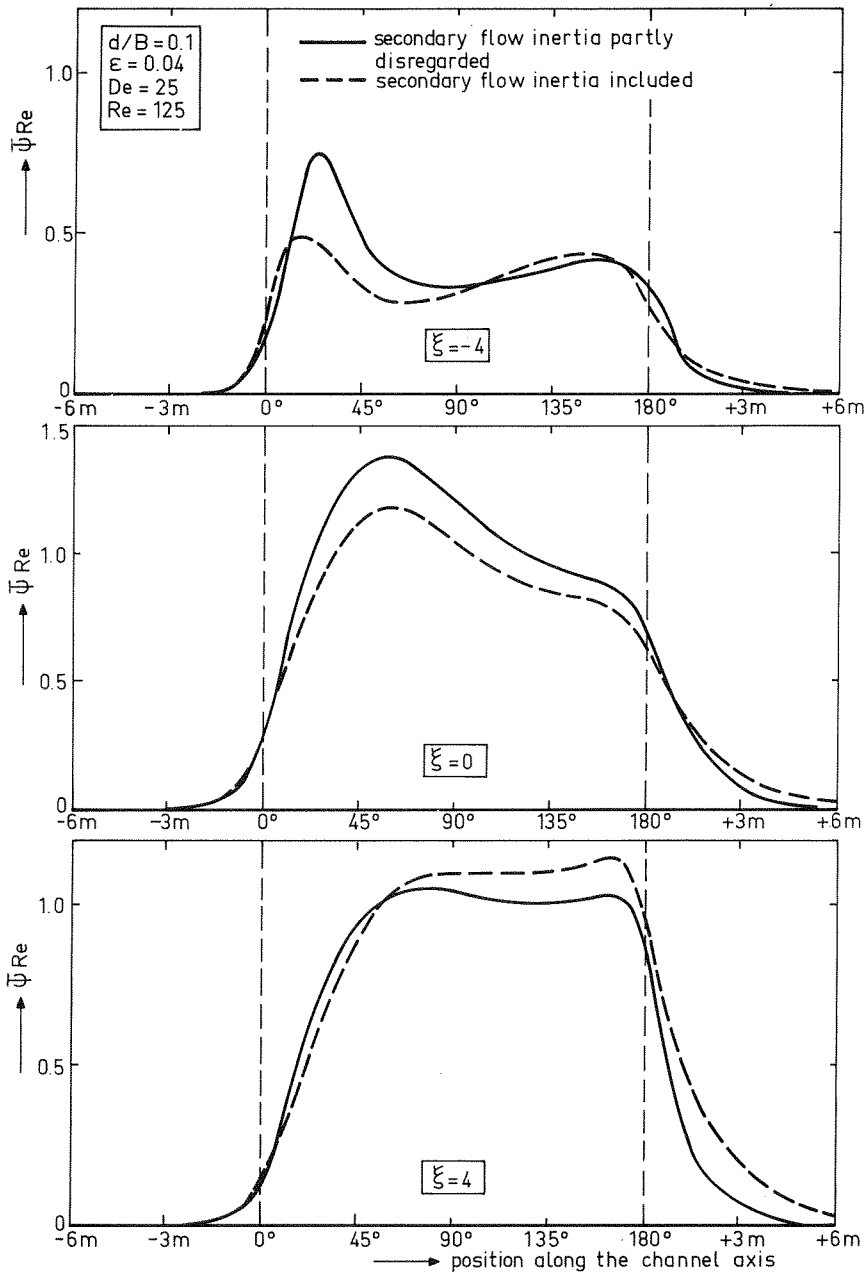

Figure 30. Influence of the partial neglect of the streamwise inertia of the secondary flow

(a) Secondary flow intensity

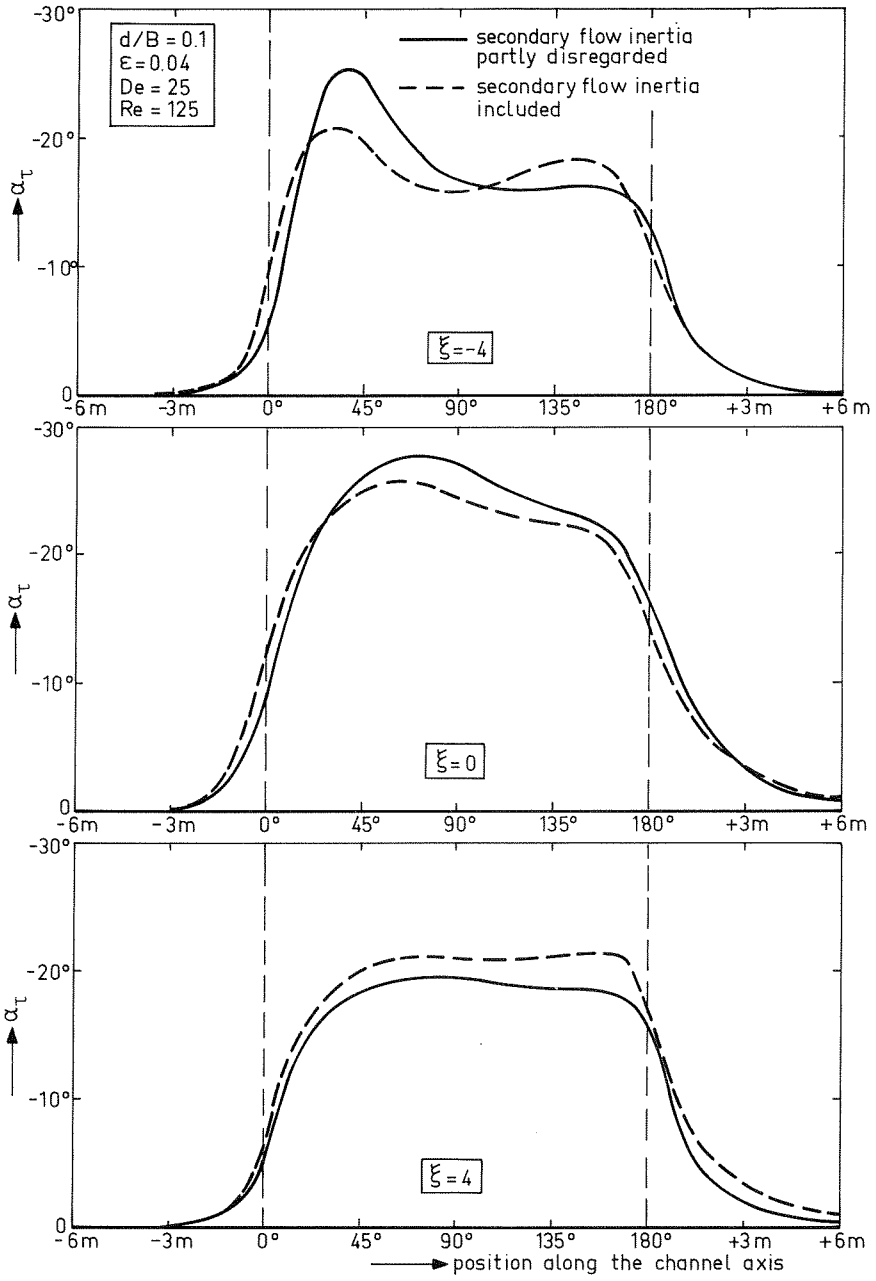

Figure 30. Influence of the partial neglect of the streamwise inertia of the secondary flow

(b) Direction of the bottom shear stress

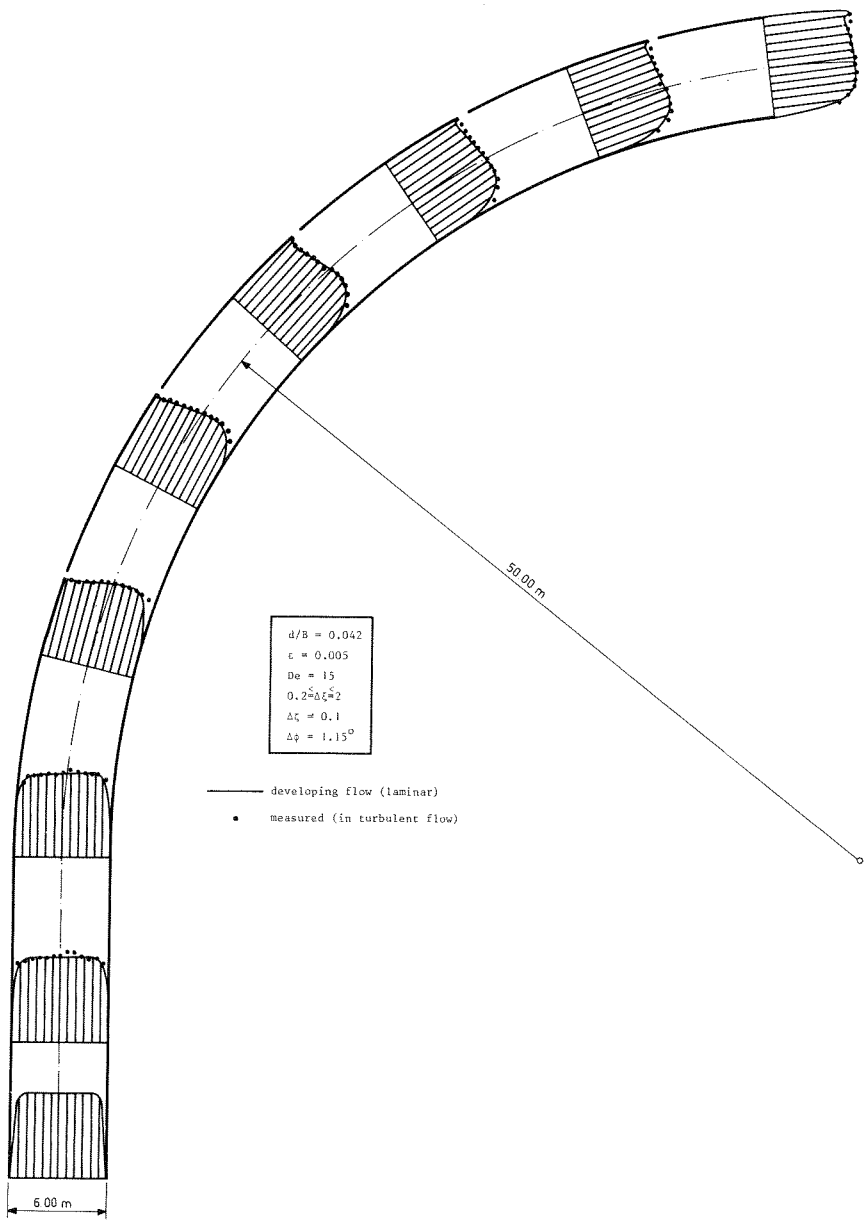

Figure 31. Qualitative comparison with turbulent flow experiments
(a) Depth-averaged main flow in the DHL-flume

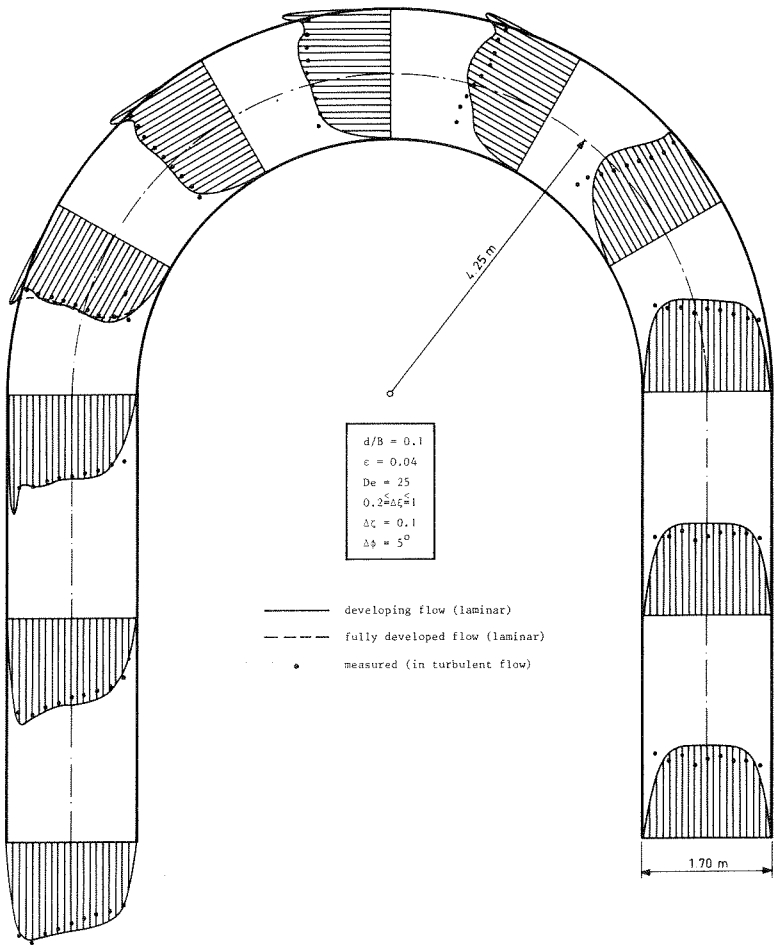

Figure 31. Qualitative comparison with turbulent flow experiments
(b) Depth-averaged main flow in the LFM-flume

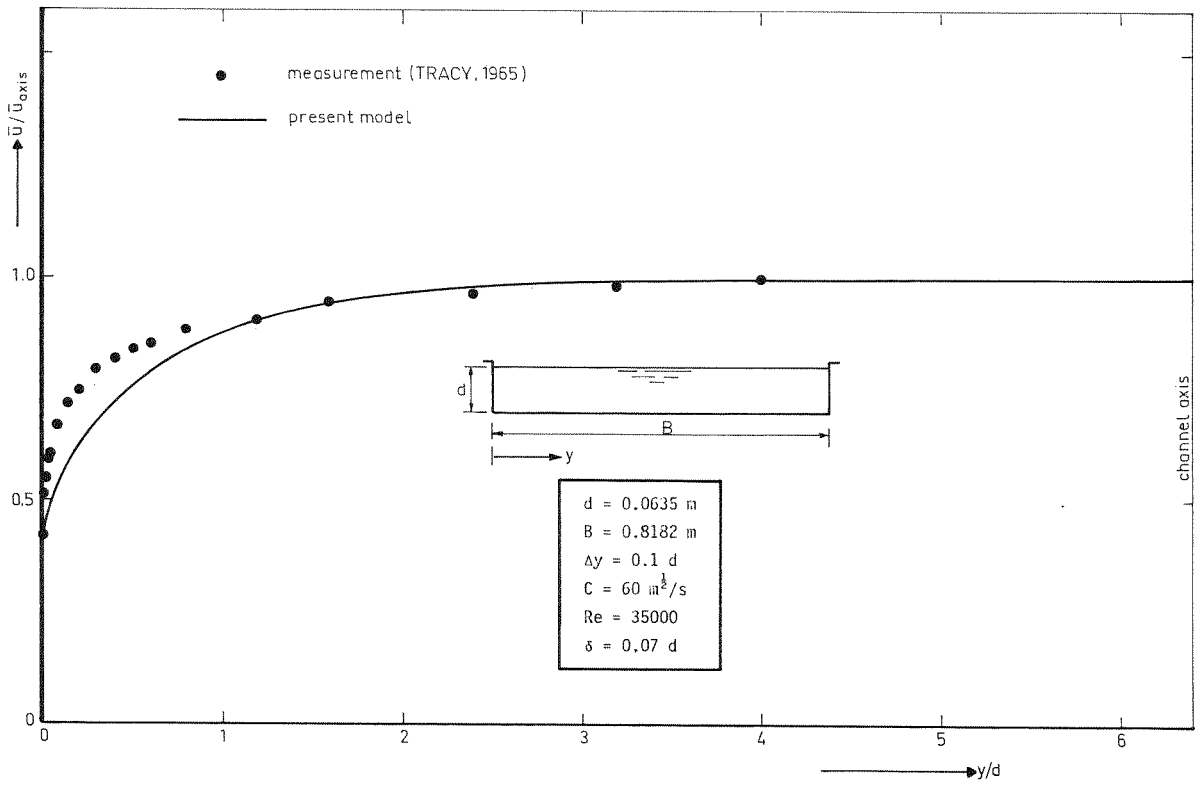

Figure 32. Fully-developed turbulent flow in a straight channel of finite width
(a) Comparison with Tracy's measurements

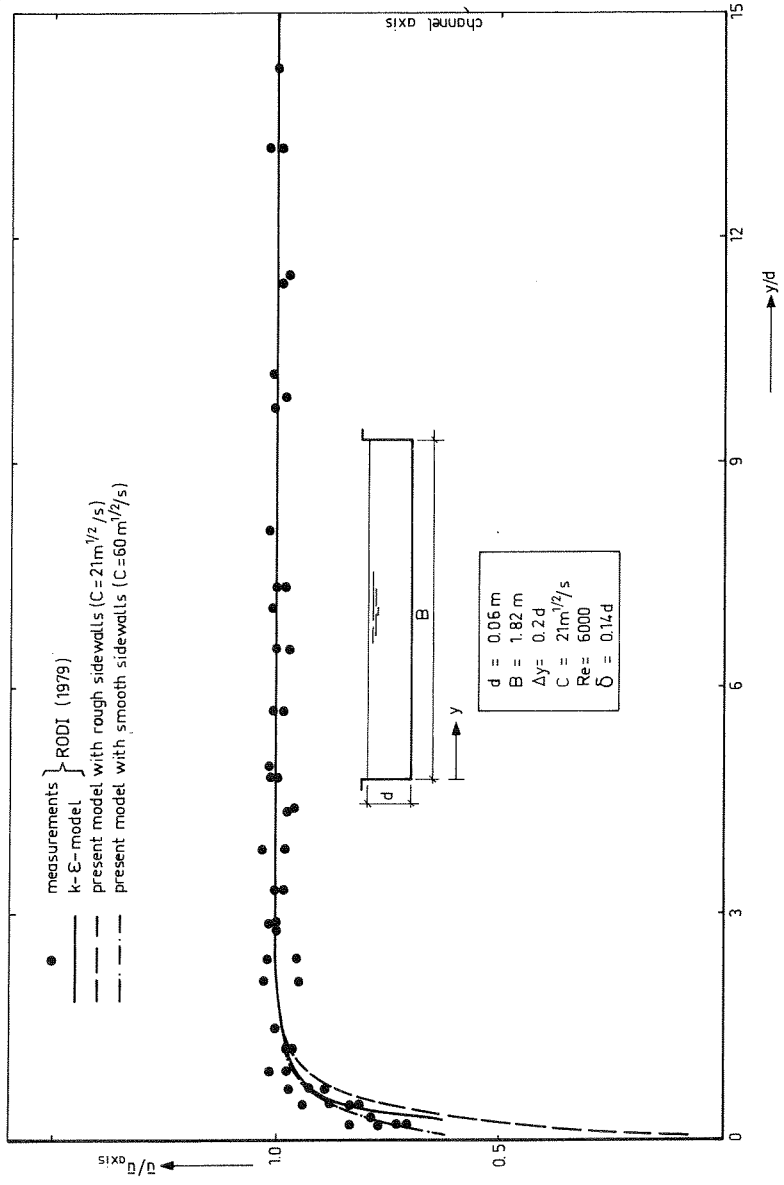

Figure 32. Fully-developed turbulent flow in a straight channel of finite width
(b) Comparison with the k-ε-model

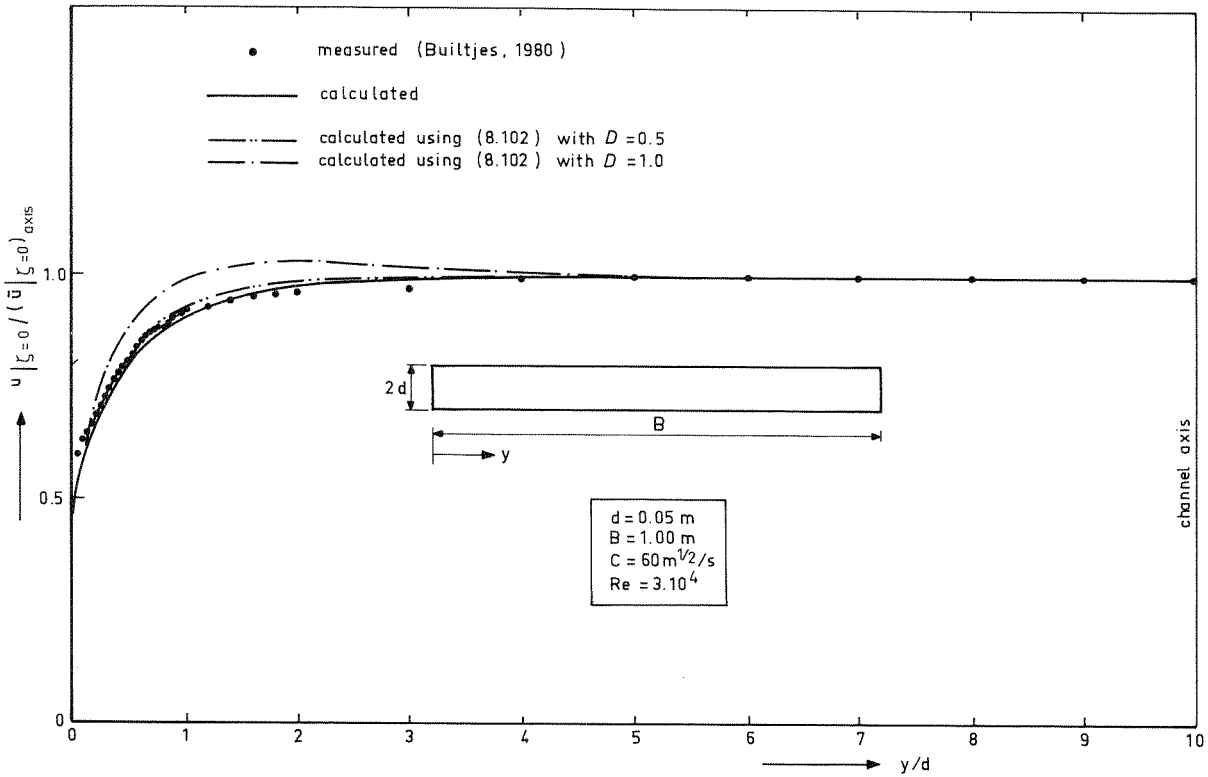

Figure 32. Fully-developed turbulent flow in a straight channel of finite width

(c) Comparison with Builtjes' measurements

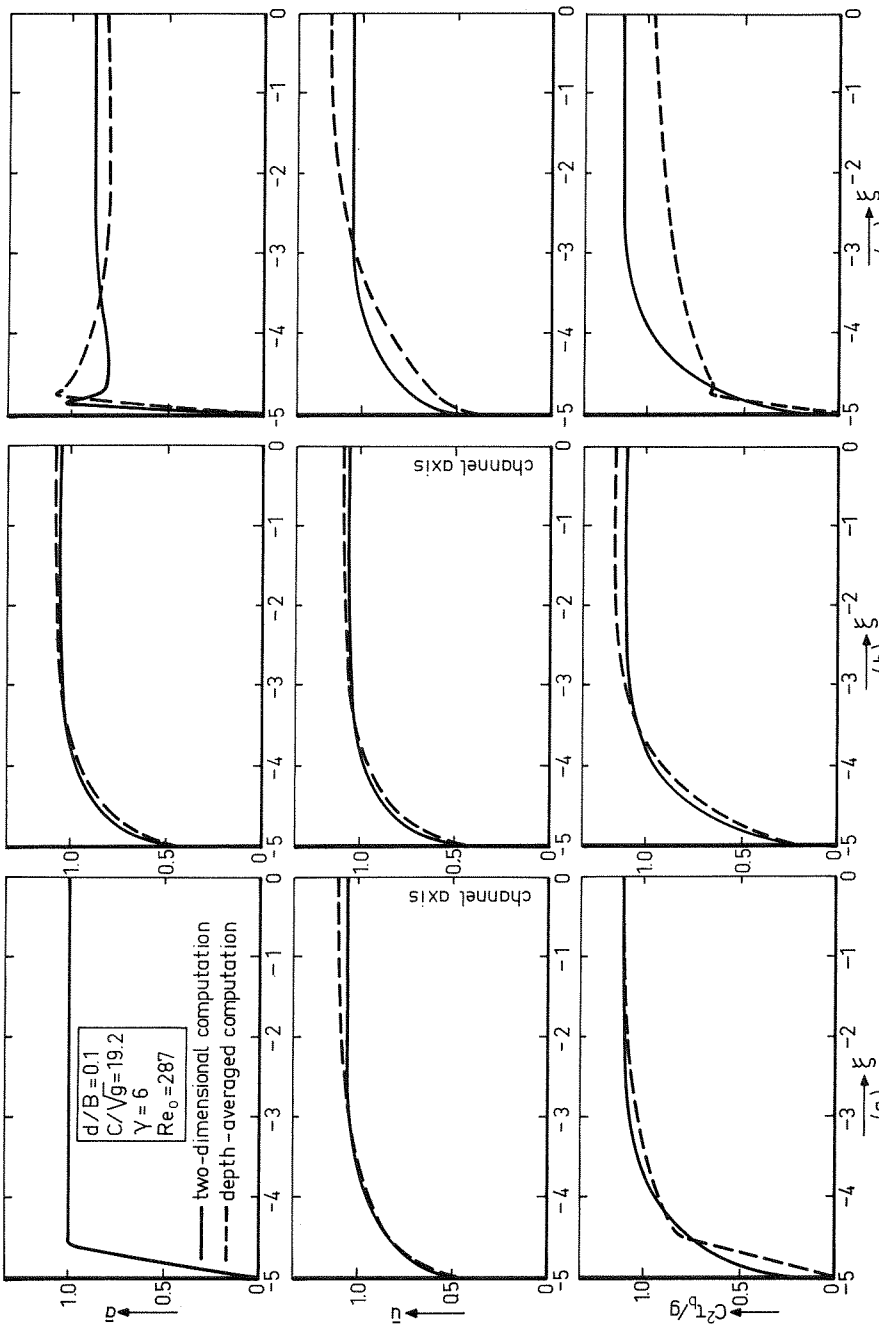

Figure 33. Influence of depth-averaging the momentum equation and the turbulence model in straight channel flow

(a) Parabolic turbulence viscosity; $\overline{\alpha}$ fixed (b) id.; $\overline{\alpha} = \overline{u}$ (c) mixing length model

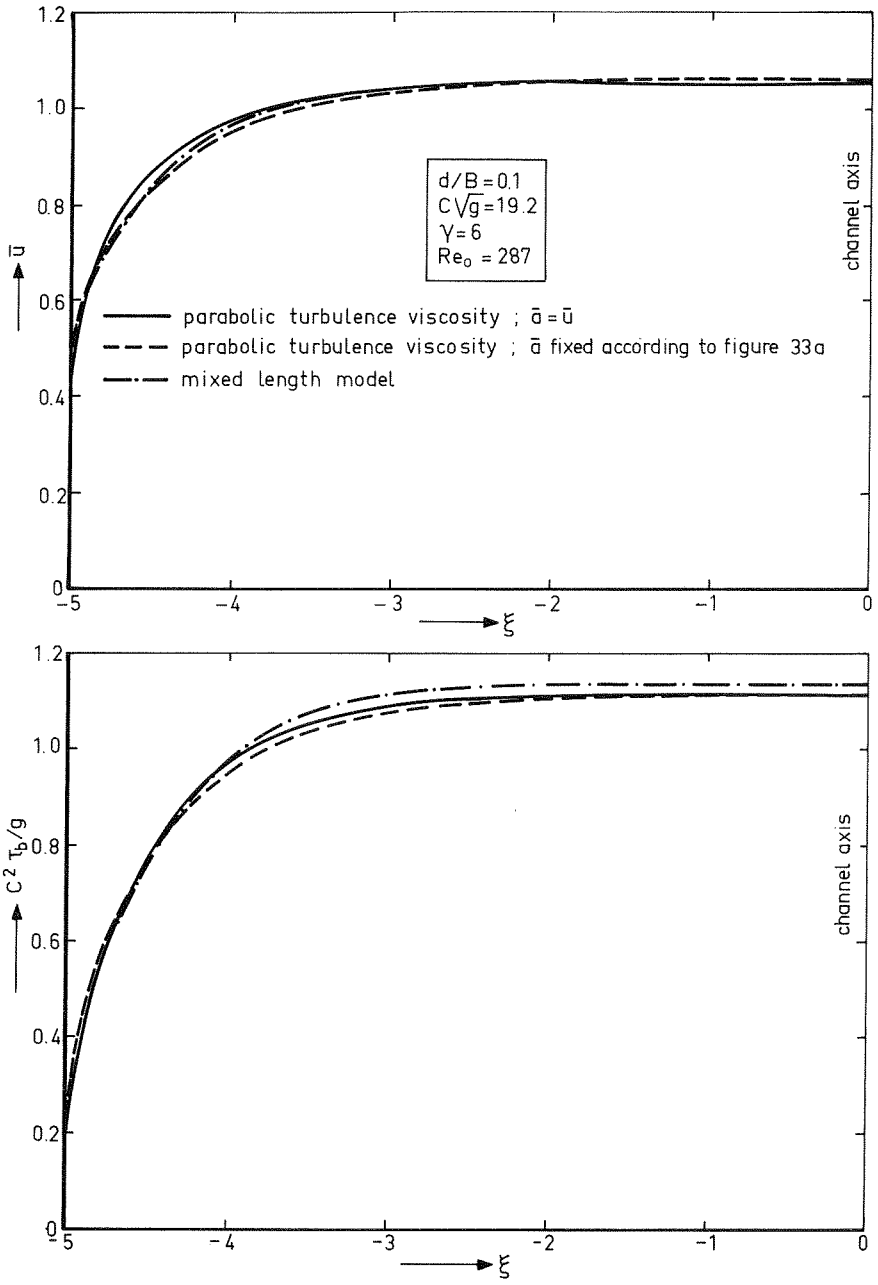

Figure 34. Influence of the turbulence model on straight channel flow

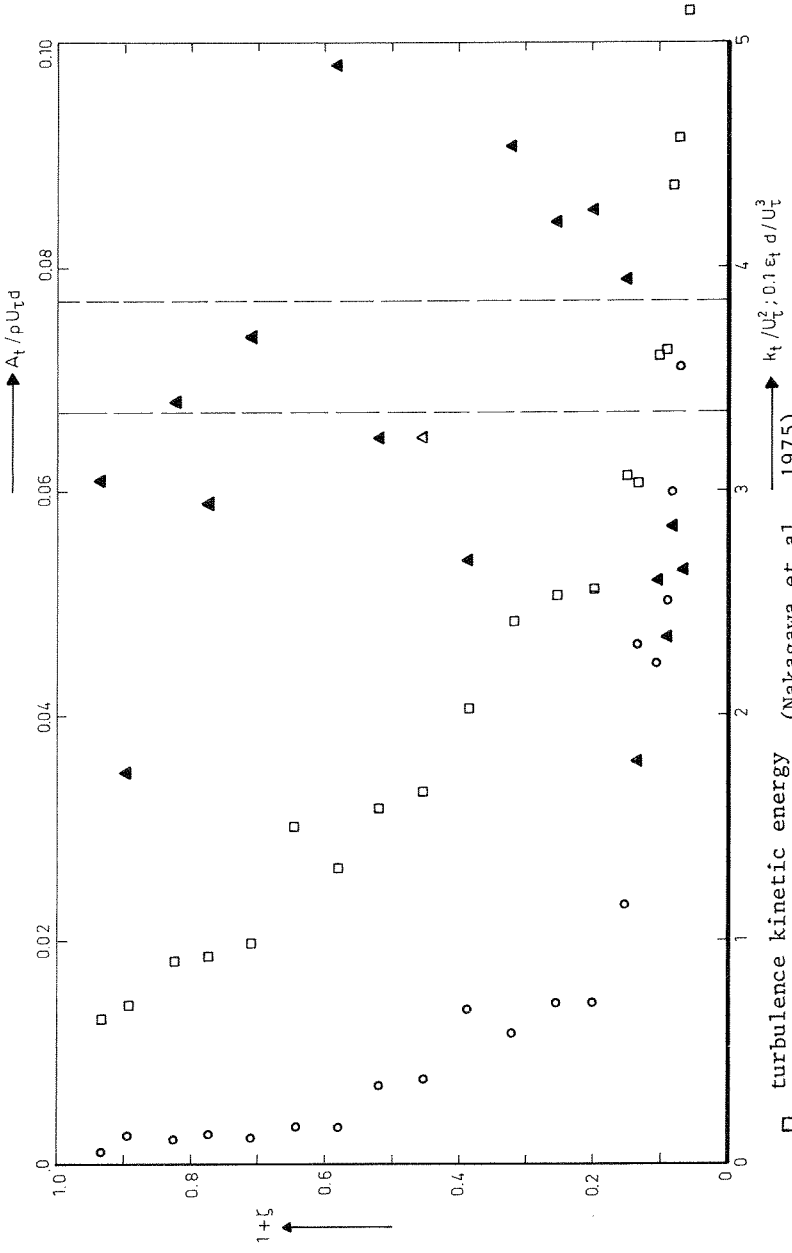

Figure 35. Turbulence viscosity based on measured turbulence data

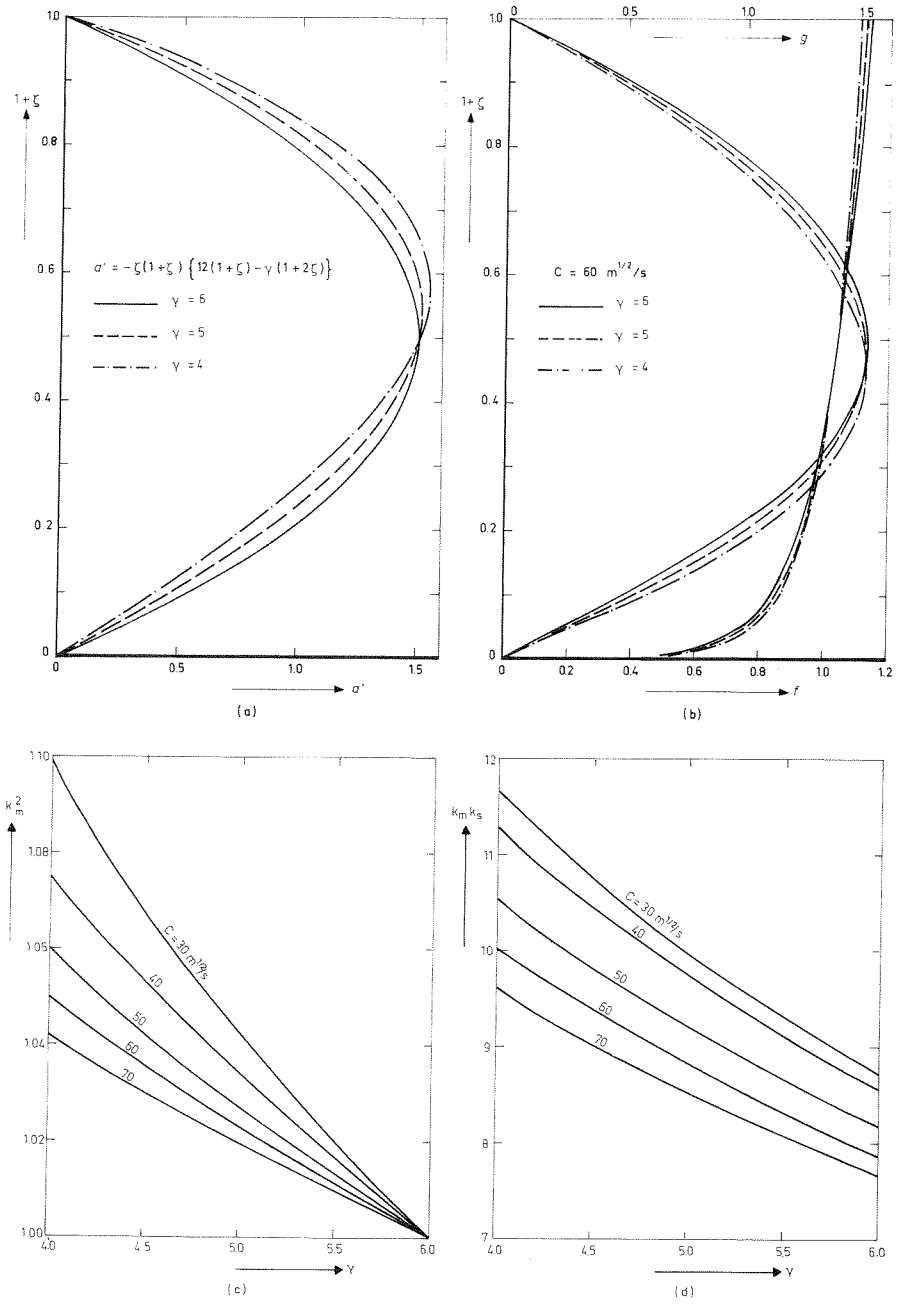

Figure 36. Influence of the overall mean value of the turbulence viscosity (a) Turbulence viscosity (b) Main and secondary velocity profiles (c)-(d) Bottom shear stress factors for main and secondary flow

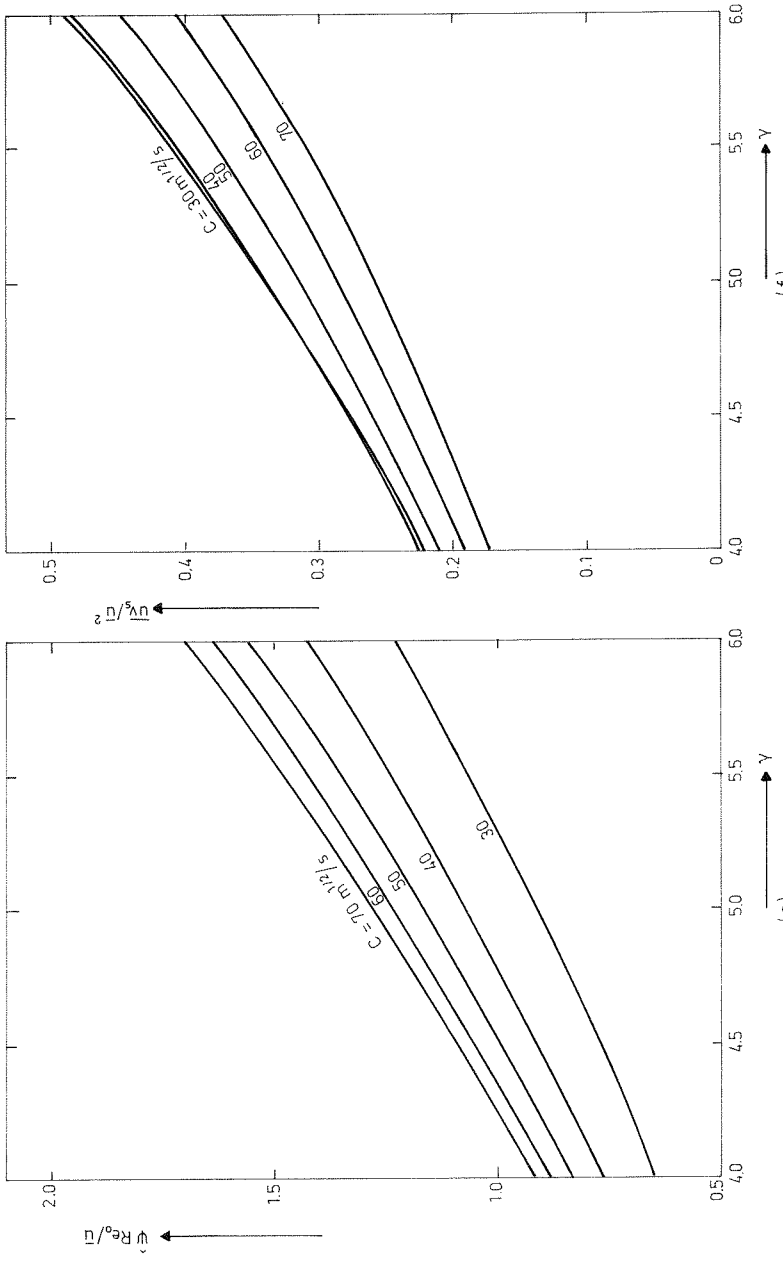

Figure 36. Influence of the overall mean value of the turbulence viscosity (e) Secondary flow intensity (f) Secondary flow convection factor

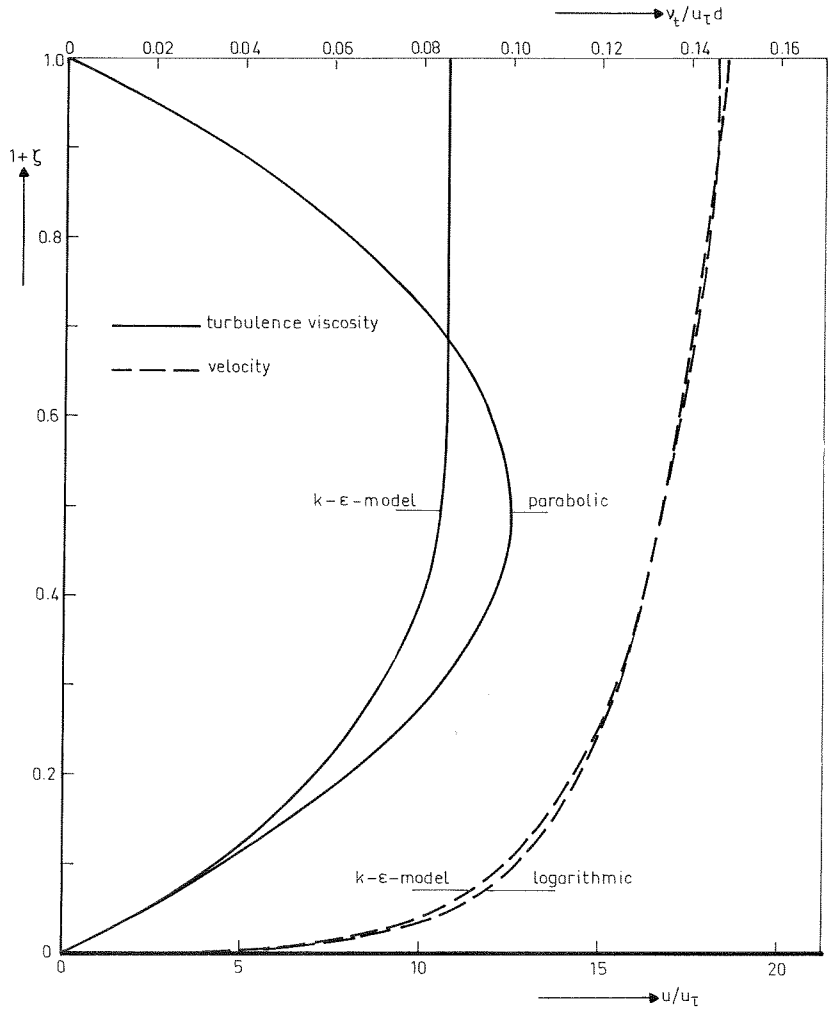

Figure 37. Parabolic turbulence viscosity vs. k-ε-model in uniform rectilinear shear flow

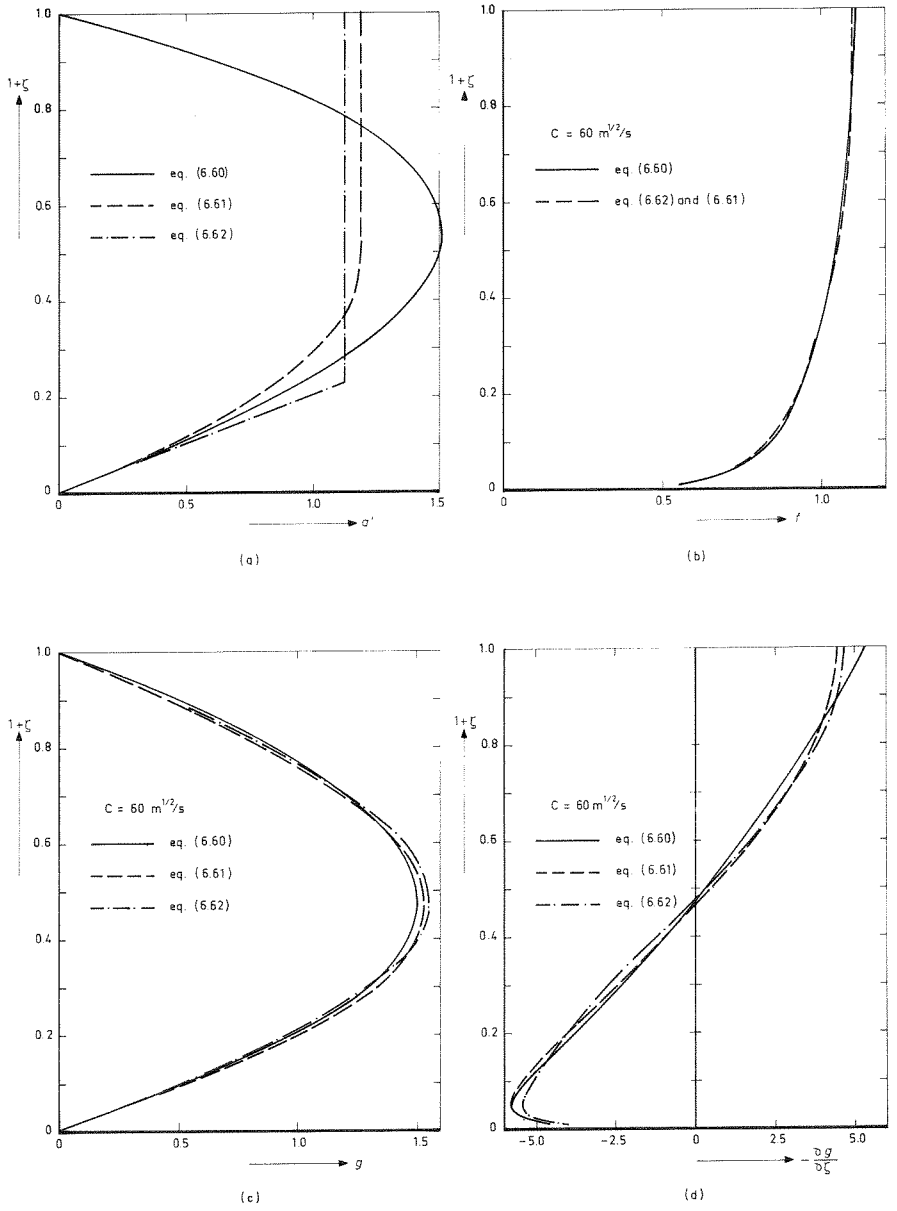

figure 38. Influence of the vertical distribution of the turbulence viscosity on the vertical distribution functions

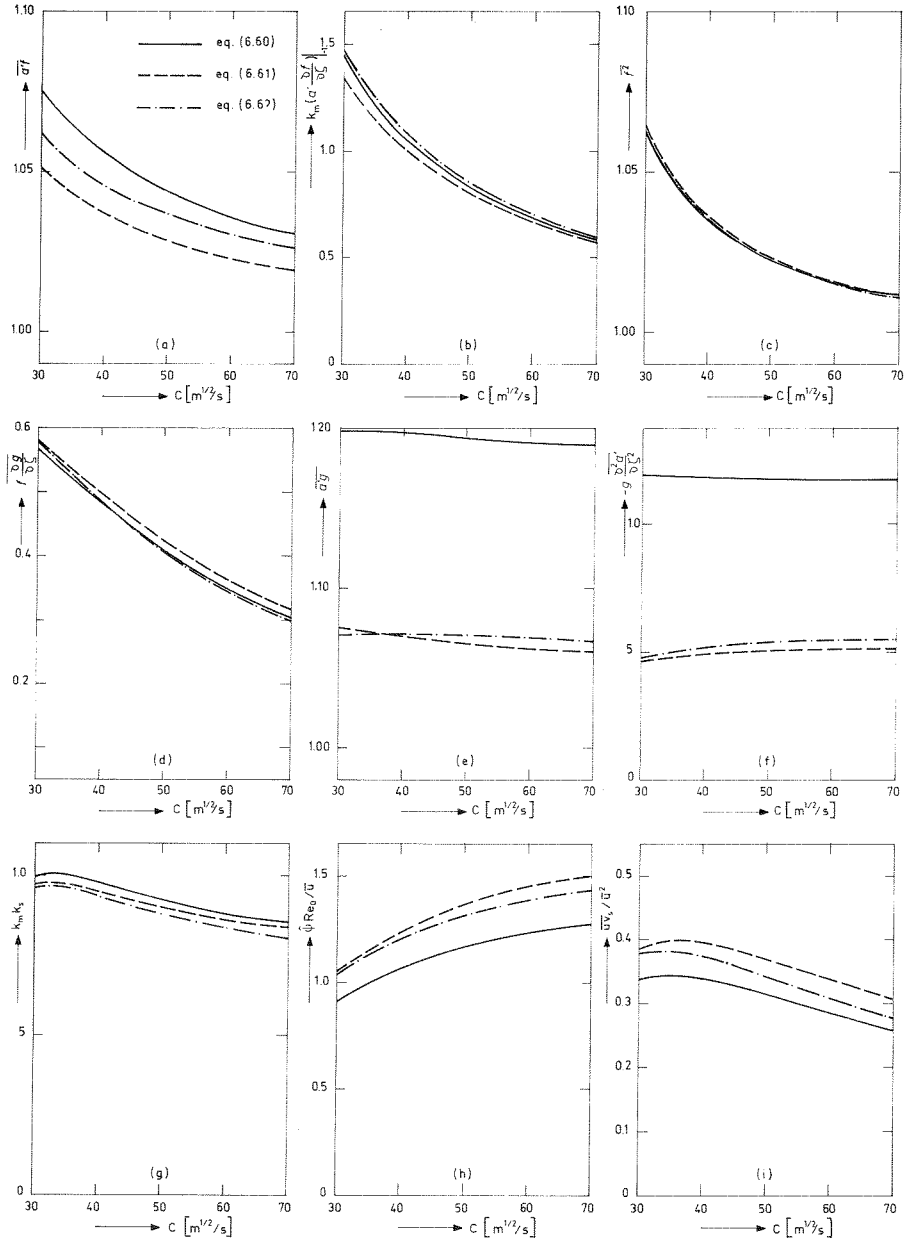

Figure 39. Influence of the vertical distribution of the turbulence viscosity on the coefficients in the depth-averaged equations

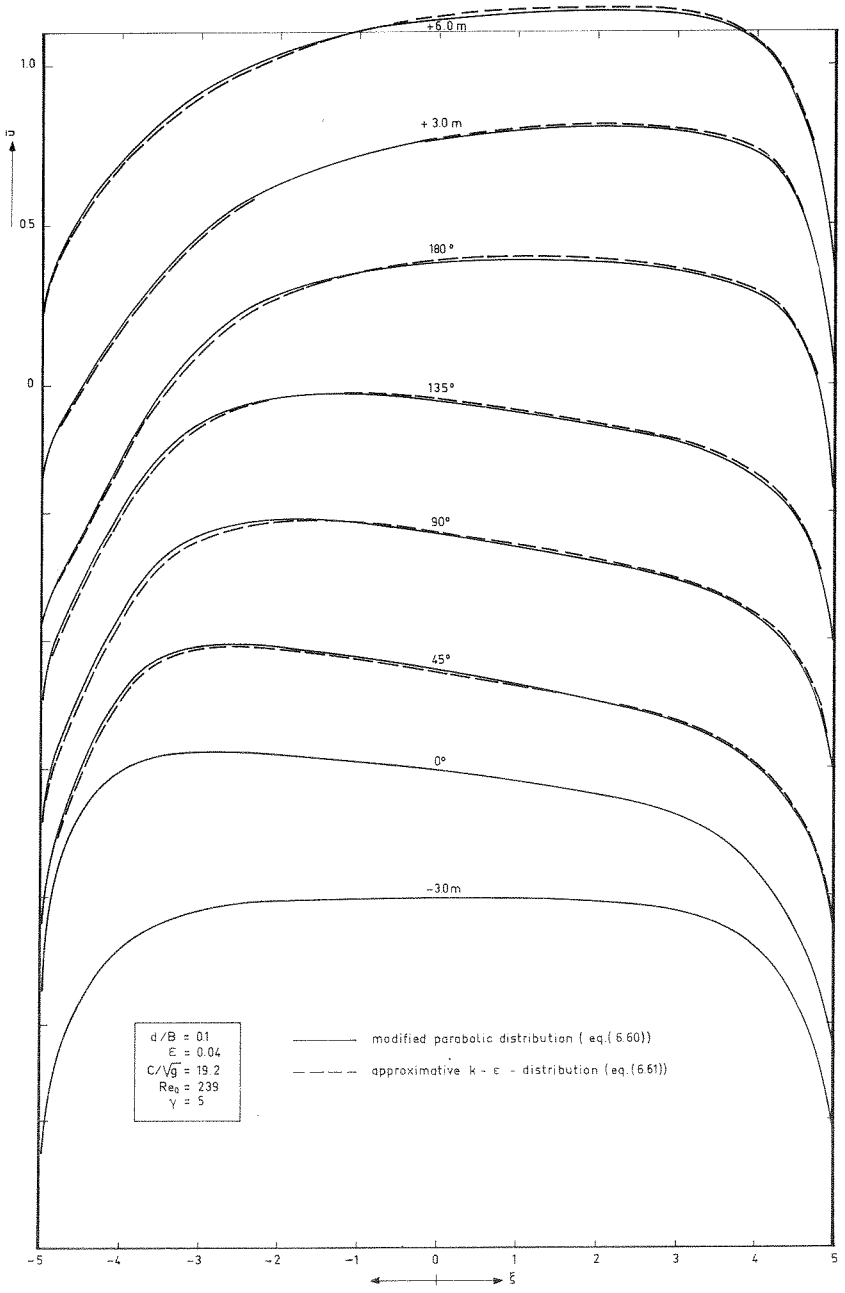

Figure 40. Influence of the vertical distribution of the turbulence viscosity on the flow in the LFM-flume
(a) Depth-averaged main velocity

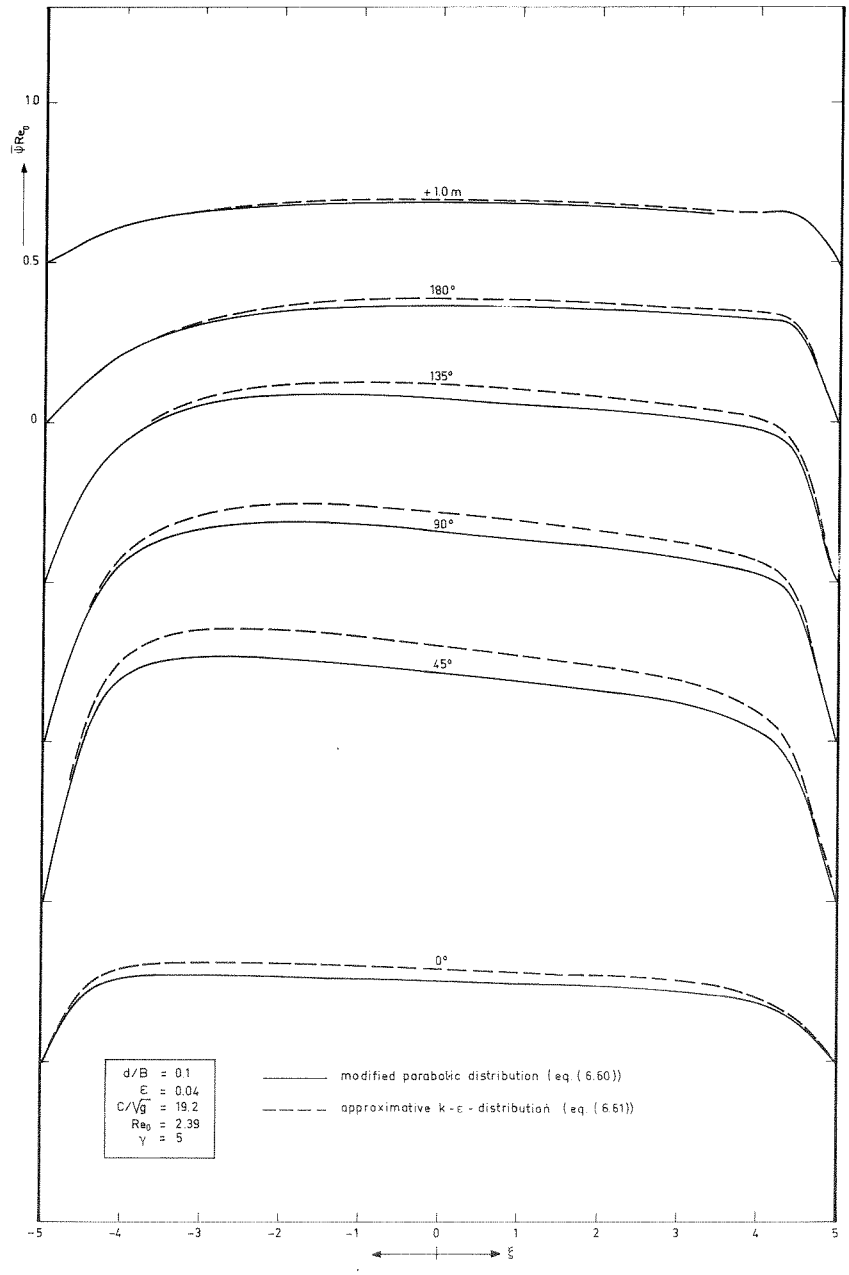

Figure 40. Influence of the vertical distribution of the turbulence viscosity on the flow in the LFM-flume

(b) Depth-averaged stream function of the secondary flow

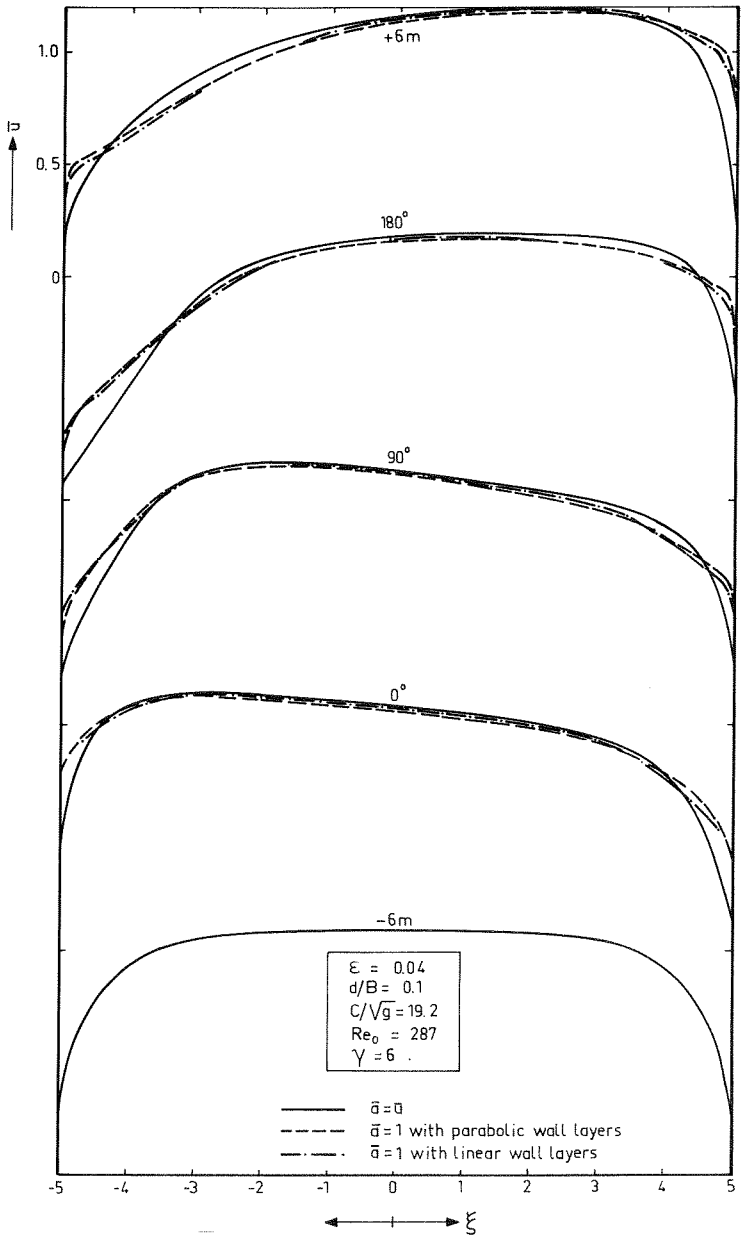

Figure 41. Influence of the horizontal distribution of the turbulence viscosity on the flow in the LFM-flume

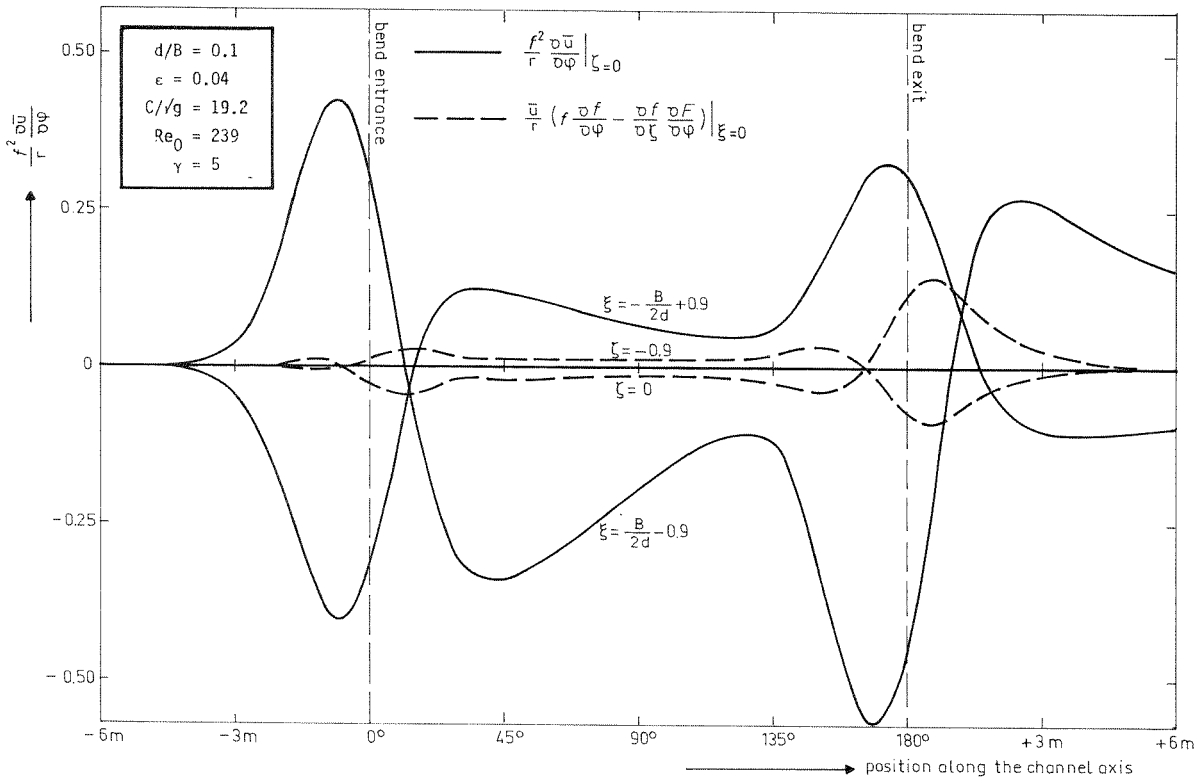

Figure 42. Influence of the simplification of the main flow convection terms

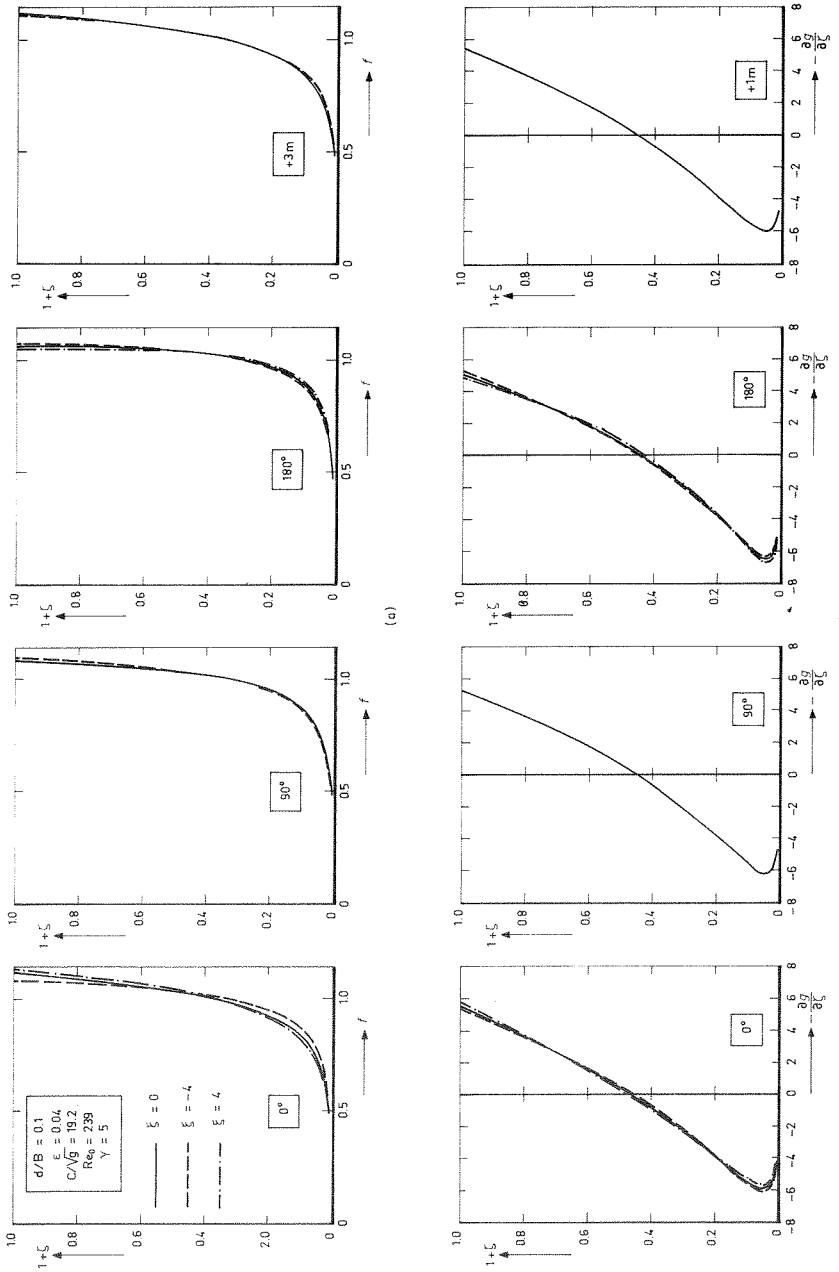

Figure 43. Influence of the streamwise accelerations on the vertical distribution functions
(a) Main velocity (b) Horizontal component of the secondary flow

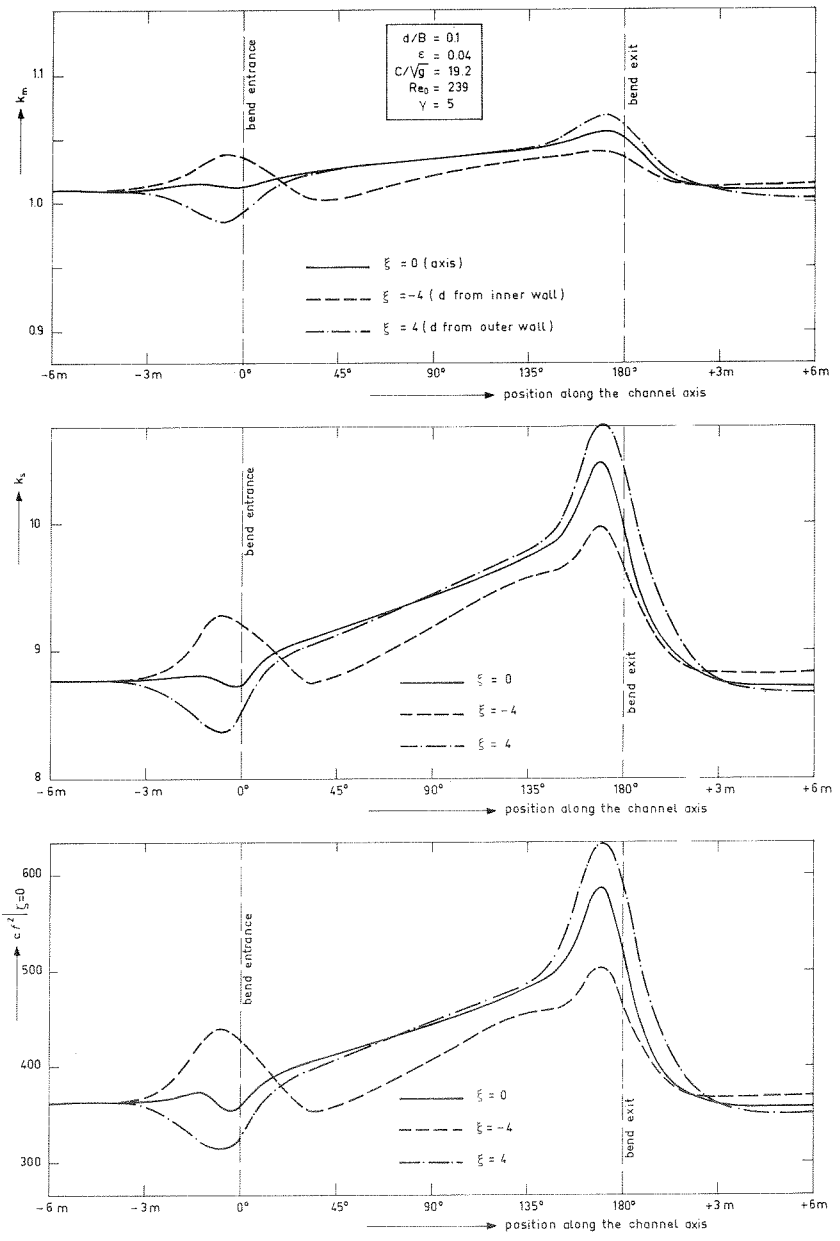

Figure 43. Influence of the streamwise accelerations on the vertical distribution functions

(c) Constants

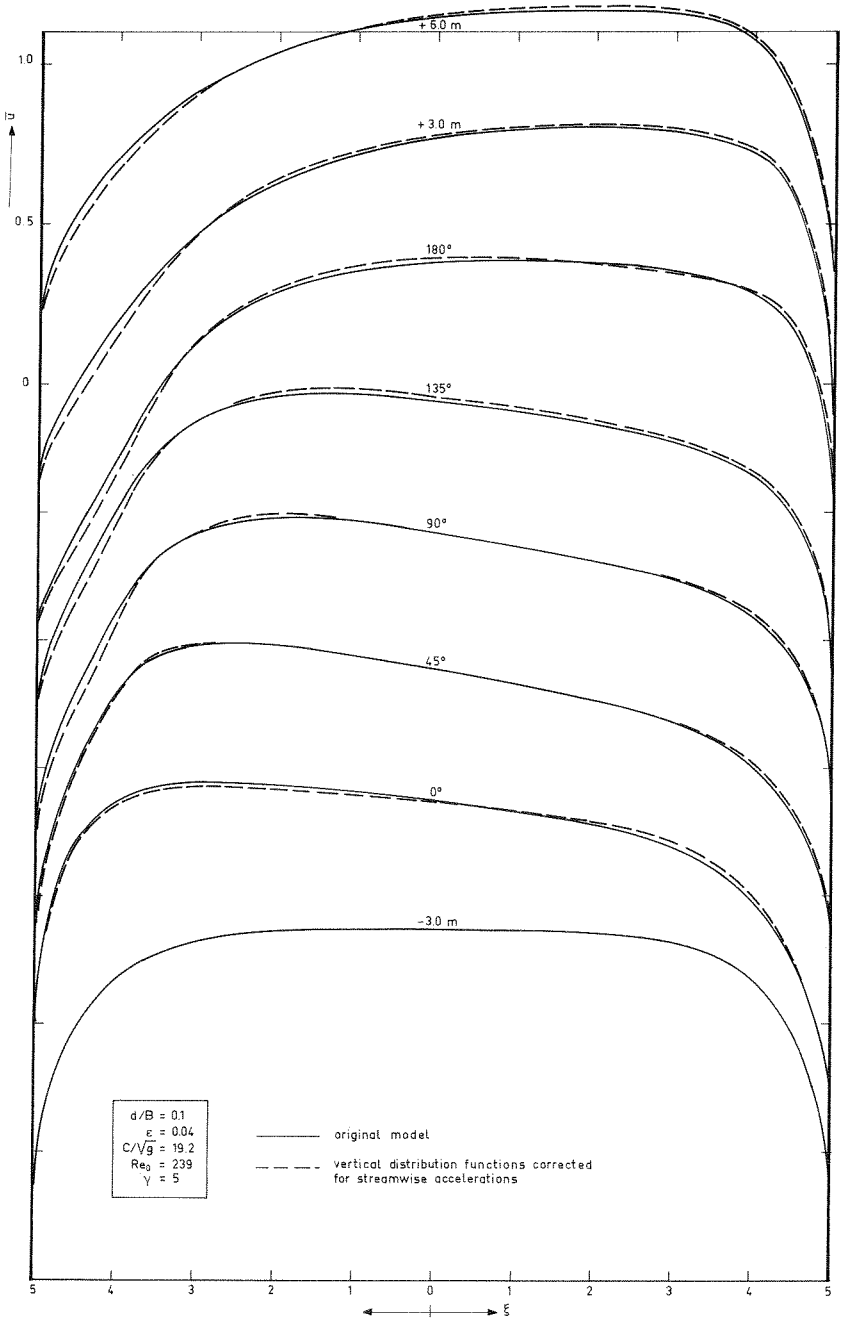

Figure 44. Influence of the streamwise accelerations of the main flow on the depth-averaged flow

(a) Depth-averaged main velocity

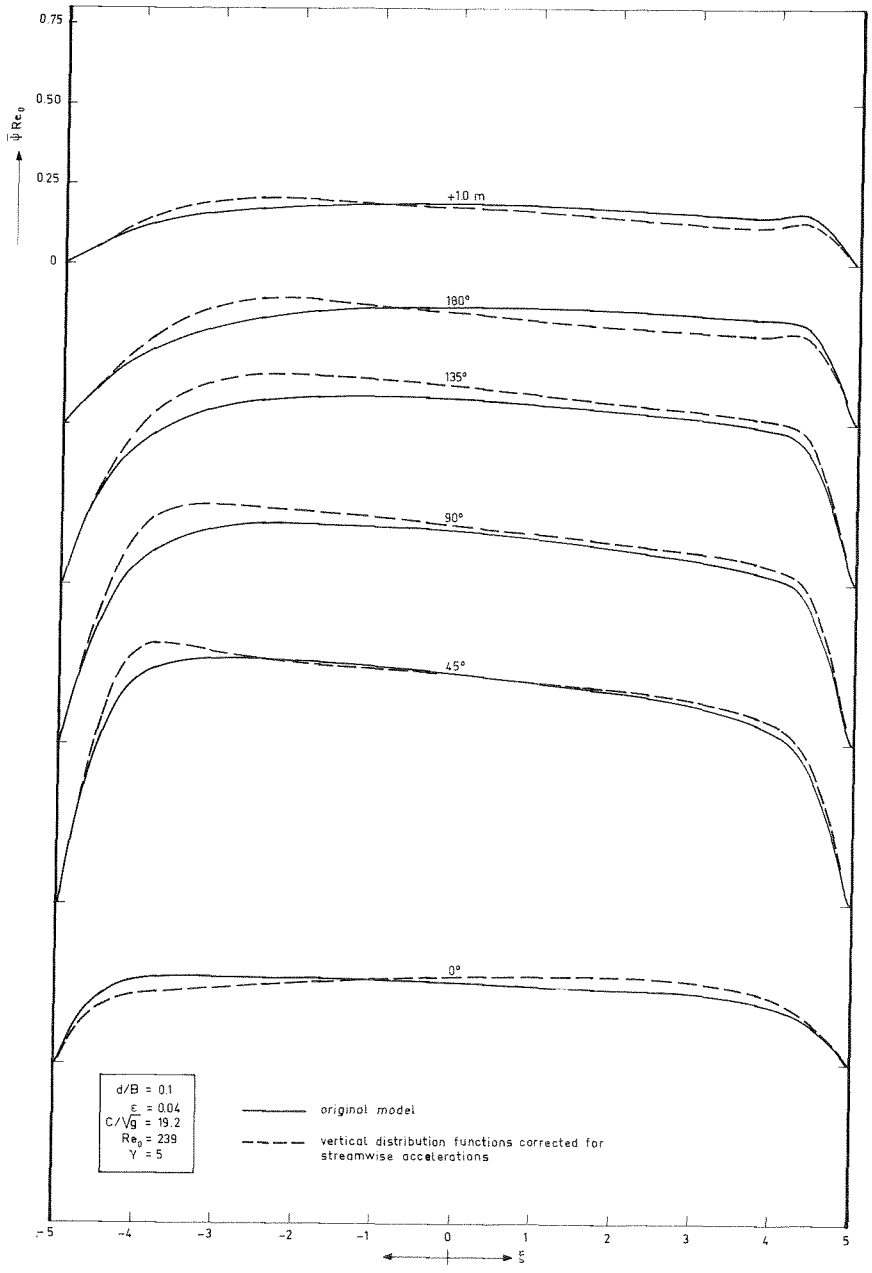

Figure 44. Influence of the streamwise accelerations of the main flow on the depth-averaged flow
(b) Secondary flow intensity

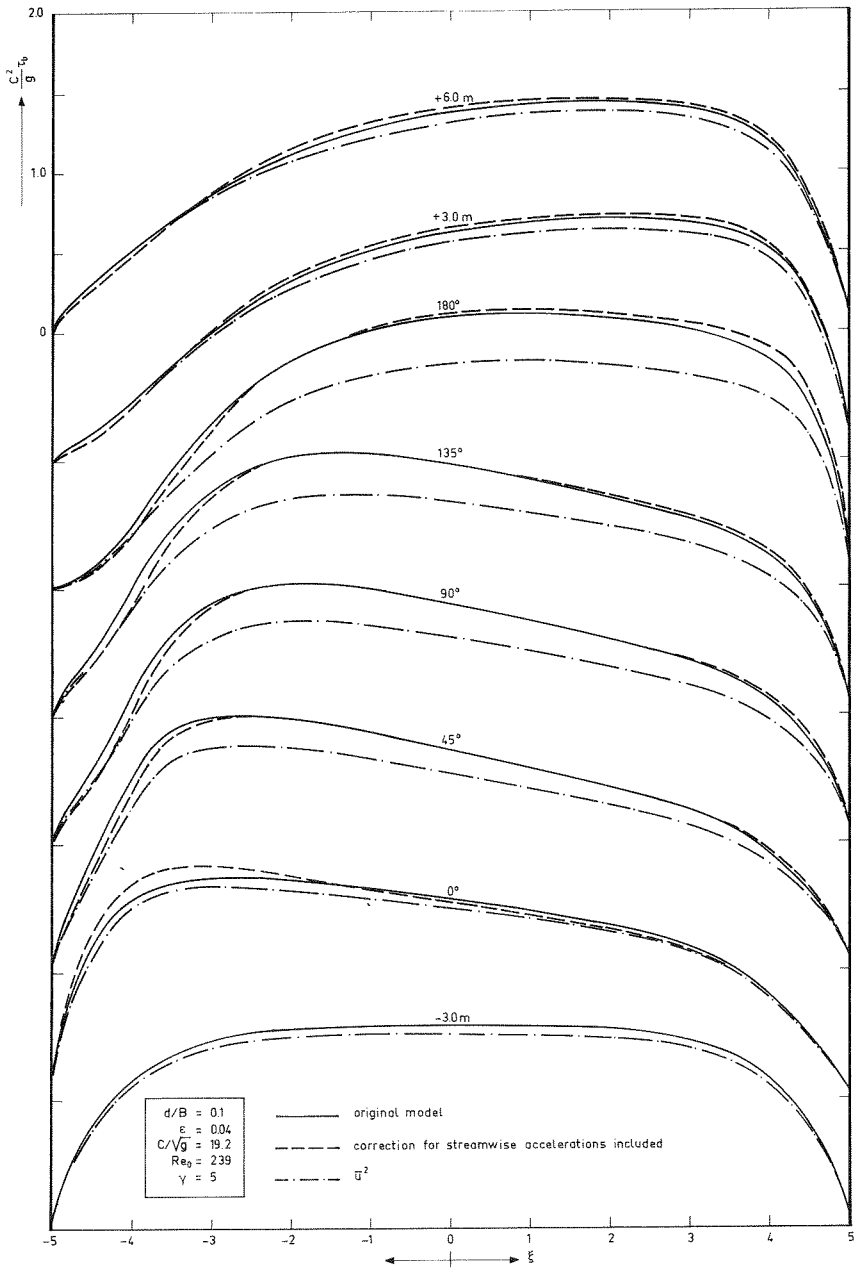

Figure 45. Influence of the streamwise accelerations of the main flow on the bottom shear stress

(a) Magnitude of the total bottom shear stress

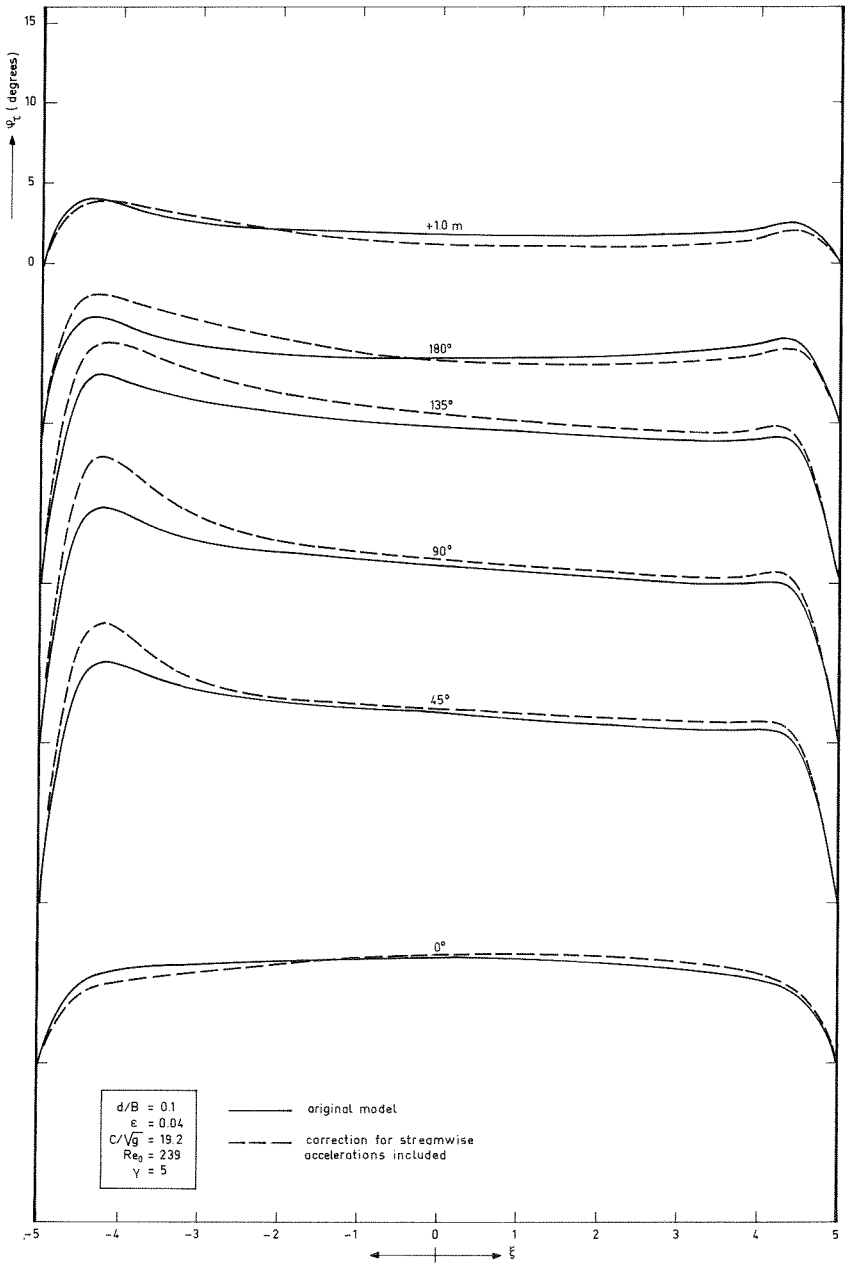

Figure 45. Influence of the streamwise accelerations of the main flow on the bottom shear stress
(b) Direction of the bottom shear stress

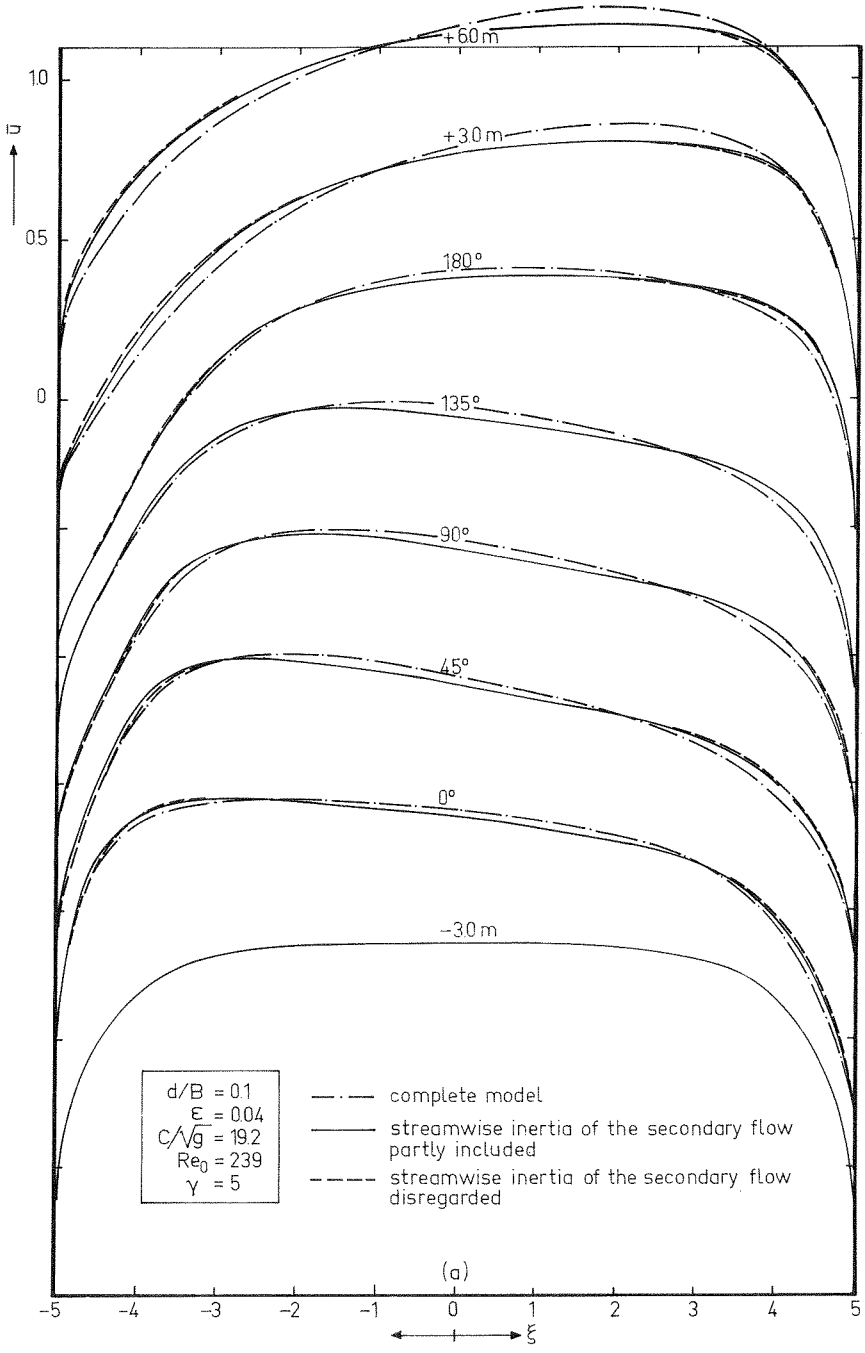

Figure 46. Influence of the streamwise inertia of the secondary flow
(a) Depth-averaged main velocity

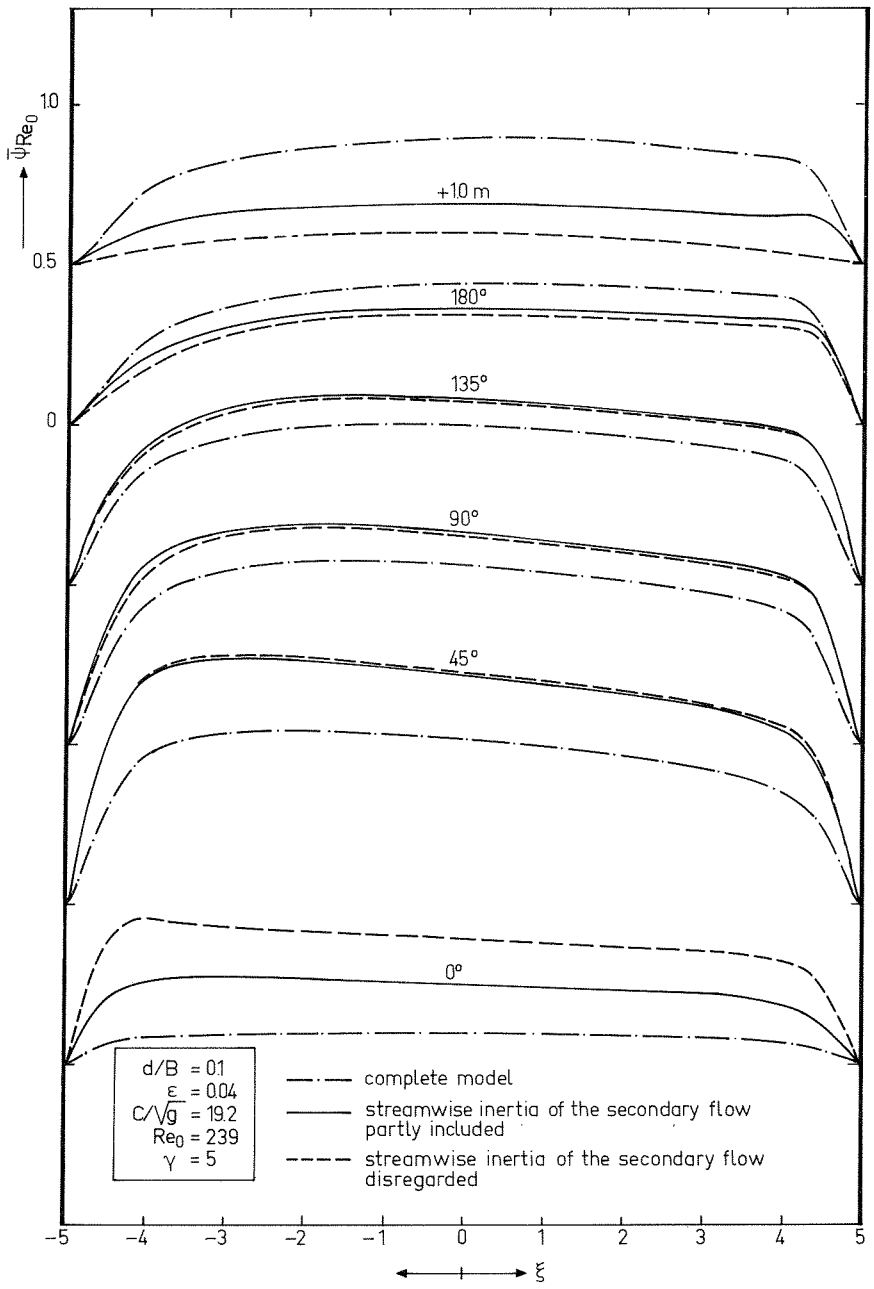

Figure 46. Influence of the streamwise inertia of the secondary flow

(b) Depth-averaged stream function of the secondary flow

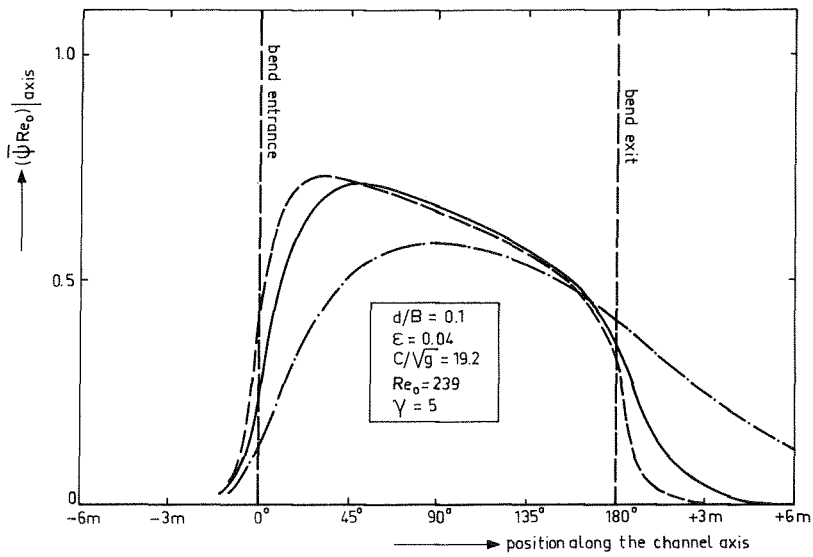

(c)

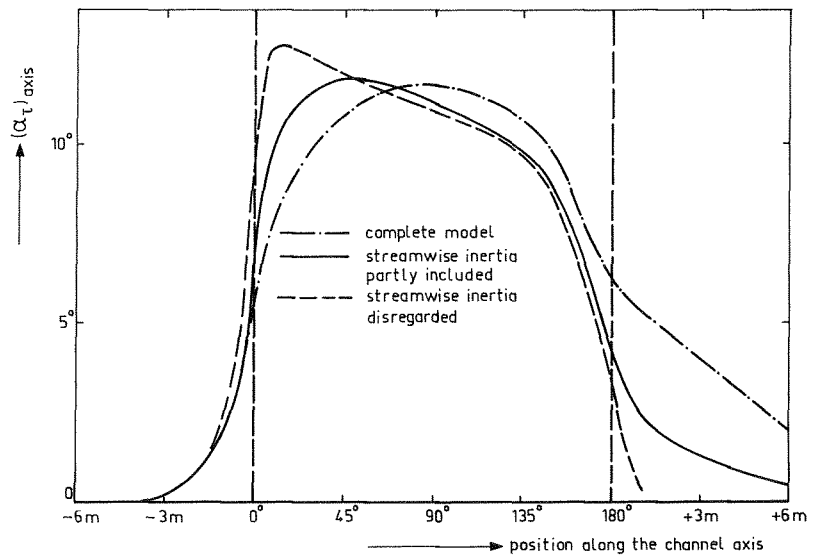

(d)

Figure 46. Influence of the streamwise inertia of the secondary flow
(c) Depth-averaged stream function in the axis
(d) Direction of the bottom shear stress in the axis

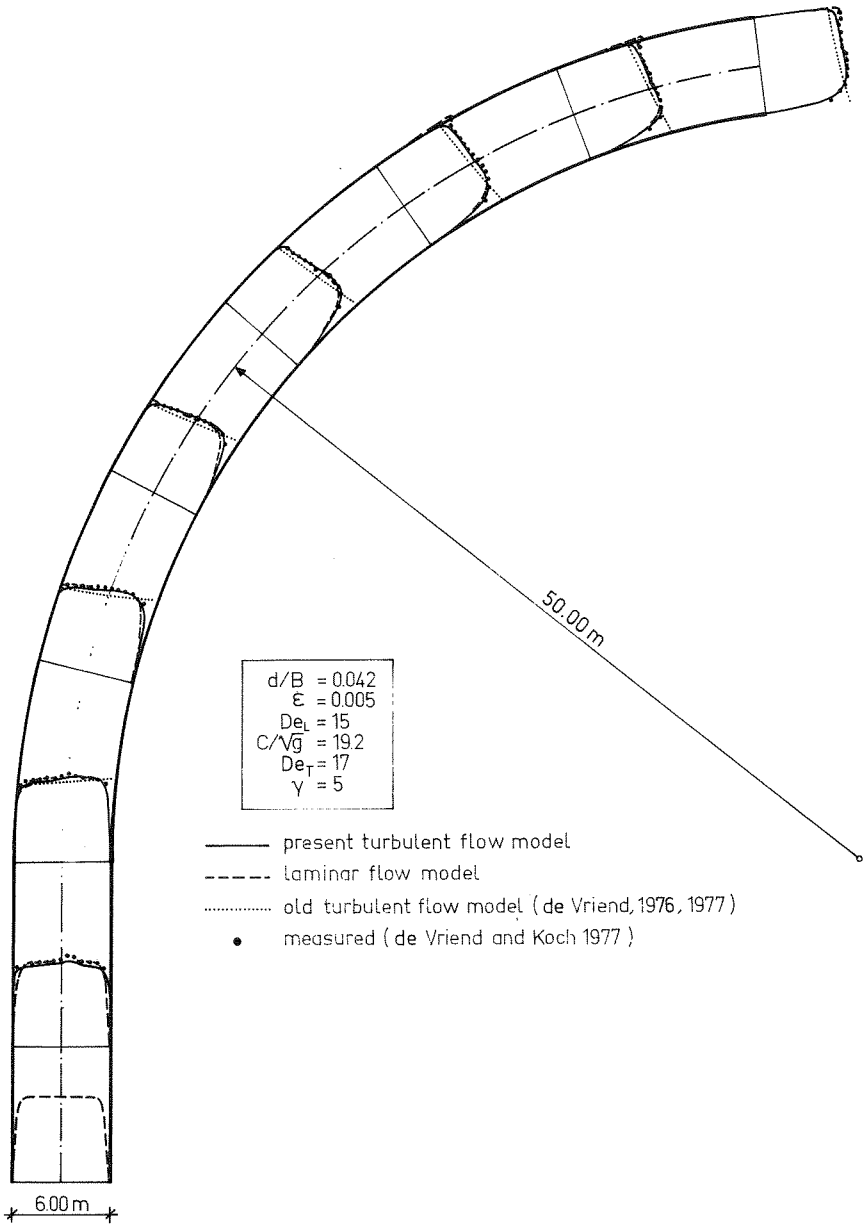

Figure 47. Preliminary comparison of the turbulent flow model with other models and measured data
(a) Depth-averaged main flow in the DHL-flume

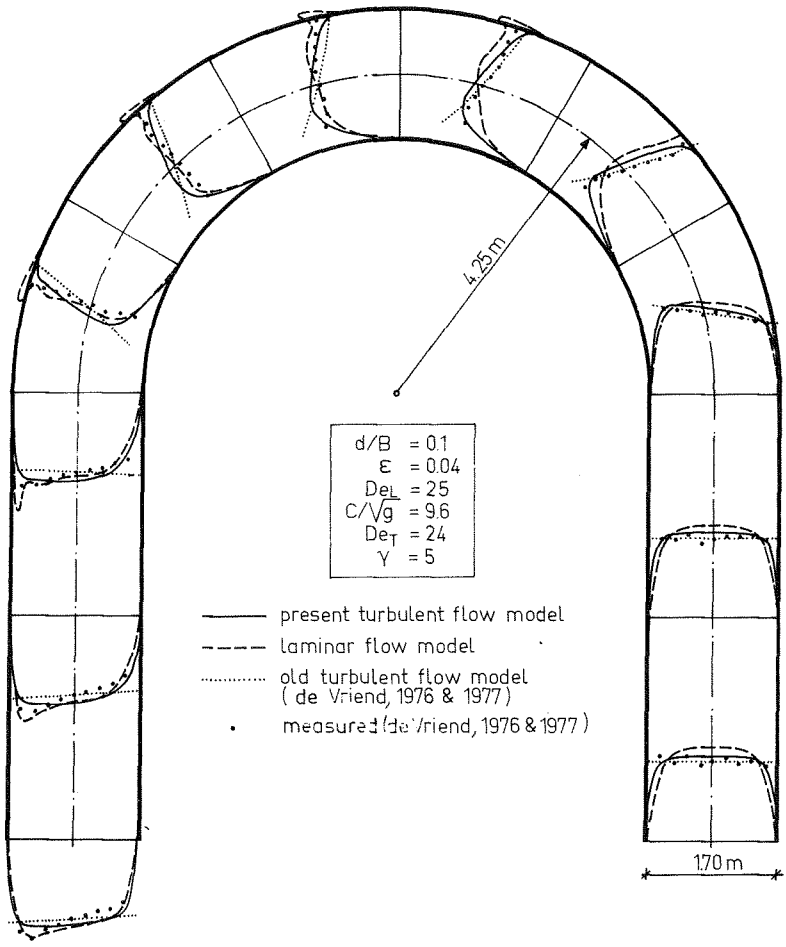

Figure 47. Preliminary comparison of the turbulent flow model with other models and measured data
(b) Depth-averaged main flow in the LFM-flume

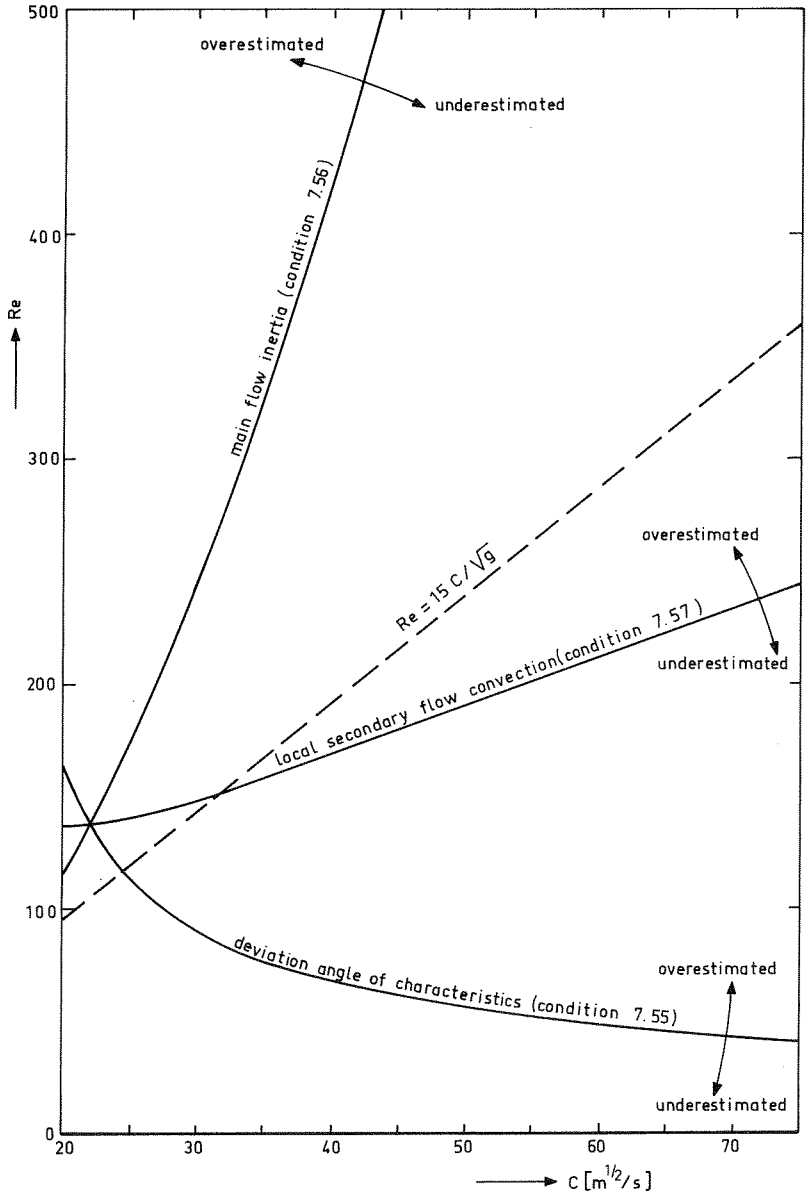

Figure 48. Simulation of turbulent flow by the laminar flow model

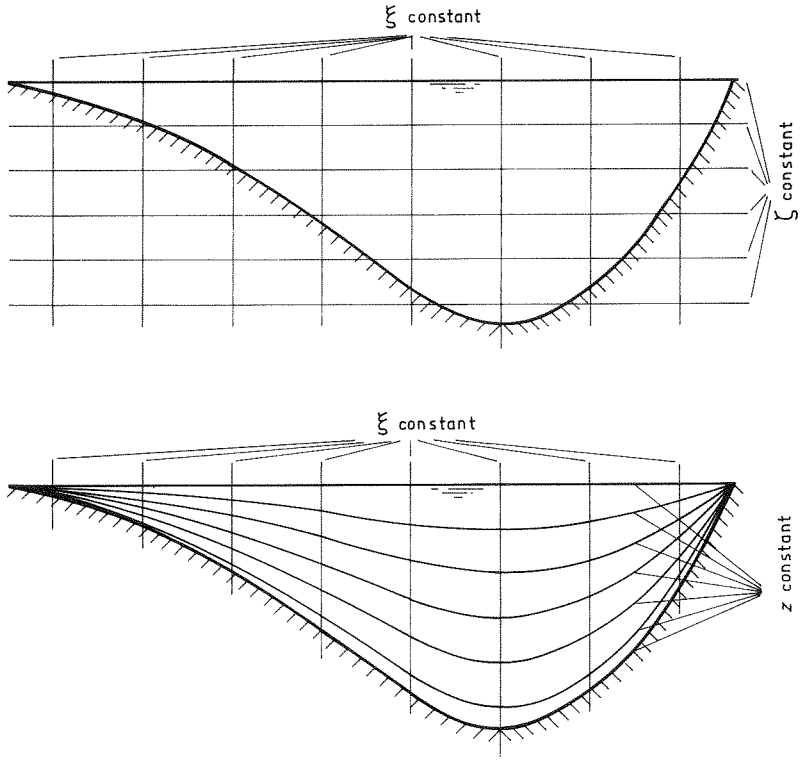

Figure 49. Transformation of the cross-section

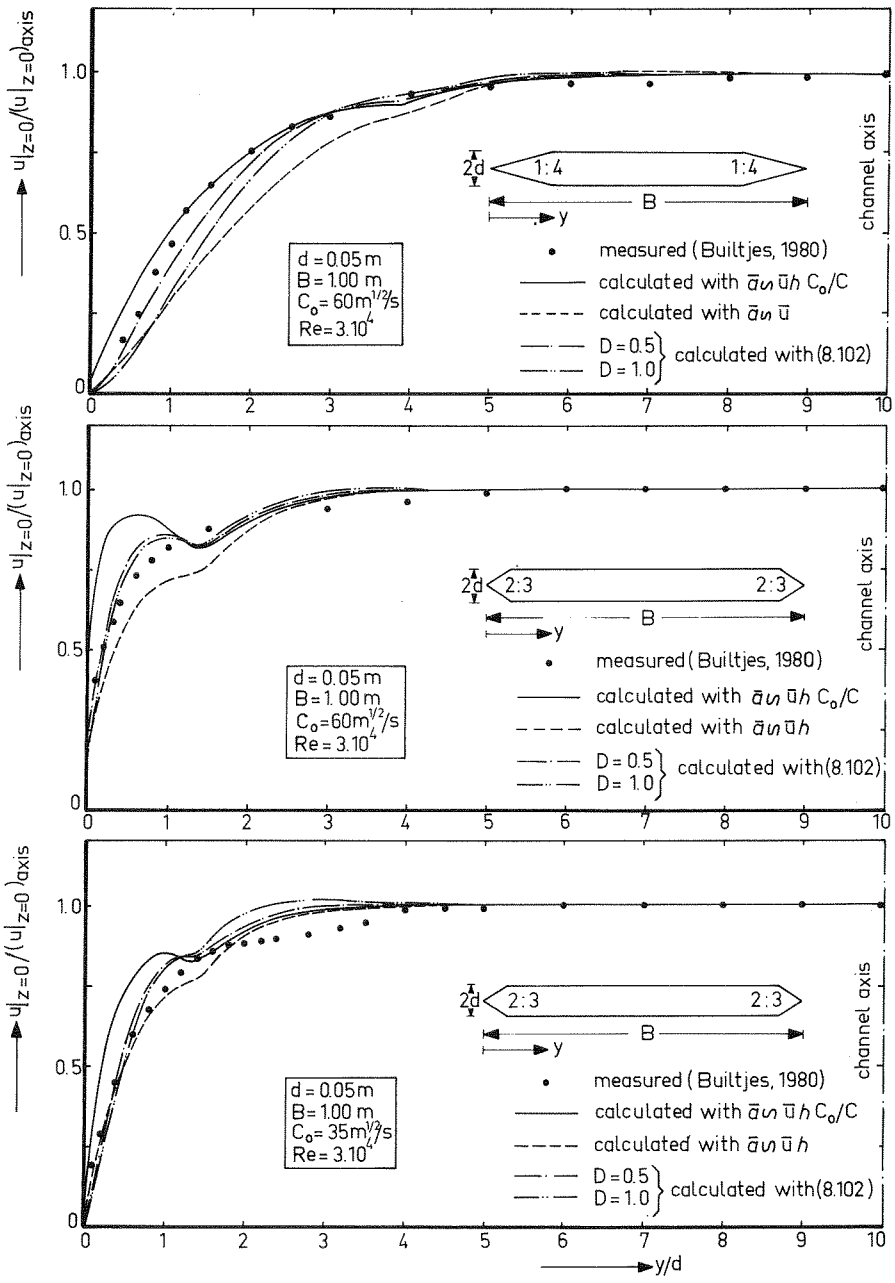

Figure 50. Fully-developed flow in straight non-rectangular channels

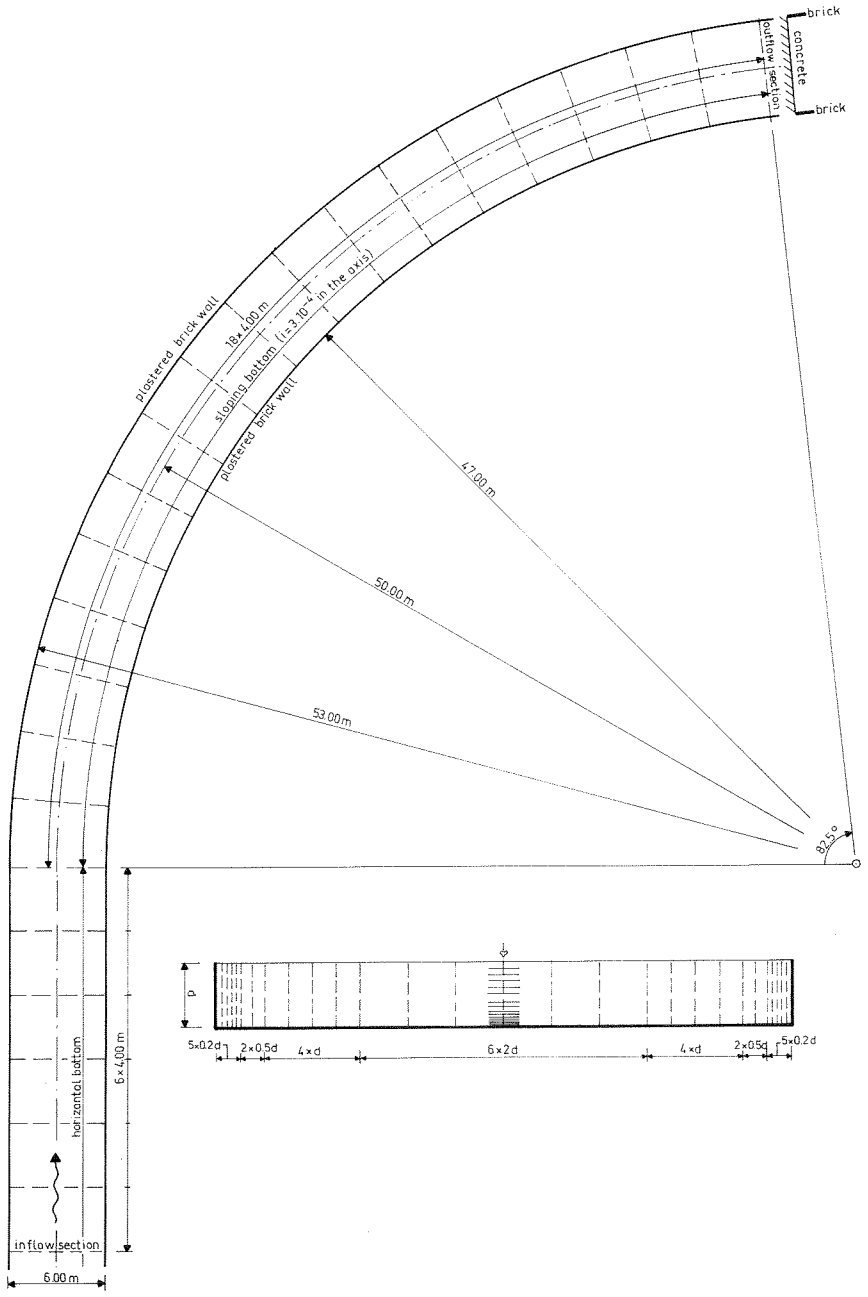

Figure 51. Simulation of the flat bed experiments in the DHL-flume: flume geometry and computational grid

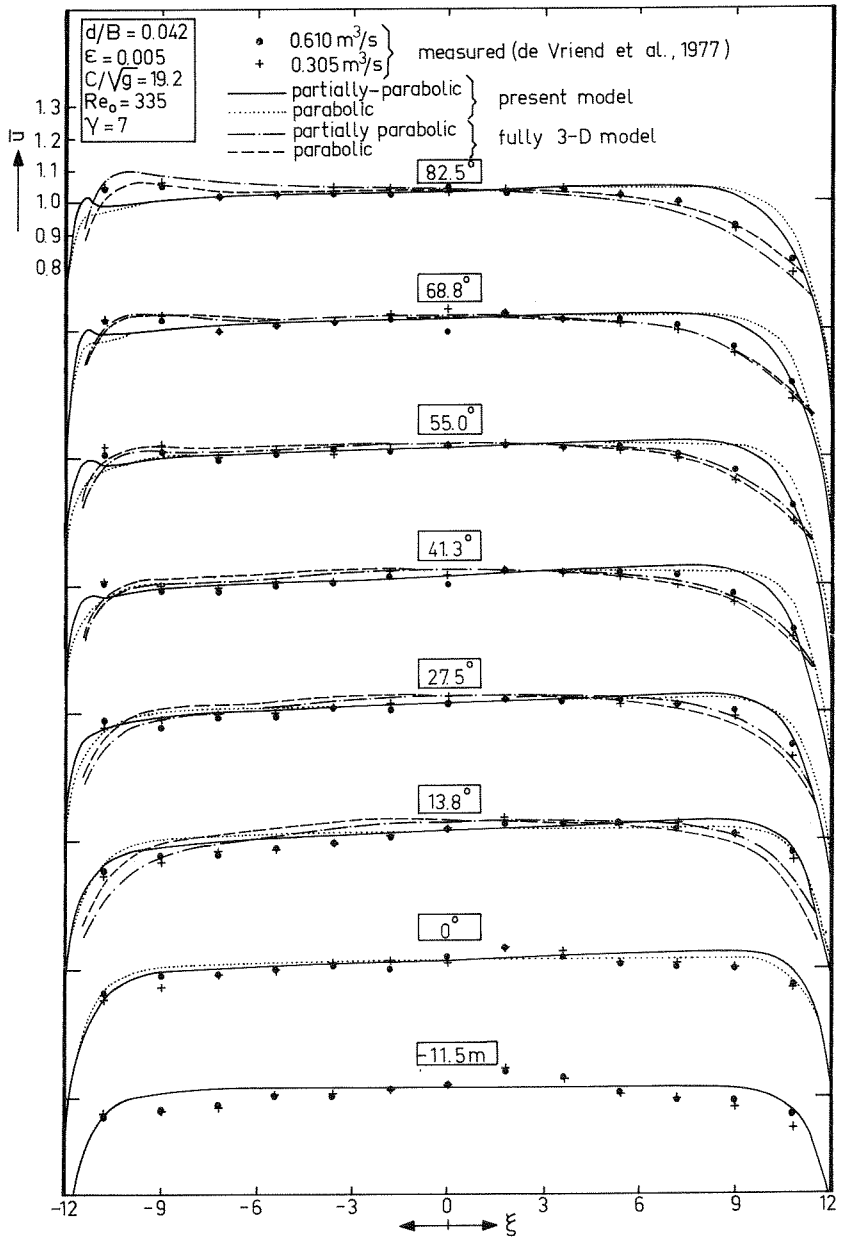

Figure 52. Simulation of the flat bed experiments in the DHL-flume: main velocity

(a) Depth-averaged main velocity

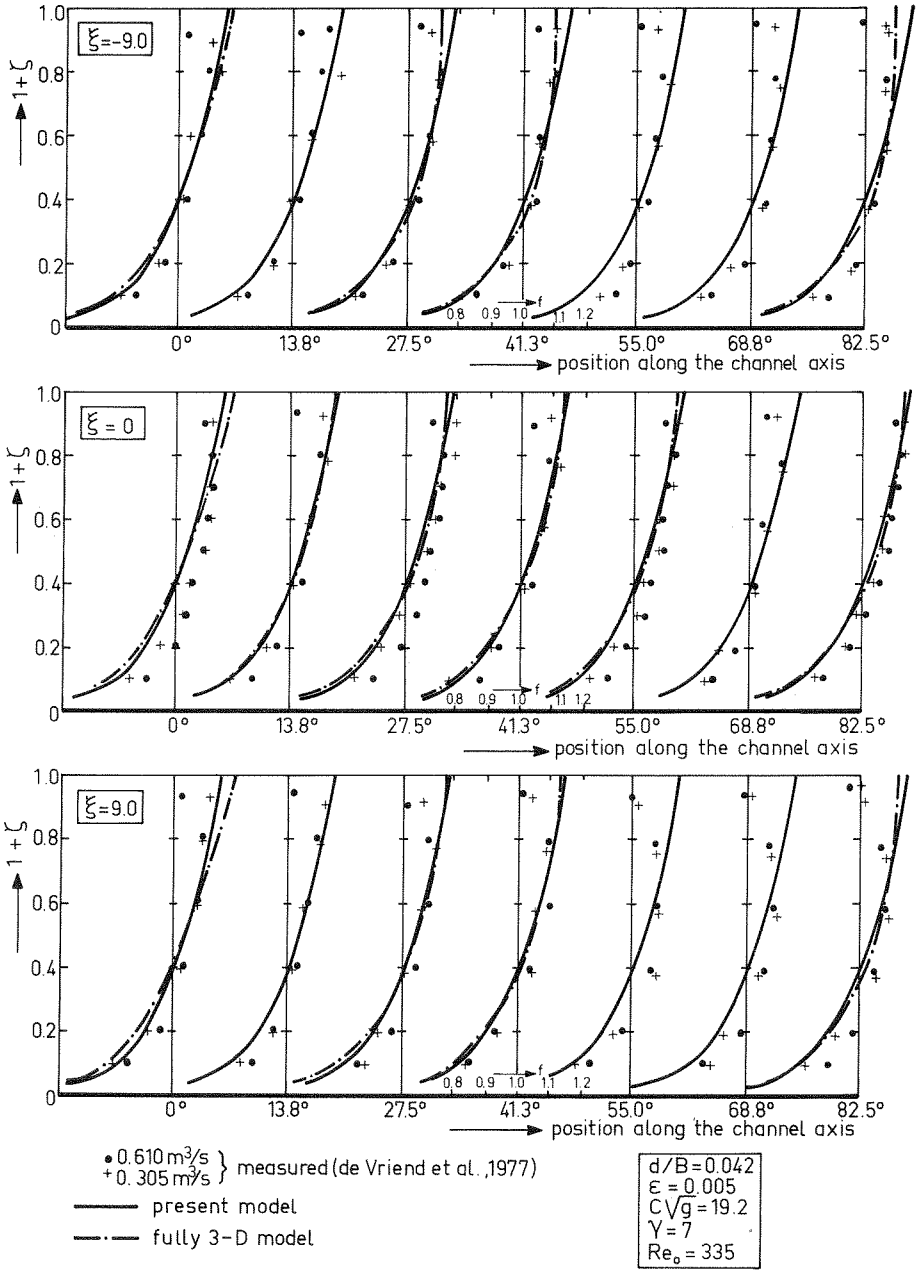

Figure 52. Simulation of the flat bed experiments in the DHL-flume:
main velocity
(b) Vertical distribution of the main velocity

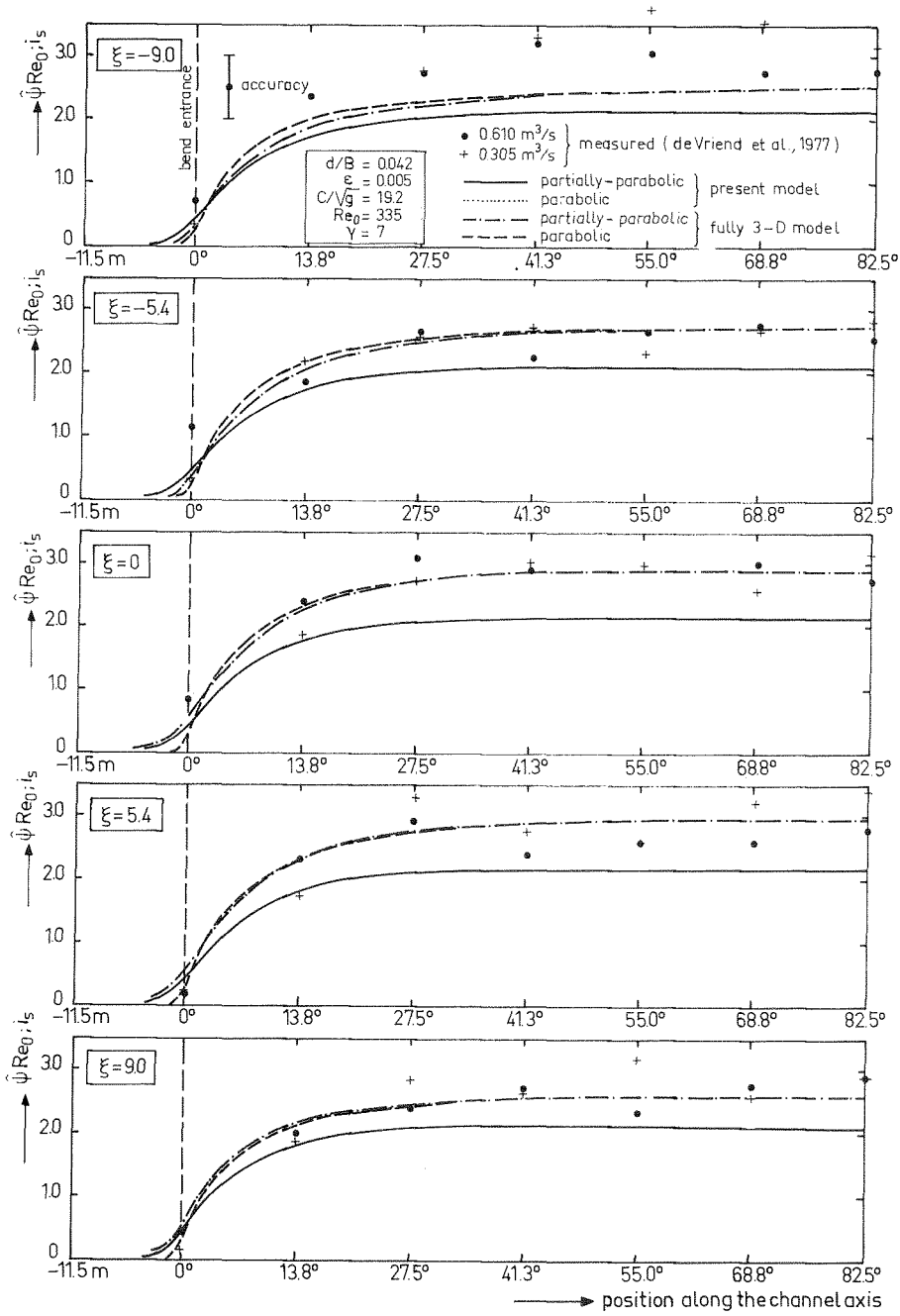

Figure 53. Simulation of the flat bed experiments in the DHL-flume: secondary flow

(a) Secondary flow intensity in longitudinal sections

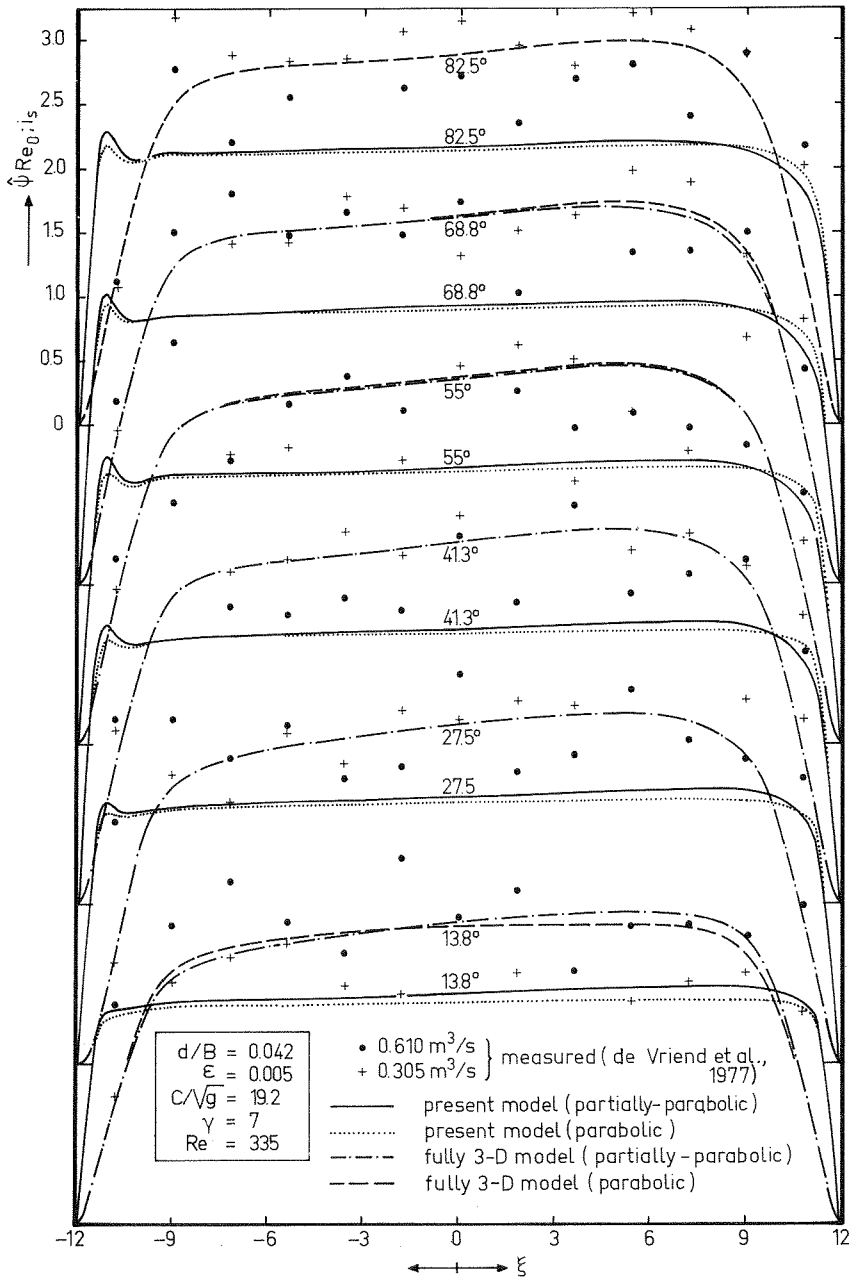

Figure 53. Simulation of the flat bed experiments in the DHL-flume: secondary flow

(b) Secondary flow intensity in cross-sections

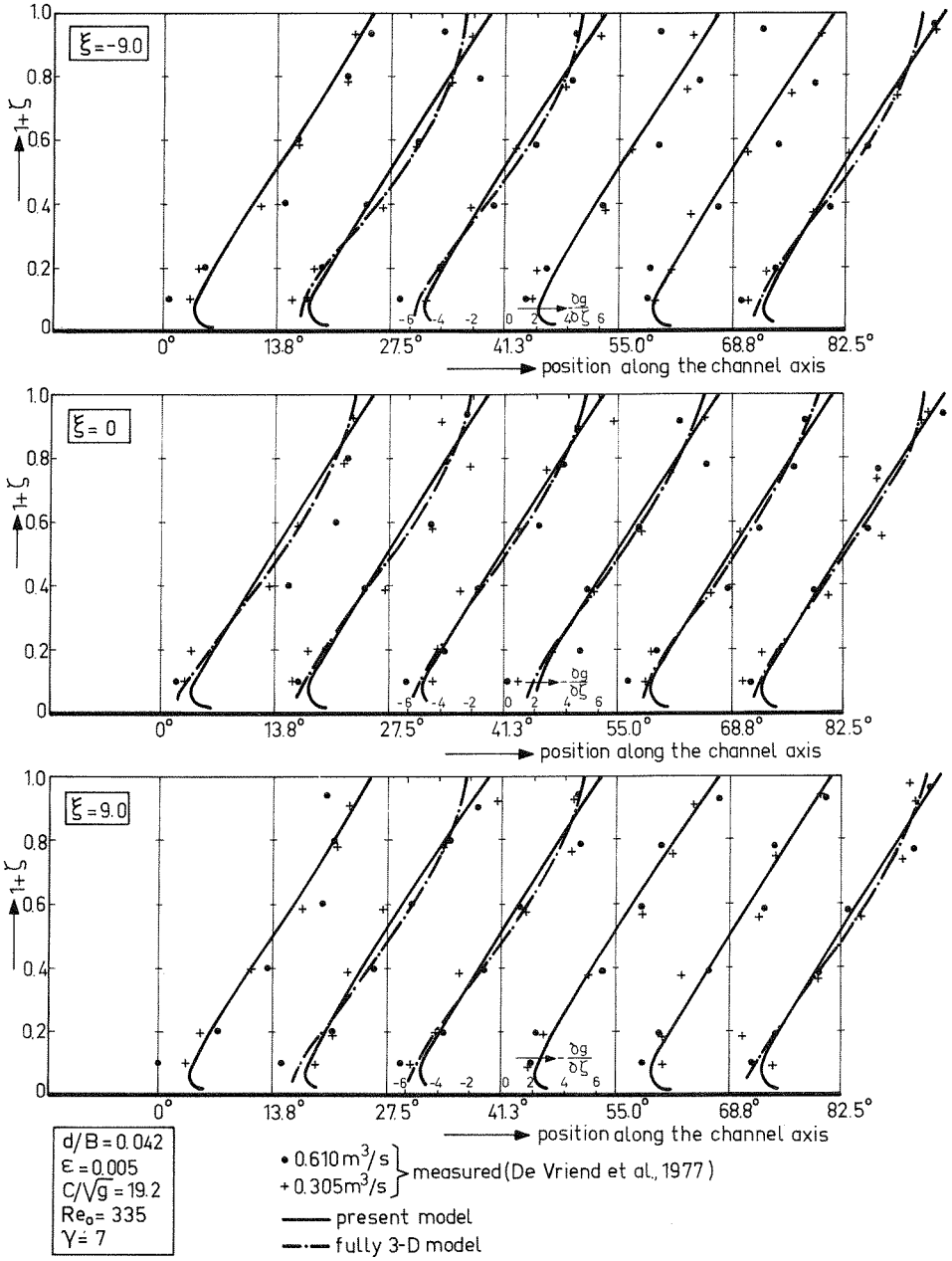

Figure 53. Simulation of the flat bed experiments in the DHL-flume: secondary flow

(c) Vertical distribution of the horizontal component

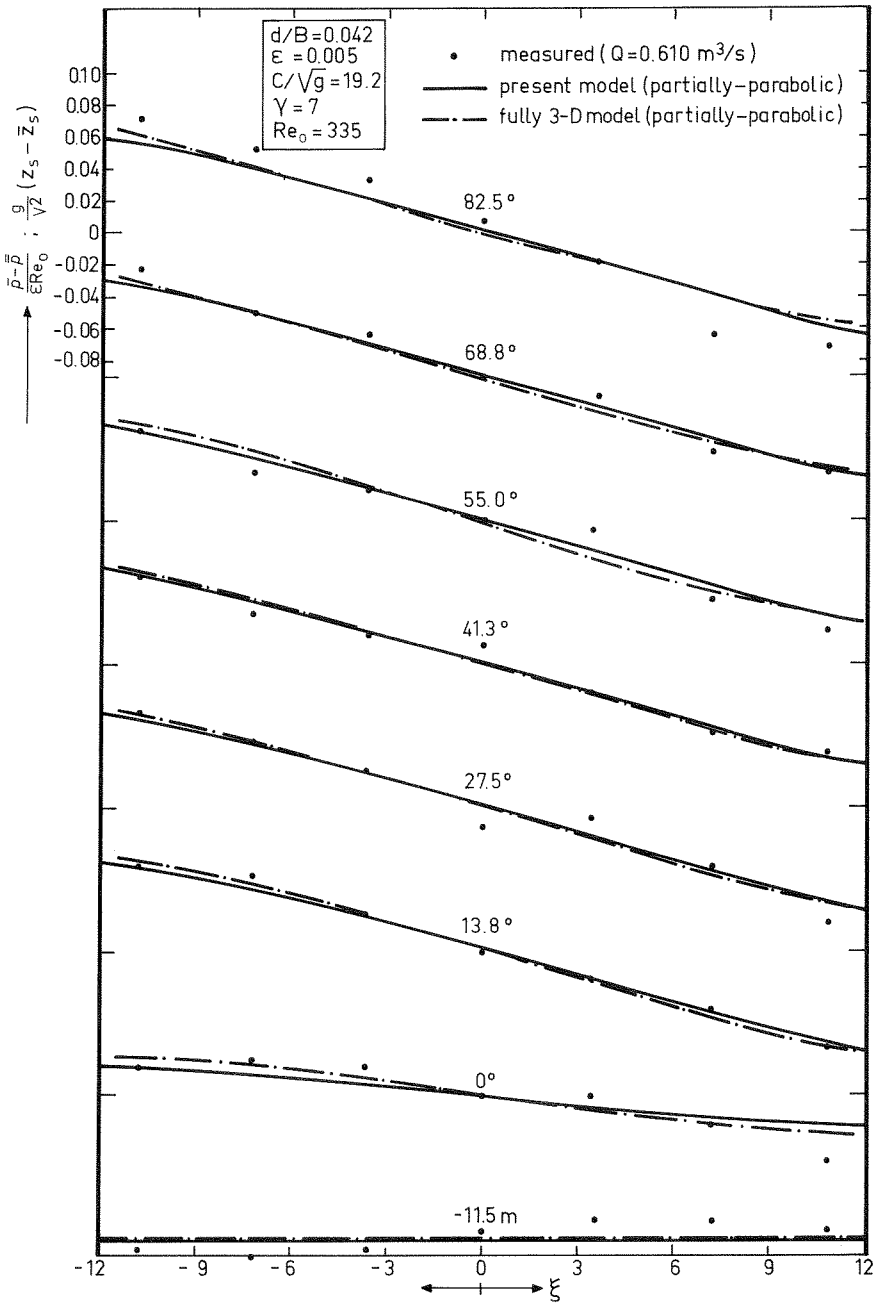

Figure 54. Simulation of the flat bed experiments in the DHL-flume: total pressure

(a) Transverse distribution

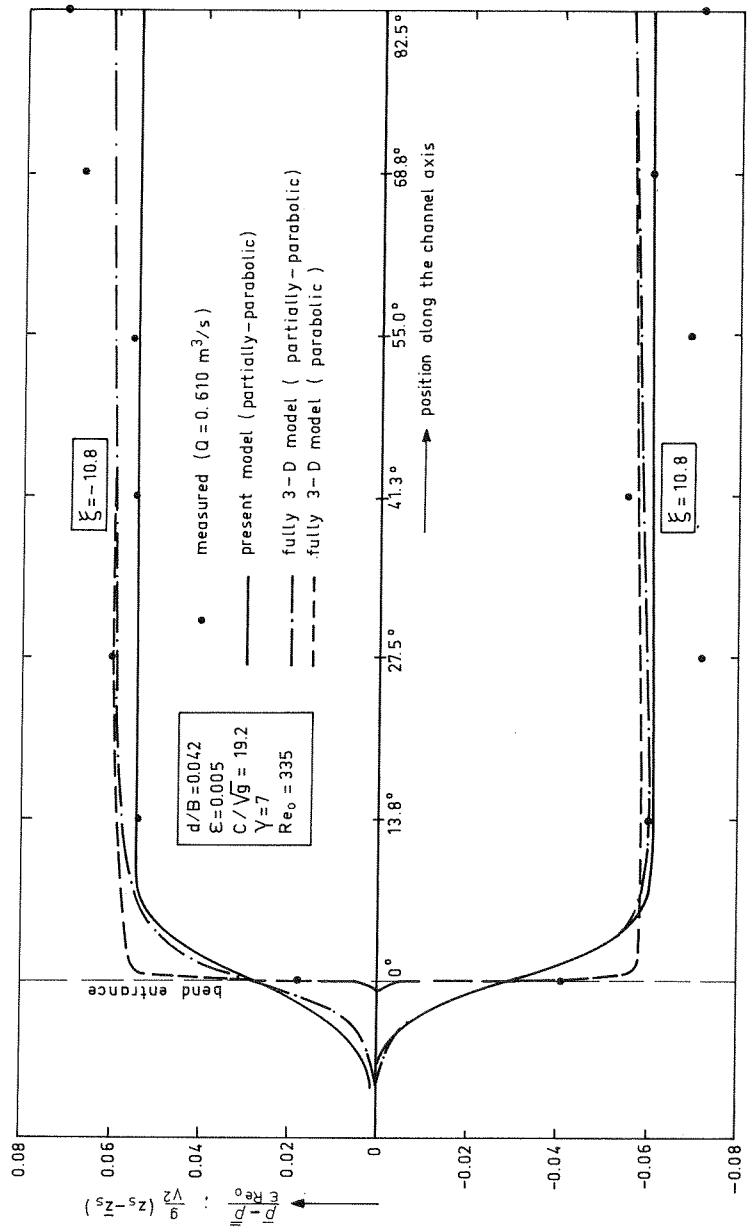

Figure 54. Simulation of the flat bed experiments in the DHL-flume:
total pressure
(b) Transverse pressure drop

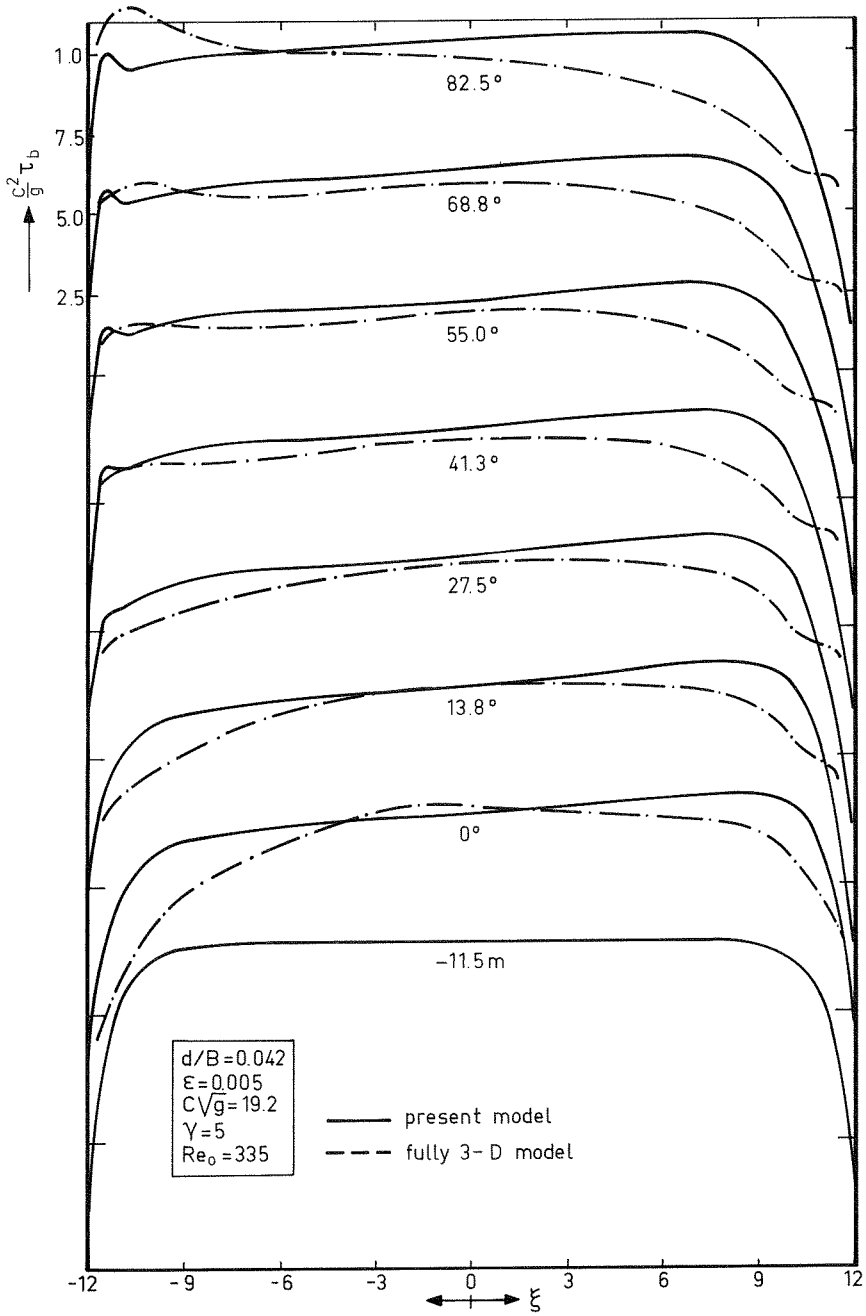

Figure 55. Simulation of the flat bed experiments in the DHL-flume: bottom shear stress

(a) Transverse distribution of the total bottom shear stress

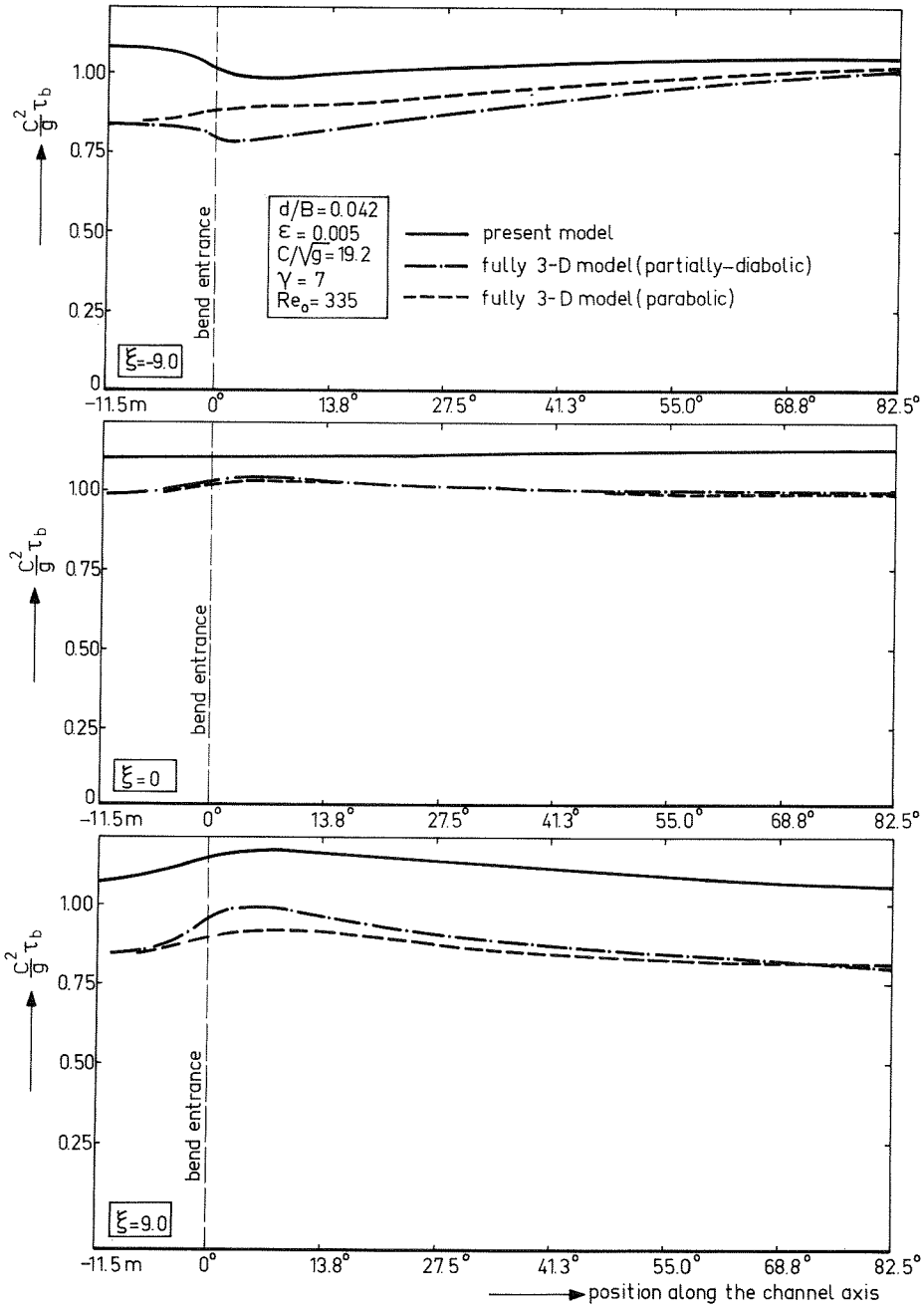

Figure 55. Simulation of the flat bed experiments in the DHL-flume: bottom shear stress

(b) Longitudinal distribution of the total bottom shear stress

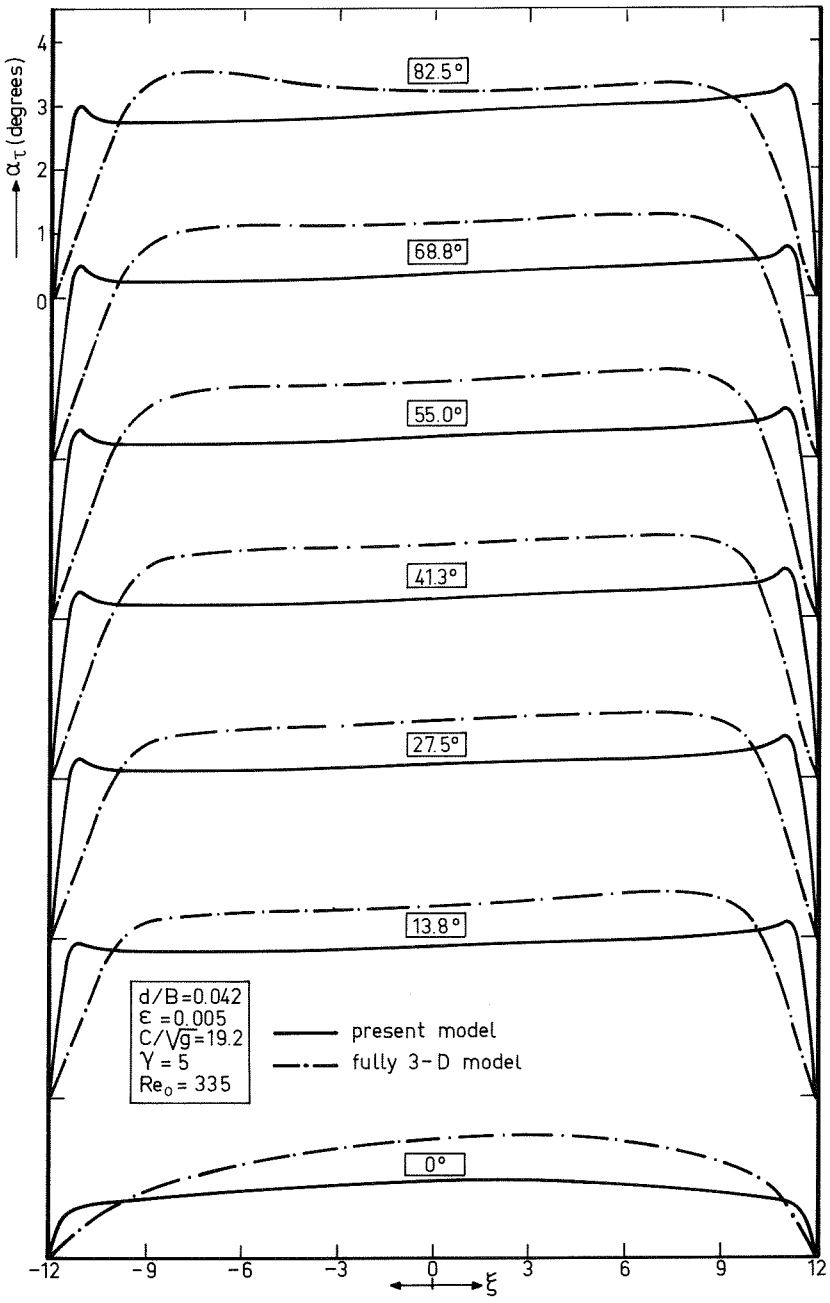

Figure 55. Simulation of the flat bed experiments in the DHL-flume: bottom shear stress

(c) Transverse distribution of the deviation angle

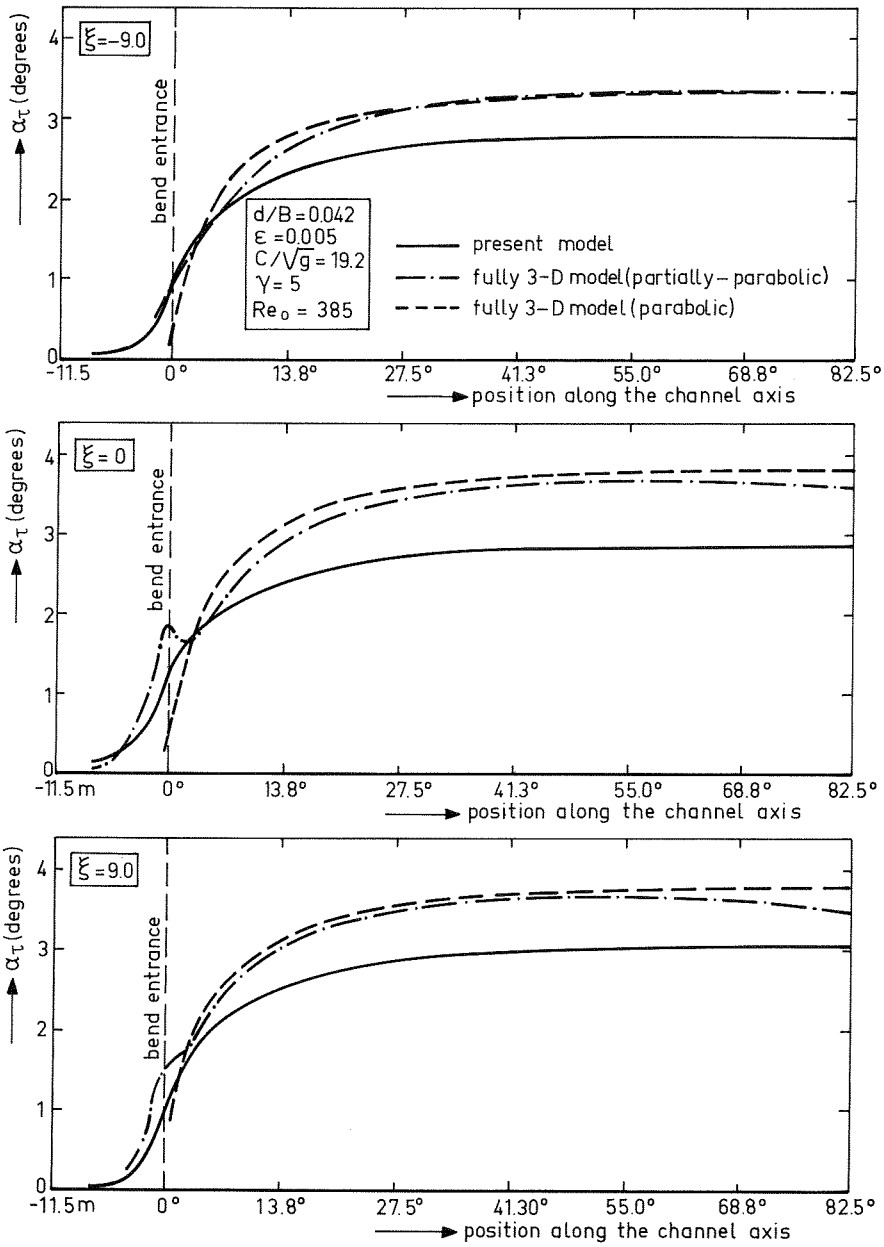

Figure 55. Simulation of the flat bed experiments in the DHL-flume: bottom shear stress

(d) Longitudinal distribution of the deviation angle

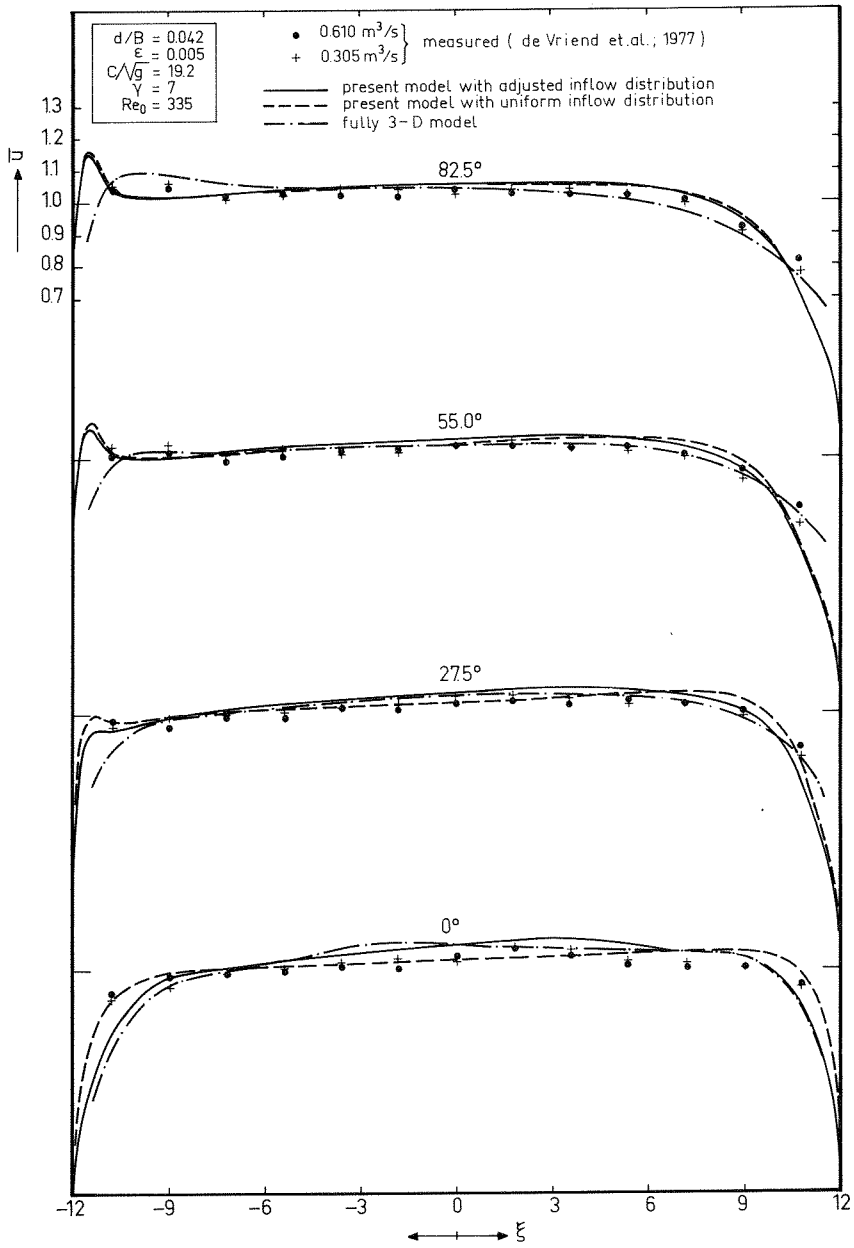

Figure 56. Influence of the inflow distribution in the DHL-flume

(a) Depth-averaged main velocity

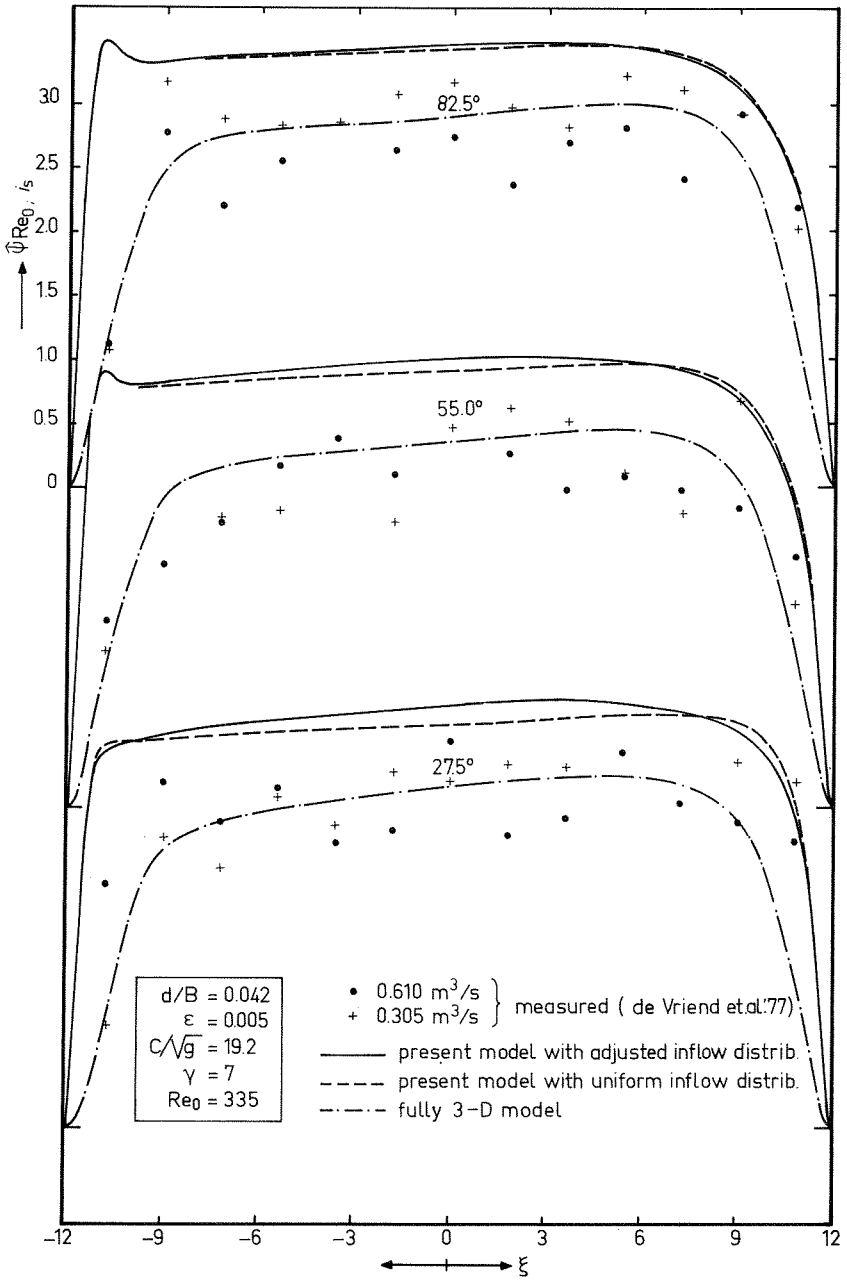

Figure 56. Influence of the inflow distribution in the DHL-flume
(b) Secondary flow intensity

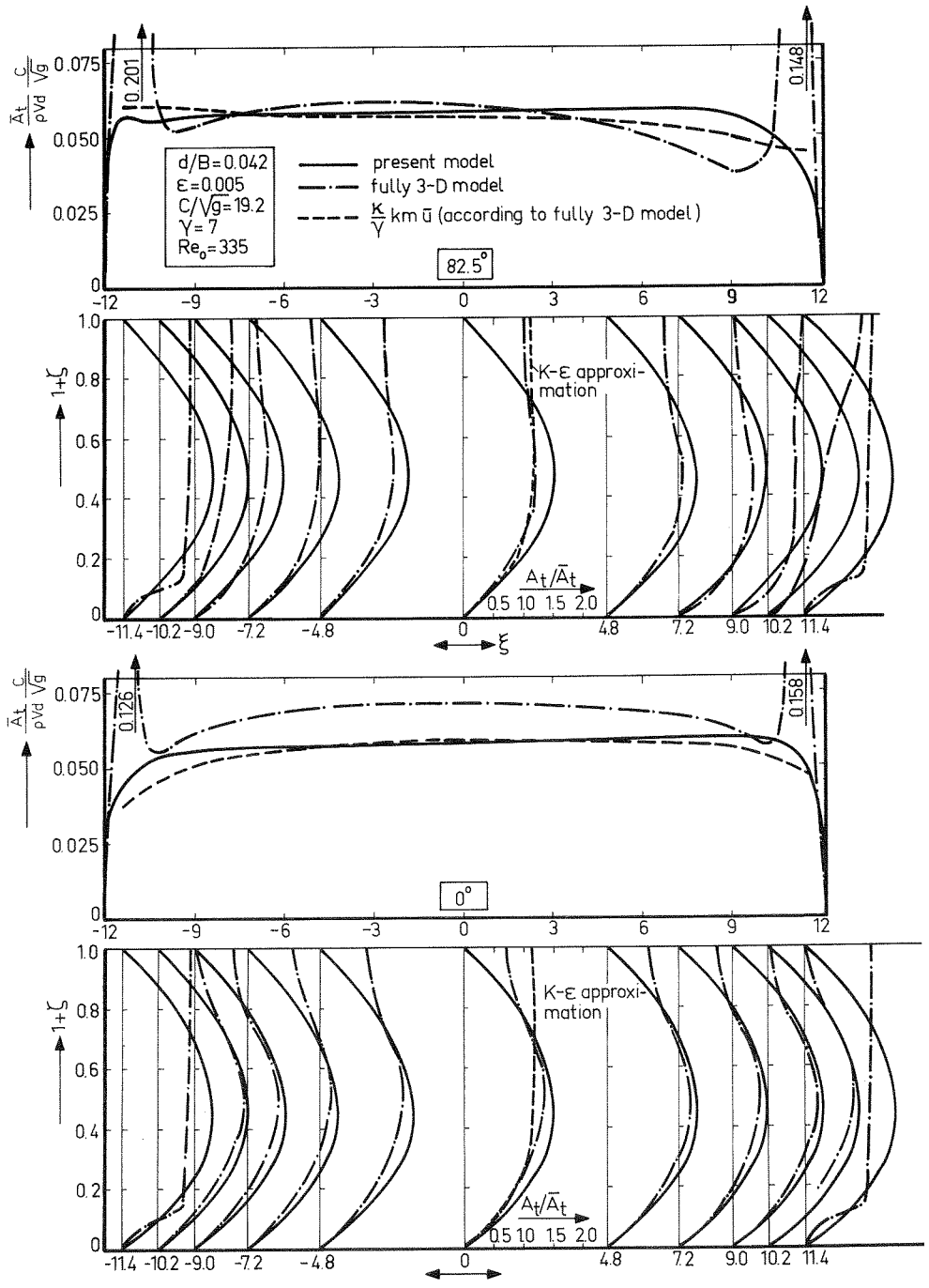

Figure 57. Analysis of the shortcomings of the model for the DHL-flume

(a) Turbulence viscosity

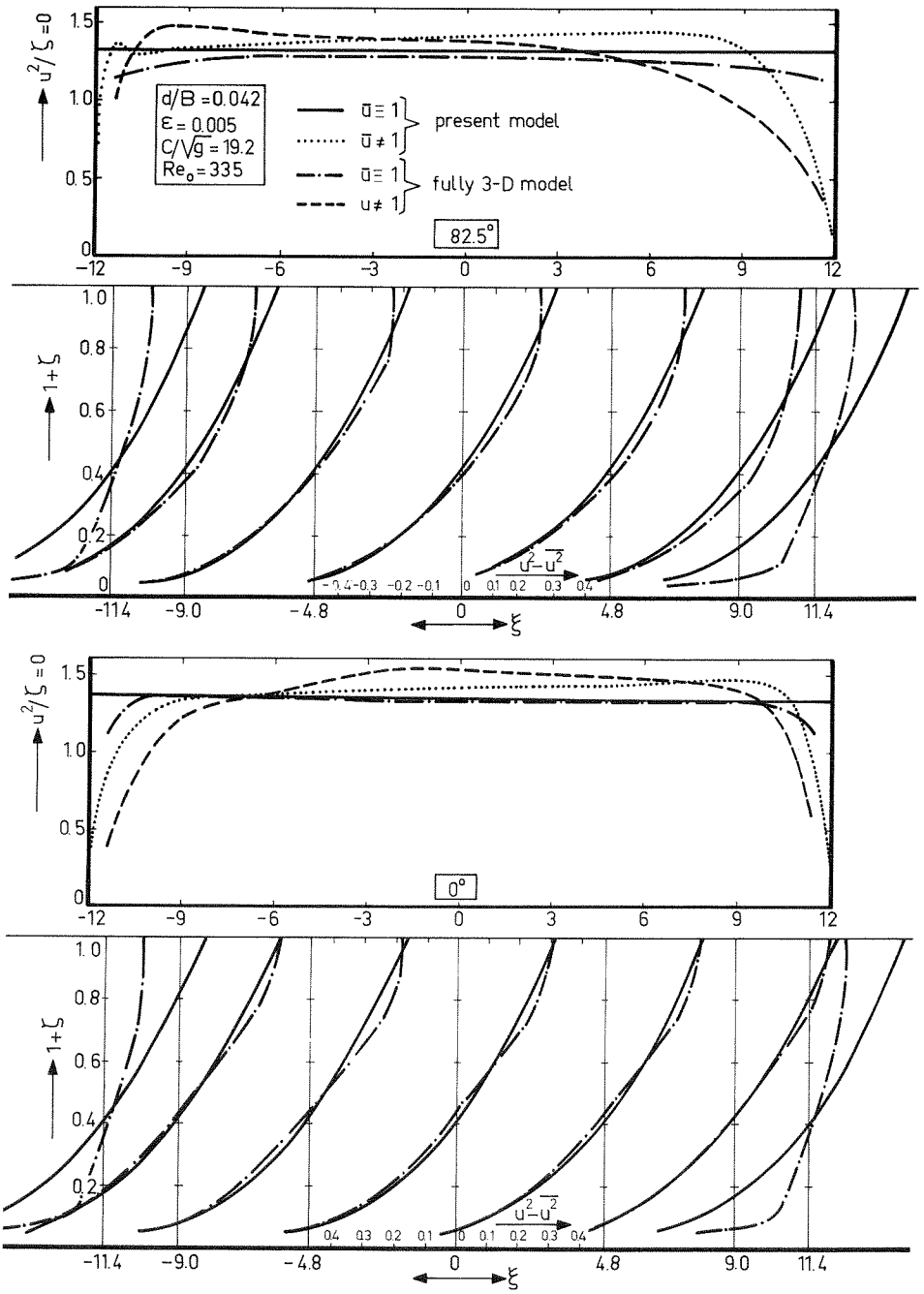

Figure 57. Analysis of the shortcomings of the model for the DHL-flume
(b) Source of secondary flow

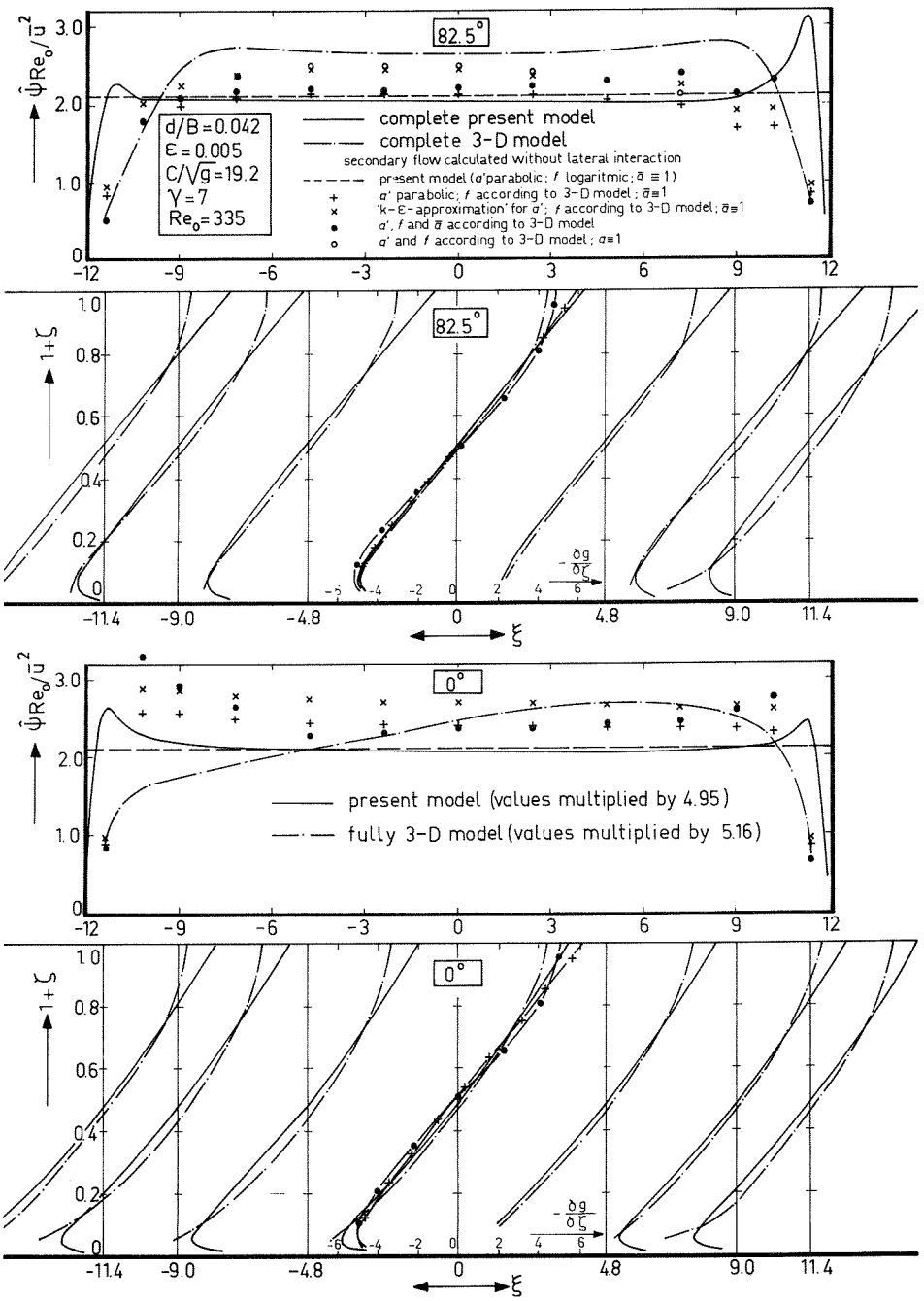

Figure 57. Analysis of the shortcomings of the model for the DHL-flume
(c) Secondary flow predictions

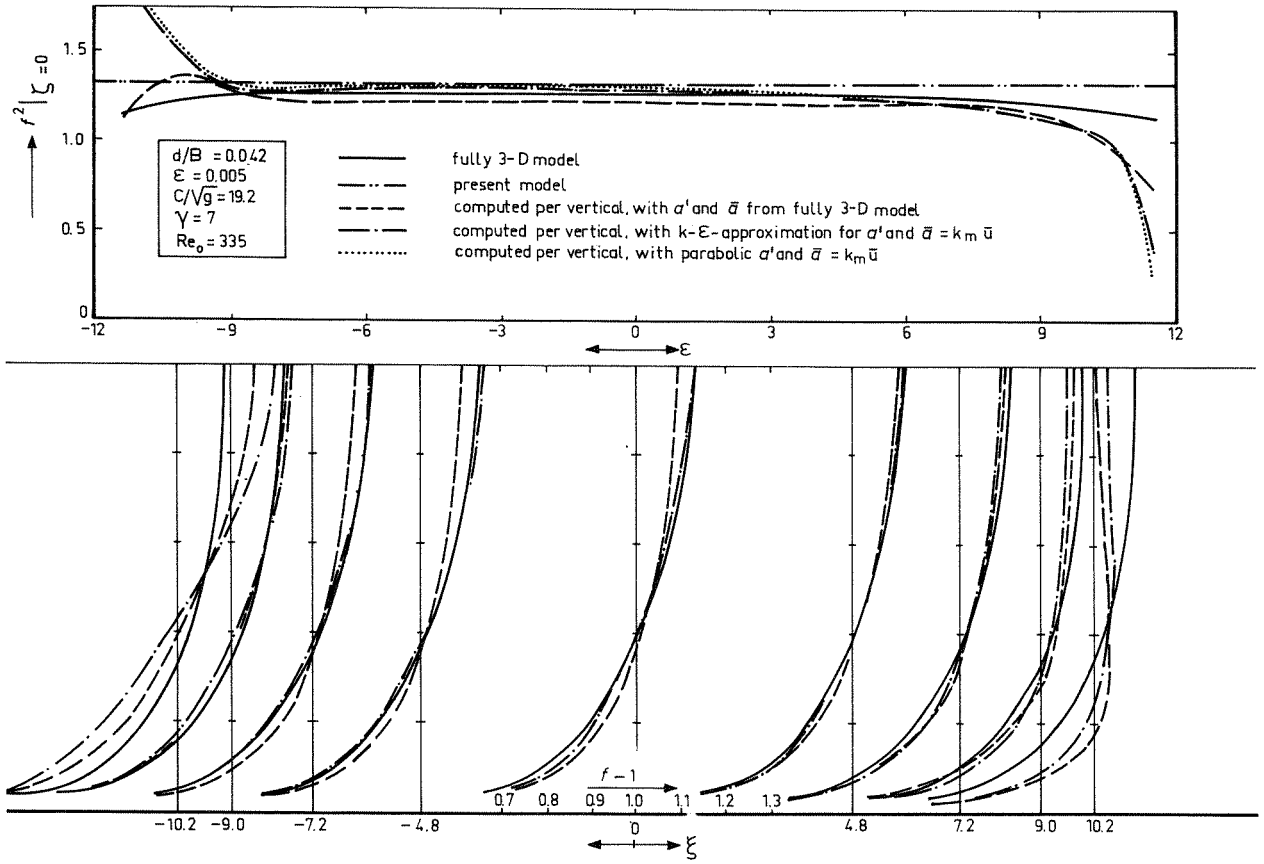

Figure 57, Analysis of the shortcomings of the model for the DHL-flume
(d) Main velocity profile calculated in separate verticals

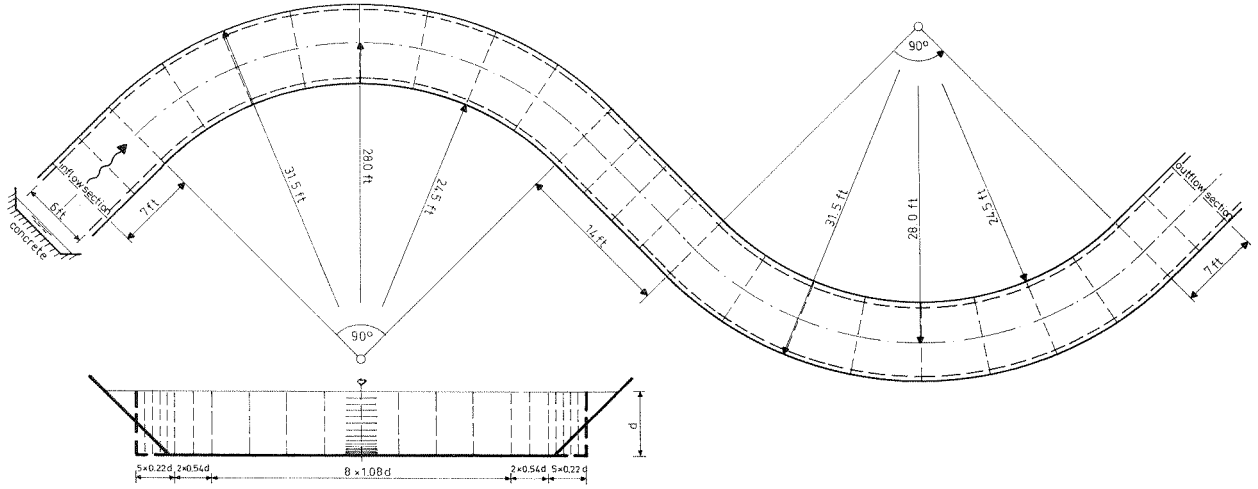

Figure 58. Simulation of one of the flat bed experiments in the IIHR-flume: flume geometry and computational grid

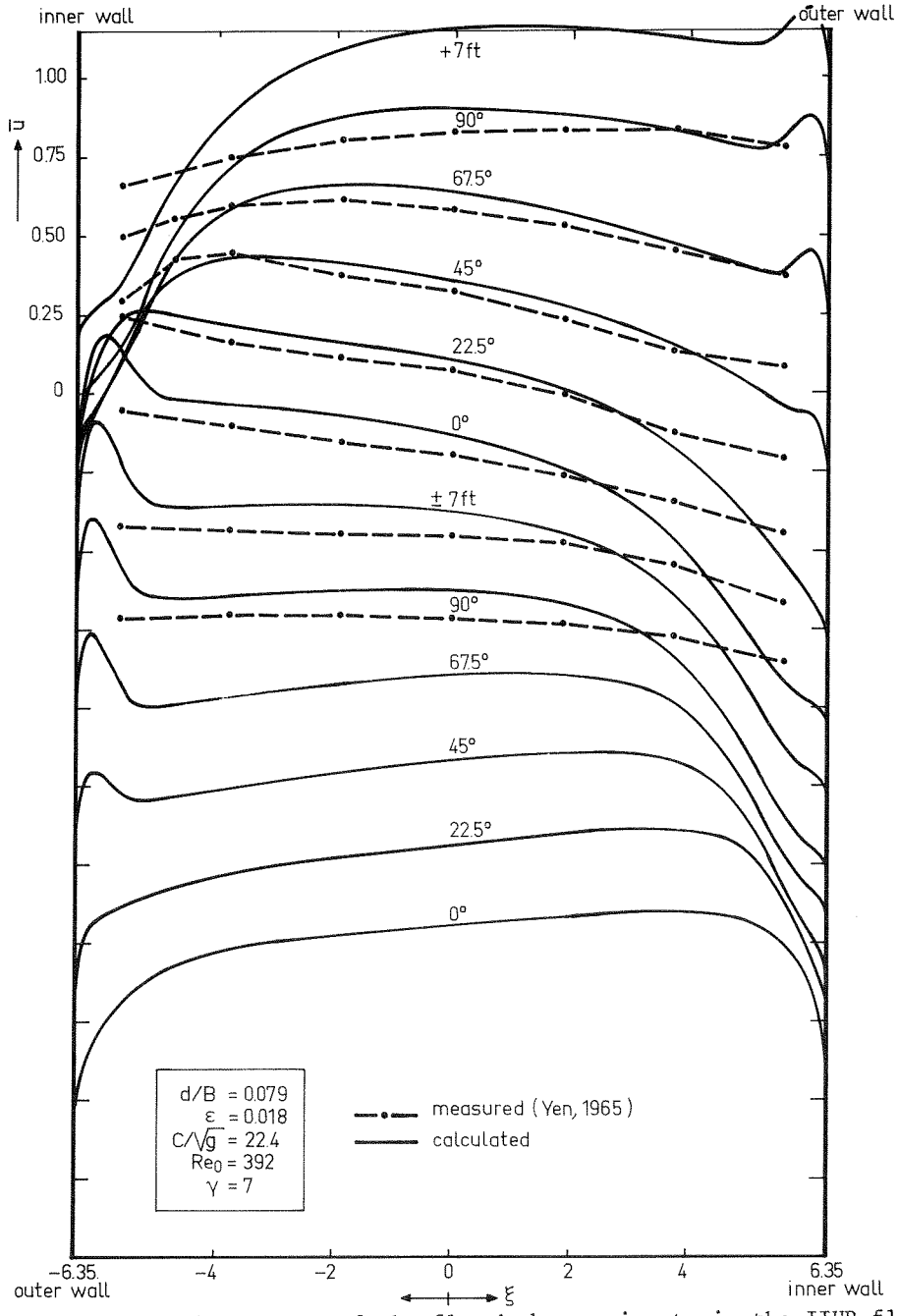

Figure 59. Simulation of one of the flat bed experiments in the IIHR-flume: main velocity

(a) Depth-averaged main velocity

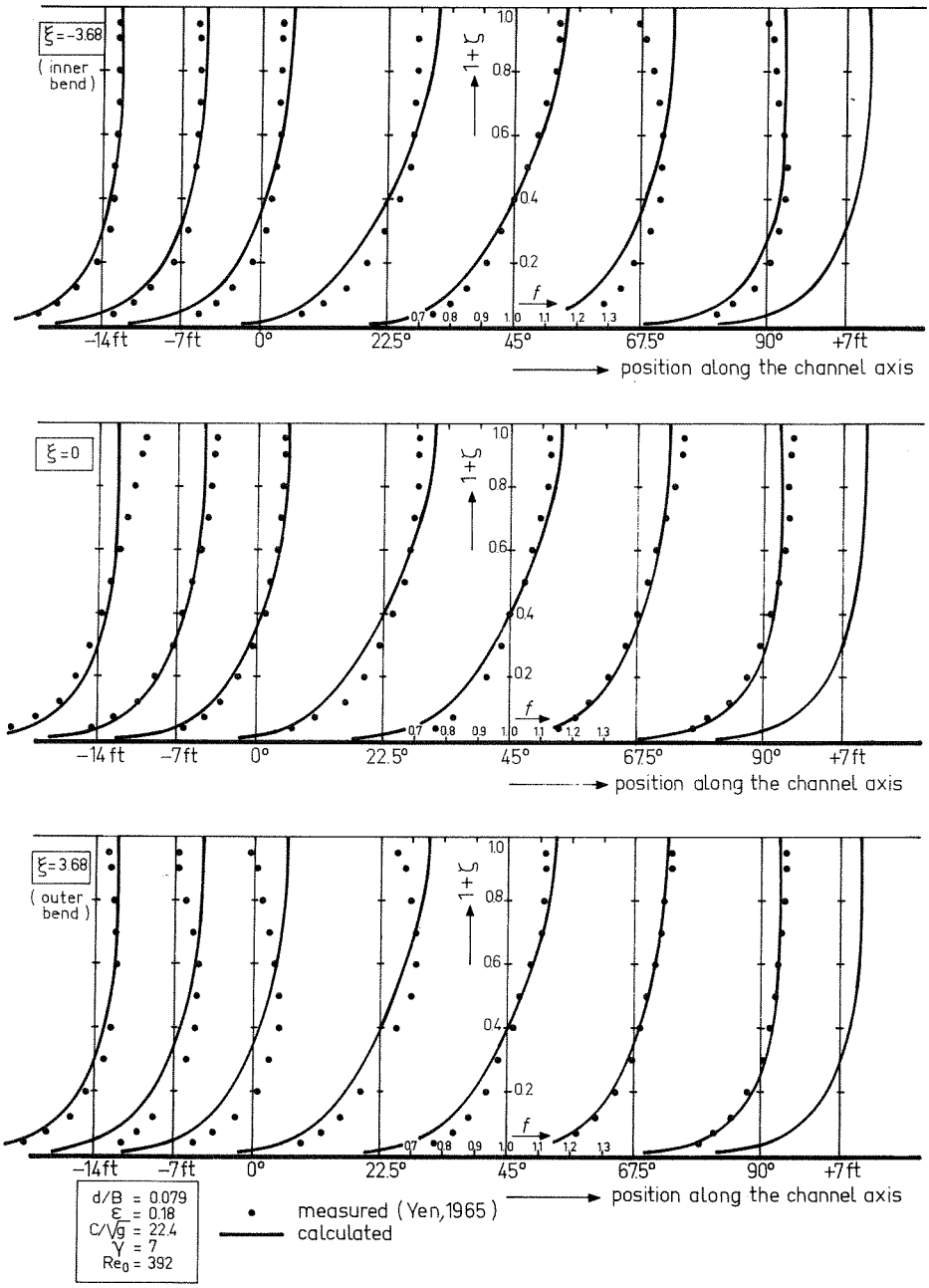

Figure 59. Simulation of one of the flat bed experiments in the IIHR-flume: main velocity

(b) Vertical distribution of the main velocity

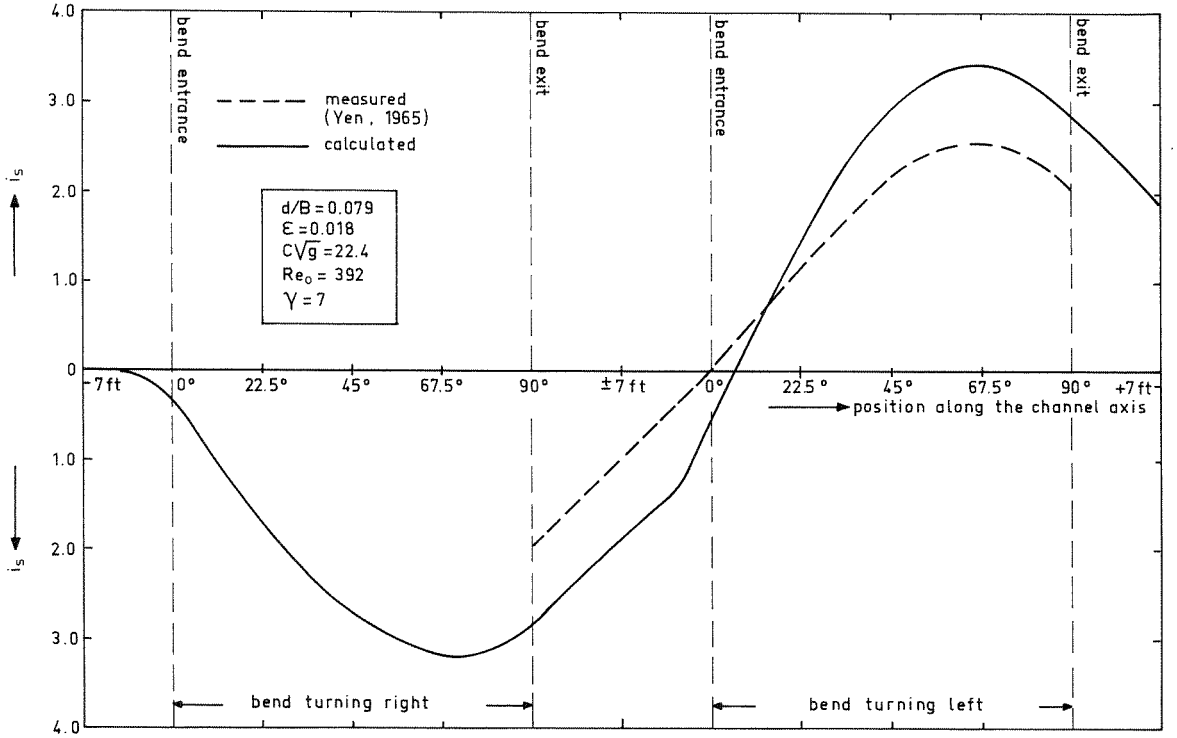

Figure 60. Simulation of one of the flat bed experiments in the IIHR-flume: secondary flow

(a) Secondary flow intensity in the channel axis

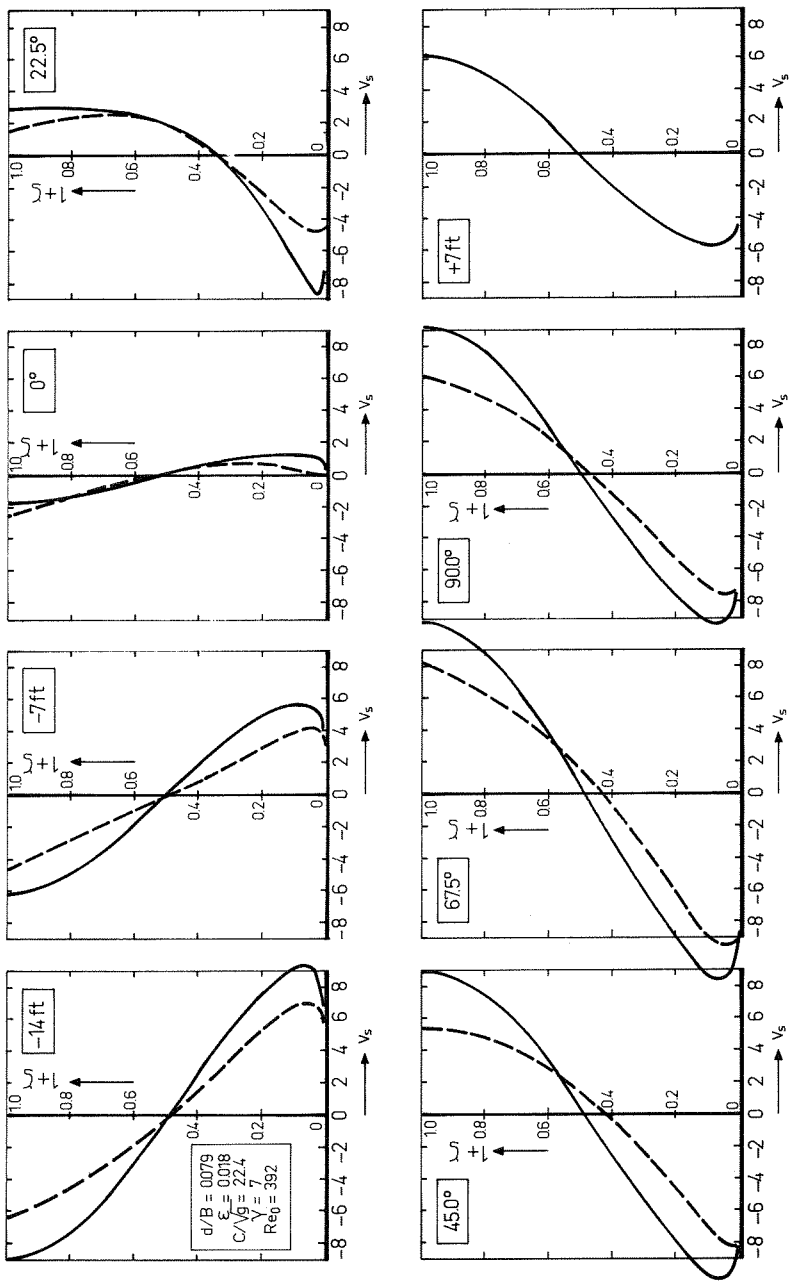

Figure 60. Simulation of one of the flat bed experiments in the IIHR-flume:
secondary flow
(b) Vertical distribution of the horizontal component

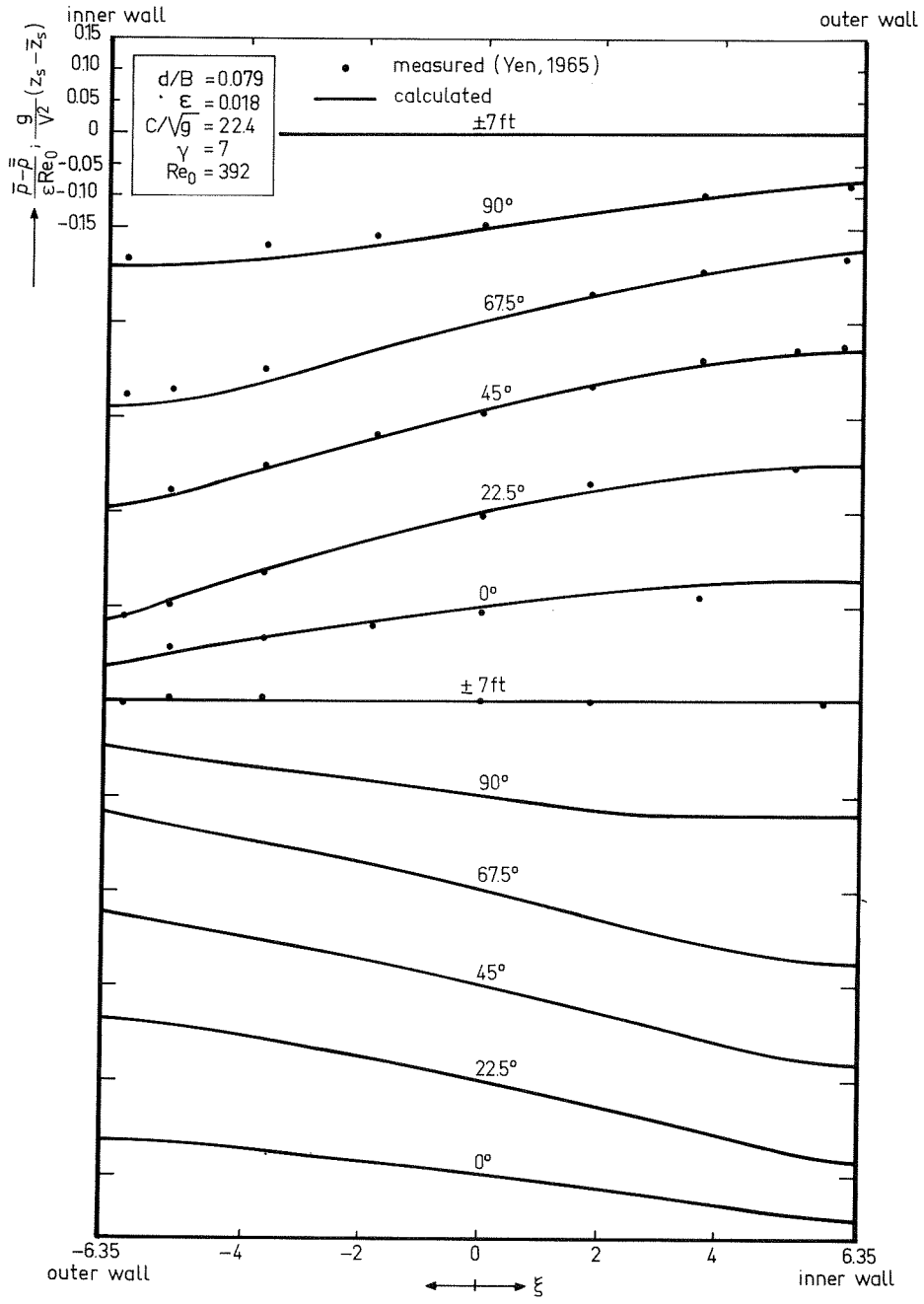

Figure 61. Simulation of one of the flat bed experiments in the IIHR-flume: total pressure

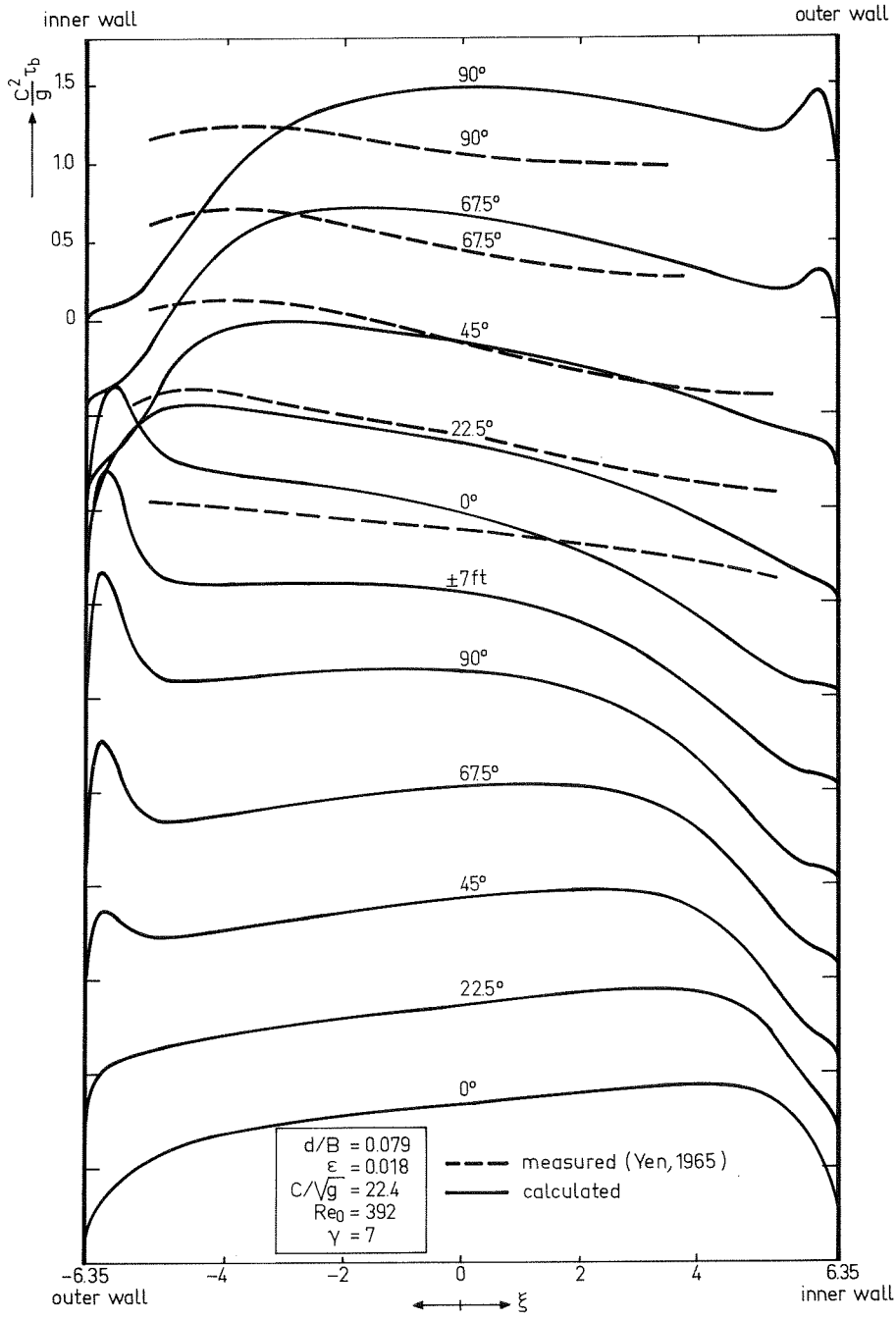

Figure 62. Simulation of one of the flat bed experiments in the IIHR-flume: bottom shear stress

(a) Transverse distribution of the total bottom shear stress

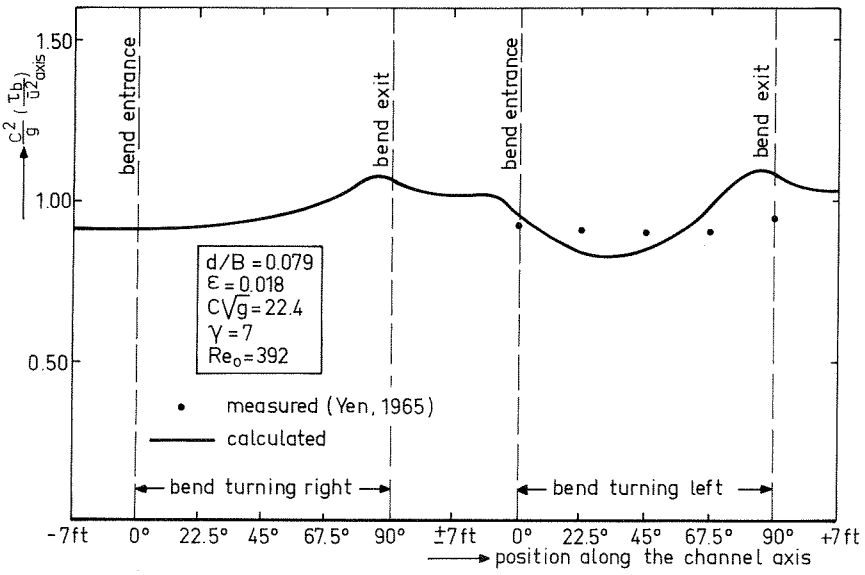

Figure 62. Simulation of one of the flat bed experiments in the IIHR-flume: bottom shear stress

(b) Longitudinal distribution of the bottom shear stress factor

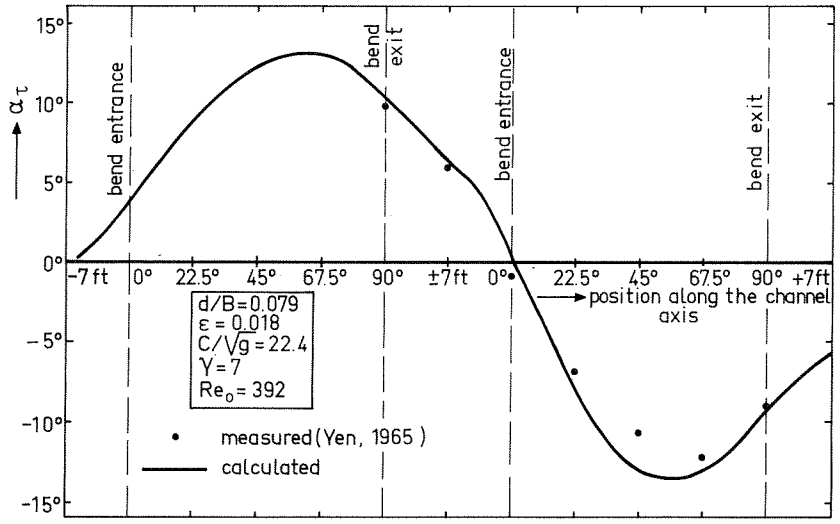

Figure 62. Simulation of one of the flat bed experiments in the IIHR-flume: bottom shear stress

(c) Longitudinal distribution of the deviation angle

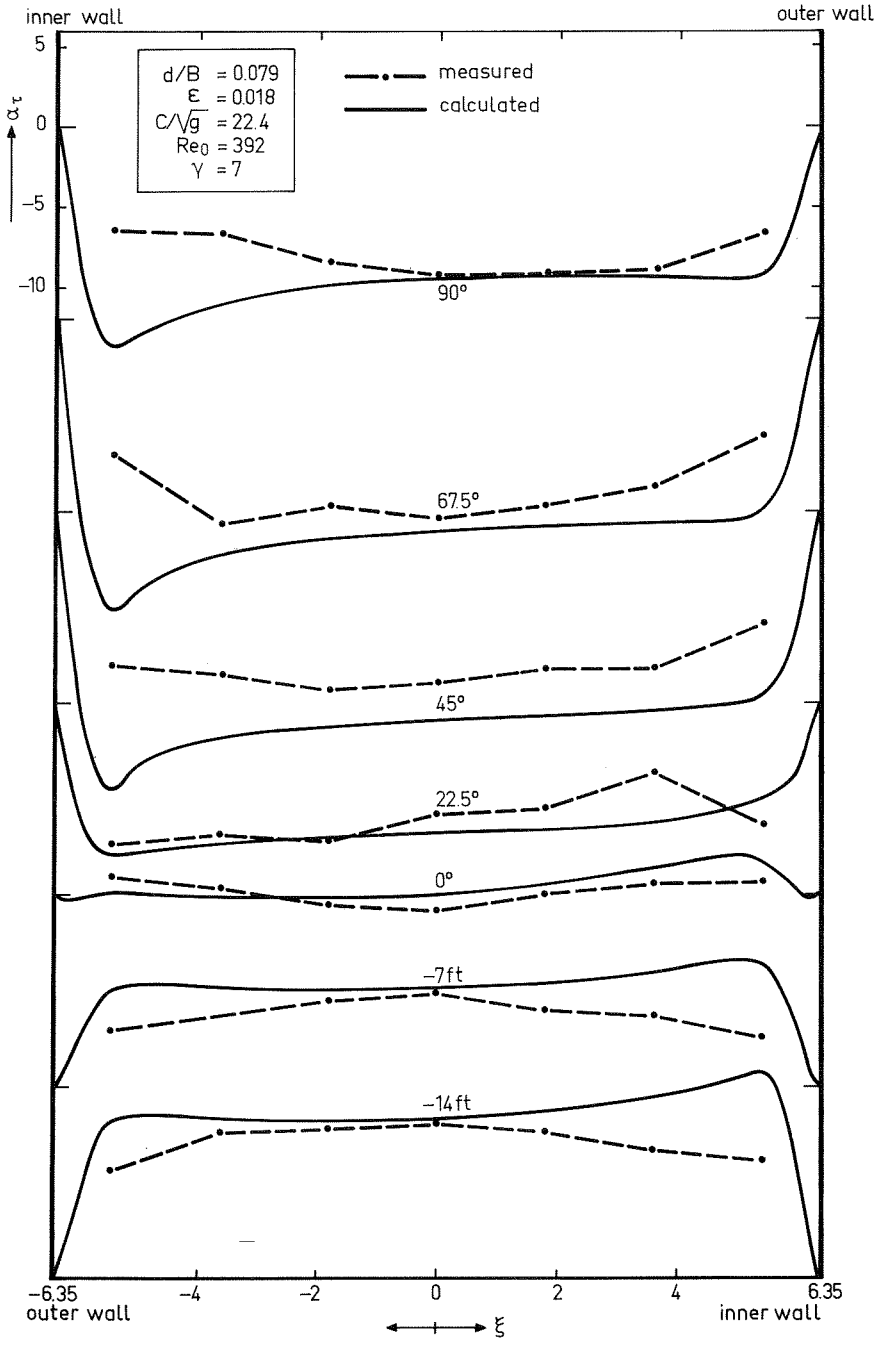

Figure 62. Simulation of one of the flat bed experiments in the IIHR-flume: bottom shear stress

(d) Transverse distribution of the deviation angle

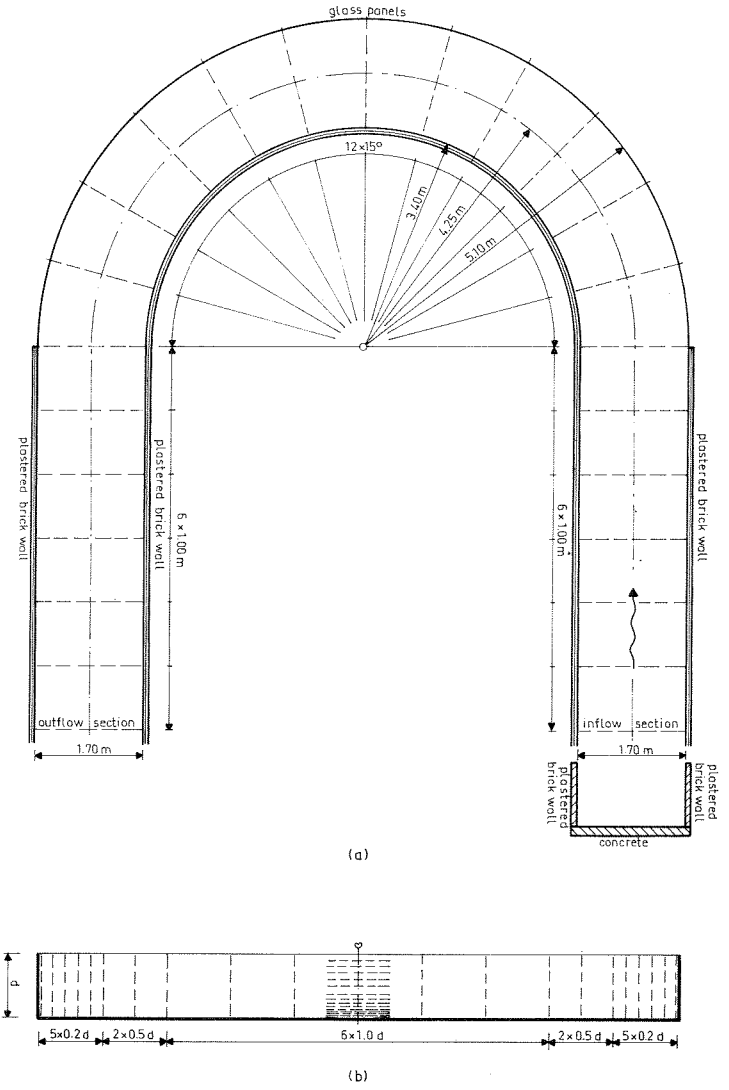

Figure 63. Simulation of the smooth bed experiment in the LFM-flume: flume geometry and computational grid

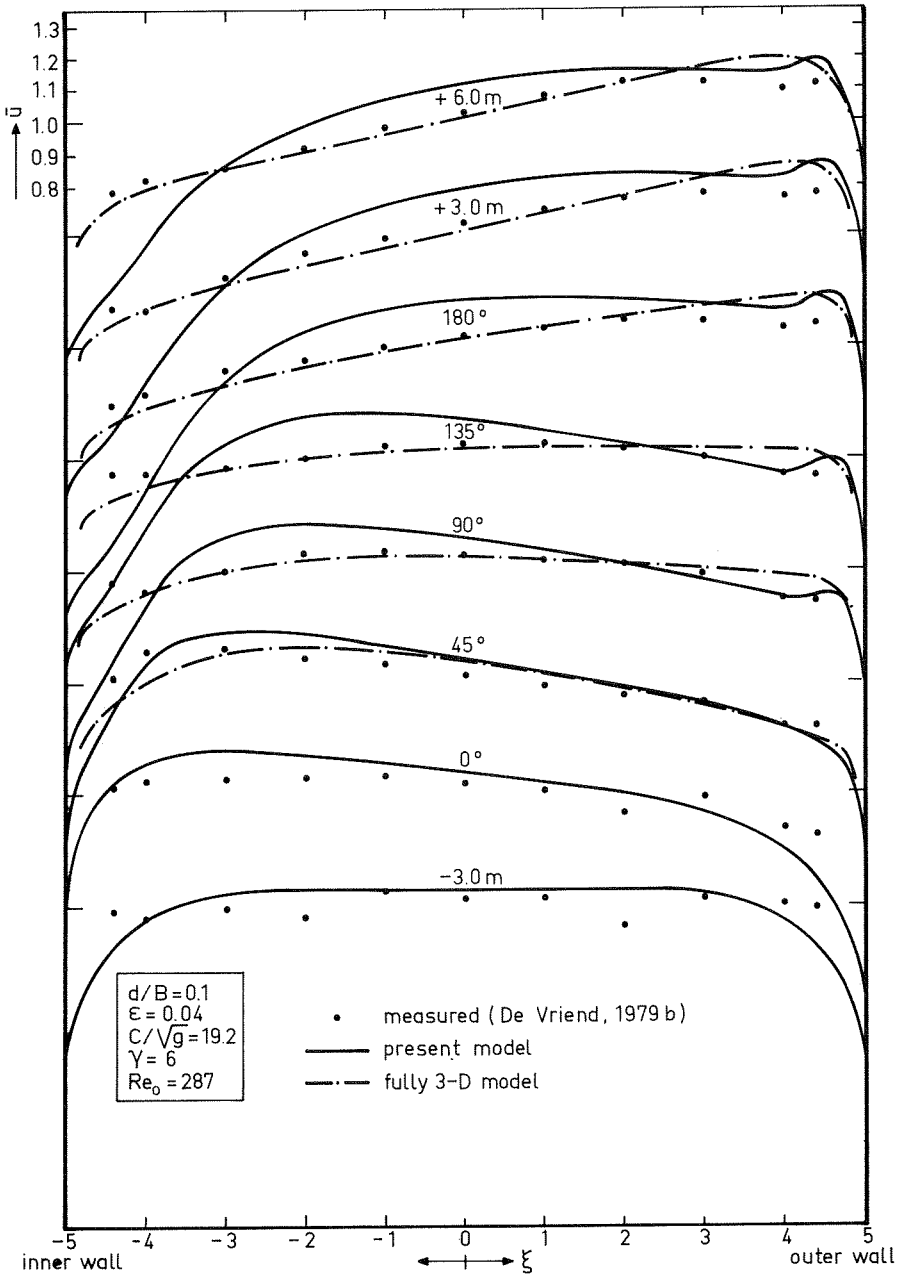

Figure 64. Simulation of the smooth bed experiment in the LFM-flume: main velocity

(a) Depth-averaged main velocity

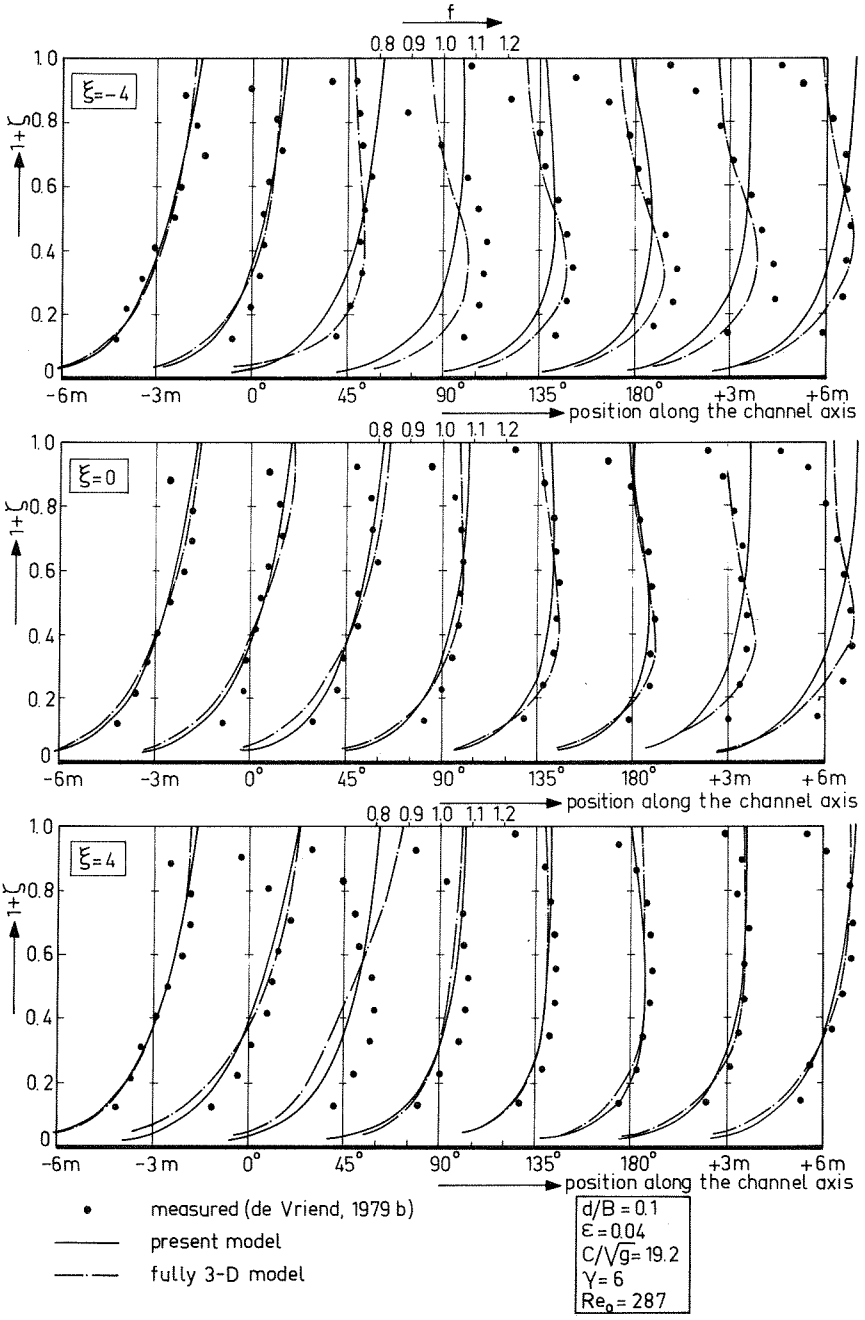

Figure 64. Simulation of the smooth bed experiment in the LFM-flume: main velocity

(b) Vertical distribution of the main velocity

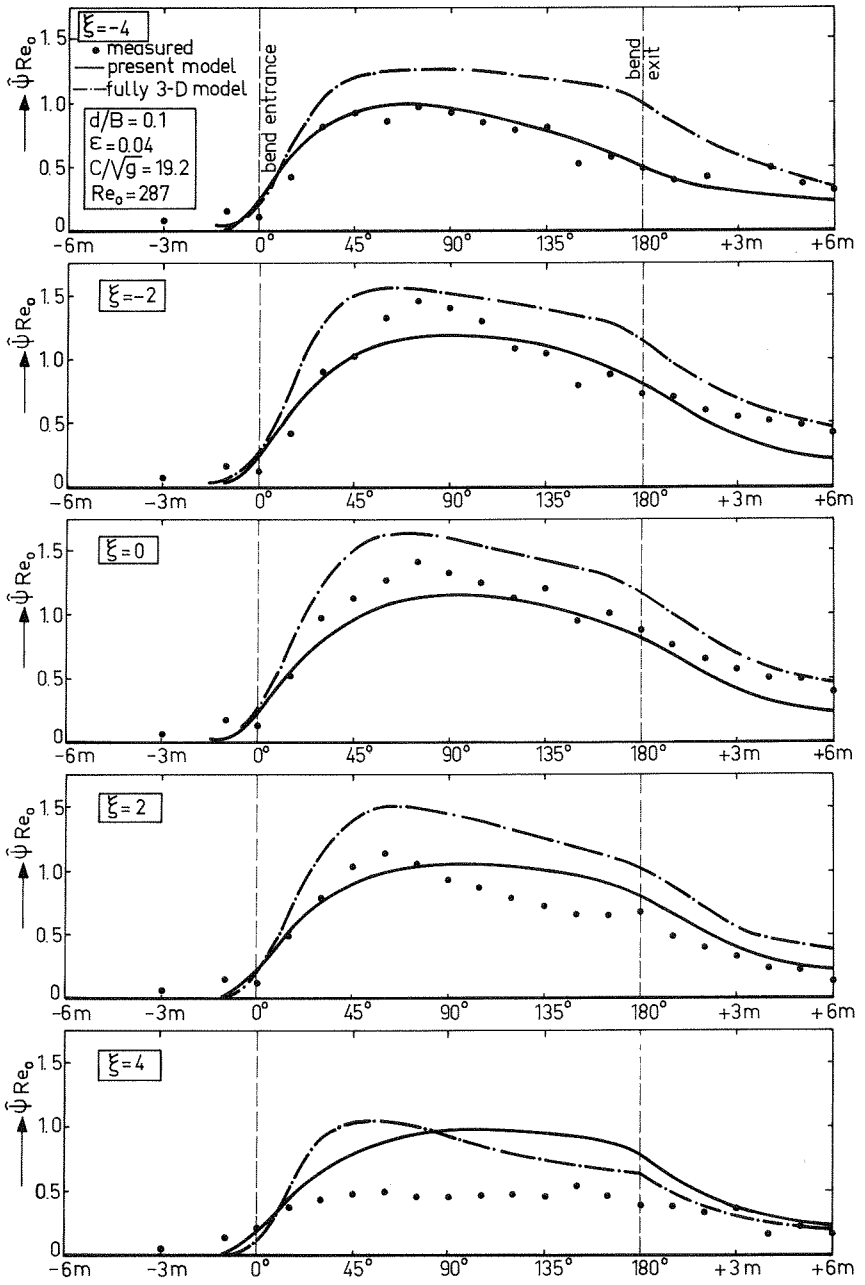

Figure 65. Simulation of the smooth bed experiment in the LFM-flume: secondary flow

(a) Longitudinal distribution of the secondary flow intensity

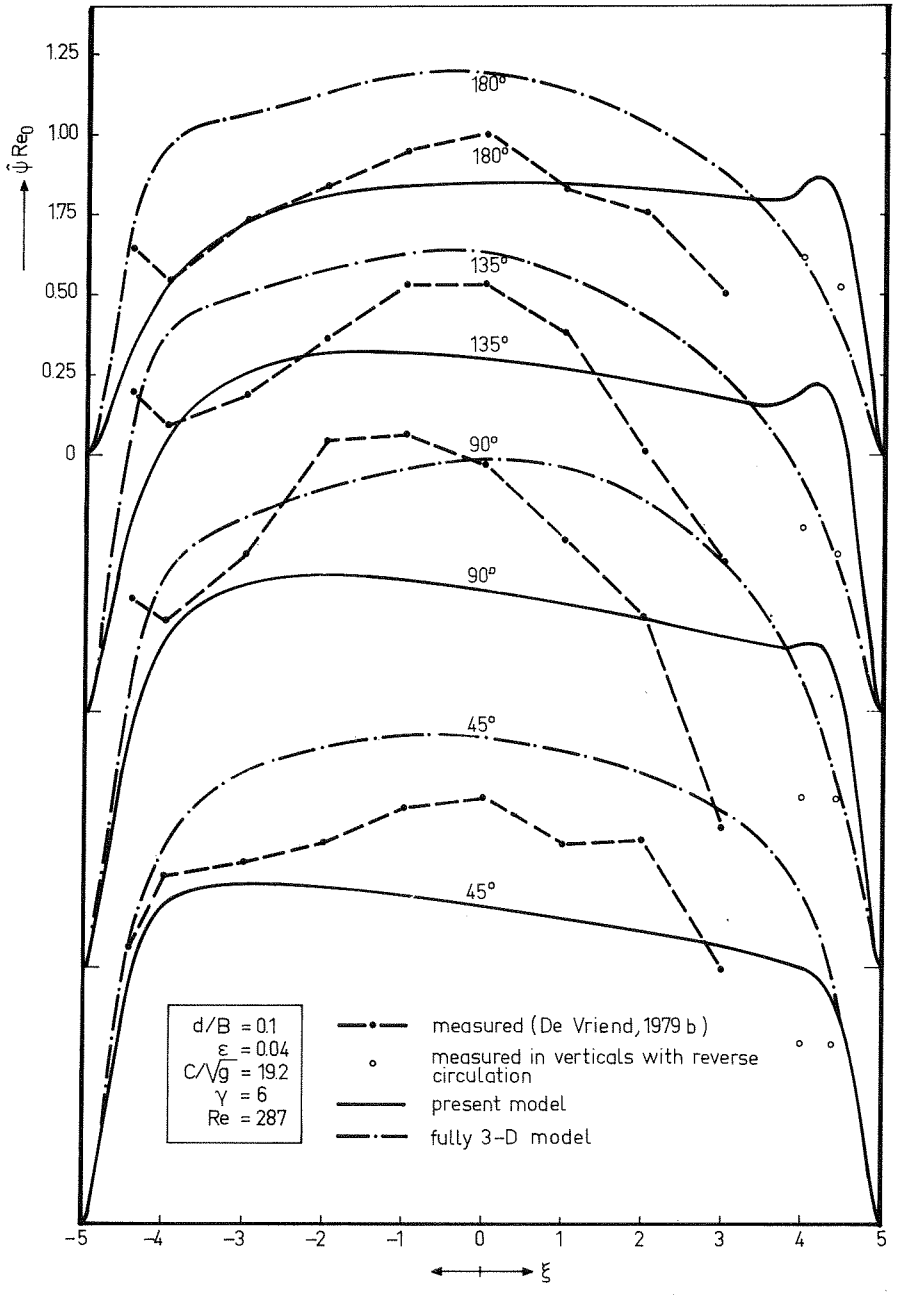

Figure 65. Simulation of the smooth bed experiment in the LFM-flume: secondary flow

(b) Transverse distribution of the secondary flow intensity

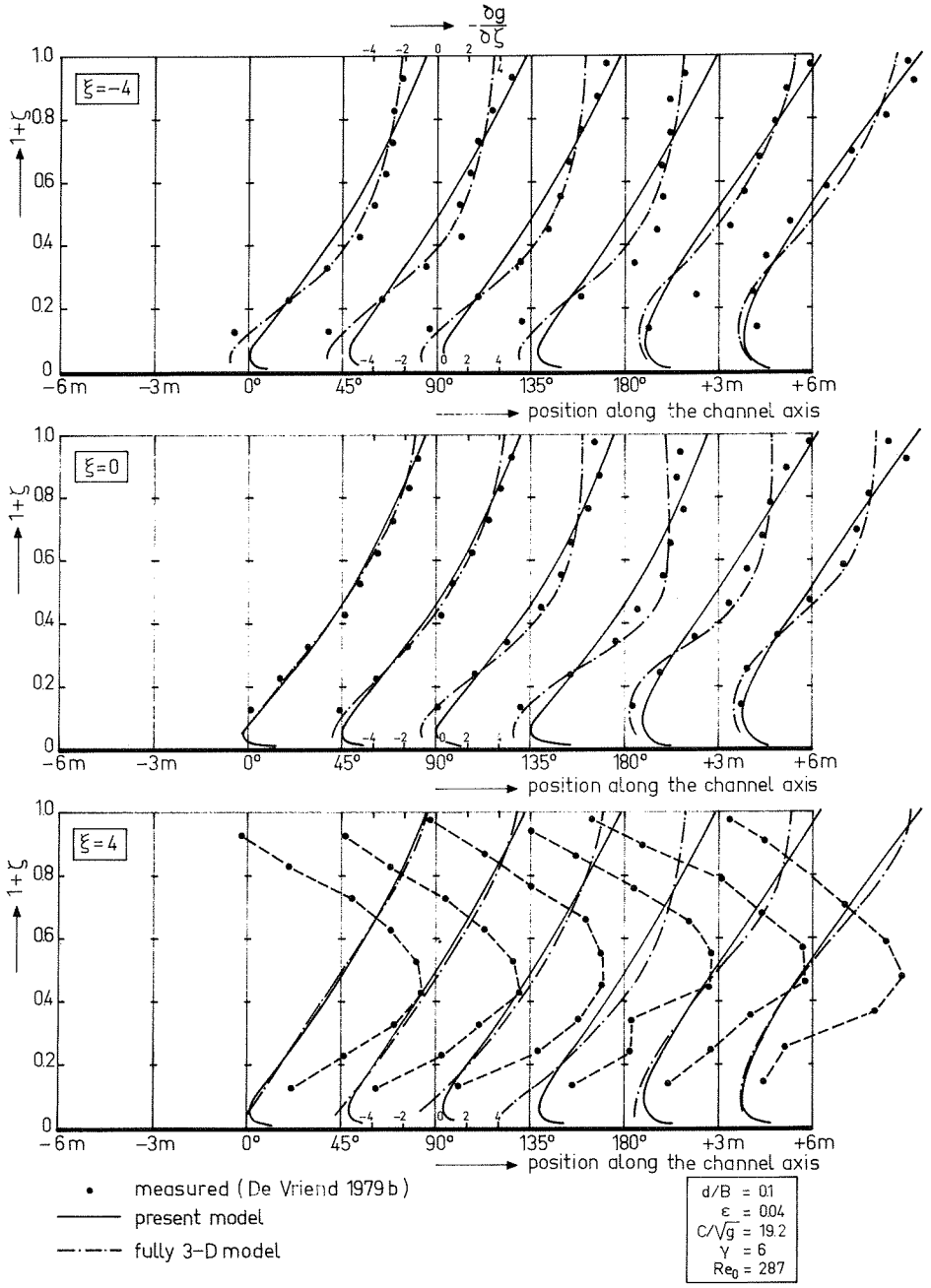

Figure 65. Simulation of the smooth bed experiment in the LFM-flume: secondary flow

(c) Vertical distribution of the horizontal component

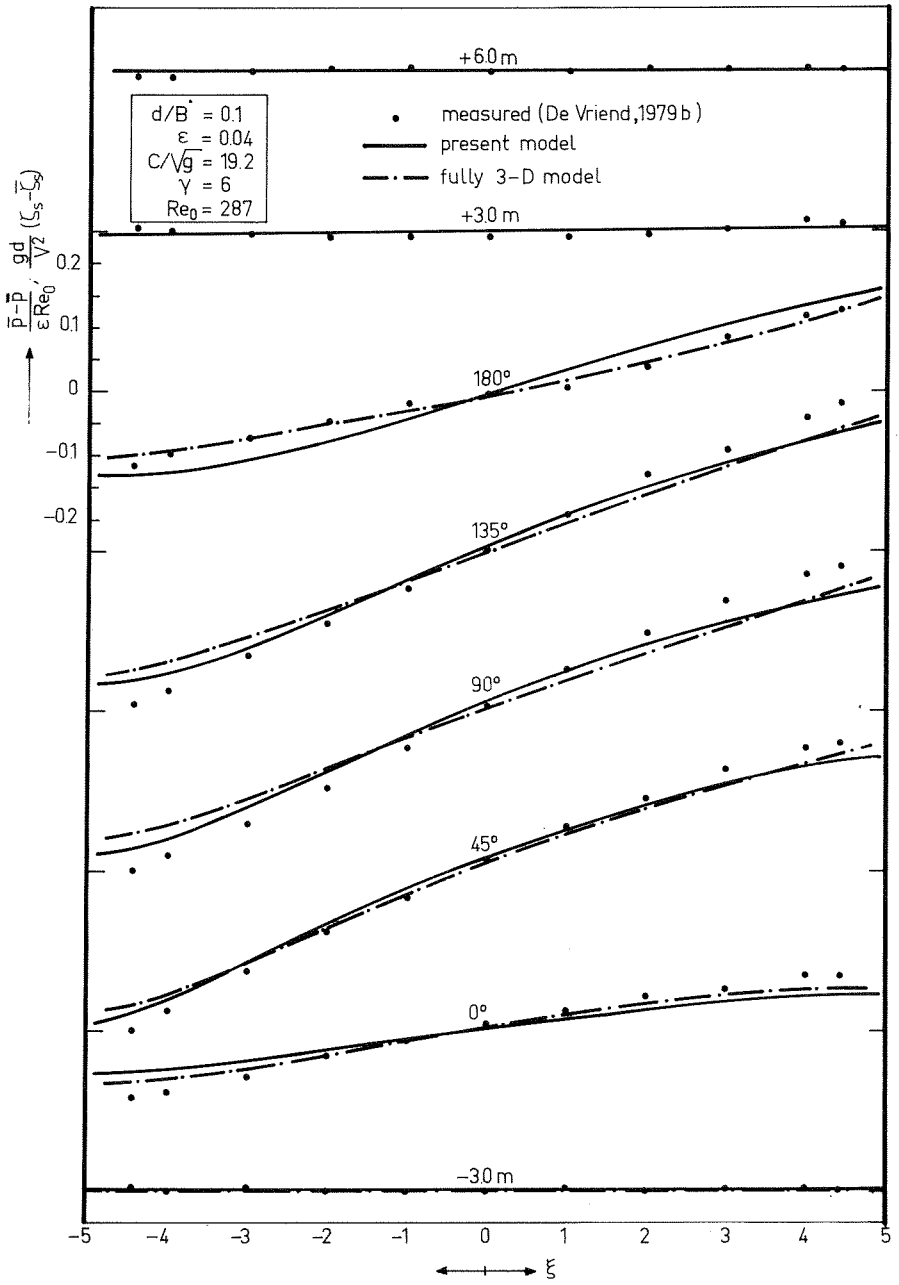

Figure 66. Simulation of the smooth bed experiment in the LFM-flume: total pressure

(a) Transverse pressure distribution

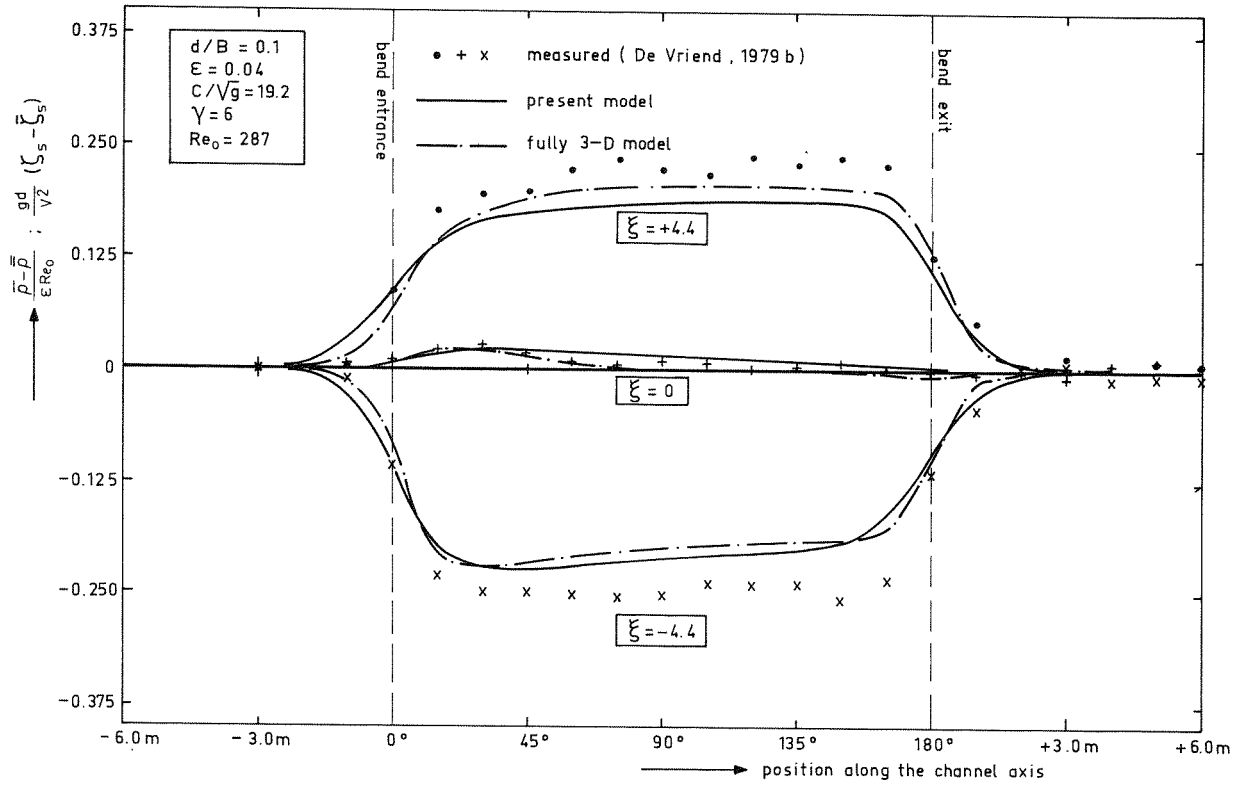

Figure 66. Simulation of the smooth bed experiment in the LFM-flume:
total pressure
(b) Transverse pressure drop

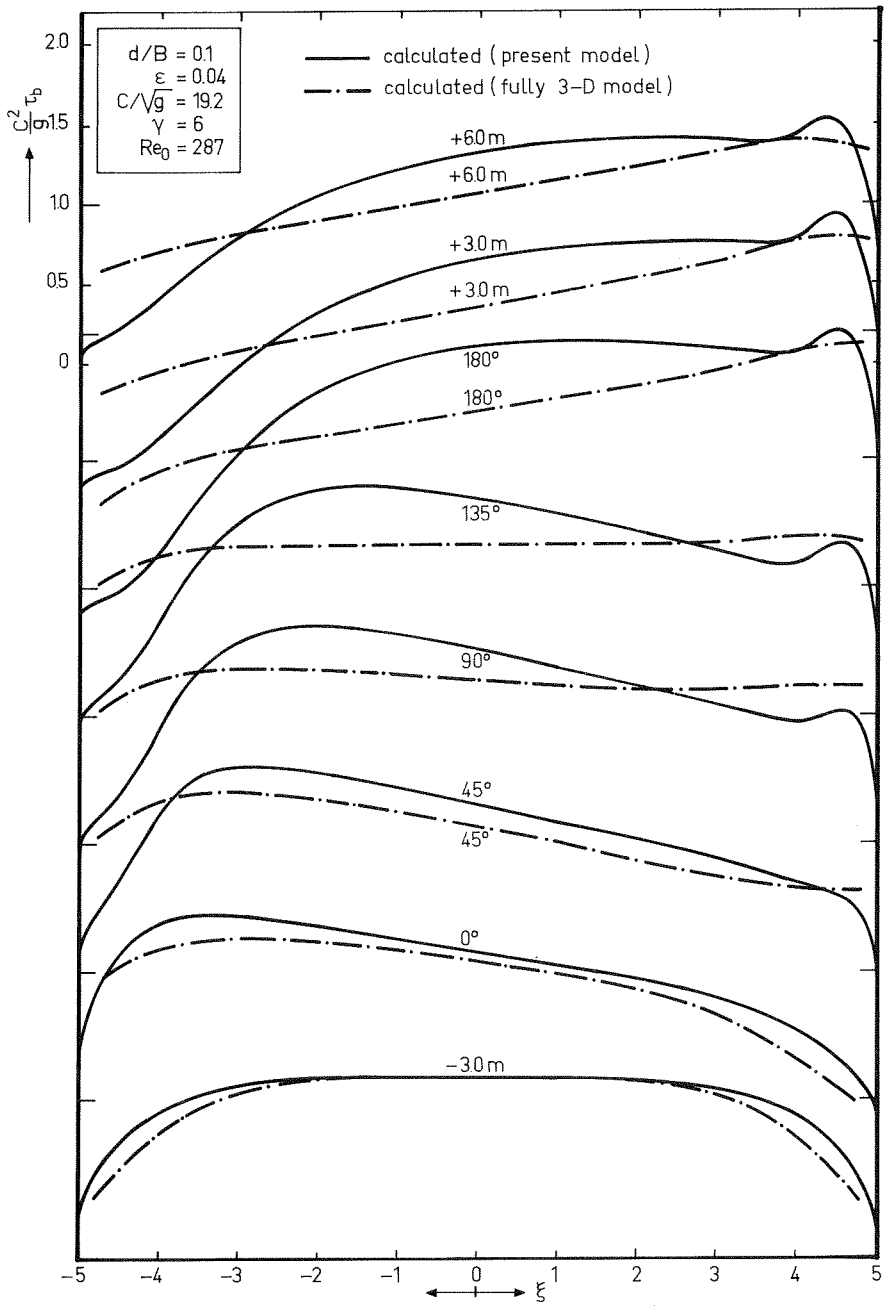

Figure 67. Simulation of the smooth bed experiment in the LFM-flume: bottom shear stress

(a) Transverse distribution of the total bottom shear stress

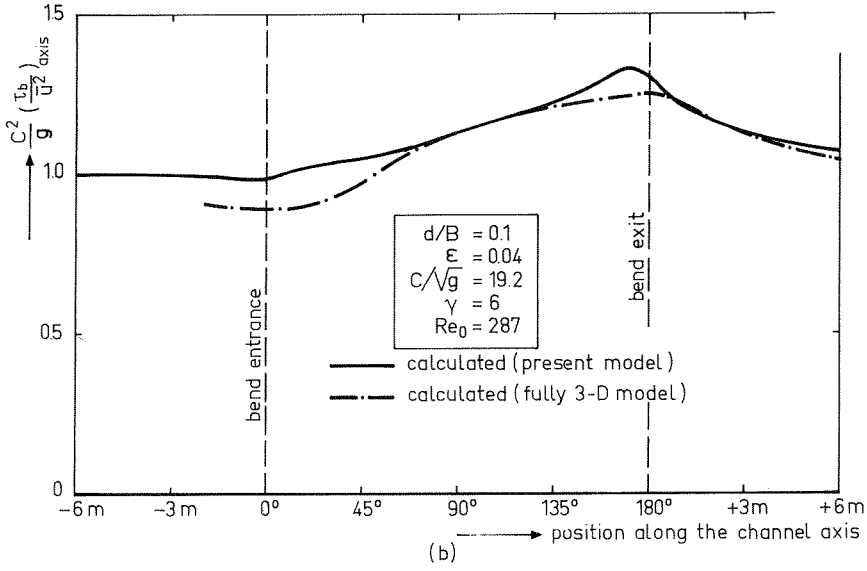

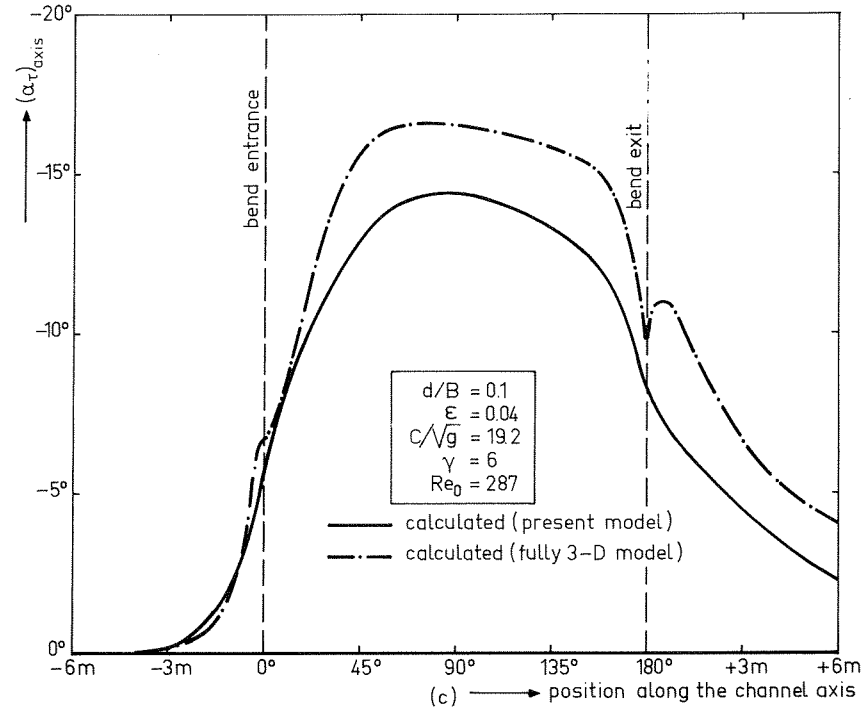

Figure 67. Simulation of the smooth bed experiment in the LFM-flume: bottom shear stress

(b) Bottom shear stress factor (c) Deviation angle in the axis

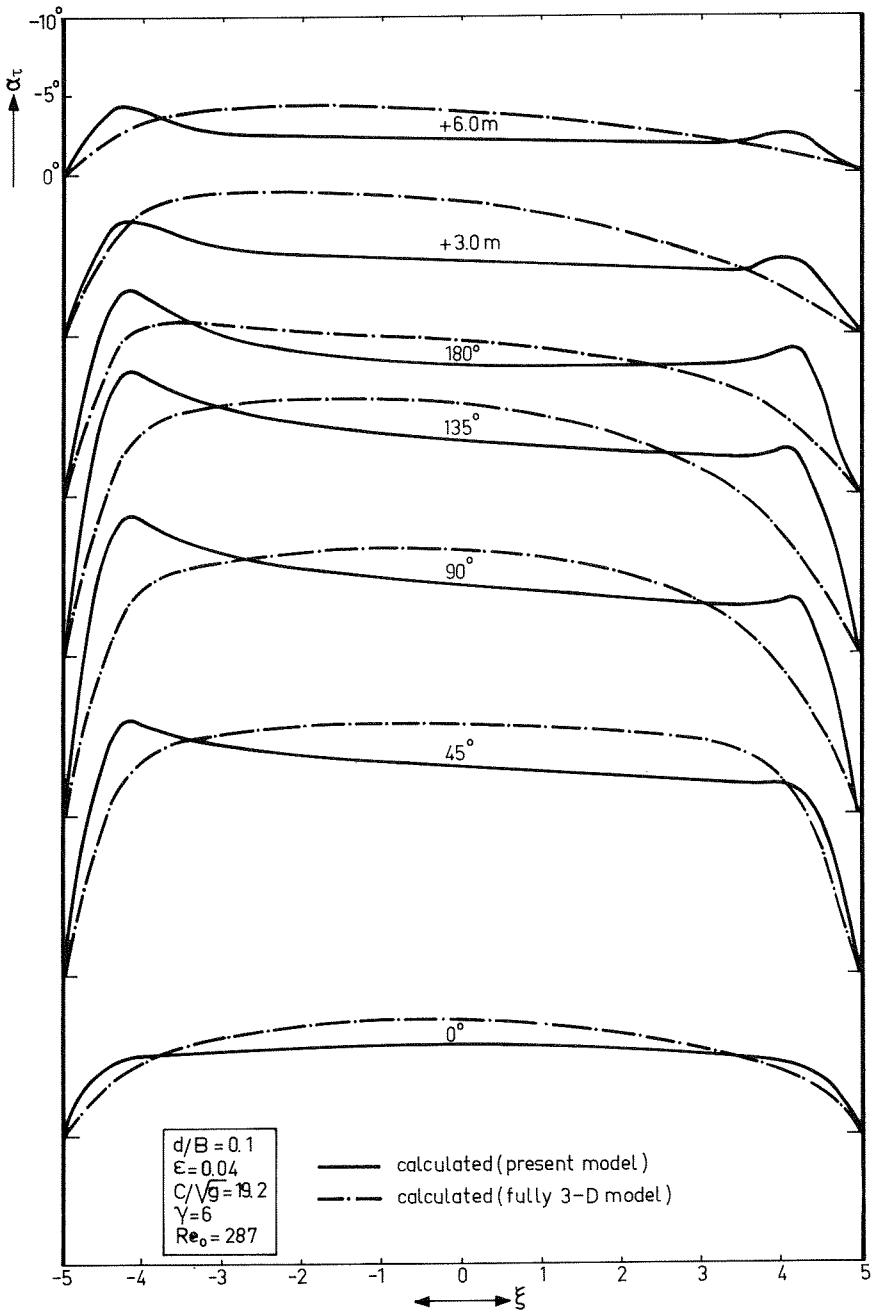

Figure 67. Simulation of the smooth bed experiment in the LFM-flume: bottom shear stress

(d) Transverse distribution of the deviation angle

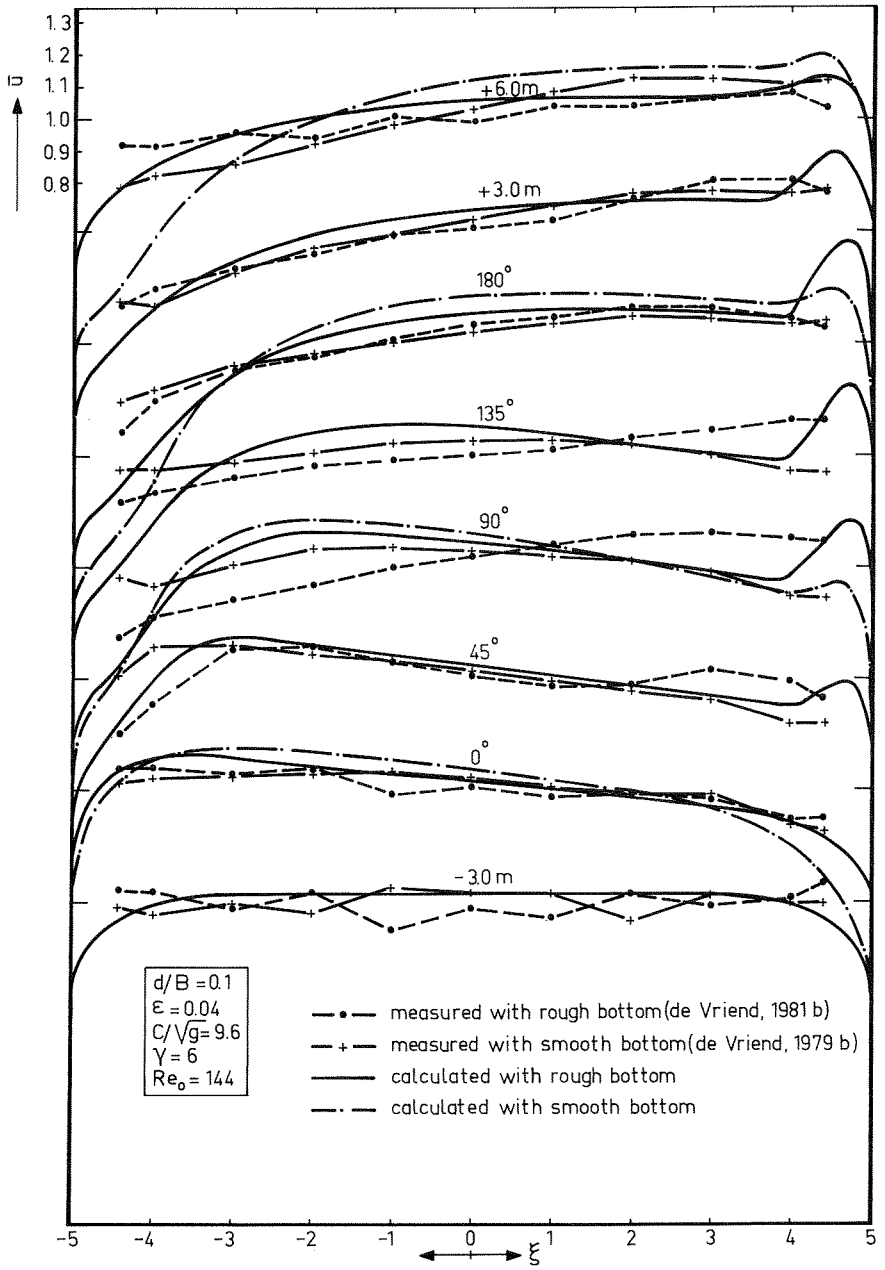

Figure 68. Simulation of the rough bed experiment in the LFM-flume: main velocity

(a) Depth-averaged main velocity

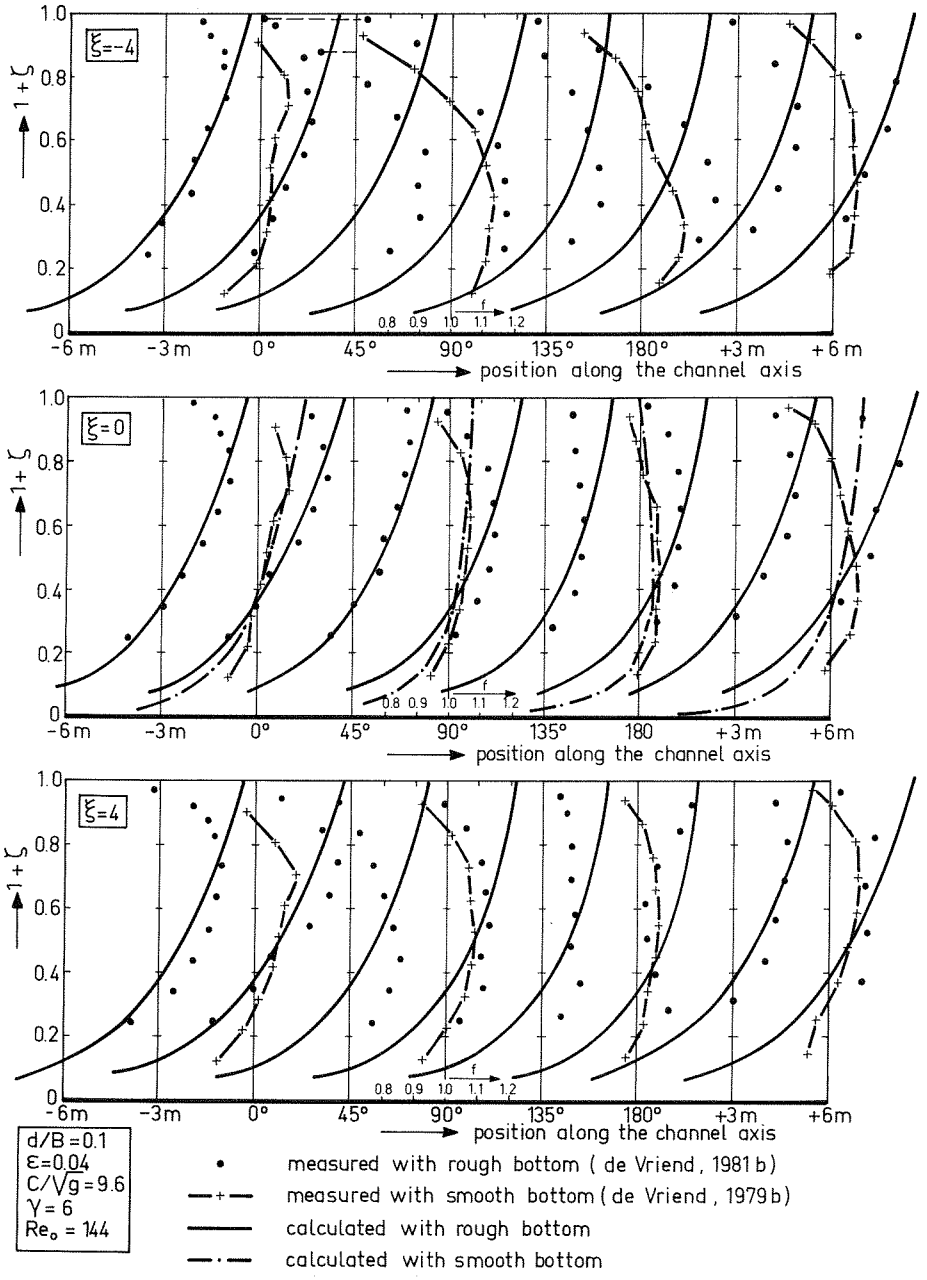

Figure 68. Simulation of the rough bed experiment in the LFM-flume: main velocity

(b) Vertical distribution of the main velocity

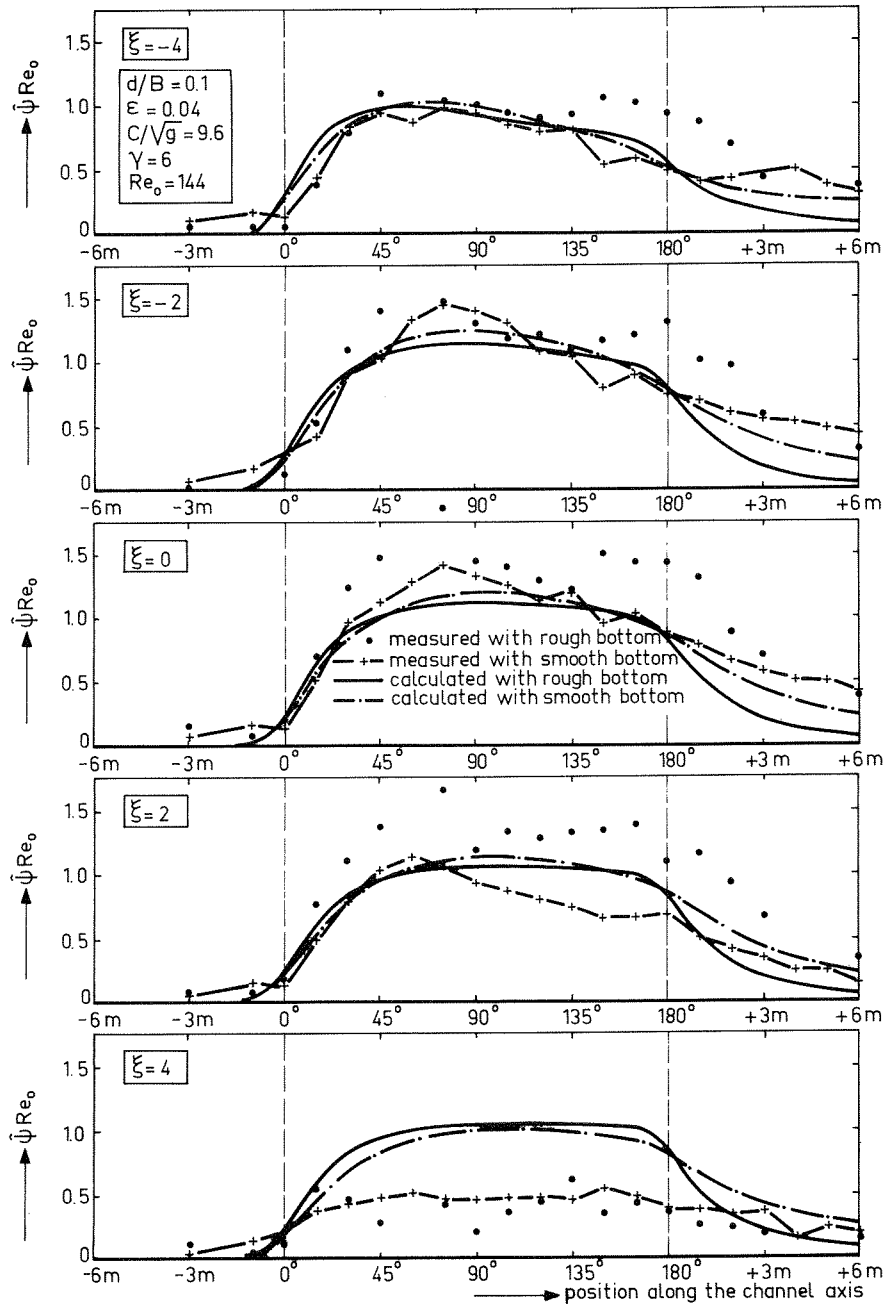

Figure 69. Simulation of the rough bed experiment in the LFM-flume: secondary flow

(a) Longitudinal distribution of the secondary flow intensity

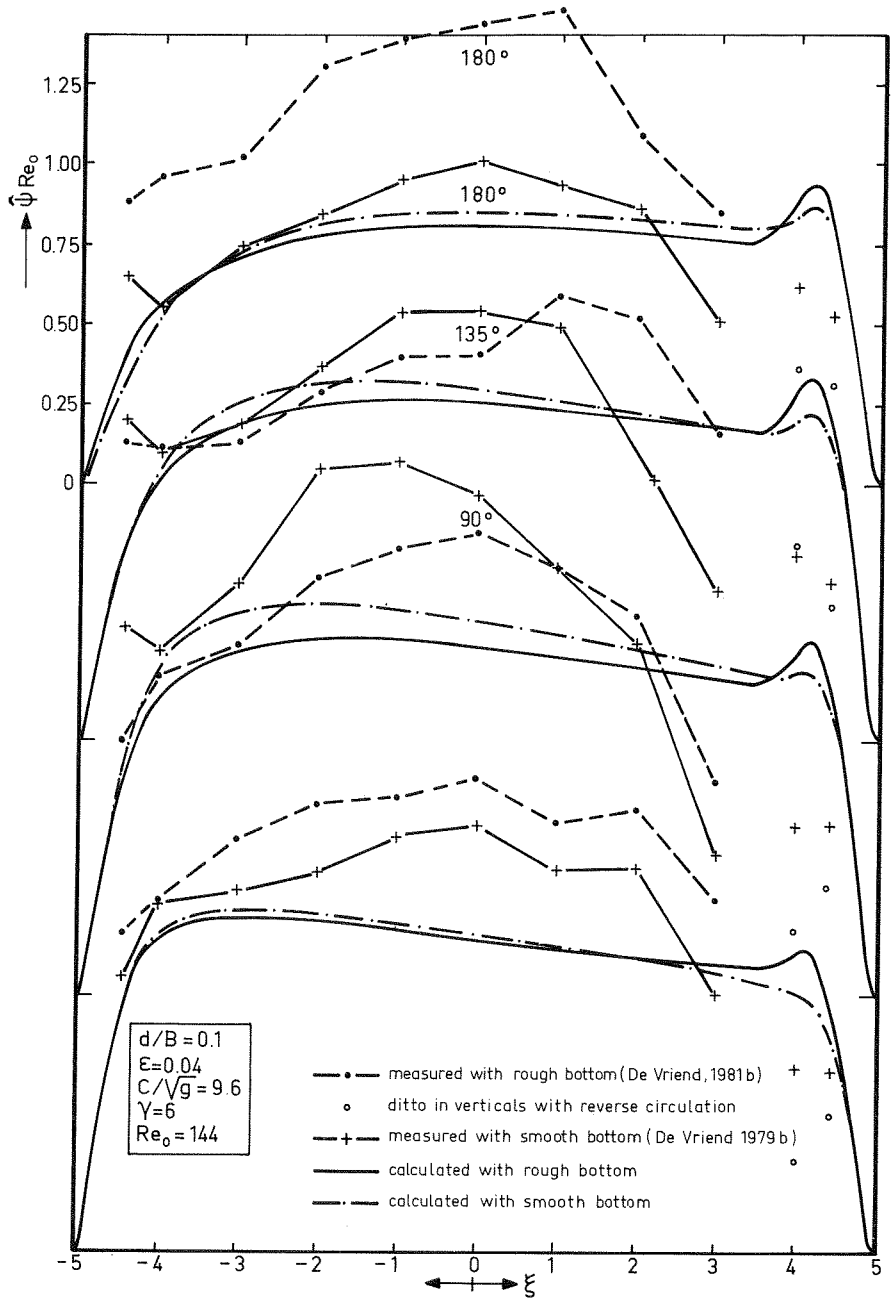

Figure 69. Simulation of the rough bed experiment in the LFM-flume: secondary flow

(b) Transverse distribution of the secondary flow intensity

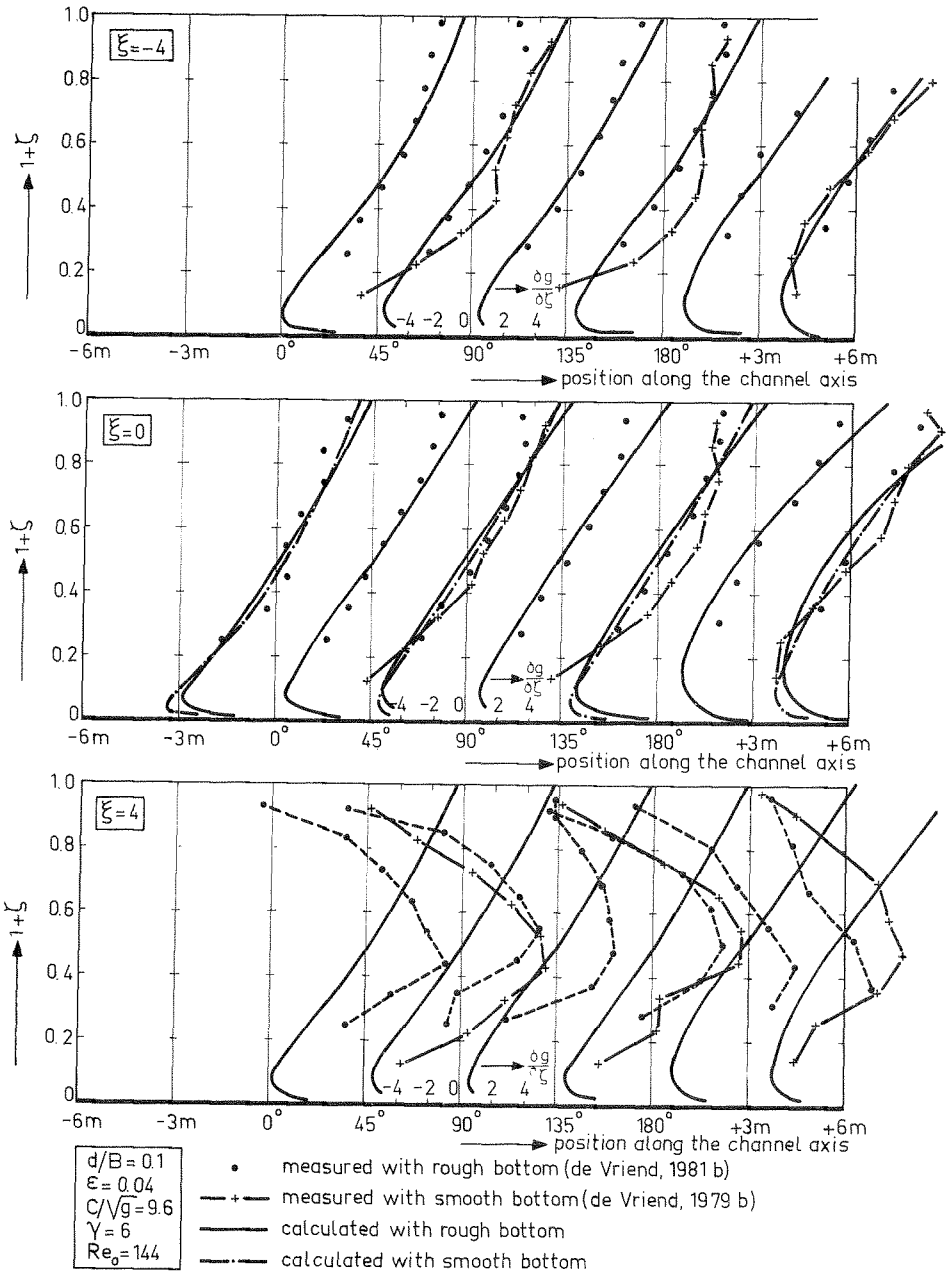

Figure 69. Simulation of the rough bed experiment in the LFM-flume: secondary flow

(c) Vertical distribution of the horizontal component

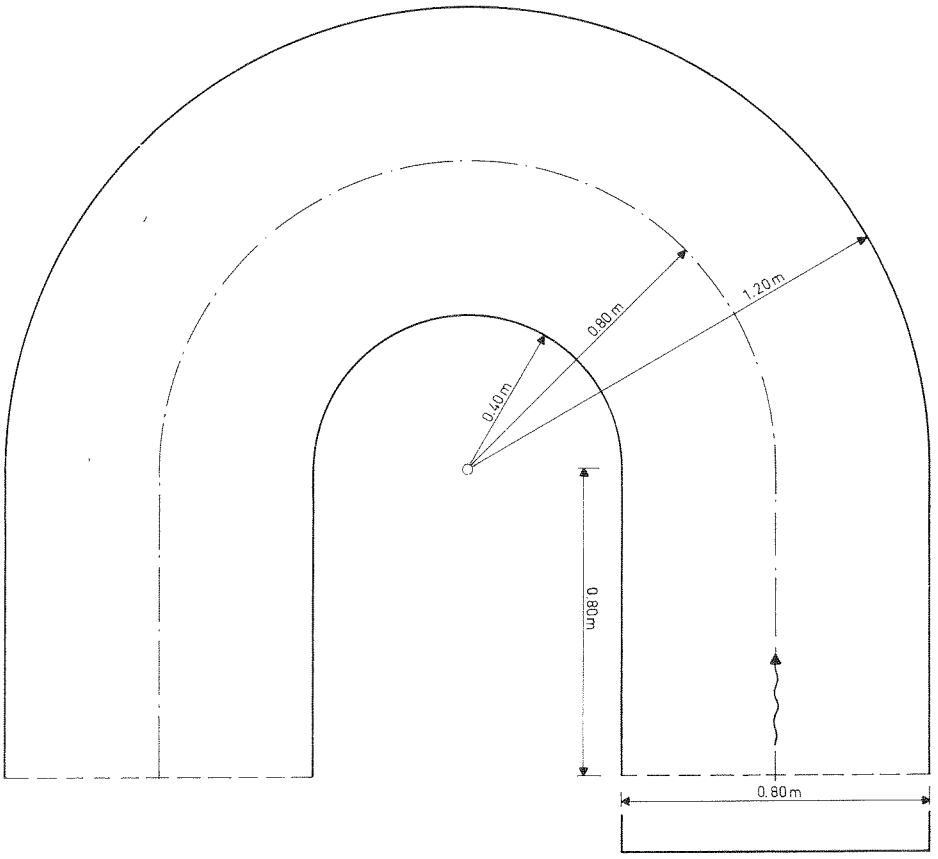

Figure 70. Simulation of one of the experiments in the IHHE-flume: flume geometry

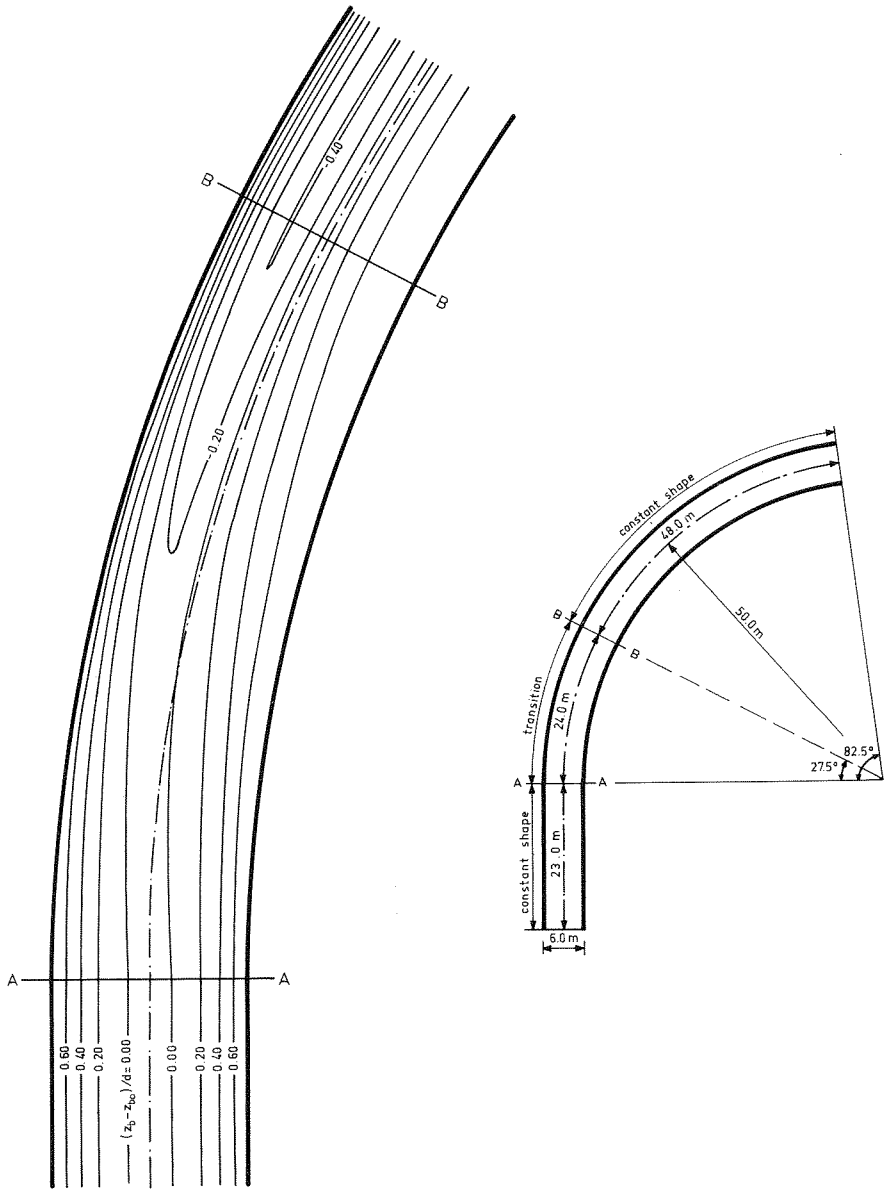

Figure 71. Simulation of the non-rectangular channel experiments in the DHL-flume: channel geometry

(a) Bottom contour lines for horizontal mean bottom

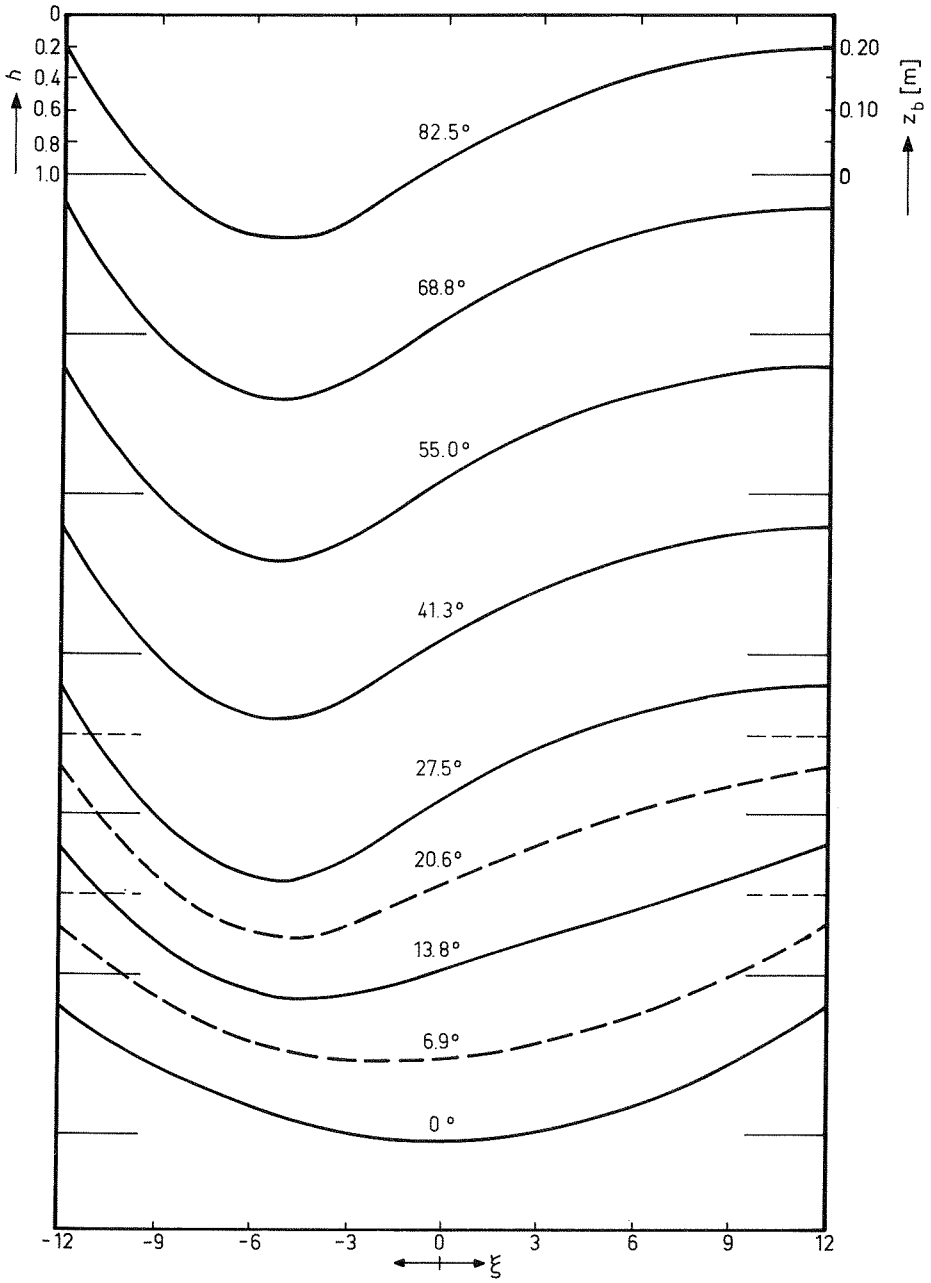

Figure 71. Simulation of the non-rectangular channel experiments in the DHL-flume: channel geometry

(b) Bottom level and depth of flow in the computation

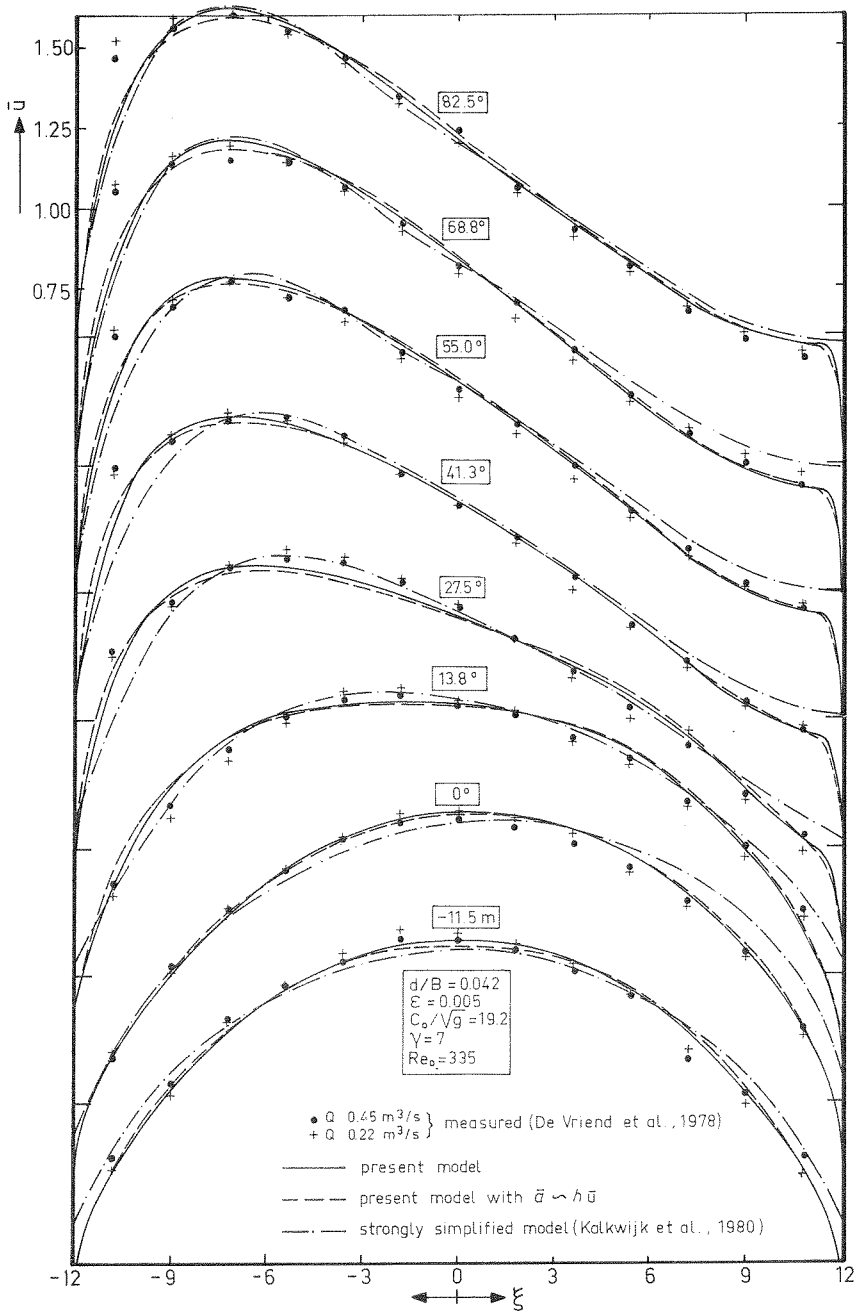

Figure 72. Simulation of the non-rectangular channel experiments in the DHL-flume: main velocity

(a) Depth-averaged main velocity

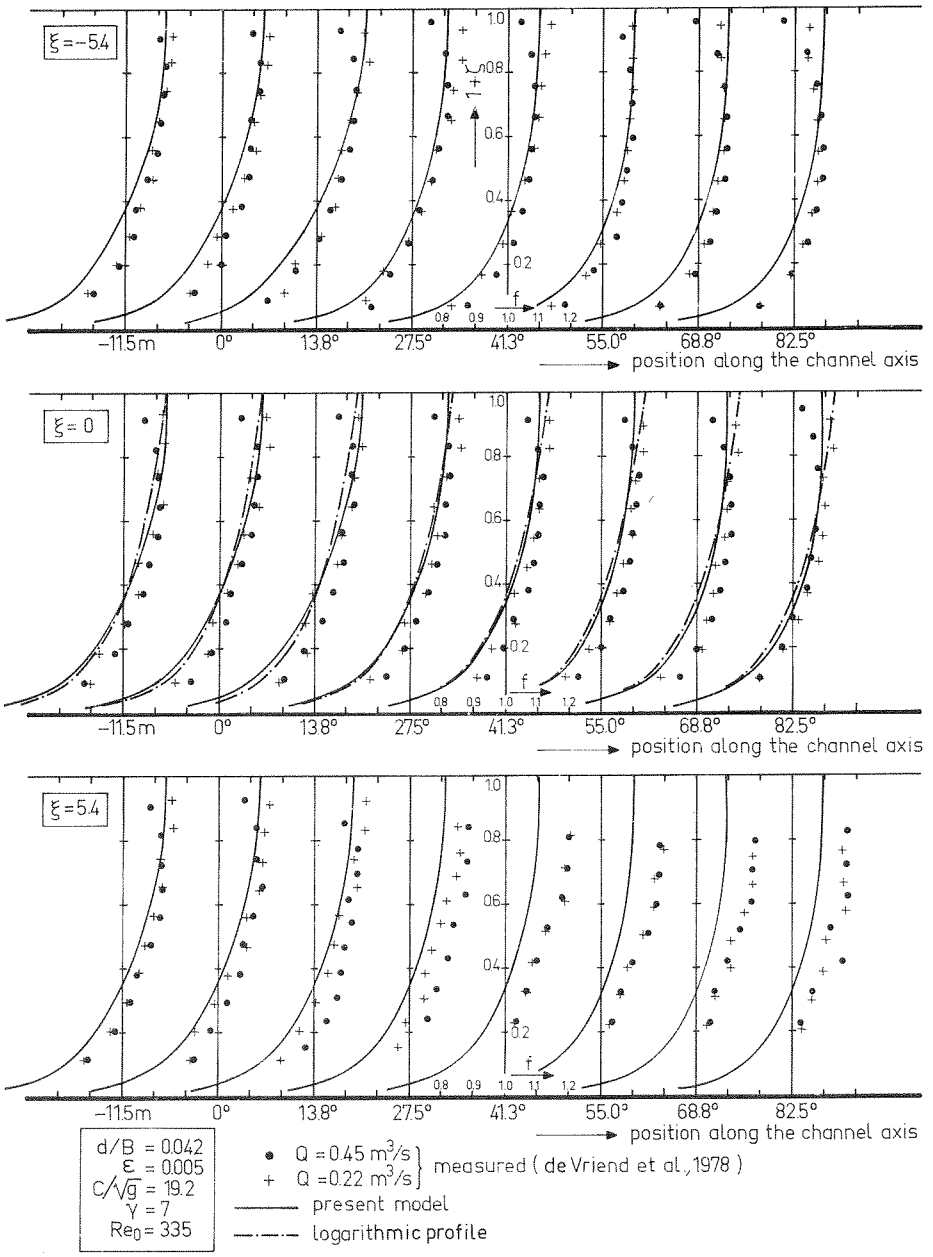

Figure 72. Simulation of the non-rectangular channel experiments in the DHL-flume: main velocity

(b) Vertical distribution of the main velocity

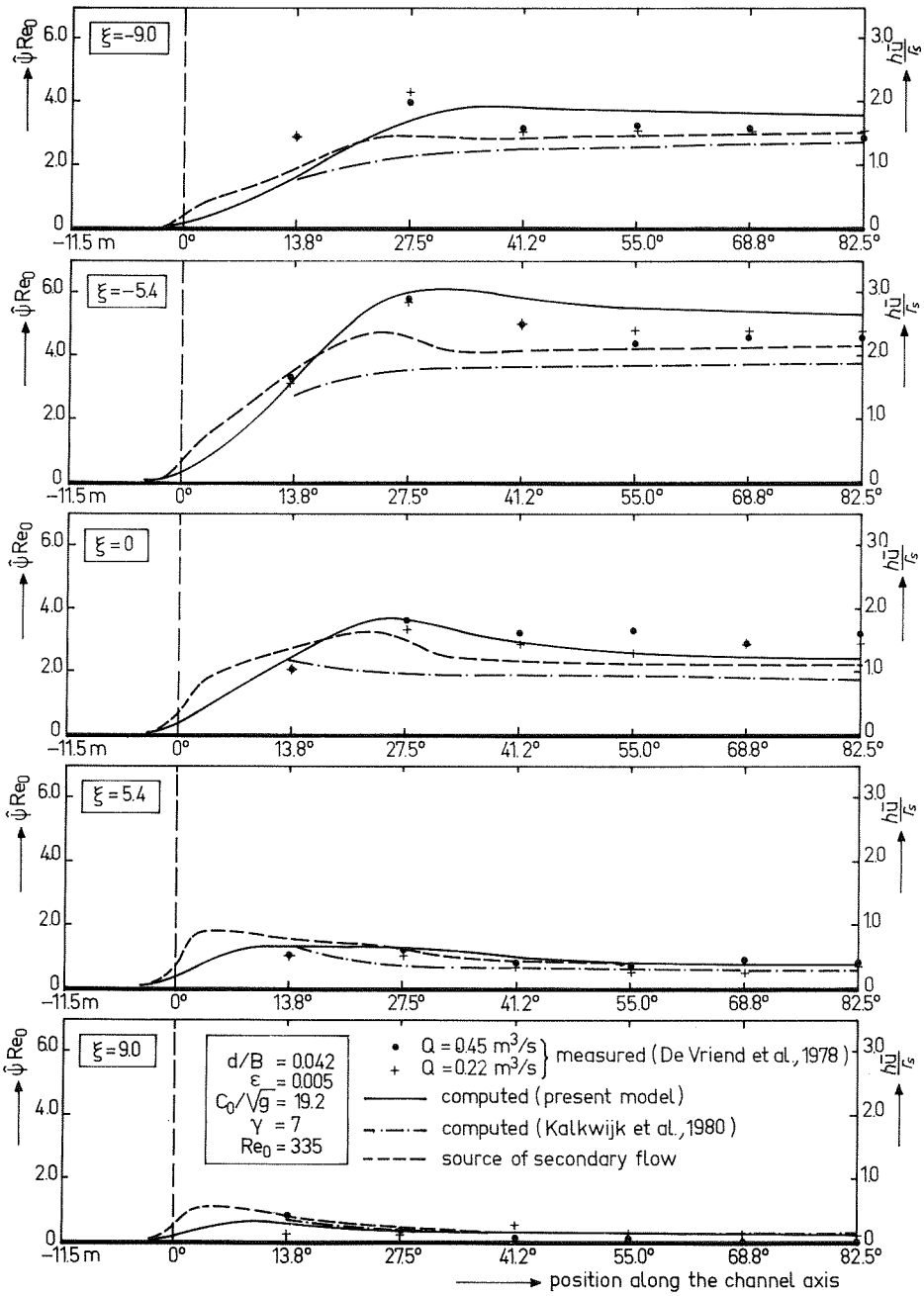

Figure 73. Simulation of the non-rectangular channel experiments in the DHL-flume: secondary flow

(a) Longitudinal distribution of the secondary flow intensity

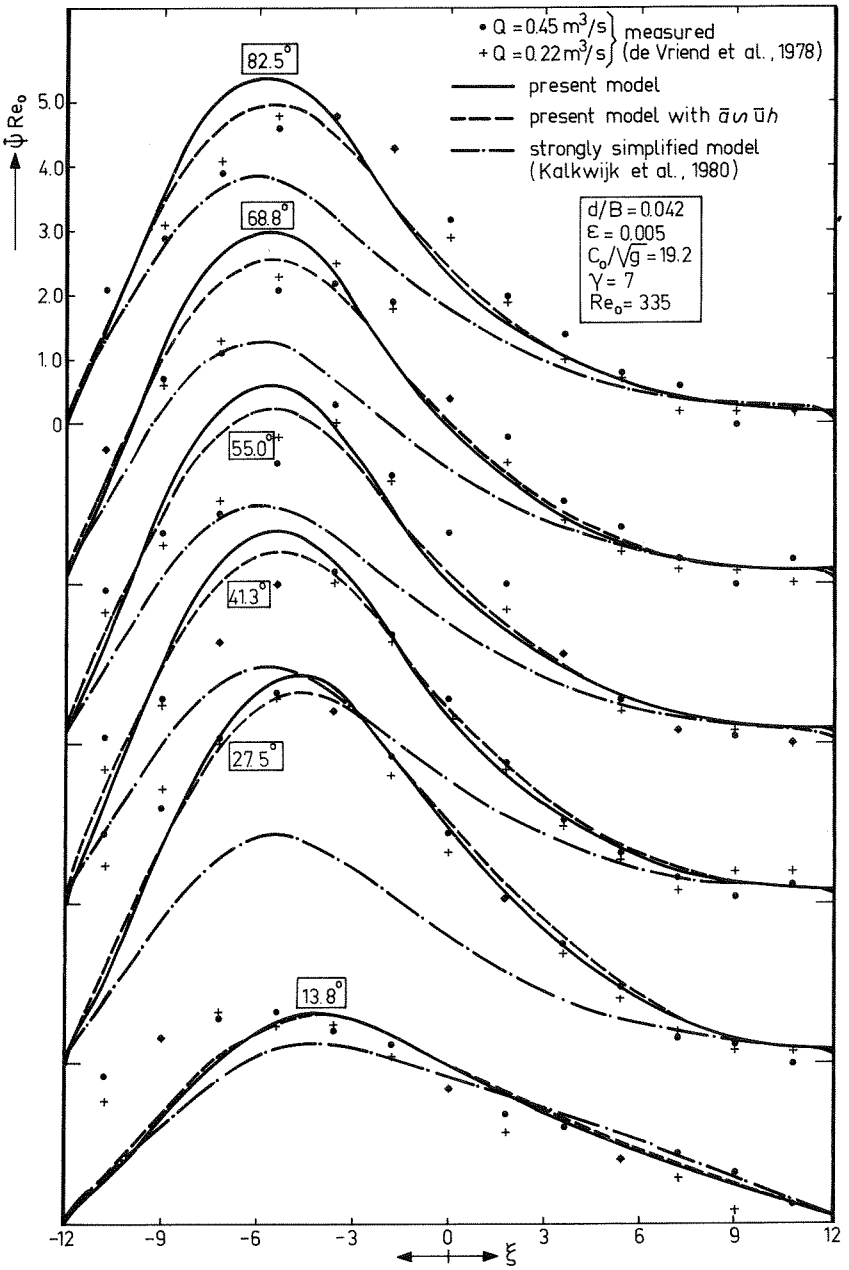

Figure 73. Simulation of the non-rectangular channel experiments in the DHL-flume: secondary flow

(b) Transverse distribution of the secondary flow intensity

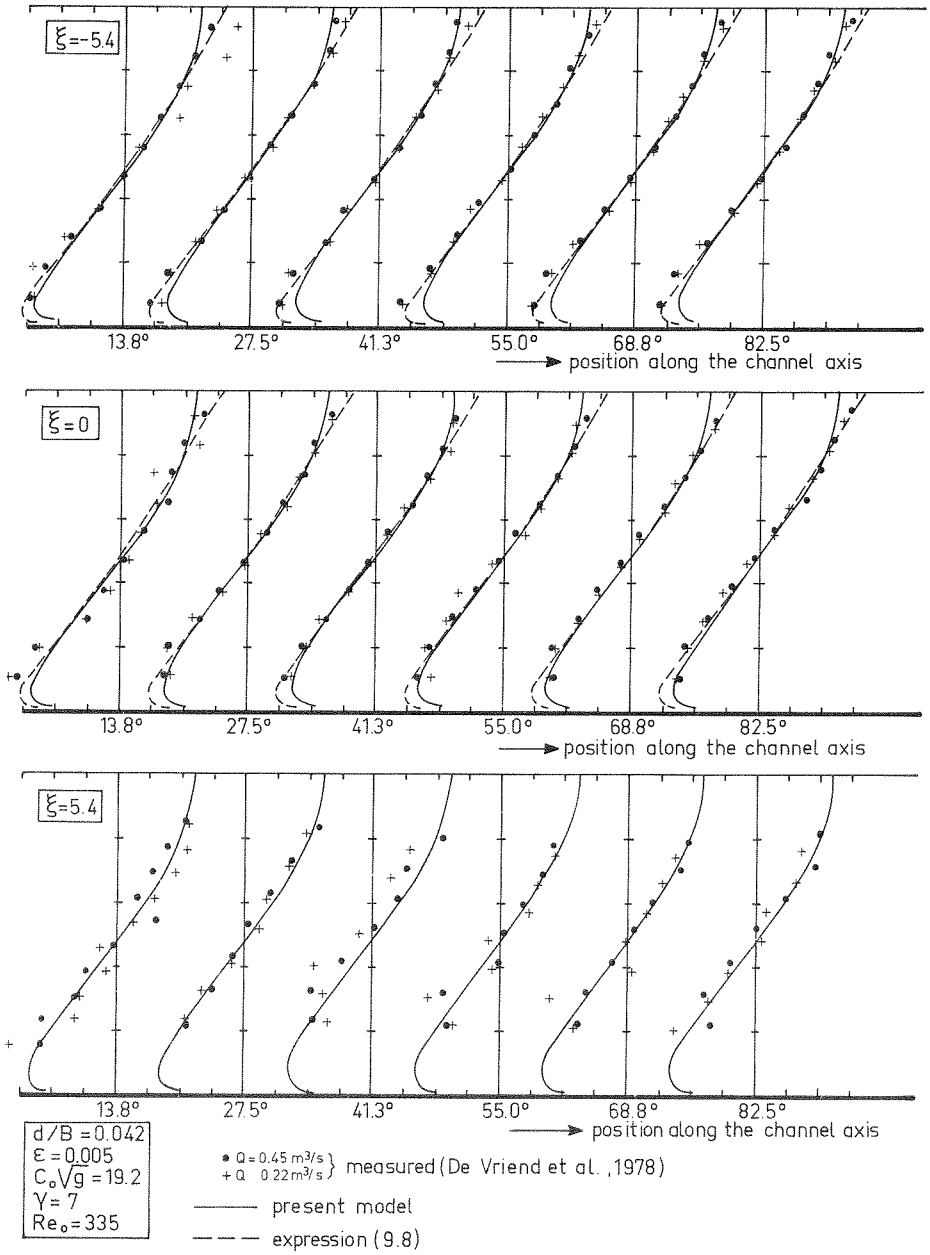

Figure 73. Simulation of the non-rectangular channel experiments in the DHL-flume: secondary flow

(c) Vertical distribution of the horizontal component

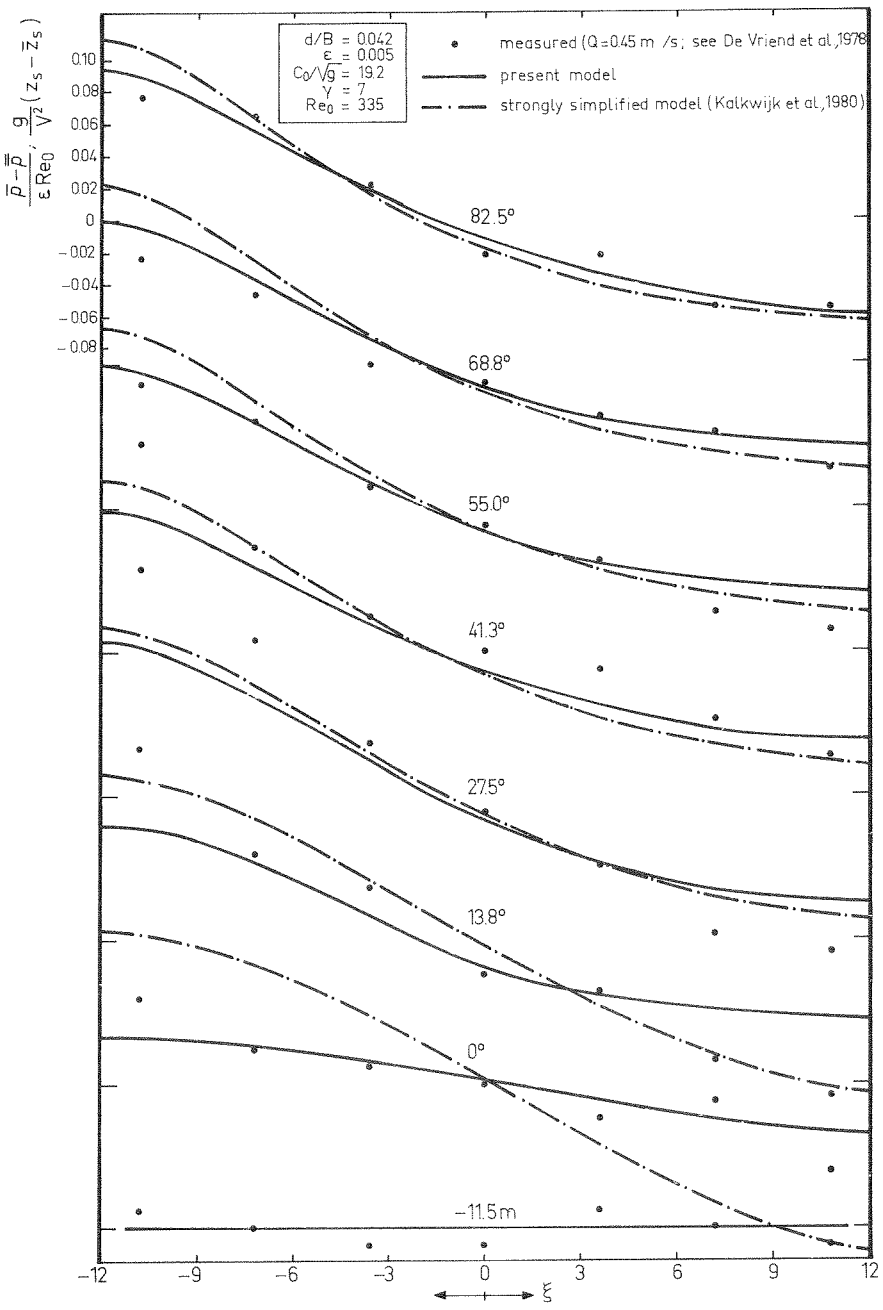

Figure 74. Simulation of the non-rectangular channel experiments in the DHL-flume: total pressure

(a) Transverse pressure distribution

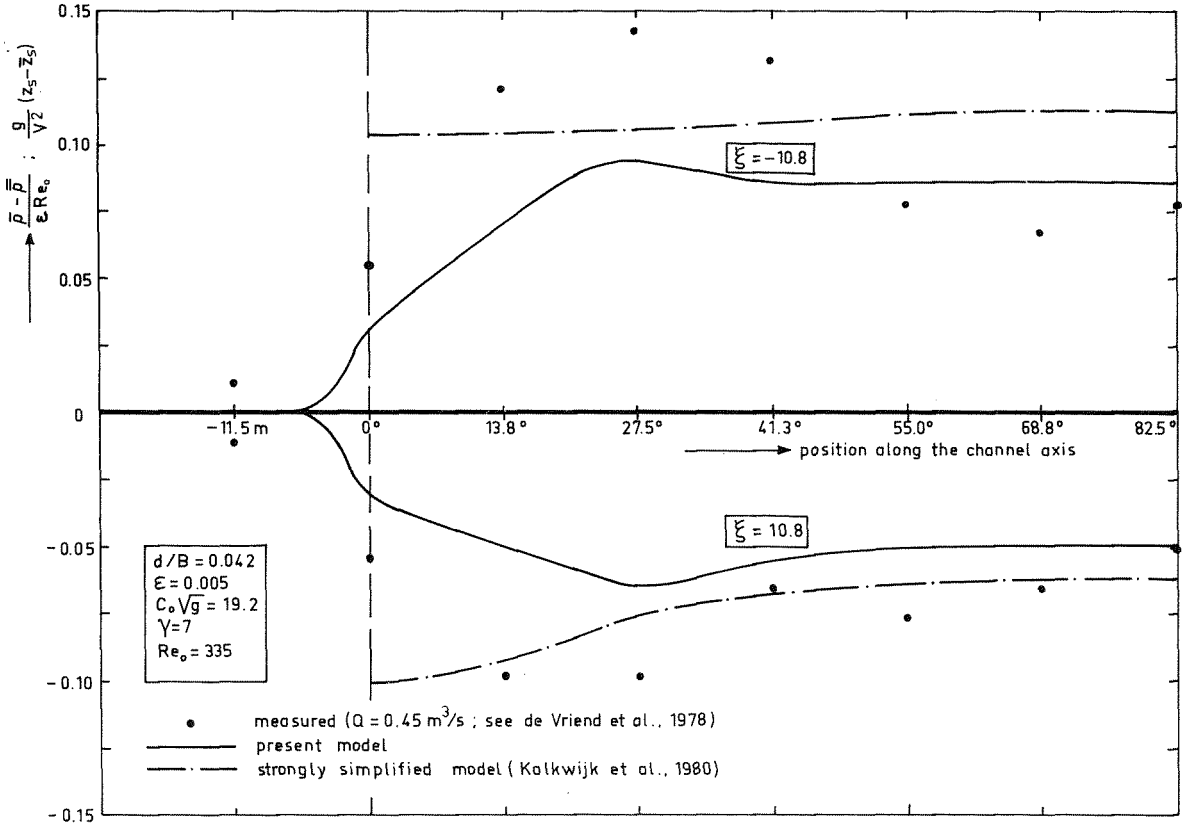

Figure 74. Simulation of the non-rectangular channel experiments in the DHL-flume: total pressure

(b) Transverse pressure drop

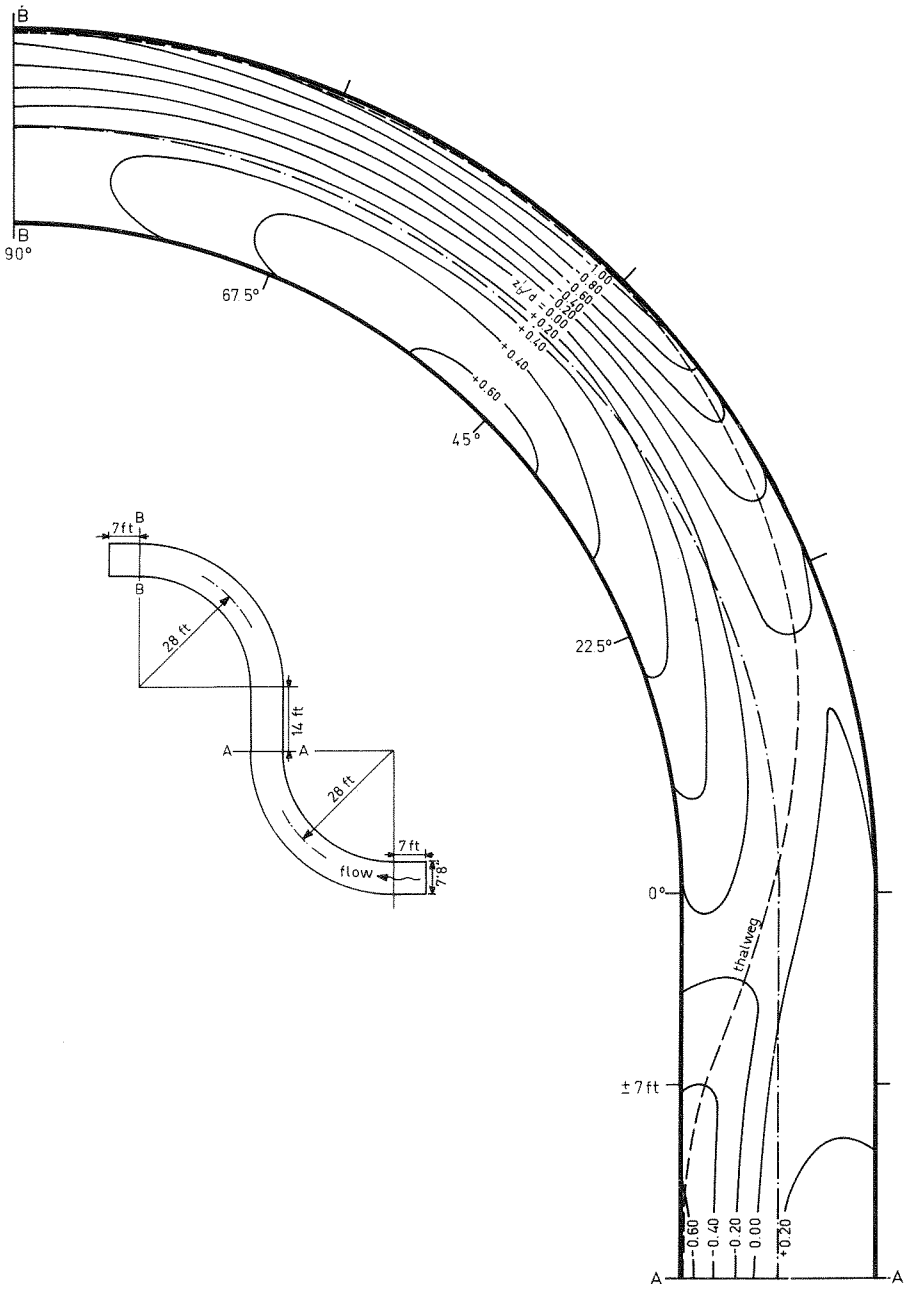

Figure 75. Simulation of the non-rectangular channel experiment in the IIHR-flume: channel configuration

(a) Bottom level contours

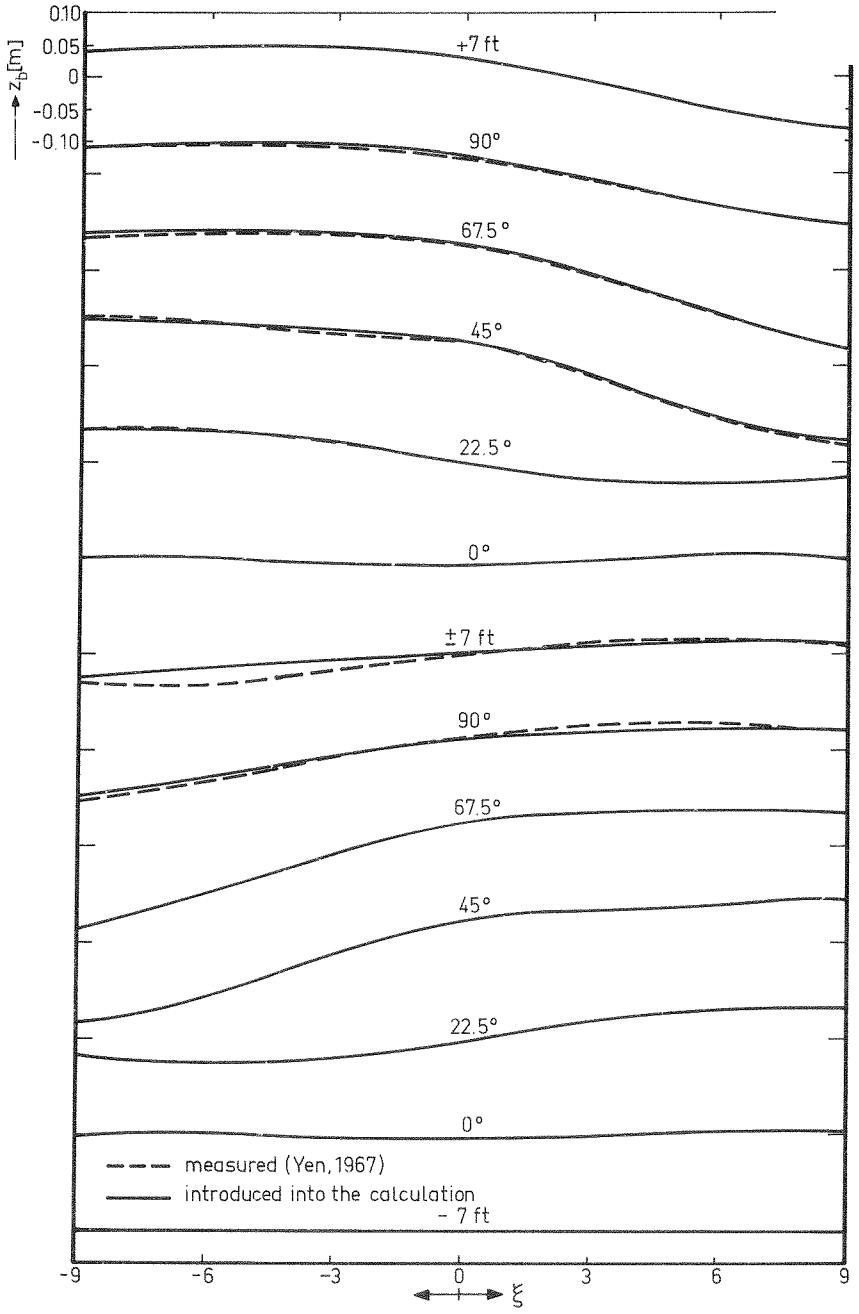

Figure 75. Simulation of the non-rectangular channel experiment in the IIHR-flume: channel configuration

(b) Transverse bottom profiles

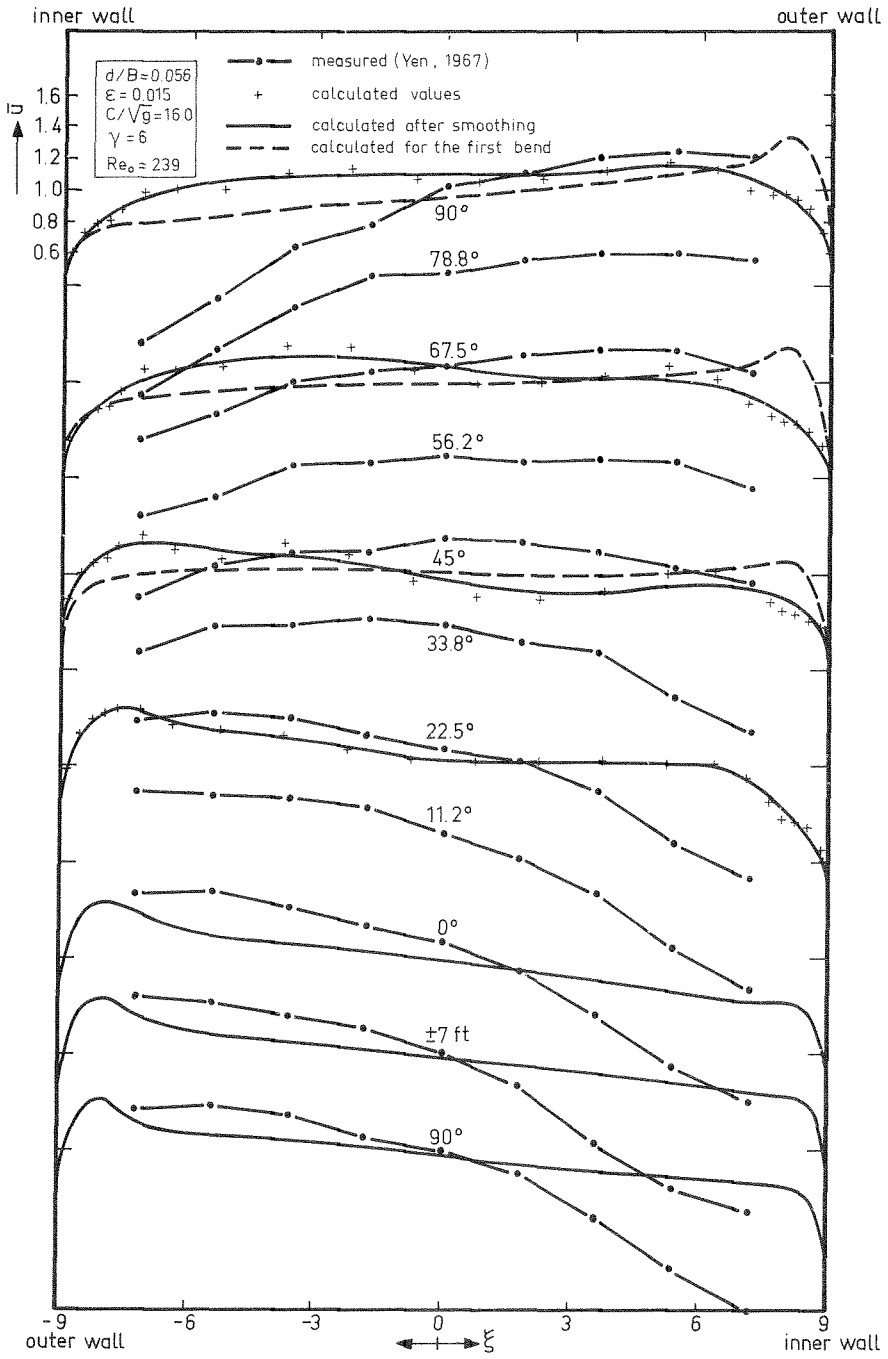

Figure 76. Simulation of the non-rectangular channel experiment in the IIHR-flume: depth-averaged main velocity distribution